

Lecture Notes in Mechanical Engineering

Puneet Verma

Olusegun D. Samuel

Tikendra Nath Verma

Gaurav Dwivedi *Editors*

# Advancement in Materials, Manufacturing and Energy Engineering, Vol. I

Select Proceedings of ICAMME 2021

 Springer


# Lecture Notes in Mechanical Engineering

## Series Editors

Francisco Cavas-Martínez, Departamento de Estructuras, Universidad Politécnica de Cartagena, Cartagena, Murcia, Spain

Fakher Chaari, National School of Engineers, University of Sfax, Sfax, Tunisia

Francesca di Mare, Institute of Energy Technology, Ruhr-Universität Bochum, Bochum, Nordrhein-Westfalen, Germany

Francesco Gherardini , Dipartimento di Ingegneria, Università di Modena e Reggio Emilia, Modena, Italy

Mohamed Haddar, National School of Engineers of Sfax (ENIS), Sfax, Tunisia

Vitalii Ivanov, Department of Manufacturing Engineering, Machines and Tools, Sumy State University, Sumy, Ukraine

Young W. Kwon, Department of Manufacturing Engineering and Aerospace Engineering, Graduate School of Engineering and Applied Science, Monterey, CA, USA

Justyna Trojanowska, Poznan University of Technology, Poznan, Poland

**Lecture Notes in Mechanical Engineering (LNME)** publishes the latest developments in Mechanical Engineering—quickly, informally and with high quality. Original research reported in proceedings and post-proceedings represents the core of LNME. Volumes published in LNME embrace all aspects, subfields and new challenges of mechanical engineering. Topics in the series include:

- Engineering Design
- Machinery and Machine Elements
- Mechanical Structures and Stress Analysis
- Automotive Engineering
- Engine Technology
- Aerospace Technology and Astronautics
- Nanotechnology and Microengineering
- Control, Robotics, Mechatronics
- MEMS
- Theoretical and Applied Mechanics
- Dynamical Systems, Control
- Fluid Mechanics
- Engineering Thermodynamics, Heat and Mass Transfer
- Manufacturing
- Precision Engineering, Instrumentation, Measurement
- Materials Engineering
- Tribology and Surface Technology

To submit a proposal or request further information, please contact the Springer Editor of your location:

**China:** Ms. Ella Zhang at [ella.zhang@springer.com](mailto:ella.zhang@springer.com)

**India:** Priya Vyas at [priya.vyas@springer.com](mailto:priya.vyas@springer.com)

**Rest of Asia, Australia, New Zealand:** Swati Meherishi  
at [swati.meherishi@springer.com](mailto:swati.meherishi@springer.com)

**All other countries:** Dr. Leontina Di Cecco at [Leontina.dicecco@springer.com](mailto:Leontina.dicecco@springer.com)

To submit a proposal for a monograph, please check our Springer Tracts in Mechanical Engineering at <https://link.springer.com/bookseries/11693> or contact [Leontina.dicecco@springer.com](mailto:Leontina.dicecco@springer.com)

**Indexed by SCOPUS. All books published in the series are submitted for consideration in Web of Science.**

More information about this series at <https://link.springer.com/bookseries/11236>

Puneet Verma · Olusegun D. Samuel ·  
Tikendra Nath Verma · Gaurav Dwivedi  
Editors

# Advancement in Materials, Manufacturing and Energy Engineering, Vol. I

Select Proceedings of ICAMME 2021

 Springer



*Editors*

Puneet Verma  
School of Earth and Atmospheric Science  
Queensland University of Technology  
Brisbane, QLD, Australia

Olusegun D. Samuel  
Department of Mechanical Engineering  
Federal University of Petroleum Resource  
Effurun, Nigeria

Tikendra Nath Verma  
Department of Mechanical Engineering  
Maulana Azad National Institute  
of Technology, Bhopal  
Bhopal, India

Gaurav Dwivedi  
Energy Centre  
Maulana Azad National Institute  
of Technology, Bhopal  
Bhopal, India

ISSN 2195-4356

ISSN 2195-4364 (electronic)

Lecture Notes in Mechanical Engineering

ISBN 978-981-16-5370-4

ISBN 978-981-16-5371-1 (eBook)

<https://doi.org/10.1007/978-981-16-5371-1>

© The Editor(s) (if applicable) and The Author(s), under exclusive license to Springer Nature Singapore Pte Ltd. 2022

This work is subject to copyright. All rights are solely and exclusively licensed by the Publisher, whether the whole or part of the material is concerned, specifically the rights of translation, reprinting, reuse of illustrations, recitation, broadcasting, reproduction on microfilms or in any other physical way, and transmission or information storage and retrieval, electronic adaptation, computer software, or by similar or dissimilar methodology now known or hereafter developed.

The use of general descriptive names, registered names, trademarks, service marks, etc. in this publication does not imply, even in the absence of a specific statement, that such names are exempt from the relevant protective laws and regulations and therefore free for general use.

The publisher, the authors and the editors are safe to assume that the advice and information in this book are believed to be true and accurate at the date of publication. Neither the publisher nor the authors or the editors give a warranty, expressed or implied, with respect to the material contained herein or for any errors or omissions that may have been made. The publisher remains neutral with regard to jurisdictional claims in published maps and institutional affiliations.

This Springer imprint is published by the registered company Springer Nature Singapore Pte Ltd. The registered company address is: 152 Beach Road, #21-01/04 Gateway East, Singapore 189721, Singapore

# Preface

This book presents a collection of research and review articles on different aspects of science and engineering of advance materials from the International Conference on Advancement in Materials, Manufacturing and Energy Engineering (ICAMME), which was organized by the Department of Materials and Metallurgical Engineering in association with Energy Centre and Department of Mechanical Engineering, Maulana Azad National Institute of Technology, Bhopal, Madhya Pradesh, India, from February 18 to 20, 2021. The conference aims to provide a platform for academicians, scientists, and researchers across the globe to share their scientific ideas and vision in the areas of materials and metallurgical engineering, energy-efficient systems, nanomaterials, composites, process metallurgy, extractive metallurgy, physical metallurgy, and mechanical behavior of materials, and other related fields of materials science. ICAMME-2021 played a key role in setting up a bridge between academician and industry. Due to the COVID-19 outbreak around the world, the meetings and gatherings were banned, besides strict immigration policy. Based on most authors' appeal and health considerations, after careful discussion, the conference committee changed this event to an online conference.

The conference presented more than 100 participants to interchange scientific ideas. During the three days of the conference, researchers from educational institutes and industries offered the most recent cutting-edge findings, went through several scientific brainstorming sessions, and exchanged ideas on practical socio-economic topics. This conference also provided an opportunity to establish a network for collaboration between academician and industry. The major emphasis was given on the recent developments and innovations in various fields of materials science and metallurgy technologies through plenary lectures. This book presents various chapters addressing the science and engineering of various advance materials and technologies in the form of mathematical- and computer-based methods and models for designing, analyzing, and measuring the characterization of material processing. The book brings together different aspects of engineering design and will be useful for researchers and professionals working in this field.

The editors would like to acknowledge all the participants who have contributed to this volume. We also deeply express our gratitude to the generous support provided by MANIT, Bhopal. The editors also thank the publishers and every staff and student volunteer of the departments and institute who has directly or indirectly assisted in accomplishing this goal. Finally, the editors would also like to express their gratitude to the Respected Director of MANIT, Dr. N. S. Raghuwanshi, for providing all kinds of support and blessings.

Despite sincere care, there might be typos and always a space for improvement. The editors would appreciate any suggestions from the reader for further improvements to this book.

Brisbane, Australia  
Effurun, Nigeria  
Bhopal, India  
Bhopal, India  
April 2021

Puneet Verma  
Olusegun D. Samuel  
Tikendra Nath Verma  
Gaurav Dwivedi

# Contents

<b>Computational Investigation of Chatter for Face Mill Tool on VMC Using Different Shim Material with Experimental Validation . . . . .</b>	<b>1</b>
N. B. Gandhi and D. H. Pandya	
<b>Multispectral Imaging for Identification of Water Stress and Chlorophyll Content in Paddy Field Using Vegetation Indices . . . . .</b>	<b>11</b>
S. Madhura and T. V. Smitha	
<b>Condition Monitoring of Used Engine Oil by FTIR Spectroscopy—A Review . . . . .</b>	<b>21</b>
Afreen Nissar, M. Hanief, and Fasil Qayoom Mir	
<b>Next-Generation Electrochemical Energy Conversion and Storage Based on Three-Dimensional Nanostructures with Improved Performance: Insights and Perspectives . . . . .</b>	<b>31</b>
Shubhadip Paul	
<b>Algae Biofuel as a Substitute for Compression Ignition Engine: A Review . . . . .</b>	<b>43</b>
S. Charan Kumar, Amit Kumar Thakur, and J. Ronald Aseer	
<b>Economic Growth in Maharashtra and India with Particular Reference to Electricity Consumption . . . . .</b>	<b>53</b>
Anand Vijay Satpute and E. Vijay Kumar	
<b>Analysis of Centrifugal Pump Impeller Guide Vane by Using CFD Technique with Different Materials . . . . .</b>	<b>63</b>
Seshaiah Turaka, P. Chiranjeevi, K. Vijaya Kumar Reddy, and Satishkumar	
<b>Study of Kinematic Chains of Group IV-D, E, and F: Part-Distinct Mechanisms . . . . .</b>	<b>75</b>
Ali Hasan	

<b>Intermittency Reduction Techniques in Hybrid Renewable Energy Systems: A Review</b> . . . . .	85
Neil Singh, Krish Patel, Krishi Patel, Siddhi Vinayak Pandey, Pankaj Singh, Anoop Kumar Shukla, and Gaurav Dwivedi	
<b>Multi-objective Optimization of Cutting Parameters in Turning Process for Minimization of Carbon Emission and Processing Time</b> . . .	93
Gunjan Agarwal, M. K. Khare, Ankit Kumar Singhal, and Ravi Prakash	
<b>Numerical Heat Transfer Analysis of a Rectangular Microchannel Heat Sink with Graphene-based Nanofluids</b> . . . . .	107
Sasmita Bal and Koustav Bandyopadhyay	
<b>Study on Design and Performance Specifications of the Prosthetic Hands</b> . . . . .	119
Mohd Azeem and Aasiya Parveen	
<b>A Multi-stage Evolutionary Tomographic Reconstruction Algorithm Using Ultrasound Time-of-Flight Projections</b> . . . . .	137
Shyam Prasad Kodali and Boggarapu Nageswara Rao	
<b>Recent Trends on Furnace Design and Stirrer Blade Geometry Used in Stir Caster: A Focused Review</b> . . . . .	147
Ashish Kumar Singh, Sanjay Soni, and R. S. Rana	
<b>Design Consideration for e-Rikshaw with Regeneration Capability</b> . . . .	161
Manoj Kumar and Amit Ojha	
<b>Liquid-Phase Exfoliation of 2D-MoS<sub>2</sub> Nanostructures at Varying Sonication Times and Their Subsequent Analysis</b> . . . . .	177
Mariam Gada, Mohammad Zaid, Mohd. Mudassir Husain, and S. S. Islam	
<b>Grid Synchronization Techniques: A Review</b> . . . . .	187
Pragya Gawhade and Amit Ojha	
<b>Removing Error and Estimating an Accurate Finite Element Model of Graphite-Epoxy Composite Laminate Structure Using Direct Updating Method</b> . . . . .	197
Abhishek Sharma, Dinesh Kumar Shukla, Ashok Kumar Bagha, Shashi Bahl, and Devaki Nandan	
<b>Human-Powered Flywheel Motor (HPFM): A Review</b> . . . . .	209
H. K. Baitule, P. B. Maheshwary, and J. P. Modak	
<b>Finite Element Analysis-Based Geometry Optimization of a Disk Brake</b> . . . . .	225
Faraz Ahmad, Vishvajet, Viveksheel Yadav, and Shalini Chauhan	
<b>Modeling and Simulation of Electrical Discharge Machining—A Review</b> . . . . .	241
Abhishek Verma and Sudhanshu Kumar	

<b>Structural, Optical and Magnetic Properties of Cobalt Ferrite Nanomaterials, Synthesized by a Green Technological Approach Using Lemon Juice</b> . . . . .	249
Shashank Bhushan Das, Vivek Kumar, Rakesh Kumar Singh, Nishant Kumar, Harendra Kumar Satyapal, and Atul Jyoti	
<b>Automation in Inventory Management in MSME (Micro, Small, Medium Enterprises) Warehouse by Use of Robots</b> . . . . .	263
Meet Savla, Amar Pandhare, Shubham Gulunjkar, Pranav Pandit, and Prathamesh Dhawale	
<b>A Review of the Mechanical Properties and Erosion Behavior of HVOF Sprayed Nanocomposite Coatings</b> . . . . .	277
Rajinder Kumar, Deepak Bhandari, and Khushdeep Goyal	
<b>Kitchen Waste Utilization Using Biogas Plant—Need of the Hour</b> . . . . .	289
Bhamre Hrishikesh, Shimpi Abhishek, and Gadhe Prakash	
<b>Biosensor Based on One-Dimensional Photonic Crystal for Poliovirus Detection</b> . . . . .	303
Sapna Dinodiya and Anami Bhargava	
<b>Assessment of Local River Sand Mould Property at Different Curing Temperatures</b> . . . . .	311
Jatin Sadarang, Ramesh Kumar Nayak, and Isham Panigrahi	
<b>Microstructure and Interfacial Characterization Near Grain Boundary of Al<sub>2</sub>O<sub>3</sub>/SiC Reinforced AA 6061 Semi-solid Squeeze Cast Composite</b> . . . . .	319
Nitin Srivastava and Mohd Anas	
<b>Utilization of Stone-dust in Sand Mould Casting Process</b> . . . . .	331
Jatin Sadarang, Ramesh Kumar Nayak, and Isham Panigrahi	
<b>Effect of Fe-Cr Mold Temperature on Mold Hardness, Compressive and Shear Strength</b> . . . . .	339
Jatin Sadarang, Ramesh Kumar Nayak, and Isham Panigrahi	
<b>A Comprehensive Study on Electrical and Electronic Waste Management</b> . . . . .	347
V. Iswarya and T. Yuvaraj	
<b>Investigating the Effect of Annealing Temperature on Structural, Luminescence, and Magnetic Properties of Nickel and Zinc Aluminate</b> . . . . .	357
Sampurnanand, Nishant Kumar, Rakesh Kumar Singh, Atul Jyoti, and Vikash Kumar	

<b>Review of Battery Technologies Available for Promoting Electric Mobility in Urban India</b> . . . . .	367
Rahul Tiwari, Umang Patel, and Atmagya Raj	
<b>Application of Combined Compromise Solution Method for Material Selection</b> . . . . .	379
Farheen Jahan, Manoj Soni, Aasiya Parveen, and Mohammad Waseem	
<b>Analysis of Performance and Emission Parameters in Direct Injection Diesel Engine by Using Biodiesel Blended with Additives</b> . . . . .	389
Mamuni Arya, Akshaya Kumar Rout, and Samiran Samanta	
<b>Femur Bone Implant Plate Design Analysis Under Varying Fracture Conditions</b> . . . . .	403
Nilesh Tipan, Ajay Pandey, and Girish Chandra	
<b>Study of Electrical and Mechanical Parameters of Electromagnetic Railgun</b> . . . . .	423
Shreyas Maitreya, Ritwik Mishra, Ayush Vatsa, and Amit Ojha	
<b>Performance Analysis of Optimal Designed Photovoltaic/Diesel Generator-Based Hybrid Energy System Coupled to Utility Grid</b> . . . . .	435
Anurag Chauhan, Ashish Srivastava, Mohd Tauseef Khan, Altaf Alam, and Subho Upadhyay	
<b>Effective Control of Response of a Reinforced Concrete Building Under Seismic Loads Using Tuned Liquid Damper</b> . . . . .	449
Mukul Srivastava, Shailja Bawa, and Ujjwal Sharma	
<b>A Review on Tribo-Mechanical Behaviour and Corrosion Performance of AA8000 Based Composites</b> . . . . .	465
Rajesh Sharma, Mohan K. Pradhan, and Pankaj Jain	
<b>Plasma Processing of Carbon Dioxide</b> . . . . .	475
Kali Charan Sabat, Archana Singh, and Satyabrata Das	
<b>Metal-Inorganic Nickel Complexes-Derived Nanostructured Nickel Oxide as an Efficient Water Oxidation Catalyst</b> . . . . .	485
Kamlesh, Deepika Tawar, Kali Charan Sabat, and Archana Singh	
<b>Synthesis and Morphological Study of Ethylene Diamine-Based Nickel Oxide Flower-Like Nanostructure</b> . . . . .	493
Deepika Tawar, Kamlesh Goyre, Diksha Choudhary, Kali Charan Sabat, and Archana Singh	
<b>Automated Real-Time Transformer Health Monitoring System Using the Internet of Things (IoT)</b> . . . . .	503
P. Venkat Subramanian, Venkatesh Boddapati, and S. Arul Daniel	

**A Comprehensive Study on Adaptive MPPT Control Techniques for Efficient Power Generation** . . . . . 513  
 Pushpendra Dangi, Amit Ojha, Shiv Pratap Singh, Suresh Kr. Gawre, Sangharsh Meshram, and Arvind Mittal

**Preliminary Design and Flow Analysis of Domestic Chimney for Water Boiling Using Finite Volume Analysis** . . . . . 525  
 Faraz Ahmad, Shubham Pal, Viveksheel Yadav, and Vimlesh Bijalwan

**Revivification of Spent Lubricating Oil by Ecofriendly Extraction Flocculation Method** . . . . . 535  
 Sayantan Sarkar, Deepshikha Datta, K. S. Deepak, and Bimal Das

**Effect of Sintering Temperature on the Microstructure and Properties of the Copper Synthesized by Powder Metallurgy Route** . . . . . 549  
 Manish Dixit and Rajeev Srivastava

**Assessment of the Chambal River Quality at Kota Metropolis Through the Drinking Water Quality Index and Irrigation Water Quality Index** . . . . . 559  
 Kuldeep, Sohil Sisodiya, and Anil K. Mathur

**Virtual Plan of the Domestic Enlistment Warming Framework to Reproduce Electromagnetic Boundaries** . . . . . 575  
 V. Geetha, M. Pushpavalli, P. Abirami, P. Sivagami, and R. Harikrishnan

**Assessment of Urban Air Quality for Jodhpur City by the Air Quality Index (AQI) and Exceedance Factor (EF)** . . . . . 585  
 Kuldeep, Sohil Sisodiya, Anil K. Mathur, and Puneet Verma



## About the Editors

**Dr. Puneet Verma** has worked on wide areas of biodiesel, environmental science, air quality, and diesel particulate matter. He has completed his bachelor's degree in mechanical engineering from Punjab Technical University and M.Tech. from IIT Roorkee under the umbrella of MHRD fellowship, India. He was awarded QUTPRA Scholarship for his Ph.D. in environmental engineering, Queensland University of Technology (QUT), Australia. Currently, he is working as Air Quality Scientist, ASK Consulting Engineers, Brisbane, Australia, where he has delivered multiple projects of emission, odor, noise, and dust monitoring at industrial and construction sites. He has also worked as Quality Control Chemist and HSE Specialist, Intertek Testing Services, Australia, and Environmental Research Intern, Puma Energy, Australia. He has published more than 33 research articles in international journals and conferences. He is Member of Clean Air Society of Australia and New Zealand, The American Association for Aerosol Research and Professional Mechanical Engineer (Engineers Australia).

**Dr. Olusegun D. Samuel** is Full-Time Lecturer and Research Fellow in the Department of Mechanical Engineering, Federal University of Petroleum Resources, Effurun, Delta State, Nigeria. He does research in the process intensification of biofuel production, upgrading of pyrolytic bio-oil and its efficacy of soft computing in its modelling, techno-economic analysis, and general mechanical engineering. He has trained many students in areas of production, renewable energy, tribology, diesel engine performance and emission parameter optimization techniques, degradation of elastomers in alternate fuel, corrosion of automotive parts in biodiesel-based fuel, biogas, residual stress, energy conversion, renewable energy, and thermo-fluids. Their current project is entitled "CFD studies and exergetic analysis of mechanical systems, and techno-economic and sustainability assessments of various combustion-related energy technologies." He has published more than 70 papers in reputed journals and two chapters in Nova Science Publishers and one in Intech Open. He has widely participated at national and international seminars as keynote and invited speakers and as an external examiner

of Ph.D./M.Sc. thesis. He serves as Reviewer to Elsevier (*Energy, Journal of Cleaner Production, Fuel*, etc.) and Taylor and Francis. He is the editorial board member of reputed journals published by Springer and other SCI indexed Journals.

**Dr. Tikendra Nath Verma** received his Bachelor of Engineering (B.E.) degree in mechanical engineering with securing first division from Pt. R.S.U. Raipur (C.G.) in 2006. He did his master's degree in thermal engineering in 2009 from the Department of Mechanical Engineering, Maulana Azad National Institute of Technology Bhopal (M.P.). He has obtained his Ph.D. degree from National Institute of Technology, Raipur (Chhattisgarh). He joined National Institute of Technology Manipur as Assistant Professor in September 2015. Presently, he is working as Assistant Professor (Grade—I) in the Department of Mechanical Engineering, Maulana Azad National Institute of Technology Bhopal. His areas of interest include computational fluid dynamics, heat and mass transfer, renewable energy, and alternative fuels in internal combustion engines. He has published more than 65 papers in SCI and Scopus indexed journals. He has published ten chapters with reputed publishers. He also serves as a potential reviewer for various journals such as *Energy, Energy Conversion and Management, Applied Energy, Fuel, Journal of Cleaner Production, Journal of Building Engineering, Waste Management, Journal of Hazardous Material*, etc. (Elsevier); *Journal of Thermal Analysis and Calorimetry* (Springer), *International Journal of Ambient Energy* (Springer); and *Journal of Thermal Engineering* (Begell House Journals).

**Dr. Gaurav Dwivedi** has completed his B.Tech. in mechanical engineering from IKGPTU Jalandhar, M.Tech. in energy systems from IIT Roorkee, and Ph.D. in the field of renewable energy (biofuel) from IIT Roorkee, India. He has 8 years of teaching experience in the field of mechanical and energy engineering and taught various subjects like IC engine, thermodynamics, fluid machinery, bioenergy, and others at various institutes like VIT University Vellore and Amity University Noida. Currently, he is working as Assistant Professor in the Energy Centre at Maulana Azad National Institute of Technology Bhopal, India. His area of interest is biodiesel production methodology, enhancement in fuel properties, and application of biofuel on engine operation. He has published more than 85 papers in various international journals and conferences. He has published more than 50 papers in SCI and Scopus indexed journals. He has published one book with International Publisher; along with that, he has contributed five chapters. He got Young Scientist Award at NIT Trichy for his contribution in the field of renewable energy. He is Active Member of Institution of Engineers (India) and Solar Energy Society of India and IEEE. He also served as Guest Editor for *Materials Today Proceedings* and *Journal of Traffic and Transportation*.

# Computational Investigation of Chatter for Face Mill Tool on VMC Using Different Shim Material with Experimental Validation



N. B. Gandhi and D. H. Pandya

## 1 Introduction

During machining, noise and chatter is a major problem in VMC (vertical milling centre) at high-speed operation. Today precision and accuracy with high-speed machining is very essential to cut cost and increase productivity. The chatter is one of the major hurdles in achieving the automation of machining operations such as milling, drilling, boring and turning [1, 2]. The chatter in machining create problems like poorer surface finish, excess amount of noise, reduction in tool life and in worst case breakdown of the tool components, which reduce productivity [3–6].

These chatter are present due to an absence of dynamic rigidity of the machine tool structure including required cutting attachments on machine. Successful machining operations depend upon the active connection between the workpiece and cutting tool. Under certain circumstances, the motion of the tool against the work can produce a chatter, subsequent in great amplitude of pulsations. This chatter adversely disturbs the feature of the cut, the tool life and sound.

Rogov [1] inspected the excellence of machined apparent and the efficiency of turning using shim with high restraining properties in the fasten of insert. Five shims made of ceramic, epoxy granite, sandstone, granite and chlorite schist are planned. Computational and experimental examination are delivered to study the stress–strain in the fasten set structure of insert. Stationary and active features of cutting tool with shim made of dissimilar materials are studied. Liu et al. [2] highlight on learning limiting coating checking tool receptacle for chatter and its steadiness development in turning action. Author has been examined four dissimilar types of viscoelastic resources and decided that (Polyurethane rubber) was the utmost appropriate viscoelastic material for collective restraining ratio. Tarneg et al. [7] offered a system of escalating the piezoelectric actuator on a cutting tool and does as a damper with tuning to reduction the vibration in turning. In which, the N.

---

N. B. Gandhi (✉) · D. H. Pandya  
Mechanical Department, KSV University, Gandhinagar, Gujarat, India

F of the cutting tool must be equal to the N.F of the damper. Additionally, a superior amount of DR is mandatory for damper. Cardi et al. [8] examined a technique of self-excited chatter lessening for yielding workpiece material.

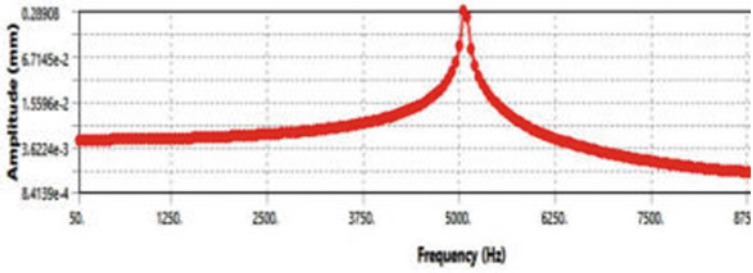
Our goal is to reduce chatter and to improve surface finish in VMC—vertical milling centre this kind of computational and experimental work is not found in literature review and industry. The chatter can be reduced by using shim which provides damping in face milling. High-speed cutting of hard material creates pressure on the insert. So we need to develop shim which acts as a shock absorber for the insert and workpiece. Planned shim should protect both insert and tool holder from damage due to high cutting forces. In this research work, the Carbide shim, SS—Stainless Steel shim and conventional face mill tool are analysed to find out possible method to reduce vibration. Finite element analysis (FEA) is done for finding the damping ratio for different shim material using ANSYS software and followed by experiment for validation. This research paper includes computational and experimental investigation of face mill tool using SS—Stainless Steel and Carbide shims and conventional face mill tool.

## 2 Computational Analysis of Face Mill Tool

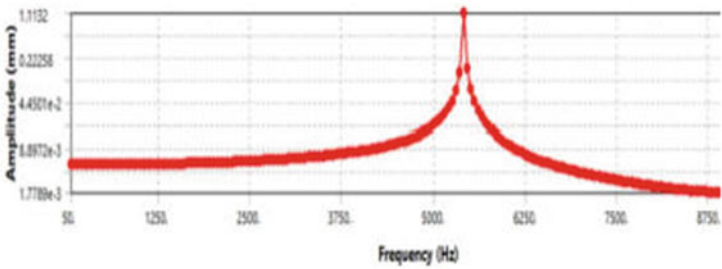
The computational analysis is done with modal analysis followed by harmonic analysis of face mill tool using SS—Stainless Steel shim, Carbide shims and Without shim face mill tool [9–15]. Computational analysis (FEA) is carried out by using the ANSYS work bench 14.1 and calculated damping ratio using SS—Stainless Steel shim, Carbide shims and Without shim face mill tool. The purpose of ANSYS 14.1 modal analysis is to investigate the dynamic characteristics of free vibration of face mill. By this modal analysis, we can find out efficient frequency and inefficient frequency. The assembly model of face mill tool consists of tool holder, insert, shim and bolt which developed with the use of creo2.0 is exported to ANSYS to perform the modal analysis and harmonic analysis. The frequency response curve generated by harmonic analysis by using ANSYS as follow Fig. 1a–c for Carbide shim, SS—Stainless Steel shim and Without shim face mill tool.

## 3 Findings of Computational Analysis

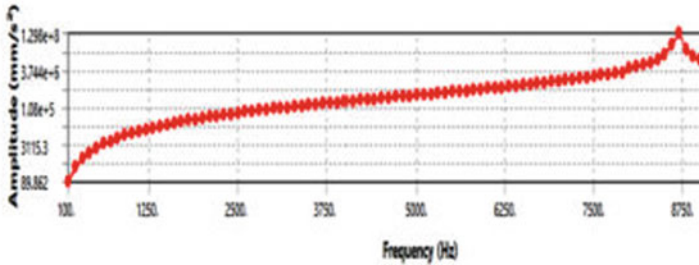
Damping ratio of SS—Stainless Steel shim, Carbide shim and Without shim face mill tool is found out by half power bandwidth method which is given in Table 1. The frequency response curve derived for Carbide shim—Fig. 1a, SS—Stainless Steel shim—Fig. 1b and Without shim face mill tool—Fig. 1c is used to calculate the damping ratio.



(a) With Carbide shim



(b) With SS-Stainless Steel shim



(c) Without shim face mill

**Fig. 1** Frequency response plot

**Table 1** Damping ratio for different shim material

Shim	Natural frequency Fr (Hz)	Max amplitude (mm)	Half power point	$F_1$ (Hz)	$F_2$ (Hz)	Damping ratio
Carbide	6392.2	1.21E-02	8.55E-03	6356.812	6437.238	0.0063
SS—Stainless Steel	6961.3	8.66E-03	6.14E-03	6913.755	6983.120	0.0049
Without shim	8700.3	1.298E+08	9.17E+7	8655.81	8756.435	0.0057

Above Table 1 gives following conclusion from the computational analysis—harmonic analysis. Finite element analysis shows that the damping ratio is changing with changing shim materials. As per the above Table 1, Carbide has the highest value for damping ratio followed by Without shim face mill and SS—Stainless Steel shim. SS—Stainless Steel shim has the lowest value for damping ratio followed by Without shim face mill and Carbide shim.

## 4 Experimental Analysis

After computational analysis, experiment is carried out on VMC—vertical milling centre milling machine with CoCo 80 dynamic signal analyser and surface roughness tester ( $200\text{--}150\ \mu\text{m}$ ) to validate computational analysis. This set-up used for the collection of vibration signals is as shown in Fig. 2a. Vibration signals are taken with use of Try axial sensor attached to VMC—vertical milling centre tool holder. Analyser gives the displacement–time, velocity–time, acceleration–time and frequency–amplitude relations in reference to each other which help to plot motion study graphs. The experiments were carried out on the CVM 640 (VMC—vertical milling centre) milling machine with two face milling tool, first is special purpose Kyocera make face milling tool  $\text{\O} 63\ \text{mm}$  with 5 inserts cutting tool and second is Kyocera make face milling tool  $\text{\O} 63\ \text{mm}$  with 5 inserts and with shim as shown in Fig. 2b, and workpiece plate of  $75 * 25 * 300\ \text{mm}$  of 2062 mild steel 130 BH work material was used for the experiments. The machining was done using TNMG 120412 (Carbide) insert. The experiments were conducted at three cutting speeds (250, 200, 150 m/min), three feed per tooth (0.15, 0.1, 0.05 mm/tooth), three depth of cut (1.2, 1.0, 0.8 mm) and four shim materials (SS—Stainless Steel, Carbide and Without shim face mill) are taken for experiments.

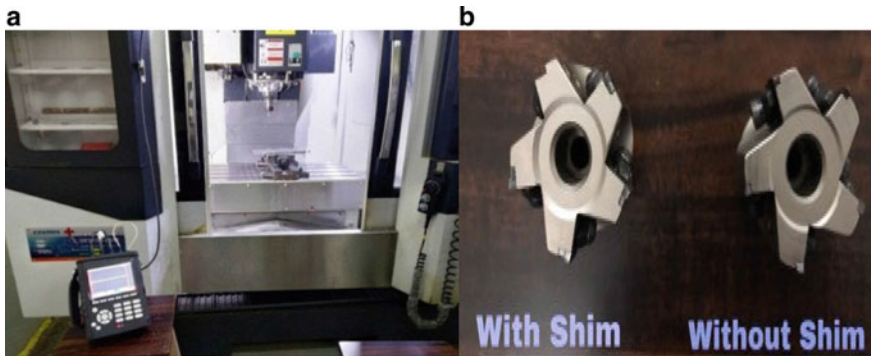


**Fig. 2** a CVM milling machine with CoCo 80 dynamic signal analyser with try axial sensor  
b face milling tool 63 mm dia. with shim and Without shim face mill

The displacement data collected using CoCo 80 dynamic analyser. EDM software is used to plot displacement data. MATLAB is used to generate the fast Fourier transformation (FFT) graphs to find the behaviour of face mill tool. From FFT graphs, we found that rotational frequency, chatter frequency and three types of responses for face mill tool behaviour are as sub-harmonic and super harmonic as shown in Fig. 3.

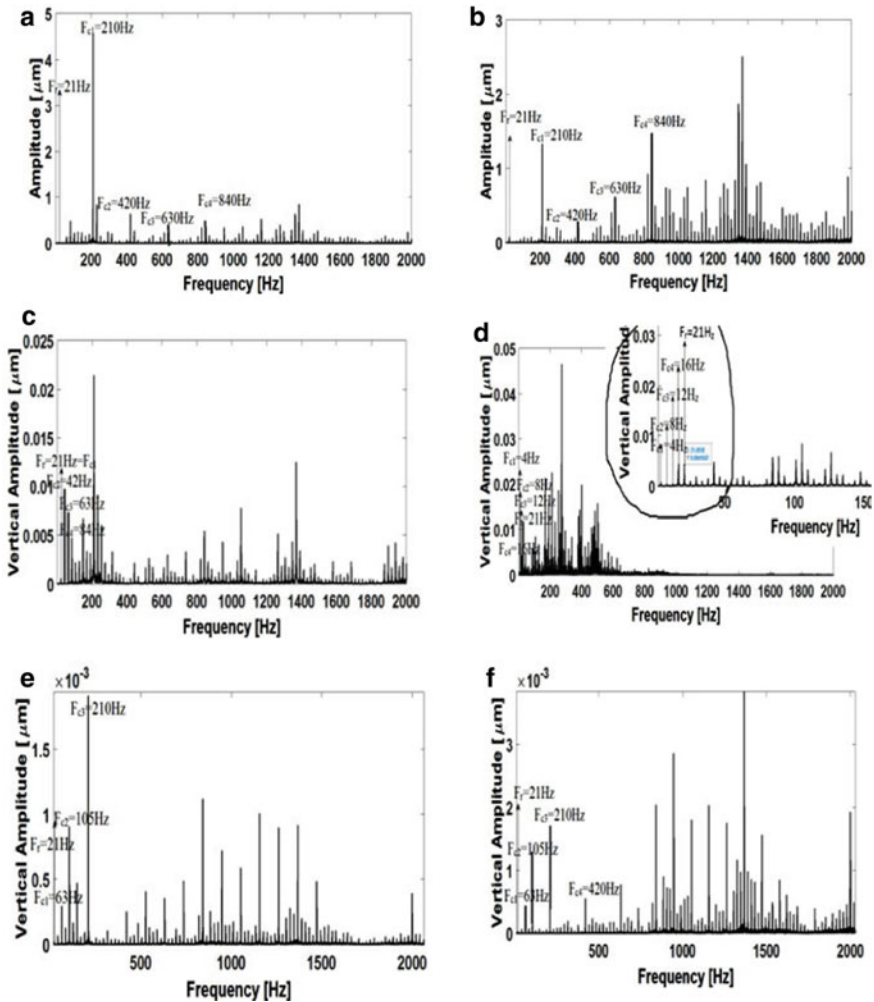


**Fig. 3** a Experimental FFT responses in X-direction—longitudinal. b Experimental FFT responses in Y-direction—cross feed for carbide shim with cutting speed 250 m/min, depth of cut 0.8 mm and feed 0.05 mm/tooth. c Experimental FFT responses in X-direction—longitudinal. d Experimental FFT responses in Y-direction—cross feed for SS—Stainless Steel shim with cutting speed 250 m/min, depth of cut 0.8 mm and feed 0.05 mm/tooth. e Experimental FFT responses in X-direction—longitudinal. f Experimental FFT responses in Y-direction—cross feed for Without shim with cutting speed 250 m/min, depth of cut 0.8 mm and feed 0.05 mm/tooth

## 5 Data Collection of Vibration and Dynamic Motion Behaviour Analysis

### 5.1 Data Collection

Data collection is the process of converting the vibration signals of physical components (CoCo 80 dynamic signal analyser) into the numerical data which can be precisely studied and analyzed. To find out chatter, vibration signals are taken with double cut, with different cutting condition and with different shim. TDR (Time Displacement Response) and FFT (Fast Fourier Transformation) graphs were generated with the help of EDM and MATLAB software. Rotational frequency, chatter frequency and dynamic motion behaviour for above conditions have been studied and analysed by using TDR and FFT graphs.

### 5.2 Dynamic Motion Behaviour Analysis

To find dynamic motion behaviour, different combination of depth of cut, feed and cutting speed for Without shim face mill and with shim face mill (Carbide shim and SS—Stainless Steel shim) are used, and experiments has been carried out and obtained time domain graphs and FFT graphs. Time-varying signal is given as input to FFT spectrum analyser; FFT computes the magnitude of its sine and cosine components and displays the spectrum of these frequency components. These FFT graphs are amplitude versus frequency (Hz). This graph consists of  $X$ -longitudinal feed direction and  $Y$ -cross feed direction. Thus, motion analysis is done with the help of time domain graphs, FFT graphs to analyse the dynamic motion behaviour and to find out rotational frequency and chatter frequency. The two types of pattern of FFT responses which are discussed for face mill tool behaviour are sub-harmonic and super harmonic. Figure 3a–f shows the different FFT graphs for carbide shim, SS—Stainless Steel shim and Without shim face mill tool with cutting speed 250 m/min, depth of cut 0.8 mm and feed 0.05 mm/tooth.

## 6 Result and Findings of Experimental Analysis

In this paper, the face mill tool behaviour is observed for different machining conditions that are given in Table 2. The result of FFT graphs shows that pattern of FFT responses of face mill tool is as sub-harmonic and super harmonic. Table 2 shows  $X$ -longitudinal feed and  $Y$ -cross feed of FFT graphs frequency in Hz.

From Table 2, it clearly shows that Carbide shim face mill tool has highest  $F_c$ —chatter frequency than Without shim face mill and SS—Stainless Steel shim face mill in all cutting condition, followed by Without shim face mill and SS—Stainless



**Table 2** Face mill chatter frequency ( $F_c$ ), rotational frequency ( $F_r$ ) and pattern of FFT responses

Sr. no	Cutting speed (m/min), DOC (mm), feed (mm/tooth)	Shim material	Rotational frequency $F_r$ (Hz)	Chatter frequency $F_c$ (Hz)		Pattern of FFT responses
				X	Y	
1	250/0.8/0.05	Carbide shim	21	210	210	Super harmonic
2		SS—Stainless Steel shim	21	21	4	Sub-harmonic
3		Without shim	21	63	63	Super harmonic
4	200/1/0.05	Carbide shim	17	169	169	Super harmonic
5		SS—Stainless Steel shim	17	17	17	Sub-harmonic
6		Without shim	17	84	51	Super harmonic
7	150/1/0.05	Carbide shim	13	63	63	Super harmonic
8		SS—Stainless Steel shim	13	13	13	Sub-harmonic
9		Without shim	13	51	25	Super harmonic

Steel shim face mill. Table 2 also shows that  $F_c$ —chatter frequency is higher than  $F_r$ —rotational frequency in case of Carbide shim and Without shim face mill tool, but in case of SS—Stainless Steel shim,  $F_c \leq F_r$  (chatter frequency is equal to or less than rotational frequency) in all cutting condition. Further carbide shim  $F_c$ —chatter frequency is higher by 5–10 times than  $F_r$ —rotational frequency. In case of Without shim face mill,  $F_c$ —chatter frequency is higher by 2–3 times than  $F_r$ —rotational frequency. But in case of SS—Stainless Steel shim,  $F_c$ —chatter frequency is equal to or less than  $F_r$ —rotational frequency.

If we apply  $F_c$  (self-excited vibration)  $\leq F_r$  (Forced excited vibration), in case of SS—Stainless Steel shim face mill, then moderate chatter would be generated. In case of Carbide shim,  $F_c$  is ten times higher than  $F_r$ , and in case of Without shim face mill,  $F_c$  is three times higher than  $F_r$  at higher cutting speed [(250m/min) and (200m/min)]. In case of Carbide shim,  $F_c$  is five times higher than  $F_r$ , and in Without shim face mill,  $F_c$  is two times higher than  $F_r$  at lower speed (150m/min). But in case of SS—Stainless Steel shim,  $F_c \leq F_r$  (chatter frequency is equal to or less than rotational frequency), and then, minimum chatter would be generated. Pattern of FFT responses shows as sub-harmonic and super harmonic.

## 7 Conclusions

Following conclusion is derived after computational simulation and experimental validation of the face mill tool using different shim material and different cutting conditions as described above in Tables 1 and 2. Following conclusions are given on basis of computational data and experimental work. Observation of this research can be used to reduce the chatter in VMC—vertical milling centre by using face mill tool.

- Carbide shim has the highest damping ratio followed by Without shim face mill and SS—Stainless Steel shim. Carbide shim gives maximum vibrations compare to Without shim face mill and SS—Stainless Steel shim in all cutting conditions, followed by Without shim face mill and SS—Stainless Steel shim face mill. So carbide shim is not useful for reducing chatter at high-speed VMC—vertical milling centre.
- Without shim face mill damping ratio is lower than carbide shim and higher than SS—Stainless Steel shim. Without shim face mill,  $F_c$  is lower than carbide shim and higher than SS—Stainless Steel shim in all cutting condition as verified by dynamic motion behaviour. Without shim face mill gives higher vibrations compare to SS—Stainless Steel shim and lesser than carbide shim in all cutting condition. This is current scenario of VMC—vertical milling centre operation of face mill.
- SS—Stainless Steel shim has the lowest damping ratio, and SS—Stainless Steel shim has  $F_c \leq F_r$  (chatter frequency is equal to or less than rotational frequency), in all cutting condition, so it is concluded that SS—Stainless Steel shim face mill is most desirable as it generates least chatter in comparison with Without shim and Carbide shim face mill tool. So SS—Stainless Steel shim can be justified for face mill to reduce chatter.

**Acknowledgements** Authors would like to acknowledge the support received by Green KSV Skill Development Centre, LDRP-ITR campus, Gandhinagar, GUJARAT

## References

1. Rogov VA (2017) Improvement of cutting tool performance during machining process by using different shim. Arch Civil Mech Eng 17(2017):694–671
2. Liu Y, Liu Z, Song Q, Wang B (2019) Analysis and implementation of chatter frequency dependent constrained layer damping tool holder for stability improvement in turning process. J Mater Process Technol 266:687–695
3. Mevada CJ, Trivedi HM, Darji AA, Pandya DH. Experimental investigation of chatter in CNC turning using different shim materials. In: Gupta VK, Varde PV, Kankar PK, Joshi N (eds) Reliability and risk assessment in engineering. Lecture notes in mechanical engineering. Springer Singapore, Singapore, pp 253–259. [https://doi.org/10.1007/978-981-15-3746-2\\_23](https://doi.org/10.1007/978-981-15-3746-2_23)
4. Shrivastava MA, Patel MV, Pandya DH (2017) Experimental study and analysis for chatter of face milling tool. 5(4):5
5. Wang P, Davies P, Starkey JM, Routson RL (1992) A torsional vibration measurement system. IEEE Trans Instrum Measur 41(6):5
6. Antoniou S, Pinho R (2004) Advantages and limitations of adaptive and non-adaptive force-based pushover procedures. J Earthquake Eng 8(4):497–522. <https://doi.org/10.1080/13632460409350498>
7. Tarnag YS, Kao JY, Lee EC (2000) Chatter suppression in turning operations with a tuned vibration absorber. J Mater Process Technol 105(1–2):55–60
8. Cardi AA, Firpi HA, Bement MT, Liang SY (2008) Workpiece dynamic analysis and prediction during chatter of turning process. Mech Syst Signal Process 22(6):1481–1494
9. Moon FC. An introduction for applied scientists and engineers. 6

10. Nobukawa S, Nishimura H, Yamanishi T, Liu J-Q (2015) Analysis of chaotic resonance in Izhikevich neuron model. Cymbalyuk G (ed) PLoS ONE 10(9):e0138919. <https://doi.org/10.1371/journal.pone.0138919>
11. Wen G, Yin S, Xu H, Zhang S, Lv Z (2016) Analysis of grazing bifurcation from periodic motion to quasi-periodic motion in impact-damper systems. *Chaos, Solitons Fractals* 83:112–118. <https://doi.org/10.1016/j.chaos.2015.11.039>
12. Li P, Jiang Z (2018) Bifurcation analysis of stick-slip motion of the vibration-driven system with dry friction. *Math Probl Eng* 2018:1–10. <https://doi.org/10.1155/2018/2305187>
13. Prajapati NB, Desai JV, Pandya DH (2020) Experimental investigation of chatter in boring operation using shim. In: Gupta VK, Varde PV, Kankar PK, Joshi N (eds) *Reliability and risk assessment in engineering. Lecture notes in mechanical engineering*. Springer Singapore, Singapore, pp 253–259. [https://doi.org/10.1007/978-981-15-3746-2\\_23](https://doi.org/10.1007/978-981-15-3746-2_23)
14. Moon FC (1992) *Chaotic and fractal dynamics: an introduction for applied scientists and engineers*. Wiley
15. Lian X, Liu J, Zhang J, Wang C (2019) Chaotic motion and control of a tethered-sailcraft system orbiting an asteroid. *Commun Nonlinear Sci Numer Simul* 77:203–224. <https://doi.org/10.1016/j.cnsns.2019.04.026>

# Multispectral Imaging for Identification of Water Stress and Chlorophyll Content in Paddy Field Using Vegetation Indices



S. Madhura and T. V. Smitha

## 1 Introduction

India is basically an agriculture-based country, and it is the second-largest producer of rice in the world. Around 58% of the Indian population has made agriculture as a primary source of livelihood [1]. The problems faced by the farmers during paddy cultivation can be broadly classified into two categories: (1) excess water supply and (2) insufficient water supply. Paddy is grown in the eastern and southern parts of the country which include brown and white rice. One of the major problems with the paddy cultivation is the enormous amount of water stress due to the inadequate or excess rainfall. Let us consider each case in detail: firstly, the water stress, if the water supply is not adequate for the crop, then the stomata present in the leaves will close automatically to conserve water content which adversely affects the plant growth and also yield [2]. Secondly, if the water is supplied in excess, the yield of the crop will be reduced as per previous study.

The proposed work identifies the water stress of the paddy crop through the variation in the vegetation color of the crop at two different stages. The qualitative analysis is made over Vegetation Water Stress Index (VWSI) which is important factor for management of irrigation system of paddy crop. The identified cultivation land is situated in Mandya district, Karnataka, India.

---

S. Madhura (✉)

Department of Electronics and Communication Engineering, RV Institute of Technology and Management, Bangalore 560076, India  
e-mail: [madhuras.rvitm@rvei.edu.in](mailto:madhuras.rvitm@rvei.edu.in)

T. V. Smitha

Department of Mathematics, RV Institute of Technology, Bangalore 560076, India  
e-mail: [smithatv.rvitm@rvei.edu.in](mailto:smithatv.rvitm@rvei.edu.in)

## 2 Related Work

Some of the factors that determine the water stress in paddy field include evaporation transpiration (ET), moisture in the soil, water holding capacity of leaf, and the water content in the leaf. The holistic development of the crops as monitored by the remote sensing system was very well estimated by identification of spatial and temporal information indicating the crop stress [3]. The following information aids in the spectral analysis of the leaf, pigmentation of the leaf is determined by the visible band, water content by mid-intra red region (MIR), and cellular structure by near infrared (NIR) regions [4]. The classical method of water management includes ground-based method which uses surface renewable systems, scintillometers, ratio, and covariance systems. The collection of data from ground using the common techniques like manual inspection was very slow process and not accurate [5]. The ground-based system will not only be tedious but erroneous [6]. The absorption of the light by the leaf pigment varies resulting in decrease of chlorophyll content in the leaf in the stressed regions. The variation in the spectral band can be analyzed as decreased green band and increased blue and red band in the stressed regions due to inadequate supply of water. For a better analogy, short wave infrared band is used to determine water thickness and near-infrared band for dry land content [7]. These color bands can be utilized to provide the vegetation condition along with normalized VWWSI. Short wave infrared (SWIR) can detail water indices for water stress and drought condition detection [8].

Yet another challenge in stress assessment is the collection of data from the paddy field. Several remote sensing techniques were adopted for image collection from the field which involved undesirable weather condition that limits the data acquisition [9]. Satellite images posed a spatial and temporal resolution constraints in assessing the crop image [10]. Many water stress analyses were done on the wheat crop in Haryana [7, 11, 12] where they have introduced vegetation condition index along with Landsat TM infrared bands. There is a need to identify a robust, flexible, and accurate crop water management that is very essential to improve the yield and productivity of the crop. Some of the researcher have collected chlorophyll content, leaf area indicator, and biomass details using remote sensing technology [13–15]. However, the major drawback in this process is the weather conditions like the cloud and fog which results in poor quality image [16].

## 3 Methodology

The images of the paddy field were obtained from a village called Hodagatta, Mandya district, Karnataka state, India. The entire image covers nearly 1.5 acres of paddy crop with a verity by name Mukthi (CTH-1) which is one of the most

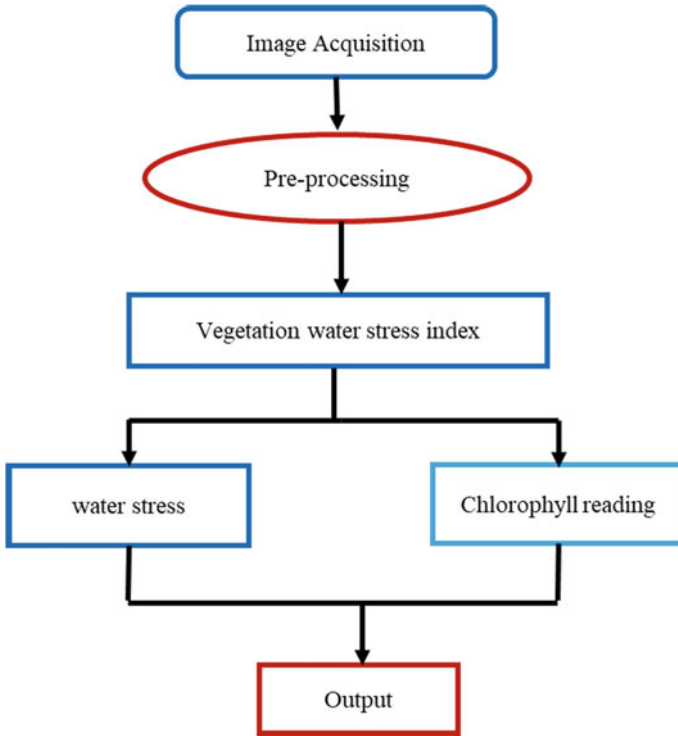


**Fig. 1** Flowchart of the proposed work

popular type of rice variety grown in this region. This crop Mukthi (CTH-1) was planted on February 2, 2019, in the location stated. The flow diagram of the methodology is shown in Fig. 1.

The rice is a five-month crop which was monitored from February to June, and the vegetation indices was studied during the month of April. The content of the water stress and chlorophyll to estimate the crop yield can be better understood by the red band with 720 nm and near-infrared band with 800 nm wavelength. The images from the site under consideration were taken from site using multispectral camera. The image obtained is with lower color reflectance from the crop which makes the analysis of VWSI erroneous. Thus, the image acquired was preprocessed using spatial and temporal filters to remove impulse and Gaussian noises present due to weather conditions like rain and fog using spatiotemporal trilateral filter (STTF) [17, 18].

### 3.1 Vegetation Water Stress Index

Vegetation Water Stress Index is a 2D image indexing system proposed by [19–22] relayed on SWIR and NIR wavelengths. The waterlines with minimum and maximum water stress was identified using the slope equation

$$y = mx + c \quad (1)$$

The vertical waterline was named as  $V_1$  and  $V_2$ , and horizontal waterline was named as  $H_1$  and  $H_2$ .

VWSI is generated by:

$$\text{VWSI} = 1 - \frac{(V_1 - V) * (\text{NIR} - V_2 * \text{SWIR} - H_2)}{(V_1 - V_2) * (\text{NIR} - V * \text{SWIR}) - (V_1 - V) * H_2 + (V_2 - V) * H_1} \quad (2)$$

The above numerical values can be analyzed in meshed method using [19, 20].

## 4 Result and Discussion

The vegetation indices should be made sensitive to water content and not disturbed by soil moisture. Differentiating the land as two different waterlines as stated in methodology and implementing in Eq. 2 gives a better analysis profile. The paddy crop was harvested in the month of February after harvest of sugarcane one month before that is in January. Figure 2 shows the site location with two-month-old paddy filed which was taken on April 03, 2019. The preprocessing is done using STTF as depicted in Fig. 3. The enhanced harvested image gives better reflectance and wave band absorption details for comparison with the multispectral image data for identification of water stress and chlorophyll content. Figure 4 gives the multispectral image showing the waveband details.

VWSI during this month was 0.12 which indicated no water stress in this plot along with the reflectance of uniform green color that is indication of good chlorophyll content. The imaging was carried out after one month that is on May 12, 2019, Fig. 5 shows the captured image from the plot.

Since the acquired image was visually color distinguishable, there was no pre-processing being done on this image. The multispectral image obtained for the same plot can be seen in Fig. 6.

For the normal growth of the crop, VWSI should be less than 0.3, its value between 0.3 and 0.5 depicted moderate water stress, and VWSI with a value greater than 0.5 shows sever water stress condition that affects the yield abruptly [7]. VWSI for the third month crop showed 0.43, which means it falls under moderate water



**Fig. 2** Two-month-old paddy field



**Fig. 3** Enhanced image of paddy field using spatiotemporal trilateral filter

stress and accordingly the color of the crop was yellow to light orange indicating the chlorophyll deficiency as observed in Fig. 6. Table 1 shows the quantification of VWSI with the crop growth and chlorophyll content.



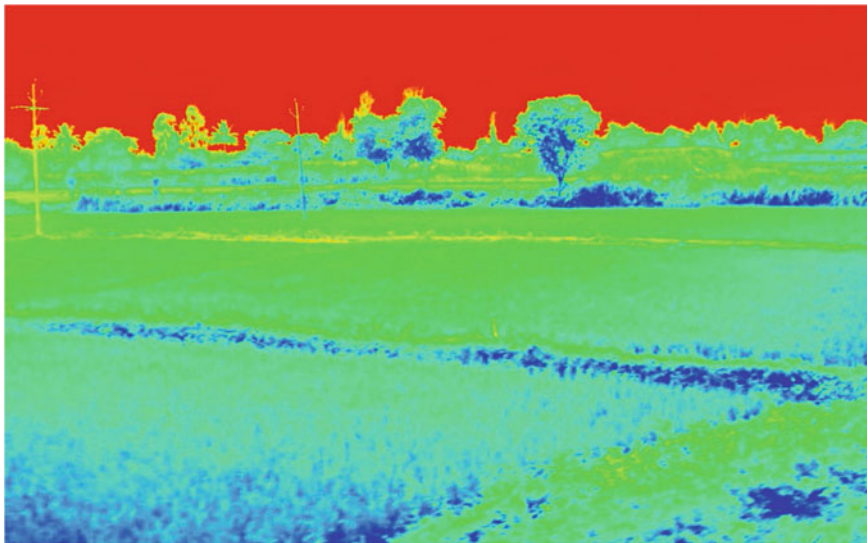


**Fig. 4** Multispectral image of the two-month-old paddy crop



**Fig. 5** Three-month-old paddy field

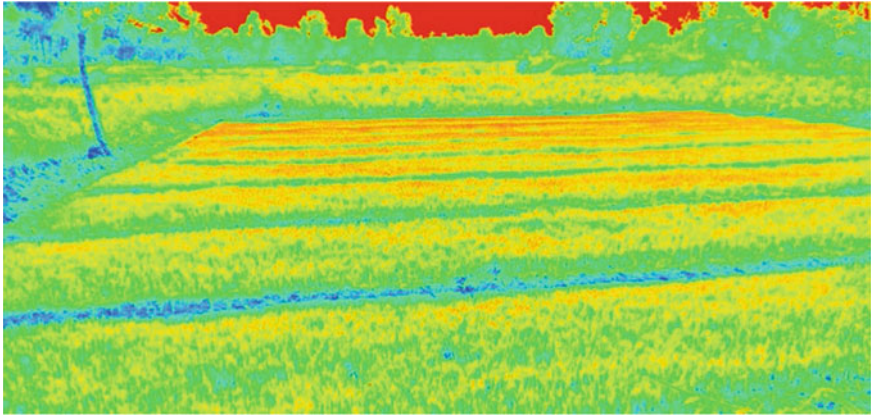


**Fig. 6** Multispectral image of three-month-old paddy crop

**Table 1** Quantification of VWSI with crop growth and leaf color

Water stress index (VWSI)	Crop condition	Color of the crop (Chlorophyll content)
<0.3	Normal growth	Green
0.3 > VWSI < 0.5	Moderate growth	Light yellow
>0.5	Less growth	Orange to brown

## 5 Conclusion

This paper proposed a method to identify the water stress in paddy crop grown in southern part of India using VSWI derived from multispectral data acquired from the field. The VSWI was used to estimate the water stress with the data from multispectral images with different spectral bands. The data can be mapped to identify the chlorophyll content in the leaf, wherein the indices and the color mapping was found to successfully identify the water stress during the different month of cultivation. This was one of the good methods of identifying the crop condition through color of the crop which provides overview for the cultivators to calibrate the water input but either increasing the supply for stressed areas or to reduce the supply to healthy areas. During the first two months, the water content was adequate, stress was detected, and VSWI was 0.2 indicating no water stress. During the third month, the indices was detecting moderate water stress with VSWI as 0.43 that needed attention from the crop owner. Thus, there was a good agreement between the calculated stress indices and color observation which would result in better yield if treated on time. As future work, the precision of the output can be increased to help the farmers to get better yield through controlled and sustainable cultivation.

## References

1. Kinkaid E (2020) Trent brown: farmers, subalterns, and activists: social politics of sustainable agriculture in India. *Agric Hum Values* 37:929–930. <https://doi.org/10.1007/s10460-020-10033-9>
2. Porporato A, Daly E, Rodriguez-Iturbe I (2004) Soil water balance and ecosystem response to climate change. *Am Nat* 164:625–632
3. Campbell JB (1987) Introduction to remote sensing (1987). Fung T Drew E *PERS* 53:1649–1658
4. Ripple WJ (1986) Spectral reflectance relationships to leaf water stress. *Photogr Eng Remote Sens* 52:1669–1675. (ISSN 0099–1112)
5. Valente J, Sanz D, Barrientos A, del Cerro J, Ribeiro A, Rossi C (2011) An air-ground wireless sensor network for crop monitoring. *Sensors* 11(6):6088–6108
6. Zhang G, Xiao X, Dong J, Kou W, Jin C, Qin Y, Biradar C (2015) Mapping paddy rice planting areas through time series analysis of MODIS land surface temperature and vegetation index data. *ISPRS J Photogr Remote Sens* 106:157–171
7. Ghulam A, Li Z-L, Qin Q, Yimit H, Wang J (2008) Estimating crop water stress with ETM + NIR and SWIR data. *Agric For Meteorol* 148:1679–1695
8. Kim HJ (2006) Combined use of vegetation and water indices from remotely-sensed AVIRIS and MODIS data to monitor riparian and semiarid vegetation. The University of Arizona, Tucson (AZ)
9. Nguy-Robertson A, Gitelson A, Peng Y, Viña A, Arkebauer T, Rundquist D (2012) Green leaf area index estimation in maize and soybean: combining vegetation indices to achieve maximal sensitivity. *Agro J Abs—Biometry, Model Stat* 104(5):1336–1347
10. Mukherjee A, Misra S, Raghuvanshi NS (2019) A survey of unmanned aerial sensing solutions in precision agriculture. *J Netw Comput Appl* 148:1–24
11. Kogan FN (1995) Application of vegetation index and brightness temperature for drought detection. *Adv Space Res* 15:91–100
12. Xiao X, Boles S, Liu J, Zhuang D, Frolking S, Li C, Salas W, Moore B III (2005) Mapping paddy rice agriculture in southern China using multi-temporal MODIS images. *Remote Sens Environ* 95:480–492
13. Abdullah S, Tahar KN, Rashid MFA, Osoman MA (2019) Camera calibration performance on different non-metric cameras. *Pertanika J Sci Technol* 27(3):1397–1406
14. Wang K, Huggins DR, Tao H (2019) Rapid mapping of winter wheat yield, protein, and nitrogen uptake using remote and proximal sensing. *Int J Appl Earth Obs Geoinf* 82:1–10
15. Fu Y, Yang G, Wang J, Song X, Feng H (2014) Winter wheat biomass estimation based on spectral indices, band depth analysis and partial least squares regression using hyperspectral measurements. *Comput Electron Agric* 100:51–59
16. Verger A, Vigneau N, Chéron C, Gilliot JM, Comar A, Baret F (2014) Green area index from an unmanned aerial system over wheat and rapeseed crops. *Remote Sens Environ* 152:654–664
17. Madhura S, Suresh K (2020) A new parallel DSP hardware compatible algorithm for noise reduction and contrast enhancement in video sequence using Zynq-7020. *Int J Comput Aided Eng Technol* 13(1/2):14–27
18. Madhura S, Suresh K (2016) Adaptive spatio-temporal filtering with motion estimation for mixed noise removal and contrast enhancement in video sequence. In: FICTA-2016 and publication in Springer AISC series, 16, 17 Sept, Bhuvaneshwar, Odisha
19. Smitha TV, Nagaraja KV (2019) Application of automated cubic-order mesh generation for efficient energy transfer using parabolic arcs for microwave problems. *Energy* 168:1104–1118
20. Smitha TV, Nagaraja KV (2019) An efficient automated higher-order finite element computation technique using parabolic arcs for planar and multiply-connected Energy problems. *Energy* 183:996–1011

21. Jayanth KG, Boddapati V, Geetha RS (2018) Comparative study between three-leg and four-leg current-source inverter for solar PV application. In: Proceedings of the 2018 international conference on power, instrumentation, control and computing (PICC), Thrissur, India, 18–20 Jan 2018. <https://doi.org/10.1109/PICC.2018.8384793>
22. Boddapati V, Sathesh Kumar T, Prakash N et al. Current droop control of parallel inverters in an autonomous microgrid. Mater Today: Proc. <https://doi.org/10.1016/j.matpr.2020.09.496>

# Condition Monitoring of Used Engine Oil by FTIR Spectroscopy—A Review



Afreen Nissar, M. Hanief, and Fasil Qayoom Mir

## 1 Introduction

Engine oil or lubricating oil is used for the purpose of lubrication of IC engines. Its prime function is reducing friction and wear on the moving parts as it forms a film of material between the surfaces and thus preventing the surfaces to come into direct contact with each other. It also helps to remove the sludge and varnish from the engine and thus cleaning it. Lubricating oil neutralizes the acids that originate from the fuel and prevents heating of engine by carrying heat which is produced by friction between parts which convert the kinetic energy into heat, away from moving parts and thereby cooling it.

There are many additives that are blended with the lubricating oil for specific purposes, and these include metallic detergents, ash-less dispersants, anti-foam, zinc di-thiophosphates, anti-oxidants, etc. These additives improve oil's detergency, prevent corrosion of engine parts, and enable extreme pressure performance. Used engine oil is an extremely dangerous pollutant as it contains heavy metals in considerable amount. Also, it contains high concentrations of PAH which are carcinogenic compounds. Lubricants can save billions of dollars if optimally adjusted. Engine oil does not wear out after using it; it just gets dirty as many contaminants get added to it along the way. The main contaminants found in used engine oil are water, dissolved gasoline and gas-oil, solvents, aromatics and cleaning fluids, sediments, lead, and polymeric and non-polymeric additives [1].

Used oil analysis is a significant part of engine maintenance, and FTIR plays a massive role in the same. The main aim of conducting used oil analysis is to assess

---

A. Nissar (✉) · M. Hanief  
Mechanical Engineering Department, NIT Srinagar, Srinagar,  
Jammu and Kashmir 190006, India

F. Q. Mir  
Chemical Engineering Department, NIT Srinagar, Srinagar,  
Jammu and Kashmir 190006, India

the condition of the oil as it gives information about the suitability of oil for advanced use and also the right time when the oil should be changed. It also gives us the information about the condition of the engine by identifying the contaminants and size of the wear particles. The use of degraded lubricant, if gone unnoticed, can offer substandard protection from mechanical wear and lead to permanent and/or costly damages [2].

## 2 FTIR Spectroscopy

Spectroscopic method such as FTIR can give us substantial information about condition of the engine oil and about the system where the oil is being used. Source is the first component in the spectroscopic system which will emit infrared energy, and this energy is sent through an aperture. The beam is encoded in the interferometer from where it enters next by means of series of stationary and movable mirrors. After this, the beam then enters the sample where some energy frequencies are absorbed. The detector then measures the energy that manages to escape, and then, the computer performs the Fourier transformation on the measured signal. FTIR spectroscopy is used for assessing industrially manufactured material and often serves as the first step in material analysis process for quality control. If there is change in normal pattern of absorption bands, then it clearly shows a change in the composition of the material, hence confirming the presence of contaminants. Contaminants have the capability of reducing lubricating capacity of the oil, which in turn increases wear of the machine parts (Fig. 1).

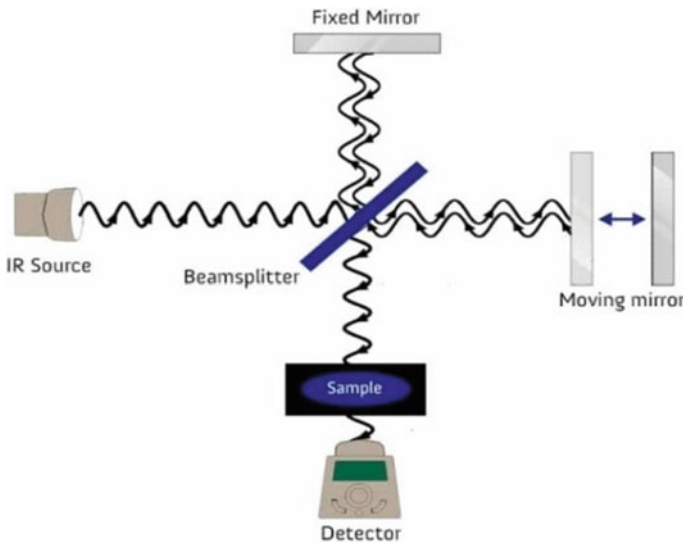


**Fig. 1** Working of FTIR Spectrometer

### 3 Condition Monitoring of Used Engine Oil by FTIR Spectroscopy (a Review)

FTIR spectroscopy is a proven technique that helps us to analyze and characterize used engine oil samples. When the engine oil sample is exposed to infrared radiation, the molecules absorb these radiations at different wavelengths and the detector placed at the other side of the samples identifies the molecules. The identification of molecules is accurate as no two molecules can produce same pattern or wavelength. The spectral location of the various components in the oil is as under (Table 1).

Detection of various impurities that have been added to the engine oil during its usage is very important as it provides us with the information about the condition of the engine by identifying the wear components and also the probability of recycling the used engine oil. Engine oil condition parameters such as viscosity, color, and odor also provide information about the condition of the engine. By removing the said impurities, it can be re-used for various purposes, thus making the whole process economical and also saving the environment. FTIR spectroscopy plays an important role by identifying these impurities/parameters, and the usually identified impurities/parameters are:

#### 3.1 Oxidation

FTIR spectroscopy is considered to be the most commonly used methodology to measure oxidation level in used engine/ lubricating oils. The FTIR spectra studied

**Table 1** Spectral location of various components in used engine oil

Component	Spectral location ( $\text{cm}^{-1}$ )
Soot	2000
Oxidation	1750
Nitration	1630 1650–1600 [3]
Sulfation	1150
Water	3400
Glycol	880
Diesel	800
Gasoline	750
ZDDP (AW)	980
Carbonyl absorption region	1820–1650
Ketones	1705–1725
Carboxylic acid	1700–1725
Ester	1725–1750

**Table 2** Spectral location of various oxidation related problems in used engine oil

Spectral location	Purpose
1725–1650 $\text{cm}^{-1}$	Detection of oil degradation related to thermal stress
835–735 $\text{cm}^{-1}$	Detection of fuel contamination
1775–1725 $\text{cm}^{-1}$	Detection of fuel dilution problems
1750–1725 $\text{cm}^{-1}$	Detection of ester content

**Table 3** Spectral location of various oxidation-related problems in used engine oil [6]

Spectral location ( $\text{cm}^{-1}$ )	Functional group
3100–3600	Alcohols
2500–3200	Carboxylic acids in polar environment
1650–1730	Aldehydes and ketones
1680–1710	Carboxylic acids
1700–1740	Esters
1780	Lactones
1050–1450	(C–O) aromatic compounds
1000–1250	(C–C) aromatic compounds
1440–1650	(C=C) aromatic compounds

by Wolak et al. [4] stated that oxidation causes the aging changes in the engine oil. Agoston et al. [5] observed that the used oil detects the oxidation around the spectral location of  $1710 \text{ cm}^{-1}$ . The spectral locations mentioned below are observed and studied for the following purposes (Tables 2 and 3).

### 3.2 Hydrocarbons and Carbonyl Groups

The following bands of spectral locations are observed for hydrocarbons and carbonyl groups (Tables 4 and 5).

### 3.3 Infiltration of Diesel Fuel into Engine/Lubricating Oil

Exposure of engine oil to high temperature, pressure, and other contaminants creates degradation of products, and contaminant infiltration from outside cause additives to deplete. Infiltration of fuel into engine oil affects the basic parameters such as viscosity, viscosity index, TBN, and flash point. Fuel dilution in diesel engines usually occurs by extreme idling, faulty injectors, or loose connections.



**Table 4** Spectral location of hydrocarbons and carbonyl groups in used engine oil

Spectral location	Hydrocarbons/Carbonyl group detected
1704.29–1603 cm <sup>-1</sup>	Carbonyl groups from esters, ketones, or acids (Short chain compounds) [7]
1157.92 cm <sup>-1</sup>	Per-oxide compounds [7]
704.29–1603.13 cm <sup>-1</sup>	Unsaturated additives [8]
1229–724 cm <sup>-1</sup>	Nitrates formation derived from the oxidation of nitrogen oxide compounds [7, 9]
600–1300 and 1500–2000 cm <sup>-1</sup>	Additives (Zn, Ca, and Mg salts) or organic acids [7, 10]
Split band at 2925, 1460 and 1376 cm <sup>-1</sup>	Presence of hydrocarbon compounds having a small chain lengths
869.4, 813.2 and 1603.1 cm <sup>-1</sup>	Presence of aromatics (and/or PAHs) in the used engine oil representing hydrocarbons in the aromatic ring [10]

**Table 5** Spectral location of hydrocarbons and carbonyl groups detected by FTIR analysis of oil residues (over 150 days weathering in the plant root zone) [11]

Spectral location	Hydrocarbons/Carbonyl group detected
2957–2850 cm <sup>-1</sup>	Bands which are related to C–H vibrations
1460 cm <sup>-1</sup> (Intense band) 1377 cm <sup>-1</sup> (Less intense band)	Bands produced by a combination of compounds having small chain lengths and splitting vibrations from C–H of methylene (–C–H <sub>2</sub> –) chains in used oil
3424 cm <sup>-1</sup> (Intense band) 1645 cm <sup>-1</sup> (New band)	Bands associated with the O–H stretching band and also the H–O–H bending vibrations of water
1740 cm <sup>-1</sup>	Band linked with carbonyl groups (ketones, aldehydes and/or acids)
1707 and 1709 cm <sup>-1</sup>	Bands associated with new carbonyl groups (from microbial oxidation of the oil)
1708 and 1740 cm <sup>-1</sup> (New bands)	New carbonyl-based compounds (ketones or aldehydes produced by microbial oxidation processes)

The main peaks detected that are associated with main functional groups are (Tables 6 and 7):

Zinc di-alkyl di-thiophosphates (ZDDPs) are the principal anti-wear additives currently used by automotive engine/lubricating oils and transmission fluids. They also function as anti-oxidants, providing a main part of the anti-oxidant action in many lubricant preparations [18].

**Table 6** Spectral location of functional groups in used engine oil produced by infiltration of diesel fuel into engine/lubricating oil

Spectral location	Functional group
2954, 2920, 2848 $\text{cm}^{-1}$	CH bonds of saturated <i>n</i> -alkyl groups [12]
1707 and 1156 $\text{cm}^{-1}$	Polymethacrylate
1456 $\text{cm}^{-1}$	CH deformation of $\text{CH}_2$ and $\text{CH}_3$ groups [13]
1376 and 1156 $\text{cm}^{-1}$	$\text{CH}_3$ peaks of <i>n</i> -alkanes
974 $\text{cm}^{-1}$	Spectral band linked with the P–O–C bond of zinc di-alkyl di-thiophosphates (ZDDPs)
835–688 $\text{cm}^{-1}$	Spectrum meant for new oil and diesel fuel
700–850 $\text{cm}^{-1}$	Large number of skeletal vibration of many ring structures [14]
803, 764, 740 722, 697 $\text{cm}^{-1}$	These well-separated peaks correspond to out-of-plane aromatic CH stretching and these vibrations show stronger intensity [15]
650–784 $\text{cm}^{-1}$	For gasoline determination, the region is attributed for aromatics [16]

**Table 7** Fourier transform infrared (FTIR) spectrometer for used motor oil [17]

Frequency $\text{cm}^{-1}$	Bond	Functional group
725.21	C–H	Alkanes
813.46	C–H	Aromatic
884.53	C–H	Aromatic
1033.48	C–O	Carboxylic acid
1158.63	C–O	Carboxylic acid
1374.89	C–H	$\text{CH}_3$
1448.16	C–H	Alkanes
1603.88	C=C	Aromatic
1743.74	C=O	Carbonyl compounds
2335.07	O–H	Carboxylic acid
2727.21	H–C = O:CH	Aldehydes
2922.01	C–H	Alkanes
3379.41	–OH	Water

### 3.4 Moisture

Presence of moisture or water content in the lubricant can weaken the effectiveness of the lubricant as it can cause wear to the machine by corrosion. It is thus considered to be one of the most extensive and damaging lubricant contaminants (Tables 8 and 9).

**Table 8** Parameters and their measurement regions (Petroleum crankcase lubricants) [19]

Parameter	Measurement region (cm <sup>-1</sup> )
Water	3500–3150
Soot loading	2000
Oxidation	1800–1670
Nitration	1650–1600
Anti-wear components	1025–960
Gasoline	755–745
Diesel (JP-5, JP-8)	815–805
Sulfate by-products	1180–1120
Ethylene glycol	1100–1030

**Table 9** Oil quality parameters from single-point measurements in the mid-IR region [20, 21]

Parameter	Wavenumber (cm <sup>-1</sup> )
Heptane-insolubles	4000
Heptane-insolubles	2500
Water	3430
Fuel	3040
Fuel	700
TBN	1170

### 3.5 Operating Effect

Intensity of the bands (2850–2960 cm<sup>-1</sup>) and (1385 cm<sup>-1</sup>–1464 cm<sup>-1</sup>) decrease with the distance travelled by the engine of the vehicle. However, bands (1570–1614 cm<sup>-1</sup>) and 1095 cm<sup>-1</sup> become more intense with the distance travelled by the engine of the vehicle. They correspond to presence of the silicates, phosphates, and sulfates consequential from the additives present in the lubricating oils.

There is also the depletion of nitrile contained in the new lubricating oil as it is believed that the nitrile is depleted during operation of the engine. Fresh strip of C-N band is formed around 1360 cm<sup>-1</sup>. There is formation of a C-O band around 1200 cm<sup>-1</sup> which depicts production of ester. Appearance of carbonyl group (1740 cm<sup>-1</sup>—intense band) occurs due to oxidation of lubricating oil.

## 4 Conclusion

There are many other parameters that can be identified using FTIR spectroscopy which include kinematic viscosity, viscosity index, base number, soot, etc. FTIR spectroscopy has proven to be a very useful technique for condition monitoring of engine and analyzing the engine oil. The technique can be applied in both industrial and automobile sectors to prevent costly failure of machine as well as to encourage

recycling of the used oil. Spectral data for artificial neural network has been used to authenticate the edible oil adulterants over the FTIR spectrum. Infrared spectrometry has provided us with a useful alternative to the age-old conventional methods for monitoring oil samples. FTIR spectrometry is considered to be a very versatile tool and finds a very wide range of application for the samples taken from aviation industry, geology, biology, chemistry, etc.

## References

1. Ciora Jr et al (2000) Refining of used oils using membrane- and adsorption-based processes. US6024880A
2. Stellman CM, Ewing KJ, Bucholtz F, Aggarwal ID (1999) Monitoring the degradation of a synthetic lubricant oil using infrared absorption, fluorescence emission and multivariate analysis: a feasibility study ©Lubrication Engineering
3. Robinson N (2000) Monitoring oil degradation with infrared spectroscopy. <http://www.wearcheck.co.za>
4. Wolak A, Krasodowski W, Zajac G (2020) FTIR analysis and monitoring of used synthetic oils operated under similar driving conditions. *Friction* 8(5):995–1006
5. Agoston A, Ötsch C, Zhuravleva J, Jakoby B (2004) An IR-absorption sensor system for the determination of engine oil deterioration. *IEEE* 0-7803-8692-2/04/©2004
6. Gracia N, Thomas S, Bazin P, Duponchel L, Thibault-Starzyk F, Lerasle O (2010) Combination of mid-infrared spectroscopy and chemometric factorization tools to study the oxidation of lubricating base oils. *Catal Today* 155:255–260
7. Kadam AN, Zingde MD (1985) Infrared spectroscopic analysis of used crankcase oil. *Res Ind* 30:382–385
8. Zieba-Paulus J, Koscielniak JP (1999) Differentiation of motor oils by infrared spectroscopy and elemental analysis for criminalistic purposes. *J Mol Struct* 482–483:533–538
9. Rashid HA, Alhassan AA, Abdulsalam A (1990) Analysis of used oil by IR-spectroscopic and synthesis of dispersions of a highly basic petroleum calcium sulfonate additive. *Fuel Sci Technol Int* 8:899–910
10. Geach A (1996) Infrared analysis as a tool for assessing degradation in used lubricants. <http://www.wearcheck.ca/literature/techdoc/WZA002.html>
11. Dominguez-Rosado E, Pichtel J (2003) Chemical characterization of fresh, used and weathered motor oil via GC/MS, NMR and FTIR techniques. *Proc Ind Acad Sci* 112(2):109–116
12. Hirri A, Bassbasi M, Oussama A (2013) Classification and quality control of lubricating oils by infrared spectroscopy and chemometric. *Int J Adv Technol Eng Res* 3:59–62
13. Kupareva A et al (2012) Chemical characterization of lube oils. *Energy Fuels* 27(1):27–34
14. Marinović S et al (2012) Prediction of diesel fuel properties by vibrational spectroscopy using multivariate analysis. *J Anal Chem* 67(12):939–949
15. Andrade JM, Garrigues S, De La Guardia M et al (2003) Non-destructive and clean prediction of aviation fuel characteristics through Fourier transform-Raman spectroscopy and multivariate calibration. *Analytica Chimica Acta* 482(1):115–128
16. Borin A, Poppi RJ (2005) Application of mid infrared spectroscopy and iPLS for the quantification of contaminants in lubricating oil. *Vib Spectrosc* 37(1):27–32
17. Abu-Elella R, Ossman ME, Farouq R, Abd-Elfatah M (2015) Used motor oil treatment: turning waste oil into valuable products. *Int J Chem Biochem Sci.* ISSN 2226-9614

18. Willermet PA, Mahoney LR, Bishop CM (1980) Lubricant degradation and wear II antioxidant capacity and IR-spectra in systems containing zinc dialkyl dithiophosphates. *ASLE Trans* 23(3):217–224
19. Van De Voort FR, Sedman J, Cocciardi RA, Pinchuk D (2006) FTIR condition monitoring of in service lubricants: on-going developments and future perspectives. *Tribol Trans* 49(3):410–418
20. Stuart AD, Trotman SM, Doolan KJ, Fredericks PM (1989) Spectroscopic measurement of used lubricating oil quality society for applied spectroscopy. 0003-7028/89/4301-0055/©1989
21. Pandurangan MK, Murugesan S, Gajivaradhan P, Shettu N (2017) Application of artificial neural networks to authenticate virgin groundnut oil adulterants using FTIR spectral data. *Pharm Chem J* 4(4):33–38

# Next-Generation Electrochemical Energy Conversion and Storage Based on Three-Dimensional Nanostructures with Improved Performance: Insights and Perspectives



Shubhadip Paul

## 1 Introduction

To address various challenges arising due to global warming, increasing environmental pollutions, and limited state of fossil fuels, the necessity for developing sustainable renewable energy conversion and storage has come into surface [1, 2]. The sources of renewable energy—solar and wind—are having intermittent properties. The significant use of these alternative source of energies for achieving the increasing demand of energy has led to the abrupt technological advancement of electrochemical energy conversion and storage, which is seen in case of rechargeable batteries, supercapacitors, (Photo-)electrochemical fuel cells [3, 4]. The development of wind turbines and photovoltaics, in the past decades, helped in the process of conversion of wind and solar energy to electricity. But, the supercapacitors and rechargeable batteries, which are becoming as the crucial media, have added a flavor in the storage and deliver of fluctuating electricity [5]. Beside this production, the (photo-)electrochemical production of chemical fuels from carbon dioxide ( $\text{CO}_2$ ), water ( $\text{H}_2\text{O}$ ), and nitrogen ( $\text{N}_2$ ) by virtue of solar energy or renewable electricity is an optimistic way for making a sustainable energy future [6–9].

A series of physiochemical reactions on the electrode surface or at electrode interface for the purpose of electrochemical energy conversion and storage are linked with the transport behavior of ions and electrons. Thus, the optimization of electrode materials and electrons/ions transport is the main criteria for the improvement of electrochemical energy conversion and storage [10–12]. The major two strategic issues which can help in the improvement of the efficiency of electrochemical energy conversion and storage devices are:

---

S. Paul (✉)

Department of Metallurgical and Materials Engineering, National Institute of Technology Durgapur, Durgapur, West Bengal, India

- Material design [12, 13],
- Design of electrode [9–14].

Basically, three-dimensional nanostructured materials consist of arrayed one-dimensional/two-dimensional nanostructures, three-dimensional nanoporous structures, and three-dimensional hierarchical nanostructures that are having combination of unique properties: (i) Highly specific surface area (For increasing number of active sites for ion accessibility). (ii) Increased transportation of ion and electrons (To assist reaction kinetics) [15–17]. The prime motive is to get new insights, opinions, and various perspectives through various updated advantages and challenging factors related to the applications of three-dimensional nanostructures in the hydrogen generation from photoelectrocatalytic conversion of  $\text{CO}_2$  and  $\text{N}_2$  to chemical fuels, photoelectrochemical (PEC) water splitting, supercapacitors, and rechargeable metal-ion batteries for next-generation electrochemical energy conversion and storage to achieve sustainable energy future by utilizing renewable energy.

## 2 Three-Dimensional Nanostructures: Overview

The three-dimensional structure having active materials with porous configuration furnishes stability of supercapacitor electrodes with larger efficiency, proper channels for electrolyte outflow, larger surface area, and higher mechanical stability to supercapacitor electrodes as shown in Fig. 1. Generally, the construction of three-dimensional electrodes is done by—(a) Three nanostructures by assembling active materials, (b) Using metal foam acting as a template. The nanostructured materials are grouped into following divisions:

- (1) Zero-dimensional (0D) nanomaterials (nanospheres, nanoparticles);
- (2) One-dimensional (1D) nanomaterial (nanowires, nanorods);
- (3) Two-dimensional (2D) nanomaterials (nanoplates);
- (4) Three-dimensional (3D) nanomaterials.

All the dimensions (length, breadth, and height) are considered as one parameter. In case of detailed explanation of nanosized particles, it is known that if the materials are having their length and width within the nanometer range dimension less than 100 nm belong to zero dimensional. We all know that, in one-dimensional nanomaterial, one dimension is outside the nanoscale, and in two-dimensional nanomaterials, two dimensions are outside the nanoscale. But if we want to discuss about three-dimensional nanomaterials, then it should be mentioned here that the confinement of materials in nanoscale are not in any of the dimension. Constructing 3D nanostructures gives an exposure to a new domain which perform manipulation and integration of multiple nanoscale units at a larger scale, thus linking various gaps between nanoscale (indicating individual nanometer units) with microscales and macroscales (indicating nanounit-based devices) [18–21]. Three-dimensional

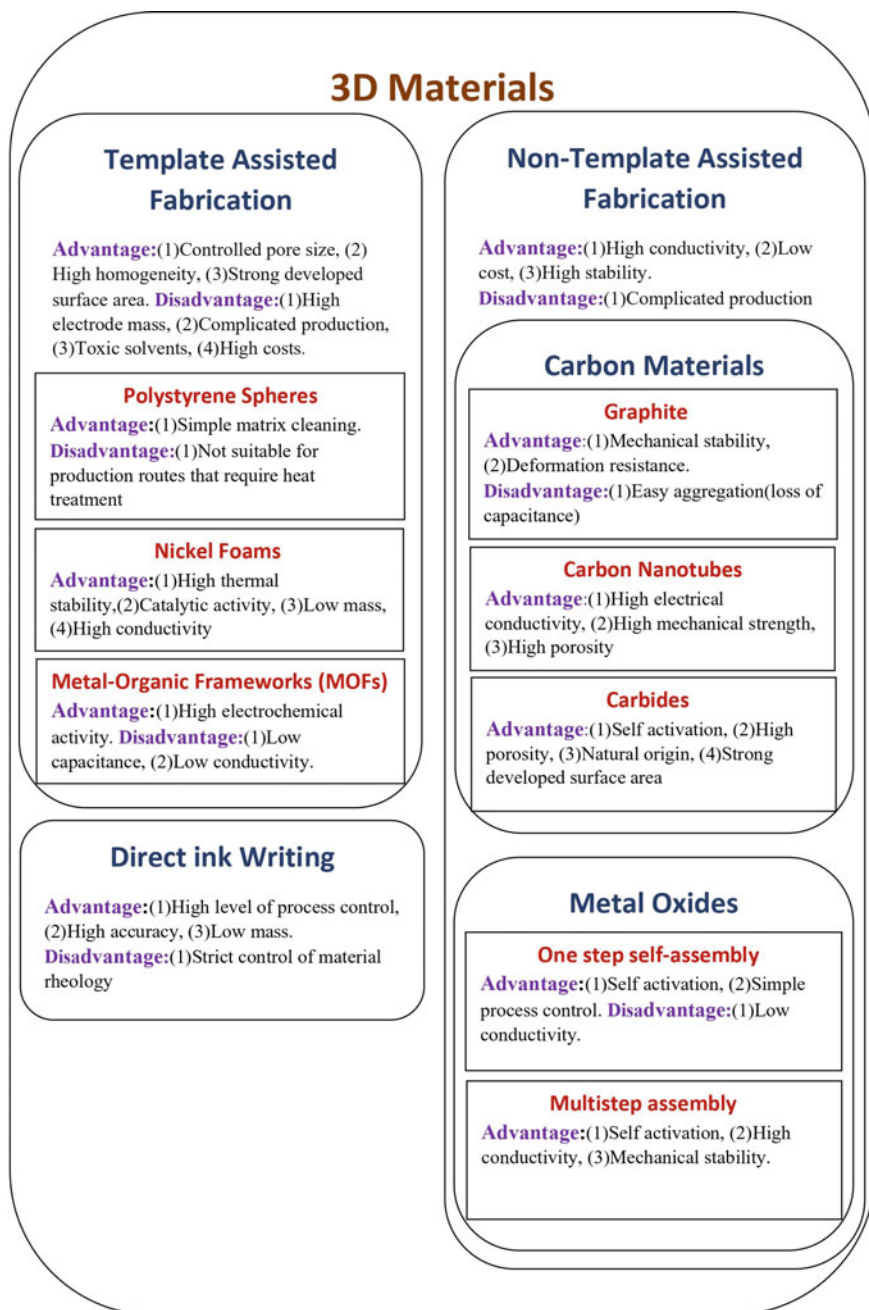


**Fig. 1** Advantages and disadvantages of 3D materials



nanostructures can demonstrate various properties by virtue of novel electronic, optical, and magnetic nature [22]. Thus, it can be stated that 3D nanostructures act as building blocks to design, construct, and optimize nanodevices like sensors, electronics, photonics, and also for the purpose of energy conversion and storage.

### 3 Electrochemical Energy Conversion

#### 3.1 Photoelectrochemical Water Splitting

Solar-driven  $H_2$  generation from the process of photoelectrochemical (PEC) water splitting portrays a profound solution which can help in achieving the increasing demand of energy and combat the issue of problem of environmental pollution. But, the efficiency of current conversion of solar to  $H_2$  is still not sufficient for implementation in practice and has transformed into a major challenging issue. During an archetypal process of PEC water splitting under solar irradiation as shown in Fig. 2, a semiconductor photoelectrode firstly absorbed photons for the production of electron–hole pairs. Then, the holes and electrons emerged by photogeneration get separated rapidly and migrate to the anode and cathode surface and get engaged in hydrogen evolution reaction (HER) and oxygen evolution reaction (OER). In particular, improvement in the efficiency of solar-to- $H_2$  conversion depends not only on the discovery of novel semiconductor photoelectrodes having high internal potential of catalyst but also depends on optimization of photoelectrode architectures for promoting the charge separation, light-harvesting capability enhancement, reducing the recombination of electron/hole by facilitating kinetics of such fast reactions occurring on photoelectrodes surface. Accordingly, fabrication of photoelectrodes with the aspects of 3D nanostructures can be considered as predominant tactics for improving the performance of PEC [23–26]. In case of PEC water splitting along with different PEC energy conversion devices, the most significant features of 3D nanoporous MOFs are the versatilities of structures. By tailoring the metal centers and organic ligands, the optimization of catalytic activities, bandgap, and porosity of three-dimensional nanoporous MOFs can be done for the enhancement of the performance of the catalysts [27–29]. The advantages of three-dimensional nanostructures for the purpose of PEC water splitting means are: (1) Trapping of light largely leads to the photonic, antireflection crystal effects prevailing in the increment of the absorption and utilization of solar irradiation of 3D nanomaterials. (2) High surface area provides enough space in the decoration of co-catalysts on the surface of photoelectrode, thus making it suitable for designing heterojunctional photoelectrode by optimizing the PEC performance. (3) Within the electrode, redox species mass transport due to the presence of huge number of open spaces in 3D nanomaterials help in the accelerating the reaction kinetics. But, the demerits for water splitting by PEC means of 3D nanomaterials are: (1) The reduction of the photocurrent due to high surface area would give rise to increasing recombination of interfacial charge for the development of PEC devices [23] (2) It

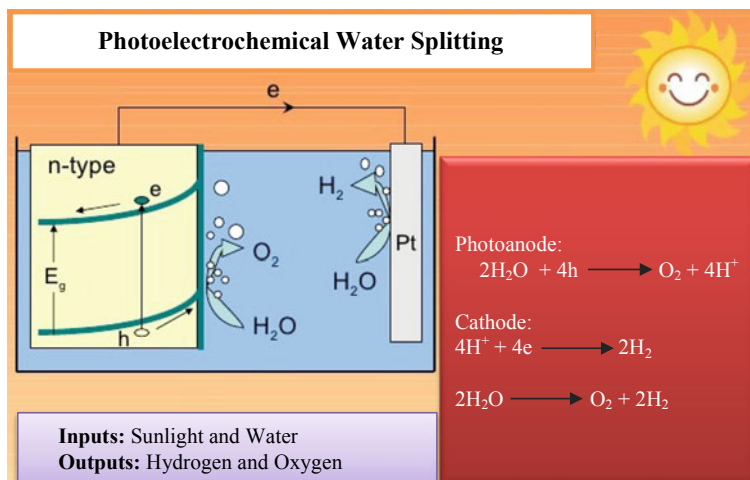
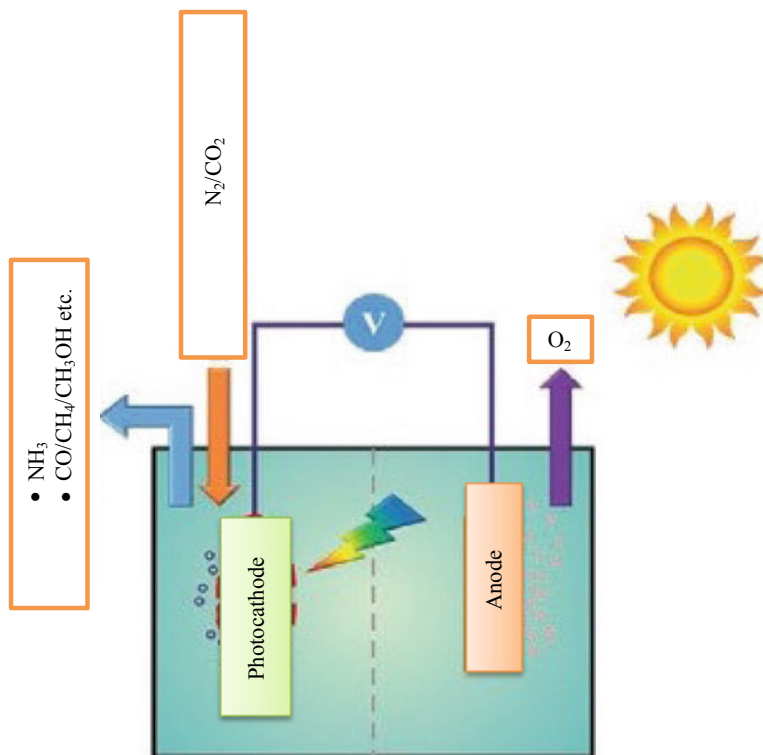


Fig. 2 Photoelectrochemical water splitting

is hard to explain a uniformity of the fabricated co-catalysts on the larger surface of photoelectrodes containing three-dimensional nanostructured materials [30]. Solutions to these challenging issues would be crucial for constructing three-dimensional nanostructured photoelectrodes with more efficient solar-to-H<sub>2</sub> conversion.

### 3.2 Conversion of N<sub>2</sub> and CO<sub>2</sub> Photoelectrocatalytically to Chemical Fuels

In order to produce H<sub>2</sub> by PEC water splitting, three-dimensional nanomaterials have been experimented significantly for the conversion of CO<sub>2</sub> and N<sub>2</sub> photoelectrocatalytically to chemical fuels, leading to above-mentioned advantages of 3D nanostructured materials for PEC water splitting [31–33]. Apart from a fertilizer, ammonia (NH<sub>3</sub>) is not only a significant intermediate of renewable energy storage but also a carrier of clean energy [34, 35]. If compared with the famous Haber–Bosch process, the photoelectrocatalytic conversion paved the way for converting from N<sub>2</sub> and H<sub>2</sub>O for the formation of NH<sub>3</sub> in presence of solar energy which is highly energy intensive as shown in Fig. 3. There is a profound similarity between PEC water splitting process and photoelectrocatalytic N<sub>2</sub> reduction reaction (NRR) process. In brief, it should be mentioned here that, the system involves the light absorption for the generation, separation, and transportation of electron–hole pairs with the formation of oxygen by the holes during the oxidation of H<sub>2</sub>O. It also involves production of NH<sub>3</sub> by the electron after getting reduction of N<sub>2</sub>.



**Fig. 3** N<sub>2</sub> and CO<sub>2</sub> conversion photoelectrocatalytically to chemical fuels

The photoelectrocatalytic process would help in the conversion of CO to hydrocarbon fuels, for example, ethylene, methane, methanol, carbon monoxide, and ethanol. In comparison with the conversion of NH<sub>3</sub> from N<sub>2</sub> by photoelectrocatalytic means, the CO<sub>2</sub> reduction reaction (CO<sub>2</sub>RR) follows the major factors which includes generation of electron-hole pairs undergoing the process of light absorption followed by separation and transfer on the catalyst surface. Thereby, some reactions on the surface are found which are oxidation of H<sub>2</sub>O and reduction of CO<sub>2</sub> [36, 37]. At the molecular or atomic scale of catalysts by virtue of surface engineering, a large number of CO<sub>2</sub>RR catalysts have been fabricated to upgrade the process of chemisorption of carbon dioxide on the surface of the electrode most of which are in the form of powder [38, 39]. Similar to the 3D nanostructured NRR electrode, the fabricated CO<sub>2</sub>RR catalyst nanoparticles (such as silicon nanowire arrays and gallium nitride nanowire arrays) get congregated on of 3D nanostructure surface [40, 41].

The fabrication of 3D nanostructured catalysts in case of both CO<sub>2</sub>RR and NRR should include homogenous stated nanounits having uniform crystal faces with controlled doping of heteroatom and abundant vacancies in stable phase. Hence, the 3D nanostructured catalysts will be having the capacity of huge light absorption,

high exposure to reactive sites, and functional charge-carrier migration followed by separation with highly stable structure. Thus, all these factors would help in upgrading the efficiency of solar-to-fuels conversion via either CO<sub>2</sub>RR or NRR.

## 4 Electrochemical Energy Storage Devices

### 4.1 Rechargeable Metal-Ion Batteries

The necessity to store and deliver the intermittent and fluctuating electricity can be provided efficiently by sodium, lithium-ion batteries recognized as rechargeable metal-ion batteries. The evolutionary progression from bulky macroscale to nanoscale electrode materials has provided the upgradation of performance in the energy storage of rechargeable metal-ion batteries due to the fact that electroactivity of electrode materials can be increased by nanomaterials. But, various challenging factors in agglomeration arise if the nanostructured electrode materials (nanowires, nanotubes, nanosheets, nanoparticles) are in the powder form [42]. Moreover, the dissociation of this powder form of electrode materials could be done after continuous cycling process which can diffuse the separators and accumulate on the surface of opposite electrode resulting in capacity loss.

In case of rechargeable metal-ion batteries, assembling one-dimensional and two-dimensional nanostructured materials into self-sustaining three-dimensional nanomaterials to fulfill the potential of nanomaterials has helped in tackling various challenges of agglomeration purposes faced by 1D and 2D nanomaterials [16, 18, 43, 44]. Ideal 3D self-supported nanostructures consist of 1D and 2D nanounits [45] having following features—(a) Nanounits spatially separated from each other in case of 3D nanomaterials (for avoiding agglomeration). (b) Self-sustaining three-dimensional nanomaterials bonded directly to current collectors (for avoiding dissociation of active materials). (c) Interconnected porous network (help in rapid transport of ion). (d) Nanostructures by virtue of various mechanisms (pseudocapacitance, surface-based adsorption of ion) can help in storing charge. (e) Fabrication of 3D nanostructured materials is more complicated to 1D and 2D powder nanomaterials, thus affecting adversely in the applications at a larger scale of 3D nanostructured materials.

### 4.2 Supercapacitors

Alternative or complement to batteries, on the basis of fast charging-discharging rate, fast energy storage as well as delivery and also for high-power density, the supercapacitors are the better option. But, the most disadvantageous factor of supercapacitor is that they possess low energy density. Supercapacitors store energy by—(i) Ionic adsorption/desorption at the interface of the electrode or the

electrolyte (double-layered electrochemical capacitor). (ii) Surface redox reactions in between the electrolyte and electrode which is fast and reversible in nature (pseudocapacitors). Developing active materials into 3D nanostructures with the enlargement of the surface area of active materials helps in the upgradation of energy density of supercapacitors [17, 46–48]. The most advantageous factors of using supercapacitors are as follows—(i) Interconnected porous network. (ii) Low charge transfer resistance. (iii) Large specific surface area. These factors help in the more storage of charge and diffusion of ions rapidly. But various disadvantages are also present in supercapacitors such as—(i) Low tap density of 3D nanostructured materials leading to low power density of supercapacitors. (ii) Mass loading for the functional materials if becomes less than slurry-cast electrode, then it creates problem [49]. Thus, mechanical stability should be high in case of 3D nanostructured materials during the assembly process for the nanodevice development with the subunits having predefined spatial arrangements and orientations (Table 1).

**Table 1** On the basis of various nanostructures, properties of supercapacitors electrode materials under 3D category [50]

Classification	Patterns	Summary	References
Three-dimensional metal foam	Nickel foam with Ni <sub>0.61</sub> Co <sub>0.39</sub> oxide on it	At 2 A g <sup>-1</sup> , it is having 1523.0 F g <sup>-1</sup> ; After 1000 cycles, capacitance retention is 95.3%	[51]
	Three-dimensional nickel foam with CoO-PPy on it	At 1 mA cm <sup>-2</sup> , it is having 2223 F g <sup>-1</sup> ; From 1 to 50 mA cm <sup>-2</sup> , rate capability is of 29.1%; After 2000 cycles, capacitance retention is 99.8%	[52]
	Three-dimensional porous structure in MnO <sub>2</sub> /Mn core shell	At 5 mVs <sup>-1</sup> , it is having ~1200 F g <sup>-1</sup> ; From 5 to 500 mVs <sup>-1</sup> , rate capacity is of 83%; After 2000 cycles, capacitance retention is 96%	[53]
Three dimensional carbonaceous materials	Wrinkled graphene-balls	At 0.1 A g <sup>-1</sup> , it is having 150 F g <sup>-1</sup> ; From 0.1 to 2.5 A g <sup>-1</sup> , rate capability is of 40%; After 5000 cycles, the capacitance retention is ~100%	[54]
	Coating of Ni (OH) <sub>2</sub> coating on vertically aligned carbon nanotube-graphene	At 22.1 A g <sup>-1</sup> , it is having 1065 F g <sup>-1</sup> ; From 5 to 30 mV s <sup>-1</sup> , the rate capability is of 70%; After 20 000 cycles, capacitance retention is 96%	[55]
	CNTs/GO/β-Ni (OH) <sub>2</sub>	At 2 A g <sup>-1</sup> , it is having 1815 F g <sup>-1</sup> ; From 2 to 20 A g <sup>-1</sup> , rate capacity is of 47.2%; After 2000 cycles, capacitance retention is 97%	[56]

(continued)

**Table 1** (continued)

Classification	Patterns	Summary	References
Three-dimensional pseudocapacitive materials	Three-dimensional NiO nanoflowers	At 0.5 A g <sup>-1</sup> , it is having 480 F g <sup>-1</sup> ; From 0.5 to 5 A g <sup>-1</sup> , rate capacity is of 52.5%; After 400 cycles, capacitance retention is ~90%	[57]
	Three-dimensional nanostructures like Co <sub>3</sub> O <sub>4</sub> urchin	At 0.5 A g <sup>-1</sup> , it is having 781 F g <sup>-1</sup> ; From 0.5 to 8 A g <sup>-1</sup> , the rate capacity is of 78.2%; After 1000 cycles, capacitance retention is 97.8%	[58]

## 5 Conclusion

This article gives an overview with various insights and perspectives regarding common electrode materials for the purpose of fabrication of energy storage devices based on carbon-based 3D architectures. Above all, the ceaseless advancement of the fundamental researches along with various technological innovations in modern nanofabrication will help for achieving a cost-effective and renewable energy future. The road for developing ideal energy storage device though is still very long, but the reasonable effective development of the proposed structure can uplift the idea of scientific research to achieve success.

## References

1. Quaschnig V (2019) Renewable energy and climate change, 2nd edn. Wiley, Chichester, UK
2. Chu S, Cui Y, Liu N (2017) Nat Mater 16:16
3. Tilley SD (2019) Adv Energy Mater 9:1802877
4. Li Q, Liu Y, Guo S, Zhou H (2017) Nano Today 16:46
5. Yang Z, Zhang J, Kintner-Meyer MCW, Lu X, Choi D, Lemmon JP, Liu J (2011) Chem Rev 111:3577
6. Yan Z, Hitt JL, Turner JA, Mallouk TE (2020) Proc Natl Acad Sci USA:201821686. <https://doi.org/10.1073/pnas.1821686116>
7. Giménez S, Bisquert J (2016) Photoelectrochemical solar fuel production. Springer, Switzerland
8. Fukuzumi S (2017) Joule 1:689
9. Wang Q, Lei Y, Wang D, Li Y (2019) Energy Environ Sci 12:1730
10. Chen X, Guo Y, Du X, Zeng Y, Chu J, Gong C, Huang J, Fan C, Wang X, Xiong J (2020) Adv Energy Mater 10:1903172
11. Ross MB, De Luna P, Li Y, Dinh C-T, Kim D, Yang P, Sargent EH (2019) Nat Catal 2:648
12. Sun Y, Guo S, Zhou H (2019) Adv Energy Mater 9:1800212
13. Yan Z, Ji M, Xia J, Zhu H (2020) Adv Energy Mater 10:1902020
14. Wang H-F, Xu Q (2019) Matter 1:565
15. Lukatskaya MR, Dunn B, Gogotsi Y (2016) Nat Commun 7:12647

16. Xu Y, Zhou M, Lei Y (2016) *Adv Energy Mater* 6:1502514
17. Zhao H, Liu L, Vellacheri R, Lei Y (2017) *Adv Sci* 4:1700188
18. Zhou M, Xu Y, Lei Y (2018) *Nano Today* 20:33
19. Li W, Liu J, Zhao D (2016) *Nat Rev Mater* 1:16023
20. Salian GD, Koo BM, Lefevre C, Cottineau T, Lebouin C, Tesfaye AT, Knauth P, Keller V, Djenizian T (2018) *Adv Mater Technol* 3:1700274
21. Zhao Y, Chang C, Teng F, Zhao Y, Chen G, Shi R, Waterhouse GIN, Huang W, Zhang T (2017) *Adv Energy Mater* 7:1700005
22. Nie Z, Petukhova A, Kumacheva E (2010) *Nat Nanotechnol* 5:15
23. Fang M, Dong G, Wei R, Ho JC (2017) *Adv Energy Mater* 7:1700559
24. Deng J, Su Y, Liu D, Yang P, Liu B, Liu C (2019) *Chem Rev* 119:9221
25. Zhou M, Bao J, Xu Y, Zhang J, Xie J, Guan M, Wang C, Wen L, Lei Y, Xie Y (2014) *ACS Nano* 8:7088
26. Mi Y, Wen L, Xu R, Wang Z, Cao D, Fang Y, Lei Y (2016) *Adv Energy Mater* 6:1501496
27. Gong Y-N, Ouyang T, He C-T, Lu T-B (2016) *Chem Sci* 7:1070
28. Meyer K, Ranocchiaro M, van Bokhoven JA (1923) *Energy Environ Sci* 2015:8
29. Wang W, Xu X, Zhou W, Shao Z (2017) *Adv Sci* 4:1600371
30. Wang S, Liu G, Wang L (2019) *Chem Rev* 119:5192
31. Gu Z, Shen H, Shang L, Lv X, Qian L, Zheng G (2018) *Small Methods* 2:1800121
32. Ali M, Zhou F, Chen K, Kotzur C, Xiao C, Bourgeois L, Zhang X, MacFarlane DR (2016) *Nat Commun* 7:11335
33. Yu Y, Zhang Z, Yin X, Kvit A, Liao Q, Kang Z, Yan X, Zhang Y, Wang X (2017) *Nat Energy* 2:17045
34. Giddey S, Badwal SPS, Munnings C, Dolan M (2017) *ACS Sustain Chem Eng* 5:10231
35. Valera-Medina A, Xiao H, Owen-Jones M, David WIF, Bowen PJ (2018) *Prog Energy Combust Sci* 69:63
36. Zheng T, Jiang K, Wang H (2018) *Adv Mater* 30:1802066
37. Li R, Zhang W, Zhou K (2018) *Adv Mater* 30:1705512
38. Wang Y, Han P, Lv X, Zhang L, Zheng G (2018) *Joule* 2:2551
39. Zhang L, Zhao Z, Wang T, Gong J (2018) *Chem Soc Rev* 47:5423
40. AlOtaibi B, Fan S, Wang D, Ye J, Mi Z (2015) *ACS Catal* 5:5342
41. Chu S, Fan S, Wang Y, Rossouw D, Wang Y, Botton GA, Mi Z (2016) *Angew Chem Int Ed* 55:14262
42. Guo Y-G (2019) *Nanostructures and nanomaterials for batteries: principles and applications*. Springer, Singapore
43. Ellis BL, Knauth P, Djenizian T (2014) *Adv Mater* 26:3368
44. Liang L, Xu Y, Wang C, Wen L, Fang Y, Mi Y, Zhou M, Zhao H, Lei Y (2015) *Energy Environ Sci* 8:2954
45. Chabi S, Peng C, Hu D, Zhu Y (2014) *Adv Mater* 26:2440
46. Zhao H, Wang C, Vellacheri R, Zhou M, Xu Y, Fu Q, Wu M, Grote F, Lei Y (2014) *Adv Mater* 26:7654
47. Grote F, Lei Y (2014) *Nano Energy* 10:63
48. Yu Z, Tetard L, Zhai L, Thomas J (2015) *Energy Environ Sci* 8:702
49. Lei Z, Liu L, Zhao H, Liang F, Chang S, Li L, Zhang Y, Lin Z, Kröger J, Lei Y (2020) *Nat Commun* 11:299
50. Yu Z, Tetard L, Zhai L, Thomas J (2015) Supercapacitor electrode materials: nanostructures from 0 to 3 dimensions. *Energy Environ Sci* 8:702
51. Wang Y-M, Zhang X, Guo C-Y, Zhao Y-Q, Xu C-L, Li H-L (2013) *J Mater Chem A* 1:13290–13300
52. Deng M-J, Ho P-J, Song C-Z, Chen S-A, Lee J-F, Chen J-M, Lu K-T (2013) *Energy Environ Sci* 6:2178–2185
53. Zhou C, Zhang Y, Li Y, Liu J (2013) *Nano Lett* 13:2078–2085
54. Luo J, Jang HD, Huang J (2013) *ACS Nano* 7:1464–1471
55. Ma X, Liu J, Liang C, Gong X, Che R (2014) *J Mater Chem A* 2:12692–12696

56. Du F, Yu D, Dai L, Ganguli S, Varshney V, Roy AK (2011) *Chem Mater* 23:4810–4816
57. Kim S-I, Lee J-S, Ahn H-J, Song H-K, Jang J-H, *Appl ACS (2013) Mater Interfaces* 5:1596–1603
58. Xiao Y, Liu S, Li F, Zhang A, Zhao J, Fang S, Jia D (2012) *Adv Funct Mater* 22:4052–4059



# Algae Biofuel as a Substitute for Compression Ignition Engine: A Review



S. Charan Kumar, Amit Kumar Thakur, and J. Ronald Aseer

## 1 Introduction

Energy is an indispensable element for mankind to sustain global prosperity, in this regard crude oil has played an essential role. The transportation sector is utterly dependent on crude oil. Consumption of crude oil has continued to surge to date due to the climb in motor vehicles. Various toxic compounds are produced from engine emissions (particulate matter, CO, NO<sub>x</sub>, and unburnt hydrocarbons), which are perilous for the environment and human beings. Environmental degradation and crude oil dwindling are the main factors that need to be addressed quickly. If the above obstacles are not addressed severe environmental hazards will persist on living things. Millions of animals will become endangered and billions of humans will risk their lives if global temperature increments by 2 °C on average. Oil crisis, energy immoderate demand in transport sector led to analyze substitute for petro-diesel. Zero sulfate emissions, minimal toxicity, and biodegradable make biofuel (advantages and disadvantages in Table 1) a good swap for petro-diesel. Edible (first generation), non-edible (second generation), algal (third generation), modified algae (fourth generation) biomass are the categorization of biofuel based on their production and origin [1–4] (in Fig. 1). Biggest downside of edible biomass is the possibility of a clampdown in the food supply which leads to an increment in food products cost. The flaw of edible biomass has engaged investigators to focus on non-edible biomass. The upside and downside of non-edible biomass are it exterminates food inequality and low plant yield, land usage. It is foremost to identify biomass feedstock that can swap edible and non-edible biomass in biofuel production.

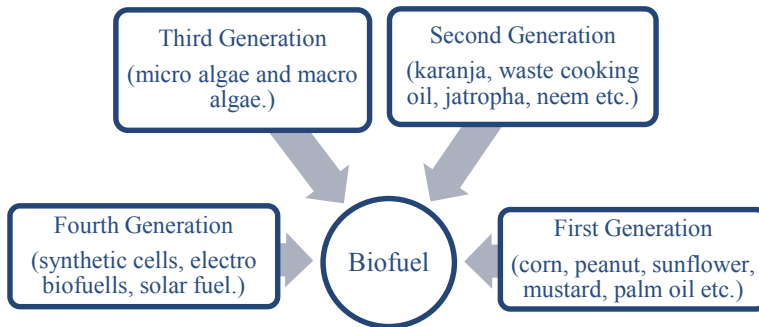
---

S. C. Kumar · A. K. Thakur (✉)  
Department of Mechanical, LPU, Phagwara, Punjab, India  
e-mail: [amit.25010@lpu.co.in](mailto:amit.25010@lpu.co.in)

J. R. Aseer  
Department of Mechanical, NIT Karaikal, Karaikal, Puducherry, India

**Table 1** Biofuel disadvantages and advantages

Disadvantages	Advantages
Viscosity is high	CO <sub>2</sub> emissions are low
No <sub>x</sub> emissions are high	Can be used as a lubricant
Less volatile	Flashpoint is high
Energy content is less	Non-toxic

**Fig. 1** Biofuels generations

## 2 Algae Biofuel

Algae are photosynthetic aquatic organisms, don't have vascular tissue, stems, leaves, roots, and are categorized into macro algae and microalgae [5–7]. Multicellular and large organisms are referred to as seaweeds or macro algae and are further divided depending on pigmentation, like red seaweed (*Rhodophyceae*), green seaweed (*Chlorophyceae*), brown seaweed (*Phaeophyceae*). Unicellular and small organisms are referred to as phytoplankton or microalgae. And these are further classified as blue-green algae (*Cyanophyceae*), yellow-green algae (*Xanthophyceae*), euglenoids (*Euglenophyceae*), golden-brown algae (*Chrysophyceae*), fire algae (*Phaeophyceae*). Till now only a few species have been analyzed for extraction of biodiesel from algae such as blue-green which includes *Azolla* [8–11], *Chlorella protothecoides* [12, 13], *spirulina* [14–16], etc. Green algae which includes *Botryococcus barauinii* [17–19], *Neochloris oleoabundans* [20, 21], *chlorella* variables [22], *Chlorella Vulgaris* [23–25], etc. Red algae which include *Melanothamnus afaqhusainii*, etc. Algae biodiesel extraction consists of four stages (in Fig. 2).

- Stage 1 Cultivation of algae [6, 26, 27].
- Stage 2 Algae harvesting [6, 28, 29].
- Stage 3 Algal oil extraction [6].
- Stage 4 Algal oil conversion to biodiesel [6].

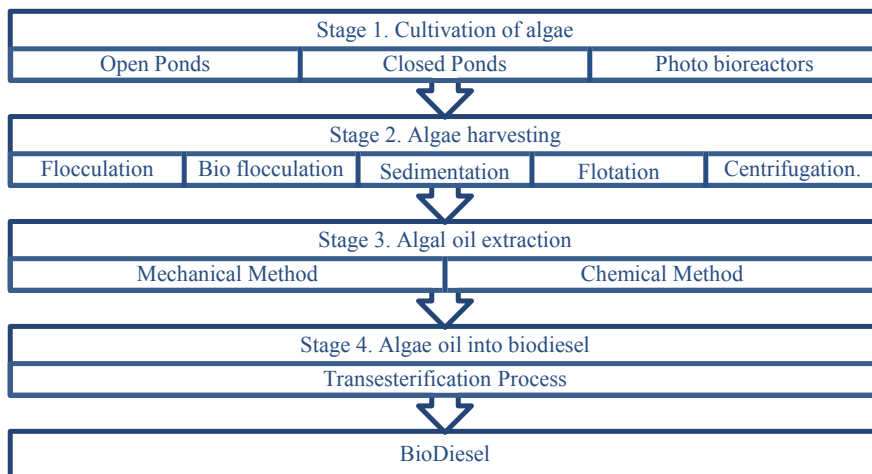


**Fig. 2** Stages for converting algae into biodiesel

## 2.1 Cultivation of Algae

Open ponds are shallow, oldest, simplest, and widely used microalgae cultivation on a larger scale and designed like a raceway. It consists of a paddlewheel which helps in mixing and circulating nutrients. The paddle wheel is run by a motor. Raceways are made from concrete or caved into the ground and covered with a plastic liner. Depth ranges from 15 to 45 cm. Algae that are cultivated in open ponds use photosynthesis to generate food. Advantages and disadvantages are given in Table 2.

Closed ponds are not revealed to atmospheric air and are covered with greenhouse. The growth and production of microalgae are more compared to open ponds. Larger cultivation due to the control environment. Contamination problems from other bacteria are eliminated in closed ponds. Operation and construction cost is high compared to open ponds. Photobioreactors are closed vessels that ensure a controlled environment that enables higher productivity. The major advantages of photobioreactors are evaporation and carbon dioxide losses are less when compared to open and closed ponds. Higher growth rates and efficiency are achieved by photobioreactors. The main disadvantage is its higher operating cost.

**Table 2** Advantages and disadvantages of open pond

Advantages	Disadvantages
Easy to construct	Evaporation losses
Operating cost is low	Contamination risk from other bacteria
Easy Maintenance	Cannot control the temperature

## 2.2 *Algae Harvesting*

It is one of the most adulterate processes and the cost for harvesting algae for biodiesel is high which accounts for 30% of the price of algal biomass. Harvesting is referred to as algae separation from the medium. Based on the algal type it is divided into two processes thickening and bulk harvesting. Thickening and bulk harvesting are further classified as centrifugation, electrical-based methods, flotation, sedimentation, bio-flocculation, flocculation. Above all the methods, the fastest one is centrifugation which employs centripetal force to separate and harvest cells and it is a continuous or semi-continuous process. The main downside is its operating cost. Gravitational force is employed in sedimentation which causes solid or liquid particles to detach from a liquid of dissimilar density. The sedimentation process is very slow. Chemical is added in the flocculation process to the mixture of algae and water which causes aggregation of algae and forms colloids. Ferric chloride and alum are the chemicals that are being used in this technique. In flotation air bubbles are being sent, so that algae can aggregate at the surface as a float. It requires chemical flocculants.

## 2.3 *Algae Oil Extraction*

It consists of two techniques mechanical and chemical techniques, and are further categorized as ultrasonic-assisted extraction, expeller press and supercritical fluid extraction, hexane solvent. In an expeller press, algae biomass is first dried and then dried biomass is pressed to extract oil. Only 70–80% of oil can be collected using this process. In ultrasonic-assisted, bubbles are created in a solvent by sending ultrasonic waves with the aid of an ultrasonic reactor. Bubbles cause the breakdown of algae cells which in turn release the oil. More effective than expeller press. In the hexane solvent process, biomass is first pressed and oil is extracted, hexane is mixed in leftover algae to extract the remaining oil. 95% oil can be collected by this method. Separating one element (extract) from another element (solvent) using a supercritical fluid such as carbon dioxide is referred to as supercritical fluid extraction. Up to 100% oil can be collected by this process. Through transesterification extracted oil is converted into biodiesel.

Environmental parameter plays a major role in growth and production of algae such as temperature, light intensity, pH, nutrients, and water evaporation rate [30, 31]. Biodiesel which is produced from algae is more volatile and its yield is more when compared with other biodiesel generations. In India very small amount of work is done on the extraction of biodiesel from algae and the use of algae as fuel for CI engines and extensive work is carried out on applications of microalgae in the pharmaceutical and food sector. Institutes working on algal biodiesel in India are shown in Table 3.

**Table 3** Institutes working in India on algal research

Name of the Institute	Biodiesel
Central Salt and Marine Chemicals Research Institute	Jatropha and algae
Fisheries College and Research Institute, Tuticorin Marine	Microalgae
Institute of Chemical Technology	Algal biohydrogen
Madras University	Algal biotechnology
Phycological Society of India	Algal research
The energy Research Institute	Algae
University of Delhi	Algae
University of Pune	Algae
Vivekananda Institute of Algal Technology	Microalgae
Madurai Kamraj University	Genetically-modified cyanobacteria

Advantages of algae:

- Eco-friendly.
- The non-requirement of farmland.
- Less water consumption.
- High yield, can grow in fresh, saline, and wastewater.

### 3 Emission and Performance Characteristics

Kannan et al. [8] has performed an investigation on water cooled diesel engine for knowing the feasibility of nano BaO blended *Azolla*. 20% by volume of *Azolla* was taken and blended in base fuel, termed as B20 and nano BaO of diverse composition 50, 100 ppm was in it. The study unveiled a downturn in CO, HC (in Figs. 3 and 4) and a rise in NO<sub>x</sub> emission for nano fuels.

Narayanaswamy et al. [10] has done observation on constant speed water cooled diesel engine. Nano TiO<sub>2</sub> of varied composition 100, 75, 50, 25 ppm was blended in *Azolla* biodiesel (B20). Authors revealed 13.38, 8.79, 8.49, 2.60% surge in BTE and 57.30, 54.80, 51.92, 21.15% deduce in CO and 12.97, 10.04, 8.36, 7.53 drop in HC for 100, 75, 50, 25 ppm nano blended fuel. Al-lwayzy et al. [12] evaluated chlorella protothecoides (B100, B50, B20) as a substitute for diesel on air cooled, 4-stroke engine. Rise in BSFC and surge in BTE for blends were illustrated. Rajak et al. [14] performed an experiment for knowing spirulina biodiesel feasibility on water cooled diesel engine. B100, B80, B60, B40, B20 are the varied composition of test fuel. As per the investigators BTE was 29.8, 30.1, 30.5, 30.9, 31.32, 32.3% and BSFC was 329, 321, 309, 304.1, 301, 291 g/kwh for B100, B80, B60, B40,

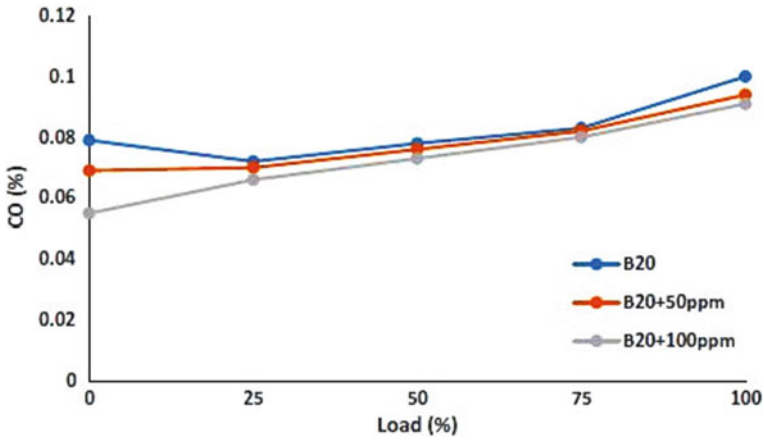


Fig. 3 CO versus load [8]

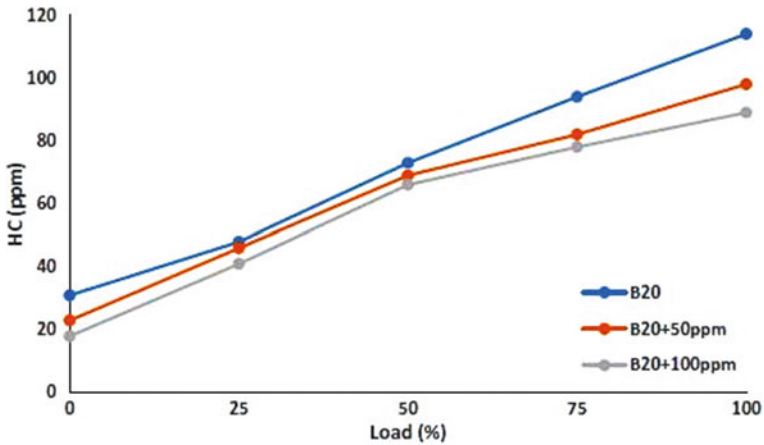


Fig. 4 HC versus load [8]

B20, B0 (in Fig. 5), diesel respectively. Rajak et al. [15] has investigated water cooled, 17.5:1 CR diesel engine in order to check the viability of spirulina (B100, B80, B60, B40, B20) by volume. Their study found SFC of diesel is lower and downturn in BTE for blends in comparison to diesel. SFC was 307.9, 296.4, 285.01, 273.85, 266.3, 252.27 g/kwh and BTE was 32.1, 32.5, 33.0, 33.18, 33.3, 33.51% for B100, B80, B60, B40, B20 and B0 respectively.

Karthikeyan et al. [18] performed experiments on a CRDI engine to know the feasibility of nano additive ( $La_2O_3$ ) and botryococcus barauinii (B20) blends. 50, 75, and 100 ppm were the compositions of nano additives. All the tests were carried out at a constant speed of 1500 rpm. The authors illustrated a drop in CO, HC, and

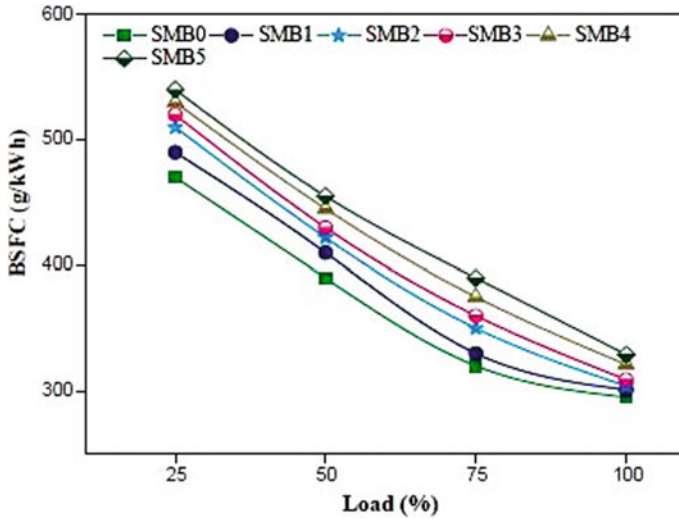


Fig. 5 BSFC versus load [14]

rise in  $NO_x$  for nano blends with increased dosage levels of additives. Karthikeyan et al. [19] experimented to know the viability of botryococcus braunii (B20) with fuel catalyst nano  $CeO_2$  of diverse proportion 100, 75, 50 ppm. Because of shorter ignition delay and complete combustion drop in CO and HC emissions was observed. Nirmala et al. [22] analyzed blends of waste cooking oil and chlorella variables biodiesel on a CI engine. Test fuels were W100, C100, C10W90,

Table 4 Investigations on emissions and performance

References	Biodiesel	Composition	Interpretation
Narayanasamy et al. [10]	<i>Azolla</i>	B20, B20 + $TiO_2$	BSFC, CO, HC deduced and rise in BTE, $NO_x$ on inclusion of $TiO_2$
Al-lwayzy et al. [12]	<i>Chlorella protothecoides</i>	B100, B50, B20	B100 found to be optimal blend. B100 deduced $NO_x$ and CO by 7.4 and 28% contrast to diesel
Rajak et al. [14]	<i>Spirulina</i>	B100, B80, B60, B40, B20	B20 was found to be optimal blend. For B20 $NO_x$ and BTE declined by 4.9 and 3.03% with respect to diesel
Nautiyal et al. [16]	<i>Spirulina</i>	B100, B20, B10	The optimal blend was B20. Less HC, CO and climb in $NO_x$ for blends
Karthikeyan et al. [18]	<i>Botryococcus braunii</i>	B20, B20 + $La_2O_3$	$NO_x$ rises and CO, HC declined on the addition of $La_2O_3$ when compared with B20
Kalaimurugan et al. [22]	<i>Neochloris oleoabundans</i>	B20, B20 + $CeO_2$	Upon addition of $CeO_2$ HC, CO deduced drastically
Mathimani et al. [25]	<i>Chlorella vulgaris</i>	B60, B50, B40, B30	BTE dwindled and climb in $NO_x$ for all blends

C20W80, C50W50, and C70W30. The authors conclude that W100 has better BTE, BSFC compared to C100. Waste cooking oil-chlorella variables blends emitted lesser CO, and HC concerning diesel which was in the range of 53.8–60.3%, and 85.86–86.72% respectively. The effect of algal biofuel on emissions and performance is shown in Table 4.

## 4 Conclusion

On the whole, it is concluded that high productivity and low land requirement make algae biofuel as a good swap for fossil fuels. Algae consume CO<sub>2</sub> and have the ability to cut down CO<sub>2</sub> up to 50–60% in contrast to diesel. The research on algae biofuels is in the early stages. More research is needed to achieve high yields and more cost-effective production processes for third-generation biofuels. The majority of the study is performed in blue-green algae (*Azolla, spirulina*) and green algae (*B. barauinii, N. oleoabundans, C. Vulgaris*) species regarding biodiesel production. Algal biofuel blends (B10 to B30) are ideal for enhancing engine performance and deduce emissions.

## References

1. Dwivedi G, Sharma MP (2014) Potential and limitation of straight vegetable oils as engine fuel—An Indian perspective. *Renew Sustain Energy Rev* 33:316–322
2. Dwivedi G, Sharma MP (2014) Prospects of biodiesel from Pongamia in India. *Renew Sustain Energy Rev* 32:114–122
3. Dwivedi G, Sharma MP (2015) Investigation and improvement in cold flow properties of Pongamia biodiesel. *Waste Biomass Valor* 6(1):73–79
4. Dwivedi G, Sharma MP (2014) Impact of cold flow properties of biodiesel on engine performance. *Renew Sustain Energy Rev* 31:650–656
5. Peng L, Fu D, Chu H, Wang Z, Qi H (2020) Biofuel production from microalgae: a review. *Environ Chem Lett* 18:285–297
6. Mata TM, Martins AA, Caetano NS (2010) Microalgae for biodiesel production and other applications: a review. *Renew Sustain Energy Rev* 14:217–232
7. Shuba ES, Kifle D (2018) Microalgae to biofuels: ‘Promising’ alternative and renewable energy, review. *Renew Sustain Energy Rev* 81:743–755
8. Kannan D, Christraj W (2018) Emission analysis of Azolla methyl ester with BaO nano additives for IC engine. *Energy Sources, Part A: Recov Util Environ Effects* 40:1234–1241
9. Venkatraman V, Sugumar S, Sekar S, Viswanathan S (2019) Environmental effect of CI engine using microalgae biofuel with nano-additives. *Energy Sources, Part A: Recov Util Environ Effects* 41:2429–2438
10. Narayanasamy B, Jeyakumar N (2019) Performance and emission analysis of methyl ester of Azolla algae with TiO<sub>2</sub> Nano additive for diesel engine. *Energy Sources, Part A: Recov Util Environ Effects* 41:1434–1445
11. Kannan D, Christraj W (2018) Emission analysis of Azolla methyl ester with Bi<sub>2</sub>O<sub>3</sub> nano additives for IC engine. *Energy Sources, Part A: Recov Util Environ Effects* 40:1183–1189



12. Gaur A, Mishra S, Chowdhury S, Baredar P, Verma P (2020) A review on factor affecting biodiesel production from waste cooking oil: an Indian perspective. *Mater Today Proc*
13. Satputaley SS, Zodpe DB, Deshpande NV (2017) Performance, combustion and emission study on CI engine using microalgae oil and microalgae oil methyl esters. *J Energy Inst* 90 (4):513–521
14. Rajak U, Nashine P, Verma TN (2020) Effect of spirulina microalgae biodiesel enriched with diesel fuel on performance and emission characteristics of CI engine. *Fuel* 268:117305
15. Rajak U, Nashine P, Verma TN (2019) Assessment of diesel engine performance using spirulina microalgae biodiesel. *Energy* 166:1025–1036
16. Nautiyal P, Subramanian KA, Dastidar MG, Kumar A (2020) Experimental assessment of performance, combustion and emissions of a compression ignition engine fuelled with *Spirulina platensis* biodiesel. *Energy* 193:116861
17. Karthikeyan S, Dharma Prabhakaran T (2018) Emission analysis of *Botryococcus braunii* algal biofuel using Ni-Doped ZnO nano additives for IC engines. *Energy Sources, Part A: Recov Util Environ Effects* 40:1060–1067
18. Karthikeyan S, Dharma Prabhakaran T, Prathima A (2018) Environment effect of  $\text{La}_2\text{O}_3$  nano-additives on microalgae-biodiesel fueled CRDI engine with conventional diesel. *Energy Sources, Part A: Recov Util Environ Effects* 40:179–185
19. Karthikeyan S, Prathima A (2017) Microalgae biofuel with  $\text{CeO}_2$  nano additives as an eco-friendly fuel for CI engine. *Energy Sources, Part A: Recov Util Environ Effects* 39:1332–1338
20. Karthikeyan S, Prathima A (2017) *Neochloris oleoabundans* microalgae oil as a fuel for diesel engines *Energy Sources, Part A: Recov Util Environ Effects* 39:606–612
21. Kalaimurugan K, Karthikeyan S, Periyasamy M, Mahendran G (2020) Emission analysis of CI engine with  $\text{CeO}_2$  nanoparticles added *neochloris oleoabundans* biodiesel-diesel fuel blends. *Mater Today: Proc*
22. Nirmala N, Dawn SS, Harindra C (2020) Analysis of performance and emission characteristics of waste cooking oil and *Chlorella variabilis* MK039712.1 bio-diesel blends in a single cylinder, four strokes diesel engine. *Renew Energy* 147:284–292
23. Thirugnanasambantham R, Elango T, Elangovan K (2020) *Chlorella vulgaris* sp. microalgae as a feedstock for biofuel. *Mater Today: Proc*
24. Tayari S, Abedi R (2019) Effect of *Chlorella vulgaris* methyl ester enriched with hydrogen on performance and emission characteristics of CI engine. *Fuel* 256:115906
25. Mathimani T, Senthil Kumar T, Chandrasekar M, Uma L, Prabaharan D (2017) Assessment of fuel properties, engine performance and emission characteristics of outdoor grown marine *Chlorella vulgaris* BDUG 91771 biodiesel. *Renew Energy* 105:637–646
26. Singh RN, Sharma S (2012) Development of suitable photobioreactor for algae production—a review. *Renew Sustain Energy Rev* 16:2347–2353
27. Kumar K, Mishra SK, Shrivastav A, Park MS, Yang JW (2015) Recent trends in the mass cultivation of algae in raceway ponds. *Renew Sustain Energy Rev* 51:875–885
28. Milledge JJ, Heaven S (2013) A review of the harvesting of micro-algae for biofuel production. *Rev Environ Sci Biotechnol* 12:165–178
29. Barros AI, Gonçalves AL, Simões M, Pires JCM (2015) Harvesting techniques applied to microalgae: a review. *Renew Sustain Energy Rev* 41:1489–1500
30. Schnurr PJ, Allen DG (2015) Factors affecting algae biofilm growth and lipid production: a review. *Renew Sustain Energy Rev* 52:418–429
31. Singh SP, Singh P (2015) Effect of temperature and light on the growth of algae species: a review. *Renew Sustain Energy Rev* 50:431–444

# Economic Growth in Maharashtra and India with Particular Reference to Electricity Consumption



Anand Vijay Satpute and E. Vijay Kumar

## 1 Introduction

Electricity is considered as the supreme and competent form of energy that is greatly responsible for the overall progress of the economy. The electricity supply–demand is swiftly rising with a cumulative population and industrial development. Its importance is evident in the policy circle as well. To satisfy the energy demand of an emerging economy and developing nation, India’s power sector has seen a fast growth [1]. With the vision of “Electricity to Everyone,” the Government of India (GoI) launched “Saubhagya” scheme in 2017 meant to offer power to all houses situated in rural areas [2]. To reduce the technological glitches and commercial problems that are affecting the power industry, numerous strategies and reforms have been made since 1992 [3]. Maharashtra is particularly shortlisted for the study as it is the foremost state which is having high perspective of fast growth in future. With good climate throughout the year and transport connectivity, the state attracts the most investment from foreign and local capital investors. For constant fiscal growth, it is essential to study the trend of electricity use by different sectors in aggressively developing state like Maharashtra. The gross domestic product (GDP) of Maharashtra for 2018–19 was 6% and is projected be 9.3% in future, with agriculture sector rising by 13%, industries up with 31%, and service increasing through 56% [4], with all are at balance with national growth rates of 6.1%, 15.4%, 23%, and 61.5%, respectively [5, 6]. Maharashtra has a vast population of about 11.2 crore people which is 9.3% of India’s total population [7, 8]. In the scenario of a high number of people shifting from the rural area to urban cities for employment, constant and reliable power supply plays a vital role in economic growth. Consequently, the research paper examined electricity consumption pattern in Maharashtra and linked it with the country. The analysis aims to explore the

---

A. V. Satpute (✉) · E. V. Kumar  
Department of Electrical Engineering, Sarvepalli Radhakrishnan University, Bhopal,  
Madhya Pradesh 462026, India

electricity picture over time in state and recommends specific directions to eliminate power shortage.

## 2 Electricity Generation

Growth in energy is the most significant building block and intrinsically acts as an important link in determining the financial enlargement of all of the countries. Electricity generation sector has seen a fast progress to meet the requirements of a hugely populated nation like India [9]. Coal usage as fuel was highest which accounts for maximum energy generation. Industrial, domestic, and transport sectors were on forefront for the consumption of energy. Figure 1 shows the electricity generation progress. Installation capacity growth rate remains in 4–6% bracket [3].

## 3 Non-conventional Energy

Coal is the major fuel for energy. Non-conventional power percentage share in overall electricity generation remains more than 60% till 2019 from 1992 [10]. GoI is shifting its dependence on coal power to cleaner energy as committed to the Paris agreement, United Nations Framework Convention on Climate Change [11], and reduce carbon emission [12]. Installation capacity rises from 274,904.37 MW in year the 2015 to 370,047.97 MW in the starting of the year 2020. Maharashtra is the aggressor in revolutionizing industries and allied sectors, and economic

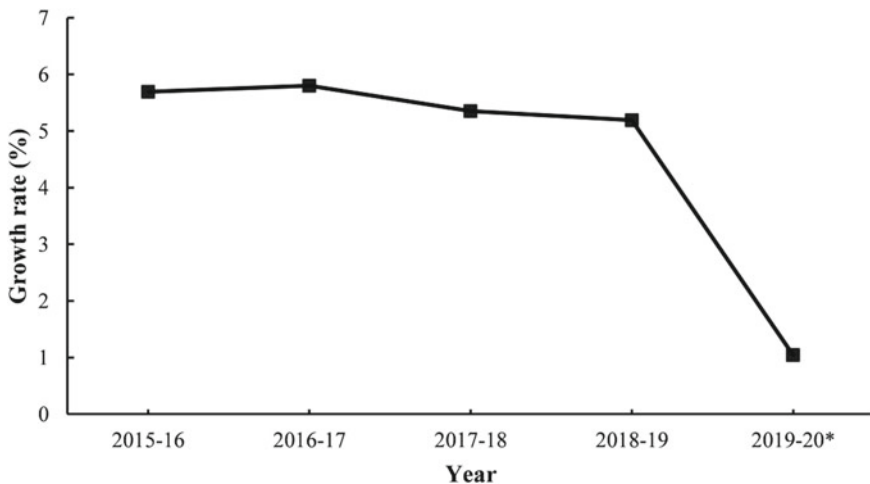


Fig. 1 Electricity generation growth rate [3] (\*Provisional)

development in the country contributes 10% power to India’s overall generation [13–17]. Figure 2 shows the installation capacity added from 2015 to 2020. Keeping the GoI green energy target [18], the percentage share of energy generation from coal power thermal plant is gradually reduced and can be observed from Fig. 3.

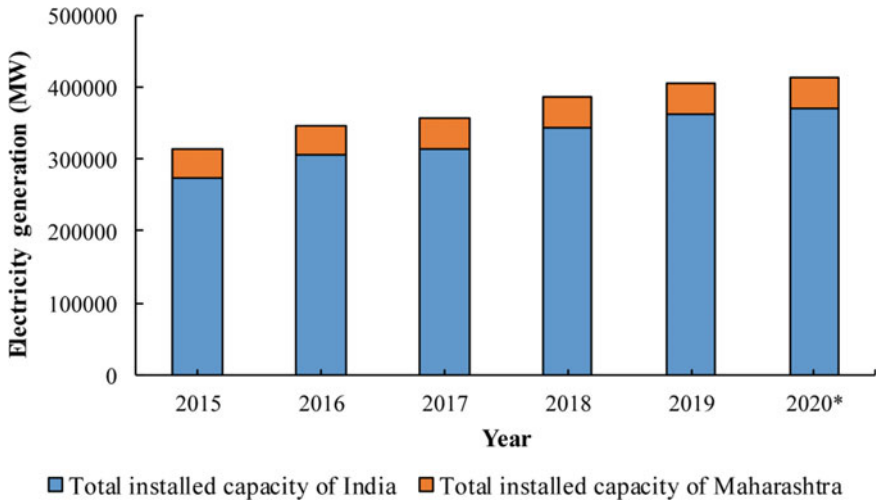


Fig. 2 Installed capacity of India and Maharashtra [13–17] (\*Till March 31, 2020)

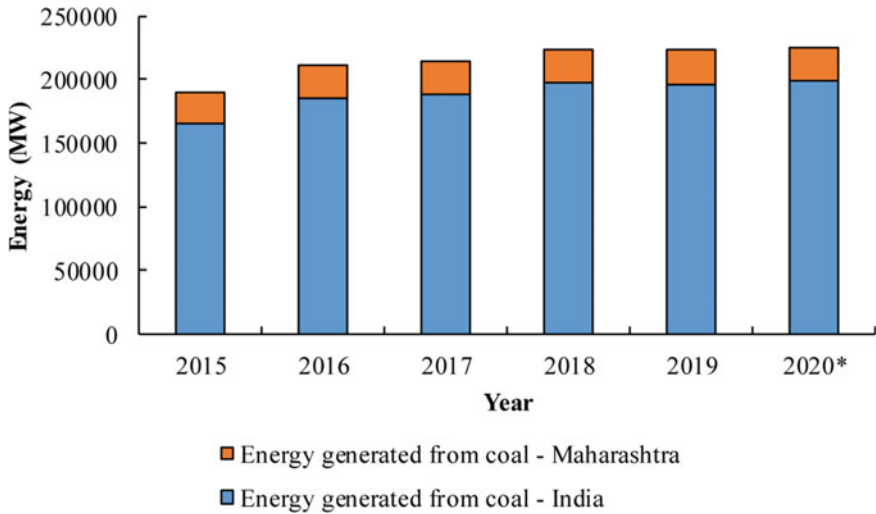


Fig. 3 Contribution of coal to energy generation—India and Maharashtra [13–17] (\*Till March 31, 2020)

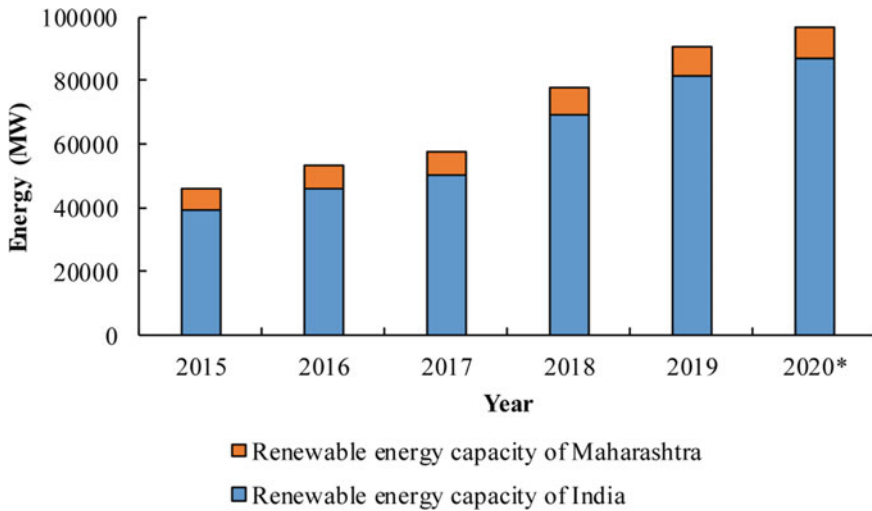


Fig. 4 Renewable energy growth [13–17] (\*Till March 31, 2020)

## 4 Renewable Energy

To reduce carbon footprint and its effect on the global climate, the international energy agency has recognized the advancement of sustainable energy [19, 20] and has projected India to be a front-runner in energy demand [19]. GoI is gradually moving in the direction of accomplishing its green and clean energy target by the year 2030 [21] by generating more power from renewable rather than conventional sector. India's clean energy sector share to overall power contribution has risen to 23% in 2020 (March 31, 2020) from 14% in 2015 [13–17]. In the case of Maharashtra, renewable energy growth is gradually increasing. Its installed capacity has seen rapid growth from 6987.83 MW in 2015 to 9710.4 MW in 2020 (March 31, 2020). Figure 4 demonstrates the combined growth of renewable energy in India and Maharashtra.

## 5 Rural Electrification

GoI aims at electrifying each households (HHs) situated in rural villages and areas far away from urban towns. Deendayal Upadhyaya Gram Jyoti Yojana (DDUGJY) in 2015 [22] and Saubhagya in 2017 [2] were the schemes started by the authorities aimed at complete electrification across the country and state that household in every urban and rural region must be electrified. As given in Table 1, electrification status in India and going by current growth 100% HHs electrification will be achieved by the end of year 2021. Table 2 indicates the status of electrification in

**Table 1** Status of HHs electrification, India [26]

Description	2001	2011
Total numbers of HHs	191,963,935	246,740,228
Total numbers of HHs electrified	107,209,054	165,935,192
Percentage	55.8	67.25
Total numbers of rural HHs	138,271,559	167,874,291
Total numbers of rural HHs electrified	60,180,658	92,845,936
Percentage	43.5	55.31
Total numbers of urban HHs	53,692,379	80,888,766
Total numbers of urban HHs electrified	47,026,369	73,089,256
Percentage	87.6	92.68

**Table 2** Status of HHs electrification, Maharashtra [26]

Description	2001	2011
Total numbers of HHs	19,063,149	23,830,580
Total numbers of HHs electrified	14,773,940	20,004,164
Percentage	77.5	83.9
Total numbers of rural HHs	10,993,623	13,016,652
Total numbers of rural HHs electrified	7,167,842	9,605,299
Percentage	65.2	73.7
Total numbers of urban HHs	8,069,526	10,813,928
Total numbers of urban HHs electrified	7,609,563	10,398,865
Percentage	94.3	96.1

Maharashtra and its way ahead that of national percentage in terms of rural HHs electrified. According to the latest report available, 100% rural electrification is achieved [23]. Rural electrification is most important as it expands people's capabilities [24]. As agriculture is the main occupation in India, the electrification of rural areas directly contributes in increase of farming yields [25] thereby contributing to the overall economic growth of the country.

## 6 Electricity Consumption

As India is a majorly agriculture-driven economy [27] and lately due to the industrial revolution, the major energy is consumed by these two sectors [28]. As the energy demand per capita is increasing with the population as shown in Fig. 5, it is important to meet the energy demand of various sectors [29]. As per the report published by the Department of Statistics, GoI, the industrial sector takes the biggest share for energy consumption followed by the domestic and agriculture

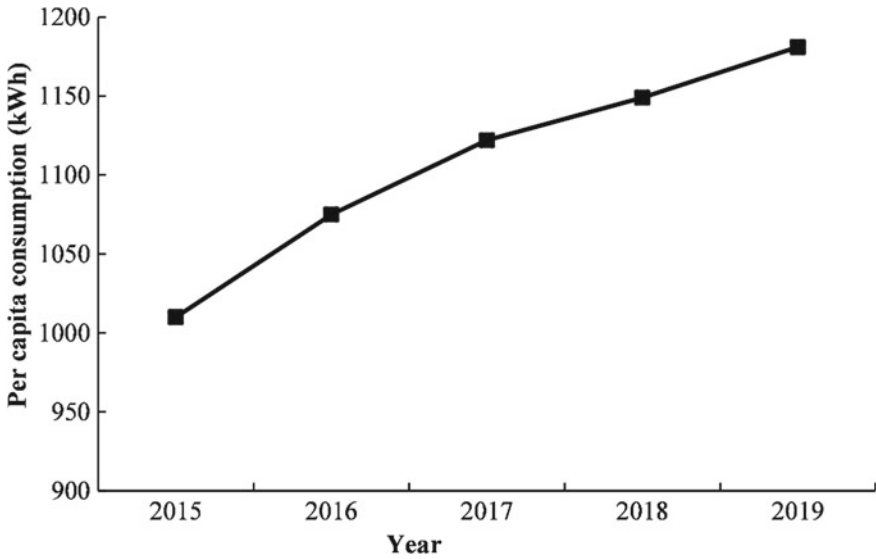


Fig. 5 Energy consumption [29]

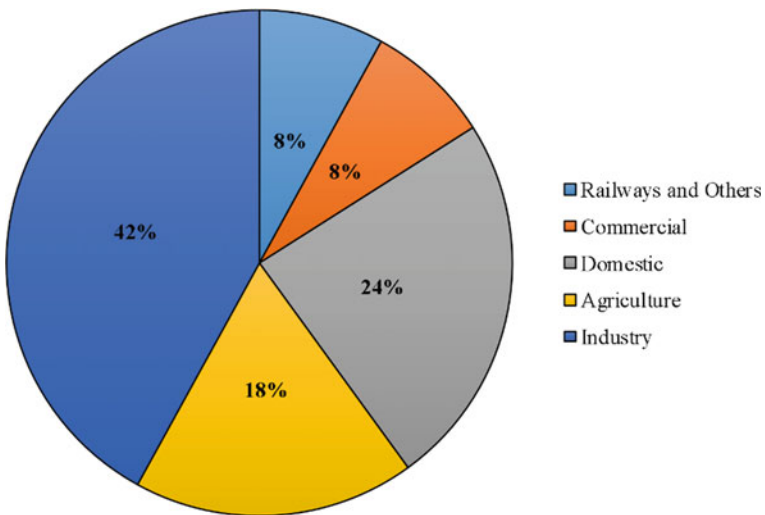


Fig. 6 Sector-wise energy consumption in India [30]

sectors during 2018–19 [30]. Sector-wise consumption is shown in Fig. 6. It is seen that energy rise in generation and installation capacity is mainly driven by industrial growth.

Maharashtra being the geographically blessed state is pioneering the development of agriculture and the industrial and allied sectors in the country. Its energy usage pattern is the same as that of a national trend, agriculture, and industrial being

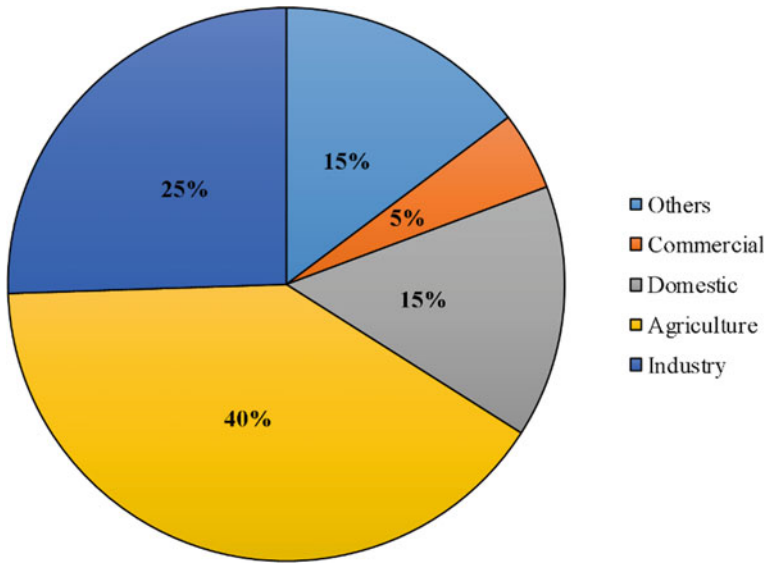


Fig. 7 Sector-wise energy consumption in Maharashtra [31]

the largest consumers for the same considered period as shown in Fig. 7 [31]. The only difference is that the agriculture sector is the biggest consumer as it is the backbone of Maharashtra’s economy. Further, it can be observed that other sectors which include government hospitals, schools, offices, and domestic sector share the same percentage of energy consumption.

## 7 Economics

As per the reports released by International Monetary Fund, India is one of the finest growing economies in Asia and the world [32]. India was the most progressively growing key economy globally from 2014 to 2018 surpassing China with GDP growth rate of 7% [33]. Two-third of the country’s GDP is dominated by domestic and industrial consumption. India ranks second in agriculture food production with an export of more than \$35 billion [34]. With its large workforce, IT sector is one of the biggest sectors in the country and with its services has generated revenue more than \$180 billion [35]. In comparison, Maharashtra’s economy leads the country [36] with 6% GDP growth for 2018–19 [4]. Although agriculture is accepted as a major occupation [37], the state is also a key contributor in industries with a share of 13% in the country’s industrial output. Industries contribute almost 46% to the state GDP [38]. Mumbai, the capital of Maharashtra, also known as the finance capital of India is home to Asia’s oldest and largest stock exchange. Almost all the major multinational companies and national banks, insurance companies,



**Table 3** Sector-wise GDP of India and Maharashtra [4, 5]

GDP by sector	India	Maharashtra
Agriculture (%)	15.4	13
Industry (%)	23	31
Services (%)	61.5	56

and mutual funds have headquarters and corporate offices located in Mumbai [39]. The association of India's and Maharashtra's GDP is given in Table 3. It is clear that Maharashtra dominates the nation's economy in all sectors leading from agriculture to industrial and financial institutions.

## 8 Conclusion

In this study, the electricity generation scenario in India and Maharashtra and its consumption pattern have been studied. Maharashtra mirrors the national trend. The energy consumption pattern by different sectors also supports the same. The country's GDP growth rate and the state's GDP growth rate have a close association with each other. The state share in national power generation is more than 10%, and its renewable power contribution is 11% which supports GoI vision of clean energy. The energy share is increasing with its growing population. The government of Maharashtra along with the national scheme of electrification has 100% electrified all the households in rural villages. Running of solar pump and solar home lighting scheme, it has improved the agricultural yield and living standard of the people present in villages. As agriculture is still the main occupation for living in Maharashtra, easy availability of electricity has improved the farm output and thus contributed to the national growth of GDP. Industries and allied sectors have created more employment in Maharashtra than any other state in the country. Industrial sector growth drives the national economy as it remains a major contributor for it followed by agriculture. Maharashtra is the leader in all the departments from the country's GDP to its target of clean energy generation, rural electrification, agriculture, and industries. Its development and inclination define the national picture.

## References

1. Government of India, Ministry of Statistics and Programme Implementation Energy statistics 2020, pp 1–117
2. Ministry of Power. <https://saubhagya.gov.in/>. Last accessed 2020/12/29
3. Ministry of Power. <https://powermin.nic.in/en/content/about-ministry>. Last accessed 2020/12/29
4. PRS Legislative Research. Maharashtra budget analysis 2020–21. <https://www.prsindia.org/parliamenttrack/budgets/maharashtra-budget-analysis-2020-21>. Last accessed 2020/12/29

5. Central Intelligence Agency. The World Factbook, India. <https://www.cia.gov/the-world-factbook/static/265961bcafce29e6b74fd3ffd37b56a0/IN-summary.pdf>. Last accessed 2020/12/29
6. International Monetary Fund. World economic outlook database. <https://www.imf.org/en/Countries/IND>. Last accessed 2020/12/29
7. UNICEF Annual Report 2013—India. [https://www.unicef.org/about/annualreport/files/India\\_COAR\\_2013.pdf](https://www.unicef.org/about/annualreport/files/India_COAR_2013.pdf). Last accessed 2020/12/29
8. Size, growth rate and distribution of population. [https://censusindia.gov.in/2011-prov-results/data\\_files/india/final\\_ppt\\_2011\\_chapter3.pdf](https://censusindia.gov.in/2011-prov-results/data_files/india/final_ppt_2011_chapter3.pdf). Last accessed 2020/12/29
9. Government of India, Central Statistics Office, Ministry of Statistics and Programme Implementation Energy statistics 2019, pp 1–123
10. Lahiri-Dutt K (2016) The diverse worlds of coal in India: Energising the nation, energising livelihoods. *Energy Policy* 99:203–213
11. Gi K, Sano F, Akimoto K, Hiwatari R, Tobita K (2020) Potential contribution of fusion power generation to low-carbon development under the Paris Agreement and associated uncertainties. *Energy Strat Rev* 27(2020):100432
12. Wang Z, Meng J, Zheng H, Shao S, Wang D, Mi Z, Guan D (2018) Temporal change in India's imbalance of carbon emissions embodied in international trade. 231:914–925
13. Central Electrical Authority. Monthly report, 2016. [http://www.cea.nic.in/reports/monthly/executivesummary/2016/exe\\_summary-03.pdf](http://www.cea.nic.in/reports/monthly/executivesummary/2016/exe_summary-03.pdf). Last accessed 2020/12/29
14. Central Electrical Authority. Monthly report, 2017. [http://www.cea.nic.in/reports/monthly/executivesummary/2017/exe\\_summary-02.pdf](http://www.cea.nic.in/reports/monthly/executivesummary/2017/exe_summary-02.pdf). Last accessed 2020/12/29
15. Central Electrical Authority. Monthly report, 2018. [http://www.cea.nic.in/reports/monthly/executivesummary/2018/exe\\_summary-02.pdf](http://www.cea.nic.in/reports/monthly/executivesummary/2018/exe_summary-02.pdf), last accessed 2020/12/29
16. Central Electrical Authority. Monthly report, 2019. [http://www.cea.nic.in/reports/monthly/executivesummary/2019/exe\\_summary-02.pdf](http://www.cea.nic.in/reports/monthly/executivesummary/2019/exe_summary-02.pdf). Last accessed 2020/12/29
17. Central Electrical Authority. Monthly report, 2020. [http://www.cea.nic.in/reports/monthly/installedcapacity/2020/installed\\_capacity-03.pdf](http://www.cea.nic.in/reports/monthly/installedcapacity/2020/installed_capacity-03.pdf). Last accessed 2020/12/29
18. United Nations Treaty Collection. Paris agreement. [https://treaties.un.org/Pages/ViewDetails.aspx?src=IND&mtdsg\\_no=XXVII-7-d&chapter=27&clang=\\_en](https://treaties.un.org/Pages/ViewDetails.aspx?src=IND&mtdsg_no=XXVII-7-d&chapter=27&clang=_en). Last accessed 2020/12/29
19. India Energy Outlook. <https://www.iea.org/reports/india-2020>. Last accessed 2020/12/29
20. Nazir MS, Mahdi AJ, Bilal M, Sohail HM, Ali N, Iqbal HM (2019) Environmental impact and pollution-related challenges of renewable wind energy paradigm—a review. *Sci Tot Environ* 683:436–444
21. Eren BM, Taspinar N, Gokmenoglu KK (2019) The impact of financial development and economic growth on renewable energy consumption: empirical analysis of India. *Sci Tot Environ* 663:189–197
22. Ministry of Power. Launch of DUGJY. <http://pib.nic.in/newsite/PrintRelease.aspx?relid=123595>. Last accessed 2020/12/29
23. Rural electrification status. <http://garv.gov.in/dashboard>. Last accessed 2020/12/29
24. Ray S, Naylor RL (2019) Rural electrification in agricultural intensification across India. In: AGUFM 2019: GC43H-1409
25. Malakar Y (2018) Evaluating the role of rural electrification in expanding people's capabilities in India. *Energy Policy* 114:492–498
26. Census of India 2011. <http://censusindia.gov.in/2011census/Hlo-series/HH11.html>. Last accessed 2020/12/29
27. Singh P, Agrawal G (2020) Development, present status and performance analysis of agriculture insurance schemes in India. *Int J Soc Econ*
28. Wang Q (2020) Comparative analysis of drivers of energy consumption in China, the USA and India: a perspective from stratified heterogeneity. *Sci Tot Environ* 698:134117
29. Central Electricity Authority. Growth of electricity sector in India from 1947–2019. [https://cea.nic.in/wp-content/uploads/pdm/2020/12/growth\\_2020.pdf](https://cea.nic.in/wp-content/uploads/pdm/2020/12/growth_2020.pdf). Last accessed 2020/12/29
30. Government of India, Ministry of Statistics and Programme Implementation, Energy Statistics 2020

31. State energy calculator. <https://www.mahadiscom.in/daily-power-position/>. Last accessed 2020/12/29
32. International Monetary Fund\_India. <https://www.imf.org/en/Countries/IND>. Last accessed 2020/12/29
33. World Economic Outlook. <https://www.imf.org/en/Publications/WEO/Issues/2018/09/24/world-economic-outlook-october-2018>. Last accessed 2020/12/29
34. Business Standard. India: an agricultural powerhouse of the world. [https://www.business-standard.com/article/b2b-connect/india-an-agricultural-powerhouse-of-the-world-116051800253\\_1.html](https://www.business-standard.com/article/b2b-connect/india-an-agricultural-powerhouse-of-the-world-116051800253_1.html). Last accessed 2020/12/29
35. NASSCOM. Annual report 2018–19. [https://nasscom.in/sites/default/files/NASSCOM\\_Annual\\_Report\\_2018-19.pdf](https://nasscom.in/sites/default/files/NASSCOM_Annual_Report_2018-19.pdf). Last accessed 2020/12/29
36. Government of Maharashtra, Planning Department, Directorate of Economy and Statistics, Economic survey of Maharashtra 2019–20
37. De Roy S. Ind J Agri Econ Econ Polit Weekly 52(9):67–72
38. IBEF. Maharashtra state. [https://www.ibef.org/download/Maharashtra\\_271211.pdf](https://www.ibef.org/download/Maharashtra_271211.pdf). Last accessed 2020/12/29
39. Rawal P (2015) Indian stock market and investors strategy, 16 April 2015, pp 12. ISBN 978-1-5053-5668-7

# Analysis of Centrifugal Pump Impeller Guide Vane by Using CFD Technique with Different Materials



Seshaiah Turaka, P. Chiranjeevi, K. Vijaya Kumar Reddy, and Satishkumar

## 1 Introduction

Comprehensive simulation of the centrifugal pump impeller guide vane has been made possible by developments in the field of computational fluid dynamics and measurable demonstrating alongside elite PC frameworks. A siphon is a mechanical framework expected to move a liquid from a lower to a higher position or from a lower to a higher weight zone. The siphon would be provided with mechanical energy and afterward changed over to pressure driven liquid energy. At bay weight, siphons make negative weight with the end goal that the pneumatic stress powers the liquid into the pump [1, 2]. The liquid coming into the siphon is pushed toward the source precisely where positive weight is created. Siphons are arranged in number of the ways dependent on their motivation, determinations, plan, climate, etc. [3]. The liquid enters the siphon impeller along or close to the pivoting hub and is quickened by the impeller, streaming radially outward or pivotally into a diffuser or volute chamber, from where it exits into the downstream funneling framework. Radiating siphons are commonly utilized for enormous release through more modest heads [1, 4]. At the point when the source edge point is expanded from 20° to 50°, the head is expanded by over 6%; however, the pressure driven effectiveness was diminished by 4.5%. Nonetheless, at high stream rates, the expansion of the source sharp edge point caused a critical improvement of the water driven efficiency [5]. The inward stream fields and qualities of the radial siphons with various In noncavitation and cavitation conditions, edge numbers are reproduced and extended utilizing CFD [6]. The pivotal composite impeller was fabricated utilizing different

---

S. Turaka (✉) · P. Chiranjeevi (✉) · Satishkumar (✉)  
Department of Mechanical Engineering, QIS College of Engineering and Technology,  
Ongole 523272, India

K. V. K. Reddy  
Department of Mechanical Engineering, JNTU College of Engineering,  
Hyderabad 500085, India

Kevlar 49, carbon and S-glass fortified epoxy grid composite materials. It is broke down as a static and transient examination for the diverse working rates of the impeller, and the redirection and stress focus districts of the predefined materials are analyzed [7]. The stream recreation of the radiating siphon impeller was tried utilizing ANSYS-CFX [8]. To quicken the siphon plan process [8, 9], the convoluted interior streams in water siphon impellers that are not notable can be very much anticipated with the guide of the CFD approach. The static and dynamic investigation of a radiating siphon impeller made of three diverse amalgam materials (i.e., Inconel combination 740, Inconel compound 803 and Waspaloy) was examined to rough its performance [10].

Based on the exhaustive literature, no author has been to study the comparative analysis on the static, model and CFD analysis is performed on the different models of the centrifugal impeller of a single-stage pump by changing the vane angles  $12^\circ$ ,  $14^\circ$  and  $18^\circ$  of the impeller, which is made up of stainless steel, aluminum metal matrix composite and Kevlar 49. To determine stresses, strains deformations and frequencies by applying the rotational velocity of fluid for different models of the centrifugal impeller by using ANSYS-CFD. As a result of these performance, curve becomes smoother and flatter with the increase outlet blade angle at  $14^\circ$  with Kevlar 49.

## 2 Materials

Commercially available stainless steel, aluminum metal matrix composite and Kevlar 49: from Tirven ventures Pvt Ltd., Balanagar, and Hyderabad. Stainless steel contains carbon as the primary alloying component, and it is containing 0.4% of silicon and 1.2% of manganese. Molybdenum, chromium, nickel, copper and aluminum are available in little amounts. The light weight and toughness qualities of evaluation of aluminum metal matrix composite are exceptionally utilized in the car, airplane and aviation industries. Kevlar 49 is containing a combination of Kevlar, and other compound components have high elasticity and durability (even at extraordinary temperatures). They are light in weight and have phenomenal erosion obstruction and the capacity to withstand outrageous temperatures [11]. The itemized mechanical properties of chosen materials are in Table 1.

**Table 1** Mechanical properties of materials

Materials	Young's modulus (MPa)	Tensile strength (MPa)	Poisson's ratio	Density (kg/mm <sup>3</sup> )
Stainless steel	700,000	690	0.29	0.00000785
Aluminum MMC	71,700	280	0.33	0.00000028
KEVLAR 49	110,000	862	0.31	0.000000450

### 3 Computational Tools

#### 3.1 *Modeling and Analysis*

CATIA offers the occasion to 3D picture ventures. This thought was progressive when it was executed. Since Dassault Systems had no advertising experience, they had a connection with IBM to share income, which demonstrated exceptionally productive for the two organizations to sell CATIA. CATIA was utilized intensely in the development of the Mirage airplane in the beginning phases; however, the product's potential immediately made it a typical choice in the car business also. Dassault adjusted the item assignment from CAD/CAM applications to Project Lifecycle Management, when CATIA was grasped by increasingly fabricating firms. The association has broadened the product's scope. [12]. ANSYS is a product bundle for universally useful limited component investigation. Finite element analysis (FEA) is a computational strategy for deconstructing a confounded structure into little parts called segments (of client assigned size). The program applies and settles all conditions that control the conduct of these segments, making a nitty gritty portrayal of how the framework functions overall. It is then conceivable to show this information in arranged or graphical manners. For the design and improvement of a framework too muddled to even think about studying by hand, this technique for examination is generally utilized. Because of their calculation, size, or overseeing equations [13], structures that could fall into this classification are excessively muddled. ANSYS is the fundamental FEA showing instrument at a few universities inside the Department of Mechanical Engineering. In common and electrical designing, just as in the Physics and Chemistry offices, ANSYS is likewise utilized.

#### 3.2 *Centrifugal Pump Impeller*

The fundamental element of a diffusive siphon is the impeller. It is comprised of a bunch of vanes which are blended. These are typically sandwiched between two circles (an enclosed impeller). In Fig. 1a–c separately, an open or semi-open impeller (upheld by a solitary circle) is picked for liquids with solids. Liquid joins the impeller at its pivot (the 'eye') and exits between the vanes around the circuit. In the contrary side of the eye, the impeller is appended to an engine by a drive shaft and turned at rapid (regularly 500–5000 rpm). The impeller's rotational movement quickens the liquid through the siphon packaging through the impeller vanes.



**Fig. 1** Centrifugal impeller types **a** open; **b** semi-enclosed or semi-open; **c** enclosed

### 3.3 Mesh Generation and CFD Methodology

In this cycle, the model of outward siphon that is done on CATIA is imported in ANSYS, and afterward network age is applied on it. Subsequent to cross section is applied we apply the channel and source limit condition for CFD investigation is finished. After the CFD is done, we get the weight and speed conditions. According to the form plot, the greatest static weight at corner parts of the limit of delta and least static weight at the limit of outlet. The imported model (radial cutting edges) and lattice model of vane point at  $12^\circ$  boundary conditions for water gulf—water source of vane point at  $12^\circ$  as appeared in Figs. 2 and 3.

## 4 Results and Discussion

### 4.1 CFD Analysis of Centrifugal Pump Impeller

The mean pressure is  $8.41e+07$  Pa relying upon the form map, and the base pressure is  $2.56e+06$  Pa. The general speed of the impeller inside the limit, as per the form map, and the base speed extent outside the limit. The middle speed is

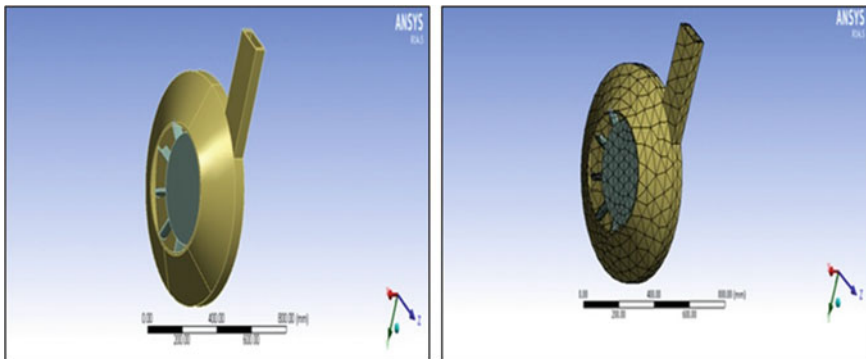


**Fig. 2** Comparison of Imported model (Radial blades) and mesh model of vane angle at  $12^\circ$

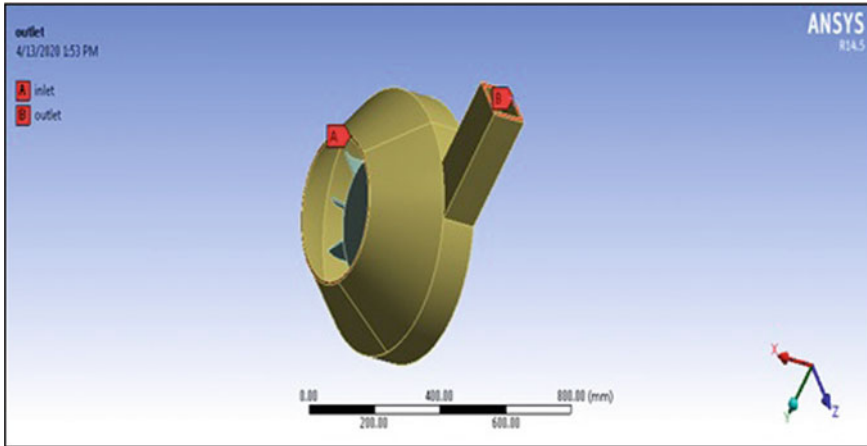


**Fig. 3** Boundary conditions for water inlet–water outlet of vane angle at 12°

**Table 2** CFD analysis results

Impeller vane angle (°)	Pressure (Pa)	Velocity (m/s)	Mass flow rate (kg/sec)
12	8.41e+07	1.61e+03	64.796
14	4.22e+05	4.18e+02	3.105
18	4.91e+07	9.02e+02	38.232

1.61e+03 m/s as indicated by the form plot above, and the base speed is 1.61e +02 m/s. As found in Table 2, the pressure and speed form plot for 12°, 14°, 18° is found in Figs. 4, 5 and 6. The weight and speed for edge points are high at 12° from these weight and speed forms for different edge points [14].

### 4.2 Static Analysis of Centrifugal Siphon Impeller Vane

In this examination, the fit model is imported and afterward we apply limit conditions like weight and speed are applied on edges at 12°, 14°, 18° and apply the materials steel, aluminum, Kevlar 49, and subsequently we compute deformation, stress, strain as shown in Figs. 7, 8 and 9 and their values as shown in Table 3. From these figures, the twisting is high in material Kevlar 49 at cutting edge angle 14°, the stress is high as same in materials steel, aluminum, Kevlar 49 at 12°, and stain is additionally high in material aluminum at 12°. Also, compare the A plot between maximum pressure, maximum velocity and maximum flow rates of centrifugal pump impeller blade type by FSI approach as shown in Fig. 10. From the plot, the variation of maximum deformation occurs at impeller blade angle at 14°



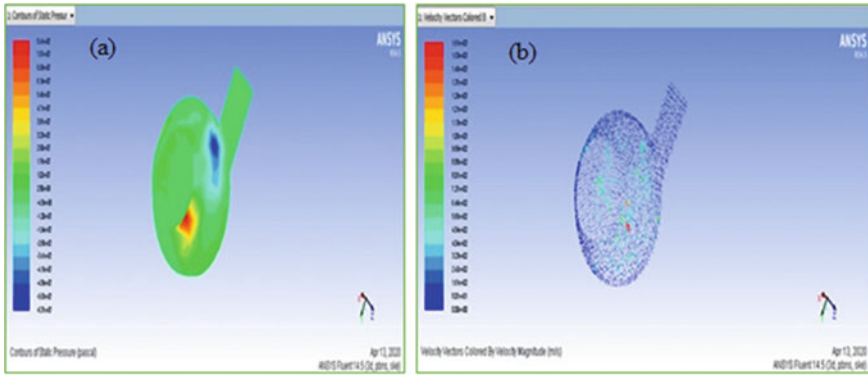


**Fig. 4** a Pressure contours for water inlet–water outlet of vane angle at 12°; b velocity contours for water inlet–water outlet of vane angle at 12°

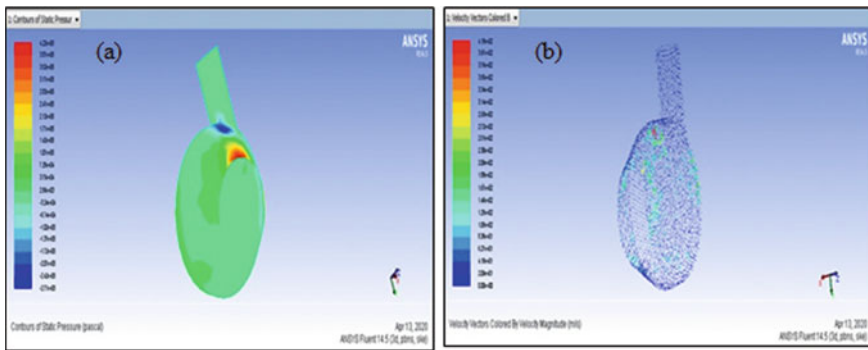


**Fig. 5** a Pressure contours for water inlet–water outlet of vane angle at 14°; b velocity contours for water inlet–water outlet of vane angle at 14°

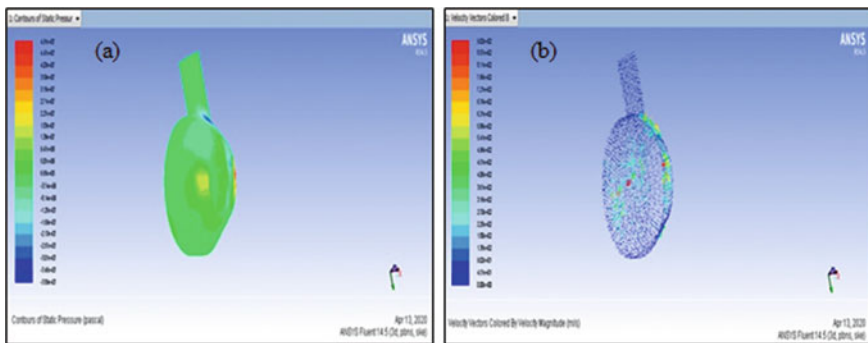


**Fig. 6** a Pressure contours for water inlet–water outlet of vane angle at 18°; b velocity contours for water inlet–water outlet of vane angle at 18°

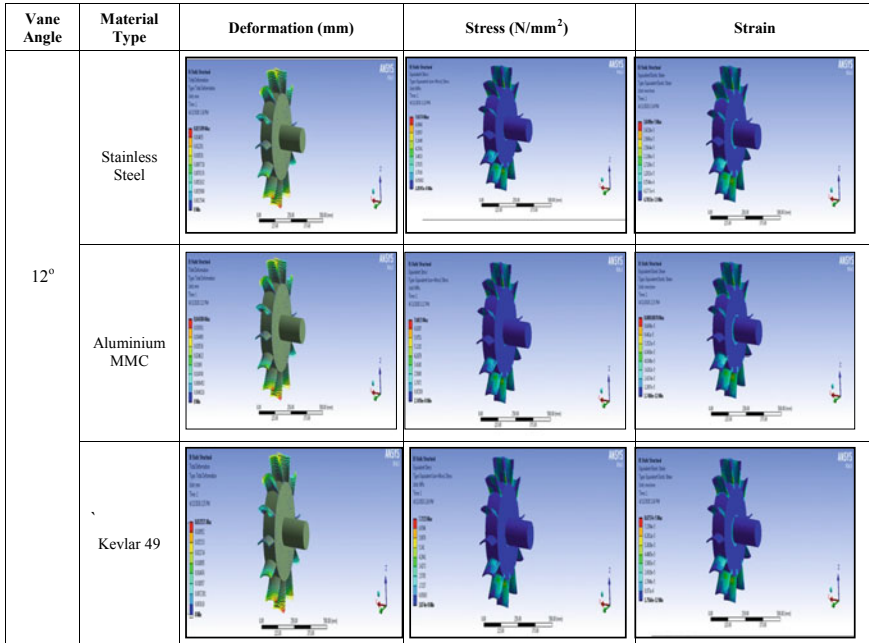


Fig. 7 Static analysis of impeller vane angle at 12° for different materials

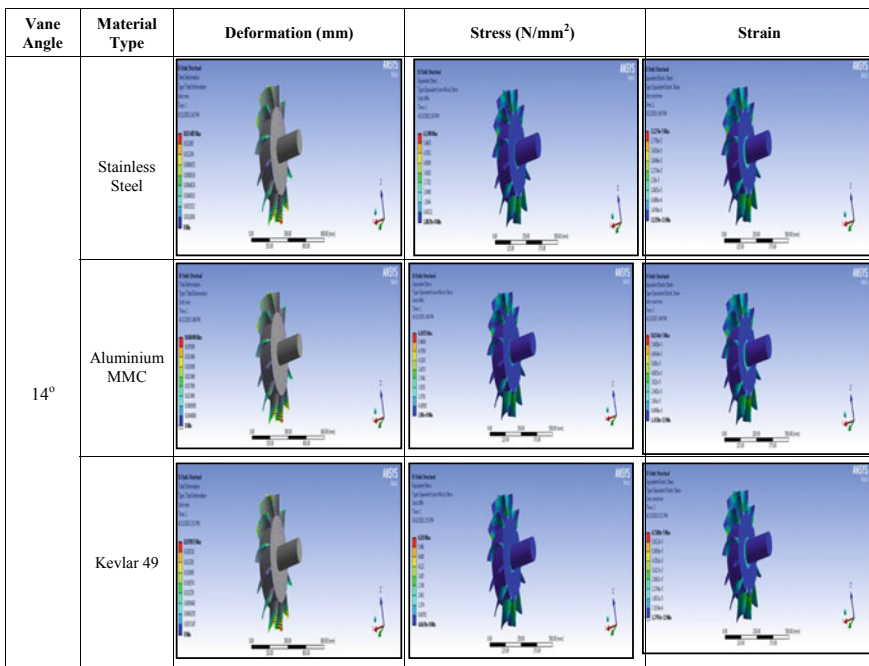
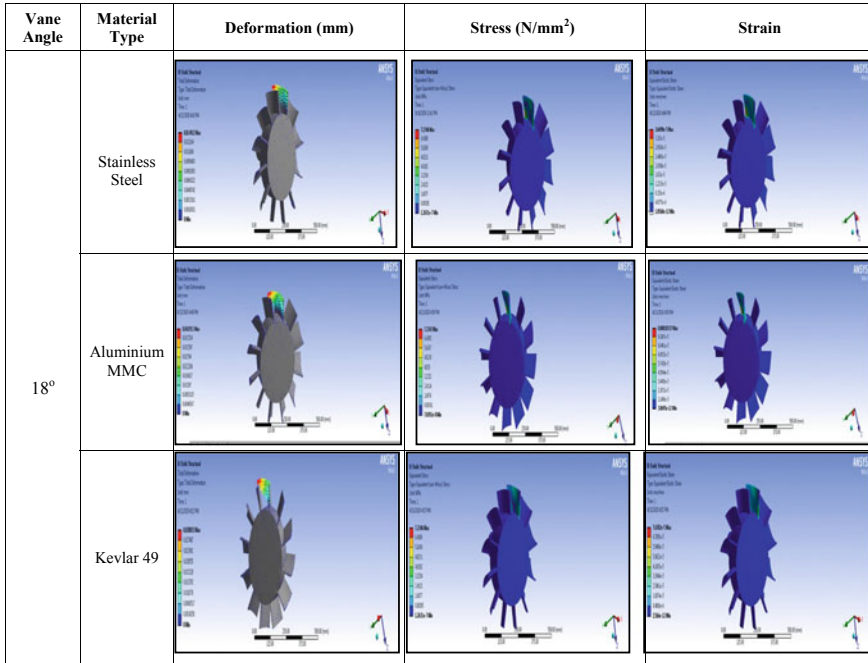


Fig. 8 Static analysis of impeller vane angle at 14° for different materials



**Fig. 9** Static analysis of impeller vane angle at 18° for different materials

**Table 3** Static analysis results

Impeller vane angle (°)	Materials	Deformation (mm)	Stress (N/mm <sup>2</sup> )	Strain
12	Stainless steel	0.015789	7.6574	3.84e-5
	Aluminum MMC	0.044304	7.6823	0.00010878
	KEVLAR 49	0.0032571	7.7115	8.07e-5
14	Stainless steel	0.014405	6.1498	3.12e-5
	Aluminum MMC	0.040498	6.1655	8.824e-5
	KEVLAR 49	0.29833	6.183	6.53e-5
18	Stainless steel	0.014922	7.2275	3.66e-5
	Aluminum MMC	0.041911	7.2343	0.00010337
	KEVLAR 49	0.030833	7.2346	7.638e-5

for Kevlar 49 material, minimum stress occurs at impeller blade angle 14° for aluminum alloy material and minimum strain occurs at impeller blade angle 14° for stainless steel material as shown in Fig. 11.

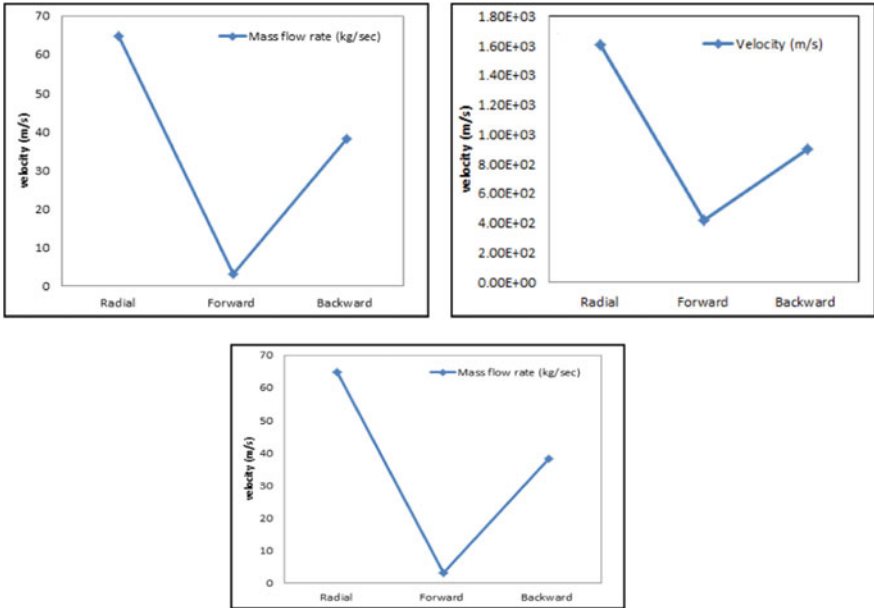


Fig. 10 Variation of a pressure; b velocity; c mass flow rates for different impeller vanes

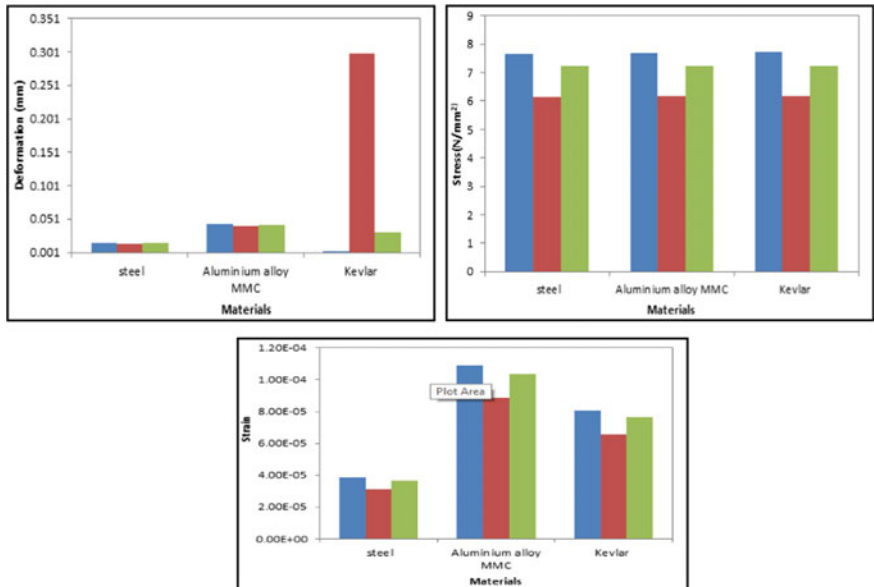


Fig. 11 Variation of a deformation; b stress; c strain for different impeller vanes materials

## 5 Conclusion

In this examination of centrifugal pump, impeller is done in CFD and FSI method for various geometries utilizing ANSYS to decide liquid weight, speed, stress dispersion, strain and even distortion, and a radial siphon impeller is considered utilizing computational liquid elements and liquid strong communication strategy with various calculations. Utilizing CATIA programming, the radial siphon impeller is demonstrated in 3D. Three materials, for example, steel, aluminum composite and Kevlar 49, were considered for deformation and stress examination.

By checking the final outcome of the process, the strength and speed of the radial impeller blade were improved by investigating the impacts of the CFD concentrate when contrasted with different calculations. Maximum deformation occurs at backward impeller of Kevlar 49. The pressure esteems are limited by in reverse edges in static examination, and the weight esteems are taken from CFD investigation. For aluminum content, the pressure esteem is lower than for tempered steel and Kevlar 49. Minimum strain occurs at backward impeller of stainless steel.

## References

1. Filios AE, Bacharoudis EC, Mentzos MD, Margaris DP (2008) Radial siphon parametric investigation by shifting the point of the source cutting edge. *The free mechanical designing diary*, pp 75–83
2. Houlin L, Yong W, Shouqi Y, Minggao T, Kai W (2010) Impacts of blade number of centrifugal pump characteristics. *Chin Mech Eng J*
3. Mohan B, Kumar BE (2014) Fem axial flow compressor impeller structural analysis. *Int J Eng Sci Technol*. ISSN: 2278-0181
4. Rajendran S, Purushothaman K (2012) Investigation of a radial siphon impeller utilizing ANSYS-CFX. *Int J Eng Sci Technol* 1(3)
5. Syam Prasad A, Lakshmipathi Rao BVVV, Babji A, Kumar Babu P (2013) Static and dynamic study of a centrifugal pump impeller. *Int J Sci Eng Res* 4(10)
6. Neelambika V (2014) Blended stream impeller CFD audit. *Int Acad Eng Technol J*
7. Srivastava S, Roy AK, Kumar K (2014) Improvement of and approval of a blended stream siphon impeller utilizing FEM research. *Science Direct, Procedia Technol* 14:181–187
8. Shukla S, Roy AK, Kumar K (2015) Material selection for mixed flow pump impeller blades using ANSYS. *Science Direct Mater Today: Proc* 2:2022–2029
9. Basawaraj HH (2016) An examination investigation on radial siphon impeller manage vane with fem approach by utilizing diverse material. *IJES* 2016(8)
10. Pode VP, Channapattanna S (2014) Surveying divergent siphon yield by CFD while changing the east release attractions hand. *Int Eng Technol Res J*. eISSN: 2319-1163
11. Gavande SN, Deshmukh PD, Kulkarni SS (2014) A multi-admission radial siphon release improvement strategy, 2249–8974
12. Cheng B, Yonghaiyu (2012) CFD recreation and advancement for horizontal redirection and admission siphoning stations, 122–127

13. Honggeng Z, Rentian Z, Guoqiang L (2012) Worldwide gathering on current water driven designing, procedural designing, request of water powered attributes of a volute-type release section, 27–322
14. Asok SP, Sankaranarayanan K, Sundararajan T, Vaidyanathan G, Kumar KU (2011) Pressure drop and cavitation studies on static helical-notched square shape, fluid maze seals of three-sided and bended depression, atomic designing and engineering, 843–853

# Study of Kinematic Chains of Group IV-D, E, and F: Part-Distinct Mechanisms



Ali Hasan

## 1 Introduction

Isomorphism checking among kinematic chains and mechanisms has been a non-reliable, difficult to apply, and lack of grasping mechanism in real environment. Therefore, eliminating the duplicate mechanisms is a difficult task from the beginning. A number of researchers have proposed several new reliable and easy techniques for the purpose. He et al. [1] proposed a method with the application of variable high-order adjacency link values for identification of isomorphism among kinematic chains. The authors redefined the high-order adjacency link values. Later, these redefined values were used in the characteristics of the kinematic chains in depth. These values were determined again and again through reassignment manner according to the presentation of one kinematic chain element. In the last, the isomorphisms were found matching both the higher order adjacency link strings from both the kinematic chains. The authors tested their proposed method using 8-bars, 15-bars, and 28-bars kinematic chains. Sun et al. [2] used graph theory to design the gear trains applicable for transplanting mechanism. The authors screened the topology graphs among the gear trains use a specific gear train mechanism for pot seedling transplantation. In the end, the authors verified the feasibility of proposed scheme. Rajneesh and Sunil [3] proposed a new algorithm for labeling the bars of kinematic chains along with binary code. The method was used for the verification of isomorphism among kinematic chains of 6, 8, 9, 10, 11, 12, and 15 links having simple joints as well as 4, 5, and 6 links epicyclic gear chains. Rizvi et al. [4] developed a new algorithm with adjacency matrices to calculate the distinct mechanisms of a closed kinematic chain. The worth of the developed algorithm was proved with the help of several examples. Sun et al. [5] proposed a novel method for isomorphism calculation of planar kinematic chains along with

---

A. Hasan (✉)

Faculty of Engineering and Technology, Jamia Millia Islamia, New Delhi, India  
e-mail: [ahasan@jmi.ac.in](mailto:ahasan@jmi.ac.in)

multiple joints using joint–joint matrix. A joint–joint matrix was defined, and then links and joints details were taken from the matrix. The scientist developed link code and joint code for the purpose. The author showed their proposed method with the help of examples. Dharanipragada and Chintada [6] work on the revolute as well as prismatic pairs. Here, joint–joint matrices were used by labeling the revolute joint first and then prismatic pair. It was used the method like hamming number technique and split the matrices into three parts. The authors used a computer program for one degree of freedom, six bar chains having simple joints. Sun et al. [7] proposed a hamming number technique for isomorphism finding among kinematic chains with multiple joints. They used joint–joint matrix to define the chain. They discussed the joint hamming number, chain hamming number, and joint hamming string with the help of examples. Rao [8] proposed fuzzy logic for calculating inversions and isomorphism in kinematic chains. The investigators proposed several parameters like symmetry, parallelism, and mobility for distinct chains. Sarkar and Khare [9] proposed a theoretical method for finding the flexibility, isomorphism, and effect of uncertainty among kinematic chains. The idea of direct graph was used for motion flow from link to link. Ding and Huang [10] gave an approach based on new topological graph for mechanisms kinematic chains. They used the characteristics of adjacency matrix to represent kinematic chains. Later, the authors gave the characteristic representation code for one to one correspondence to sketch the topological graphs automatically. Ding and Huang [11] worked on isomorphism of graphs by unique representation of graphs. It was re-labeled the graph to obtain canonical perimeter graph. Using canonical adjacency matrix set, the unique graph was obtained. Dargar et al. [12] worked on finding of isomorphism in kinematic chains. The authors proposed a new method by proposing first adjacency chain link string and second adjacency chain link string. The degrees of freedom of links and type of joints were considered in the procedure. Two invariants were suggested to check the isomorphism among all kinematic chains. Yang et al. [13] invented a new technique applying incident matrices to check isomorphism among topological graphs. The proposed technique is useful in finding correspondence of separate vertices and sufficient isomorphism identification condition. Zeng et al. [14] invented DMA algorithm to establish connection among vertices of kinematic chains for the purpose of isomorphism checking. The proposed algorithm divides the vertices into sets. Validation of reliability of developed algorithm is also provided in the study. Ding et al. [15] invented an automatic method for designing the planar non-fractionated kinematic chains taking two multiple pairs. The investigators proposed a better algorithm for achieving the characteristic number of topological graphs considering two multiple pairs to increase the efficiency of isomorphism checking. Hasan [16] suggested a new method in which kinematic chains are represented in the form of the joint–joint matrix. Two structural invariants, sum of absolute characteristic polynomial coefficients, and maximum absolute value of the characteristic polynomial coefficient are derived from the characteristic polynomials of the joint–joint matrix of the kinematic chains. Author has taken several figures and other data from Jensen [17].



## 2 The Joint–Joint Matrix

This is joint-based matrix square symmetric matrix of size  $n \times n$ , where  $n$  is the number of Kinematic pairs in a KC.

$$[A] = \{E_{ij}\}_{n \times n} \quad (1)$$

where

$E_{ij}$  {=2 for binary, 3 for ternary, 4 for quaternary, —,  $n$  for  $n$ -nary link, between  $i$ th and  $j$ th pairs if they are connected directly else zero including diagonal elements}.

## 3 Methodology

A KC is converted into joint–joint  $[A]$  matrix. When, we framed any bar (link) of a KC, a mechanism is achieved. If we changed the elements of rows and columns of the corresponding pairs of the framed bar with zero elements, then a mechanism is obtained for that framed bar. Then, this new  $[A]$  matrix is written as  $[A-a]$  matrix. The identification numbers of this  $[A-a]$  matrix are calculated using MATLAB. The identification numbers ‘AS-a’ and ‘AM-a’ are the identification numbers for the first mechanism.

The same procedure is adopted for all mechanisms by fixing every bar in turn. We achieve the pairs of identification numbers equal to the number of bars in the KC. Now, we check the pairs of achieved identification numbers carefully and note that some of the identification numbers are similar and remaining different. Similar identification numbers means similar mechanism and are counted equal to one mechanism. The bars of similar mechanisms are known as similar bars.

## 4 Illustrative Example

We are considering an example of six bars, seven pairs, 1F Stephenson’s KC drawn in Fig. 1. The joint–joint matrix for Fig. 1 is represented by  $[A]$ .

$$[A] = \begin{pmatrix} 0 & 3 & 0 & 0 & 2 & 0 & 3 \\ 3 & 0 & 2 & 0 & 0 & 0 & 3 \\ 0 & 2 & 0 & 3 & 0 & 3 & 0 \\ 0 & 0 & 3 & 0 & 2 & 3 & 0 \\ 2 & 0 & 0 & 2 & 0 & 0 & 0 \\ 0 & 0 & 3 & 3 & 0 & 0 & 2 \\ 3 & 3 & 0 & 0 & 0 & 2 & 0 \end{pmatrix}$$

The pair of identification numbers from matrix [A] is:  $9.7560e+003$  and  $3.6000e+003$ .

The pair of identification numbers if bar-a is framed:  $12,280$  and  $4.8500e+003$ .

The pair of identification numbers if bar-b is framed:  $7.1960e+003$  and  $3.1920e+003$ .

The pair of identification numbers if bar-c is framed:  $8.0320e+003$  and  $3.1110e+003$ .

The pair of identification numbers if bar-d is framed:  $7.1960e+003$  and  $3.1920e+003$ .

The pair of identification numbers if bar-e is framed:  $1.2280e+004$  and  $4.8500e+003$ .

The pair of identification numbers if bar-f is framed:  $8.0320e+003$  and  $3.1110e+003$ .

Here, we note that:

Bar-a and bar-e are similar as their identification numbers are same.

Bar-b and bar-d are similar as their identification numbers are same.

Bar-c and bar-f are similar as their identification numbers are same.

Therefore,

The mechanism obtained by framing bar-a and bar-e will be similar and taken as 1.

The mechanism obtained by framing bar-b and bar-d will be similar and taken as 1.

The mechanism obtained by framing bar-c and bar-f will be similar and taken as 1.

As a result, we get three different mechanisms from this KC drawn in Fig. 1. Here, our results are in complete agreement as already reported in the literature.

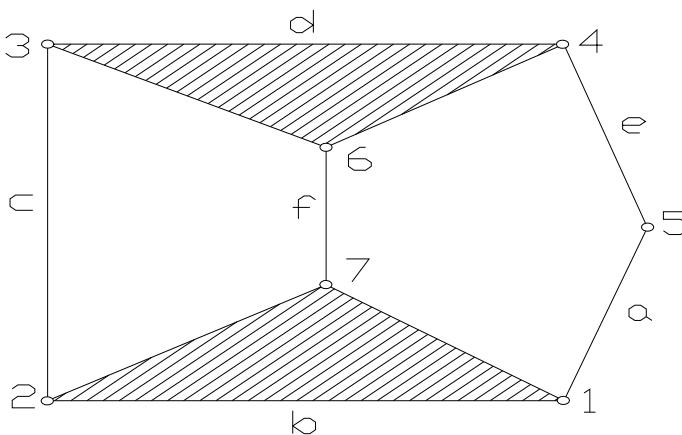


**Fig. 1** Six bar, seven pairs, 1F Stephenson's KC

### 5 Results and Discussion

The identification number [AS] and [AM] can be may be utilized for checking of isomorphism as well as the similar and dissimilar mechanisms of KCs. The technique is equally applicable for simple as well as multiple paired KCs. The detailed identification numbers (values of AS and AM) of all 1-F KCs and different mechanisms of 6 bars, 8 bars and 10-bars have been calculated by the author [16]. The figures of KCs having ten bars, thirteen pairs, 1F Group ‘IV-D, E, and F’ are redrawn in Figs. 2, 3, and 4 from Jensen [17]. The collection of similar and dissimilar bars along with mechanisms obtained from ten bars, thirteen pairs, 1F KCs of Group ‘IV-D, E and F’ are summarized in Table 1. The total number of different mechanisms identified from ten bars, thirteen pairs, 1F KCs of Group

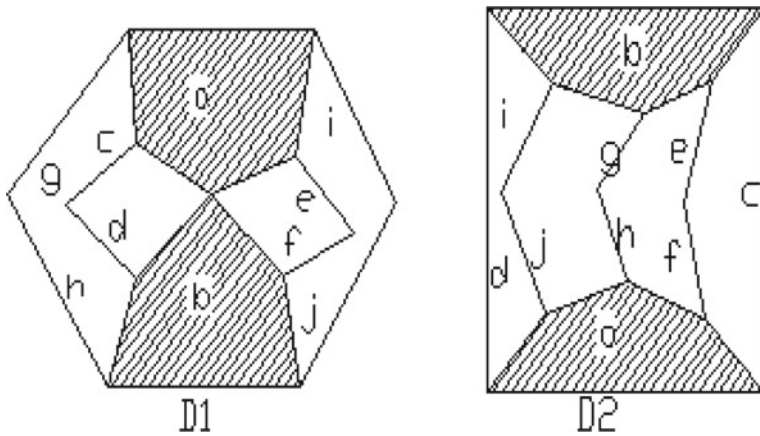


Fig. 2 Ten bars 13 pairs 1F closed chains of Group IV-D

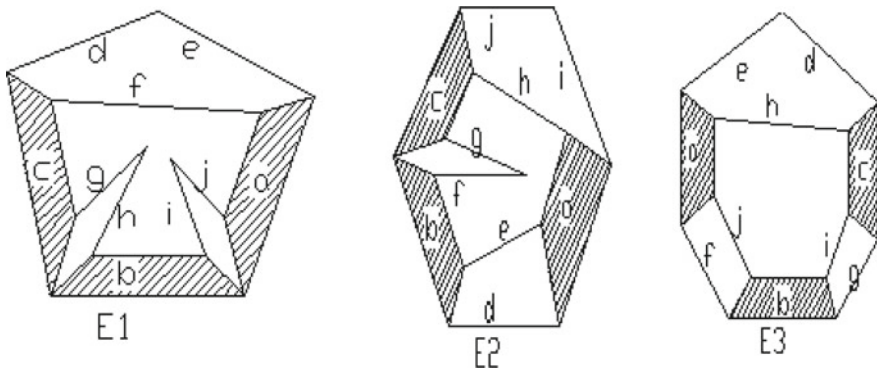
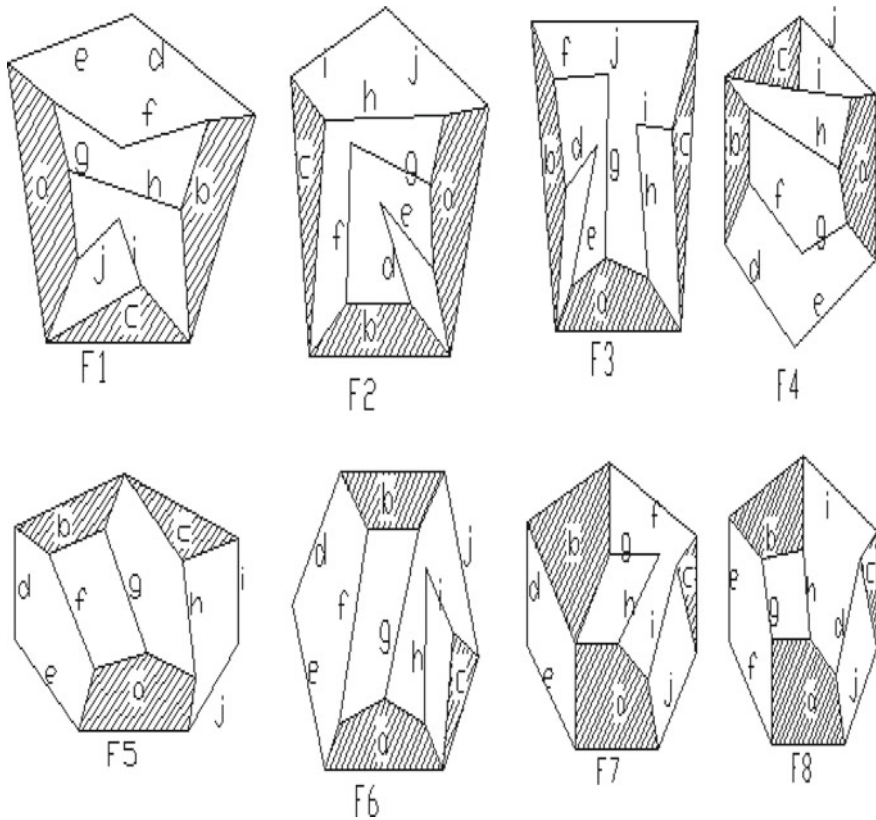


Fig. 3 Ten bars 13 pairs 1F closed chains of Group IV-E



**Fig. 4** Ten bars 13 pairs 1F closed chains of Group IV-F

'IV-D, E and F' are 7, 20, and 77, respectively. The identification numbers of each chain of Group 'IV-D, E, and F' are presented in Appendix D, E, and F, respectively.

## 6 Conclusions

The suggested identification numbers [AS] and [AM] are fully capable to differentiate between similar and dissimilar bars in a kinematic chain and its mechanisms. As a result, we can determine total number of mechanisms from kinematic chains with simple joints or multiple joints to facilitate the designer in the initial stage of design. The suggested technique is dependent on the type of links (binary, ternary, —). These proposed identification numbers are quite general in nature and can be used for identification and characterization of kinematic chains and their inversions

**Table 1** Distinct mechanisms of ten bars 13 pairs 1F closed chains of Group IV-D, E, and F

Kinematic chain	$n_5 n_4 n_3 n_2$	Similar and dissimilar bar	Mechanism
D1	2008	$a = b, c = d = e = f, g = h = i = j$	3
D2	2008	$a = b, c = d, e = f = i = j, g = h$	4
E1	0307	$a = c, b, d = e, f, g = j, h$	6
E2	0307	$a, b, c, d, e, f, g = i, h, j$	9
E3	0307	$a = c, b, d = e, f = g = i = j, h$	5
F1	1117	$a, b, c, d, e, f, g, h, i, j$	10
F2	1117	$a, b, c, d, e, f, g, h, i, j$	10
F3	1117	$a, b, c, d, e, f, g, h, i, j$	10
F4	1117	$a, b, c, d, e, f, g, h, i, j$	10
F5	1117	$a, b, c, d, e, f, g, h, i, j$	10
F6	1117	$a, b, c, d, e, f, g, h, i, j$	10
F7	1117	$a, b, c, d = g, e = h, f, i = j$	7
F8	1117	$a, b, c, d, e, f, g, h, i, j$	10

having single or multiple degrees of freedom. The detailed analysis of the kinematic chains is with the author and numerical values obtained with the help of MATLAB from kinematic chains of Group IV D, E, and F are listed in Appendix D, E, and F, respectively.

**Appendix D** Identification numbers [AS] and [AM] of kinematic chains Group IV-D

Inv. (Chain)	Bar-a	Bar-b	Bar-c	Bar-d	Bar-e	Bar-f	Bar-g	Bar-h	Bar-i	Bar-j
AS(D1)	1.2228	1.2228	1.4824	1.4824	1.4824	1.4824	1.2685	1.2685	1.2685	1.2685
AM(D1)	4.1637	4.1637	3.5514	3.5514	3.5514	3.5514	3.5841	3.5841	3.5841	3.5841
AS(D2)	3.2671	3.2671	2.5995	2.5995	3.1467	3.1467	3.0218	3.0218	3.1467	3.1467
AM(D2)	13.166	13.166	11.708	11.708	98,326	98,326	86,809	86,809	98,326	98,326

Note Multiplying factors (e+008) and (e+007) are common to [AS] and [AM], respectively

**Appendix E** Identification numbers [AS] and [AM] of kinematic chains Group IV-E

Inv. (Chain)	Bar-a	Bar-b	Bar-c	Bar-d	Bar-e	Bar-f	Bar-g	Bar-h	Bar-i	Bar-j
AS(E1)	1.7504	1.7895	1.7504	1.7984	1.7984	1.5916	1.7023	1.7269	1.7269	1.7023
AM(E1)	5.3427	6.1102	5.3427	5.4426	5.4426	5.3350	4.8312	4.9275	4.9275	4.8312
AS(E2)	2.0646	1.9894	1.8819	1.8043	1.7182	1.9239	1.8829	1.6529	1.8829	1.8330
AM(E2)	5.1692	5.3892	5.2951	6.1850	6.0662	6.4609	6.3616	5.9597	6.3616	6.2520
AS(E3)	1.8269	1.8242	1.8269	1.5551	1.5551	1.4881	1.4881	1.5722	1.4853	1.4853
AM(E3)	1.8269	1.8242	1.8269	1.5551	1.5551	1.4881	1.4881	1.5722	1.4853	1.4853

Note Multiplying factors (e+007) and (e+006) are common to [AS] and [AM], respectively

**Appendix F** Identification numbers [AS] and [AM] of kinematic chains Group IV-F

Inv. (Chain)	Bar-a	Bar-b	Bar-c	Bar-d	Bar-e	Bar-f	Bar-g	Bar-h	Bar-i	Bar-j
AS(F1)	3.0226	3.7195	2.8914	3.5436	3.5961	3.2060	3.2696	3.2463	3.9188	4.0071
AM(F1)	1.1376	1.1687	1.1436	1.3398	1.3933	1.2202	1.2600	1.3049	1.3500	1.4728
AS(F2)	8.3596	5.3880	5.6584	4.8962	5.5675	6.1054	6.2056	7.0011	8.2362	8.9849
AM(F2)	3.1455	2.3103	2.0621	2.0159	2.4039	2.4949	2.5451	2.4935	2.9034	3.1356
AS(F3)	5.2049	4.8555	4.4802	4.5811	4.8498	4.0736	4.0614	5.8360	5.4351	4.5256
AM(F3)	1.4838	1.3757	1.2304	1.2715	1.4359	1.2537	1.2473	1.7790	1.6402	1.3467
AS(F4)	17.861	15.138	1.0034	12.804	14.373	16.415	17.598	15.760	12.759	12.465
AM(F4)	5.5078	3.9894	2.5470	3.5734	3.7515	4.5930	5.1185	4.5213	3.9591	4.0937
AS(F5)	12.909	8.9432	77.161	95.238	10.611	9.1248	10.187	9.0481	11.708	13.253
AM(F5)	3.7667	3.0509	2.1532	3.0061	2.9489	3.1138	3.0940	3.0520	2.8715	3.2825
AS(F6)	3.2576	5.3160	3.2498	3.3455	3.1104	3.9814	2.6986	5.2156	4.9308	3.6346
AM(F6)	1.3356	1.5210	1.3205	1.5730	1.5010	1.6362	1.3832	1.8710	1.6691	1.5160
AS(F7)	11.421	11.433	5.2468	11.440	11.494	7.4130	11.440	11.494	7.3869	7.3869
AM(F7)	5.4698	4.9899	2.0156	3.9516	4.4271	3.5824	3.9516	4.4271	3.5700	3.5700
AS(F8)	17.057	19.229	9.1504	11.335	13.638	14.603	16.314	13.264	13.693	11.498
AM(F8)	5.7522	6.5529	2.9791	4.3792	4.2220	4.6279	4.9586	4.6421	4.2300	4.3391

Note A multiplying factor (e+007) is common to both [AS] and [AM]







## References

1. He L, Liu F, Sun L, Wu C (2019) Isomorphic identification for kinematic chains using variable high-order adjacency link values. *J Mech Sci Technol* 33:4899–4907. <https://doi.org/10.1007/s12206-019-0930-9>
2. Sun L, Chen X, Wu C, Zhang G, Xu Y (2017) Synthesis and design of rice pot seedling transplanting mechanism based on labeled graph theory. *Comput Electron Agr* 143:249–261. <https://doi.org/10.1016/j.compag.2017.10.021>
3. Rajneesh KR, Sunil P (2019) A new algorithm of links labelling for the isomorphism detection of various kinematic chains using binary code. *Mech Mach Theory* 131:1–32. <https://doi.org/10.1016/j.mechmachtheory.2018.09.010>
4. Rizvi SH, Hasan A, Khan RA (2016) An efficient algorithm for distinct inversions and isomorphism detection in kinematic chains. *Persp Sci* 8:251–253. <https://doi.org/10.1016/j.pisc.2016.03.022>. Get rights and content
5. Sun W, Kong J, Sun L (2018) A joint–joint matrix representation of planar kinematic chains with multiple joints and isomorphism identification. *Adv Mech Eng* 10(6):1–10. <https://doi.org/10.1177/1687814018778404>
6. Dharanipragada V, Chintada M (2016) Split hamming string as an isomorphism test for one degree-of-freedom planar simple-jointed kinematic chains containing sliders. *ASME J Mech Des* 138(8):082301–1–082301–8. <https://doi.org/10.1115/1.4033611>
7. Sun W, Kong JY, Sun LB (2017) The improved hamming number method to detect isomorphism for kinematic chain with multiple joints. *J Adv Mech Des Syst Manuf* 11(5):17–00479–1–10
8. Rao AC (2000) Application of fuzzy logic for the study of isomorphism, inversions, symmetry, parallelism and mobility in kinematic chains. *Mech Mach Theory* 35(8):1103–1111. [https://doi.org/10.1016/S0094-114X\(99\)00060-9](https://doi.org/10.1016/S0094-114X(99)00060-9)

9. Sarkar SC, Khare AK (2004) Detecting the effect of uncertainty and isomorphism in 10 bar kinematic chains using all possible paths for motion transmission. *Mech Mach Theory* 39 (8):893–900. <https://doi.org/10.1016/j.mechmachtheory.2004.02.006>. Get rights and content
10. Ding H, Huang Z (2007) A unique representation of the kinematic chain and the atlas database. *Mech Mach Theory* 42(6):637–651. <https://doi.org/10.1016/j.mechmachtheory.2006.06.010>. Get rights and content
11. Ding H, Huang Z (2009) Isomorphism identification of graphs: Especially for the graphs of kinematic chains. *Mech Mach Theory* 44(1):122–139. <https://doi.org/10.1016/j.mechmachtheory.2008.02.008>. Get rights and content
12. Dargar A, Khan RA, Hasan A (2010) Application of link adjacency values to detect isomorphism among kinematic chains. *Int J Mech Mater Des* 6(2):157–162
13. Yang F, Deng Z, Tao J, Li L (2012) A new method for isomorphism identification in topological graphs using incident matrices. *Mech Mach Theory* 49:298–307. <https://doi.org/10.1016/j.mechmachtheory.2011.09.008>. Get rights and content
14. Zeng K, Fan X, Dong M, Yang P (2014) A fast algorithm for kinematic chain isomorphism identification based on dividing and matching vertices. *Mech Mach Theory* 72:25–38. <https://doi.org/10.1016/j.mechmachtheory.2013.09.011>
15. Ding H, Yang W, Zi B, Kecskeméthy A (2016) The family of planar kinematic chains with two multiple joints. *Mech Mach Theory* 99:103–116. <https://doi.org/10.1016/j.mechmachtheory.2016.01.003>
16. Hasan A (2007) Some studies on characterization and identification of kinematic chains and mechanisms. Ph D thesis, Jamia Millia Islamia, New Delhi, India
17. Preben JW (1991) *Classical and modern mechanism for engineers and inventors*. Marcel Dekker Inc, New York

# Intermittency Reduction Techniques in Hybrid Renewable Energy Systems: A Review



Neil Singh , Krish Patel , Krishi Patel ,  
Siddhi Vinayak Pandey , Pankaj Singh ,  
Anoop Kumar Shukla , and Gaurav Dwivedi

## 1 Introduction

The villages in India have acute shortage of electricity. Renewable sources of energy are a good option to bridge the demand–supply gap [1]. However, the transient and inconsistent nature of renewable energy causes fluctuation and leads to intermittency in HRES [2, 3]. The HRES system is basically the combination of wind- and solar-based power generation. Due to the dependency of wind and solar energy generation on the environmental factors, it causes fluctuations and intermittency within HRES.

This paper analyses various approaches, both conventional and modern, which are utilized to reduce the intermittency within a HRES. The advancement in energy

---

N. Singh

Commack High School, Commack School District, New York, USA

K. Patel

United World College of South East Asia, Dover Road, Dover, Singapore

K. Patel

Department of Biotechnology, Rutgers University, New Jersey, USA

S. V. Pandey

Department of Electrical Engineering, Adani Institute of Infrastructure Engineering, Ahmedabad, Gujarat, India

P. Singh

Department of Strategy and Consulting, Adani Institute of Infrastructure Management, Ahmedabad, Gujarat, India

A. K. Shukla

Department of Mechanical Engineering, Amity University, Uttar Pradesh, Noida 201313, India

G. Dwivedi (✉)

Energy Center, Maulana Azad National Institute of Technology, Bhopal 462003, India

© The Author(s), under exclusive license to Springer Nature Singapore Pte Ltd. 2022

P. Verma et al. (eds.), *Advancement in Materials, Manufacturing and Energy Engineering, Vol. I*, Lecture Notes in Mechanical Engineering,

[https://doi.org/10.1007/978-981-16-5371-1\\_9](https://doi.org/10.1007/978-981-16-5371-1_9)



storage technology and its lowering cost can reduce intermittency and optimize the usage of renewable energy [4, 5]. Paper also gives insight about leveraging optimization techniques and predictive analytics for better forecasting of energy demand. Cattle power generation, biogas and fuel cells can be used to address the shortage of supply from HRES and thereby reduce the intermittency within the system.

## 2 Intermittency Reduction Using Energy Storage Systems

Demand–supply equilibrium is critical for proper utilization and consumption of electricity. In the past few years, solar, wind and other forms of renewable energy have grown. Renewable energy generation does not have a steady supply pattern due to the nature of these sources of energy. Solar generation is impacted by irradiance and wind power also varies with wind speed. So, the demand may not be properly met by renewable energy, due to the irregular pattern of supply to renewable energy. Due to this reason, it becomes difficult to supply renewable energy to the grid using a HRES. So, we need to use energy storage systems to store and supply when there is an imbalance between supply–demand [6].

Changes in supply of renewable energy, weather and behaviour of consumers lead to fluctuations in electrical requirement and load in smart buildings [7, 8]. This requires the usage of building energy management systems (BEMSs) to handle intermittencies by real-time corrections to maintain optimal power supply [9]. Advancement of technologies and reduction in costs of energy storage systems is leading to higher usage energy storage in conjunction with sources of renewable energy [10, 11]. Currently, lithium–ion and lead acid-based batteries are the pioneer storage systems utilized to store and supply the energy in HRES.

The energy storage systems can store/supply the energy when HRES system is directly connected to load. If HRES generates more amount of energy with respect to demand of the load, then it will store the energy. Also, it can supply the energy when HRES-based energy generation is not sufficient to fulfil the load demand in real-time domain. It is good for environment and economically advantageous to leverage renewable energy along with energy storage [12].

## 3 Intermittency Reduction Using Data Analytics and Forecasting-Based Approach

The data analytics and forecasting-based approach are utilized to reduce the intermittency of HRES system by monitoring the past datasets and forecasting the upcoming values in real-time domain [13]. These types of analytical methods are used to forecast the parameters on which the energy generation of HRES system

depends. In HRES system, mostly the hybrid combination of wind- and solar-based energy generating stations are used to fulfil the load demand [14].

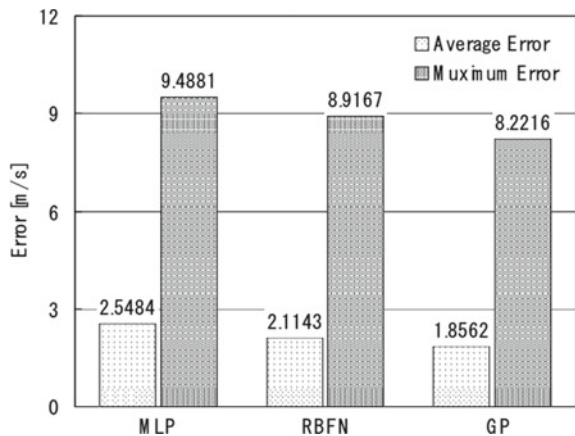
Due to the continuous variations in wind speed, air density, irradiance and environmental temperature; the energy generation through solar- and wind-based power plants vary continuously [15]. These types of perpetual variations affect the supply–demand chain and hence cause the lack of balance within a system. As the intermittency of HRES system is directly dependent on the parameters such as wind speed, air density, irradiance and environmental temperatures. The intermittency within a system is directly proportional to these parameters; so, if there will be more fluctuations within a parameter, the more will be the overall intermittency within a system [16].

As mentioned in Lorenz et al. [17], the three days ahead irradiance have been forecasted for the prediction of power generation through solar PV array using European Centre for Medium-Range Weather Forecasts (ECMWF) datasets. The hourly based irradiance has been forecasted with a root mean square error (RMSE) of 37% for the first forecast day, while the 46% RMSE has been observed on the third forecast day.

Alzahrani et al. [18] forecasted the irradiance using deep recurrent neural network (DRNN) by utilizing the real-world datasets from the natural resources in Canada. Further, the prediction through DRNN has been compared with support vector regression (SVR) and feedforward neural network (FNN) approach. The experimental result depicts that DRNN system is having higher accuracy with RMSE of 0.086, while the SVR and FNN are having lower accuracy with RMSE of 0.16 and 0.11, respectively.

Mori and Kurata [19] have used the Gaussian process (GP) method for forecasting the uncertainty of wind speed. The kernel machine technique and Bayesian estimation approach have been utilized for predictions. This method has reduced the average error of multilayer perception (MLP) and radial basis function network (RBFN) by 27% and 12%, respectively. While the maximum error for MLP and

**Fig. 1** Average and maximum error of MLP, RBFN and GP [19]



RBFN has been reduced by 13% and 7.8%, respectively, the average and maximum error of MLP, RBFN and GP have been mentioned in Fig. 1.

Various forecasting techniques such as numeric weather prediction (NWP), statistical approaches, various machine learning and neural network-based algorithms are utilized to forecast the wind speed, air density and irradiance in real-time domain. These types of forecasting techniques will give us the estimated report of the next day, and based on the data, we can forecast the amount of energy that will be generated in future. Based on this dataset, forecasting of intermittency could be calculated and need of proper resources can be arranged to establish a perfect balance between supply and demand [20, 21].

## 4 Intermittency Reduction Using Cattle Power-Based Energy Generating Stations

Livestock is an internal part of India's rural areas with each farmer owning an average at least one or two pairs of bullocks. They are used for ploughing the farms, but during the non-farming season, they do not contribute to farmers income and yet they have to be fed. So, the bullocks can be used to save energy cost by generating electricity. Cattle/bullock-generated electricity can be an opportunity for income all year round and enhances the quality of life for farmers in villages. It also increases the reach of renewable energy. It is an alternate solution to stop sending livestock to slaughterhouses. Cattle/bullock-generated electricity is easy to generate, and the electricity can be stored for consumption as and when needed. Electricity generated by a group of bullocks can be stored and used to power electric vehicles [22]. Each cattle/bullock can produce energy ranging from 2 to 7 HP energy for a cleaner greener and brighter future.

Cattle dung can be converted into biogas economically by using anaerobic digestion technology (shown in Fig. 2). Methane produced can be used for renewable electrical energy, fuel and heat. The microbial populations that develop during anaerobic hydrolysis can be used to increase the rate of hydrolysis–acidification and the overall anaerobic digestion can be enhanced by the generation of microbial population during the hydrolysis. Electricity generated from fossil sources can reduce by increasing the microbial fuel cell (MFC) powered renewable energy. MFC can be used for wastewater treatment.

The electricity can also be generated from organic waste using a device like the cassette—electrode microbial fuel cells [23].

As mentioned in Cantrell et al. [24], the biofuel production can reduce fossil fuel usage and enhance the quality of air, water and soil. Income of farmers can be increased and cost reduced by converting cattle waste to bioenergy by using platforms like thermochemical and biochemical as shown in Fig. 3. The products from this conversion process are fuel, power, heat and chemicals. A key by-product is slurry, which can be used as a fertilizer.

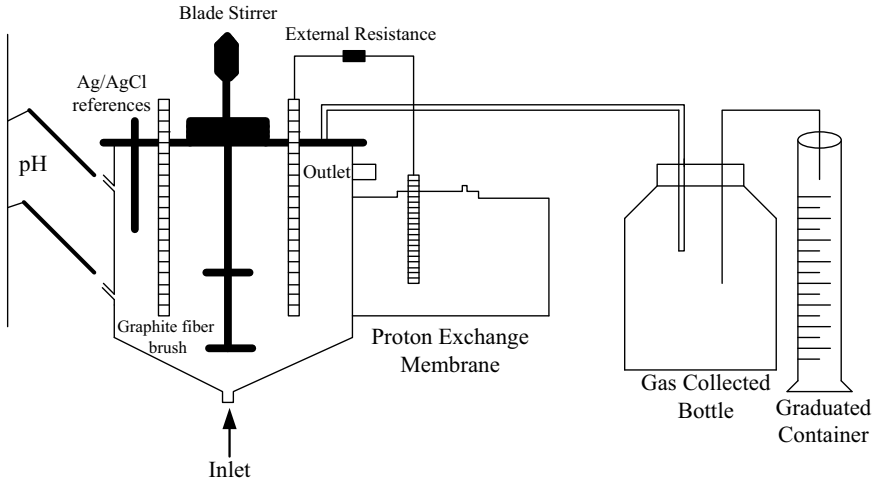
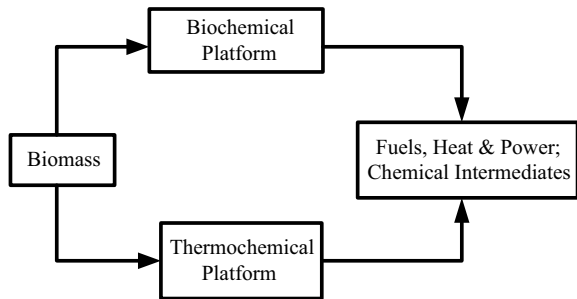


Fig. 2 Schematic diagram of bioreactor [22]

Fig. 3 Conversion platform for livestock waste to bioenergy conversion [24]



## 5 Intermittency Reduction Using Biogas and Fuel Cells

Breakdown of biodegradable organic matter in an anaerobic condition leads to the production of a mixture of gases, known as biogas. The raw organic materials that can be used to produce biogas include agricultural waste, municipal waste, sewage, manure, plant material and leftover food. Calorific value of biogas is 22.4 MJ/m<sup>3</sup> and contains over 50% methane [25], 30–45% CO<sub>2</sub>, and a small percentage of ammonia, carbon monoxide, hydrogen, hydrogen sulphide and water vapour [26]. The main source of biogas that we are focusing on is Gobar, also known as cow dung. Gobar gas is a special type of biogas that can be used to reduce intermittency and provide energy.

The production of biogas is done anaerobically (in the absence of oxygen). As shown in Fig. 4, it involves a closed system called an anaerobic digester or a bio-digester, an inlet pipe, a gas outlet, a gas tank and an outlet. The biodegradable

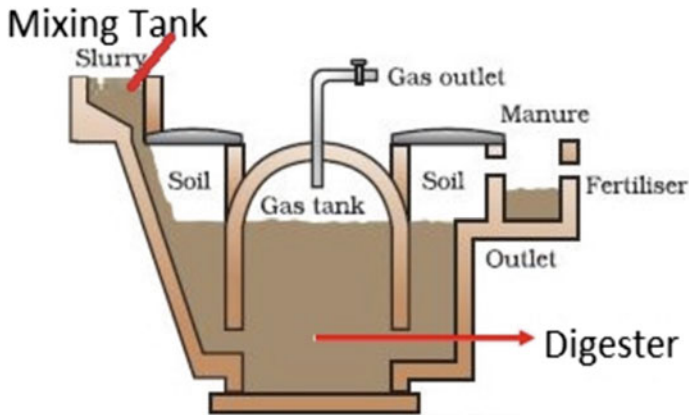


Fig. 4 Production of biogas [27]

raw materials known as bio-waste are converted into smaller pieces and slurrified in the latrine. Liquid is added to the bio-waste to make it easier to process. This is known as slurrifying. Next, bacteria such as methanogens and acetogens secrete enzymes which break down the biomass into an even finer consistency. These microbes and microorganisms can work without the presence of oxygen. They need warm conditions to act on the bio-waste so it is heated to around 37 °C. Through their action, these complex molecules are converted into a mixture of methane and carbon dioxide: biogas. Lastly, purification of the biogas by removing impurities and carbon dioxide is done. In the final stage, the gas is transported via a gas pipeline network.

To make the energy produced by Gobar gas even more efficient, we can create a HRES by incorporating fuel cells in the system. Fuel cells technology makes use of the chemical energy stored in hydrogen and oxygen to generate electricity. Fuel cells are more efficient than other heat engines because they are quieter and more manageable as they do not have any moving parts. Moreover, because fuels cells directly convert chemical energy into electrical energy, “the conversion efficiency can be much higher; they may be cheaper to operate, and there will be less heat produced, resulting in small radiator and exhaust systems” [27, 28]. In certain applications, such as space missions and remote site operations, fuel cells have proved to be viable power sources. Fuel cells are currently being developed for widespread commercial applications. While the advantages of fuel cells over other heat engines could tip the scales in their favour, the relatively high development costs necessitate substantiation.

A HRES of biogas and fuel cells will be greatly beneficial because they complement each other in the best way possible. Biogas will be able to produce energy that generates way less CO<sub>2</sub> as compared to fuel cells and the fuel cells will provide backup energy for the biogas plant to work more efficiently.

## 6 Conclusion

In this paper, various techniques to reduce the intermittency within hybrid renewable energy system has been explicated in detail. Techniques such as energy storage system, data analytics and forecasting-based approach, cattle power and biogas are the few methods that can be coupled with HRES system to reduce the intermittency and balance the supply–demand chain in real-time domain. The energy storage system is tending to store and supply the energy with respect to demand of the load. Other techniques such as hydro/thermal power plant can supply the electricity when the generation power of HRES is shorted and not able to withstand the load demand in real-time domain. The only disadvantage with this kind of generating stations is—it can only supply the energy when HRES power is not enough with respect to demand of the load; but it cannot store the energy when HRES system generates excess quantum of electricity with respect to demand in real-time domain. The cattle-based power, biogas and fuel cell-based approaches can also be implemented to fulfil the entire power demand by solely using the green energy generation. The forecasting-based approach also helps to understand the energy generation scenario of the near future by analysing the previous datasets of that system. In future, better estimation techniques by use of data-driven methods can be implemented in real system to forecast the energy generation through HRES.

## References

1. Mishra S, Verma S, Chowdhury S, Dwivedi G (2020) Analysis of recent developments in greenhouse dryer on various parameters—a review. *Mater Today Proc.* <https://doi.org/10.1016/j.matpr.2020.07.429>
2. Verma S et al (2020) Solar PV powered water pumping system—a review. *Mater Today Proc.* <https://doi.org/10.1016/j.matpr.2020.09.434>
3. Arul PG, Ramachandramurthy VK, Rajkumar RK (2015) Control strategies for a hybrid renewable energy system: a review. *Renew Sustain Energy Rev* 42:597–608
4. Barton JP, Infield DG (2004) Energy storage and its use with intermittent renewable energy. *IEEE Trans Energy Convers* 19(2):441–448
5. Teleke S, Baran ME, Bhattacharya S, Huang AQ (2010) Rule-based control of battery energy storage for dispatching intermittent renewable sources. *IEEE Trans Sustain Energy* 1(3):117–124
6. Sundararaghavan S, Baker E (2012) Evaluating energy storage technologies for wind power integration. *Sol Energy* 86(9):2707–2717
7. Zhao H, Wu Q, Hu S, Xu H, Rasmussen CN (2015) Review of energy storage system for wind power integration support. *Appl Energy* 137:545–553
8. El-Batawy SA, Morsi WG (2018) Optimal design of community battery energy storage systems with prosumers owning electric vehicles. *IEEE Trans Ind Inf* 14(5):1920–1931
9. Shafie-khah M, Siano P (2017) A stochastic home energy management system considering satisfaction cost and response fatigue. *IEEE Trans Ind Inf* 14(2):629–638
10. Terlouw T, AISkaif T, Bauer C, Van Sark V (2019) Multi-objective optimization of energy arbitrage in community energy storage systems using different battery technologies. *Appl. Energy* 239:356–372

11. Mehrjerdi H, Bornapour M, Hemmati R, Ghiasi SMS (2019) Unified energy management and load control in building equipped with wind-solar-battery incorporating electric and hydrogen vehicles under both connected to the grid and islanding modes. *Energy* 168:919–930
12. Nicholls A, Sharma R, Saha TK (2015) Financial and environmental analysis of rooftop photovoltaic installations with battery storage in Australia. *Appl Energy* 159:252–264
13. Negi S, Mathew L (2014) Hybrid renewable energy system: a review. *Int J Electron Electr Eng* 7(5):535–542
14. Goud BS, Rao BL, Reddy CR (2021) An intelligent technique for optimal power quality reinforcement in a grid-connected HRES system. EVORFA technique. *Int J Num Model: Electron Netw Dev Fields* 34(2)
15. Anvari M, Lohmann G, Wächter M, Milan P, Lorenz E, Heinemann D, Tabar MR, Peinke J (2016) Short term fluctuations of wind and solar power systems. *New J Phys* 18(6):1–15
16. Sovacool BK (2009) The intermittency of wind, solar, and renewable electricity generators: technical barrier or rhetorical excuse. *Utilities Policy* 3(4):288–296
17. Lorenz E, Hurka J, Heinemann D, Beyer HG (2009) Irradiance forecasting for the power prediction of grid-connected photovoltaic systems. *IEEE J Sel Top Appl Earth Obs Remote Sens* 2(1):2–10
18. Alzahrani A, Shamsi P, Dagli C, Ferdowsi M (2017) Solar irradiance forecasting using deep neural networks. *Procedia Comput Sci* 217:304–313
19. Mori H, Kurata E (2008) Application of gaussian process to wind speed forecasting for wind power generation. In: 2008 IEEE international conference on sustainable energy technologies, vol 24, pp 956–959
20. Soman SS, Zareipour H, Malik O, Mandal P (2010) A review of wind power and wind speed forecasting methods with different time horizons. In: North American power symposium, pp 1–8
21. Liu H, Tian HQ, Chen C, Li YF (2010) A hybrid statistical method to predict wind speed and wind power. *Renewable Energy* 35(8):1857–1861
22. Zhao G, Ma F, Wei L, Chua H, Chang CC, Zhang XJ (2012) Electricity generation from cattle dung using microbial fuel cell technology during anaerobic acidogenesis and the development of microbial populations. *Waste Manage* 32(9):1651–1658
23. Inoue K, Ito T, Kawano Y, Iguchi A, Miyahara M, Suzuki Y, Watanabe K (2013) Electricity generation from cattle manure slurry by cassette-electrode microbial fuel cells. *J Biosci Bioeng* 116(5):610–615
24. Cantrell KB, Ducey T, Ro KS, Hunt PG (2018) Livestock waste-to-bioenergy generation opportunities. *Biores Technol* 99(17):7941–7953
25. Asher MI, Keil U, Anderson HR, Beasley R, Crane J, Martinez F, Mitchell EA, Pearce N, Sibbald B, Stewart AW (1995) International study of asthma and allergies in childhood (ISAAC). *Ration Meth* 8(3):483–491
26. Echiegu EA. Operation of a domestic biogas plant in an urban setting in a developing country-a field experience. OMICS International, 25 July 2017
27. CBSE NCERT Notes Class 8 Biology Cell. [www.examfear.com/notes/Class-10/Physics/Sources-of-Energy/714/Bio-Mass.htm](http://www.examfear.com/notes/Class-10/Physics/Sources-of-Energy/714/Bio-Mass.htm). Last accessed 24 Aug 2020
28. Fuel cells: essay on fuel cells: devices: energy management. In: Engineering notes, India. Last accessed 24 Aug 2020

# Multi-objective Optimization of Cutting Parameters in Turning Process for Minimization of Carbon Emission and Processing Time



Gunjan Agarwal, M. K. Khare, Ankit Kumar Singhal,  
and Ravi Prakash

## 1 Introduction

In the world, India stands 12th in production and 7th in consumption of machine tools as per the Gardner Business Media survey 2019 [1]. Machining processes have number of inputs in the form of energy, material and information and produce different outputs [2] (Fig. 1).

In machining process, 99% of environmental impact is due to energy consumption in machine tool [3]. Cutting fluids are also having significant environmental impact on machining processes [4]. So machining processes should be taken into account for study to reduce material resources and bad environmental impacts.

## 2 Literature Review

To reduce the bad environmental impact in the form of carbon emission, researchers have done work in this direction. In 2000s, work has been done by Gutowski [5] to analyze material and energy consumption and their effect on environment in different machining processes. CNC machining parameters have been optimized by Anderberg et al. [6] to reduce specific energy consumption and increasing material removal rate. This will lead to increase in energy efficiency and reduce cost of manufacturing a component.

In machining, parameters were optimized on minimum energy and carbon footprints by Mativenga and Rajemi [7]. Li et al. [8] had done the quantity analysis of carbon emission in CNC machining system. In the work by Kant and Sangwan [9], cutting parameters have been optimized to minimize power consumption and surface roughness using gray relational analysis and response surface analysis.

---

G. Agarwal (✉) · M. K. Khare · A. K. Singhal · R. Prakash  
Department of Mechanical Engineering, College of Engineering Roorkee, Roorkee, India



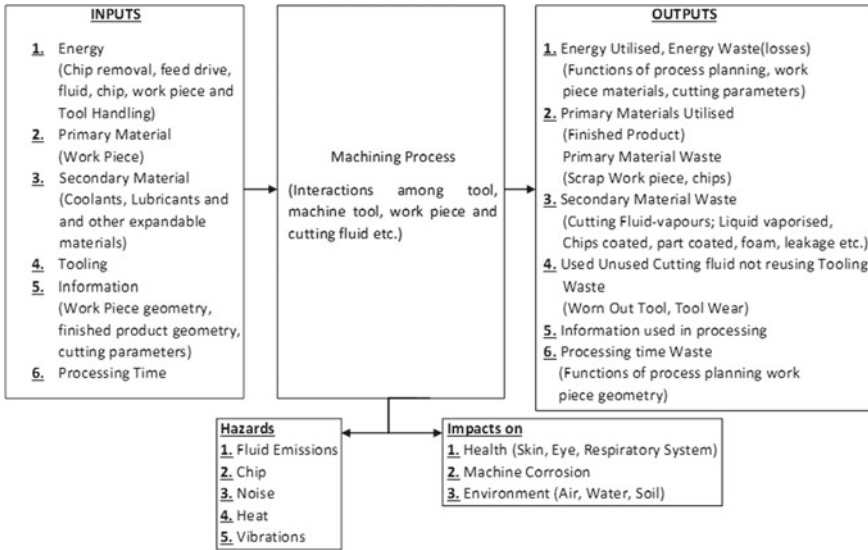


Fig. 1 Machining process with wastes [2]

As per the results, feed is more important machining parameter followed by depth of cut and cutting speed. In the work by Dambhare et al. [10], the effect of process parameters, the machining environment and the type of cutting tool on the response were observed. Analysis of variance (ANOVA) was applied to test data. Process analysis was done using response surface methodology (RSM). Liu et al. [11] had done multi-objective optimization of parameters of cutting processes using low-carbon emission cost.

In the work by Zhang et al. [12], multipass dry milling process has been optimized for high efficiency and low-carbon emission. In multi-objective optimization model, processing time and carbon emissions are to be minimized with surface roughness as a constraint (Sihag and Sangwan [13]). RSM is used to design the experiments. GA has been used to optimize the parameters.

Models of carbon emissions, surface roughness and processing time were obtained through input–output response surface and theoretical analysis by Jiang et al. [14]. Experiments were conducted on lathe machine using AISI1045 steel. NAGAI were applied to solve the equations. TOPSIS method is used to find the optimized parameters.

Sihag and Sangwan [15] developed a multi-objective optimization model to minimize energy consumption and maximize material removal rate while obtaining good quality product. Response surface method has been applied.

In the work, Pawan et al. [16] optimized two objectives, surface roughness and power consumption, using TOPSIS method. As per findings, the depth of cut is a more significant factor than feed rate and speed. The optimized results were

compared with gray relational methods. Both methods have different results, and best method should be selected on the basis of confirmation experiments. Experiments have been performed on heavy duty lathe machine.

In the various work done by researchers, amount of energy and hence the carbon emission have been minimized without taking cutting fluid, cutting tool, etc., into consideration. In the present work, wet runs are also taken into account to study the effect of cutting fluid in carbon emission along with cutting tool and cutting energy in machining process.

### 3 Methodology

In the present work, study of carbon emission has been done by using not only energy consumption in turning process but also cutting tool and cutting fluid taking into considerations. Experiments have been carried out to measure energy and processing time in different conditions in dry and wet run. Amount of carbon emission due to cutting energy, cutting fluid and cutting tool have been calculated. Mathematical model is established, and effect of parameters such as cutting speed ( $v$ ), feed ( $f$ ) and depth of cut ( $d$ ) on carbon emission have also been studied. RSM has been used to conduct the experiments. Analysis of variance (ANOVA) is used to analyze the parameters. Multi-objective optimization is to be done using desirability function to optimize the parameters to minimize processing time (PT) and carbon emission (CE).

#### a. Objective function

$$\begin{aligned} &\text{Minimize } [CE(X), PT(X)] \\ &X = w(v, f, d), \end{aligned}$$

where

$w$  is function of  $v$ ,  $f$  and  $d$ .

CE( $X$ ) = Carbon emission.

PT( $X$ ) = Processing time.

The problem is to be optimized within the range of cutting parameters selected for experimentation.

The methodology for solving multi-objective optimization is presented in Fig. 2 (Table 1).

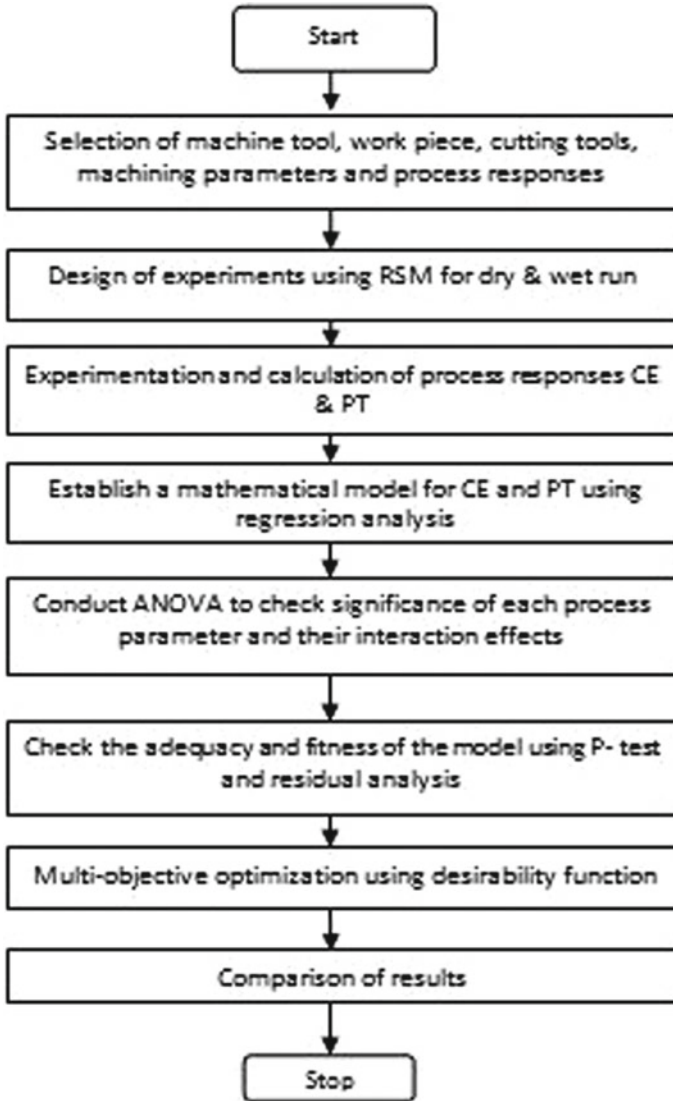


Fig. 2 Methodology for multi-objective optimization

Table 1 Cutting tool coefficients [17]

Cutting tool coefficients	$C_1$	$p$	$q$	$r$
	$5.02 \times 10^{10}$	4.55	1.55	0.55

### 3.1 Calculation of Carbon Emission

The carbon emission (CE) in a metal cutting process is directly caused by various factors such as energy consumption in machine tool, use of cutting tools and use of cutting fluid. The amount of all three depends upon cutting parameters  $v$ ,  $f$  and  $d$ . The carbon emission (CE) in a metal cutting process caused by other factors is not considered as they are not dependent on the cutting parameters of metal cutting process. Amount of carbon emission due to different factors is shown in Table 2.

$$\text{Total carbon emission } CE_T = CE_{\text{Energy consumption}} + CE_{\text{Cutting fluid}} + CE_{\text{Cutting tool}}$$

$CE_{\text{Energy consumption}}$  = Carbon emission due to energy consumption.

$CE_{\text{Cutting fluid}}$  = Carbon emission due to cutting fluid.

$CE_{\text{Cutting tool}}$  = Carbon emission due to cutting tool.

#### Carbon emission due to amount of energy consumption

Amount of energy consumption can be taken from each experimental run. This amount can be multiplied by carbon emission per kWh.

#### Carbon emission due to cutting tool wastes

$W_{\text{cutting tool}}$  = No. of tool expended after all possible regrinds  $\times$  mass of one tool  
 = (Time for one pass  $\times$  mass of one tool)/(Tool life  $\times$  No of possible regrinds or No. of cutting edges).

$$\text{Cutting tool waste per pass} = \frac{\pi L(D_i - d)v f^{q-1} d^r m_t}{1000 C_1 n_g}$$

where  $L$  is cutting length,  $D_i$  = initial diameter,  $q$ ,  $r$  and  $C_1$  constants whose values are given in Table 1,  $m_t$  = mass of tool, and  $n_g$  = No. of cutting edges.

Carbon emission due to cutting tool waste = Cutting tool waste  $\times$  carbon emission per unit mass.

#### Carbon emission due to Cutting fluid wastes

= Processing time  $\times \delta \times [CE_{\text{cf production}} \times V_{\text{in}} + CE_{\text{cf disposal}} \times V_{\text{dis}}]$ /Time of CF flow.

**Table 2** Carbon emission due to different machining process element [13]

Carbon emission for cutting energy	1.41 KgCO <sub>2</sub> /KWh
Carbon emission for coolant	500 KgCO <sub>2</sub> /m <sup>3</sup>
Carbon emission for coolant dis	200 KgCO <sub>2</sub> /m <sup>3</sup>
Carbon emission-cutting tool	31.5 KgCO <sub>2</sub> /Kg

$\delta$  = Cutting fluid concentration.

$CE_{cf \text{ production}}$  = Carbon emission due to cutting fluid production.

$CE_{cf \text{ disposal}}$  = Carbon emission due to cutting fluid disposal.

$V_{in}$  = Volume of cutting fluid in during machining run (ml).

$V_{dis}$  = Volume of cutting fluid dispose during machining run (ml).

## 4 Case Study

For the above work, experiments were conducted on a HMT lathe powered by 10.3 kW motor using AISI1040 steel and SNUN120412 throwaway carbide-cutting tool inserts under dry and wet conditions. The size of the specimen was  $\phi 48$  mm  $\times$  108 mm. Soluble cutting oil METAKOOL is used in machining process with 10% water. Delivery rate of the pump was 1250 ml/min. Amount of cutting fluid delivered and disposed has been measured for each experimental run. The cutting fluid of same concentration was added to the tank as per the requirement. The wear of tool per pass is calculated as it is very less to measure it. Time and power have been measured to calculate the amount of energy consumption for each pass using stopwatch and energy meter, respectively. In Tables 1 and 2, various

**Table 3** Processing energy for dry and wet run

S. No.	Cutting speed (m/min)	Feed (mm/rev)	Depth of cut (mm)	Energy consumption dry run (kJ)	Carbon emission dry run (KgCO <sub>2</sub> )	Energy consumption wet run (kJ)	Carbon emission wet run (KgCO <sub>2</sub> )
1	150	0.09	2	262.12	0.102664	351.33	0.137604
2	90	0.09	2	427.66	0.1675	463.77	0.181643
3	120	0.05	2	593.5	0.232454	664.82	0.260388
4	120	0.13	2	267.22	0.104661	306.88	0.120195
5	150	0.09	0.5	237.89	0.093174	273.44	0.107097
6	120	0.13	0.5	202.32	0.079242	251.94	0.098677
7	120	0.05	0.5	511.37	0.200287	648.1	0.253839
8	90	0.09	0.5	283.46	0.111022	464.27	0.181839
9	90	0.05	1.25	700.35	0.274304	844.17	0.330633
10	120	0.09	1.25	353.12	0.138305	397.81	0.155809
11	120	0.09	1.25	356.57	0.139657	393.63	0.154172
12	120	0.09	1.25	342.97	0.13433	393.86	0.154262
13	120	0.09	1.25	347.33	0.136038	402.38	0.157599
14	120	0.09	1.25	353.55	0.138474	383.99	0.150396
15	150	0.05	1.25	505.19	0.197866	542.43	0.212452
16	90	0.13	1.25	315.60	0.12361	336.40	0.131757
17	150	0.13	1.25	262.38	0.102766	328.97	0.128847

**Table 4** Carbon emission due to cutting energy, cutting fluid and cutting tool

S No	Cutting speed (m/min)	Feed (rev/min)	Depth of cut (mm)	Processing time (Sec)	CE <sub>Cutting tool</sub> (Kg)	CE <sub>Cutting fluid</sub> (Kg)	CE <sub>Energy consumption</sub> (Kg)	CE <sub>T</sub> (Kg)
1	150	0.09	2	77	0.000264	0.815319	0.137604	0.953187
2	90	0.09	2	125.83	4.31E-05	1.333822	0.181643	1.515508
3	120	0.05	2	175.88	8.65E-05	2.083547	0.260388	2.344021
4	120	0.13	2	69.28	0.000146	0.481531	0.120195	0.601872
5	150	0.09	0.5	97.8	0.000123	1.149118	0.107097	1.256339
6	120	0.13	0.5	67.63	6.83E-05	0.715254	0.098677	0.813999
7	120	0.05	0.5	172.8	4.04E-05	1.882286	0.253839	2.136166
8	90	0.09	0.5	124.15	2.01E-05	1.328054	0.181839	1.509913
9	90	0.05	1.25	230.26	2.41E-05	2.5877	0.330633	2.918357
10	120	0.09	1.25	98.9	9.23E-05	1.042594	0.155809	1.198495
11	120	0.09	1.25	97.7	9.23E-05	1.025794	0.154172	1.180058
12	120	0.09	1.25	98.9	9.23E-05	1.038694	0.154262	1.193048
13	120	0.09	1.25	97	9.23E-05	1.014581	0.157599	1.172272
14	120	0.09	1.25	97.91	9.23E-05	1.034253	0.150396	1.184741
15	150	0.05	1.25	127.2	0.000148	1.350328	0.212452	1.562927
16	90	0.13	1.25	88.32	4.07E-05	0.924636	0.131757	1.056433
17	150	0.13	1.25	52.59	0.00025	0.554981	0.128847	0.684077

data for calculating cutting tool waste and cutting fluid waste carbon emission have been given. In Table 3, experimental data are presented. In Table 4, amount of carbon emission due to different sources has been shown.

#### 4.1 Mathematical Modeling of Responses

The second-order mathematical models for energy (dry and wet), processing time and carbon emission have been obtained.

$$\begin{aligned}
 \text{Energy, } E_d = & + 1339.62 - 3.49 * \text{speed} - 17,777.88 * \text{feed} \\
 & + 448.12 * \text{depth of cut} + 29.57 * \text{speed} * \text{feed} \\
 & - 1.33 * \text{speed} * \text{depth of cut} + 58,123.28 * \text{feed}^2 \\
 & - 89.07 * \text{depth of cut}^2.
 \end{aligned}$$

$$\begin{aligned} \text{Energy, } E_w = & + 2655.61 - 14.35 * \text{speed} - 23,525.78 * \text{feed} \\ & + 5.41 * \text{depth of cut} + 61.31 * \text{speed} * \text{feed} \\ & + 0.87 * \text{speed} * \text{depth of cut} + 318.50 * \text{feed} * \text{depth of cut} \\ & + 0.022 * \text{speed}^2 + 61,997.19 * \text{feed}^2 - 45.50 * \text{depth of cut} \end{aligned}$$

$$\begin{aligned} \text{Processing time} = & + 644.09571 - 3.34949 \text{ Speed} - 5353.21042 \text{ feed} \\ & + 17.71861 \text{ Depth of cut} + 14.02708 \text{ Speed} * \text{feed} \\ & - 0.249778 \text{ Speed} * \text{Depth of cut} - 11.91667 \text{ feed} * \text{Depth of cut} \\ & + 0.006282 \text{ Speed}^2 + 13,035.31250 \text{ feed}^2 \\ & + 13,035.31250 \text{ feed}^2 + 4.37156 \text{ Depth of cut}^2 \end{aligned}$$

$$\begin{aligned} \text{Carbon emission} = & 8.50 - 0.052 * \text{speed} - 68.437 * \text{feed} \\ & + 0.584 * \text{depth of cut} + 0.205 * \text{cutting speed} * \text{feed} \\ & - 0.0034 * \text{cutting speed} * \text{depth of cut} \\ & - 3.4998 * \text{feed} * \text{depth of cut} + 0.00011 * v^2 \\ & + 167.189 * f^2 + 0.036 * d^2 \end{aligned}$$

Effect of process parameters on process response has been studied using ANOVA analysis. The ANOVA analysis of processing time is shown in Table 5.

The model *F*-value of 42.77 implies the model is significant. There is only a 0.01% chance that an *F*-value this large could occur due to noise—values less than 0.0500 indicate model terms are significant. In this case, *A*, *B*, *AB* and *B*<sup>2</sup> are significant model terms.

**Table 5** ANOVA for quadratic model—response processing time

Source	Sum of squares	df	Mean square	<i>F</i> -value	<i>p</i> -value	
<b>Model</b>	32,030.71	9	3558.97	42.77	<0.0001	significant
<i>A</i> -Speed	5722.90	1	5722.90	68.78	<0.0001	
<i>B</i> -Feed	22,932.25	1	22,932.25	275.62	<0.0001	
<i>C</i> -Depth of cut	25.88	1	25.88	0.3111	0.5944	
<i>AB</i>	1133.33	1	1133.33	13.62	0.0077	
<i>AC</i>	126.34	1	126.34	1.52	0.2576	
<i>BC</i>	0.5112	1	0.5112	0.0061	0.9397	
<i>A</i> <sup>2</sup>	134.60	1	134.60	1.62	0.2440	
<i>B</i> <sup>2</sup>	1831.55	1	1831.55	22.01	0.0022	
<i>C</i> <sup>2</sup>	25.46	1	25.46	0.3060	0.5974	
<b>Residual</b>	582.42	7	83.20			
Lack of fit	579.74	3	193.25	287.95	<0.0001	Significant
Pure error	2.68	4	0.6711			
<b>Cor Total</b>	32,613.13	16				

**Table 6** ANOVA for quadratic model—carbon emission

Source	Sum of squares	df	Mean square	<i>F</i> -value	<i>p</i> -value	
<b>Model</b>	5.71	9	0.6342	34.63	<0.0001	Significant
A-Speed	0.8088	1	0.8088	44.16	0.0003	
B-Feed	4.21	1	4.21	229.99	<0.0001	
C-Depth of cut	0.0114	1	0.0114	0.6217	0.4563	
AB	0.2416	1	0.2416	13.19	0.0084	
AC	0.0238	1	0.0238	1.30	0.2915	
BC	0.0441	1	0.0441	2.41	0.1647	
$A^2$	0.0440	1	0.0440	2.40	0.1651	
$B^2$	0.3013	1	0.3013	16.45	0.0048	
$C^2$	0.0018	1	0.0018	0.0994	0.7618	
<b>Residual</b>	0.1282	7	0.0183			
Lack of fit	0.1278	3	0.0426	395.51	<0.0001	Significant
Pure error	0.0004	4	0.0001			
<b>Cor total</b>	5.84	16				

The ANOVA analysis for carbon emission has been shown in Table 6. The model *F*-value of 34.63 implies the model is significant. There is only a 0.01% chance that an *F*-value this large could occur due to noise—values less than 0.0500 indicate model terms are significant. In this case, *A*, *B*, AB and  $B^2$  are significant model terms.

## 4.2 Multi-objective Optimization

Multi-objective optimization is done to obtain optimum set of cutting parameters using desirability function of Design-Expert 13 Software. The parameters, responses to their goal and ranges are shown in Table 7. The optimizations results are shown in Table 8.

**Table 7** Constraints used for optimization in wet run

Condition	Goal	Lower limit	Upper limit
<i>v</i> : Cutting speed (m/min)	In range	90	150
<i>f</i> : Feed (mm/rev)	In range	0.05	13
<i>d</i> : Depth of cut (mm)	In range	0.5	2
PT: Processing time (sec)	Minimize	52.0	217.33
CE: Carbon emission (kg-CO <sub>2</sub> )	Minimize	0.60	2.92



**Table 8** Optimization solutions

Number	Speed	feed	Depth of cut	Processing time	Carbon emission	Desirability	Speed	
1	150.000	0.125	2.000	55.563	0.568	0.992	150.000	Selected
2	149.999	0.126	2.000	55.563	0.567	0.992	149.999	
3	149.999	0.126	2.000	55.565	0.566	0.992	149.999	
4	149.998	0.126	2.000	55.565	0.567	0.992	149.998	
5	150.000	0.125	2.000	55.566	0.569	0.992	150.000	
6	149.997	0.125	2.000	55.575	0.570	0.992	149.997	
7	149.999	0.127	2.000	55.579	0.565	0.992	149.999	
8	149.998	0.124	2.000	55.585	0.571	0.992	149.998	
9	150.000	0.125	1.992	55.593	0.570	0.992	150.000	
10	149.999	0.125	1.992	55.597	0.571	0.992	149.999	

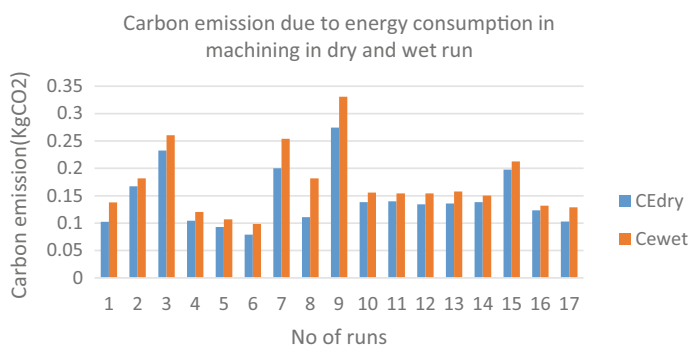


**Fig. 3** Comparison of carbon emission due to energy consumption for dry and wet run

## 5 Results and Discussion

The variation of carbon emission in dry and wet run is shown in Fig. 3.

For the present problem for all 17 experimental runs, the values of carbon emission for energy consumption are compared for dry and wet run (Fig. 3). In each run, the value of carbon emission for wet run is more in comparison with dry run. These excess values are due to the extra power required for coolant pump used in wet run. It may also be due to the increase in specific cutting energy as hardness of workpiece may increase due to decrease in interface temperature due to the use of cutting fluid. The same has been found by Anderberg [6] that specific cutting energy is dependent on workpiece material, presence of cooling, cutting tool geometry, process parameters and micro-geometry of cutting tool.

Figure 4 shows the effect of cutting speed, feed and depth of cut on carbon emission. Due to increase in cutting speed and feed, there is decrease in processing

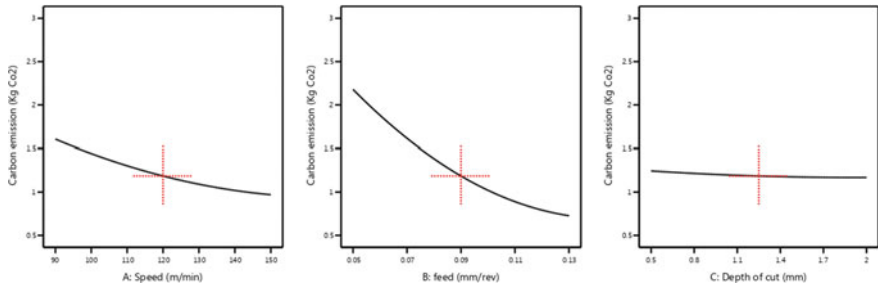


Fig. 4 Effect of parameters on carbon emission

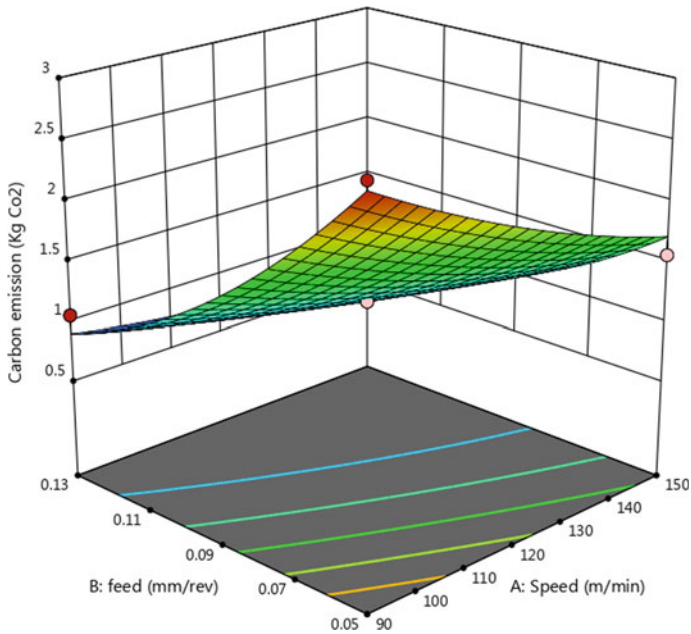
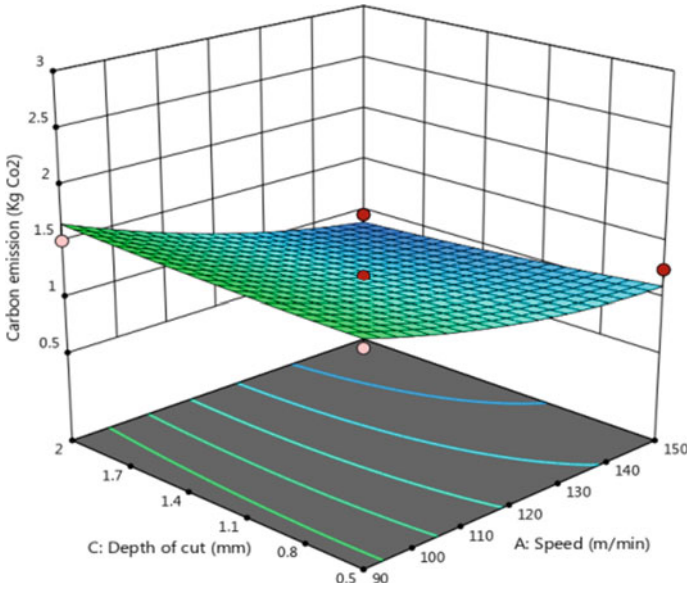
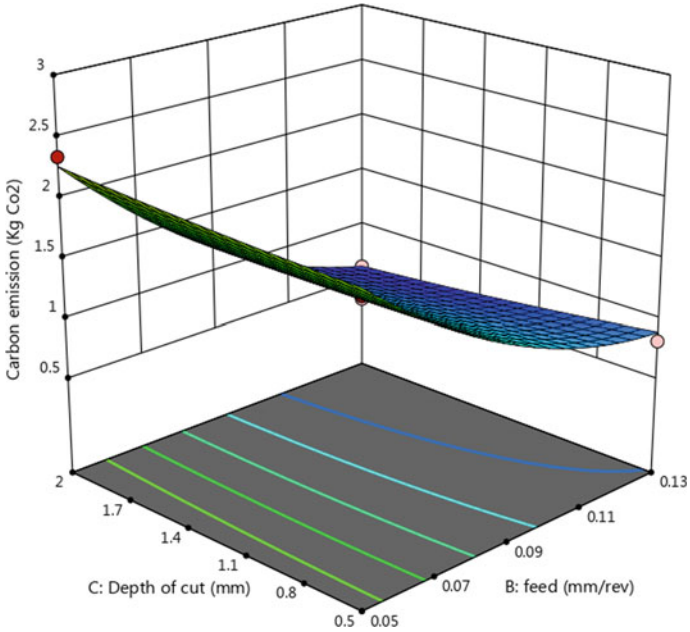


Fig. 5 Surface graph for interaction effects of feed and cutting speed at constant depth of cut on carbon emission

time. This will lead to decrease in energy consumption as well as fluid delivered in the process. Due to increase in depth of cut, there is an increase in tool waste and hence more carbon emission, but amount of carbon emission due to tool waste is very less as shown in Fig. 8. The three-dimensional surface graphs for interaction effect of cutting speed, feed and depth of cut are shown in Figs. 5, 6, and 7 for wet run. From Fig. 5, it can be seen that there is decrease in carbon emission when there is increase in values of cutting speed and feed. In Figs. 6, and 7, the effect of depth of cut on carbon emission is not much, but at higher values of cutting speed and feed, it shows less carbon emission at high depth of cut.



**Fig. 6** Surface graph for interaction effects of depth of cut and cutting speed at constant feed on carbon emission



**Fig. 7** Surface graph for interaction effects of feed and depth of cut at constant speed on carbon emission

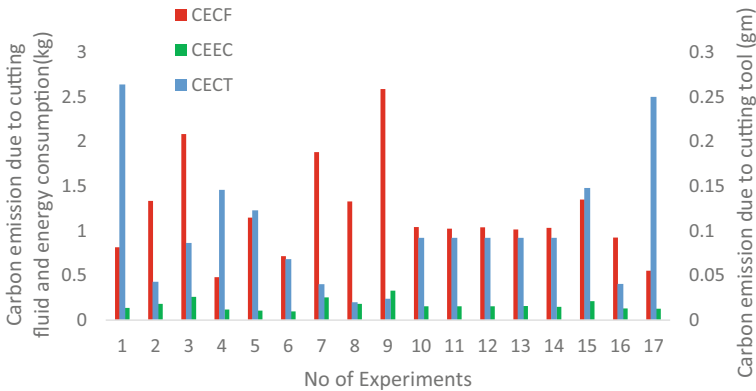


**Fig. 8** Carbon emission in turning process

On the basis of experimental data and their calculations, the graph (Fig. 8) is drawn between experimental runs and values of carbon emission. The values of carbon emissions are varying in each run as per the variation in the values of cutting parameters. The values of carbon emission due to cutting fluids are more in comparison with carbon emission due to energy consumption in machining. The values of carbon emission due to cutting tool material are negligible.

## 6 Conclusions

In the present study, a multi-objective optimization has been done to find out cutting parameters to minimize carbon emission and processing time in machining. For values of carbon emission, cutting tool, cutting fluid and energy consumption all are considered. For this, experiments have been performed on center lathe machine. Experiments have been designed using Box–Behnken method for RSM using design expert software. During each experiment, data for energy, processing time and cutting fluid delivered and dispose of with chips are measured and collected. Mathematical equations have been obtained. Effect of cutting parameters on carbon emission and processing time have been obtained. At higher values of cutting speed and feed, the value of carbon emission is less because of less energy consumption which is due to decrease in processing time. Fluid consumption is also less as fluid delivered will be less in shorter processing time. In surface graph, at low values of cutting speed and feed, the effect of depth of cut is uniform. At higher values of cutting speed and feed, the value of carbon emission is less at high depth of cut than at low depth of cut. This surface graph can be used for selection of cutting parameters. Optimization has been done using desirability function.

**Acknowledgements** The authors are thankful to the affiliating institute, College of Engineering Roorkee, Roorkee, India, for providing necessary support to carry out this research work.

## References

1. IMTMA-Annual-Report 2019–2020
2. Agarwal G (2018) Optimization of process parameters for the minimization of wastes in a machining system. PhD Thesis
3. CECIMO (2009) Concept description for CECIMO's self-regulatory initiative SRI for the sector specific implementation of the direct 2005/32/EC. Available online <http://www.eco-design.info.eu/documentations/Machine-tool-VA2009>
4. Allen D, Bauer D, Brass B, Gutowski T, Murphy C, Piwonka T (2002) Environmentally benign manufacturing: trends in Europe, Japan, and the USA. *J Manuf Sci Eng* 124:908–920
5. Gutowski T (2007) The carbon and energy intensity of manufacturing. In: 50th Seminar CIRP, Keynote Address, Liverpool, pp 1–6
6. Anderberg SE, Kara S, Beno T (2009) Impact of energy efficiency on computer numerically controlled machining. *Proc I Mech E Part B: J Eng Manuf* 22:531–541
7. Mativenga PT, Rajemi MF (2011) Calculation of optimum cutting parameters based on minimum energy footprint. *CIRP Ann Manuf Technol* 60(1):149–152
8. Li C, Tang Y, Cui L, Yi Q (2013) Quantitative analysis of carbon emissions of CNC-based machining systems. In: 10th IEEE international conference on networking, sensing and control, ICNSC 2013, pp 869–874
9. Kant G, Sangwan KS (2014) Prediction and optimization of machining parameters for minimizing power consumption and surface roughness in machining. *J Clean Prod*
10. Dambhare S, Deshmukh S, Borade A, Digalwar A, Phatee M (2015) Sustainability issues in turning process: a study in indian machining industry. *Procedia CIRP* 26:379–384
11. Liu Z, Sun D, Lin C, Zhao X, Yang Y (2016) Multi-objective optimization of the operating conditions in a cutting process based on low carbon emission costs. *J Clean Prod* 124:266–275
12. Zhang H, Deng Z, Fu Y, Lv L, Yan C (2017) A process parameters optimization method of multi-pass dry milling for high efficiency, low energy and low carbon emissions. *J Clean Prod* 148:174–184
13. Sihag N, Sangwan KS (2018) Development of a multi-criteria optimization model for minimizing carbon emission and processing time during machining. *Procedia CIRP* 69:300–305
14. Jiang Z, Gao D, Lu Y, Liu X (2019) Optimization of cutting parameters for trade off among carbon emissions, surface roughness, and processing time. *Chin J Mech Eng* 32:94. <https://doi.org/10.1186/s10033-019-0408-9>
15. Sihag N, Sangwan KS (2019) Multiobjective optimization for energy efficient machining with high productivity and quality for a turning processes. *Procedia CIRP* 80:67–72
16. Pawanr S, Garg GK, Routroy S (2019) Multiobjective optimization of machining parameters to minimize surface roughness and power consumption using TOPSIS. *Procedia CIRP* 86:116–120
17. Agarwal G, Khare MK. Multiobjective optimisation of cutting parameters in machining-a sustainable approach. *Mater Today: Proc* (in press)

# Numerical Heat Transfer Analysis of a Rectangular Microchannel Heat Sink with Graphene-based Nanofluids



Sasmita Bal and Koustav Bandyopadhyay

## 1 Introduction

The introduction and development of commercial computers since 1950s have given rise to a digital age. With time, the increasing demand for computing power has sparked an exponential rise in development and advancement of chips in terms of processor density and capacity. High-density packaging in electronic industry creates a high heat flux which is responsible for system failure [1, 2]. It is of paramount importance to employ appropriate cooling mechanisms to reduce the operating temperature of the electronic equipment. Thus, an effective but compact cooling system is continuously being explored.

Many researchers have found that nanofluids show an increasing trend in thermal conductivity with its concentration in base fluid and, therefore, an excellent candidate for heat transfer [3–6]. Suspension of nanofluids like  $\text{TiO}_2$ ,  $\text{Al}_2\text{O}_3$ , and  $\text{CuO}$  in base fluid has been proved to improve heat dissipation capability [7–10]. Several experimental studies have been reported on heat transfer behavior of graphene as nanofluid within a microchannel. The mass flow rate of nanofluid and concentration of graphene nanoparticles were used as major variables within those experiments [11–15]. The variation of thermal conductivity of graphene with temperature, for different concentrations of graphene, has also been studied by several researchers [16–18].

As it is very difficult to do experiments with nanofluids of different concentrations and to see its impact on heat transfer, significant number of papers are not available in the literature. So, an attempt has been made to show numerically the contribution of graphene nanofluid to transfer heat significantly in a microchannel.

---

S. Bal (✉)  
Alliance University, Bangalore, India

K. Bandyopadhyay  
KIIT Deemed University, Bhubaneswar, India

In the present numerical work, graphene nanoplatelets (Gnp) suspended in distilled water (base fluid) as nanofluid has been studied for different concentrations and mass flow rates in a rectangular microchannel. The geometry of the model and the simulation analysis were done in CATIA V5R20 and Ansys R19.2, respectively. The analysis was performed by solving a couple of governing equations for a set of input parameters and required boundary conditions. The effect of various parameters like mass flow rate and concentration of nanofluids on pressure drop, surface temperature, and heat absorbed by the fluid were studied.

## 2 Methodology

### 2.1 Microchannel Heat Sink Modeling

The current study aims to evaluate the heat transfer and cooling of an electronic chip aided by a microchannel device placed directly over the chip. The heat dissipated from the top layer of the chip is considered as conduction at the interface between the chip and the base of the cooling device. Heat flow from this base to the cooling fins is also considered as conduction. Further, both conductive and convective heat transfers are considered at the fluid interface with the fin and device base. Continuity, momentum, and energy equations are used for the simulation. Table 1 presents the measurements of the device base, fin, and channel dimensions. The operating conditions and thermophysical properties of the nanofluid and solid are provided in Tables 2, 3, and 4. Thermophysical properties are calculated using equations suggested in the literature [13]. Figure 1 shows the base plate with vertical cooling fins, regularly inter-spaced at 0.5 mm. It is noted that the microchannels are presented between two consecutive fins through which the fluid flows. It is to be noted that the experiment was performed on a 30 microchannel device [19]. However, due to computation power limitation, the modeling and the subsequent analysis were done on a representative 5-channel model. Given that the analysis incorporates area of the heat sink plate, a 5-channel model would produce similar results as the experimental setup.

**Table 1** Dimensions of the cooling device

Parameter	Value
Length of channel ( $L$ ) (mm)	30
Width of channel ( $W$ ) (mm)	0.5
Height of channel ( $H_1$ ) (mm)	5
Height of base plate ( $H_2$ ) (mm)	1
Width of fin ( $w$ ) (mm)	0.5
Height of fin ( $H_3$ ) (mm)	5
Area of base plate [model] (mm <sup>2</sup> )	315

**Table 2** Operating conditions

Operating conditions	Value
Inlet fluid temperature $T_{in}$ (°C)	20
Heat load (W)	50, 100, 150, 200
Mass flow rate (kg/s)	0.01, 0.02, 0.03
Nanofluid concentration (vol%)	0, 0.05, 0.1, 0.15, 0.2

**Table 3** Thermophysical properties of graphene nanofluid at different concentrations and 20 °C

Concentration (vol%)	Density ( $\rho_{nf}$ ) (kg/m <sup>3</sup> )	Viscosity ( $\mu_{nf}$ ) (Ns/m <sup>2</sup> )	Thermal conductivity ( $K_{nf}$ ) (W/mK)	Specific heat capacity ( $c_{nf}$ ) (J/kgK)
0	1000	0.004	0.59	4182
0.05	1025	0.009	0.61	3358
0.1	1055	0.0095	0.625	2807
0.15	1075	0.0104	0.630	2366
0.2	1095	0.013	0.630	1925

**Table 4** Thermophysical properties of copper (used as heat sink material)

Density ( $\rho_s$ ) (kg/m <sup>3</sup> )	Thermal conductivity ( $K_s$ ) (W/mK)	Specific heat capacity ( $c_s$ ) (J/kgK)
8940	386	385

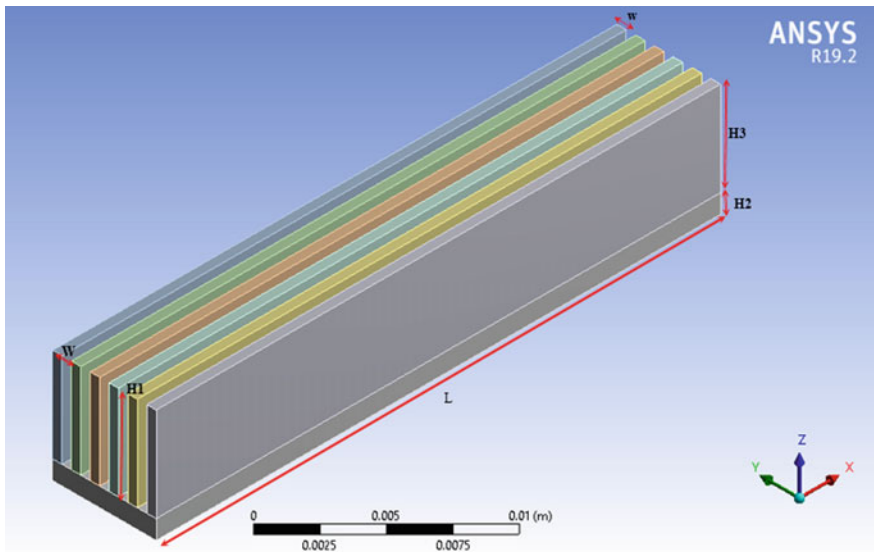


**Fig. 1** Isometric view of the model comprising five channels and six fins



## 2.2 Simulation Setup

The geometry was created in CATIAV5R20, and meshing was done in the meshing [Ansys Autodyn PrepPost] packaged within Ansys R19.2. The analysis was done on Fluent 19.2. For the computational analysis, Fluent solves a coupled governing equation for a set of input parameters and required boundary conditions. A uniform tetrahedral meshing with edge size 0.25 mm was used (Fig. 2). The SIMPLE algorithm was used to analyze the model. Second-order discretization was used to solve the pressure equation, and second-order upwind discretization was used to solve the momentum and energy equations. Given that this problem is energy predominant, a convergence criterion of  $10^{-6}$  was used for the energy equation and  $10^{-3}$  was used for velocity residual.

## 2.3 Governing Equation and Boundary Conditions

The base plate and the fins are solid copper. The values of thermal conductivity, density, and specific heat capacity are set to the Fluent database default values for copper.

For each combination of mass flow rate, fluid concentration, heat load, and constant inlet temperature of 20 °C, the analysis was executed as per the convergence criteria mentioned previously. Outputs were recorded for temperature of outlet, average temperature of the base plate, fluid pressure at inlet, and pressure at outlet. Using the values of inlet temperature ( $T_{in}$ ) and outlet temperature ( $T_{out}$ ), the

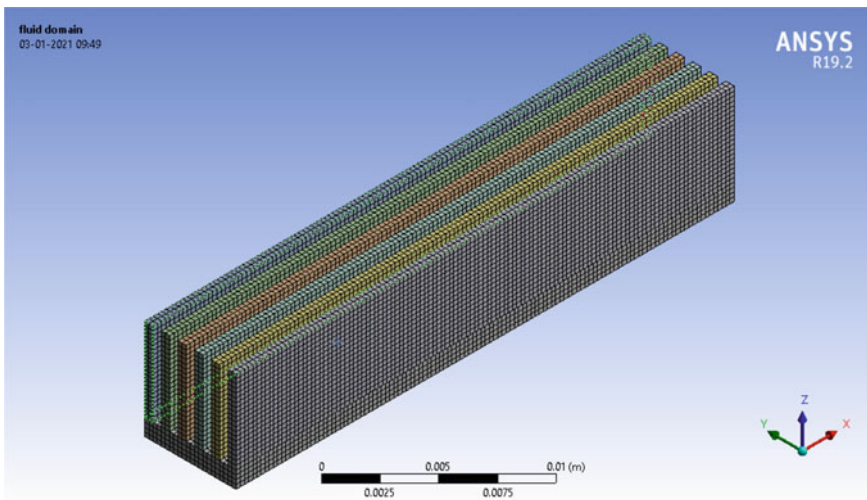


Fig. 2 Isometric view of the model showing tetrahedral meshing

heat absorbed by the fluid was calculated using the following Eqs. (1) and (2). The different parameters used in equations are inlet and outlet temperatures of the fluid, inlet, and outlet pressures of the fluid and mass flow rate of the fluid.

$$Q = mC_p\Delta T \quad (1)$$

$$\text{where } \Delta T = T_{\text{out}} - T_{\text{in}} \quad (2)$$

Given that the heat taken up by the fluid is a representative of the total heat transfer between the heat sink base and the fluid, this  $Q$  was utilized to calculate the heat transfer coefficient for this problem using Eq. (3). The average temperature of the base ( $T_{\text{avg}}$ ) was recorded using area-weighted average and substituted in the Eq. (4).

$$Q = hA\Delta t \quad (3)$$

$$\text{where } \Delta t = T_{\text{avg}} - ((T_{\text{in}} + T_{\text{out}})/2) \quad (4)$$

Here, the area in Eq. (3) represented by  $A$  refers to the total area of heat transfer, which is calculated using Eq. (5).

$$\text{Area} = \text{No. of channels} \times L \times (W + 2 \times H_1) \quad (5)$$

The pressure drop associated with each mass flow rate has been calculated by recording the values of pressure at inlet ( $p_{\text{in}}$ ) and pressure at outlet ( $p_{\text{out}}$ ) and putting in Eq. (6).

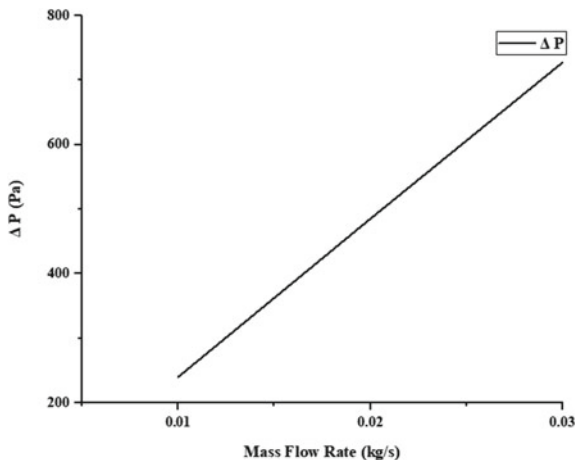
$$\Delta p = p_{\text{in}} - p_{\text{out}} \quad (6)$$

### 3 Results and Discussion

#### 3.1 Effect of Mass Flow Rate on Pressure Drop

It is well-known that there is a drop in pressure along the length of the flow. This is due to the frictional and viscous losses that occur. The calculated  $\Delta p$  as a function of mass flow rate at volumetric concentration of 0.1% and heat load of 150 W is shown in Fig. 3. It is noted that the drop in pressure rises linearly with increasing flow rate. Due to the constant area of the inlet, increasing mass flow rate results in higher velocity. At higher velocities, more frictional and viscous losses occur, which aid the drop in pressure.

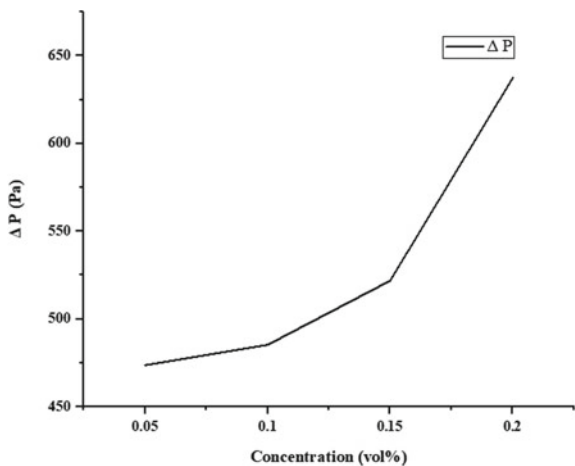
**Fig. 3** Variation of pressure drop with increasing mass flow rate



### 3.2 Effect of Nanoparticle Concentration on Pressure Drop ( $\Delta p$ )

An increase in concentration of nanoparticles in the base fluid increases the viscosity of the fluid. As viscosity is defined as the resistance of a liquid to flow, a higher viscosity requires a higher driving force to induce flow, which manifests as the pressure drop along the length of the flow. From Fig. 4, it is evident that the  $\Delta p$  increases in a nonlinear manner with increase in volumetric concentrations for mass flow rate of 0.02 kg/s and heat load of 100 W.

**Fig. 4** Variation of  $\Delta p$  with increasing concentration of nanoparticles within the coolant



### 3.3 *Effect of Volumetric Concentration on Heat Absorbed by the Fluid*

Using the inlet and outlet temperatures of the fluid and average temperature of base and thermophysical properties of the fluid at different concentrations, the heat absorbed was calculated using Eq. (3). Figure 5 shows the variation of  $Q$  (amount of heat absorbed by the fluid per sec) with varied concentrations for a fixed mass flow rate of 0.03 kg/s and heat load of 100 W. It was noted that with increase in concentration of the nanoparticles within the fluid, the amount of heat absorbed increases, thereby, indicating a higher efficiency of cooling capability.

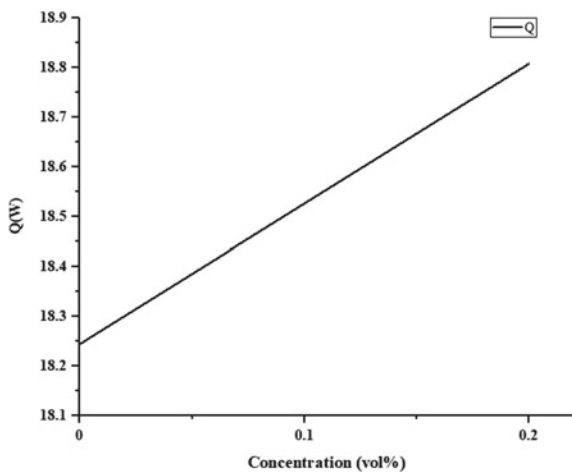
### 3.4 *Effect of Concentration on Fluid Temperature*

Figure 6 shows the variation of  $\Delta T$  with concentration of nanoparticles within the base fluid. The  $\Delta T$  is calculated by obtaining the difference of the fluid at the outlet and the inlet. The rise in  $\Delta T$  implies that the fluid absorbs more heat with increasing concentration. This is because with increase in concentration of nanoparticles, conductivity of the nanofluid and its cooling capability increase.

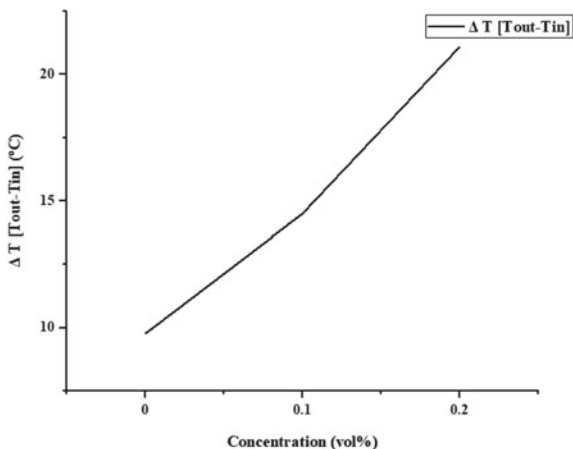
### 3.5 *Effect of Heat Load/Input on Temperature of Fluid*

With increasing heat load on fluid from 50 to 200 W, it is noted that the temperature difference between the outlet and inlet of the fluid rises linearly. The temperature of

**Fig. 5** Variation of  $Q$  as a function of concentration



**Fig. 6** Variation of  $\Delta T$  as a function of volumetric concentration of nanoparticles at 150 W



fluid outlet was recorded for volumetric concentration of 0% (water) and 0.2% at constant mass flow rate of 0.03 kg/s as shown in Fig. 7. The graph shows that the cooling liquid absorbs more heat with increasing the heat load on the cooling device.

### 3.6 Effect of Mass Flow Rate on $\Delta T$

With increase in mass flow rate of the cooling fluid, the velocity of the fluid increases and, hence, the time of contact of the fluid with the heated base and fins decreases. This results in lower amount of heat absorbed by the fluid and, hence,

**Fig. 7** Variation of  $\Delta T$  as a function of heat load on the cooling device

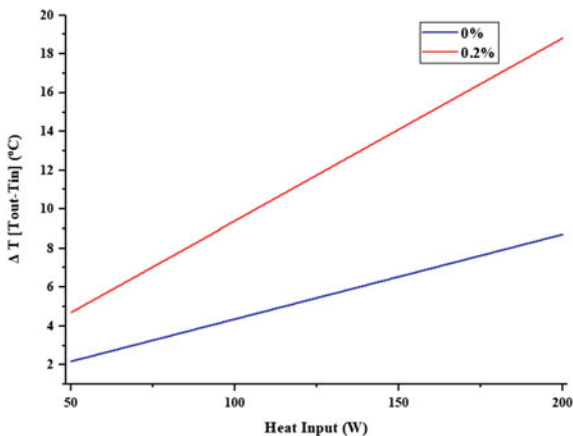
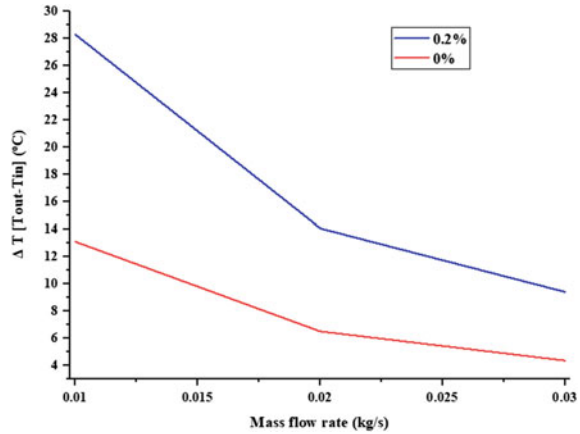


**Fig. 8** Variation of  $\Delta T$  as a function of mass flow rate



decrease in the difference between the inlet and outlet temperature. From Fig. 8, it is noted that  $\Delta T$  decreases with increase in the mass flow rate as expected.

### 3.7 Variation of Surface Heat Transfer Coefficient Along Flow Length

The heat transfer coefficient ( $h$ ) varies locally as a function of local temperature difference between the fluid and the heated solid. As the local temperature difference between the fluid and the solid is maximum at the inlet, it is expected that the heat transfer coefficient would also be maximum at the entry of the channel and would gradually decrease along the length of flow as the fluid temperature increases. Figure 9 shows the variation of surface heat transfer coefficient at 0.01 kg/s, 100 W, and 0% volumetric concentration. It is noted that the heat transfer coefficient decreases nonlinearly with length.

### 3.8 Validation of Model

As mentioned in the objective, an effort has been made to compare the results of the model with the experimental data obtained. In Fig. 10, comparison of average heat transfer coefficient between the experimental and computational analysis for different mass flow rates has been made. This was done at constant values of volumetric concentration of nanofluid (0%) and heat load (100 W). It was noted that the heat transfer coefficient value of the model matches satisfactorily with the experimental value, with minor deviation.

**Fig. 9** Variation of local heat transfer coefficient along the length of flow

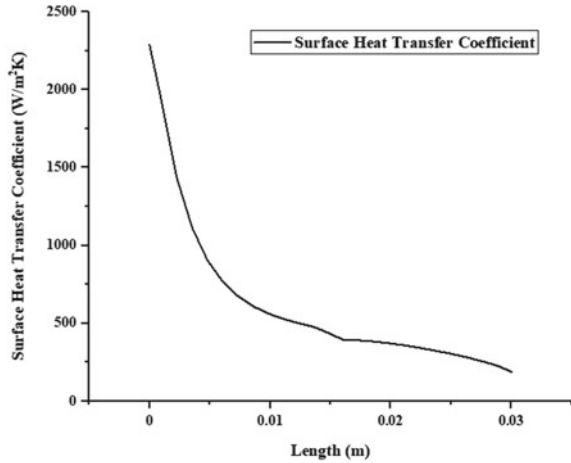
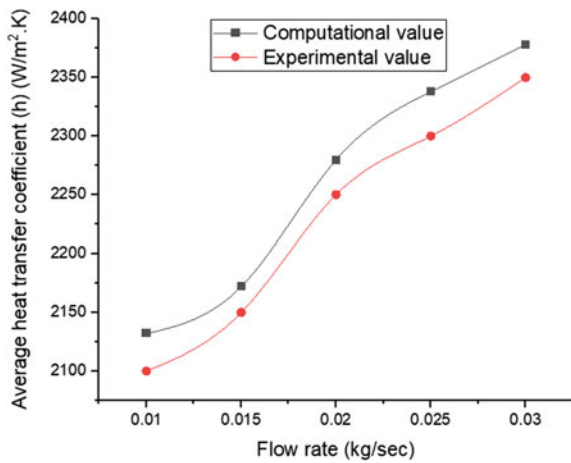


**Fig. 10** Comparison of experimental [19] and computational heat transfer coefficient values for different flow rates of nanofluid



### 4 Conclusions

The heat transfer analysis has been performed using Ansys Fluent 19.2 commercial software. Significant gradient in the heat transfer coefficient could be observed along the length of channel. However, an average value of the same has been used for subsequent analysis. It was noted that the pressure drop in microchannel increased with the mass flow rate of nanofluid and concentration of nanoparticles in the base fluid. Further, increase in volumetric concentration of nanoparticles increased the total heat transferred from the base plate and conducting fins, resulting in higher outlet fluid temperature. The increased heat load on the base plate resulted in increased temperature difference between outlet and inlet temperatures of the coolant. This indicates a higher amount of heat absorption by the nanofluid. Further,

due to the increase in velocity with mass flow rate, the contact time between the fluid and the heated solid surface decreases and, hence, lowers the coolant outlet temperature. Reasonable agreement could be established between the calculated average “h” with those of literature-reported experimental values.

## References

1. Saidina DS, Abdullah MZ, Hussin M (2020) Metal oxide nanofluids in electronic cooling: a review. *J Mater Sci: Mater Electron* 1–18
2. Mantelli MBH (2021) Electronics cooling. In: *Thermosyphons and heat pipes: theory and applications*, pp 363–382. Springer, Cham
3. Heydari A, Akbari OA, Safaei MR, Derakhshani M, Alrashed AA, Mashayekhi R, Nguyen TK (2018) The effect of attack angle of triangular ribs on heat transfer of nanofluids in a microchannel. *J Therm Anal Calorim* 131(3):2893–2912
4. Thakur PP, Khapane TS, Sonawane SS (2021) Comparative performance evaluation of fly ash-based hybrid nanofluids in microchannel-based direct absorption solar collector. *J Therm Anal Calorim* 143:1713–1726
5. Amini Y, Akhavan S, Izadpanah E (2020) A numerical investigation on the heat transfer characteristics of nanofluid flow in a three-dimensional microchannel with harmonic rotating vortex generators. *J Therm Anal Calorim* 139(1):755–764
6. Keshavarz F, Lavasani AM, Bayat H (2019) Numerical analysis of effect of nanofluid and fin distribution density on thermal and hydraulic performance of a heat sink with drop-shaped micropin fins. *J Therm Anal Calorim* 135(2):1211–1228
7. Khaleduzzaman SS, Sohel MR, Saidur R, Selvaraj J (2015) Convective performance of 0.1% volume fraction of TiO<sub>2</sub>/water nanofluid in an electronic heat sink. *Proc Eng* 105:412–417
8. Al-Rashed AA, Shahsavari A, Entezari S, Moghimi MA, Adio SA, Nguyen TK (2019) Numerical investigation of non-Newtonian water-CMC/CuO nanofluid flow in an offset strip-fin microchannel heat sink: thermal performance and thermodynamic considerations. *Appl Therm Eng* 155:247–258
9. Sajid MU, Ali HM, Sufyan A, Rashid D, Zahid SU, Rehman WU (2019) Experimental investigation of TiO<sub>2</sub>-water nanofluid flow and heat transfer inside wavy mini-channel heat sinks. *J Therm Anal Calorim* 137(4):1279–1294
10. Xia GD, Liu R, Wang J, Du M (2016) The characteristics of convective heat transfer in microchannel heat sinks using Al<sub>2</sub>O<sub>3</sub> and TiO<sub>2</sub> nanofluids. *Int Commun Heat Mass Transfer* 76:256–264
11. Mohammed HA, Bhaskaran G, Shuaib NH, Saidur R (2011) Heat transfer and fluid flow characteristics in microchannels heat exchanger using nanofluids: a review. *Renew Sustain Energy Rev* 15(3):1502–1512
12. Bahiraei M, Heshmatian S (2018) Thermal performance and second law characteristics of two new microchannel heat sinks operated with hybrid nanofluid containing graphene–silver nanoparticles. *Energy Convers Manage* 168:357–370
13. Arshad W, Ali HM (2017) Graphene nanoplatelets nanofluids thermal and hydrodynamic performance on integral fin heat sink. *Int J Heat Mass Transf* 107:995–1001
14. Ali HM, Arshad W (2017) Effect of channel angle of pin-fin heat sink on heat transfer performance using water-based graphene nanoplatelets nanofluids. *Int J Heat Mass Transf* 106:465–472
15. Sarafraz MM, Yang B, Pourmehran O, Arjomandi M, Ghomashchi R (2019) Fluid and heat transfer characteristics of aqueous graphene nanoplatelet (GNP) nanofluid in a microchannel. *Int Commun Heat Mass Transfer* 107:24–33



16. Akbari A, Fazel SAA, Maghsoodi S, Kootenaie AS (2019) Pool boiling heat transfer characteristics of graphene-based aqueous nanofluids. *J Therm Anal Calorim* 135(1):697–711
17. Sarsam WS, Amiri A, Kazi S, Badarudin A (2016) Stability and thermophysical properties of non-covalently functionalized graphene nanoplatelets nanofluids. *Energy Convers Manag* 116:101–111
18. Mehrli M, Sadeghinezhad E, Latibari ST, Kazi SN, Mehrli M, Zubir MNBM, Metselaar HSC (2014) Investigation of thermal conductivity and rheological properties of nanofluids containing graphene nanoplatelets. *Nanosc Res Lett* 9(1):15
19. Balaji T, Selvam C, Lal DM, Harish S (2020) Enhanced heat transport behavior of micro channel heat sink with graphene based nanofluids. *Int Commun Heat Mass Transfer* 117:104716

# Study on Design and Performance Specifications of the Prosthetic Hands



Mohd Azeem and Aasiya Parveen

## 1 Introduction

World Health Organization (WHO) estimates that around 650 million individuals suffering from disability worldwide and 80% of those 650 million individuals are in developing countries [1]. The number of upper limb amputees is approximately 2.4 million [2]. Rehabilitation devices for overcoming disability are so rare and expensive that just 3% of the amputees in the developing countries can afford them [1]. To address this problem and to make prosthesis readily available to the user, extensive research is being done. In the course of the most recent couple of decades, there have been extraordinary steps in the improvement of novel prosthetic hands and terminal devices that exploit the most recent mechanical advances, moving toward more dexterous, practical hand devices [3]. Nonetheless, there is as yet an incredible hole between the present status of the arts and devices that have the ideal mix of being exceptionally useful, tough, corrective, and cheap.

In this paper, we survey the plan details of a wide scope of commercial prosthetic terminal devices and exploration hands, focusing primarily on anthropomorphism in such devices. The physical performance specifications as well as any justification provided by the developer regarding the scientific validity of design parameters are discussed. Various surveys are taken into account to corroborate various claims or comment stated in this paper.

---

M. Azeem

Department of Mechanical Engineering, Jamia Millia Islamia, New Delhi, India

A. Parveen (✉)

Department of Mechanical and Automation Engineering, Indira Gandhi Delhi Technical University for Women, New Delhi, India

## 2 Prominent Models

### 2.1 Ability Hand: 2019

Ability hand as shown in Fig. 1 is a developed, multi-action prosthetic hand having 6 degrees of freedom (DOF), with an application for natural or acquired amputees. It works with most third-party myoelectric pattern recognition system, myoelectric direct control, linear transducers, or force-sensitive resistors [4]. For the power supply, the PSYONIC Battery Pack, a high capacity, high throughput, 7.4 V DC lithium polymer battery of at least 2200mAh, is used. The temperature limit for hand to function is  $-5\text{ }^{\circ}\text{C}$  to  $50\text{ }^{\circ}\text{C}$ . The hand offers at least five grip patterns, which are sufficient for executing a sufficient number of ADLs. The hand is quite fast with power grasp done in 200 ms. The weight of hand is 460 g, which is 20% less than the actual human hand. The fingers of a hand are made up of polyurethane and silicone which can absorb  $10\times$  more stress as compared to rigid finger designs. It is launched recently and is mainly focused on providing prosthetic services in the developing countries where amputees cannot afford to get expensive prosthetic systems like bionic, etc.

### 2.2 University of Illinois Hand (2015)

Figure 2 shows the TACT hand which is an open-source, myoelectric, and anthropomorphic prosthetic hand. Most of the hand is 3D printed. It is designed to

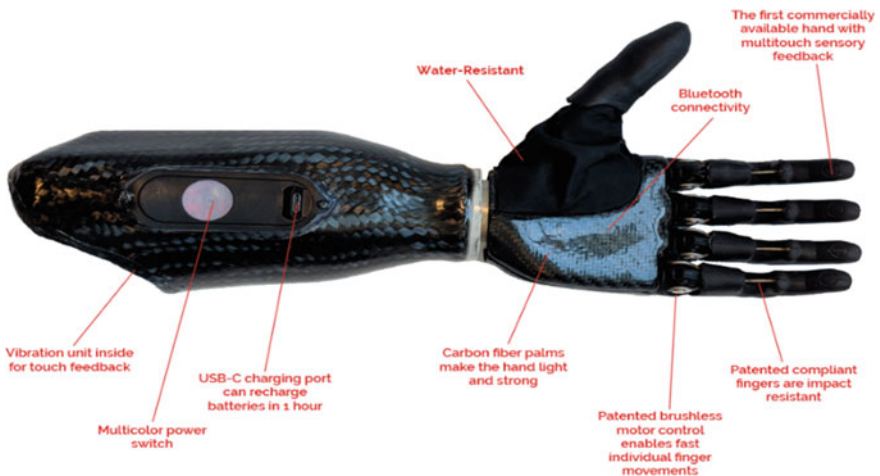
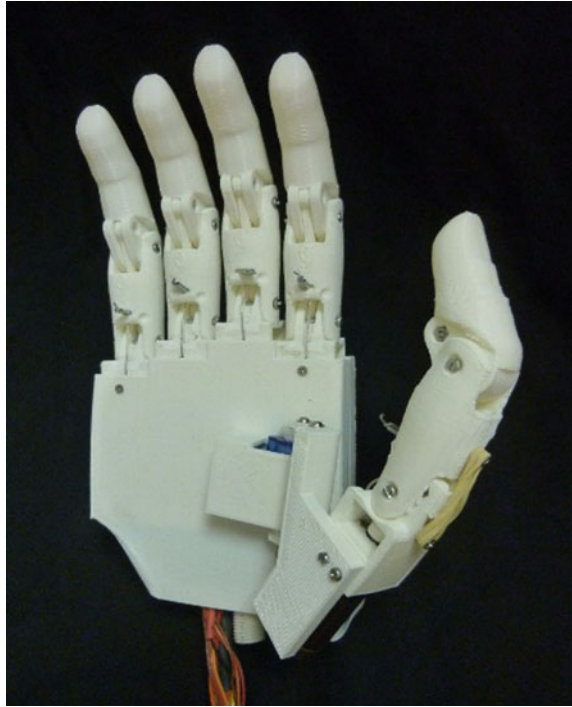


Fig. 1 Ability hand [4]

**Fig. 2** Tact hand [5]

meet the requirement of user in developing countries. Greater emphasis is given on the availability, cost, and robustness of the hand.

To minimize the cable use and other components, a directly coupled cable to the finger for flexion and extension is actuated by the DC motor [5]. The electrical signals received by the electrodes placed over the residual limb muscles are sent to an EMG board, which is then in turn sent to a microprocessor that contains a machine learning algorithm interpreting the signal [2]. It causes the hand to move. The hand has 6 degrees of freedom and uses 6 motors for actuation. The consistent movement is produced through a finger joint mechanism by using four-bar linkage and greater force at the fingertip than a purely tendon-based design [5]. This TACT hand can be produced through 3D printing and off-the shell components with an average cost of \$250.

### ***2.3 University of Washington (UW) Hand (2013)***

An advanced research hand with 20 DOF is designed to provide fast and easy accessibility for modification of design parameters. The methodology used is a combination of rapid prototyping, adaptive design along with custom-designed software. It takes 20 h for 3D printing and 4 h for assembly.

**Fig. 3** UW hand [6]

As evident in Fig. 3, the cable-driven transmission system is used since it provides hand with a unique characteristic of being fully actuated and underactuated with very less modification. Tactile sensing field is formulated of 16 separate skin pads which in turn have three layers. The actuation system is comprised of a pneumatic control unit and actuation unit. The actuation unit consists of 36 M9 Airpel cylinders (Airpot Corp., CT) for finger tendons and 4 M16 Airpel cylinders for wrist tendons [6]. The hand demonstrates its motion without any control algorithms and joint sensors, using only pneumatic actuation. Hence, for the further development, optimal control programs are to be developed. The cost of hand is just \$100 excluding actuation systems.

#### **2.4 Biomimetic Hand (2016)**

It has a highly biomimetic anthropomorphic robotic hand as shown in Fig. 4. The hand is 3D printed by laser scanning of actual human hand skeleton. To achieve biomechanics similar to actual human hand elements like artificial joint capsules, crocheted ligaments and tendons, laser-cut extensor hood, and elastic pulley mechanisms is used [7]. Since the brain is responsible for controlling prosthetic hands, neuroprosthetic technologies are more effective when the design of the prosthesis is more similar to its biological counterpart, i.e., human hand. Thus, a

**Fig. 4** Biomimetic hand [7]

highly biomimetic approach is used to elaborate on the characteristics of the human hand efficient control and a wider application. These complicated components are held together with a series of artificial ligaments, rendered by high-strength spectra strings, with laser-cut latex sheets to copy the soft tissue of human joints. Actuation is carried out with 10 dynamixel servos which impart 8 DOF to the hand. These servos are smart actuators with fully integrated DC motor, reduction gearhead, controller, driver, network [8].

Currently, it is the most advanced hand in the field of prosthetic robotics. It uses biocompatible materials, which are 3D printed from bone structure scans and thus provides a unique opportunity of generating artificial human limbs. Thus, such neuroprosthesis research combined with biological research can provide very favourable results in the field of the prosthesis.

## 2.5 *Hero Arm (2018)*

It is the first medically approved 3D printed bionic arm developed by Open Bionics, a startup in Bristol, UK. Hero arm uses electromyographic (EMG) sensors to sense muscle activity and give proportional control of the arm. The hand weight ranges 280–346 g depending on the configuration and size whereas the whole arm weighs less than 1 kg. As shown in Fig. 5, arm is completely 3D printed according to the bone structure of each recipient.

The hand has 6 DOF (1 for each finger and 2 for thumb) and offers 6 grip patterns with a dynamic socket which offers tolerance for change in size. The arm

**Fig. 5** Hero arm [9]

has 4 motors or 3 motors depending on the hand size. The arm has maximum force capability for 8 kg load and uses Li-ion 7.5 V 2600 mAh battery [9]. The arm price starts from \$3000 and is currently available in the UK, USA, France, and Spain through prosthetic clinics.

## 2.6 *Dextrus Hand (2013)*

Dextrus hand as shown below in Fig. 6 is a research project by open hand which aims at providing technical knowledge and support in the field of the prosthesis. The hand is 5 fingered, 3D printed and has 6 DOF. It has been developed as an open-source project and thus can be used by individuals without any issues related to patents [10]. It uses EMG electrodes for receiving signals from the muscles and has a DC tendon mechanism for actuation using 6 motors. The weight of hand is 428 g which is mainly concentrated in the palm which has actuation and sensory systems. The hand is fairly cheap and can be readily used as a prototype for further research in the field of the prosthesis.

## 2.7 *Vincent Evolution 3 (2018)*

It has an anatomically shaped bionic prosthetic hand (Fig. 7) developed by Vincent systems. This is an upgrade to the previous hands launched by the company with the first hand, i.e., Vincent hand being launched in 2010. The material used for this hand is the combination of stainless steel and Mg–Al alloy which makes hand prosthesis extremely robust and light. The hand comes in 5 sizes with the smallest size being the smallest and lightest multiarticulate hand with 6 motors of all prosthetic hand currently available, and it weighs 386 g along with transcarpal wrist [11].

The 6 DC motors along with 6 planetary gearheads provide with 14 grip types which can be selected with patented single trigger control (STC) concept just by 1 trigger response. There can be many intermediate grip types as the hand has

Fig. 6 Dextrus hand [10]



Fig. 7 Vincent evolution 3 [11]

powered thumb rotation so it more or less behaves like an actual human hand. User can learn to operate the hand via an app which is compatible with the microcontrollers of the hand.

Vibrotactile feedback (small vibrations on the skin) provides the user with feedback in terms of force measured by the index finger. This feedback helps in



alerting user when the force exceeds the specified threshold, and this feature is present only in this prosthesis system. There are 11 joints in the hand. Elastic lining, flexible arched springs, and artificial sense of touch provide a safe, non-slip grip. Index finger and thumb always remain in contact with high-precision pinch grasp and flattened fingertips facilitates in gripping of objects without any problems. The wrist joint is a major advantage of this system as it provides with 2 kinds of wrists—"quick-snap" and "short," which combined with flexion makes 4 wrist options for users. Flexion of the wrist has a range from  $-54^\circ$  to  $54^\circ$  [12]. The hand is currently used for research purposes and is not available for public use.

## 2.8 *Bebionic3 (2012)*

Initially developed by RSL steeper, it is now a product of Ottobock health care. *Bebionic3* is the third-generation bebionic hand-launched in 2012 as shown in Fig. 8. It comes in 3 sizes ranging from 390 to 600 g [13]. It has 6 DOF, uses 5 Faulhaber DC SR series motors which are lightweight and compact providing with enough torque for hand to function efficiently as illustrated in Table 1. These motors are fitted into palm itself. It uses 4 bar link mechanism for transmission in each finger, and a lead screw is used for flexion and extension of the fingers. MIP and PIP joints are coupled. Aerospace industry-grade aluminum makes hand light and robust. *Bebionic3* has manual thumb rotation and thumb fits in only 2 positions, i.e., non-opposed and opposed, and it offers 14 grip patterns. Unlike Vincent's hand, there is no sensory feedback and thus all the patterns and forces are preplanned and must remain in the limit for hand to function properly. It also uses EMG sensors and has 2 50/60 Hz electrodes in the prosthesis shaft for receiving and transmitting. The hand offers 4 wrist options—electric quick disconnect, short wrist, friction wrist, threaded stem, all these wrists are compatible with different models and offer flexion and rotation. These wrists are incorporated with the complete bionic arm housing EMG sensors. A hand runs at the nominal voltage of 7.4 V and has a battery range of 1300–2200 mAh. *Bebalance3* software present in the hand is used to customize and operate the hand. With this tool, the user has access to all the hand features and can accordingly control them. One major benefit of *Bebionic3* is the active index finger which is available only in this bebionic model. There is provision for hand cover as well which are made of silicon and look like actual human skin. The hand is priced at \$35,000 and is one of the most advanced systems commercially available.

**Table 1** Prosthetic hands general characteristics [2, 3, 6, 8, 11, 12, 14, 15]

Prosthesis	Developer	Weight (g)	Size (mm) (length × width × thickness)	Joints	Number of actuators*	Degree of freedom	Actuation method	Joint coupling method
Ability hand	Psyonic	460	200 L × 110 W × 55 D (large) 189 L × 110 W × 55 D (small)	9	6	6	Brushless DC motor —Worm gear**	Linkage spanning MCP to PIP
Tact hand	University of Illinois	350	200 × 98 × 27	11	6	6	DC motor —Tendons	Tendon linking MCP to PIP
UW hand	University of Washington	660	280 × 160	19	40 double acting cylinders	20	pneumatic control—tendons	Tendons linking cylinders, MCP, PIP, DIP
Biomimetic hand	—	942	—	19	10	8	Dynamixel servos—tendons, elastic pulleys	Tendons linking MCP to DIP
Hero arm	Open bionics	280–346	—	11	3/4	6	DC motor—tendons	Tendon Linking MCP to PIP
Dextrus hand	Open hand project	428	205 × 88 × 45	11	6	6	DC motor—tendons	Tendon and free spinning pulleys

(continued)

Table 1 (continued)

Prosthesis	Developer	Weight (g)	Size (mm) (length × width × thickness)	Joints	Number of actuators*	Degree of freedom	Actuation method	Joint coupling method
Vincent evolution 3	Vincent systems	386 (XS)	145 × 65 (XS) 150 × 70 (S) 160 × 75 (M) 170 × 80 (L) 180 × 85 (XL)	11	6	6	Brushed DC motors—planetary gearheads	Linkage spanning MCP to PIP
Bebionic3	Ottobock	390–600	200 × 92 × 50 (L) 190 × 84 × 50 (M)	11	5	6	DC motor—lead screw	Linkage spanning MCP to PIP

(\*\*) estimation based on images/videos

(\*) indicates motors (DC or servo) unless specified

**Fig. 8** Bebionic3 [13]

### 3 Specifications of Prosthetics

#### 3.1 Hand Weight and Size

Weight and size of the prosthesis are one of the major parameters in designing as it is the comfort of the user that matters. Weight of human hand on average is approximately 400 g [16] (wrist to the distal and excluding extrinsic muscle of forearm). That being said, prosthetic end effector devices of similar weight are perceived as surprisingly heavy by users [17]. Methods used in the attachment of these prosthetics with the user are one of the primary reasons for this anomaly. To address this problem, researchers are working on osseointegrated attachment mechanisms. 79% of myoelectric prosthetic users in an Internet survey claimed that their prosthetic was too heavy [17]. Similarly, findings from Biddiss' survey [18] concluded that on a scale of 0 (not important) to 100 (very important), users rated the weight of the device as 70 in terms of design precedence of prosthetic hands. Since there is no set of rules for setting the weight limit of prosthetics, capabilities and function of the hand can be termed as the sole reason for the weight and size of the hand. There are many claims for the optimum weight of the hand, like a study by Pons [16], according to which an adult-sized prosthetic hand should be less than 400 g in weight. Belter [3] and Bergman [19] in their study concluded that a weight limit of 500 g is appropriate. The size for anthropomorphic prosthetic hand should be the size and shape of a natural hand. The bebionic hand and Vincent's hand have the facility of silicone gloves which closely resembles the actual human skin. As these gloves are designed according to human hand dimensions, the prosthetic hand

should have a length between 180 and 198 mm and a width of 75–90 mm to match normal human hand size [3].

### 3.2 *Actuator Characteristics*

Direct current (DC) motors are the most commonly used motors in the prosthetic hands. Limited space is one of the most crucial design considerations in the case of prosthetic hands. These motors have a unique characteristic of being installed in that limited space because they are very compact and lightweight. Hence, DC motors are among the most widely used motors in prosthetic hands. Transmission components like gearheads—planetary, worm, or leadscrews are used to control the motion and torque, though less speed and more torque are desired. Servo motors are widely used as well. They are mainly used to provide more manoeuvrability as it provides 180° rotation. Also, feedback potentiometer allows the servo to rotate at a specific angle by keeping track of its initial position. Thus, these properties of servos are realized in the biomimetic hand, which used 10 dynamixel servos for actuation. That being said the weight of hand is considerably more (981 g), which would increase even more once the casing is installed. The UW hand uses pneumatic actuators for controlling hand. The use of pneumatic systems offers more control over speed and torque components, its usage and installation are very easy which lead to additional economic and time investment and thus the overall cost of prosthetic. Non-back drivable mechanisms are incorporated in many hands so that the hand may be able to exert grip force on the object without power being supplied to the motors. There are many options like Maxon, Faulhaber, etc., while selecting motors for various hand depending on the parameters like speed, torque, weight, and expense. Table 2 provides with information about motors and battery used in the hands.

### 3.3 *Grip Force*

Grip force is one of the major influential parameters in designing the prosthetic hand. During most of the ADLs like typing, writing, waving, and gestures, we need more speed and less force/torque, whereas prerequisite in the case of prosthetic hand is more torque and less speed. Actuation, transmission, hand dimensions, and spatial arrangement can be termed as the controlling factors of the grip force. Prosthetic hands administer different grasp forces for different object sizes. However, it is very exacting to forecast the required grasp force to hold an object in a particular grasp as the grasp force is chiefly a function of friction acting between the hand and object. According to Wier [20], human hand exerts 95.6 N of force in precision grasp, and in other grasps like power grasp, the force can reach as high as 400 N. Also, an analysis by Wier [20] accomplished that a grip force of a mere

**Table 2** Battery and actuators in considered hands [2, 3, 6, 8, 11, 12, 14, 15]

Prosthesis	Actuator	Battery
Ability hand	Self-developed patent-pending motor	7.4 V 2200 mAh Li-pol
Hero arm	Maxon DCX 12 L	7.5 V 2600 mAh Li-ion
Bebionic3	Faulhaber DC 1024 SR	7.4 V 1300 mAh–2200 mAh Li-pol
Vincent evolution 3	Maxon DCX 10	6–8 V 1300 mAh–2600 mAh Li-pol
Tact hand	Escap 16G 214E MR 19	–
Dextrus hand	Escap 16G 214E MR 19	–
UW hand	36 cylinders of M9 Airpel, 4 cylinders of M16 Airpel	N/A
Biomimetic hand	Robotis Dynamixel motors—9 MX-12W and 1 AX-12A	–

68 N is sufficient to execute activities of daily living. Interestingly Vinet [21] suggested that a limiting grip force of 45 N for prosthetic hands is required for practical use. Hands like Vincent, bebionic, biomimetic, and UW, execute different grasp force depending on the object sizes and have adaptive grip. Adaptive grip enhances hand's maneuverability, and durability as excessive forces just flex the finger in place of shearing gears or sabotaging linkages. There is not much available information on grip forces as these hands are latest and not much review has been done thus proper literature is absent on physical details. Moreover, nowadays force is measured on components like fingertip and joints during simulation rather than on the hand as a whole. It provides with information in much details about all the kinematic aspects of the hand. Table 3 provides with elaborate information about the functioning parameters of the hands discussed.

### 3.4 Joint Coupling Method

In prosthetic hands, joints are the critical points where most of the failure takes place and hence their designing plays a significant role in the functioning of the hand. Before discussing the coupling methods and their significance, it is important to visualize the various joints in the human hand. Figure 9, shown below, provides an important visualization of the human hand. The number of joints is more than the number of actuators, and therefore, multiple joints are coupled together to function as a single unit and aiding in achieving optimum functionality. Such methodology can be observed in Vincent, bebionic, hero arm, tact, ability hand, in all these models the MCP and PIP joints are coupled.

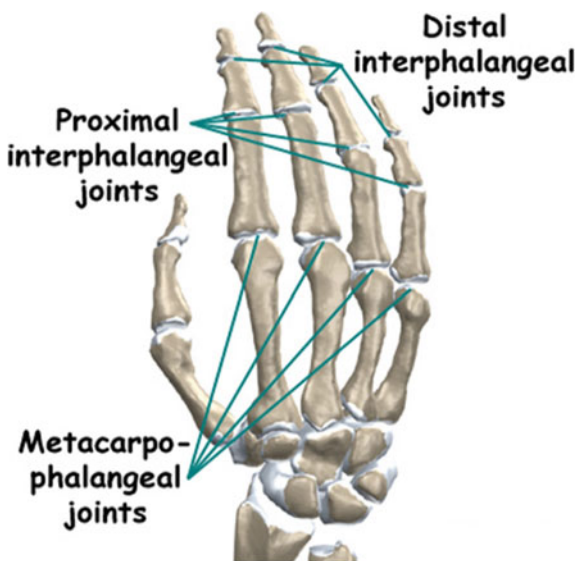
**Table 3** Hand operating parameters [3–16]

Prosthetic hand	Grip patterns	Range of motions (degrees)		
		MCP joint	PIP joint	DIP joint
Ability hand	5	0–90*	0–90*	20*
Hero arm	6, 4	0–90*	0–90*	20*
Bebionic3	14	0–90	0–90	20
Vincent evolution 3	14+	0–90	0–100	–
Tact hand	5	0–90	23–90	20
Dextrus hand	5*	0–90	0–90	0–90
UW hand		0–90	0–90	0–90
Biomimetic hand	15+	0–90	0–110	0–70

(\*) Inferred from videos

Thus, the process of coupling is accountable for the degree of freedom, according to which 1 degree of freedom is the motion of hand indicated by 1 parameter. Due to this fact, each finger in the hands discussed in this paper (except UW hand and biomimetic hand) have 1 DOF, despite having multiple joints. The coupling can also be done through under actuation, a process involving the use of a single actuator to control multiple independent degrees of freedom. The process of under actuation is adaptive since it permits multiple links of fingers to conform to the shape and position of an object without any resistance and while using a single actuator. In adaptive under actuation, it is irrelevant to use a single actuator parameter to render the position of joints since they are subject to the state of contact of each finger link with the object. Underactuation is used in UW hand,

**Fig. 9** Joints in hand



biomimetic hand, and also in hero's arm. In UW hand, biomimetic hand under actuation is used to control little and ring fingers, also, in hero's arm—3 motor version, index and middle finger are coupled as well. In UW hand, there is a convention for under actuation for fingers by replacing 4 separate tendons by a single tendon with pulleys. This reduces the DOF of fingers from 4 to 3. One of the major shortcomings of under actuation is the probability of prompting fingers into unknown postures when fingers flex or extend between furthest positions and respective finger configuration is highly dependent on object contact [22]. Bergman et al. [19] in 1992 claimed non-adaptive conventional prosthesis substantiated “significantly better results” in terms of grip width, grip force, and standardized grip function test when equated to a similar adaptive prosthesis. That being said, adaptive finger designs facilitate the interaction force between the finger and object in a more distributed manner, which enables the machine to operate a greater range of configurations for the same number of actuators. Kargov et al. [23] stated that even though the contact forces are larger when a fixed coupling is used in fingered prosthetic, the joint torques of adaptive fingered hands are more or less equal to the joint torques of the human hand.

Adaptability is widely used in available prosthetic hands like bebionic and Vincent, and advantages of such hands widely overshadow their disadvantages in terms of object perception and operability.

## 4 Conclusions

This paper presented the collection of empirical and published characteristics and performance parameters of the latest prosthetic hands. The main area of focus was the mechanical characteristics and techniques of the hand rather than its other electronics, electrical, sensing, control, and power requirement aspects. It is not relevant to substantiate fixed mechanical and performance requirements, since a hand, similar to any other tool, has multiple applications and thus sufficient performance for one purpose can be useless or not adequate for another. Eventually, the final choice of hand characteristics and specification is an interrelation among tradeoffs in complexity, weight, control methods, cost, and dexterity (e.g., achievable grasps). Moreover, each of these parameters is dependent on the recipient's particular need which involves the nature and level of amputation, as well as the level of activity, professional needs, the intensity of usage, and others.

Even the hands discussed above have no clear winner. It all depends on the needs of the end user. Some hands outdo others in some parameters but there no hand stands alone. This is an important characteristic of prosthetic hands. Thus, the entire prosthesis must work as a coherent system to accomplish tasks. A set of clinical standards for performance, including techniques for evaluating anthropomorphic hand designs, would be beneficial. In doing so, a familiar set of standards (or range of standards) would facilitate the probability of extensive research efforts which can be implemented in a successful commercial device thereby improving



the lives of amputees. With the advancements in the prosthesis, healthcare industry, especially biomedical technologies have developed at a very fast pace. Such advancements facilitate in the development of humanoid robots. Even though there is not a perfect prosthetic hand, these technological breakthroughs are milestones which will help in the development of the artificial human hand.

## References

1. Hussain S, Shams S, Jawaid Khan S (2019) Impact of medical advancement: prostheses. *Comput Archit Ind Biomech Biomed Eng*. <https://doi.org/10.5772/intechopen.86602>
2. Phillips B, Zingalis G, Ritter S, Mehta K (2015) A review of current upper-limb prostheses for resource constrained settings. <https://doi.org/10.1109/GHTC.2015.7343954>
3. Belter JT, Dollar AM (2011) Performance characteristics of anthropomorphic prosthetic hands. *IEEE Int Conf Rehabil Robot*. <https://doi.org/10.1109/ICORR.2011.5975476>
4. Kragten GA, Kool AC, Herder JL (2009) Ability to hold grasped objects by underactuated hands: performance prediction and experiments. In: *Proceedings 1992 IEEE international conference on robotics and automation*, pp 2493–2498
5. Slade P, Akhtar A, Nguyen M, Bretl T (2015) Tact: Design and performance of an open-source, affordable, myoelectric prosthetic hand. In: *Proceedings IEEE international conference on robotics and automation*, 2015 June, pp 6451–6456
6. Xu Z, Kumar V, Todorov E (2015) A low-cost and modular, 20-DOF anthropomorphic robotic hand: design, actuation and modeling. In: *IEEE-RAS International conference on humanoid robots*, 2015 Feb, pp 368–375
7. Schmerler J, Chant I (2016) Tomorrow's prosthetic hand. *Sci Am Mind* 27:16–16
8. Fras J, Althoefer K (2018) Soft biomimetic prosthetic hand: design, manufacturing and preliminary examination. In: *IEEE international conference on intelligent robots and systems*, pp 6998–7003
9. Wong TH, Asnaghi D, Leung SWW (2019) Mechatronics enabling kit for 3D printed hand prosthesis. In: *Proceedings of the international conference on engineering design ICED 2019Aug*, pp 769–778
10. Gibbard J (2013) Dextrus. <http://www.openhandproject.org/index.php>
11. Belter JT, Segil JL, Dollar AM, Weir RF (2013) Mechanical design and performance specifications of anthropomorphic prosthetic hands: a review. *J Rehabil Res Dev* 50:599–618
12. Xu Z, Kumar V, Todorov E. The UW hand: a low-cost, 20-DOF Tendon-driven hand with fast and compliant actuation
13. Clement RGE, Bugler KE, Oliver CW (2011) Bionic prosthetic hands: a review of present technology and future aspirations. *Surgeon* 9:336–340
14. Xu Z, Todorov E (2016) Design of a highly biomimetic anthropomorphic robotic hand towards artificial limb regeneration. In: *Proceedings IEEE international conference on robotics and automation*. Institute of Electrical and Electronics Engineers Inc., pp 3485–3492
15. Slade P, Akhtar A, Nguyen M, Bretl T (2015) Tact: design and performance of an open-source, affordable, myoelectric prosthetic hand. In: *Proceedings IEEE international conference on robotics and automation*. Institute of Electrical and Electronics Engineers Inc., pp 6451–6456
16. Pons JL, Rocon E, Ceres R, Reynaerts D, Saro B, Levin S, Van Moorleghe W (2004) The MANUS-HAND dextrous robotics upper limb prosthesis: mechanical and manipulation aspects. *Auton Robots* 16:143–163
17. Light CM, Chappell PH (2000) Development of a lightweight and adaptable multiple-axis hand prosthesis. *Med Eng Phys* 22:679–684

18. Biddiss E, Beaton D, Chau T (2007) Consumer design priorities for upper limb prosthetics. *Disabil Rehabil Assist Technol* 2:346–357
19. Bergman K, Örnholmer L, Zackrisson K, Thyberg M (1992) Functional benefit of an adaptive myoelectric prosthetic hand compared to a conventional myoelectric hand. *Prosthet Orthot Int* 16:32–37
20. Weir RF (2004) Design of artificial arms and hands for prosthetic applications. *Stand Handb Biomed Eng Des* 1–61
21. Vinet R, Beaudry N, Drouin G (1995) Design methodology for a multifunctional hand prosthesis
22. Gustus A, Stillfried G, Visser J, Jörntell H, van der Smagt P (2012) Human hand modelling: kinematics, dynamics, applications. *Biol Cybern* 106:741–755
23. Kargov A, Pylatiuk C, Martin J, Schulz S, Döderlein L (2004) A comparison of the grip force distribution in natural hands and in prosthetic hands. *Disabil Rehabil* 26:705–711

# A Multi-stage Evolutionary Tomographic Reconstruction Algorithm Using Ultrasound Time-of-Flight Projections



Shyam Prasad Kodali and Boggarapu Nageswara Rao

## 1 Introduction

Identification and characterization of internal defects in engineering systems will be helpful in assessing their criticality in service and also in minimizing the catastrophic failures. The extensive utilization of computed tomography (CT) in medical field has also evolved as an effective process in majority of engineering applications in detecting internal defects and also identifying the defect material [1, 2]. The two principal phases in CT are illustrated in Fig. 1. To begin with, the object or specimen to be inspected is irradiated with some form of energy (like the X-rays, ultrasound, etc.). The recorded resulting energy, after interaction with the specimen, is referred as the projection data (which could be the intensity, amplitude, or time-of-flight (TOF) of the input energy after attenuation, due to interactions with the object material). In the next step, the acquired projection data serves as an input to the reconstruction algorithm, for processing the input, to reveal the cross section of the object [3]. Several reconstruction algorithms can be broadly grouped into three classes: in the first group, the transform methods include the filtered back projection algorithms and the convoluted back projection algorithms [3]. In the second group, the series expansion methods include algorithms like algebraic reconstruction techniques and the multiplicative algebraic reconstruction techniques [3]. The relatively new third group of reconstruction algorithms is designed on evolutionary optimization methods particularly the genetic algorithms (GAs) [4–7].

Development of one-step tomographic reconstruction using real-coded genetic algorithms is discussed in [4]. An elaborate discussion of a reconstruction procedure based on a variation of the principles of binary-coded genetic algorithm is presented in [5]. However, the methodology is applicable, only when the number of

---

S. P. Kodali · B. N. Rao (✉)

Department of Mechanical Engineering, Koneru Lakshmaiah Education Foundation, Vaddeswaram, Guntur, Andhra Pradesh 522 502, India  
e-mail: [shyamprasad.k@kluniversity.in](mailto:shyamprasad.k@kluniversity.in)

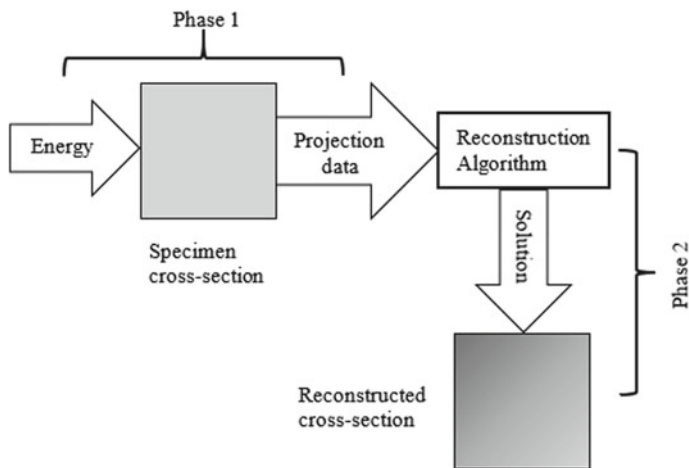


**Fig. 1** Principal phases of tomographic reconstruction process

materials present in the object cross section is limited to three. Kishore et al. [6] have presented a binary GA tomographic reconstruction procedure with cluster analysis, for identification of defects in composite plates. Kodali et al. [7] have made comparative studies on four different tomographic reconstruction procedures. They have used a GA-based algorithm and three variations of multiplicative algebraic reconstruction technique (MART), for the reconstruction of synthetic test cross sections. The influence of parameters in the algorithm and the effects of random noise in the projection data are reported.

This article presents the details on the development of a multiple-step tomographic reconstruction algorithm using real-coded genetic algorithms (RGAs). The input to the proposed algorithm (namely the time-of-flight of ultrasound rays interacting with the test specimen) is generated following the procedures in [5]. The reconstruction results of numerical studies on various specimens demonstrate the efficacy of the proposed methodology.

## 2 Proposed Reconstruction Methodology

The reconstruction problem is formulated as an optimization problem, of minimizing the objective function given by Eq. (1). This is essentially the sum of the squares of the deviation, of the TOF of each of the ultrasound rays irradiating the solution guess, from the corresponding rays irradiating the specimen under examination. In this work, the same objective function is also used to estimate the fitness of solutions in the GA population which is a measure of the goodness of a solution [5]. This simply means the fitness of every solution guess in the population is estimated and solutions having lower fitness get the chance to participate in the

```

initialize the algorithm parameters
initialize starting resolution
initialize the population of solutions
do
  for each population member evaluate fitness
  initialize solution = population member with best fitness
  do
    apply tournament selection operator
    apply simulated binary crossover operator
    apply polynomial mutation operator
    apply elitism operator
    for each population member evaluate fitness
    update solution with the new best fitness population member
  until (termination criteria of evolution is met)

  update resolution of population members
  perform refine operation
  perform freeze operation
  update population members from coarser to finer resolution
until (resolution exceeds the final resolution required)
return solution

```

**Fig. 2** Pseudocode outlining the significant hierarchical steps in the proposed multi-step elitist real-coded genetic algorithm reconstruction approach

subsequent GA operations. The pseudo-code outlining the significant hierarchical steps, in the proposed multi-step elitist real-coded genetic algorithm reconstruction approach, is presented in Fig. 2.

$$\varphi(i) = \sum_{c=1}^C \sum_{t=1}^T \sum_{r=1}^R \left\{ \text{TOF}_{\text{Pop}}^{(i)}(c, t, r) - \text{TOF}_{\text{Specimen}}(c, t, r) \right\}^2 \quad (1)$$

Here,  $C$  is the number of configurations. In each configuration,  $T$  is the number of transmitters and  $R$  is the number of receivers.  $\text{TOF}_{\text{Pop}}^{(i)}(c, t, r)$  and  $\text{TOF}_{\text{Specimen}}(c, t, r)$  are, respectively, the time-of-flight, of the rays connecting the  $t$ th transmitter and the  $r$ th receiver in the  $c$ th configuration, considering the  $i$ th population member and the test specimen.

The algorithm is developed from the principles of real-coded genetic algorithms, in contrast to the conventional binary-coded genetic algorithms used in earlier reported work. In each iteration or GA generation, solutions are arrived using the tournament selection operator, simulated binary crossover operator, and the polynomial mutation operator. The tournament selection operator is used, to create a mating pool of relatively better solutions, from the randomly initialized population of solutions or those available at the beginning of the current generation [8, 9]. Next

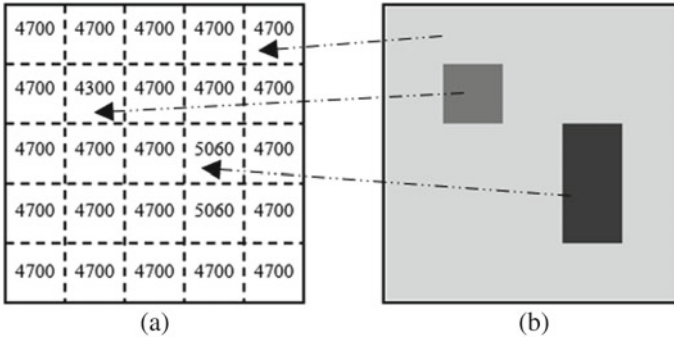


**Fig. 3** Specimen cross section; **a** computational code **b** visual display

the simulated binary crossover is applied to pairs of solutions in the mating pool to create new and hopefully improved solutions as in [10, 11]. It is to be noted that in any population-based search algorithms, maintaining diversity in the population of solutions ensures or reduces the chances of the algorithm converging to a local optimum. This task is taken care of in GA by the mutation operator, which in this work is facilitated with the use of polynomial mutation operator as in [12, 13]. GA being stochastic in nature, there is a chance of losing the best solution found with increasing number of iterations, which is prevented with the use of elitism principle as in [14, 15]. The reconstruction algorithm stores, processes, and outputs a discretized cross section of the object under examination, as a matrix of real values like the one shown in Fig. 3a. The real value assigned to each of the discretized grid cells corresponds to the characteristic property of the material in the object. The characteristic property is nothing but the velocity of propagation of ultrasound through the physical material present in the object. For the convenience, the discretized cross section is displayed in Fig. 3b as an image with different grey levels distinguishing the different materials [5].

### 3 Results and Discussions

The adequacy of the proposed algorithm is examined on several synthetic object cross sections. Results of reconstructions with  $16 \times 16$  and  $32 \times 32$  grid resolutions are discussed in this section. Recognizing the fact that genetic algorithms are stochastic in nature and their performance depends on various parameters at execution time, GA parametric studies are carried out to study the influence of maximum number of GA iterations or generations, GA population size, probability of crossover for applying the simulated binary crossover operator, and probability of mutation for applying the polynomial mutation operator. Other parameters like  $\eta$ -c and  $\eta$ -m are chosen from the recommended values in [8–12]. Table 1 gives the setting of GA parameters used in the study.

**Table 1** GA parameters values used in the study

Parameters	Set value
Maximum number of generations	Starting with 2000, increased by three times the current value with every update in grid resolution
Population size	Final grid resolution
Crossover probability	0.8
	0
	0
	$\theta_3$
Mutation probability	Starting with $1/(\text{current grid resolution})^2$ , updated to one-fourth the current value with every update in grid resolution
eta_c	10
eta_m	20

Figures 4 and 5 show the reconstruction results with resolutions of  $16 \times 16$  and  $32 \times 32$  for the cross section having a central defect of square shape. Figure 4a is the visual display of test specimen cross section, which is irradiated with ultrasound, and the time-of-flight of the ultrasound rays, after interaction with the cross-section materials is recorded. This recorded data is fed as input to the proposed algorithm. The results are illustrated in Fig. 4b–d. As briefed in the previous section, the algorithm starts with a population of randomly created initial guesses to the specimen cross section; one of such solution guesses is shown in Fig. 4b. It should be noted that the resolution of initial solutions is  $8 \times 8$ , which is half of the final desired resolution of  $16 \times 16$ . Following the multiple stage strategy, the algorithm gives an intermediate best solution, with the current coarser resolution of  $8 \times 8$  as shown in Fig. 4c. At this stage, the algorithm updates the population of solutions with  $8 \times 8$  resolutions, to a finer resolution of  $16 \times 16$ , by subjecting the former population to the operators: refine, freeze, and update. Next, the defined GA operators, simulated binary crossover, polynomial mutation, and elitism, are applied repeatedly, on the updated population resulting in the final solution as shown in Fig. 4d. Figure 4e illustrates the trend of convergence (showing variation of fitness or error as a function of the number of iterations or generations of the algorithm) in a semi-log plot. The intermediate spike in the fitness is noticed at generation number 2000. The spike corresponding to the point of the intermediate solution in Fig. 4c is the start of the second stage of algorithm. The sudden degradation in fitness is noticed when the current population of solutions with  $8 \times 8$  coarser resolution are exploded to solutions of  $16 \times 16$  finer resolution.

The estimated characteristic property, in each of the pixels of the reconstructed solution, is compared with the corresponding values in the test specimen. The difference between them (i.e. the error in reconstructed characteristic property) is shown in the stem plot of Fig. 4f). It is observed that the maximum error in all the 256 pixels is approximately 30 units indicating below 1%. Comparison of two solutions by looking at the errors in each pixel is a difficult task. To overcome such situations, an overall quality metric, namely the root mean square error, in Eq. (2) is

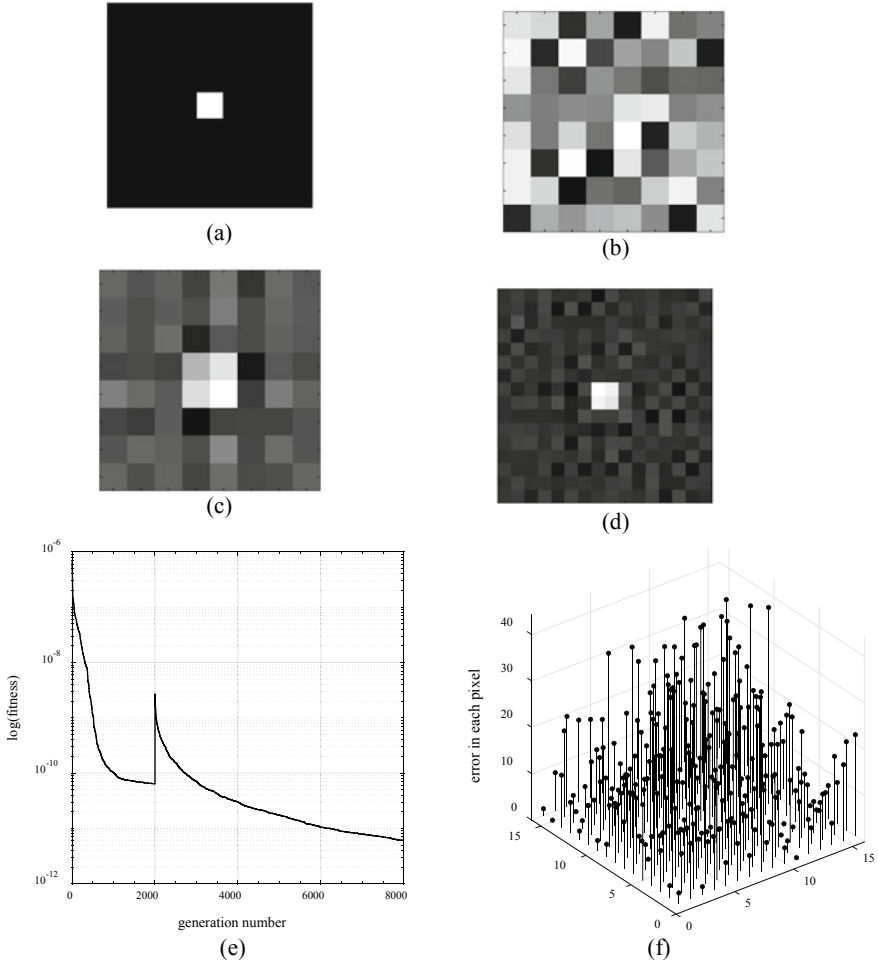


**Fig. 4** Results of reconstruction (RUN3) with resolution of  $16 \times 16$ : **a** test cross section to be reconstructed, **b** initial random solution, **c** reconstructed solution with  $8 \times 8$  resolution, **d** reconstructed solution with final resolution of  $16 \times 16$ , **e** fitness history plot, **f** error in each pixel of the reconstructed cross section

introduced considering the errors in all pixels into a single value. However, this comparison of different solutions is feasible only when working with synthetic cross sections.

$$\text{RMSE} = \sqrt{\sum_{i=1}^{\text{res}} \sum_{j=1}^{\text{res}} (\text{prop\_specimen}(i,j) - \text{prop\_solution}(i,j))^2} \quad (2)$$



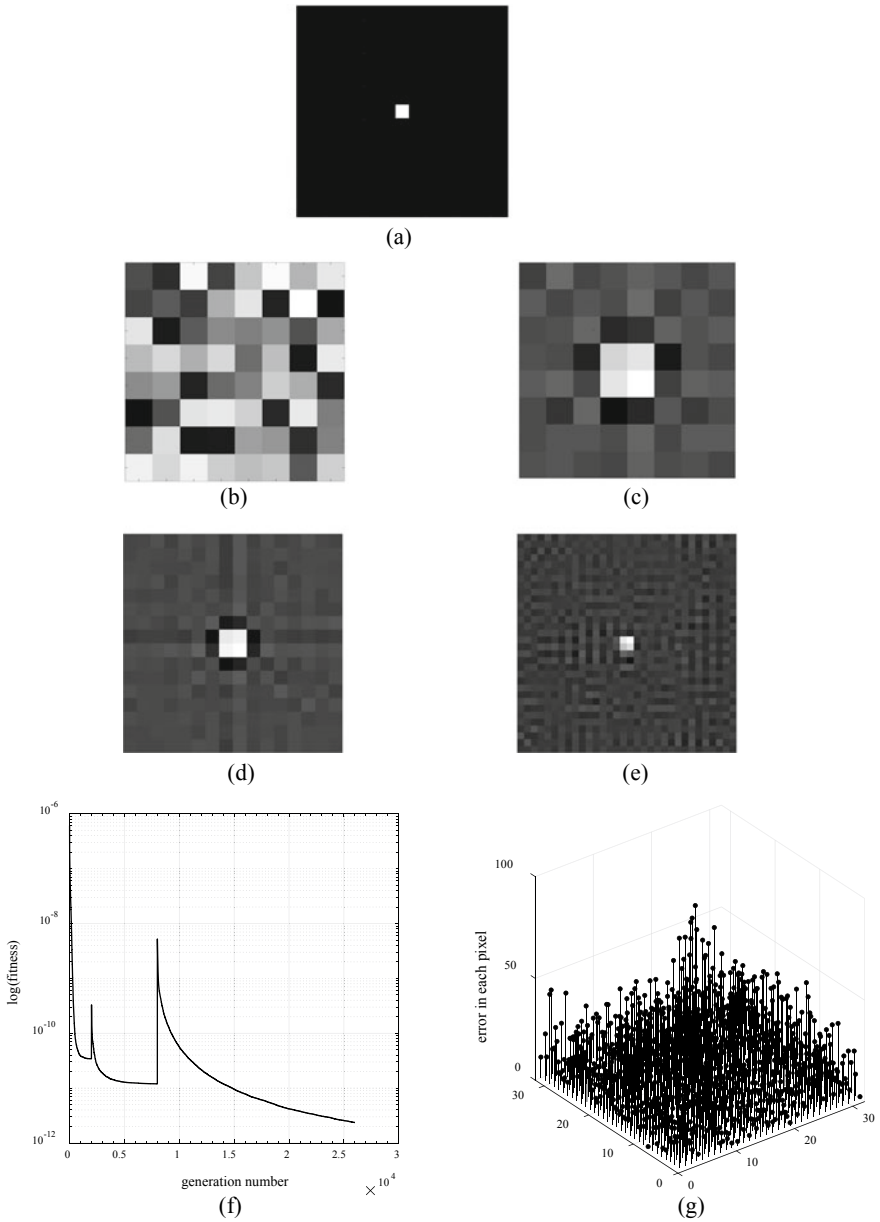


**Fig. 5** Results of reconstruction (RUN5) with resolution of  $32 \times 32$ : **a** test cross section to be reconstructed, **b** initial random solution, **c** reconstructed solution with intermediate resolution of  $8 \times 8$ , **d** reconstructed solution with intermediate resolution of  $16 \times 16$ , **e** reconstructed solution with final resolution of  $32 \times 32$ , **f** fitness history plot, **g** error in each pixel of the reconstructed cross section

where RMSE is the overall quality metric,  $(i, j)$  corresponds to a pixel in the discretized cross section,  $res$  is the resolution of reconstructed solution, and  $prop\_specimen$  and  $prop\_solution$  are matrices of real values representing the characteristic properties of material distribution across the cross sections of the specimen and reconstructed solution, respectively.

The adequacy of the proposed methodology is examined further by applying for reconstruction of test cross section with higher resolution of  $32 \times 32$  in Fig. 5a. The results in Fig. 5 are similar to those obtained from lower resolution of  $16 \times 16$  in Fig. 4. It should be noted that the algorithm solves the problem at hand in three steps—starting with a coarse resolution of  $8 \times 8$  (Fig. 5c), updating to an intermediate solution of  $16 \times 16$  (Fig. 5d) resolution, and finally giving the solution with required resolution of  $32 \times 32$  (Fig. 5e). The two intermediate peaks in Fig. 5f correspond to the points, where the solutions are updated from a coarser grid resolution to relatively finer grid resolution. Figure 5g illustrates the error in reconstructed characteristic property value in each of the pixels. It is observed from Figs. 4 and 5 that the algorithm starts with a wide range of randomly generated property values, narrows down as it progresses (from one stage to the next stage), and matches finally the range of characteristic property values in the test specimen cross section.

## 4 Conclusions

This paper presents a modified real-coded genetic algorithm, which is well suited for the reconstruction of the cross section of engineering test specimens. The principal modification to earlier reported work is the use of real GA principles, in place of binary-coded GA principles. These modifications provide the user with the flexibility of supplying necessary input within the acceptable wide range of limits, in contrast to the requirement of specification of the exact discrete values of input in earlier reported studies. The adequacy of the proposed algorithm is demonstrated considering several simulation studies with different synthetic test specimens. The multiple-step strategy is shown to take less time when compared to the single-step strategy of previous studies utilizing the binary-coded GA. It is to be noted that the results in general depend on the setting parameters of the algorithm. In this study, parameters are set after several trial simulations with different values of GA parameters, including the probability of crossover, probability of mutation, and the maximum number of generations. Future work is directed towards the identification of robust parameter settings by performing extensive parametric studies using statistical approaches.

## References

1. Vicente MA, Mínguez J, González DC (2017) Computed tomography—advanced applications. IntechOpen, Rijeka
2. DeChiffre L, Carmignato S, Kruth JP, Schmitt R, Weckenmann A (2014) Industrial applications of computed tomography. *CIRP Ann* 63(2):655–677
3. Kak AC, Slaney M (1998) Principles of computerized tomographic imaging. Society for Industrial and Applied Mathematics, Philadelphia
4. Kodali SP, Rao BN (2020) An evolutionary tomographic reconstruction procedure for defect identification using time-of-flight of ultrasound. In: Proceedings on ICEM2020, In Press, Jaipur
5. Kodali SP, Rao BN (2020) Tomographic reconstruction of isotropic materials using genetic algorithms with ultrasound time-of-flight projection data. *J Comput Appl Res Mech Eng*, In Press
6. Kishore NN, Munshi P, Ranamale MA, Ramakrishna VV, Arnold W (2011) Tomographic reconstruction of defects in composite plates using genetic algorithms with cluster analysis. *Res Nondestr Eval* 22(1):31–60
7. Kodali SP, Deb K, Munshi P, Kishore NN (2009) Comparing GA with MART to tomographic reconstruction of ultrasound images with and without noisy input data. In: Proceedings on 2009 IEEE congress on evolutionary computation, pp 2963–2970, IEEE, Trondheim
8. Miller BL, Goldberg DE (1995) Genetic algorithms, selection schemes and the varying effects of noise. IlliGAL report no. 95009, University of Illinois at Urbana-Champaign
9. Lavinias Y, Aranha C, Sakurai T, Ladeira M (2018) Experimental analysis of the tournament size on genetic algorithms. In: Proceedings on 2018 IEEE international conference on systems, man, and cybernetics (SMC), pp 3647–3653, Miyazaki, Japan
10. Deb K, Kumar A (1995) Real-coded genetic algorithms with simulated binary crossover-Studies on multi-modal and multi-objective problems. *Complex Syst* 9(6):431–454
11. Deb K, Agrawal RB (1995) Simulated binary crossover for continuous search space. *Complex Syst* 9(2):115–148
12. Deb K, Deb D (2014) Analyzing mutation schemes for real-parameter genetic algorithms. *Int J Artif Intell Soft Comput* 4(1):1–28
13. Razvan C (2017) Comparative study between the improved implementation of 3 classic mutation operators for genetic algorithms. *Proc Eng* 181:634–640
14. Yong L, Kwong-Sak L (2011) Genetic Algorithm with adaptive elitist-population strategies for multimodal function optimization. *Appl Soft Comput* 11(2):2017–2034
15. Deb K, Pratap A, Agarwal S, Meyarivan T (2002) A fast and elitist multi-objective genetic algorithm-NSGA-II. *IEEE Trans Evol Comput* 6(2):181–197

# Recent Trends on Furnace Design and Stirrer Blade Geometry Used in Stir Caster: A Focused Review



Ashish Kumar Singh, Sanjay Soni, and R. S. Rana

## 1 Introduction

Over the past few years, a considerable increase in the development of lightweight metal matrix composites (MMCs) has been realized so that they could be introduced into several significant applications such as automobiles, aerospace, marine, and structures. Aluminum metallic composites (AMCs) are greatly attractive in such applications owing to their superior physical and mechanical applications [1]. AMCs can be defined as materials composed of pure Al alloy (Al) as matrix phase and ceramic and organic compounds as reinforcing phase incorporated in volume % or weight % and various forms such as particulates, fibers, and whiskers [1, 2]. The choice of reinforcing phases relies on the anticipated outcomes and intended applications of the produced composite. The lighter reinforcing materials open up the opportunity of applications where reduced weight has emerged as a major priority [3]. In this review article, specific attention has been made to particulate reinforced AMCs, because of their abundant availability, economics, and ease in distribution inside the matrix phase during production. Particle reinforced composites exhibit isotropic properties with easier and cost-effective production and thus are more interesting over continuous fiber reinforced composites [4]. Particulate reinforced AMCs are largely employed in aerospace, automobiles, and structural applications owing to their higher stiffness, improved strength-to-weight ratio, better fatigue resistance, greater wear resistance, better stability at elevated temperature, and superior conductivities (electrical and thermal) over the conventionally used engineering materials, which provide the capability to meet the various design criteria of a wide range of elements in advanced engineering fields [5, 6]. Among all ceramic particulates, SiC, Al<sub>2</sub>O<sub>3</sub>, and B<sub>4</sub>C were recognized as fre-

---

A. K. Singh (✉) · S. Soni · R. S. Rana  
Mechanical Engineering Department, Maulana Azad National Institute of Technology,  
Bhopal 462003, India

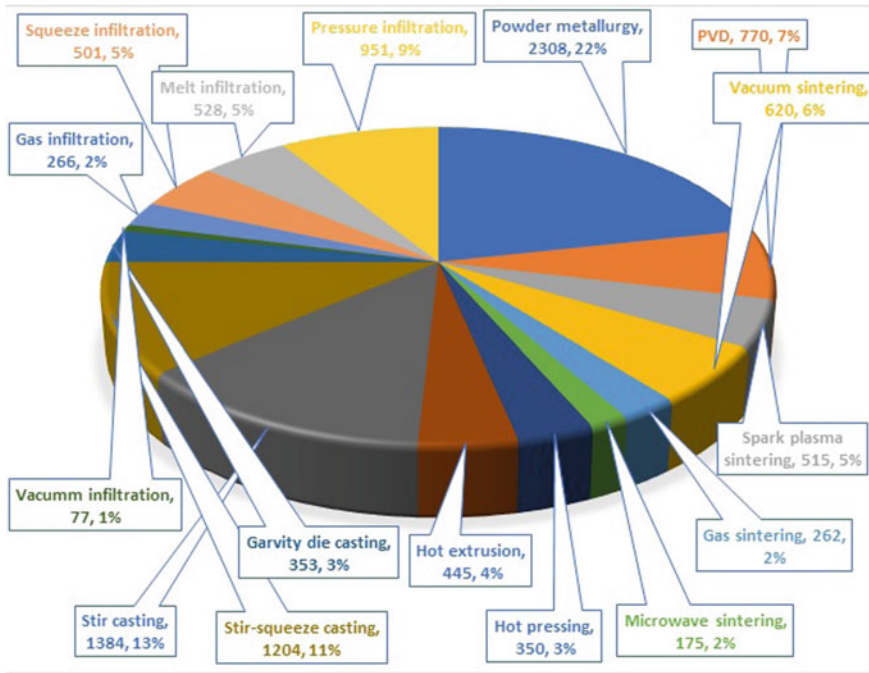


**Fig. 1** Publications on several production methods for AMCs. Source [www.scopus.com](http://www.scopus.com)

quently used particulates in the manufacturing of AMCs which offer enhanced mechanical properties at fairly reduced production cost [7].

The anticipated properties from AMCs also significantly rely upon the production method; thus, the choice of processing technique plays a vital character to conform with engineering demands and to offer competent features. The economics of a processing method of AMCs is a very important aspect to upgrade their applications. The primary processing techniques adopted for bulk AMCs are comocasting, stir casting, direct melt oxidation method, infiltration, and powder metallurgy [8, 9]. In addition, as per the Scopus Search ([www.scopus.com](http://www.scopus.com)) database, a pie chart (refer Fig. 1) has been shown to portray the various processing methods for the past one decade, which clearly shows that stir casting underlying liquid state processing method is the most commonly adopted production method. In a study, Shirvanimoghaddam et al. [10] reported nineteen review articles available in the field of metallic composites from the year 2000, where ten out of these articles were found to deal with processing techniques. In another review study, Torralba et al. [11] made attention on the processing of MMCs by using the powder metallurgy method. Mg metallic composites were the focus of Ye and Liu [12] where only one subsection was dealt with the processing routes. Furthermore, Miracle [13] only focused on the fabrication methods briefly where the attention was made on the MMCs properties making them appropriate for many engineering

applications. Similarly, Ye et al. [14] made focus on the fabrication of MMCs through the injection molding method. Casati and Vedani [15] focused on MMCs reinforced with nano-sized particulates. Another study made by Qu et al. [16] was concentrated on metallic composites for thermal applications. Kala et al. [17] presented tribo-mechanical characteristics of AMCs produced through the stir casting route. Silvestre [18] and Bakshi et al. [19] reviewed metallic composites dispersed with carbon nanotubes (CNTs) and therefore very explicit where a wide spectrum of reinforcing phases and the processing methods are yet to be covered.

Based on the available literature, it is very apparent that comprehensive reviews especially on furnace design and stirrer blade geometry of stir caster used to produce AMCs are very scarce. Therefore, in the existing review article, a critical assessment has been carried out to deliver an extensive overview of the furnace design and various associating factors to stirrer blade geometry involved in the production of AMCs through stir casting method.

## 2 Liquid State Stir Casting Method

This method comprises of dispersal of reinforcement (particulates or fibers) into the melt of matrix material and subsequent mixing of these elements using rotating stirrer [20], refer Fig. 2. In a study, Rohatgi et al. [21] synthesized A356-FAP composites using a melt stirring route and found that composites can be effectually applied in numerous lightweight components with limited economics. Reddy et al. [22] produced Al 6061/SiCp/B4Cp metallic composites by stir casting method and

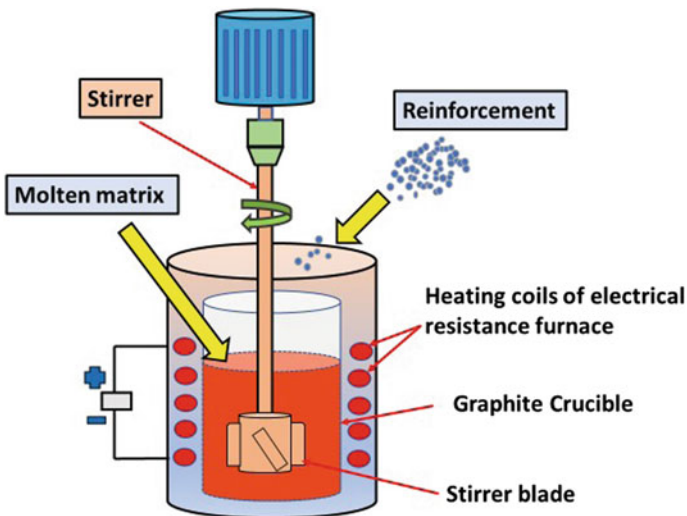


Fig. 2 Stir casting route [23]

detected better wettability and noteworthy improvements in the strength and hardness.

In several studies, the geometry of reinforcing phases [24], melt temperature of matrix [25], type of furnace used for the heating of matrix [7], preheating of reinforcing phases [26] and mold [27], mode of pouring [28], design of stirrer blade assembly [29], and some other process variables such as feed rate [24] and stirrer rotation time and rotational speed [29] have been reported as major factors that affected the quality of castings. In the following sections, two of these, namely furnace design and stirrer blade geometry, have been discussed exclusively.

### 2.1 Casting Furnace Design

Based on the melting process, several furnaces are being adopted during the development of AMCs using stir caster. Amongst, electrical resistance type of furnace is being prominently used as it offers better flexibility with a wide range of possible modifications that can be effectively incorporated in this furnace [7, 30]. Going through several research studies, the following modifications (refer Fig. 3) were found in the furnace design used in the production of AMCs.

#### Coal-fired Heating Furnace

This method involves heating of matrix material using a coal-fired furnace, and a blower is employed to draw the generated heat inside the furnace as well as to distribute it all over in the crucible. Reinforcement is brought into the matrix melt

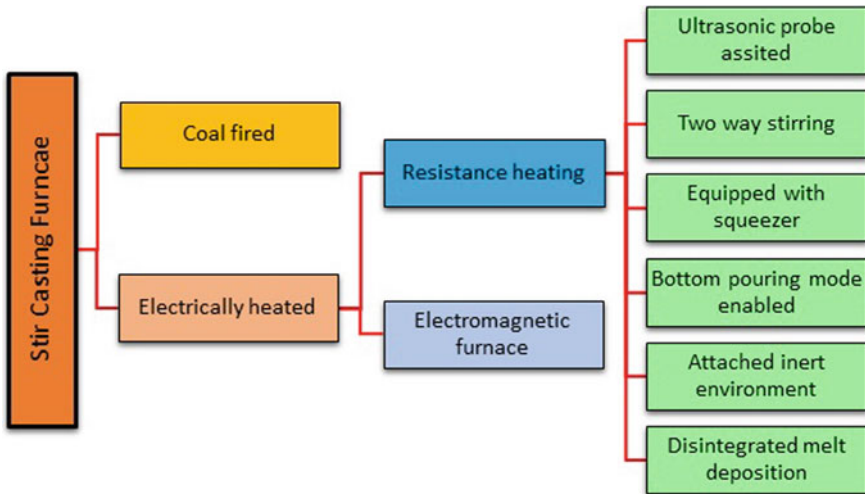


Fig. 3 Heating furnace designs used in stir caster

after mechanical stirring. In an investigation, Annigeri and Veeresh Kumar [31] reviewed different methods used in the manufacturing of the Al metallic composites and reported the coal-fired furnace as the basic among all other casting furnaces.

### **Electrically Heated Stir Caster**

These types of furnaces are the most commonly used casting furnaces, where electrical resistance heating furnace has been noted to be one of the most commonly employed furnaces and is thereby being discussed in subsections ahead.

#### *Stir Caster Assisted with Ultrasonic Transducer*

This type of casting furnace is being mainly used while dealing with nano-sized particulates in the production of Al-based composites. This furnace mainly involves an extra element, namely an ultrasonic probe, to agitate the composite mixture so that proper mixing can be imparted [32]. In a study, Patel et al. [33] inspected the impact of ultrasonic stirrer onto the micro-mechanical behavior of AA 5083/TiCp in-situ composites and reported uniform dispersion of TiCp, leading toward upgraded strength and hardness. Srivastava and Chaudhari [34] also employed an ultrasonic transducer for 3 min with a 20 kHz frequency during producing AA 6061/Al<sub>2</sub>O<sub>3</sub>np and resulted in outstanding particle spreading throughout the mixture.

#### *Two-way (Modified) Stir Caster*

Herein, stirring is conducted at two phases, i.e., semi-solid (mixed) phase and complete liquid phase in the molten mixture, which indorses very even mixing of reinforcements and superior bonding between the elements [35]. In a study, Sambathkumar et al. [36] used this furnace to cast AA 7075/SiCp/TiCp-based composites and perceived enhanced tensile strength and hardness in the comparison with unreinforced matrix alloy.

#### *Stir Caster with Inert Environment and Bottom Pouring*

Herein, the conventionally used stir caster is equipped with an attachment creating an inert atmosphere and a bottom pouring component. The above setup includes the advantages of both the additional attachments and eliminates the occurrence of unsought chemical reactions due to atmospheric gases and provides improved even dispersion. In an investigation, Amirkhanlou and Niroumand [37] employed this type of stir caster in the manufacturing of A356/SiCp-based composites; herein, SiC particles were incorporated using an extra connection provided at the junction point of a flow regulator and Ar gas carrier. It was stated that using these attachments, homogeneous spreading of particles, limited porosity %, and superior bonding (wettability) between the constituents were attained and therefore leading toward enhanced mechanical properties.

#### *Stir Caster with Squeezer and Bottom Pouring*

Herein, individual merits of the two different components, namely squeezer and bottom pouring arrangements, can be obtained by assisting these components with



the conventionally used stir casting furnace [38]. Employing squeezer and bottom pouring, the better quality of castings can be achieved with very limited minor casting defects. In an investigation, Kannan and Ramanujam [39] casted AA7075/SiCnp/Al<sub>2</sub>O<sub>3</sub>np-based composites attaching these additional components and reported improved mechanical properties as compared to the unreinforced base alloy.

#### *Furnace with Disintegrated Melt Deposition*

This can be termed as an upgraded form of the formerly used spray deposition method which is being mainly employed to avoid the unevenness in the distribution of particles and to provide improved interfacial integrity between the composite elements [40, 41]. Herein, the disintegration of the poured composite melt is carried out using two inert gas jets inclined at an angle of around 90° with the stream of the melt and subsequent deposition onto a substrate. In a study, Gupta et al. [42] used this method in the production of SiCp-dispersed AMCs and observed regular distribution of particles, improved mixing, and robust interfacial wetting between the constituents and thus leading greater desired properties.

Table 1 has been provided below to summarize the salient features of different heating furnaces used in the processing of AMCs.

**Table 1** Various furnaces and their salient characteristics adopted in the development of AMCs

Furnace Design	Notable Features		References
	Advantageous	Adversative	
Conventional furnace	Easier handling	Some sites of clusters	[43]
Coal-fired furnace	Reduced consumption of electricity	By-products of Solid wastes	[31]
Electromagnetic furnace	Better dispersion of particles	Expensive, porosity with higher frequency	[30]
Stir caster assisted with an ultrasonic transducer	Outstanding dispersal of reinforcing particles	Expensive, limited with nanoparticles, agglomerated sites	[34]
Two-way (modified) caster	Superior bonding, consistent dispersal	More care required in the stirring of slurry	[36, 44]
Stir caster with squeezer and bottom pouring	A significant decrement in porosity	Expensive, slower	[39]
Stir caster with the inert environment and bottom pouring	Homogeneous dispersal, reduced % porosity and defects	–	[45–47]
Furnace with disintegrated melt deposition	Greater integrity at interface	Expensive and lengthy	[42]

## 2.2 Stirrer Blade Geometry

The design of the stirrer blade assembly has also been recognized as one of the influencing factors affecting the quality of castings [29, 48]. In this section, various associating factors such as the impeller blade angle, the height of the melt, and stirrer in the crucible have been discussed.

### Impeller Blade Staging

In several studies [29, 31], two or more than two blades were employed with the impeller to create a vortex and to obtain favorable mixing of the constituents present in the composite mixture. Furthermore, multistage blades (refer Fig. 4) were also installed with the impellers to offer greater mixing of the constituents. However, impellers with the multistage blade are being generally used in the manufacturing of chemical products, while single-stage impellers have been recognized as the most appropriate in the development of AMCs using stir caster [29].

### Blade Angle

The vortex formed by the rotating stirrer promotes the shifting of the reinforcements in the matrix melt from the free surface, and shearing offers the splintering of the gathered reinforcing elements enabling inconsistent spreading [24, 29]. Therefore, the selection of a suitable blade angle becomes a critical phase to accomplish promising shearing phenomena and axial flow (refer Fig. 5). Modeling techniques such as water models and computational fluid dynamics (CFD) are being widely used to observe the impact of blade angles on the quality of the castings. In numerous research investigations [24, 29, 48], different impeller blade angles such as 15°, 30°, 45°, 60°, and 90° were taken, and the blade angle of 30° was conveyed as the best suitable promoting homogeneous dispersion of the reinforcing

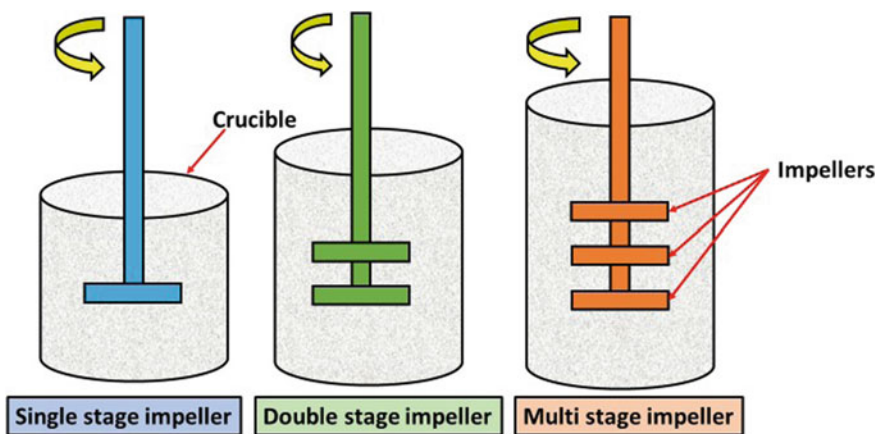
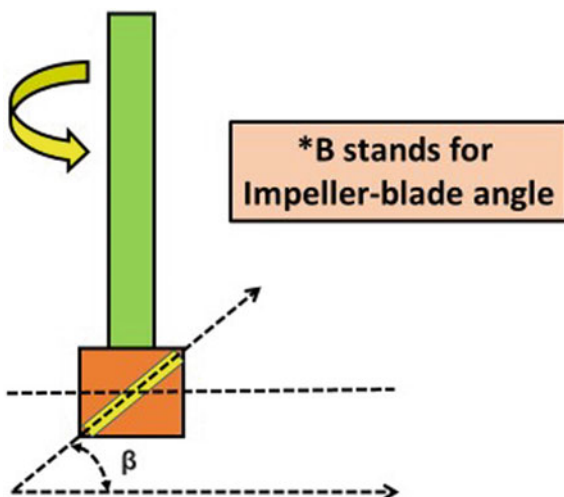


Fig. 4 Multistage in impeller blade [24]

**Fig. 5** Impeller blade angle  
[24]



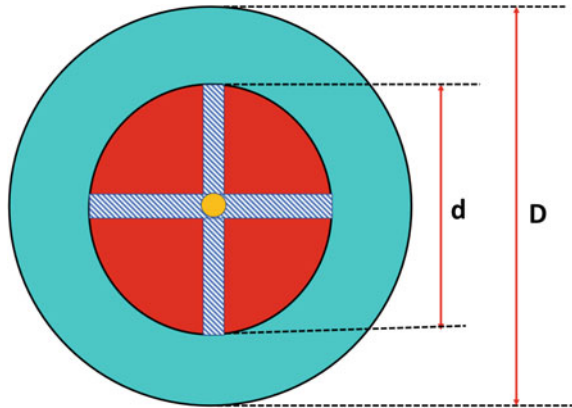
particulates with reduced agglomerated sites. Furthermore, it was also stated that at a higher angle, particles were noticed to gather in the locality of the blade tip resulting in larger radial variation. Besides, greater shearing phenomena also occurred at higher blade angles leading toward the adversative mixing of the elements. However, at the lower blade angle, embedded particles were merely distributed near the rotating stirrer leading toward inferior mixing of the elements.

### Impeller Blade Size (Diameter)

The dispersion of the reinforcing particles also relies on the size of the impeller blade (diameter) which is generally expressed in the term of the crucible diameter. Impeller blade size must be optimized as a higher impeller diameter resulted in reinforcing particulates more concentrated in the center of the bottom of the crucible, while a lower impeller diameter led more particle suspension at the crucible periphery causing a limited transfer of the particles to the center. The optimum impeller diameter ( $d$ ) should be 0.5 times of the crucible diameter ( $D$ ) for a crucible having a flat base subjected to single-stage stirring at 550 rpm [49], and it should be 0.55 times of crucible diameter ( $D$ ) for a crucible having semispherical base subjected to multistage stirrer rotating at 1000 rpm [29], refer Fig. 6, while the width of the blade ( $b$ ) should be 0.1–0.2 times of crucible diameter ( $D$ ) [50].

The boundary layer theory of Ekman related to the lifting of the particle in the whirling fluid is well predictable during the initial stirring phases. Secondary axial flow is created through the Ekman layer where momentum transfer occurred from a higher momentum region to a lower momentum region. Characteristic velocity ( $V_E$ ) in the Ekman layer and spin-up time ( $t$ ) scale are given in Eqs. (1) and (2), respectively.

**Fig. 6** Impeller and crucible diameters [24]



$$V_E = (H_2/t) \tag{1}$$

$$t = (E\Omega^2)^{-1/2} \tag{2}$$

where  $\Omega$  stands for angular velocity,  $H_2$  stands for the height of the free surface of the melt, and E stands for the Ekman number.

The correlation of the observed lifting of the particle in the layer with flow variables is given by the particle dispersion number (PDN), which is defined as a ratio of  $V_E$  and terminal falling velocity.

PDN value greater than one indicates that secondary axial flow velocity is higher than that of the settling velocity; therefore, convection of the particles happened to the top of the molten mixture, whereas the particles would remain at the bottom for the PDN values lesser than one. PDN for a rotating coaxial flow is expressed as given in the Eq. (3) [50].

$$PDN = \left[ \left\{ H_2(\mu\omega)^{1/2} \right\} / \left\{ R_i^{1/4} d^{3/4} V_t \right\} \right] \tag{3}$$

where  $V_t$  stands for settling velocity,  $\mu$  stands for slurry viscosity,  $H_2$  stands for melt height,  $d$  stands for the gap between outer and inner,  $R_i$  stands for inner radius, and  $\omega$  stands for angular velocity.

**Impeller Blade Position**

The impeller blade position into the composite mixture was also found to play a vital role during the mixing of the composite elements. In an investigation, Hashim et al. [50] recommended the optimum position of the impeller blade assembly into the mixture (refer Fig. 7) and stated that impeller height ( $H_1$ ) should be around 30% of the total free surface height ( $H_2$ ) in the composite melt. A proper position of this

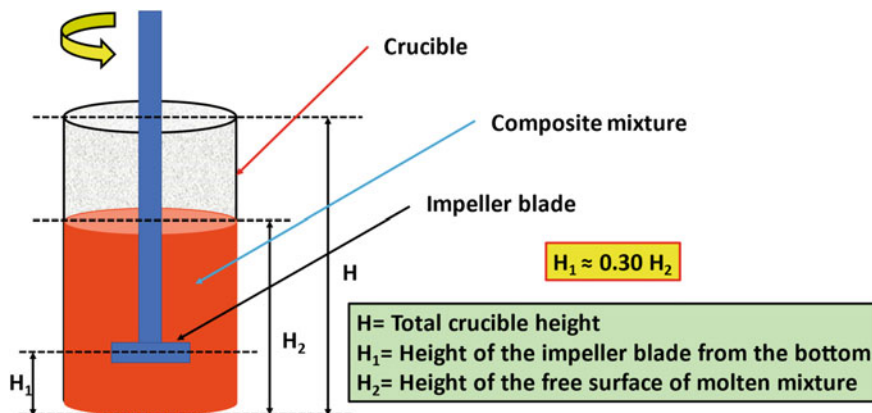


Fig. 7 Impeller blade position into the melt [49]

assembly prevents the occurrence of agglomerated sites and consequences unvarying the distribution of the embedded phases into the molten matrix.

### 3 Concluding Remarks and Future Prospects

Considering the initial treatment conducted for the matrix phase, liquid and solid state methods have been acknowledged as the prime processing routes for AMCs. However, some semi-solid state (mixed-phase) processing routes such as compocasting and thixocasting are also being used. Based on the database (Scopus search), the stir casting route has been reported as one of the prominent techniques used for the development of AMCs as this method provides informal handling of the process with limited cost. This review article recommends that depending on the requirement, appropriate modification in the casting furnace such as an ultrasonic probe, inert atmosphere, bottom pouring mode, and squeezer can be carried out during the production of AMCs. Besides, a single-stage impeller blade assembly containing three blades at an angle of  $30^\circ$  would be more suitable for stirrer blade geometry. In the existing review article, only two major aspects, namely furnace design and stirrer blade geometry, have been taken into consideration. However, there are many other factors such as stirrer rotational speed and time, melting temperature of the matrix material, the geometry of reinforcing phases, and feed rate which affect the quality of produced castings and, therefore, must be reviewed and discussed properly.

**Acknowledgements** The authors are very grateful to Director, MANIT, and Dr. S. Das, Adjunct Professor MANIT/Former Director AMPRI (CSIR), Bhopal (India), for a fruitful encouragement toward research.

## References

1. Surappa MK (2003) Aluminium matrix composites: challenges and opportunities. *Sadhana—Acad Proc Eng Sci* 28(1–2):319–334
2. Dasgupta R (2012) Aluminium alloy-based metal matrix composites: a potential material for wear resistant applications. *ISRN Metall* 2012:1–14
3. Mavhungu ST, Akinlabi ET, Onitiri MA, Varachia FM (2017) Aluminum matrix composites for industrial use: advances and trends. *Proc Manuf* 7:178–182
4. Das DK, Mishra PC, Singh S, Pattanaik S (2014) Fabrication and heat treatment of ceramic-reinforced aluminium matrix composites—a review. *Int J Mech Mater Eng* 9(1):1–15
5. Kala H, Mer KKS, Kumar S (2014) A review on mechanical and tribological behaviors of stir cast aluminum matrix composites. *Proc Mater Sci* 6:1951–1960
6. Rohatgi P (1991) Cast aluminum-matrix composites for automotive applications. *JOM* 43(4):10–15
7. Ramanathan A, Krishnan PK, Muraliraja R (2019) A review on the production of metal matrix composites through stir casting—Furnace design, properties, challenges, and research opportunities. *J Manuf Process* 42(Dec 2018):213–245
8. Das S (2004) Development of aluminium alloy composites for engineering applications. *Trans Indian Inst Met* 57(4):325–334
9. Harrigan WC (1998) Commercial processing of metal matrix composites. *Mater Sci Eng A* 244(1):75–79
10. Shirvanimoghaddam K et al (2017) Carbon fiber reinforced metal matrix composites: fabrication processes and properties. *Compos Part A Appl Sci Manuf* 92:70–96
11. Torralba JM, Da Costa CE, Velasco F (2003) P/M aluminum matrix composites: an overview. *J Mater Process Technol* 133(1–2):203–206
12. Ye HZ, Liu XY (2004) Review of recent studies in magnesium matrix composites. *J Mater Sci* 39(20):6153–6171
13. Miracle DB (2005) Metal matrix composites—from science to technological significance. *Compos Sci Technol* 65(15–16 Spcl Iss):2526–2540
14. Ye H, Liu XY, Hong H (2008) Fabrication of metal matrix composites by metal injection molding—a review. *J Mater Process Technol* 200(1–3):12–24
15. Casati R, Vedani M (2014) Metal matrix composites reinforced by nano-particles—a review. *Metals (Basel)* 4(1):65–83
16. Qu XH, Zhang L, Wu M, Bin Ren S (2011) Review of metal matrix composites with high thermal conductivity for thermal management applications. *Prog Nat Sci Mater Int* 21(3):189–197
17. Kala H, Mer KKS, Kumar S (2014) A review on mechanical and tribological behaviors of stir cast aluminum matrix composites. *Proc Mater Sci* 6:1951–1960
18. Silvestre N (2013) State-of-the-art review on carbon nanotube reinforced metal matrix composites. *Int J Compos Mater* 3(6A):28–44
19. Bakshi SR, Lahiri D, Agarwal A (2010) Carbon nanotube reinforced metal matrix composites—a review. *Int Mater Rev* 55(1):41–64
20. Rana RS, Purohit R, Soni S, Das S (2014) Comparison of mechanical properties and microstructure of aluminum alloy micron and Nano SiC composites fabricated by ultrasonic vibration. *Int J Adv Eng Res Dev* 1(12):135–146
21. Rohatgi PK, Kim JK, Gupta N, Alaraj S, Daoud A (2006) Compressive characteristics of A356/fly ash cenosphere composites synthesized by pressure infiltration technique. *Compos Part A Appl Sci Manuf* 37(3):430–437
22. Reddy PS, Kesavan R, Vijaya Ramnath B (2018) Investigation of mechanical properties of aluminium 6061-silicon carbide, boron carbide metal matrix composite. *Silicon* 10(2):495–502
23. Hashim J, Looney L, Hashmi MSJ (1999) Metal matrix composites: production by the stir casting method. *J Mater Process Technol* 92–93:1–7

24. Sahu MK, Sahu RK (2018) Fabrication of aluminum matrix composites by stir casting technique and stirring process parameters optimization. In: *Advanced casting technologies*
25. Venkatesan S, Xavier MA (2019) Characterization on aluminum alloy 7050 metal matrix composite reinforced with graphene nanoparticles. *Procedia Manuf* 30:120–127
26. Bharath V, Nagaral M, Auradi V, Kori SA (2014) Preparation of 6061Al-Al<sub>2</sub>O<sub>3</sub> MMC's by stir casting and evaluation of mechanical and wear properties. *Proc Mater Sci* 6:1658–1667
27. Soundararajan R, Ramesh A, Sivasankaran S, Sathishkumar A (2015) Modeling and analysis of mechanical properties of aluminium alloy (A413) processed through squeeze casting route using artificial neural network model and statistical technique. *Adv Mater Sci Eng* 2015
28. Raj R, Thakur DG (2016) Qualitative and quantitative assessment of microstructure in Al-B4C metal matrix composite processed by modified stir casting technique. *Arch Civ Mech Eng* 16(4):949–960
29. Su H, Gao W, Zhang H, Liu H, Lu J, Lu Z (2010) Optimization of stirring parameters through numerical simulation for the preparation of aluminum matrix composite by stir casting process. *J Manuf Sci Eng Trans ASME* 132(6):0610071–0610077
30. Kumar A, Lal S, Kumar S (2013) Fabrication and characterization of A359/Al<sub>2</sub>O<sub>3</sub> metal matrix composite using electromagnetic stir casting method. *J Mater Res Technol* 2(3):250–254
31. Annigeri UK, Veeresh Kumar GB (2017) Method of stir casting of aluminum metal matrix composites: a review. *Mater Today Proc* 4(2):1140–1146
32. Koli KD, Agnihotri G, Purohit R (2015) Influence of ultrasonic assisted stir casting on mechanical properties of Al6061-nano Al<sub>2</sub>O<sub>3</sub> composites. *Mater Today Proc* 2(4–5):3017–3026
33. Patel KK, Kumar V, Purohit R, Gupta GK, Modi OP (2017) Effect of ultrasonic stirring on changes in microstructure and mechanical properties of cast in-situ Al 5083 alloy composites containing 5wt.% and 10wt.% TiC particles. *Mater Today Proc* 4(2):3494–3500
34. Srivastava N, Chaudhari GP (2016) Strengthening in Al alloy nano composites fabricated by ultrasound assisted solidification technique. *Mater Sci Eng A* 651:241–247
35. David Raja Selvam J, Dinaharan I, Mashinini PM (2017) High temperature sliding wear behavior of AA6061/fly ash aluminum matrix composites prepared using compocasting process. *Tribol—Mater Surfaces Interfaces* 11(1):39–46
36. Sambathkumar M, Navaneethakrishnan P, and Sasikumar KS, Ponappa K (2016) Mechanical and corrosion behavior of Al7075 ( Hybrid) metal matrix composites by two step stir casting process. *Lat Am J Solids Struct* 7075:243–255
37. Amirkanlou S, Niroumand B (2010) Synthesis and characterization of 356-SiCp composites by stir casting and compocasting methods. *Trans Nonferr Met Soc China (English Ed)* 20 (SUPPL 3):s788–s793
38. Sekar K, Allesu K, Joseph MA (2014) Effect of T6 heat treatment in the microstructure and mechanical properties of A356 reinforced with nano Al<sub>2</sub>O<sub>3</sub> particles by combination effect of stir and squeeze casting. *Procedia Mater Sci* 5:444–453
39. Kannan C, Ramanujam R (2017) Comparative study on the mechanical and microstructural characterisation of AA 7075 nano and hybrid nanocomposites produced by stir and squeeze casting. *J Adv Res* 8(4):309–319
40. Tham LM, Gupta M, Cheng L (1999) Influence of processing parameters during disintegrated melt deposition processing on near net shape synthesis of aluminium based metal matrix composites. *Mater Sci Technol* 15(10):1139–1146
41. Gupta M, Lai MO, Saravananathan D (2000) Synthesis, microstructure and properties characterization of disintegrated melt deposited Mg/SiC composites. *J Mater Sci* 35(9):2155–2165
42. Gupta M, Lai MO, Soo CY (1996) Processing-microstructure-mechanical properties of an Al-Cu/SiC metal matrix composite synthesized using disintegrated melt deposition technique. *Mater Sci Forum* 217–222(PART 3):1865–1870
43. Rohatgi PK, Weiss D, Gupta N (2006) Applications of fly ash in synthesizing low-cost MMCs for automotive and other applications. *JOM* 58(11):71–76

44. Radhika N, Sai Charan K (2017) Experimental analysis on three body abrasive wear behaviour of stir cast Al LM 25/TiC metal matrix composite. *Trans Indian Inst Met* 70 (9):2233–2240
45. Mistry JM, Gohil PP (2018) Research review of diversified reinforcement on aluminum metal matrix composites: fabrication processes and mechanical characterization. *Sci Eng Compos Mater* 25(4):633–647
46. Gopalakrishnan S, Murugan N (2012) Production and wear characterisation of AA 6061 matrix titanium carbide particulate reinforced composite by enhanced stir casting method. *Compos Part B Eng* 43(2):302–308
47. Josyula SK, Narala SKR (2016) Experimental investigation on tribological behaviour of Al–TiCp composite under sliding wear conditions. *Proc Inst Mech Eng Part J: J Eng Tribol* 230 (8):919–929
48. Ravi KR et al (2007) Optimization of mixing parameters through a water model for metal matrix composites synthesis. *Mater Des* 28(3):871–881
49. Sahu MK, Sahu RK (2017) Optimization of stirring parameters using CFD simulations for HAMCs synthesis by stir casting process. *Trans Indian Inst Met* 70(10):2563–2570
50. Hashim J, Looney L, Hashmi MSJ (2002) Particle distribution in cast metal matrix composites —Part I. *J Mater Process Technol* 123(2):251–257



# Design Consideration for e-Rikshaw with Regeneration Capability



Manoj Kumar and Amit Ojha

## 1 Introduction

Electric Vehicle is gaining popularity days by days due to its inherent advantages such as no emission, very low running cost, low energy consumption, low maintenance and high performance [1–3]. e-Rikshaw belongs to the family of e-vehicle, due to the advantages of e-Rikshaw over conventional rikshaw, e-Rikshaws are gaining lots of popularity as public transport. Conventional Rikshaws are popular in most Indian cities for local short distance travel due to its ease of availability. These ordinary Rikshaws are driven by Internal Combustion Engine which has efficiency around 20% and leads to CO<sub>2</sub> emission which aggravate the environmental condition during winter [4]. Therefore, a fair amount of thrust is being given by Government of India to promote this segment. Hence, nowadays, battery powered e-Rikshaw are becoming popular due to reduction in running cost, no CO<sub>2</sub> emission, reduced maintenance, increased price of fossil fuel. E-vehicle has some disadvantages like low driving range, longer recharging time and battery cost [5]. Continual efforts are being made by researchers around the world to overcome these drawbacks [6]. Main source of energy for e-Rikshaw is battery which has limited energy and it runs around 50–60 kms per charging and recharging takes 8–10 h. A further efficiency boost and recapturing of brake energy will further glorify its popularity due to improvement in running kms per charging cycle of battery. Selection of power rating and design consideration for electric vehicles with their issues has been dealt in [7–10]. Motors and inverters for electric vehicles are dealt in [11–15]. The research which deals with regenerative braking capability of e-vehicle is covered in [16–27] Comprehensive design considerations which are

---

M. Kumar

Control Equipment Engineering Department, BHEL, Bhopal, Madhya Pradesh, India

A. Ojha (✉)

Electrical Engineering Department, MANIT, Bhopal, Madhya Pradesh, India

© The Author(s), under exclusive license to Springer Nature Singapore Pte Ltd. 2022

P. Verma et al. (eds.), *Advancement in Materials, Manufacturing and Energy Engineering, Vol. I*, Lecture Notes in Mechanical Engineering,

[https://doi.org/10.1007/978-981-16-5371-1\\_15](https://doi.org/10.1007/978-981-16-5371-1_15)

161

mandatory for designing an e-Rikshaw are rarely considered till now. Also, the various energy efficient measures specifically regenerative capability which is making e-Rikshaw most efficient are yet to touch. Therefore, author has made an exhaustive effort to concentrate the design consideration of e-Rikshaw with regenerative capability. The proposed key features will benefit researchers as well as industries for the development of an efficient e-Rikshaw with improved features such as efficiency improvement, proper selection of components and enhancement in running per charging.

## 2 e-Rikshaw Drive System

e-Rikshaw is becoming inherent part of modern transportation system now-a-days due to its various advantages over conventional auto-Rikshaw. The main components of E-Rikshaw are structure frame, battery, inverter, motor, gears and drive wheels (Fig. 1). The dynamic response of e-Rikshaw is very fast as compared to conventional auto-Rikshaw. It takes hardly a few seconds to reach its maximum speed. It is almost free from wear and tear as its uses electric braking methodology. Battery is prime source of energy when driving and it can also restore energy during braking if e-Rikshaw has regenerative capability. A three-phase voltage source inverter and its controller convert the battery voltage into 3-phase AC voltage which is fed to driving motor. The same inverter system works as boost chopper while braking and kinetic energy of e-Rikshaw is fed back to battery. Motor drive fitted with gear system finally drives wheels of e-Rikshaw.

Figure 2 shows the schematic of controller required for e-Rikshaw [28]. The controller comprises three PI controllers, Clarke, inverse Clarke and inverse park transforms, space vector modulation, phase voltage construction and sliding mode observer. The hardware of e-Rikshaw controller consists of voltage and current sensors, driving motor and metal-oxide-semiconductor field-effect transistor (MOSFET)/Insulated Gate Bipolar Transistor (IGBT) based voltage source inverter. The control command is derived from reference speed which is fed through hand operated potentiometer in e-Rikshaw. The reference speed signals ( $\omega_{r*}$ ) is

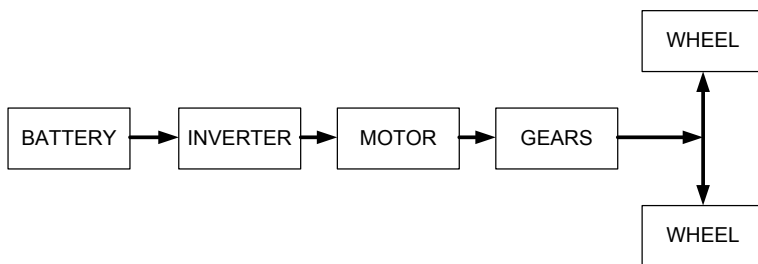


**Fig. 1** Basic block diagram of e-Rikshaw



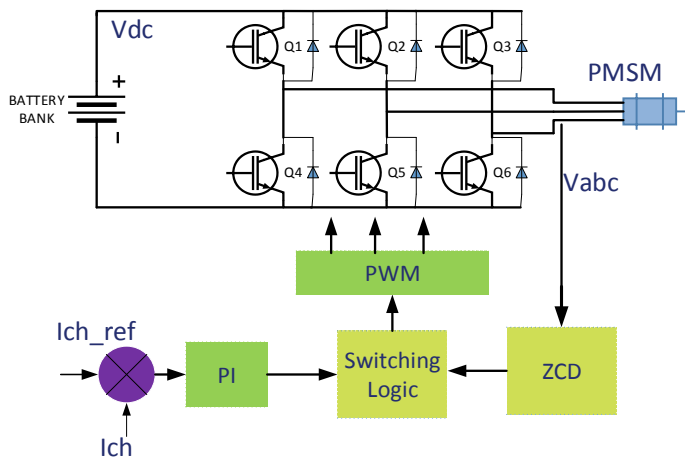


Fig. 3 Braking control block diagram of e-Rikshaw

- Load Capacity: 500–1500 kg
- Speed: 25–35 kmph
- Max running in one charging: 60 km
- Charging time: 8–10 h

To maximise the overall efficiency of e-Rikshaw, the author proposes the design considerations and explained in detail in the following sections.

### 3 Shape of e-Rikshaw

The shape of e-vehicle is very important in maximisation of its efficiency. For e-vehicle drive system efficiency enhancement, shape of vehicle must be chosen carefully. The force acting on driving body of vehicle can be calculated as:

$$F_d = \frac{1}{2} \rho A C_d v^2 \quad (1)$$

where

$F_d$  = Drag force (N-m)

$\rho$  = Air density ( $\text{kgm}^{-3}$ )

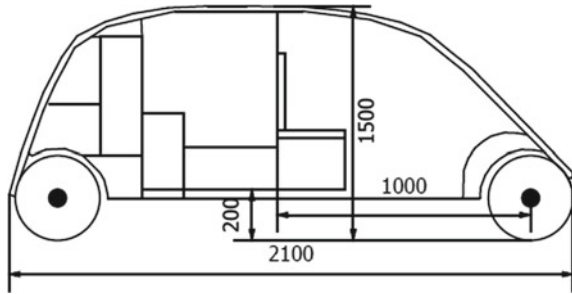
$A$  = Frontal area of vehicle ( $\text{m}^2$ )

$v$  = Speed of vehicle ( $\text{ms}^{-1}$ )

$C_d$  = Drag coefficient.

Drag force should be as minimum as possible for improvement in vehicle efficiency. Ideal body shape is similar to teardrop as shown in Fig. 4 it faces minimum

**Fig. 4** Proposed aerodynamic shape (all dimensions in mm)



drag force. Drag coefficient  $C_d$  varies from 0.1 to 0.5 and air density can be taken as  $1.2 \text{ kgm}^{-3}$ . It can be seen from Eq. 1, the drag force is directly proportional to drag coefficient. Hence, care must be taken to keep it as minimum as possible. A typical shape of e-Rikshaw showing dimension is shown in Fig. 4.

### 4 Rolling Resistance

Rolling resistance is defined as a force acting against the motion of wheel and plays a vital role in vehicle efficiency, hence, need proper attention during the design of vehicle system. It is also known as rolling friction. In general, rolling resistance consumes around 20–50% of fuel/battery energy. 10% reduction in rolling resistance improves vehicle efficiency by 3%. Out of total energy consumes by rolling resistance, 1–5% is contributed by aerodynamic drag and 9–10% by road friction and 85–95 is exhausted in internal friction or hysteresis of material, therefore, it is the main area of concern for improvement of vehicle efficiency, i.e. tyre design is very important. There are mainly three parameters such as tyre pressure, load and slip angle. Tyre pressure increases with temperature, increased pressure reduces rolling resistance. Load resistance is directly proportional to load and slip angle comes into picture while turning a vehicle.

Rolling resistance can also be defined as friction between two surfaces when one or both are free to rotate or move. It is a combination of many forces acting between wheel and ground. It is less compared to static and sliding friction, hence, wheel and ball facilitate motion. The Fig. 5 explain the phenomena of rolling friction:

Rolling drag force on a vehicle can be calculated as:

$$F_r = u_r Mg \tag{2}$$

where

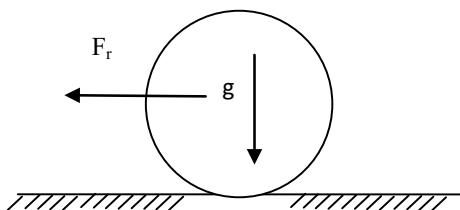
$F_r$  = Rolling drag Force (N-m)

$u_r$  = Rolling coefficient

$M$  = Weight of vehicle (kg)

$g$  = Gravitational force ( $\text{ms}^{-2}$ ).

**Fig. 5** Rolling resistance force



Rolling force is directly proportional to rolling coefficient. It varies from 0.005 to 0.015 depending upon the type of tyre. Therefore, tyre selection is very important especially for low speed vehicles.

## 5 Gear System

A transmission system is required for transfer of motion from motor to wheels in an electric vehicle. In IC engines, clutch, gearbox, propulsion shaft and differential gear are required for transmission. At each stage in a conventional system, there is power loss which makes overall efficiency of standard Rikshaw to the tune of around 20%. In e-Rikshaw, electric motor is coupled to a gear system for speed reduction that drives the wheels of a vehicle. A typical arrangement of motor and gear drive is shown in Fig. 6. Gear ratio for e-Rikshaw is normally derived using speed, motor RPM and torque requirement. Improper selection of gear ratio will lead to increased/decreased torque in a vehicle. Further, it will lead to wear and tear in vehicle, i.e. increased maintenance. The controller must be suitably designed to transmit the required tractive force to wheel. Most popular materials being used for gear manufacturing are compared in Table 1.

**Fig. 6** Speed reduction gear system

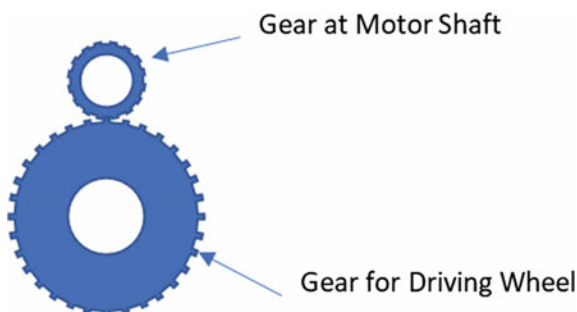


**Table 1** Gear material comparison

Gear material	Advantages	Disadvantages
Aluminium	High durability, corrosive resistance, light weight, Easy manufacturing, non-magnetic, low noise, good strength and life	Higher thermal expansion coefficient, low tensile strength
Aluminium alloy 7068	Corrosive resistance, light weight, low noise, good tensile strength and life, higher thermal conductivity, good efficiency	Cost is very high
Brass alloy	Low cost, easy processing, good hardness, good electrical and mechanical conductivity, high strength, good ductility, high corrosive resistance	Higher weight

## 6 Weight of Vehicle

Body material selection is very-very important for e-Rikshaw. Being a passenger vehicle, material selection must meet safety requirements for the segment as well as weight of material be optimum to maximise the efficiency of vehicle. Use of high-grade stainless steel (HSS) can reduce weight by 20% and further 20% weight reduction is possible by use of aluminium, plastic, polymer composite and carbon fibre composite. Use of such advanced material can reduce vehicle weight by 60%. Use of advanced material makes the initial cost higher but these are finally cheaper in long run as efficiency is directly affected by weight of vehicle, therefore, weight of any vehicle has a critical effect on the performance. Refer to Fig. 7 showing the force acting on vehicle. The force acting on a vehicle can be calculated as:

$$F_m = Mg\text{Sin}\theta \tag{3}$$

where

$F_m$  = Force due to weight (N-m)

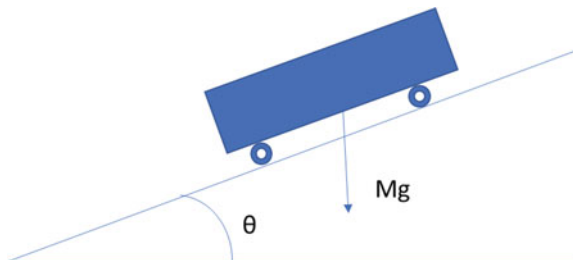
$M$  = Weight of vehicle (kg)

$g$  = Gravitational force ( $\text{ms}^{-2}$ )

$\theta$  = Climbing angle (Degree)

When the design for a flat road, i.e.  $\theta$  is zero. Force acting will also be zero.

**Fig. 7** Force on moving vehicle



## 7 Kinetic Energy

Kinetic energy of a vehicle is the energy that it possesses due to its motion. It can also be defined as the work needed to accelerate a vehicle to a defined velocity. Vehicle in motion conserves this energy. This energy can be recovered mainly during braking. The kinetic energy of a vehicle moving with a speed ( $v$ ) can be calculated as:

$$W = \frac{1}{2}Mv^2 \quad (4)$$

where

$W$  = Kinetic energy (joules)  
 $M$  = Weight of vehicle (kg)  
 $v$  = Speed of vehicle ( $\text{ms}^{-1}$ ).

When brake applies to a driving vehicle, this kinetic energy stored in rotating part of vehicle is converted into heat and resulting in wear and tear issues in vehicle. For enhance e-Rikshaw efficiency, this energy must be fed back to battery, i.e. regenerative braking [19]. The considering the conversion efficiency, the maximum recovery is around 50%. The rotating part of a vehicle also contributes to kinetic energy and it can be calculated as:

$$W_r = \frac{1}{2}Iw^2 \quad (5)$$

where

$W_r$  = Rotational kinetic energy (joules)  
 $I$  = Moment of Inertia ( $\text{kgm}^2$ )  
 $w$  = Speed of rotation ( $\text{rads}^{-1}$ ).

## 8 Motor for e-Rikshaw

In an electric vehicle, drive movement to wheels of a vehicle is given by motor. The various motor like DC motor, Induction motor, permanent magnet brushless DC motor and permanent magnet synchronous motor is in use for e-vehicle [29–32]. DC motor control is very easy but rarely used in e-vehicle due to low efficiency and higher maintenance. Permanent magnet machines and induction machines are major contenders for electric vehicles now-a-days. Efficiency, power to ratio and torque to volume ratio are higher in PM machines therefore preferred over induction motors even after higher cost. PMSM is the best choice for e-vehicle due to its various



**Table 2** Comparison of electric motors for e-Rikshaw

Characteristic	Motor		
	DC motor	Induction motor	PMSM/BLDC motor
Power density	Lowest	Medium	Highest
Controllability	Easy	Complex	Medium
Reliability	Low	Highest	High
Efficiency	Lowest	High	Highest
Technology status	Very matured	Matured	Almost matured
Cost	Lowest	High	Highest
Overall	Poor	Good	Best

advantages over other motors [33–35]. Table 2 presents the comparison of different electric motors in terms of performance required for e-Rikshaw.

The mandatory basic requirement of e-Rikshaw with respect to motor are summarised below:

- Must have high instantaneous power with high power density
- Essentially high torque at low speeds for starting and climbing, as well as a high power at high speed for cruising
- Required wide speed range, in constant-torque and constant power regions
- With good torque response, high efficiency and regenerative braking
- High reliability and robustness for various vehicle-operating conditions
- With Competitive cost

Considering the above, the selection of traction motor for an e-vehicle system is a critical step in designing the overall system. Motor can be chosen based on efficiency, cost, reliability, power density, technology and control and regeneration capability. In the current scenario: DC motor, induction motor, permanent magnet DC motor, permanent magnet synchronous motor and switched reluctance motor are available as choice. In reference [15] published in 2008, induction motor has been presented as best choice.

DC motor is a good candidate for traction application, however, its bulky construction, low efficiency, low reliability and high maintenance due to commutator and brushes makes it inferior nowadays compared to other available alternatives. It has limited regeneration capability as its need excitation. Induction motor is popular because of its ruggedness. Implementation of FOC technique makes it equivalent to DC motor. Main drawback is limited constant power operation due to breakdown torque limits. Enhancement in breakdown torque makes it bulky and it also has limited regeneration as it needs excitation. Permanent magnet machines have highest power density and efficiency. These motors have magnets at rotor, i.e. built-in excitation source resulting in good regeneration capability. High cost looks a drawback with this motor. Switched reluctance is also becoming popular due to its ruggedness. It also has good regeneration capability. The torque ripples and acoustic noise are the main issues. Table 3 presents the type of motor used in e-vehicles.

**Table 3** Type of motors in e-vehicles

Hyundai Kona EV	PMSMS
GMEV1	IM
Tata Tigor	IM
Mahindra e2o PLUS P4	IM
Toyota Prius	PMSM
Chevrolet Bolt EV	PMSM
Ford Focus Electric	PMSM
Nissan Leaf	PMSM
Honda Accord	PMSM
BMW i3	PMSM

## 9 Inverter/Converter Topology

An inverter is required to convert battery DC voltage into 3-phase PWM output to drive e-vehicle motor. A three-leg inverter is required to drive the motor used in e-vehicle. Permanent magnet synchronous motor is one of the best candidates for e-vehicle and it is being driven by an inverter. A most popular 3-leg inverter for e-Rikshaw is shown in Fig. 2. The e-Rikshaw is low voltage drive and is driven by 48 V battery. Low voltage automotive series MOSFETs are recent development by devices manufacturer such as Semikron, Toshiba, Fuji, Infineon. These devices have very low conducting resistance and very low switching frequency loss, therefore, best suited for this voltage range inverters for e-vehicles. In braking mode, 3-leg inverter is operated as boost chopper and at high switching frequency to transfer kinetic energy stored by vehicle to battery. The availability of these automotive series MOSFET have improved inverter frequency around 10–15% and it will contribute around 2–3% improvement in overall efficiency of vehicle.

The power circuit of e-Rikshaw consists of solid state power devices such as diodes, MOSFET, IGBT and associated protection elements. Table 4 highlights the recent development and contribution of power devices, controllers and sensors, etc. required for the reliable operation e-Rikshaw.

Fundamental Line–Line voltage can be calculated as

$$V_{\text{rms}L-L} = (\sqrt{3}/\sqrt{2}) * m_a * \text{battery voltage}/2$$

With modulation index ( $m_a$ ) 0.9

$$V_{\text{rms}L-L} = 1.732 * 0.9 * 48 / (2 * 1.414) = 26.5 \text{ V}$$

MOSFET with 80 V PIV is well suited for this requirement, however, suitable snubber and margin must be taken considering for protection against transient generated due to cable inductance.

**Table 4** Components of power circuit in e-Rikshaw

	Components	Important features	Manufacturers/Model
Power devices	Silicon-Carbide Based Power Devices (New solid state self commutating) such as MOSFETs, IGBTs	High voltage, high frequency SiC devices with low conduction losses	DARPA WBST HPE Program is leading for the development of High voltage, high frequency SiC devices Renesas, IXYS, ABB, etc. are the manufacturer for the power devices
Controllers	Microcontrollers, FPGA and DSPs based controller and programmable logic devices	Low cost controllers with high speed microcontrollers/DSPs required for control scheme. Low cost programmable logic devices (PLDs) are gaining popularity for non-linear controllers. Easy to implement for real time applications	XILINX, Texas Instruments, Analog Devices Lattice Semiconductor, etc. are the key manufacturers
Sensors	Current and voltage sensors	Compatible with high speed controllers	Honeywell, Life Engineer Motions, Rongtech Industry (Shanghai) Inc., etc.

## 10 Battery Bank

Battery is one of the most important components used in an electric vehicle. It stores the energy while charging and deliver stored energy to motor through inverter while driving. It ensures the running of vehicle per charging. Battery selection is a critical parameter for e-Rikshaw. Battery needs to deliver power sustained period of time. Various batteries are compared in [36–38]. Still, there are certain issues that need to be addressed to enhance the performance of battery bank and summarised in Table 5.

Main question still remains that is cost of e-Rikshaw, the development of advanced batteries such as nickel metal hydride (Ni–MH), zinc/air (Zn/Air) and lithium ion (Li-Ion) are in progress to address this problem. Major drawbacks of battery compared to gasoline are specific energy and energy density. These will be ruled out by the development of fuel cells in future and commercial growth of EVs will grow rapidly. But e-Rikshaw control system demands an efficient electric motor, power converters and electronic controllers at low cost also. Table 6 shows the available battery options for e-Rikshaw.

The available battery options are critically compared in Table 6. For e-Rikshaw in the Indian market, NiMH is a good option in terms of energy density and price.

**Table 5** Challenges for battery bank in e-Rikshaw

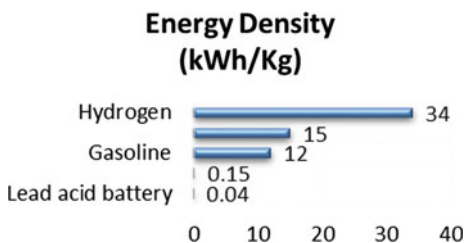
Battery capacity	The lead acid batteries are very common in e-Rikshaw for local public transport. These batteries deliver around 60–70 km running per charging and takes around 6–7 h for charging, hence, this must be improved. Limited battery energy is the main constraint
Battery weight	Battery is contributing around 20–40% of total vehicle weight in local transport vehicles and leading low energy efficiency. Weight reduction of battery will help in efficiency improvement
Battery cost	Low cost lead acid batteries are cost effective, but its energy density is very low. Recently, new batteries with 3–4 times energy density compared to lead acid battery have been announced but its cost is very high
Battery technology	In low cost public transport, lead acid batteries are in use. Lithium battery is costly nowadays and it is expected that price of lithium battery will reduce by 100% by 2025, but lithium resource is also limited like fossil fuel. A fuel cell battery has highest energy density but is yet to come in reality due to very high cost. Figure 8 represents energy density of various batteries

**Table 6** Battery options for e-Rikshaw

Battery type	Parameter				
	Cost/ Cycle	Specific density	Energy density	Specific power	Cycle life
Lead acid battery	Lowest	Low	Low	Low	Low
Nickel metal hydride battery	Moderate	Moderate	Moderate	High	High
Nickel zinc battery	Low	High	Moderate	Highest	Moderate
Lithium ion battery	<b>High</b>	<b>High</b>	<b>High</b>	<b>Moderate</b>	<b>Moderate</b>
Lithium sulphur battery	Highest	Highest	High	Moderate	Low

Lithium ion battery is superior to other types of batteries used in e-Rikshaw

**Fig. 8** Battery energy density



But Lithium Ion battery is superior and the price will reduce by 50% in coming next 5 years and market of Lithium Ion battery will increase as these batteries have advantages like high energy to volume ratio. Battery with 100 Ah capacity is generally sufficient for 60–70 km running per charging.

**Table 7** Motor rating calculation

Power	$(\text{Weight of e-Rikshaw} * \text{gravitational force} * \text{rolling friction}) * \text{velocity} + 0.5 * \text{air density} * \text{drag coefficient} * \text{area} * (\text{velocity})^3 = 712 \text{ W}$
Rating of motor required	Power requirement/system efficiency = 950 W rounded to 1 kW

## 11 Drive Motor Rating for e-Rikshaw

The input parameters for the calculation of power requirement of e-Rikshaw are weight of e-Rikshaw (500 kg), Rolling friction coefficient (0.015), aerodynamic drag coefficient (0.5), air density (1.2), system efficiency 75%. Power requirement when e-Rikshaw running at rated speed is presented in Table 7.

Hence, a 1 kW 26.5 V PMSM is sufficient to meet system requirements. A 3-phase inverter using MOSFET device STP100N8F6 meets e-Rikshaw drive requirement.

## 12 Conclusions

The paper deals with design aspects of e-Rikshaw for a better tomorrow. Every aspect which is to be considered for design of e-Rikshaw is presented. It gives a proper guideline to design engineer who is involved in designing the e-Rikshaw. It also explains the basic design requirement of various components required for e-vehicle. A comparison of various motors like DC motor, induction motor, Permanent magnet motor available for e-Rikshaw application with regeneration capacity is compared. Permanent magnet machines are the best choice nowadays due to its high regeneration capability during braking of e-vehicle. The various devices options are explored and MOSFET/IGBT is best choice for e-Rikshaw application. Different batteries are compared and Lithium Ion battery is a better choice as of now. Motor Rating is also derived considering a load of 50 N-m with key design aspects. The proposed key aspect will definitely be helpful for e-Rikshaw designers and developers. Future e-Rikshaw will consist of Solar charging and wireless charging features.

## References

1. Li Z (2019) Future prospects for electric vehicles. AIP Conf Proc 2073(1–5):020040
2. Kumar A, Prasad LB (2018) Issues, challenges and future prospects of electric vehicles: a review. In: International conference on computing, power and communication technologies (GUCON), pp 1060–1065

3. Ajanovic A (2015) The future of electric vehicles: prospects and impediments. *WIREs Energy Environ* 4:521–536
4. Majumdar D (2015) Merits and challenges of e-rickshaw as an alternative form of public road transport system: a case study in the state of West Bengal in India. In: *International conference on alternative energy in developing countries and emerging economies*, pp 307–314
5. <https://www.energysage.com/electric-vehicles/101/pros-and-cons-electric-cars/>
6. Zakaria H, Hamid M, Abdellatif EM, Imane A (2019) Recent advancements and developments for electric vehicle technology. In: *International conference of computer science and renewable energies (ICCSRE)*, pp 1–6
7. Sakai S-I, Sado H, Hori Y (2000) Anti-skid control with motor in electric vehicle. In: *Proceedings of 6th international workshop on advanced motion control*, pp 317–322
8. Ahmed A, Bhutia DD (2015) Propulsion system design and sizing of an electric vehicle. *Int J Electron Electr Eng* 3(1)
9. Sameeullah M, Chandan S (2016) Design and analysis of solar electric rikshaw: a green transport model. In: *International conference on energy efficient technologies for sustainability (ICEETS)*, pp 206–211
10. Gor CP, Shah VA, Gor MP (2016) Electric vehicle drive selection related issues. In: *International conference on signal processing, communication, power and embedded system (SCOPEs)*, pp 74–79
11. Porselvi T, Sriharikiran MK, Ashok J, Ajith Kumar S (2017) Selection of power rating of an electric motor for electric vehicles. *Int J Eng Sci Comput*, 6469–6472
12. Chauhan S (2015) Motor torque calculations for electric vehicle. *Int J Sci Technol Res* 4(8)
13. Batzel TD, Lee KY (2005) Electric propulsion with the sensorless permanent magnet synchronous motor: model and approach. *IEEE Trans Energy Convers* 20(4):818–825
14. Zeraoulia M, El Hachemi M, Benbouzid DD (2006) Electric motor drive selection issues for HEV propulsion systems: a comparative study. *IEEE Trans Veh Technol* 55(6):1756–1764
15. Hashemnia N, Asaei B (2008) Comparative study of using different electric motors in the electric vehicles. In: *Proceedings of the international conference on electrical machines*, paper ID-1257, pp 1–5
16. Xue XD, Cheng KWE, Cheung NC (2008) Selection of electric motor drives for electric vehicles. In: *Australasian universities power engineering conference (AUPEC)*
17. Zhang S, Xu J, Junak J, Fiedlerling D, Sawczuk G, Koch M, Schalja A, Podack M, Baumgartner J (2012) Permanent magnet technology for electric motors in automotive applications. In: *2nd International electric drives production conference (EDPC)*, pp 1–11
18. Shichuan D, Ming C, Chao H, Guishu Z, Wei W (2013) An energy recovery system of regenerative braking based permanent magnet synchronous motor for electric vehicles. In: *International conference on electrical machines and systems*
19. Mammosser D, Boisvert M, Micheau P (2013) Designing regenerative braking strategies for electric vehicles with an efficiency map. In: *21<sup>ème</sup> Congrès français de mécanique*
20. Long B, Lim ST, Ryu JH, Chong KT (2014) Energy-regenerative braking control of electric vehicles using three-phase brushless direct-current motors. *Energies* 7(1):99–114
21. Nian X, Peng F, Zhang H (2014) Regenerative braking system of electric vehicle driven by brushless DC motor. *IEEE Trans Indus Electron* 61(10)
22. Rajan SR, Srinivasan A, Visalakshi S (2014) Regenerative control of DC drive system. In: *IEEE international conference on advanced communication control and computing technologies (ICACCCT)*, pp 43–46
23. Boretti A (2013) Analysis of the regenerative braking efficiency of a latest electric vehicle. *SAE Int*
24. Erhan K, Özdemir E, Aktaş A (2016) Design and analysis of flywheel regenerative braking energy storage system for hybrid and electrical vehicles. *IEESE* (2016)
25. Malode SK, Adware RH (2016) Regenerative braking in electric vehicles. *IJSRD—Int J Scien Res Dev* 4(2)

26. Yanan G (2016) Research on electric vehicle regenerative braking system and energy recovery. *Int J Hybrid Inf Technol* 9(1):81–90
27. Lin Z, Zhanqun S, Yuegang L, Jing K (2016) A study of energy recovery system during braking for electric vehicle. In: 6th International conference on applied science, engineering and technology (ICASET)
28. Xiao B, Huazhong Lu, Wang H, Ruan J, Zhang N (2017) Enhanced regenerative braking strategies for electric vehicles: dynamic performance and potential analysis. *Energies* 10:1875
29. Kumar M, Ojha A (2019) Adaptive position sensorless control of pm synchronous motors-a state of art. *Int J Recent Technol Eng* 8(4):10071–10077
30. Jape SR, Thosar A (2017) Comparison of electric motors for electric vehicle application. *IJRET: Int J Res Eng Technol* 6(9)
31. Bălțățanu A, Florea LM (2013) Comparison of electric motors used for electric vehicles propulsion. In: International conference of scientific paper AFASES 201, Brasov, pp 23–25
32. Murty VS, Jain S, Ojha A (2020) Suitability linear switched reluctance motor for electric traction system. *Mech Syst Control*. Accepted for publication
33. Murty VS, Jain S, Ojha A (2020) Application of linear switched reluctance motor for sustainable electric vehicular system. *Int J Power Energy Syst* 40(1):41–48
34. Xie Y, Ge H, Yang Z, Lv S (2014) Study on key technologies of permanent magnet synchronous motor design for electric vehicles. In: 17th International conference on electrical machines and systems (ICEMS), pp 22–25
35. Menon R, Kadam AH, Azeez NA, Williamson SS (2016) A comprehensive survey on permanent magnet synchronous motor drive systems for electric transportation applications. In: IECON—42nd annual conference of the IEEE industrial electronics society
36. Omara AM, Sleptsov MA (2017) Performance assessment of battery-powered electric vehicle employing PMSM powertrain system. In: IEEE conference of Russian young researchers in electrical and electronic engineering (EIconRus), pp 963–968
37. Iclodean C, Varga B, Burnete N, Cimerdean D, Jurchis B (2017) Comparison of different battery types for electric vehicles. In: IOF Conference
38. Kumar M, Ojha A (2019) Key developments for electric vehicles in local transport. *J Instrum Inno Sci* 4(2):36–45

# Liquid-Phase Exfoliation of 2D-MoS<sub>2</sub> Nanostructures at Varying Sonication Times and Their Subsequent Analysis



Mariam Gada, Mohammad Zaid, Mohd. Mudassir Husain,  
and S. S. Islam

## 1 Introduction

TMDCs are compounds of the form MX<sub>2</sub> which are made up of transition metal (M = Mo, W, Hf, Ti, Nb, V) atoms and chalcogen (X = S, Se, Te) elements [1]. These materials are layered, with strong in-plane bonding and weak out-of-plane interactions, which enables their exfoliation into 2D layers of thickness equal to a single unit cell [2]. The layer-dependent properties of TMDCs have attracted a great deal of attention of late. This attention is attributed to the recent advances in sample preparation, optical detection, transfer and manipulation of 2D materials, and physical understanding of 2D materials learned from graphene [2]. In graphene, bandgaps can be engineered through nanostructuring, chemical functionalization, and application of a high electric field to its bilayer [3]. However, these methods make it more complex and reduce mobility [4]. On the other hand, many 2D TMDCs have tunable bandgaps, creating possibilities for interesting new FET and optoelectronic devices [5].

Moreover, a change in the overall properties of these materials is observed when they are scaled down from their bulk form to a few sheets at the nanoscale [1]. For instance, the band gap of MoS<sub>2</sub>, a transition metal dichalcogenide semiconductor

---

M. Gada (✉) · M. Zaid

Department of Electronics and Communication Engineering, Jamia Millia Islamia,  
New Delhi, India

e-mail: [inca@springer.com](mailto:inca@springer.com)

Mohd. M. Husain

Physics Department, Faculty of Science, Islamic University of Madinah, Medina,  
Kingdom of Saudi Arabia

Mohd. M. Husain

Department of Applied Sciences and Humanities, Jamia Millia Islamia, New Delhi, India

S. S. Islam

Centre for Nanoscience and Nanotechnology, Jamia Millia Islamia, New Delhi, India

© The Author(s), under exclusive license to Springer Nature Singapore Pte Ltd. 2022

177

P. Verma et al. (eds.), *Advancement in Materials, Manufacturing and Energy Engineering, Vol. I*, Lecture Notes in Mechanical Engineering,

[https://doi.org/10.1007/978-981-16-5371-1\\_16](https://doi.org/10.1007/978-981-16-5371-1_16)



[4], changes from being indirect ( $=1.2$  eV) in its bulk form to direct ( $=1.8$  eV) in a single layer [6]. This direct bandgap results in significant photoluminescence from monolayer MoS<sub>2</sub> as opposed to its absence in the bulk form, thus making it suitable for optoelectronic applications, including solar cells and light-emitting diodes [7].

The van der Waals forces in the structure of MoS<sub>2</sub> are weak enough to allow it to be exfoliated into resolvable single- and few-layers under the influence of external forces [9]. Quite a few approaches to obtain these nanosheets have already been reported in literature [1, 7–9]. Chemical vapor deposition is a method that gives extremely high yields, but it requires transfer processes and a high temperature [1]. Electrochemical Li-intercalation exfoliation is another technique widely studied; however, it sometimes results in the conversion of semiconducting properties into metallic phase [7]. Mechanical exfoliation techniques have been employed to synthesize MoS<sub>2</sub> nanosheets, but the yield remains an issue [8]. Finally, chemical exfoliation, although good in terms of simplicity, uses toxic, highly flammable acids which poses threats during research and during large-scale production. Therefore, the production of high-quality and highly soluble MoS<sub>2</sub> nanosheets on a large scale remains a challenge even today [1].

Liquid-phase exfoliation is a simple, facile process to obtain TMDC nanosheets effectively, particularly for sensing applications where a large quantity of nanosheets with inherent defects is required [9]. Coleman et al. reported a liquid exfoliation method that could produce large quantities of few layered 2D nanosheets of TMDCs [8]. They were pristine, and their structures were well retained. However, the use of solvents like NMP, which have a high boiling point [10], is an issue, since these kinds of solvents are difficult to remove from the surface of the exfoliated MoS<sub>2</sub> when it is being transferred onto a substrate [11]. These are also toxic and hence unfit for industrial purposes [10].

Therefore, low toxicity, low boiling point, and high solubility are parameters that must be considered while selecting a solvent for the liquid exfoliation of TMDCs. Hansen solubility parameters (HSP) are a way of determining the solubility of solvents. The parameter  $R_a$  (or the HSP distance) can be considered as a measure of solubility [12].  $R_a$  varies inversely with solubility, so the smaller the value of  $R_a$ , the greater is the solubility of the solvents. The procedure that we followed in this research was inspired by previous research [9], in which thin WS<sub>2</sub> nanosheets were successfully exfoliated.

In this study, we have attempted the liquid exfoliation of MoS<sub>2</sub> in a mixture of 80:20 acetone and isopropanol. These solvents have low boiling points and are comparatively safe, and the  $R_a$  value for their mixture was calculated to be 5.32 [9]. Further, this mixture along with bulk MoS<sub>2</sub> was ultrasonicated in a low-power ultrasonic bath for different periods of time. Ultrasonication-induced cavitation effect causes high temperature and pressure, which efficiently exfoliates the bulk MoS<sub>2</sub> into sheets. Finally, the samples were centrifuged to separate the prepared sheets from the bulk remains and only the top few milliliters were collected for analysis.

## 2 Materials and Methods

### 2.1 Reagents and Apparatus

#### Chemicals

Bulk MoS<sub>2</sub> (Molybdenum (IV) sulfide powder, <2 μm, 99%) from Sigma Aldrich (Germany), isopropanol (IPA extra pure AR, 99.5%) from Sisco Research Laboratories, acetone from Qualigens (M.W. 58.08 g/mol), and deionized water.

#### Synthesis

Low power bath sonicator (Elmasonic P), ultraviolet fluorescence analysis cabinet (mlabs), high-speed centrifuge (Remi R-24), measuring cylinders, glass bottles, beakers, pipettes, droppers, and vials.

#### Characterization

The morphological structure of MoS<sub>2</sub> nanosheets was characterized using FEI Nova NanoSEM 450 scanning electron microscope at 200 V–30 kV accelerating voltage. It has an ability to perform both high and low vacuum operations with an ultimate resolution of 1 nm. To perform elemental composition analysis, it houses an EDS detector, piezoelectric MiBot micromanipulators, and a nanolithography station. Raman analysis was performed using LabRAM HR800 JY (micro-Raman spectrophotometer). It gives advanced confocal Raman mapping in both two and three dimensions. Band analysis, crystallinity, polymorphism, and strain can be obtained using this spectral equipment. XRD peaks of the as-prepared samples were obtained using a high-resolution X-ray diffractometer (HR-XRD). Widely used to obtain structural information of materials, this characterization provides a plot analysis between reflected intensity and detector angle ( $2\theta$ ). The distance between parallel planes of atoms determine the location of diffraction peaks.

### 2.2 Preparation of Samples

The 10 ml mixture (of 4:1 acetone and isopropanol) was measured carefully. The 50 mg of bulk MoS<sub>2</sub> powder was added to the solvent mixture. This was repeated for six samples and then stored in glass bottles. The bottles were kept in a low power bath sonicator (set at 100 W, 37 kHz), and the dispersions (labeled 1, 2, 3, 4, and 5) were ultrasonicated for 2, 4, 8, 10, and 12 h, respectively. Sonication for variable time periods was done in order to agitate bulk particles by physical vibrations which resulted in breaking samples apart. One of the samples, bulk (labeled 0), was kept aside for comparison later on. The sonicated dispersions were left for a few days, post which they were subjected to UV irradiation (at short wavelength,  $\lambda = 254$  nm) for 30 min in an inert environment to further exfoliate bulk frameworks of our samples. Finally, the exfoliated nanostructures were separated from the unexfoliated bulk using centrifugation, at 3300 rpm for 10 min.

A part was taken from the top of the dispersions and centrifuged again. About three-fourths of the supernatants was collected and stored in fresh bottles for analysis.

The contents of the samples were then transferred onto a Si/SiO<sub>2</sub> film using a dropper, followed by magnetic stirring. The morphological and structural properties of the prepared nanomaterial films were observed under field emission scanning electron microscope (for visual distinction of exfoliated MoS<sub>2</sub>), X-ray diffractometer (to obtain the crystallographic structural changes), and Raman spectrophotometer (to determine the molecular fingerprints).

This paper provides a comparative analysis between the various characterizations of the synthesized samples. The sample specifications to interpret various figures, tables, and graphs in this article is given below.

### 3 Results and Discussion

#### 3.1 FE-SEM Imaging

Field emission scanning electron microscope (FE-SEM) is used to investigate the morphology and topology of nano- and bulk materials [13]. FE-SEM was given priority over SEM because of its ability to provide higher resolution images with a greater energy range. Furthermore, its electron beams enable analysis to be carried out at low potentials (0.02–5 kV) which helps in avoiding destruction to electron beam-sensitive specimens.

FE-SEM on the samples was employed to observe the exfoliated nanostructures. The imaging for all the samples was obtained at two different magnifications (scaled at 10 μm and 5 μm, respectively). Topographic details of the fractioned surface were observed for and the results have been illustrated in Fig. 1a–l.

As we move from Fig. 1a which is bulk MoS<sub>2</sub> dispersed in the solvent mixture toward Fig. 2b, c, i.e., the samples that were sonicated for 2 and 4 h, respectively, we notice nanosheet clusters start to appear. The FE-SEM images of sample 3 and 4 further show the formation of 2D MoS<sub>2</sub> nanostructures, thus verifying the successful exfoliation of bulk MoS<sub>2</sub>.

#### 3.2 X-ray Diffraction

X-ray diffraction (XRD) is a robust, non-destructive technique used to characterize materials that are crystalline. It tells us about structures, phases, and preferred crystal orientations [14]. XRD was conducted on the sample films to understand the atomic arrangements in the exfoliated nanomaterials. The results have been summarized in tabular form in Table 1 and illustrated graphically in Fig. 2.

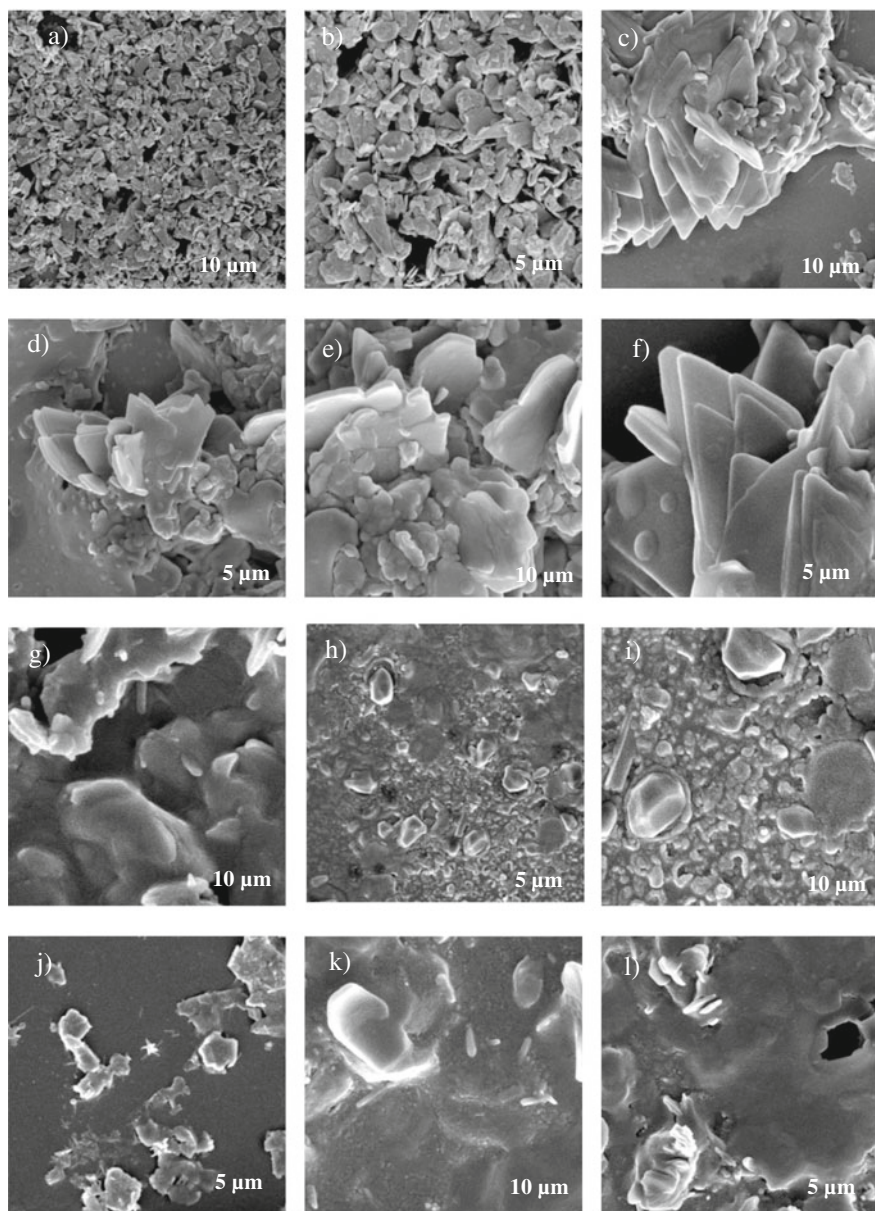


**Fig. 1** FE-SEM images of (a, b) Bulk MoS<sub>2</sub>, (c, d) Sample 1, (e, f) Sample 2, (g, h) Sample 3, (i, j) Sample 4, (k, l) Sample 5

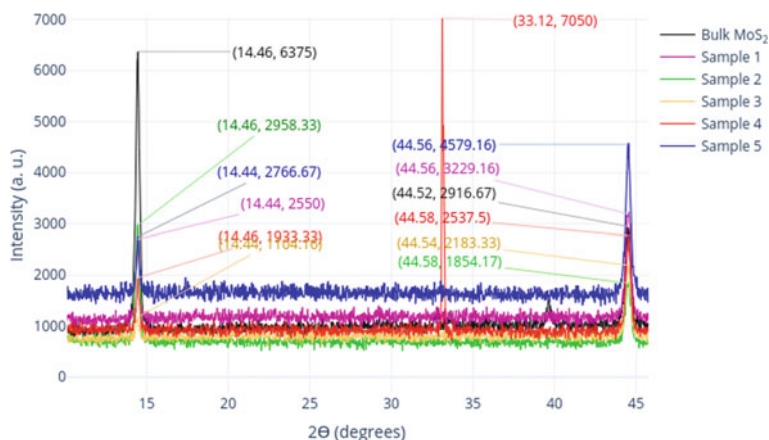


**Fig. 2** Graphical representation of XRD patterns of all samples

**Table 1** Sample specifications

Sample	Sonication time (in hours)
0 (Bulk MoS <sub>2</sub> )	0
1	2
2	4
3	8
4	10
5	12

Observed XRD pattern indicated  $2\theta$  peaks at roughly  $14.5^\circ$  and a sharp peak at  $33.12^\circ$  representing crystallographic planes (002) and (101), respectively. A significant change in intensities of XRD peaks was observed in all the samples implying a variance in counts accumulated in the orientation, i.e., having more/less atoms in a plane. A trivial, high intensity peak for (101) plane shows an exceptional extent of crystallinity at this point.

### 3.3 Raman Spectroscopy

Raman spectroscopy provides a lot of information about the molecular structure. Thus, it plays a significant role in the structural analysis of the prepared materials [15]. Figure 3 graphically depicts a comparison of different Raman spectra for different samples that were exfoliated. The data has also been given in Table 2.

As reported in literature, for a 515.4 nm laser, the  $E_{2g}^1$  and  $A_{1g}$  peaks for bulk MoS<sub>2</sub> appear at  $382\text{ cm}^{-1}$  and  $407.5\text{ cm}^{-1}$ , respectively [16]. After exfoliation, we observe  $E_{2g}^1$  peak for sample 4 at about  $382.53\text{ cm}^{-1}$ , which as has been reported

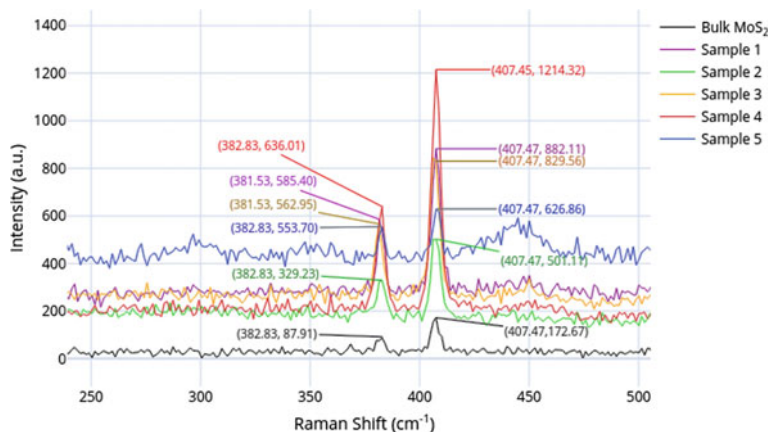


**Fig. 3** Raman spectra of all samples (0–5)

**Table 2** XRD peaks for different samples (angles and intensities)

Sample	First peak		Second peak	
	$2\theta$ (°)	Intensity	$2\theta$ (°)	Intensity
Bulk	14.46	6375	44.52	2916.67
1	14.46	2550	44.56	3229.16
2	14.46	2958.33	44.54	1854.17
3	14.44	1104.16	44.58	2183.33
4	14.46	1933.33	44.58	2537.5
5	14.46	2766.67	44.56	4579.16

**Table 3** Raman spectroscopy analysis with corresponding first and second peaks

Sample	First peak		Second peak	
	Shift (cm <sup>-1</sup> )	Intensity	Shift (cm <sup>-1</sup> )	Intensity
0	382.83	87.91	407.47	172.67
1	381.53	585.40	407.47	882.11
2	382.83	329.33	407.47	501.11
3	381.53	381.53	407.47	829.56
4	382.53	636.01	407.45	1214.32
5	382.83	553.70	407.47	626.86

earlier, corresponds roughly to tri-layered MoS<sub>2</sub> which exhibits E<sub>2g</sub><sup>1</sup> peak at 382.7 cm<sup>-1</sup> [16]. While there was no hypso/bathochromic shift in A<sub>1g</sub> peaks, a significant change in the intensities was observed, ranging from 3 to 7 times when compared to the bulk counterpart (Table 3).

## 4 Conclusion

In conclusion, MoS<sub>2</sub> nanostructures were successfully exfoliated using liquid phase exfoliation from their bulk form using the same protocol through which WS<sub>2</sub> nanosheets were fabricated previously [9].

- The properties of MoS<sub>2</sub> differed greatly from the results reported [9] of WS<sub>2</sub>, both in terms of morphology (as analyzed using FE-SEM) and structure (as observed in XRD and Raman spectra of the samples). The solvents used in this study are readily available, comparatively safe, have a low boiling point, and most importantly are highly soluble. However, exploring other solvents with a low value of HSP distance (or  $R_a$ ) could enhance the performance of the prepared nanomaterials.
- We believe that instead of low power bath sonication, if high power probe sonication is employed to exfoliate the nanosheets, it would increase the yield and give faster results.
- Further, the MoS<sub>2</sub> nanosheets fabricated in this research can be applied for sensing purposes, owing to the tunable properties that the new material exhibits. Also, the transformation from an indirect bandgap in bulk MoS<sub>2</sub> to a direct bandgap in the prepared nanosheets [6] can be exploited for their application in optoelectronic devices.

**Acknowledgements** The authors are grateful to Mr. Abid (Centre for Nanoscience and Nanotechnology, Jamia Millia Islamia) for his help in conducting the experiment, and the Director, Central Instrumentation Facility, Jamia Millia Islamia for allowing characterization of the prepared samples.

## References

1. Kim S, Park W, Kim D, Kang J, Lee J, Jang HY, Song SH, Cho B, Lee D (2020) Novel exfoliation of high-quality 2H-MoS<sub>2</sub> nanoflakes for solution-processed photodetector. *Nanomaterials* 10(6):1045
2. Wang QH, Kalantar-Zadeh K, Kis A, Coleman JN, Strano MS (2012) Electronics and optoelectronics of two-dimensional transition metal dichalcogenides. *Nat Nanotechnol* 7 (11):699–712
3. Yuan L, Li Z, Yang J, Hou JG (2012) Diamondization of chemically functionalized graphene and graphene–BN bilayers. *Phys Chem Chem Phys* 14(22):8179
4. Mir SH, Yadav VK, Singh JK (2020) Recent advances in the carrier mobility of two-dimensional materials: a theoretical perspective. *ACS Omega* 5(24):14203–14211
5. Mak KF, Lee C, Hone J, Shan J, Heinz TF (2010) Atomically thin MoS<sub>2</sub>: a new direct-gap semiconductor. *Phys Rev Lett* 105:136805
6. Radisavljevic B, Radenovic A, Brivio J, Giacometti V, Kis A (2011) Single-layer MoS<sub>2</sub> transistors. *Nat Nanotechnol* 6(3):147–150
7. Eda G, Yamaguchi H, Voiry D, Fujita T, Chen M, Chhowalla M (2011) Photoluminescence from chemically exfoliated MoS<sub>2</sub>. *Nano Lett* 11(12):5111–5116

8. Coleman JN, Lotya M, O'Neill A, Bergin SD, King PJ, Khan U, Young K, Gaucher A, De S, Smith RJ, Shvets IV, Arora SK, Stanton G, Kim H-Y, Lee K, Kim GT, Duesberg GS, Hallam T, Boland JJ, Nicolosi V et al (2011) Two-dimensional nanosheets produced by liquid exfoliation of layered materials. *Science* 331(6017):568–571
9. Jha RK, Guha PK (2016) Liquid exfoliated pristine WS<sub>2</sub> nanosheets for ultrasensitive and highly stable chemiresistive humidity sensors. *Nanotechnology* 27(47):475503
10. Halim U, Zheng CR, Chen Y, Lin Z, Jiang S, Cheng R, Huang Y, Duan X (2013) A rational design of cosolvent exfoliation of layered materials by directly probing liquid–solid interaction. *Nat Commun* 4(1)
11. Sahoo D, Kumar B, Sinha J et al (2020) Cost-effective liquid phase exfoliation of MoS<sub>2</sub> nanosheets and photocatalytic activity for wastewater treatment enforced by visible light. *Sci Rep* 10:10759
12. Zhang S-L, Jung H, Huh J-S, Yu J-B, Yang W-C (2014) Efficient exfoliation of MoS<sub>2</sub> with volatile solvents and their application for humidity sensor. *J Nanosci Nanotechnol* 14(11):8518–8522
13. Sherif El-Eskandarany M (2020) *Mechanical alloying*, 3rd edn. Elsevier
14. Bunaciu AA, Udriștioiu EG, Aboul-Enein HY (2015) X-ray diffraction: instrumentation and applications. *Crit Rev Anal Chem* 45(4):289–299
15. Kneipp K, Kneipp H, Itzkan I, Dasari RR, Feld MS (1999) Ultrasensitive chemical analysis by raman spectroscopy. *Chem Rev* 99(10):2957–2976
16. Li H, Zhang Q, Yap CCR, Tay BK, Edwin THT, Olivier A, Baillargeat D (2012) From bulk to monolayer MoS<sub>2</sub>: evolution of Raman scattering. *Adv Funct Mater* 22(7):1385–1390



# Grid Synchronization Techniques: A Review



Pragya Gawhade and Amit Ojha

## 1 Introduction

In recent few years, the use of renewable energy sources (RESs) has become very demanding and currently replacing the reliance on fossil fuels to achieve sustainable growth and management [1, 2]. Therefore, to integrate various RESs in the power system, it is important to implement advantages in environmental and economic terms. The continuous development in renewable energy resources (RES) will cause a distributed power generation to centralized power generation in coming years [3–7]. The integration of RES (wind, solar, etc.) into distribution networks has increased, as it is possible that generated power will be close to consumer which reduces power losses, rises voltage levels, and improves reliability [8, 9]. In grid-tied system, generated power supplied to the grid without any energy storage equipment has added advantage of 99% benefit compared to stand-alone system. The connection of these RESs with the grid over the power converter is called as synchronization. The major area of concern for a grid-connected PV system is synchronization and concerning power quality problems are reactive power compensation, voltage/current harmonics, voltage regulations, voltage flickering, etc. [10, 11].

The continuous efforts of the researcher have transformed the small stand-alone PV system to grid-connected PV system. This introduces a new pooling parameter for some temporary exchanges in the electricity market. With the availability of fast tracking and advanced maximum power point tracking techniques (MPPTs), maximum power is extracted from the solar. By using DC–DC converter [5], the extracted solar power is stepped to another voltage level for the desired application. For stand-alone application or grid interfacing, the shifted power at DC level is converted to AC with the help of inverter. To improve the overall efficiency of this

---

P. Gawhade · A. Ojha (✉)  
MANIT, Bhopal, India

complete system, all components such as the PV array, MPPT, DC–DC converter, inverter, and control algorithm have to be operated in synchronism.

So now, majority of the grid-tied converters can be categorized as grid feeding and grid forming converters in the PV applications to inject the maximum power to the grid. References [5, 6] one of the main problems encountered when DG system is synchronized with the grid is to obtain accurate and fast estimation of frequency and phase. By connecting nonlinear loads to the electrical networks, the problem becomes even more difficult, as transients and distortions such as phase shift and harmonics that often occur on the grid [7].

## 2 Grid Synchronization

Synchronization is defined to reduce the variations in phase, frequency, and voltage between RES output and the grid. An ideal synchronization method must approach [12–27] identification of the frequency variations efficiently, immediate response to change in utility grid, detection of phase angle of utility grid competently, effective elimination of the disturbance, and high harmonic components.

Three synchronization approaches have been categorized as: [28] active synchronization, passive synchronization, and open-transition transfer. In active synchronization, a control mechanism is used to match the frequency, voltage, and phase angle between RES and the main grid during active synchronization. Passive synchronization does not require a control mechanism, unlike active synchronization. Passive synchronization is accomplished by means of synchronization check using a synchrocheck relay which measures the magnitude, phase angle, and differences in frequency between the voltages on either side of the circuit breaker [29]. In open transition transfer method, before reconnecting RES to the main grid, the load and DGs are de-energized. This approach will not be further discussed because this method reduces the power system's reliability and does not apply to RES synchronization.

## 3 Various Methods of Synchronization

Advances of DG in power grid gave rise to the proposal of various methods of synchronization techniques which can be classified as frequency domain or time domain. The aim of this paper, therefore, is to provide a summary of the main synchronization method trends. Synchronization techniques are probably divided into 1-phase and 3-phase structures by the highest level classification. Further, these are again classified as open-loop and closed-loop methods as shown in Fig. 1.

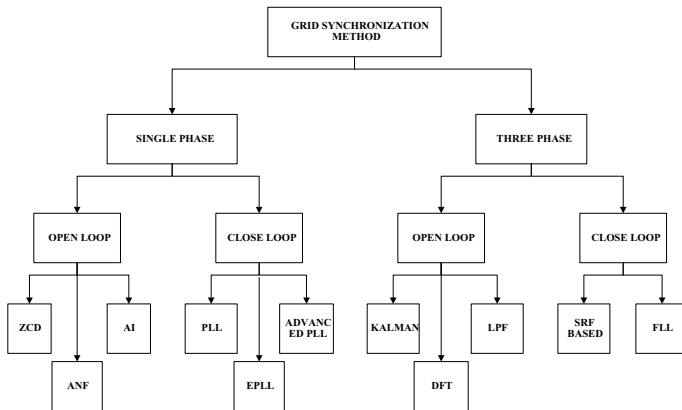


Fig. 1 Various grid synchronization techniques

### 3.1 Open-Loop Techniques

Open-loop techniques directly estimate the incoming signal magnitude, phase, and frequency, while in closed-loop methods, the phase estimation is adaptively updated through a loop mechanism. DFT-based techniques are the earliest approaches to harmonic and frequency detection [30–34]. To filter the incoming grid voltage, a recursive DFT was utilized for power converter line synchronization [19]. ANF-based techniques [22, 23], in addition to the values of their frequencies, amplitudes and phase angles, instantaneous values of the different estimated frequency components are provided. The new adaptive notch filtering approach [22]. This method is not only capable to detect amplitude in frequency variations, frequency, and phase angle but also harmonics in current. Kalman filter is a signal processing technique applied in power system signal frequency measurement. It provides an ideal estimation of the state variables of the given dynamic system. Even with frequency variations, ANN is mostly used in the observation of power system harmonics [25]. It is based on adaptive linear combiner (Adaline) that produces more accurate and faster estimates than Kalman filter [35, 36]. Other neural network techniques based on feedback from the hop field type were proposed in [37]. Zero-crossing detection is one of the easiest ways of obtaining grid information like phase by identifying the zero-crossing point of a grid voltages. During variations of voltage such as amplitude, sags, and harmonics (that are considered to be Power quality issues), the zero-crossing point can be detected only every half of the voltage/frequency utility period [34].

### 3.2 Closed-Loop Techniques

Appleton and Bellescize presented the first single-phase phase-locked loops (PLLs) as early as 1923 and 1932, respectively [38]. PLL is most acknowledged due its robustness, simplicity, and effectiveness in various grid conditions. PLL is widely used in grid synchronization.

#### (1) Basics of PLL

The PLL is a nonlinear closed-loop feedback control system that synchronizes the output signal with the input signal phase and frequency [31–33]. As shown in Fig. 2, the basic structure of PLL consists of three main blocks, the phase detector (PD), the low-pass filter (LF), and the voltage-controlled oscillator (VCO).

The two input signals will be compared by the PD, and error signal is filtered by LF which drives the VCO to produce output phase. This process continues until the phase error  $e(t) = \Delta\theta$  output and the reference phase down to the minimum value. Once the error is zero, the output is shown as the stage will be locked.

The PD block output mainly consists of a high-frequency and a low-frequency term. PI filter is mostly used as LF and is responsible for damping of high-frequency term but fails to eliminate it completely. The term low frequency is a nonlinear function of the difference between the phase angles of the input and output. The PD output magnitude depends on the input signal magnitude, and therefore, the PD gain is influenced by voltage sag.

#### (2) Advance PLL algorithm

According to recent grid regulations, the grid-connected RES system should perform stable operation during unbalanced and fault conditions. Due to the presences of other frequencies in the voltage vector (negative sequence and/or harmonics), undesired oscillations are produced which affect the accuracy of grid synchronization. Hence, to provide accurate phase information during abnormal conditions, synchronization techniques should be advanced.

Various proposals to modify and improve PLL performances in different grid conditions are there in literature like synchronous reference frame PLL (SRF-PLL), enhanced PLL (EPLL), quadrature-based PLL (QPLL), and adaptive PLL.

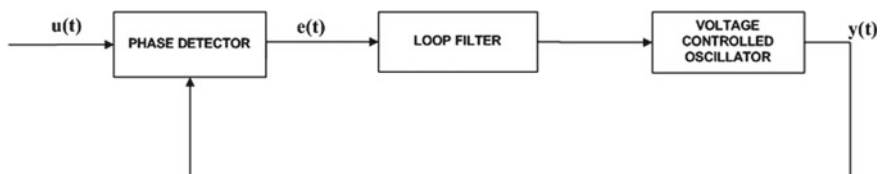


Fig. 2 Basics of PLL [40]

### (1) *Enhanced PLL*

EPLL is a nonlinear grid synchronization technique; it is a major improvement over the conventional PLL that lies in the PD mechanism which allows more flexibility. EPLL was introduced to provide the information's like magnitude, frequency, and phase angle of three-phase input systems. The working principle of EPLL is basically based on the extraction of the positive sequence component of an input signal using band-pass filter [36, 39–40]. EPLL is used to detect fundamental components, accurately and smoothly, and it provides a good transient response and minimum steady-state error. It is robust to noise, harmonics, and unbalanced input signal and also adaptive to frequency variations. EPLL provides 90 degree shift in the fundamental component of input signal. Therefore, it is an attractive solution for some single-phase system applications.

### (2) *Quadrature PLL*

Quadrature-based PLL approach estimates in-phase and quadrature-phase amplitude of input voltage. Here, the amplitude and phase angle are estimated by mathematical calculations. QPLL is very fast and accurate in frequency detection and performs well in uncertainties and disturbance, robust to harmonics and unbalanced conditions. It is applicable for both distributed communication and generation system applications.

### (3) *Adaptive PLL*

Adaptive PLL manages the system gain in an adaptive manner. Here, the phase angle, frequency, and voltage are individually controlled. The output of voltage controller used compensates reduced gain due to voltage sag. Without compromising the transient response, the frequency and phase error are eliminated. The advantage of adaptive PLL techniques is the overshooting, and settling time is low when the magnitude of AC voltage is reduced.

### (4) *Synchronous reference frame PLL*

SRF-PLL is mostly used for 3-phase grid-connected system. Under ideal grid connection, SRF-PLL is simple to implement and accurate in-phase and frequency estimation. By using park's transformation, the 3-phase voltage vector in  $abc$  frame is transformed to  $dq$  rotating frame. When the rotating reference frame is synchronized with voltage vector phase angle, the instantaneous phase angle  $\theta$  is estimated. The direct or quadrature axis voltage is set to zero with the help of PI controller to set the reference phase angle of voltage vector. The grid phase angle is obtained by integration of frequency, and the output of PI is feedback to PD. SRF-PLL measures average information of amplitude, phase, and frequency hence may not applied to single-phase system in straightforward manner. Unfortunately, SRF-PLL is sensitive to phase angle variations and hence its performance is highly degraded during unbalanced grid voltage, deviation in frequency, and in the presence of harmonics (Fig. 3).

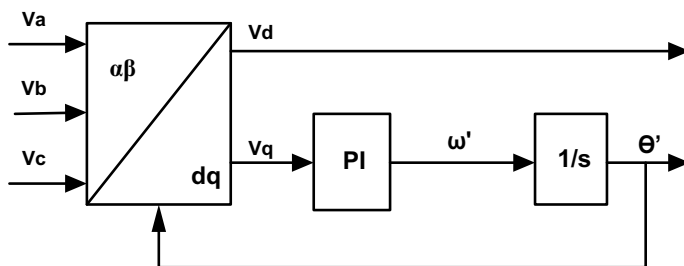


Fig. 3 Basic of SRF-PLL [39]

Decoupled double SRF-PLL method includes transformation of both negative and positive sequence of the grid voltage into double SRF and produces a decoupling network and extracts the components, which eliminates the errors produced in SRF-PLL. It is suitable for the grid interface converters controlling in both frequency variations and unbalanced condition. For unbalanced voltage condition, a decoupled double synchronous reference frame PLL (DDSRF PLL) shows fast transient response but having a disadvantage of complex structure.

In modified SRF-PLL, the PI controller is replaced with fourth-order elliptical filter. SRF is application of 3-phase system but this concept is derived from Coulon oscillation for single-phase system. It performs excellently in both steady-state and transient conditions when applied to active power shunt filter.

On the basis of grid voltage adaptive filtering, adaptive lattice SRF-PLL is developed. It is a new phase estimator for harmonic selectivity. To selectively remove harmonics, set of infinite-impulse-response (IIR) notch filters along with gradient-adaptive lattice algorithm is used. It is adaptable but its computational complexity is higher than conventional SRF-PLL.

The drawbacks and other issues in the above SRF methods mentioned, advanced SRF-PLLs, dual second-order generalized integrator PLL (DSOGI-PLL) have been projected by Golestan et al. [36]. DSOGI-PLL has same principle of extracting both fundamental positive and negative sequences as conventional SRF PLL. It utilizes a double second-order generalized integrator to implement a quadrature signal generator. A combination of LPF and BPF is used, where both LPF and BPF provide harmonic filtering and LPF provides  $90^\circ$  phase shift. It can be used for 1-phase system as  $90^\circ$  phase shift can easily be obtained.

Here, the following table compares different synchronization techniques on the basis of their advantage and disadvantage (Table 1).

**Table 1** Comparison of various synchronization techniques [3]

Synchronization methods	Merits	Demerits
Zero-crossing detection	<ul style="list-style-type: none"> <li>• It is used for both single phase and three-phase</li> <li>• Robust to frequency variations</li> </ul>	<ul style="list-style-type: none"> <li>• Poor performance in the presence of harmonics</li> <li>• It is noise-sensitive</li> </ul>
Discrete Fourier transform	<ul style="list-style-type: none"> <li>• Used for three-phase</li> <li>• Used for harmonics detection</li> <li>• Stable</li> </ul>	<ul style="list-style-type: none"> <li>• Not suitable for single phase and unbalanced condition</li> </ul>
Kalman filter	<ul style="list-style-type: none"> <li>• It is used for 1-phase and 3-phase both</li> <li>• Accurate</li> </ul>	<ul style="list-style-type: none"> <li>• Not used for harmonic detection</li> <li>• Complex structures</li> </ul>
Nonlinear least square	<ul style="list-style-type: none"> <li>• Used for single phase</li> <li>• Easy implementation</li> </ul>	<ul style="list-style-type: none"> <li>• Large transient time to frequency variations</li> </ul>
Adaptive notch filter	<ul style="list-style-type: none"> <li>• Used for both single phase and three-phase</li> <li>• Used for harmonic detection</li> </ul>	<ul style="list-style-type: none"> <li>• Slow adaption process</li> </ul>
Phase-locked loop (PLL)	<ul style="list-style-type: none"> <li>• It is used for 1-phase and 3-phase</li> <li>• Used for harmonic detection</li> <li>• Very accurate</li> </ul>	<ul style="list-style-type: none"> <li>• Not accurate in unbalanced condition</li> </ul>
Frequency-locked loop	<ul style="list-style-type: none"> <li>• Used for three-phase</li> <li>• Used for harmonic detection and harmonic elimination</li> <li>• Reliable to variation in frequency, voltage and harmonics</li> </ul>	<ul style="list-style-type: none"> <li>• Not used for single phase</li> <li>• High computation</li> <li>• In the phase error signal, double frequency oscillations are introduced</li> </ul>

## 4 Conclusion

This paper reviewed various grid synchronization methods. Various advantages and disadvantages of the synchronization techniques for harmonic component, frequency, and phase angle in grid-connected converters that have been discussed. A phase-locked loop (PLL) is a nonlinear control system and produces an output signal whose phase is related to the input signal phase. Phase-locked loops are popular technique among various synchronization techniques. Due to noise, distortions, and frequency variations, complexity of phase locking increased. To enhance and improve its performance during abrupt and large frequency and phase variations of the input signal, many modifications in the phase detector block of PLL have been made. Hence to control and detect the frequency, phase and amplitude of the inverter and grid voltage proper synchronization technique are used.

## References

1. Kamil HS, Said DM, Mustafa MW, Miveh MR, Ahmad N (2018) Low-voltage ride-through methods for grid-connected photovoltaic systems in microgrids: a review and future prospect. *Int J Power Electron Drive Syst (IJPEDS)* 9(4):1834
2. Kamil HS, Said DM, Mustafa MW, Miveh MR, Ahmad N (2019) Low-voltage ride-through for a three-phase four-leg photovoltaic system using SRFPI control strategy. *Int J Electr Comput Eng* 9(3):1524
3. Kamil HS et al (2020) Recent advances in phase-locked loop based synchronization methods for inverter-based renewable energy sources. *Indonesian J Electr Eng Comput Sci* 18(1):1–8
4. Zhong QC (2016) Virtual synchronous machines: a unified interface for grid integration. *IEEE Power Electron Mag* 3(4):18–27
5. Kroposki B et al (2017) Achieving a 100% renewable grid: operating electric power systems with extremely high levels of variable renewable energy. *IEEE Power Energy Mag* 15(2): 61–73
6. Blaabjerg F, Teodorescu R, Liserre M, Timbus AV (2006) Overview of control and grid synchronization for distributed power generation systems. *IEEE Trans Ind Electron* 53 (5):1398–1409 (An overview of assessment methods for synchronization stability of grid-connected converters under severe symmetrical grid faults Mads Graungaard Taul, Student Member, IEEE, Xiongfei Wang, Senior Member)
7. Long Y, Sun Y (2015) A new PLL simulation validation for three-phase grid under heavy distorted conditions. *Int J Online Biomed Eng (iJOE)* 11 (MESI 2014)
8. Cabana K et al (2019) Voltage sensitivity analysis to determine the optimal integration of distributed generation in distribution systems. *Int J Electr Comput Eng (IJECE)* 9:55–65
9. Sankar RSR et al (2018) Adaptive fuzzy PI current control of grid-interact PV inverter. *Int J Electr Comput Eng (IJECE)* 8:472–482
10. de Oliveira FM, da Silva SAO, Durand FR, Sampaio LP, Bacon VD, Campanhol LB (2016) Grid-tied photovoltaic system based on PSO MPPT technique with active power line conditioning. *IET Power Electron* 9:1180–1191
11. Singh B, Jain C, Goel S, Gogia R, Subramaniam U (2017) A sustainable solar photovoltaic energy system interfaced with grid-tied voltage source converter for power quality improvement. *Electr Power Compon Syst* 45:171–183
12. Verma AK, Singh B, Kaushika SC (2013) A standalone solar photovoltaic power generation using cuk converter and single phase inverter. *J Instit Eng B* 94:1–12
13. Ray S, Gupta N, Gupta RA (2016) A comprehensive review on cascaded H-bridge inverter-based large-scale grid-connected photovoltaic. *IETE Techn Rev* 1–15
14. Vainio O, Ovaska SJ (1995) Noise reduction in zero crossing detection by predictive digital filtering. *IEEE Trans Ind Electron* 42(1):58–62
15. Vainio O, Ovaska SJ, Pöllä M (2003) Adaptive filtering using multiplicative general parameters for zero-crossing detection. *IEEE Trans Ind Electron* 50(6):1340–1342
16. Weidenbrug R, Dawson FP, Bonert R (1993) New synchronization method for thyristor power converters to weak AC-system. *IEEE Trans Ind Electron* 40(5):505–511
17. Dash PK, Pradhan AK, Panda G (1999) Frequency estimation of distorted power system signals using a robust algorithm. *IEEE Trans Power Deliv* 14(3):761–766
18. Dash PK, Jena RK, Panda G, Routray A (2000) An extended complex Kalman filter for frequency measurement of distorted signals. *IEEE Trans Instrum Meas* 49(4):746–753
19. McGrath BP, Holmes DG, Galloway JJH (2005) Power converter line synchronization using a discrete Fourier transform (DFT) based on a variable sample rate. *IEEE Trans Power Electron* 20(4):877–884
20. Mojiri M, Karimi-Ghartemani M, Bakshai A (2007) Estimation of power system frequency using adaptive notch filters. *IEEE Trans Instrum Meas* 56(6):2470–2477



21. Yazdani D, Bakhshai A, Joós G, Mojiri M (2009) A real-time extraction of harmonic and reactive current in a nonlinear load for grid-connected converters. *IEEE Trans Ind Electron* 56 (6):2185–2189
22. Yazdani D, Bakhshai A, Joos G, Mojiri M (2008) A nonlinear adaptive synchronization technique for grid-connected distributed energy sources. *IEEE Trans Power Electron* 23(4):2181–2186
23. Mojiri M, Yazdani D, Bakhshai A (2010) Robust adaptive frequency estimation of three-phase power systems. *IEEE Trans Instrum Meas* 59(7):1793–1802
24. Lai L, Chan W (1999) Real-time frequency and harmonic evaluation using artificial neural networks. *IEEE Trans Power Deliv* 14(1):52–59
25. Wang YF, Li YW (2011) Analysis and digital implementation of cascaded delayed signal-cancellation PLL. *IEEE Trans Power Electron* 26(4):1067–1080
26. Jain B, Jain S, Nema RK (2015) Control strategies of grid interfaced wind energy conversion system: an overview. *Renew Sustain Energy Rev* 47:983–996
27. Lidula NWA, Rajapakse AD (2014) Voltage balancing and synchronization of microgrids with highly unbalanced loads. *Renew Sustain Energy Rev* 31:907–920
28. Bongiorno M, Svensson J, Sannino A (2008) Effect of sampling frequency and harmonics on delay-based phase-sequence estimation method. *IEEE Trans Power Deliv* 23(3):1664–1672
29. Monfared M, Golestan S (2012) Control strategies for single-phase grid integration of small-scale renewable energy sources: a review. *Renew Sustain Energy Rev* 16(7):4982–4993
30. Hsieh GC, Hung JC (1996) Phase-locked loop techniques—a survey. *IEEE Trans Ind Electron* 43(6):609–615
31. Cupertino F, Lavopa E, Zanchetta P, Sumner M, Salvatore L (2011) Running DFT-based PLL algorithm for frequency, phase, and amplitude tracking in aircraft electrical systems. *IEEE Trans Ind Electron* 58(3):1027–1035
32. Dash P, Swain D, Liew A, Rahman S (1996) An adaptative linear combiner for on-line tracking of power system harmonics. *IEEE Trans Power Syst* 11(4)
33. Lai L, Tse C, Chan W, So A (1999) Real-time frequency and harmonic evaluation using artificial neural networks. *IEEE Trans Power Delivery* 14(1)
34. Blanchard A (1976) *Phase-locked loops: application to coherent receiver design*. Wiley Interscience, New York
35. Kaura V, Blasko V (1997) Operation of a phase locked loop system under distorted utility conditions. *IEEE Trans Ind Appl* 33:58–63
36. Golestan S, Monfared M, Frejedo FD (2013) Design-oriented study of advanced synchronous reference frame phase-locked loops. *IEEE Trans Power Electron* 28(2):765–778
37. Rodríguez P, Luna A, Muñoz-Aguilar RS, Etxeberria-Otadui I, Teodorescu R, Blaabjerg F (2012) A stationary reference frame grid synchronization system for three-phase grid-connected power converters under adverse grid conditions. *IEEE Trans Power Electron* 27(1):99–112
38. Rocabert J, Azevedo GMS, Luna A, Guerrero JM, Candela JI, Rodriguez P (2011) Intelligent connection agent for three-phase grid-connected microgrids. *IEEE Trans Power Electron* 26 (10):2993–3005
39. Jaalam N et al (2016) A comprehensive review of synchronization methods for grid-connected converters of renewable energy source. *Renew Sustain Energy Rev* 59:1471–1481
40. Boyra M, Thomas J-L (2011) A review on synchronization methods for grid-connected three-phase VSC under unbalanced and distorted conditions. *IEEE Trans Ind Electron* 58 (4):1194–1204 (Guo, Xiaoqiang, Weiyang Wu, and Zhe Chen. Proceedings of multiple-complex coefficient-filter-based phase-locked loop and synchronization technique for three-phase gridinterfaced converters in distributed utility networks)

# Removing Error and Estimating an Accurate Finite Element Model of Graphite–Epoxy Composite Laminate Structure Using Direct Updating Method



Abhishek Sharma, Dinesh Kumar Shukla, Ashok Kumar Bagha , Shashi Bahl , and Devaki Nandan

## 1 Introduction

Composite materials are mainly used in aerospace, automotive, construction, mining, and marine industry. In this regard, the experimental modal analysis of the composite materials at different loadings is required to measure its spatial model (mass and stiffness matrices), modal model (natural frequencies, mode shapes, and damping coefficients), and response model (time and frequency response functions). To overcome the complexity of the experimental modal testing of the complex structures, mostly, the numerical or simulated models are developed to predict the mechanical or vibrational behavior of the materials. Finite element modeling is an important numerical tool that mostly is used for this purpose [1]. During the process to develop the finite element model of the composite structures, the various parameters are assumed. The parameters may be the in-plane material properties, fiber orientation, dimensions, and the boundary conditions of the composite structure. Due to these uncertain parameters or assumptions in the simulated finite element (FE) model, the developed model is unable to predict the exact or real

---

A. Sharma · D. K. Shukla · A. K. Bagha  
Department of Mechanical Engineering, Dr. B.R. Ambedkar National Institute  
of Technology, Jalandhar 144011, India

S. Bahl (✉)  
Department of Mechanical Engineering, I.K. Gujral Punjab Technical University  
Hoshiarpur Campus, Hoshiarpur 146001, India  
e-mail: [shashi.bahl@ptu.ac.in](mailto:shashi.bahl@ptu.ac.in)

D. Nandan  
Department of Industrial and Production Engineering, G.B. Pant University  
of Agriculture & Technology, Pantnagar 263145, India

behavior of the composite structure at different loadings or excitations. So, there is a need to correct or update the simulated finite element model of the composite structures.

The application of the finite element model updating on the composite structures has been presented in past [2]. Finite element model updating technique such as inverse eigen-sensitivity method (IESM) is used to predict the stiffness properties of the composite materials. The important parameters such as generalized mass errors, optimal location of the transducers and approximate reanalysis of eigen-solutions are addressed while doing model updating of the composite structures. A multi-model updating technique is used to predict the stiffness properties of the individual layers of the layered composite materials [3]. The main purpose to use the multi-model updating technique is to update the developed finite element model from the experimental testing so that the in-plane elastic properties of the individual layers of the laminated plate can be predicted analytically. The three important steps on which the success of the implementation of the finite element model updating for the structures depends has been investigated in past [4]. Those are a correct objective function, the correct selection of the updating parameters, and the selection of the robust optimization algorithm. They proposed to use a multi-objective optimization technique in the finite element model updating procedure. Regularized model updating technique has been developed to accurately identifying the mechanical properties of the various constituents of the composite materials [5]. It was found that the developed regularized model updating (RMU) technique can handle the random noise present in the measurements very well as compared to the conventional finite element model updating technique.

Inverse eigen-sensitivity algorithm (IESM) is used to update the developed finite element model of the composite plate so that at the constituent level the fiber and matrix elastic properties can be identified accurately [6]. A new gradient-based step size-controlled inverse eigen-sensitivity method is developed to estimate the material properties and boundary conditions of isotropic and orthotropic composite plates [7]. They found that the proposed method is capable to converge the iterations fast as compared to no-step size-controlled IESM. A finite element model updating-based inverse identification technique is developed to accurately estimate the constituent level mechanical properties of fiber reinforced plastic composite panels [8]. The error present in the boundary conditions of the FRP composite panel is removed by using the developed technique. The weighted sensitivity-based finite element model updating technique has been proposed to accurately identify the degree of composite behavior of operational bridge decks with uncertain installation of shear connectors [9]. The proposed model is limited only to predict the stiffness of the bridge deck.

Kriging metamodel is introduced in the optimization process of the frequency response function (FRF)-based model updating technique to attenuate the solving time as well as to facilitate the application of intelligent algorithms in the finite element model updating of the honeycomb composite sandwich beam [10]. A new approach named double connective layer has been developed in combination with finite element model updating for bolted joints interfaces in hybrid aluminum/

composite structures to predict its dynamic properties [11]. A sensitivity-based inverse eigen-sensitivity method (IESM) was used on 'I' shape fiber reinforced plastic (FRP) composite material to estimate the in-plane material elastic properties [12]. The experimental modal analysis (EMA) was carried out on a free-free and simply supported FRP beam. Then the experimentally measured eigenvalues are used to update the finite element model that can be used to accurately estimate the most uncertain mechanical properties of FRP beam. They concluded that the updated finite element model of the 'I' shapes FRP composite can be used for health monitoring application as well as it can successfully stand along with the actual dynamic loading conditions. A brief review about the finite element model updating techniques has been presented that can be used for the composite materials [13]. The main objective of the authors to present this review is to represent the importance of different uncertainties present in the simulated finite element model of the composite structures. However, the important issues such as parameterization and regularization are also highlighted.

IESM has been used in past to reduce the error in between the experimental modal analysis (EMA) and finite element analysis (FEA) results of a composite plate [14]. They suggested that the error in between the EMA and FEA of the composite structures is mainly due to the various discrepancies present such as different material properties, thickness of the lamina and laminates, fiber orientations, and boundary conditions. However, the authors have successfully reduced the error in between the natural frequencies of composite plate measured from EMA and FEA models by selecting the optimum parameters in the IESM optimization algorithm.

A method has been proposed which was based on model updating using uncorrelated modes [15]. The paper proposes a new method of FE model updating that can include both correlated and uncorrelated modes for updating. This is in contrast to all the current iterative modal data-based methods of model updating that are based on the assumption of availability of correlated mode pairs and hence cannot use uncorrelated mode shapes and corresponding natural frequencies in the updating process. To check the effectiveness of this method, it is applied on a beam structure and a more complex F shape structure. A review of structural dynamic model updating techniques has been presented in the past [16]. Starting with a tutorial introduction of basic concepts of model updating, the paper reviews direct and iterative techniques of model updating along with their applications to real-life systems. To remove the uncertainties, present in the analytical FE model finite element model updating techniques have been used. These techniques may be classified as direct updating techniques and iterative updating techniques. Direct updating techniques provide the solution in single step by updating the incorrect FE model. There is no problem of divergence, and it reproduces the measured data accurately. In iterative techniques, the difference between the experimental results and FE results is reduced in each of the iteration. These techniques are also called as gradient-based techniques. Iterations are stopped when the values of updating parameters stop converging or the error function is reduced to tolerable level. Error function is generally a nonlinear function of experimental and FE responses such as

eigenvalues, eigenvectors or FRFs. Iterative techniques provide symmetric and positive definite updated system matrices, which can be easily understood on a physical basis but this is not possible in case of direct updating techniques.

It is observed from the above literature review that there are few drawbacks of the IESM. The initial estimate of the uncertain parameters and the time taken to solve the iterations in the IESM algorithm is quite cumbersome. So, to overcome these limitations in this paper direct updating method has been used to improve the finite element model of the composite structure laminate. A graphite–epoxy composite material laminate is taken for the validation of direct updating method, and response curve is also plotted in time domain.

## 2 Updating of Spatial Model, Modal Model, and Response Model of the Uncertain Simulated Finite Element Model

In this section, the modal analysis characteristics such as the spatial model (mass and stiffness matrices), modal model (eigenvalues and eigenvectors), and response model (time and frequency response function curves) of the simulated FE model of the various material structures is updated.

### 2.1 Spatial Model

The spatial model represents the mass and stiffness matrices of the system. These matrices are predicted in simulated FE model by doing the assembly of the individual elements present. There are certain uncertain parameters available in the simulated FE model such as assumed material properties (Young's modulus of elasticity, density, etc.), dimensions (length, width, and thickness), boundary conditions (either simply supported or clamped–clamped), and fiber orientations [17–24]. In this regard, there is need to update or correct the spatial model of the simulated FE model.

A method known as a direct updating method (DUM) has been developed to update the mass and the stiffness matrices of the structures by using the measured eigenvalues and the eigenvectors of the structures [25]. The mass matrix is updated to ensure the orthogonality of the exact FE model modes. The mass matrix of the structure is updated as:

$$[M_u] = [M_a] + [M_a][\phi_e][\overline{M}_a]^{-1}([I] - [\overline{M}_a])[\overline{M}_a]^{-1}[\phi_e]^T[M_a] \quad (1)$$

where  $[\overline{M}_a] = [\phi_e]^T[M_a][\phi_e]$  and  $[I] = [\phi_a]^T[M_a][\phi_a]$ .

The stiffness matrix is updated by using the following equation:

$$\begin{aligned}
 [K_u] = [K_a] - [K_a][\phi_e][\phi_e]^T[M_u] - [M_u][\phi_e][\phi_e]^T[K_a] \\
 + [M_u][\phi_e][\phi_e]^T[K_a][\phi_e][\phi_e]^T[M_u] + [M_u][\phi_e][\lambda_e][\phi_e]^T[M_u]
 \end{aligned}
 \tag{2}$$

where  $[M_u]$  is the updated mass matrix,  $[M_a]$  is the analytical or simulated mass matrix,  $[\phi_m]$  is the experimental mode shape matrix,  $[I]$  is the identity matrix,  $[K_u]$  is the updated stiffness matrix,  $[K_a]$  is the analytical or simulated stiffness matrix,  $[\lambda_m]$  is the experimentally measured eigenvalues of the structure. In this paper, the finite element (FE) numerical tool is used to model and predicts the dynamic behavior of the composite laminate. Uncertain parameters are present in the FE model of the composite laminate such as constituent elastic modulus, fiber orientations, dimensions, and boundary conditions [26–33].

## 2.2 Modal Model

The modal model represents the eigenvalues (natural frequencies) and eigenvectors (mode shapes) of the structure. These are predicted by solving the eigenvalue problem (EVP) of the updated-simulated FE model.

$$[K_u][\phi_u] = \lambda_u^2[M_u][\phi_u] \tag{3}$$

where  $[K_u]$  is the updated stiffness matrix,  $[M_u]$  is the updated mass matrix,  $\lambda_u^2$  is the updated eigenvalues, and  $[\phi_u]$  is the updated mode shape matrix. The MATLAB ‘*eig*’ command is used to solve the above eigenvalue problem.

## 2.3 Response Model

The response model of the structure represents the time and frequency response function curve of the systems at various excitations. It is the ratio of the response of the system to the excitation force.

$$x/f = 1/[K_u] - \omega^2[M_u] = \alpha_u(\omega) \tag{4}$$

where  $\alpha_u(\omega)$  represents the updated frequency response function and  $\omega$  represents the excitation frequency in rad/s. The MATLAB ‘*lsim*’ command is used to predict the response in the time domain.

Figure 1 presents the flowchart which shows the procedure to update the simulated model of the structure from the simulated-experimental FE model data.

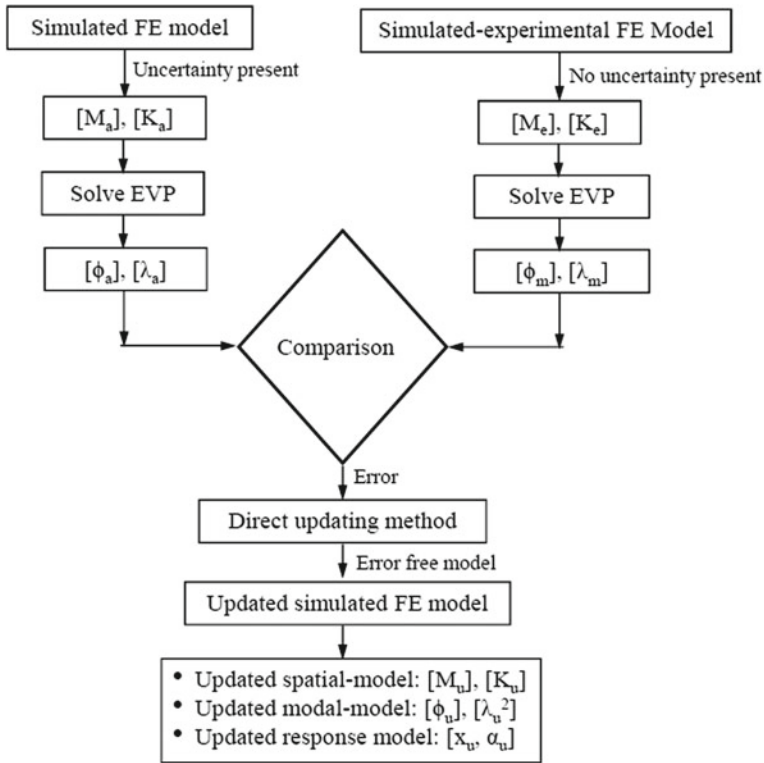


Fig. 1 Flowchart presenting the procedure to update simulated finite element model

The main objective of this paper is to update or correct the spatial model, model-model, and response model of the metallic and composite structure FE model from the simulated-experimental FE model data.

### 3 Numerical Study

In this section, the finite element model updating of a graphite-epoxy composite material laminate is carried out. Figure 2 shows the four-layer cantilever square laminated plate. A four-nodded rectangular bending element with straight edges is used to make the finite element model of the composite laminate. The elemental mass and stiffness matrices can be estimated by the following equations [34].

$$M_e = \int_{-1}^{+1} \int_{-1}^{+1} N^T I N J_S(\zeta, \eta) d\zeta d\eta \tag{5}$$

$$K_e = \int_{-1}^{+1} \int_{-1}^{+1} B^T C B J_S(\zeta, \eta) d\zeta d\eta \tag{6}$$

Table 1 represents the material properties that are used to develop the FE model of the graphite–epoxy composite laminate. It is assumed that material properties such as in-plane elastic modulus and out-of-plane elastic modulus are correct for the simulated-experimental FE model and represent the actual values. However, in the case of simulated FE model, it is assumed that the error is present in the in-plane elastic modulus. The present percentage error is 9.35%. Also, the fiber orientation is assumed incorrect in the simulated FE model.

Table 2 represents the comparison of the natural frequencies predicted by the simulated and simulated-experimental FE model. It is found that the maximum percentage error present is 18.18%. This clearly represents the mismatch between the spatial model and modal model of both the FE models. So, it is required to correct the spatial model and modal model of the simulated FE model. In the literature, as already discussed, the IESM is mostly used to update the simulated FE model of the composite structures. In this paper, the direct updating method is applied on the simulated FE model to correct it.

Table 3 shows the comparison of the updated natural frequencies of the composite laminate structure. It is observed that the error between both the models has been reduced. The percentage error now is 0.00% between both the models. It reflects that the direct updating method is also very effective on the composite laminate structures to update its modal analysis characteristics.

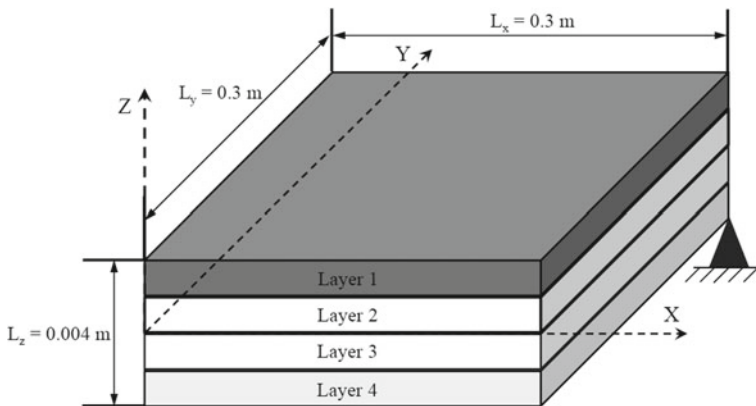


Fig. 2 Four-layer cantilever square laminated plate



**Table 1** Material properties of the graphite–epoxy composite laminate

S. No.	Material properties	Simulated FE model	Simulated-experimental FE model
1.	Number of layers	4	4
2.	Plate dimensions	0.3 m * 0.3 m	0.3 m * 0.3 m
3.	Thickness of each layer	0.001 m	0.001 m
4.	Young's modulus in x-direction	120 GPa	132.38 GPa
5.	Young's modulus in y-direction	10.76 GPa	10.76 GPa
6.	Density	1578 kg/m <sup>3</sup>	1578 kg/m <sup>3</sup>
7.	Poisson's ratio	0.24	0.24
8.	Modulus of rigidity	5.65 GPa	5.65 GPa
9.	Fiber orientation	[−30/0] <sub>s</sub>	[−35/3] <sub>s</sub>
10.	Number of elements	10 * 10	10 * 10
11.	Boundary condition	Cantilever	Cantilever

**Table 2** Comparison of the natural frequencies between simulated and simulated-experimental FE model

S. No.	Natural frequencies (Hz)		Error (Hz)	Error (%)
	Simulated FE model	Simulated-experimental FE model		
1.	0.09	0.11	0.02	18.18
2.	0.87	0.97	0.10	10.30
3.	2.46	2.40	−0.06	−2.5
4.	2.75	2.74	−0.01	−0.36
5.	3.51	3.62	0.11	3.03
6.	4.57	4.71	0.14	2.97
7.	5.43	5.32	−0.11	−2.06
8.	6.33	6.44	0.11	1.70
9.	8.46	9.45	0.99	10.47
10.	10.29	11.68	1.39	11.90

Figure 3 represents the overlay of the responses in the time domain. The tonal excitation (at fundamental frequency of the structure) is applied at certain node on the composite laminate plate and the response is predicted at the same node. It is clearly visible that the simulated FE model response is not matching with the simulated-experimental response. However, after applying the direct updating method on the simulated FE model, the updated response is completely tracking the actual (simulated-experimental) response. So, this predicted response curve completely validates the robustness of the application of the direct updating method for the composite materials.

**Table 3** Comparison of the natural frequencies between updated simulated and simulated-experimental FE model

S. No.	Natural frequencies (Hz)		Error (Hz)	Error (%)
	Updated simulated Fe model	Simulated-experimental FE model		
1	0.11	0.11	0.00	0.00
2.	0.97	0.97	0.00	0.00
3.	2.40	2.40	0.00	0.00
4.	2.74	2.74	0.00	0.00
5.	3.62	3.62	0.00	0.00
6.	4.71	4.71	0.00	0.00
7.	5.32	5.32	0.00	0.00
8.	6.44	6.44	0.00	0.00
9.	9.45	9.45	0.00	0.00
10.	11.68	11.68	0.00	0.00

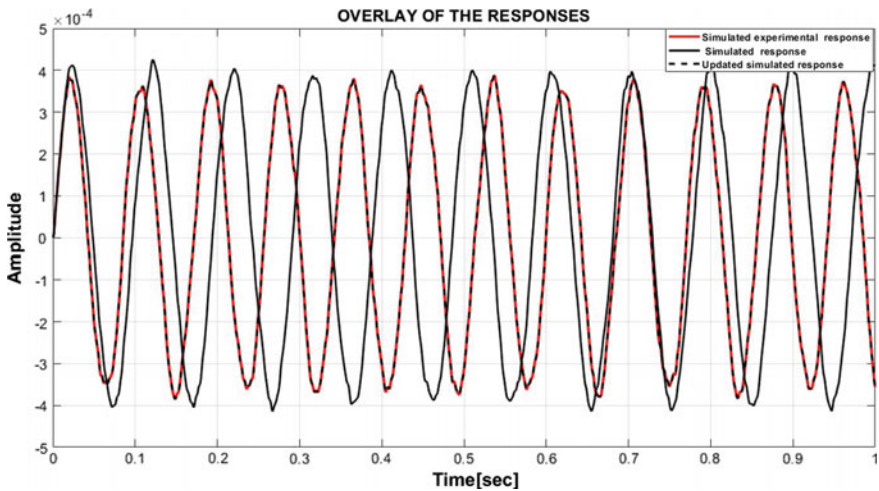


**Fig. 3** Overlay of the simulated, simulated-experimental, and updated simulated responses

### 4 Unique Ideas of the Present Study

The unique points of the present study are summarized as follows:

- By using finite element model updating (FEMU) technique, the uncertainties present in the simulated analytical finite element model can be removed.
- This method is very fast as compared to other techniques because it directly updates our spatial model, modal model, and response model.

- Updation of finite element model is required to carry out the correct vibration analysis.
- FEMU technique is widely applicable in the field of finite element (FE) model formulations, damage analysis of structures, non-destructive characterization of material properties and also for dynamic design purposes.
- In this paper, finite element model updating method is applied on the composite structure to remove the error present in the finite element models.

## 5 Conclusions

It is observed from this numerical study that the direct updating method (DUM) can be used to update the spatial model, modal model, and response model of the composite structures. The main achievement of this work is to successfully apply the direct updating method on the graphite–epoxy composite material laminate and update its simulated model by removing the uncertainties present in inelastic properties and fiber orientations. In most of the applications, direct updating method has been used for the metals, but the present paper concludes that it can be used for the composite material also. The composite materials are anisotropic materials and also found wide applications in different fields; in this regard, the successful application of DUM is having a great importance. Without consuming a large amount of time, DUM is a quick and fast algorithm to update or correct the simulated FE model. Also, in this method there is no requirement of prior estimation of the uncertain parameters, as in the case of IESM. Direct updating method directly updates the spatial model (mass matrix and the stiffness matrix) of the simulated models. This prediction directly influences on the eigenvalues and eigenvectors of the structure. If the eigenvalues and eigenvectors are predicted accurately, then it is possible to estimate the actual behavior of the system in time domain also. Also, in this paper, the response curve in time domain clearly indicates that the DUM is capable to estimate the response of the system at tonal excitations.

## References

1. Chandrupatla TR, Belegundu AD (1991) Introduction to finite elements in engineering. Prentice Hall, Englewood Cliffs
2. Cunha J, Piranda J (1999) Application of model updating techniques in dynamics for the identification of elastic constants of composite materials. *Compos Part B Eng* 30:79–85. [https://doi.org/10.1016/S1359-8368\(98\)00050-X](https://doi.org/10.1016/S1359-8368(98)00050-X)
3. Lauwagie T, Sol H, Heylen W, Roebben G (2004) Determination of the in-plane elastic properties of the different layers of laminated plates by means of vibration testing and model updating. *J Sound Vib* 274:529–546. <https://doi.org/10.1016/j.jsv.2003.05.023>

4. Jaishi B, Ren W-X (2007) Finite element model updating based on eigenvalue and strain energy residuals using multiobjective optimisation technique. *Mech Syst Sig Proc* 21:2295–2317. <https://doi.org/10.1016/j.ymsp.2006.09.008>
5. Rahmani B, Mortazavi F, Villemure I, Levesque M (2013) A new approach to inverse identification of mechanical properties of composite materials: regularized model updating. *Compos Struct* 105:116–125. <https://doi.org/10.1016/j.compstruct.2013.04.025>
6. Mishra AK, Chakraborty S (2015) Development of a finite element model updating technique for estimation of constituent level elastic parameters of FRP plates. *Appl Math Comput* 258:84–94. <https://doi.org/10.1016/j.amc.2015.02.003>
7. Goni SA, Mondal S, Chakraborty S (2015) A new gradient based step size controlled inverse eigen sensitivity algorithm for identification of material and boundary parameters of plates. *J Vib Control* 23:2619–2634. <https://doi.org/10.1177/1077546315619076>
8. Mishra AK, Chakraborty S (2016) Inverse detection of constituent level elastic parameters of FRP composite panels with elastic boundaries using finite element model updating. *Ocean Eng* 111:358–368. <https://doi.org/10.1016/j.oceaneng.2015.11.003>
9. Polanco NR, May G, Hernandez EM (2016) Finite element model updating of semi-composite bridge decks using operational acceleration measurements. *Eng Struct* 126:264–277. <https://doi.org/10.1016/j.engstruct.2016.07.057>
10. Wang JT, Wang CJ, Zhao JP (2017) Frequency response function-based model updating using Kriging model. *Mech Syst Sig Proc* 87:218–228. <https://doi.org/10.1016/j.ymsp.2016.10.023>
11. Adel F, Shokrollahi S, Jamal-Omidi M, Ahmadian H (2017) A model updating method for hybrid composite/aluminum bolted joints using modal test data. *J Sound Vib* 396:172–185. <https://doi.org/10.1016/j.jsv.2017.02.035>
12. Mishra AK, Mohammed A, Chakraborty S (2018) Improved numerical modelling of fiber reinforced plastics I-beam from experimental modal testing and finite element model updating. *Int J Acoust Vib* 23:26–34. <https://doi.org/10.20855/ijav.2018.23.11069>
13. Panwar V, Gupta P, Bagha AK, Chauhan N (2018) A review on studies of finite element model updating and updating of composite materials. *Mater Today Proc* 5:27912–27918. <https://doi.org/10.1016/j.matpr.2018.10.030>
14. Yaacob RM, Hashim MAH, Sani MSM (2019) Finite element modeling and updating of the composite plate structure. *J Phys Conf Ser* 1262. <https://doi.org/10.1088/1742-6596/1262/1/012013>
15. Modak SV (2014) Direct matrix updating of vibroacoustic finite element models using modal test data. *AIAA J* 52:1386–1392. <https://doi.org/10.2514/1.J052558>
16. Sehgal S, Kumar H (2016) Structural dynamic model updating techniques: a state of the art review. *Arch Comput Methods Eng* 23:515–533. <https://doi.org/10.1007/s11831-015-9150-3>
17. Suman R, Nandan D, Haleem A, Bahl S, Javaid M (2020) Comparative study of silicon dioxide and kaolinite ratio for temperature and humidity variations of earth energy enabled cooling system and traditional cooler. *Mater Today Proc*. <https://doi.org/10.1016/j.matpr.2020.04.847>
18. Suman R, Nandan D, Haleem A, Bahl S, Javaid M (2020) Experimental study of electroless plating on acrylonitrile butadiene styrene polymer for obtaining new eco-friendly chromium-free processes. *Mater Today Proc* 28:1575–1579. <https://doi.org/10.1016/j.matpr.2020.04.843>
19. Kumar Saini M, Kumar Bagha A, Kumar S, Bahl S (2020) Finite element analysis for predicting the vibration characteristics of natural fiber reinforced epoxy composites. *Mater Today Proc*. <https://doi.org/10.1016/j.matpr.2020.08.717>
20. Kumar Bagha A, Bahl S (2020) Strain energy and finite element analysis to predict the mechanical properties of vapor grown carbon fiber reinforced polypropylene nanocomposites. *Mater Today Proc*. <https://doi.org/10.1016/j.matpr.2020.09.034>
21. Kesharwani A, Bedi R, Kumar Bagha A, Bahl S (2020) Experimental study to measure the sound transmission loss of natural fibers at tonal excitations. *Mater Today Proc* 28:1554–1559. <https://doi.org/10.1016/j.matpr.2020.04.839>

22. Bahl S, Nagar H, Singh I, Sehgal S (2020) Smart materials types, properties and applications: a review. *Mater Today Proc* 28:1302–1306. <https://doi.org/10.1016/j.matpr.2020.04.505>
23. Bahl S (2020) Fiber reinforced metal matrix composites—a review. *Mater Today Proc*. <https://doi.org/10.1016/j.matpr.2020.07.423>
24. Bahl S (2020) Numerical simulation of the debonding behavior of fiber reinforced metal matrix composites. *Mater Today Proc* 28:1328–1334. <https://doi.org/10.1016/j.matpr.2020.04.598>
25. Berman A, Nagy EJ (1983) Improvement of a large analytical model using test data. *AIAA J* 21:1168–1173. <https://doi.org/10.2514/3.60140>
26. Chhipa SM, Kumar P, Bagha AK, Bahl S (2020) Removing uncertainty in the boundary condition of five degree of freedom spring mass vibratory system using direct updating method. *Mater Today Proc*. <https://doi.org/10.1016/j.matpr.2020.08.803>
27. Bahl S, Dolma J, Jyot Singh J, Sehgal S (2020) Biodegradation of plastics: a state of the art review. *Mater Today Proc*. <https://doi.org/10.1016/j.matpr.2020.06.096>
28. Bahl S, Cambow R, Kumar Bagha A (2020) An experimental study to measure the acoustical properties of natural fibers at real case broadband excitations. *Mater Today Proc* 28:1279–1284. <https://doi.org/10.1016/j.matpr.2020.04.228>
29. Bahl S, Bagha AK, Sehgal S (2021) Experimental investigations into sound transmission loss by different materials at aircraft noise. *Mater Today Proc*. <https://doi.org/10.1016/j.matpr.2020.12.153>
30. Bahl S, Bagha AK (2020) Finite element modeling and simulation of the fiber-matrix interface in fiber reinforced metal matrix composites. *Mater Today Proc*. <https://doi.org/10.1016/j.matpr.2020.06.160>
31. Bahl S (2020) Axisymmetric finite element analysis of single fiber push-out test for stainless steel wire reinforced aluminum matrix composites. *Mater Today Proc* 28:1605–1611. <https://doi.org/10.1016/j.matpr.2020.04.848>
32. Bagha AK, Bahl S (2020) Finite element analysis of VGCF/pp reinforced square representative volume element to predict its mechanical properties for different loadings. *Mater Today Proc*. <https://doi.org/10.1016/j.matpr.2020.06.108>
33. Bahl S, Singh T, Kumar V, Sehgal S, Bagha AK (2021) A systematic review on recent progress in advanced joining techniques of the lightweight materials. *AIMS Mater Sci* 8:62–81. <https://doi.org/10.3934/matersci.2021005>
34. Larbi W, Deü J-F, Ohayon R (2012) Finite element formulation of smart piezoelectric composite plates coupled with acoustic fluid. *Compos Struct* 94:501–509. <https://doi.org/10.1016/j.compstruct.2011.08.010>

# Human-Powered Flywheel Motor (HPFM): A Review



H. K. Baitule, P. B. Maheshwary, and J. P. Modak

## Nomenclature

HP	Horse power
RPM	Revolutions per minute
$\omega$	Angular velocity (rad/s)
$I$	Flywheel's mass moment of inertia in $\text{kg m}^2$
$R$	Input energy by the rider, $\text{kgf m}$
EM	Effectiveness of the mechanism
$G$	Speed increasing gear ratio

## 1 Introduction

The development in existing bicycles with some modification in cranking system, speed increasing gear pair and flywheel to store the pedaling energy forms the novel system known as HPFM. This HPFM has wide applications as discussed in subsequent sections. The paper has discussion on human-operated machinery.

Leg muscles are stronger than arm muscles, and hence, bicycle drive mechanisms are generally preferred. The energy of human leg powered developed in bicycle is converted into electricity. This center is used to operate mechanical systems [1]. This paper concentrates on such idea developed by Modak et al. [2, 3] known as human-powered flywheel motor (HPFM). The details of design and their various industrial and rural applications are explained in various sections [2, 4]. Ferrer-Roca et al. [5] report on influence of small changes in crank length during sub-maximal cycling. Malhi and Irwin [6] report on psychological influence on

---

H. K. Baitule (✉) · P. B. Maheshwary  
Department of Mechanical Engineering, J.D. College of Engineering and Management,  
Nagpur, Maharashtra 440019, India

J. P. Modak  
J.D. College of Engineering and Management, Nagpur, Maharashtra 440019, India

peddler while performing rapid pedaling. Rannama et al. [7] emphasize effect on muscular skeletal state of cyclist on account of cycling economy and pedaling effectiveness. Kunert et al. [8] have reported on phase space method for evaluating nonlinear analysis of pedaling forces in cycling. Ferrer-Roca et al. [9] report on influence of frontal projected area of peddler and bicycle to decide aerodynamic drag. They are suggesting new 3D method which allows feedback of the frontal area in real time.

## 2 Human-Powered Flywheel Motor (HPFM) Arrangement

### 2.1 Construction of System

This novel system of machine consists of three subsystems, viz.

- (1) Unit of energy
- (2) An appropriate required transmission unit
- (3) A process unit.

The schematic of the system is as shown in Fig. 1.

Energy unit: This comprises bicycle like peddling system, speed increasing gear pair  $G^i$  and flywheel (FW). Transmission comprises the torsionally flexible clutch (TFC) and the torque amplification gear pair  $G$  and (3) the process unit.

### 2.2 Operational Characteristic of the Machine

The process unit will be initially speeded up with high acceleration, and speed would be reduced gradually. The process units tried so far are as follows.

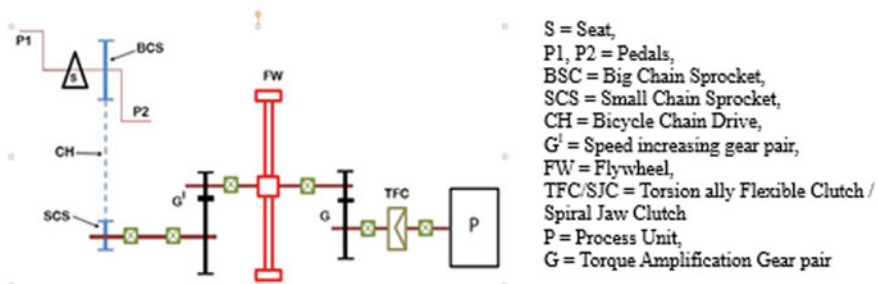


Fig. 1 Representation of the machine system [2]

Extrusion of rectangular/keyed sectioned bricks [10–18]  
 Wood turning [19]  
 Low head water lifting  
 Algae formation process [20]  
 Cloths washing [21]  
 Chaff cutting [21]  
 Food grains crushing [21]  
 Groundnut oil expulsion [21]  
 Electricity generation [22, 23].

In a nutshell, the process units needing 4–12 hp and those in which the product/process quality is not getting much affected due to constantly changing speed of input shaft can be energized by such system.

The above-stated development of this machine system is mainly done by Dr. J. P. Modak who has remained the principle investigator of this development over last 4/5 decades. Based on this work, Dr. Modak has received D.Sc. (Engg. and Tech) degree from R.T.M.N.U., has guided 20/25 PhDs and has contributed over 200 research papers.

The diameter of flywheel is 0.6 m. The flywheel attained the speed of 600–800 rpm in 5–10 min by pedaling the system. The gear pair is used to increase the torque of flywheel shaft. TFC is used to connect this energy source to process unit. The gearing arrangement with speed magnification of 2.5–3.0 and arm flywheel with approximate four arm and mass moment of inertia 22 Nm

$$E = \text{energy stored in flywheel} = 0.5 I\omega^2.$$

where  $\omega$  = angular velocity and  $N = 800$  RPM is app. 79 kN m or kJ.

Power = Energy/time, time for 60 s then.

Power = Energy/time = 79/60 = 1.32 kW/1.76 HP.

The developed power is again amplified by torque amplification gear pair and increased to 5–11 H.P. By increasing the size of flywheel diameter from 0.5 to 1 m or increasing gear ratio, more power may be developed. Figure 1 shows the HPFM system used above fundamentals for various process units as discussed above.

The speed of shaft of processing unit increases when energy unit is connected to process unit via clutch, and because of resistance offered by the process unit, its speed decreases [2].

### 2.3 Mechanism

Basically, mechanism for cranking of a bicycle has five-link chain. Mechanism consists of fixed link between seat to peddle, input as a thigh, coupler as a space between knee and ankle of leg and foot, and output as a peddle [24]. It gets converted to four bars by swapping foot. Figure 2 shows quick return ratio 1 drive with O1B as thigh, AB as size, O2A as crank, O1O2 as fixed link.



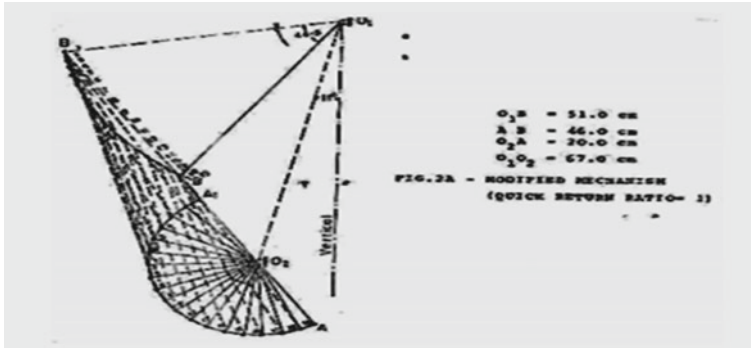


Fig. 2 Q.R.R = 1 drive [25]

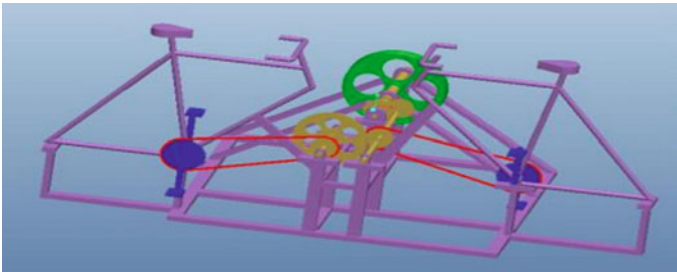


Fig. 3 CAD model [25]

The static force investigation opens the next facts: (i) One-twelfth of input link rotation is idle. (ii) Around approximate one-third is a smaller amount operative. (iii) Simply, two-third is effective one. It is improved with new mechanism. Figure 3 shows double-lever inversion drive [25] (Fig. 4).

The above figures represent cranking arrangement of the energy systems. Quick return ratio = 1 system is seventeen, and double-lever inversion drive (DLID) is thirty-five percent extra operative. The utility of the drive is to measure the ratio of energy transferred by the new drive to the current drive at smaller sprockets for an equivalent period of time. The literature proposes more effective adoption of elliptical sprocket drives [26, 27]. Various cranking setups have been proposed by Moghe and Modak [28]. The authors also discussed various experimental investigation conclusions for various cranking arrangements [29, 30].

### 3 Data-Based Model (Experimental)

The basic objectives are as follows:

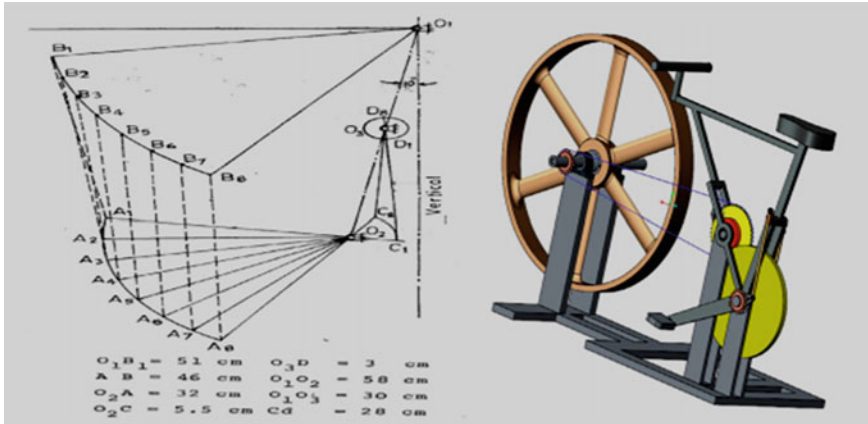


Fig. 4 Modified CAD model of HPFM [25]

1. Maximum angular velocity of the flywheel
  2. Maximum energy stored in the flywheel
  3. Maximum conversion of human powerful dynamism into K.E. of the flywheel.
- In this investigation all independent factors are diverse experimentally over broadest likely varied, and the response data is computed the analytical correlation between independent and dependent terms is recognized on the basis of this experimental knowledge. In this technique, general experimental data-based models are found, and the finest values of independent variables are applied [3].

### 3.1 Scheme of Experimentation

The authors have used the following methods for experimentation.

- Identification involved all independent, dependent and extraneous variables [H. Schanck, Jr.] of this phenomenon of energy conversion from human muscular energy form to rotational kinetic energy form of the flywheel.
- Derivation of dimensional equations.
- Test planning: This comprises (i) deciding test envelope, test points, test sequence, experimentation plan.
- Physical design of an experimental setup: This comprises decision of mechanical hardware dimensioning and instrumentation.
- Fabrication of an experimental setup: This comprises mechanical fabrication and installing instrumentation.

### 3.2 Experimentation: This is in Two Stages

Stage 1: Confirmation of appropriate functioning of subsystem, i.e., (i) mechanical hardware and (ii) instrumentation. This is for the two extreme stages of test envelope.

Stage 2: Execution of main experimentation as per earlier stated design of experimentation.

### 3.3 Formulation of Experimental Model

Based on obtained experimented data to formulate four different types of models stated as under

- (i) Exponential form
- (ii) Clubbing all independent  $\pi$  terms in to one independent  $\pi$  term form
- (iii) Getting response surface model
- (iv) ANN simulation
- (v) Reliability of models
- (vi) Optimization of model
- (vii) Experimentation.

The dimensional form of equation is

$$\omega T = f[(I/(R * T2)), (EM), (G)] \tag{1}$$

$\omega$  = The flywheel’s angular velocity in rad/s is achieved in  $T$  seconds.

$I$  = Flywheel’s mass moment of inertia in  $\text{kg m}^2$ .

$R$  = Input energy by the rider,  $\text{kgf m}$ .

$EM$  = Effectiveness of the mechanism.

$G$  = Speed increasing gear ratio.

For each independent  $\pi$  term from earlier results of Modak et al. and his associates, Table 1 presents the test envelope, test points and test series.

The test envelope was occupied by many drive mechanisms such as quick return ratio 1, double-lever inversion mechanism and elliptical sprocket from the theoretical designs. In order to confirm robustness, precision and smooth operation, the

**Table 1**

S. No.	Pi terms	Test envelope	Test sequence
01	$I$	0.255–3.48	0.255, 1.867, 1.061, 2.673, 3.48
02	EM	1–1.8	1.0, 1.3, 1.17, 1.18
03	Gear ratio	1.14–4	1.14, 1.3, 1.5, 2, 4

setup construction was approved. A further approach is designed to eliminate extraneous variables such as mood, attitude, day and test time [31].

### 3.4 Result Analysis

Figures 5, 6 and 7 show response of dependent Pi term for various independent gear ratio, efficiency of mechanisms and mass moment of inertia for all day timings [2].

### 3.5 Plan of Experimentation

The authors have conducted the experimentation by varying each independent Pi term ( $I/RT^2$ ), (EM) and ( $G$ ) in dimensionless equations and its effect on dependent Pi term  $\omega T$  observed. Also, they observed the effect of extraneous variables like enthusiasm, physical condition, environmental condition, etc., of the riders. They used experimentation as a mixed plan as it is a grouping of man-machine system [32–34].

### 3.6 Generalized Experimental Model

The exponential form of dimensional from Eq 1.

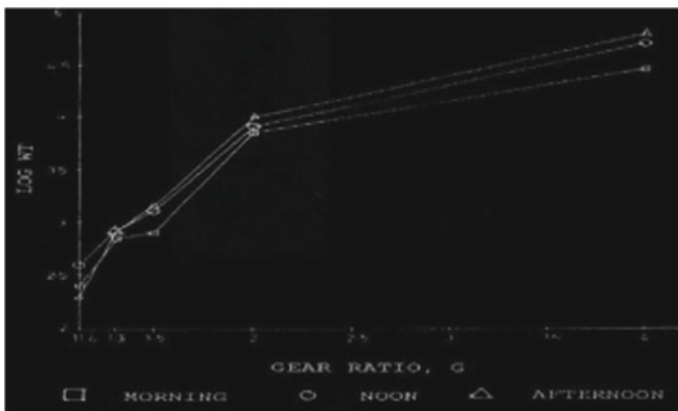


Fig. 5 Log  $\omega T$  versus GR [2]

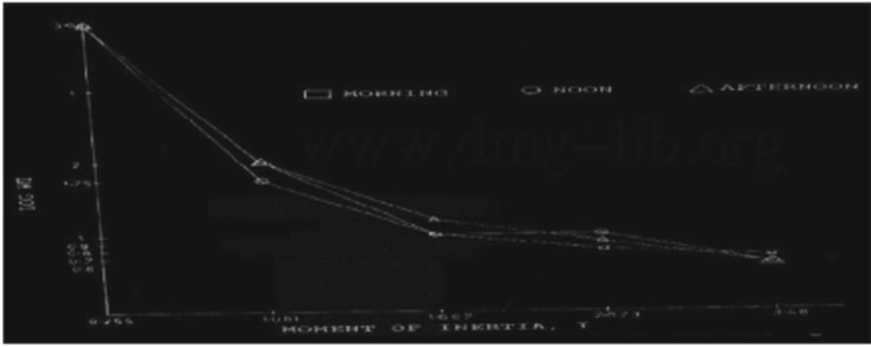


Fig. 6 Log ωT versus EM [2]

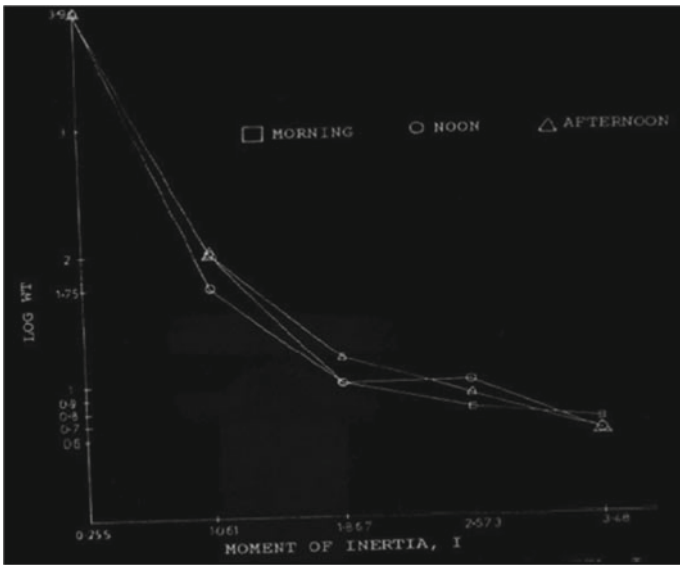


Fig. 7 Graph for log ωT versus I [2]

$$\omega T = K(I/RT^2)^a, (EM)^b, (G)^c \tag{2}$$

where  $K$  stands for a curve-fitting constant and  $a, b, c$  stand for exponential constants. The effects for these factors are found by means of multiple regression analysis and a suitable computer platform. The values of  $K, a, b$  and  $c$  are 1.28,  $-0.46, -0.87$  and  $0.40$ , respectively. Therefore, the equation can be redrafted as:

$$\omega T = 1.288(I/RT^2) - 0.46, (EM) - 0.87, (G)0.40 \tag{3}$$

### 3.7 Optimization of $I, EM, G$

The purposes of creating the experimental model for HPFM unit are as follows:

- To find maximum  $\omega T$
- To find maximum stored energy in the flywheel
- To find the maximum efficiency of the system.

As in (3) noticeably, it can be accepted that indices  $a$  and  $b$  are negative, hence  $(I/RT^2)$ , and although constant  $c$  is positive,  $(EM)$  must have a minimum value, so we have a maximum value of  $(G)$ . The improved maximum value of  $\omega T$  from the HPFM system is found, while  $I = 0.255 \text{ kg m}^2, G = 4, EM = 1$  [2].

An additional target was to achieve the full flywheel energy storage presented by Eq. 4

$$E = 0 : 5I\omega^2 \tag{4}$$

As one observes (4), we may, at some point, consider that when  $I$  and  $\omega$  are extreme,  $E$  will be extreme, but experiments reverse this principle and what analysis suggests that when  $I$  is lowest,  $E$  is maximum.

The improved maximum value of energy stored from the HPFM system is obtained when [2]

$$I = 0.255 \text{ kg m}^2, G = 4, EM = 1.$$

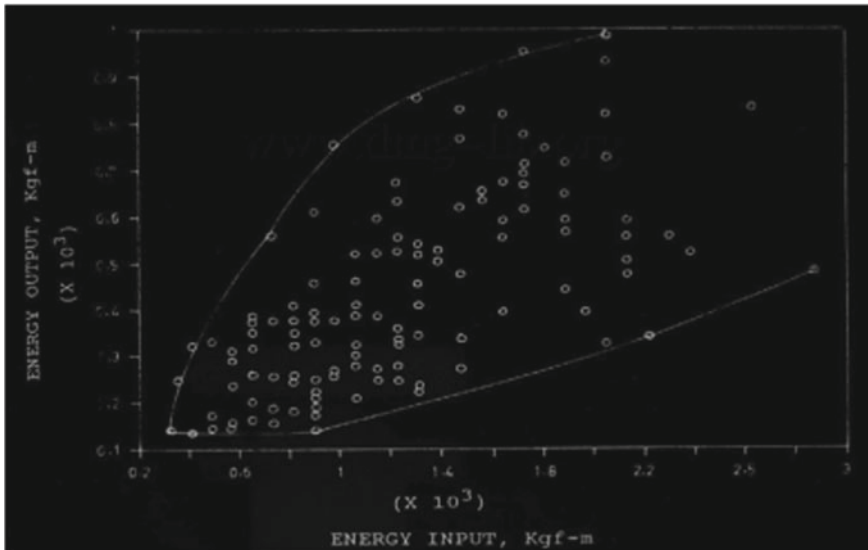


Fig. 8 Graph of input energy versus output energy [2]

Figure 8 signifies the 250 observations and their input and output energy envelope sets. On the similar appearances, thus, the improved maximum efficiency was found when  $I = 0.255$  to  $1.061 \text{ kg m}^2$ ,  $G = 2$  or  $4$ ,  $EM = 1$  [2].

## 4 Applications of HPFM [25]

### 4.1 Bamboo Sliver Cutting [26]

Bamboo sliver cutting unit is operated by HPFM having double roller and cutter. Flywheel energy is used to operate the machine through clutch. Bamboo is passed through push-in and push-out roller which cuts by sliver cutter (Fig. 9).

### 4.2 Oil Expeller Machine

Here, the author tried to extract oil by using HPFM unit when energy is stored in flywheel after pedaling 1–2 min. This energy is then supplied to process unit as shown in Fig. 10 by suitable clutch and gear ratio for torque supplied amplification. The crushing and squeezing action takes place by the auger (screw shape tool).



Fig. 9 Bamboo slivering operated by HPFM [26]

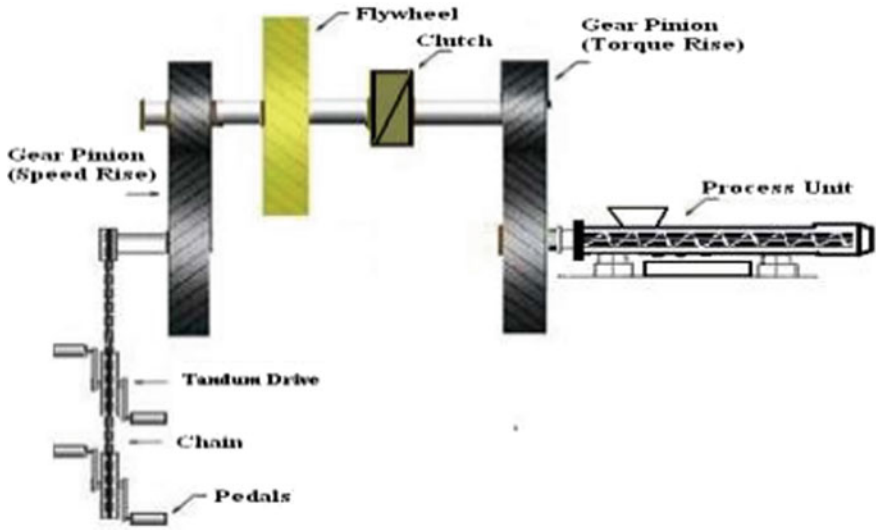


Fig. 10 Oil expeller operated by HPFM [26]

### 4.3 HPFM-Operated Chaff Cutter

The author developed the experimental HPFM-operated chaff cutter as shown in Fig. 11. They formulated the dimensionless equation for the response variables like resistive torque, no. of cuts and process time and validated using ANN [27, 32, 33].



Fig. 11 Chaff cutting machine [19]



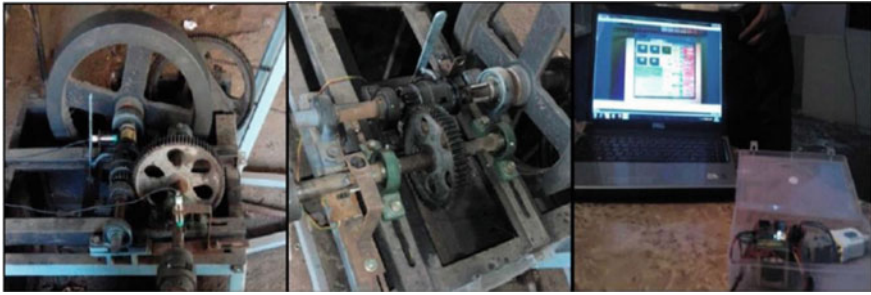


**Fig. 12** Stirrup making [6]

#### ***4.4 Stirrup Forming Operation Using HPFM***

The author investigated the HPFM-operated stirrup making process as shown in Fig. 12. In construction industry, sealed ring four-sided steel bar is used to hold the primary bar diameter ranges from 6 to 10 mm which is stirrup. Independent and dependent Pi terms were designed on the basis of this experiment to create an empirical connection for the stirrup that allows the process [32].

#### ***4.5 HPFM-Based Turmeric Polishing Machine***

The author developed turmeric polishing machine which is driven by HPFM unit as shown in Fig. 13. The machine can do washing, drying, moisture reduction, varnishing and grinding. The author also claimed for employment of semiskilled labor in rural area [35].

#### ***4.6 HPFM-Energized Fertilizer Mixer***

The drum contains soil, sand, cow dung and water that are mixed by HPFM unit using stored energy of flywheel. The slurry is taken out from the bottom of the drum. The author also gathered experimental data and simulate in MTAB and set empirical relationship [31] (Fig. 14).



**Fig. 13** Turmeric polishing machine [8]



**Fig. 14** HPFM-based fertilizer mixer [9]

### ***4.7 Pedal-Operated Paddy Thresher***

The author experimentally determined the optimum parameter of paddy thresher based on spacing and tip height of wire loop and speed of threshing drum for different types of rice. The spacing, tip height of wire loop and speed of threshing drum are found to be 39.1 mm, 60.6 mm and 339.46 m/min, respectively, by using response surface methodology (RSM) [34] (Fig. 15).

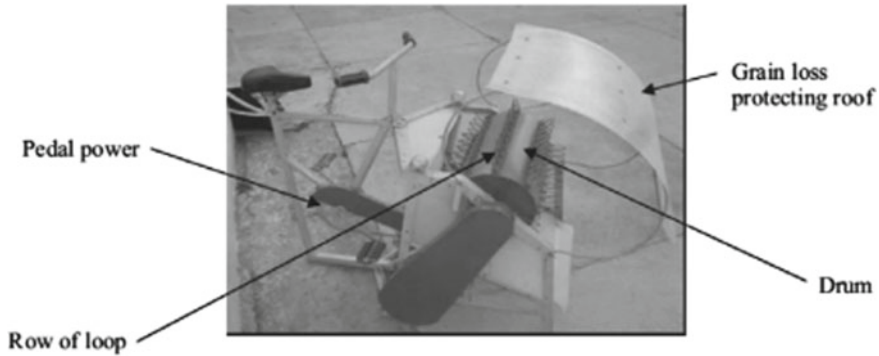


Fig. 15 Pedal-operated VL paddy thresher [34]

## 5 Conclusion

In the present work, the detailed discussion on HPFM for maximum energy stored and various applications. The various applications like chaff cutter, stirrup making, oil pressing, bamboo sliver cutting operations, food grain crusher, turmeric polishing and fertilizer mixer are discussed in detail. The development in the cranking mechanisms like elliptical chain sprocket system and TFC and flywheel could improve the efficiency. Recently, it is seen in the literature on peddler-driven system that some more cranking arrangement is developed. These should be tried for elevating terminal energy level of HPFM and reducing human body internal loss.

## References

1. Muscles C, Motors O (2009) The human-powered home: choosing muscles over motors. *World Future Rev* 01(02):92–97
2. Modak JP (2007) Proceedings of twelfth world congress in mechanism and machine science, Besancon, France: human powered flywheel motor: concept, design, dynamics and applications, IFToMM [Online]. Available: <https://www.dmg-lib.org/dmglib/streambook/index.jsp?bookid=20401009>. Accessed 03 Sep 2019
3. Modak JP (2016) Human powered flywheel motor: concept, design, dynamics and application
4. Modak J, Moghe S (1998) Design and development of a human-powered machine for the manufacture of lime-flyash-sand bricks. *Hum Power Tech J IHPVA* 13(02):3–7
5. Ferrer-Roca V, Rivero-Palomo V, Ogueta-Alday A, Rodríguez-Marroyo JA, García-López J (2017) Acute effects of small changes in crank length on gross efficiency and pedalling technique during submaximal cycling. *J Sports Sci* 35(14) (Cycling Science)
6. Malhi GS, Irwin L (2019) Rapid cycling: are we pedalling in the right direction? *Aust N Z J Psychiatry* 1–3
7. Rannama I, Reinpöld K, Pedak K, Por K (2020) The relationships between cycling economy, pedalling effectiveness and cyclist's musculoskeletal state. *World Congress of Performance Analysis of Sport XII*

8. Kunert A, Ott M, Reuter T, Koska D, Maiwald C (2019) Phases pace methods for non-linear analysis of pedaling forces in cycling, <https://doi.org/10.1371/journal.pone.0198914> April 18, 2019
9. Ferrer-Roca V, Vretos N, Chatzifolis A, Alvarez D (2017) New 3D method to estimate the cycling frontal area during pedaling. In: 5th conference of the international society of biomechanics in sports, Cologne, Germany, June 14–18, 2017
10. Askhedkar RD, Modak JP (1983) Calibration of a tachogenerator—a case study. In: Proceedings of 28th congress of ISTAM, Paper ET-5, Dec 1983
11. Shekdar AV et al (1983) An overview of methodology of experimentation. In: Proceedings of 28th congress of ISTAM, Paper ET-6, Dec 1983
12. Askhedkar RD, Modak JP (1985) Modeling of a manually driven brick making machine to simulate design data experimentally. Modeling, simulation and control, B AMSE Press France 2(4):29–64
13. Askhedkar RD, Modak JP (1994) Hypothesis for the extrusion of lime-fly-ash-S and-bricks using manually driven brick making machine. *Batim Int Build Res Pract UK* 22(1):47–54
14. Modak JP, Askhedkar RD (1993) Determination of test envelop and necessity of simplification of mathematical analysis of experimental data while studing a new phenomenon. *Adv Model Anal (AMSE Press, France)* 27(3):59–64
15. Askhedkar RD, Modak JP (1992) Development of hand moulding process for manufacture of bricks through application of techniques of methods engineering. In: Proceedings of 34th national convention of IIIE, Pune, (India) Oct 1992
16. Aware HV, Sohoni VV, Modak JP (1997) Manually powered manufacture of keyed bricks. *Build Res Inf UK* 25(N6):354–364
17. Aware HV, Sohoni VV, Modak JP (1998) Formulation of an approximate generalized experimental model for an extrusion unit of manually energized keyed bricks manufacturing machine. In: Proceedings international conference. Contribution of cognition to modelling, CCM'98, Clude-Bernard Uni of Layon, France, July-98, Paper 4.4, pp 4.12–4.15
18. Sohoni VV, Modak JP. Formulation of generalized experimental model for an extruder unit of a manually energized machine for extruding keyed bricks. *Build Res Inf U.K.* (Accepted for Publication)
19. Modak JP, Bapat AR (1993) Manually driven flywheel motor operates a wood turning process. In: Proceedings, annual conference “ergonomics and energy” of the ergonomics society. UK (Heriot watt University), April 1993, pp 352–357
20. Katpatal AG, Raman G, Modak JP (1994) Design of manually energized centrifugal drum type algae formation process unit. In: Proceedings international AMSE conference “systems analysis, control and design” Lyon, France, vol 3, 4–6, July 1994, pp 227–232
21. Modak JP (2005) Design and development of manually energized process machine having relevance to village/agriculture and other productive operations. *Hum Power USA* 57:16–21
22. Deshpande SB, Modak JP, Tarnekar SG (2003) Computer aided analysis of battery charging process adopting manually energised flywheel motor as an energy source. In: Proceedings, international conference on CAD/CAM robotics and autonomous factories. Indian Institute of Technology, New Delhi, India, August 11–14, 2003, Paper No. 289
23. Deshpande SB, Modak JP, Tarnekar SG (In Press) Modelling and simulation of battery charging process adopting human powered flywheel motor as an energy source. Paper No. 05, 302 (2A). *Int J Adv Model Simul Tech Enterprises (AMSE) France*
24. Padghan K, Warghade P, Astonkar D (2015) Kinetic energy gain in human powered flywheel motor by using quick return mechanism having ratio one. *Int J PURE Appl Res Eng Technol* 03(09):452–460
25. Kumar Dubey H, Singh MP, Modak JP et al. A review on the advancement of human powered flywheel motor (HPFM) in India and its application for rural empowerment. *Mater Today Proc.* <https://doi.org/10.1016/j.matpr.2020.04.533>
26. Undirwade SK, Singh MP, Sakhale CN (2017) Formulation of mathematical model for processing time required for bamboo sliver cutting using HPFM. *Mater Today Proc* 4:10174–10178

27. Zakiuddin KS, Singh MP, Modak J (2019) Mathematical modeling & simulation of chaff cutter energized by human powered flywheel motor. In: IFToMM world congress 2019 on mechanism and machine science. *Advances in mechanism and machine science*, pp 3551–3559
28. Modak JP, Moghe S (1997) Comparison of various bi-cycle drive mechanism designed in the light of transmission angle optimization & J. Papadopolas hypothesis part-I. In: *Proceedings on international conference on mechanical transmission and mechanisms*, IFToMM, University of Tianjian, China, pp 1087–1091
29. Modak JP, Ketkar S (1987) Design of experimentation for comparison for various bicycle drive mechanisms. *Model Simul Control B AMSE Press Fr* 09(01):33–46
30. Modak JP, Chandurkar KC, Singh MP, Yadpanawar AG (1987) Experimental verification of various bi-cycle drive mechanism part I. In: *Proceedings of AMSE conference modeling and simulation Karlsruhe West Germany*, pp 139–160
31. Bhatkulkar HS, Modak JP (2014) Design & development of nursery fertilizer mixer energized by human powered flywheel motor. *Int J Res Emerg Sci Technol* 01(5):69–73
32. Zakiuddin KS, Modak JP (2012) Postharvest crop processing machine. *Agric Eng Int CIGR J* 14(3):99–104
33. Khope PB, Modak JP (2013) Design of experimental set-up for establishing an empirical relationship for chaff cutter energized by human-powered flywheel motor. *J Agric Technol* 9(4):779–791
34. Singh KP, Pardeshi IL, Kumar M, Srinivas K, Srivastva AK (2008) Optimisation of machine parameters of a pedal-operated paddy thresher using RSM. *Biosyst Eng Elsevier* 100:591–600
35. Moghe SM, Zakiuddin KS (2013) Design and development of turmeric polishing machine energized by human power flywheel motor—a past review. In: *1st international and 16th national conference on machines and mechanisms, iNaCoMM 2013*, pp 920–923
36. Modak J, Bapat A (1990) Methodology of minimizing extraneous variables of a manually driven fly-wheel motor and approach for mathematical analysis of results. *Model Simul Control B AMSE Press Fr* 29(03):55–64
37. Schenck JH (1961) *Reduction of variables dimensional analysis. Theories of engineering experimentation*. McGraw Hill Book Co., Newyork, pp 60–81
38. Chandak PA, Lende A, Modak J (2018) Modeling of human power flywheel motor through artificial neural network—a novel approach. *Procedia Comput Sci* 125:77–84

# Finite Element Analysis-Based Geometry Optimization of a Disk Brake



Faraz Ahmad, Vishvajeet, Viveksheel Yadav, and Shalini Chauhan

## 1 Introduction

In last few years, we see a tremendous increase in fast speed automobile vehicle. A braking system reduces the velocity of a vehicle by creating friction between the rotating disk and disk pad. This friction is further converted into heat energy. This heat reduces the performance of disk brake that is why, holes are provided to improve the heat dissipation from the disk. Structural strength of braking system plays an important role because, all the static and dynamic forces were sustained by the disk. In last few years, researchers worked on structural strength improvement.

Abhishikt et al. [1] designed two types of disk brake (drilled contour and ventilated disk rotor) using SolidWorks and simulated by Ansys. Both the disk rotors were analyzed on the basis of deformation, stress, and temperature distribution. Talati et al. [2] performed the heat conduction analysis for a disk brake. Uniform wear and uniform pressure were analyzed by Limpert and Newcomb models. Choi et al. [3] analyzed a disk brake with frictional heat generation using transient thermoelastic analysis. Jian et al. [4] compared two types of ventilated disk brake using Ansys. Furthermore, the heat transfer was enhanced by using heat pipe in disk brake. Dhir [5] compared three different types of disk brake to increase the heat dissipation from the disk. The simulation result was compared on the basis of deformation and temperature distribution. In his study, the weight of the disk brake was reduced and heat transfer was increased. Shahzamanian et al. [6] analyzed the disk brake subjected to thermal, bending, frictional, and body forces. His study concludes that, in thermomechanical responses, gradation of constitutive component is a significant parameter of disk brake. Babukanth et al. [7] analyzed the heat flux distribution and temperature variation between friction surface and contacting bodies. Influence of material on temperature was analyzed for frictional contact. Chelopo et al. [8] performed the structural analysis and compared the result of

---

F. Ahmad (✉) · Vishvajeet · V. Yadav · S. Chauhan  
Dev Bhoomi Institute of Technology, Dehradun, India

aluminum and mild steel, on the basis of stress and deformation. Chouhan et al. [9] analyzed the solid and ventilated disk on the basis of static structural and thermal analysis in Ansys workbench.

From the literature, it was found that there is lack of study on disk brake geometry optimization. So in present study, geometry was optimized by topology optimization module of Ansys. Present paper is divided into following sections, first; Introduction, second; Design of Disk Structure, third; FEA Simulation and Result, forth; Optimized Design Validation with Old Geometry, fifth; Thermal Analysis of Brake Disk, sixth; Conclusion.

## 2 Design of Disk Structure

To analyze and optimize the disk of a braking system, a CAD model was prepared in Catia (see Fig. 1). Figure 2 shows the mesh model of considered disk. Meshing was done with 2 mm of mesh size, and it contains 43,282 numbers of elements and 82,051 numbers of nodes, respectively. Table 1 shows the material properties of used material.

## 3 FEA Simulation of Disk

FEA is a process of solving the physical problem of engineering by simulation. Researchers use this method to reduce the number of physical prototypes or to optimize their design [10]. In present study, the designed model of body frame was imported to static structural module. In static structural module, deformation and

**Fig. 1** Disk geometry

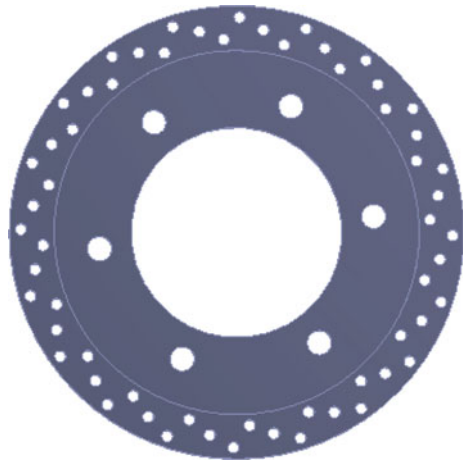




**Fig. 2** Meshing of disk

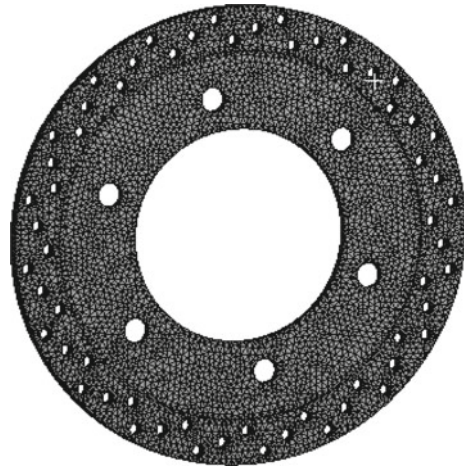


**Table 1** Material properties [3, 6]

Materials	Density (kg/m <sup>3</sup> )	Young's modulus (GPa)	Poisson ratio	Thermal conductivity (W/(mm K))
Carbon–Carbon	1800	50.2	0.3	0.05
Aluminum	2700	70	0.3	0.21

stress were calculated by applying the boundary condition. This boundary condition was fixed support, applied pressure by disk pad, and rotational velocity. Figure 3 shows the applied boundary condition, where total pressure was 1 MPa and rotational velocity was 100 rad/s. The disk was fixed from 6 positions which can be seen in Fig. 3.

The disk was tested for two different materials with same boundary conditions. Figures 4, 5, 6, and 7 show the total deformation and stress, respectively, for aluminum and carbon–carbon material made brake disk. To perform geometry optimization of disk, the simulation result of static structural was transferred to topology optimization module, (see Fig. 8). Topology optimization is a mathematical method that optimized the geometry by removing unwanted material, for a given set of boundary conditions.

Figure 9 shows the optimized result of disk, in which material was removed between each two fixed position. This optimization reduces the unwanted mass from the body frame without affecting the structural performance.



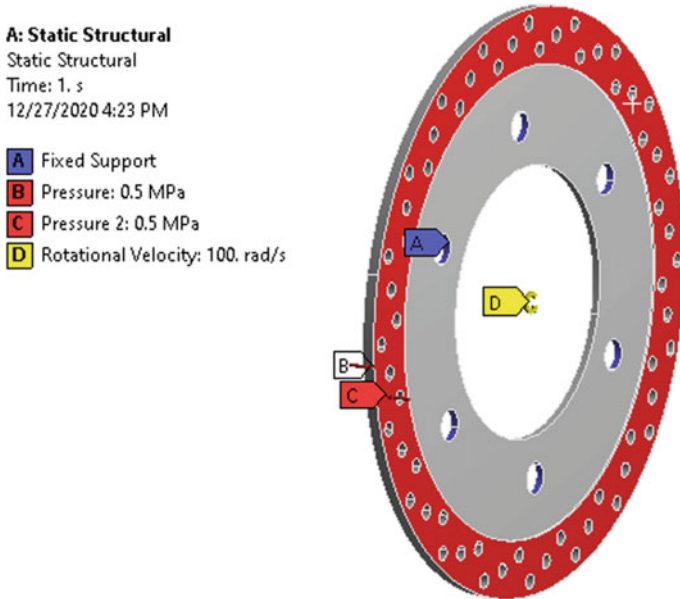


Fig. 3 All applied boundary conditions

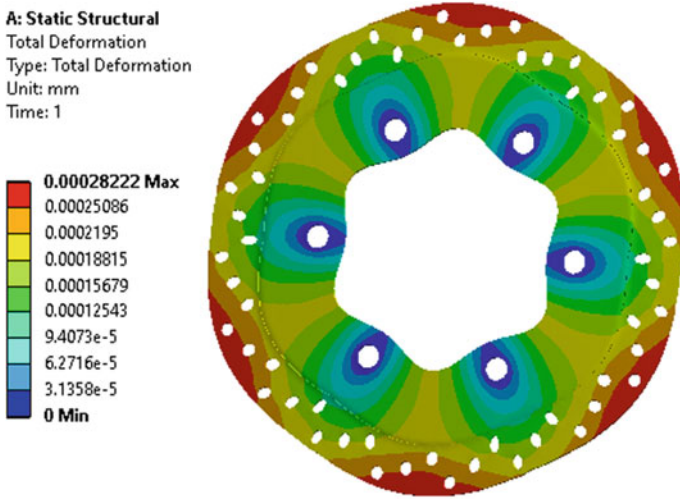


Fig. 4 Deformation in aluminum disk

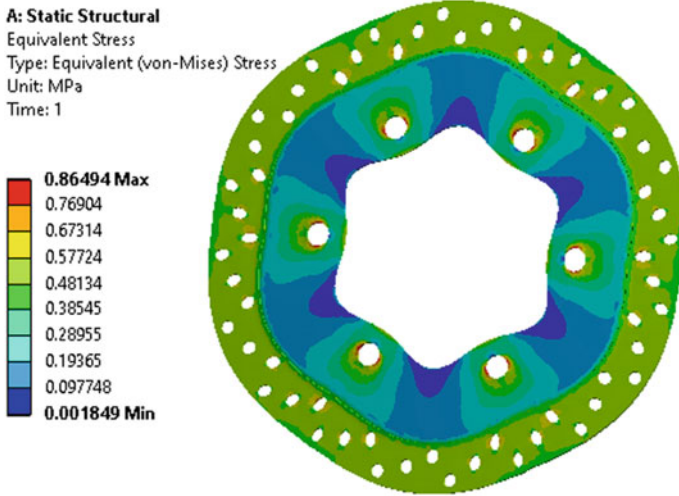


Fig. 5 Equivalent stress in aluminum disk

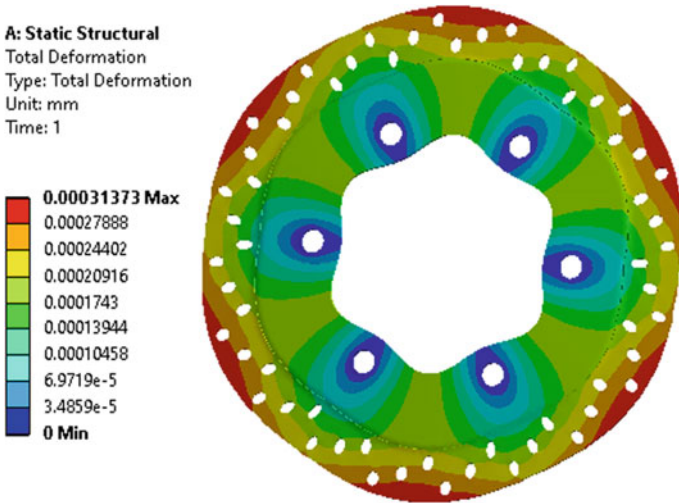


Fig. 6 Deformation in carbon-carbon disk

### 4 Optimized Design Validation with Old Geometry

Based on the optimized design produced by topology optimization, a 3D CAD model of brake disk was modeled in Catia. The new brake disk was made on the basis of optimized geometry obtained by the topology optimization. From Fig. 9, we know the position from where we can remove the unwanted mass. So the new

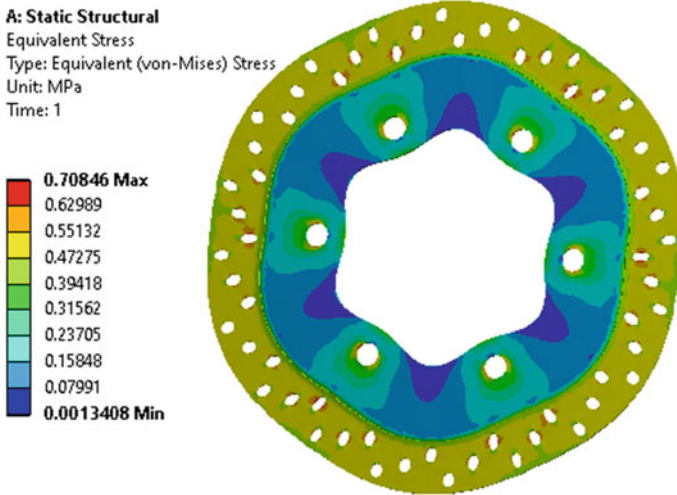


Fig. 7 Equivalent stress in carbon-carbon disk

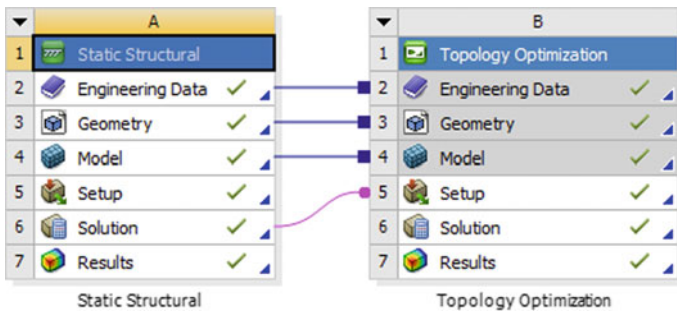


Fig. 8 Topology optimization process

CAD model of disk was designed by making circular hole at the place of unwanted portion. Figures 10 and 11 show CAD model and mesh model of new optimized disk, respectively.

The optimized disk was meshed with 2 mm of default mesh size and tested with same boundary condition (as in Sect. 3). Figure 12 shows all applied boundary condition on new optimized disk design. Figures 13 and 15, 14 and 16 show deformation and stress result of optimized disk in the form of color contour, where red color shows maximum and blue color shows minimum value.

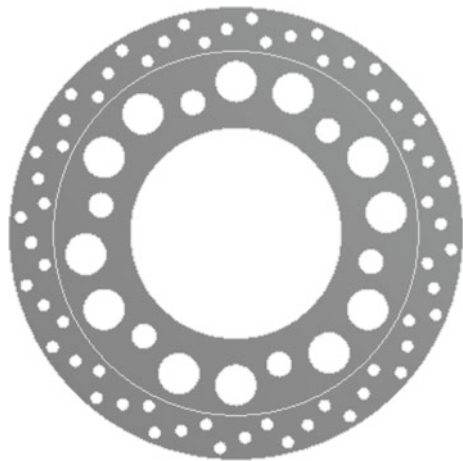
**B: Topology Optimization**  
 Topology Density  
 Type: Topology Density  
 Iteration Number: 8

- Remove (0.0 to 0.4)
- Marginal (0.4 to 0.6)
- Keep (0.6 to 1.0)



**Fig. 9** Optimized geometry by topology optimization

**Fig. 10** CAD model of new optimized design



## 5 Thermal Analysis of Brake Disk

In this section, the disk was again analyzed with temperature loading of 100 °C. Figures 17 and 18 show the applied boundary condition of old and optimized disk, respectively, where red color shows the applied temperature and yellow color shows the portion from where convection take place by air. 100 °C temperature was applied on the portion which was in contact with disk pad (see Figs. 17 and 18). The result of old and optimized brake disk was shown in Figs. 19, 20, 21, 22, 23, 24, 25 and 26. The temperature distribution of old and new aluminum material

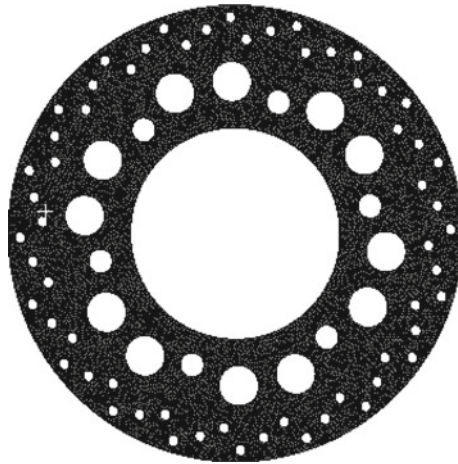


Fig. 11 Meshing of new optimized design

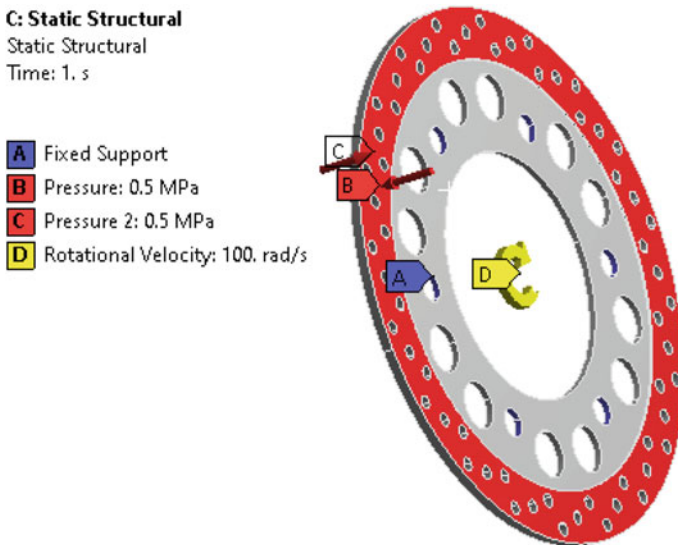


Fig. 12 Boundary condition of optimized design

based disk was demonstrated in Figs. 19 and 23, where as carbon-carbon based disk was shown in Figs. 21 and 25. Furthermore the Heat flux result of old and new aluminum based disk was demonstrated in Figs. 20 and 24, where as carbon carbon material based disk was shown in Figs. 22 and 26.

Tables 2 and 3 compare the results of old and new optimized geometry for aluminum and carbon-carbon material, respectively. From Tables 2 and 3, we can

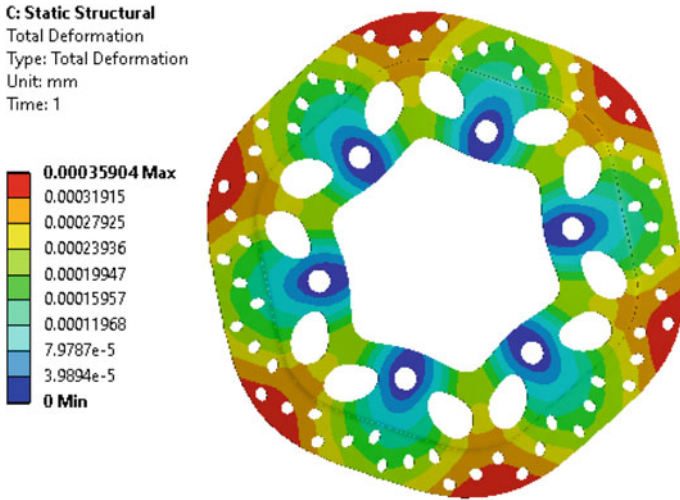


Fig. 13 Deformation in aluminum disk

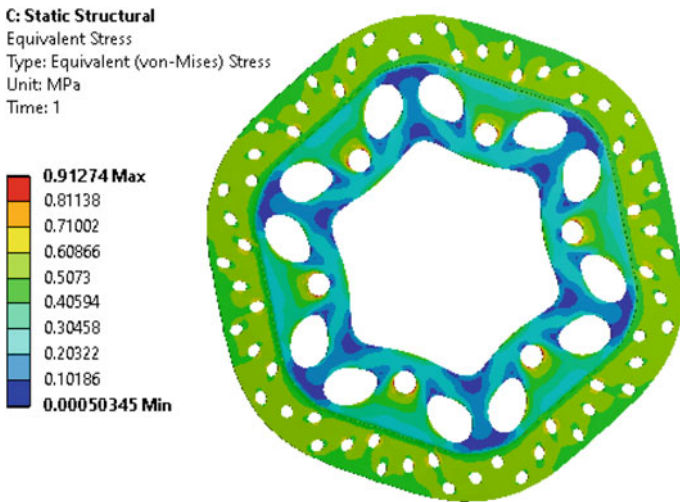


Fig. 14 Equivalent stress in aluminum disk

see that the mass is reduced to 10.7% and 10.5% for aluminum and carbon–carbon material made disk, under same loading condition, and the value of stress and deformation in both the disk is comparatively same. But the optimized disk made with carbon–carbon material gives better temperature drop (from 100 to 94.58 °C). Carbon–carbon made optimized disk can dissipate more heat from the disk surface as compared to aluminum made disk. Thus, it can be concluded that topology



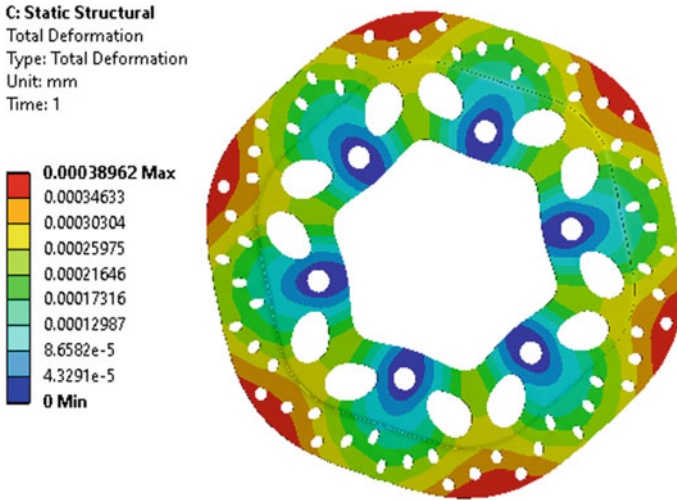


Fig. 15 Deformation in carbon-carbon disk

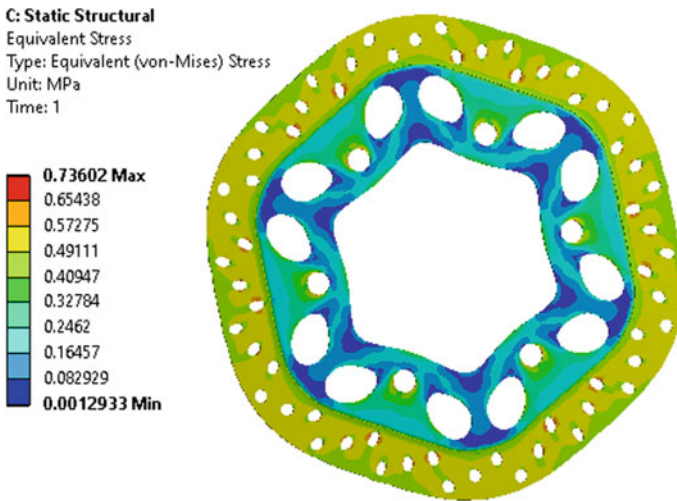


Fig. 16 Stress in carbon-carbon disk

optimization method reduces the weight within the permissible limits of geometry, without affecting the structural performance. Thermal analysis provides the material behavior under temperature loading and helps in finding out the best suited material.

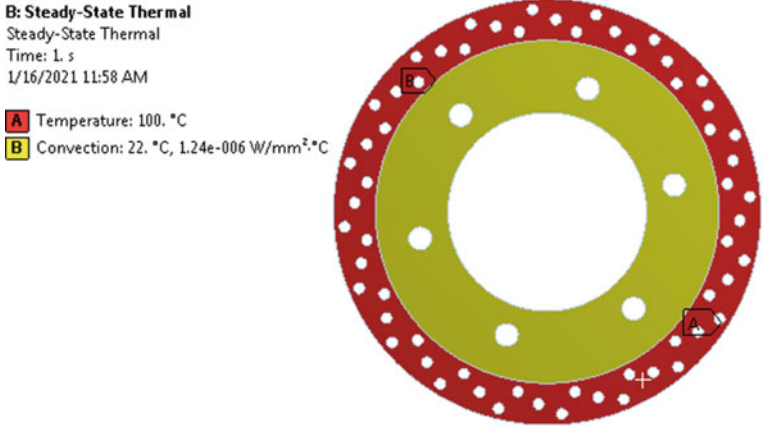


Fig. 17 Boundary conditions of old disk

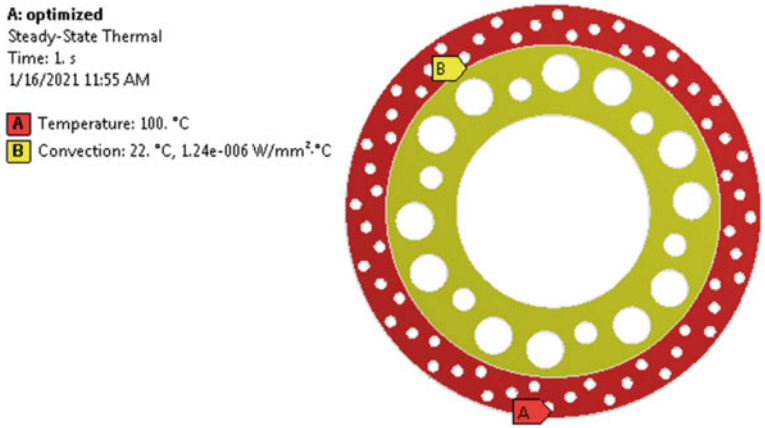


Fig. 18 Boundary conditions of optimized disk

## 6 Conclusion

A disk of a breaking system was designed in Catia and simulated in Ansys workbench. The disk was tested under static structural analysis to check the stress and deformation response with two different materials. The simulated results helped in optimizing the disk geometry by topology optimization module of Ansys. A new CAD model of disk was designed on the basis of optimized geometry and simulated for same boundary condition. The old and new optimize disk geometry gives comparatively same results of stress and deformation under given set of boundary condition. But carbon-carbon made optimized disk gives batter result in thermal



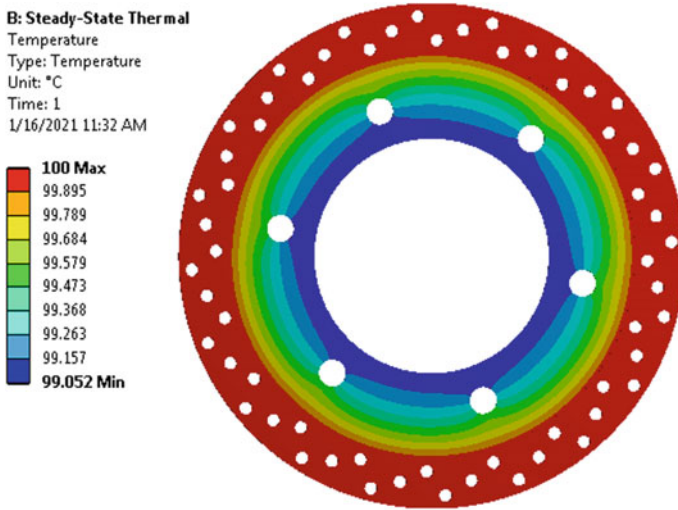


Fig. 19 Temperature distribution in aluminum disk

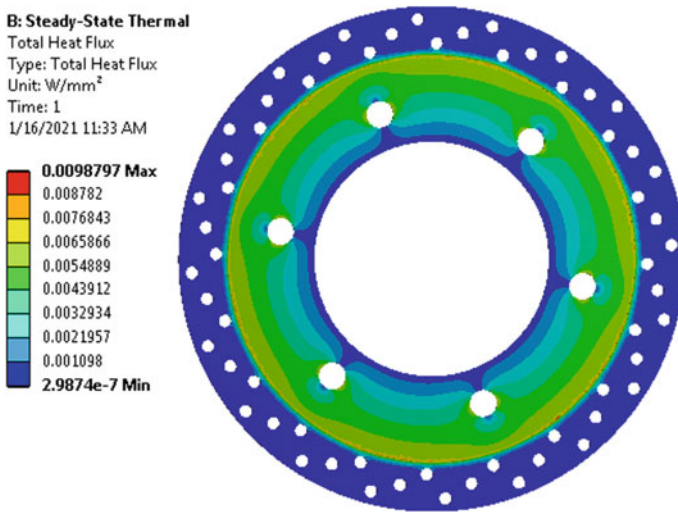


Fig. 20 Heat flux in aluminum disk

loading as compared to aluminum made disk. Thus, it can be concluded that new geometry can perform well with less mass in place of old geometry. Topology optimization reduces the mass by 10.7% and 10.5% for aluminum and carbon-carbon material made disk, respectively. The present study provides an optimization

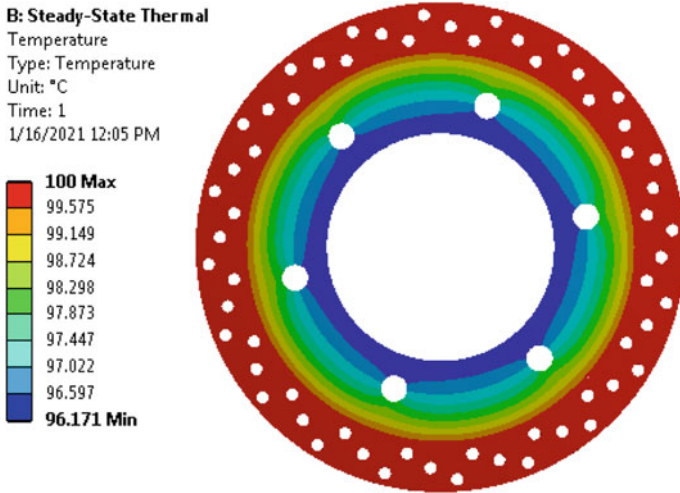


Fig. 21 Temperature in carbon-carbon disk

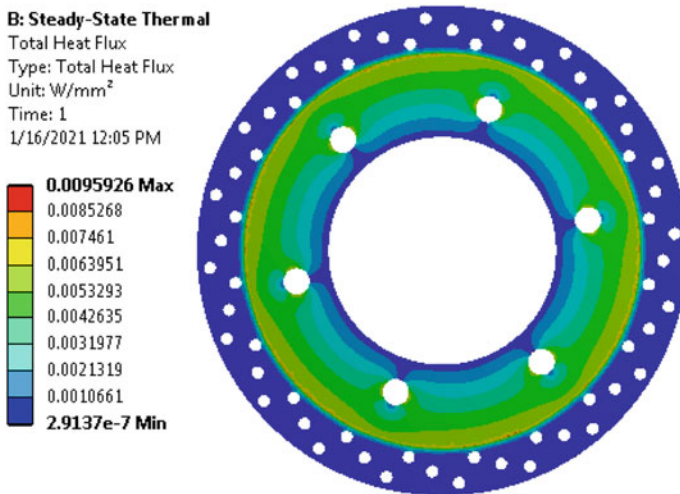


Fig. 22 Heat flux in carbon-carbon disk

technique to redesign the disk without affecting the structural performance. Furthermore, present study provides an optimization process to optimize the shape of component without affecting the performance. In case of brake disk, the optimized geometry can be performed well because the optimized geometry provides more area to dissipate heat in air.

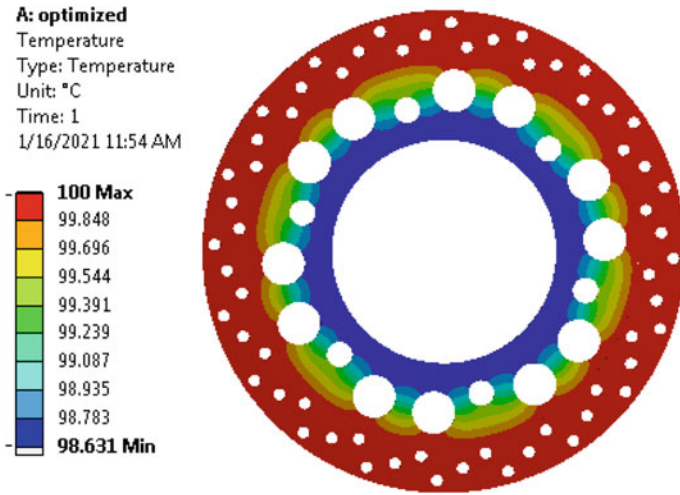


Fig. 23 Temperature in aluminum disk

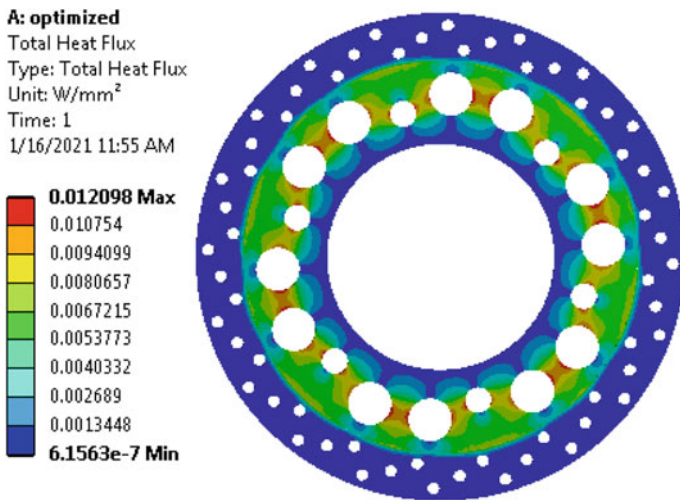


Fig. 24 Heat flux in aluminum disk

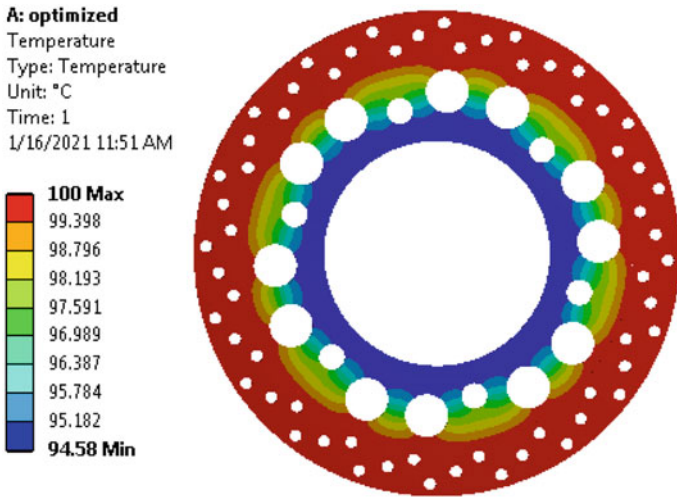


Fig. 25 Temperature in carbon-carbon disk

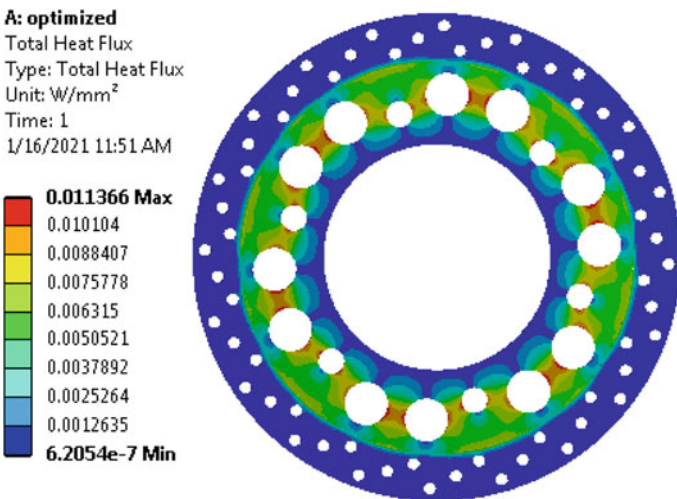


Fig. 26 Heat flux in carbon-carbon disk

Table 2 Result comparison for aluminum material disk

Brake disk	Mass (kg)	Total deformation (mm)	Stress (Mpa)	Heat flux	Temp °C	
					Max	Min
Old disk	0.5905	0.00028	0.8649	0.0098	100	99.05
Optimized disk	0.5273	0.00035	0.9127	0.0121	100	98.63

**Table 3** Result comparison for carbon–carbon material disk

Brake disk	Mass (kg)	Total deformation (mm)	Stress (Mpa)	Heat flux	Temp °C	
					Max	Min
Old disk	0.393	0.00031	0.7084	0.0096	100	96.17
Optimized disk	0.352	0.00038	0.7360	0.011	100	94.58

## References

1. Abhishikt CBNS, Ramachandran B, Alekhya GN (2020) Design and analysis of disk rotor brake under tribological behaviour of materials. *Mater Today Proc* 33:4298–4310
2. Talati F, Jalalifar S (2009) Analysis of heat conduction in a disk brake system. *Heat Mass Transf* 45(8):1047
3. Choi JH, Lee I (2004) Finite element analysis of transient thermoelastic behaviors in disk brakes. *Wear* 257(1–2):47–58
4. Jian Q, Wang L, Shui Y (2020) Thermal analysis of ventilated brake disc based on heat transfer enhancement of heat pipe. *Int J Therm Sci* 155:106356
5. Dhir DK (2018) Thermo-mechanical performance of automotive disc brakes. *Mater Today Proc* 5(1):1864–1871
6. Shahzamanian MM, Sahari BB, Bayat M, Mustapha F, Ismarrubie ZN (2010) Finite element analysis of thermoelastic contact problem in functionally graded axisymmetric brake disks. *Compos Struct* 92(7):1591–1602
7. Babukanth G, Teja MV (2012) Transient analysis of disk brake by using ansys software. *Int J Mech Ind Eng (IJMIE)* 2(1):21–25
8. Chelopo D, Gupta K (2020) Structural analysis on mild-steel and aluminium brake disk for application on belt conveyor. In: IOP conference series: materials science and engineering, vol 971, no 4. IOP Publishing, p 042056
9. Chouhan YS, Tiwari S (2020) Static structural and thermal analysis of disc brake pad model. In: IOP conference series: materials science and engineering, vol 810, no 1. IOP Publishing, p 012073
10. Kumar A, Jaiswal H, Ahmad F, Patil PP (2014) Dynamic vibration characteristics analysis of truck transmission gearbox casing with fixed constraint of vehicle frame based on FEA. *Procedia Eng* 97:1107–1115

# Modeling and Simulation of Electrical Discharge Machining—A Review



Abhishek Verma and Sudhanshu Kumar

## 1 Introduction

Electrical discharge machining (EDM) is a non-conventional machining process where the material is removed following several short discharges between the workpiece and electrode, which are submerged within a dielectric. This process of EDM is very complex and the physical aspect of material removal remains unclear [1]. In general, attempts are being made to form a more comprehensive model that can help us understand the physics of EDM better [2]. Modeling in EDM is primarily focused on finding the material removal rate based upon electrothermal mechanism [3]. In several models, approach is to find the temperature distribution within the workpiece, using single discharges, wherein assumptions are taken regarding the material properties of the workpiece. Many analytical and numerical models have been formulated to characterize EDM discharges [4].

Various models can be differentiated depending upon the definition assumed for heat source [5]. The simulation is done in these models to establish the shape of the crater and then later results are verified. The models employ various heat sources to obtain simulation results, and often the heat source is assumed to be a disk [6]. These simulated solutions still have been found to have considerable differences when compared to the original results for crater formations. Another characteristic distinguishing these models depends upon the material properties. Generally, the thermo-physical properties of the workpiece are considered not changing with temperature. Moreover, the majority of these models do not take into account the latent heat of vaporization or fusion. The main objective of writing this review paper is to reevaluate all the existing model literature in EDM process and further pave the way for future developing models. Though the information on various models is already present, unfortunately there are very few reviews available on modeling and simulation of EDM processes.

---

A. Verma (✉) · S. Kumar  
Department of Mechanical Engineering, MANIT, Bhopal, India

## 2 Modeling in Electro-Discharge Machining Process

In EDM, the workpiece and tool are submerged in a dielectric fluid separated by a small gap approximately in the range of about 5–10  $\mu\text{m}$  [7]. A spark generates due to a potential difference that breaks the dielectric medium. The high order of heat generation vaporizes some of the work and tool material due to which material removal takes place [8]. The spark is controlled due to which the material removal rate is according to the desired value. The complexity of this process is primarily due to the spark of the plasma, flushing condition of dielectric, dielectric medium, etc., and it becomes very tedious to observe the crater formation due to the spark formation [6, 9]. Thus to simplify calculations and estimate, the thickness of the layers formed in the crater modeling is done in the EDM process. Various models are modeled, and simulation is done to obtain the closest experimental values.

Modeling of EDM revolves around many aspects of the process. The models are broken down into generalized individual steps, from finding the location of discharge to estimating the input machining parameters [10]. A generalized model for electro-discharge machining is shown in Fig. 1. Usually, in the generalized model, problems are encountered in some steps, and thus, it is recommended to involve iterations. Therefore, it is impossible to formulate a simulation of the entire EDM process by copying all the steps in the generalized model. It is recommended to stimulate the specific part of the generalized model to gain a basic understanding of the mechanism involved in the EDM process, further optimization to be done related to machining parameters, and then planning the further process. In this review paper, the various models based on the generalized model pattern are discussed.

### 2.1 Simulation in EDM Process

The simulation in the EDM process is usually characterized by two aspects the simulation of the arc plasma and the simulation of the material removal. Simulation of EDM arc plasma is done to estimate the boundary conditions and hence establish the temperature distribution in the EDM process. However, it is very complicated to model the arc plasma even if the gas discharge is assumed as steady. Further, the simulation in material removal owing to a single discharge helps us to establish a result for the EDM process as it is assumed to be cumulative of many discharges. The real problem, however, remains with the concept of single discharge material removal mechanism not being entirely clear. Another simulation design is based on locating the location of discharge and deriving an algorithm to study it. Finally, the results are combined and the final geometry is established.

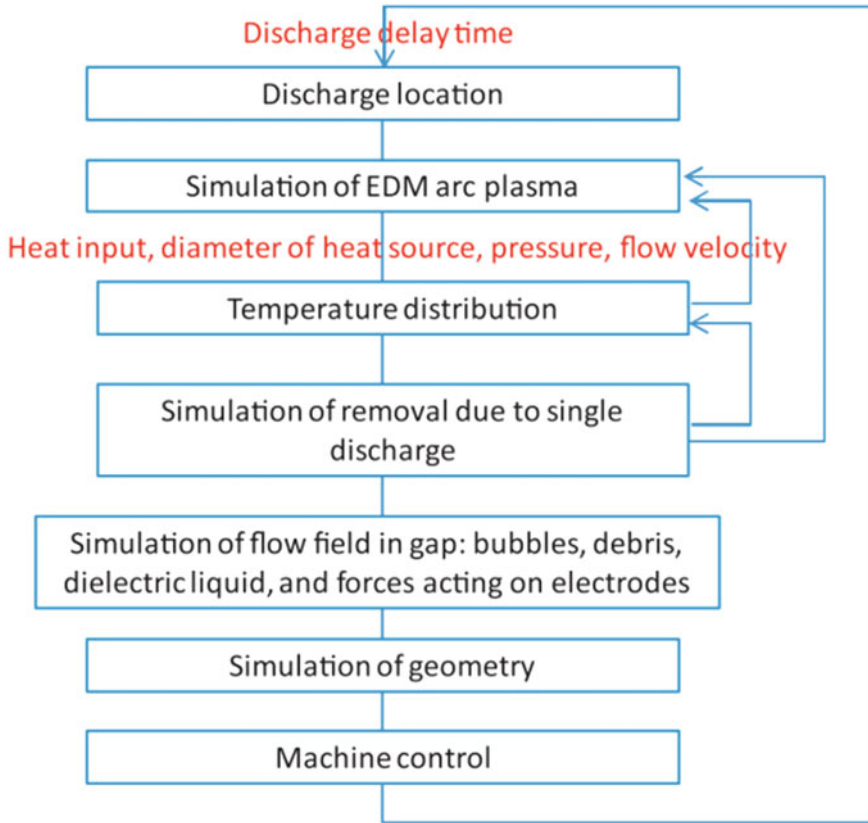


Fig. 1 Generalized model used in EDM process [11]

### 3 Various Types of Modeling in EDM Process

Since the early seventies models have been designed for electric discharge phenomena (plasma channel) and the mechanism of cathode and anode erosion in the EDM process, the two usually employed mechanisms to analyze the material removals are electromechanical analysis [12] for short discharge pulses (less than 5  $\mu$ s) and electrothermal analysis [13–15] for conventional EDM process which usually involves the removal of the material due to the intense plasma energy generated between the cathode and anode. The electrothermal EDM analysis is of primal importance today. The material removal rate in EDM is generally estimated based on an electrothermal mechanism [6, 12, 16, 17]. In most models, the temperature distribution is done based upon a specific modeled heat source, and the volume of material that achieves temperatures higher than the melting temperature is assumed to be removed.



The distinguishing factor between different models is the application of heat sources. A heat source is usually assumed to be a point heat source [18]. In several models, the heat source is assumed to be a disk and then used for modeling [19]. The use of a Gaussian distributed heat source is used to calculate the temperature distribution, and then a solution is formulated in the form of a partial differential equation [20]. Another parameter while EDM modeling is the shape of the crater. Analytical solutions are mostly derived that determine the crater and molten pool.

### ***3.1 Empirical Modeling in EDM Process***

The empirical method is employed to formulate a thermal model via an energy distribution ratio that will determine the crater geometry and help us find the material removal during the EDM process. The energy distribution is formulated by iterating a simulation model that will eventually enable us to find the energy distribution ratio, and the simulation process is repeated until the values of the simulation are close enough to the actual values [5]. Use of these empirical methods has been employed in both micro and macro EDM to evaluate the energy distribution ratio [21]. The empirical methods, however, are a little less reliable when compared to the temperature-rising methods [22]. Jeswani et al. [23] for their 3-D empirical EDM model used a dimensional analysis approach considering pulse on time, spark frequency, gap current, gap voltage, and material properties as input parameters to find out the wear of the tool.

Van Dijck et al. [24] computed the temperature distribution in the plasma channel and the surface of electrodes to form a temperature-based empirical model for EDM. The figure shown was used to evaluate the melting volume per pulse at both electrodes. This volume found from the figure is then used in reference to Pappus–Guldin theorem, and the solid volume generated is found. Further, an FEA model was also formulated to estimate the surface roughness. Various thermo-physical models were formed in EDM, a thermal–structural model was formulated to study the relation between the process variables and the output machining parameters such as MRR, tool wear, and retained stresses [25]. A model formulation was done based on understanding the EDM plasma channel formed in the heat flux during the process [26]. A more realistic numerical model is formulated based on the thermal analysis, where the analysis is done on a small portion of the workpiece around the region of spark. The small portion is assumed to be cylindrical, and the boundary conditions are evaluated using the Gaussian distribution of heat. The boundary conditions as shown in Fig. 2 are solved using FEM software Ansys [27]. The properties of the materials including thermal conductivity, specific heat, and density were taken into account while solving the boundary conditions. The simulation results were used to obtain the crater and temperature distribution. The material removal rate was evaluated using Eq. 1.

$$MRR = \{(C_v \times 60)/(T_{on} + T_{off})\} \tag{1}$$

where  $C_v$ —Volume of the cavity above melting point temperature in  $mm^3$ ,  $T_{on}$ —Pulse on time in  $\mu s$ , and  $T_{off}$ —is Pulse off time in  $\mu s$  and MRR unit is  $mm^3/min$ .

### 3.2 Semiempirical Modeling in EDM Process

Researchers developed several semiempirical models that would help us evaluate material removal rate, surface finish, and wear of the tool using the design of experiments. Patel et al. [28] designed the anode erosion empirical EDM model that used Gaussian distributed heat flux as the basis to evaluate the boundary conditions at the anode. A very unique approach to formulating an empirical EDM model via an artificial neural network was established by Gopal and Rajurkar [29]. Tsai and Wang [30] formulated the artificial neural model based on MRR and then compared the results to the actual experiments and found them to be in order. Machining parameters, namely the tool radii, depth of offset, duration of the pulse, peak current, depth of cut, were considered. Further, the ANN model was verified to give better and faster results compared to other models (Fig. 3).

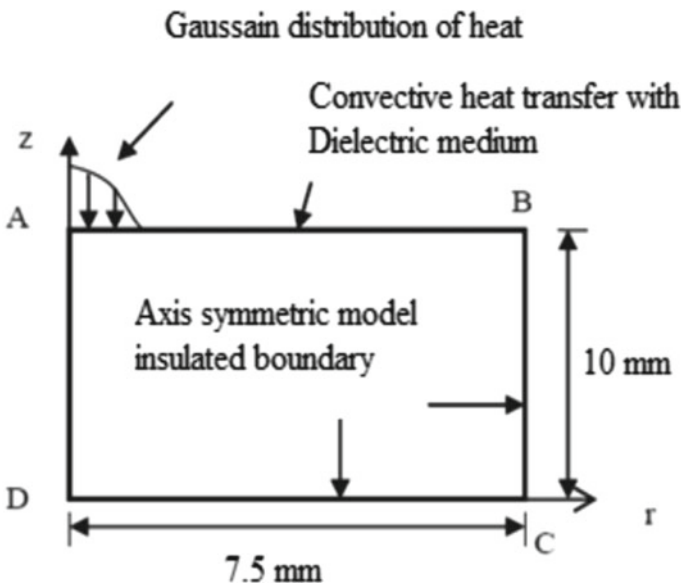


Fig. 2 Boundary conditions subjected to the workpiece [27]

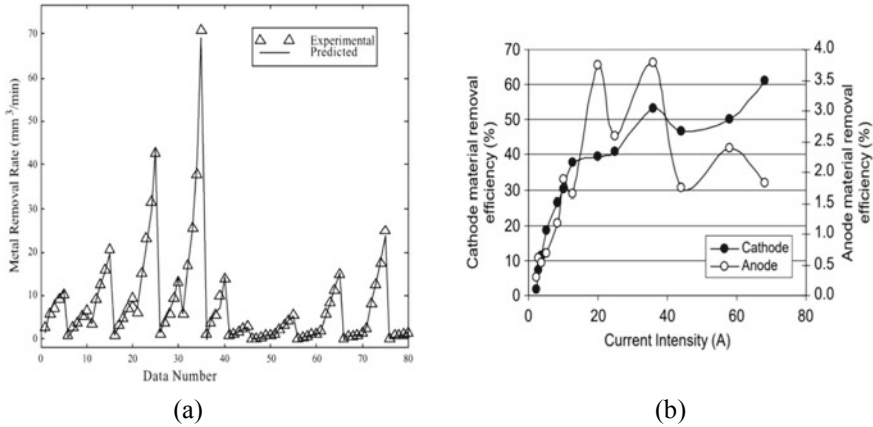


Fig. 3 Material removal rate results in (a) ANN model (b) anode erosion model [28, 29]

### 4 Conclusions

In conclusion, the empirical and semiempirical models discussed had obtained the best simulation results when they were did not assume the work material to be homogenous and the material properties were considered temperature-dependent. In addition to this, the latent heats of fusion and vaporization had a major involvement in the simulation results. The various empirical models which were based on thermal analysis have a limited scope of applicability, as they assume the spark radius to be a constant; further, the heat source is reduced to a point and thermal properties are assumed for homogenous and isotropic materials for work/tool materials. Thus, there remains a further need for developing a more realistic and concise mathematical model for thermal analysis in EDM process which can help us predict and analyze the crater more accurately by modifying the assumptions and obtaining precise experimental values. Finally, a good correlation between simulation and experimental results can be established by using a time-dependent heat source and taking into account the temperature-dependent material properties and the latent heats of fusion and vaporization.

**Acknowledgements** This research is conducted with the support of Seed Money Funds (No. Dean (R&C) 19/1015) and DST-SERB under start up-research grant (SRG/2020/000675). The authors are thankful to the agencies for supports.

## References

1. Kumar S, Verma A (2020) Surface modification during electrical discharge machining process—a review. *Mater Today Proc.* <https://doi.org/10.1016/j.matpr.2020.08.596>
2. Yeo SH, Kurnia W, Tan PC (2008) Critical assessment and numerical comparison of electro-thermal models in EDM. *J Mater Process Tech* 203(1–3):241–251. <https://doi.org/10.1016/j.jmatprotec.2007.10.026>
3. Tariq Jilani S, Pandey PC (1982) Analysis and modelling of edm parameters. *Precis Eng* 4 (4):215–221. [https://doi.org/10.1016/0141-6359\(82\)90011-3](https://doi.org/10.1016/0141-6359(82)90011-3)
4. Spur G, Schönbeck J (1993) Anode erosion in wire-EDM—a theoretical model. *CIRP Ann* 42 (1):253–256. [https://doi.org/10.1016/S0007-8506\(07\)62437-8](https://doi.org/10.1016/S0007-8506(07)62437-8)
5. DiBitonto DD, Eubank PT, Patel MR, Barrufet MA (1989) Theoretical models of the electrical discharge machining process, I. A simple cathode erosion model. *J Appl Phys* 66 (9):4095–4103. <https://doi.org/10.1063/1.343994>
6. Yeo S, Kurnia W, Tan P (2007) Electro-thermal modelling of anode and cathode in micro-EDM. *J Phys D Appl Phys* 40:2513. <https://doi.org/10.1088/0022-3727/40/8/015>
7. Hinduja S, Kunieda M (2013) Modelling of ECM and EDM processes. *CIRP Ann* 62(2):775–797. <https://doi.org/10.1016/j.cirp.2013.05.011>
8. Liao Y-S, Chen S-T, Lin C-S (2004) Development of a high precision tabletop versatile {CNC} wire-{EDM} for making intricate micro parts. *J Micromech Microeng* 15(2):245–253. <https://doi.org/10.1088/0960-1317/15/2/001>
9. Kunieda M, Lauwers B, Rajurkar KP, Schumacher BM (2005) Advancing EDM through fundamental insight into the process. *CIRP Ann* 54(2):64–87. [https://doi.org/10.1016/S0007-8506\(07\)60020-1](https://doi.org/10.1016/S0007-8506(07)60020-1)
10. “3404397 @ [www.biblio.com](http://www.biblio.com)” (Online). Available <https://www.biblio.com/micromachining-of-engineering-by-mcgeough-j-a/work/3404397>
11. Shao B (2015) Modeling and simulation of micro electrical discharge machining process
12. Masuzawa T (2000) State of the art of micromachining. *CIRP Ann* 49(2):473–488. [https://doi.org/10.1016/S0007-8506\(07\)63451-9](https://doi.org/10.1016/S0007-8506(07)63451-9)
13. Ho KH, Newman S (2003) State of the art electrical discharge machining (EDM). *Int J Mach Tools Manuf Des Res Appl (Int J Mach Tools Manuf)* 43:1287–1300. [https://doi.org/10.1016/S0890-6955\(03\)00162-7](https://doi.org/10.1016/S0890-6955(03)00162-7)
14. Li L, Guo YB, Wei XT, Li W (2013) Surface integrity characteristics in wire-EDM of Inconel 718 at different discharge energy. *Procedia CIRP* 6:221–226. <https://doi.org/10.1016/j.procir.2013.03.046>
15. Altिंग L, Kimura F, Hansen HN, Bissacco G (2003) Micro engineering. *CIRP Ann* 52 (2):635–657. [https://doi.org/10.1016/S0007-8506\(07\)60208-X](https://doi.org/10.1016/S0007-8506(07)60208-X)
16. Dornfeld D, Min S, Takeuchi Y (2006) Recent advances in mechanical micromachining. *CIRP Ann* 55(2):745–768. <https://doi.org/10.1016/j.cirp.2006.10.006>
17. Qin Y et al (2010) Micro-manufacturing: research, technology outcomes and development issues. *Int J Adv Manuf Technol* 47(9):821–837. <https://doi.org/10.1007/s00170-009-2411-2>
18. Zahiruddin M, Kunieda M (2012) Comparison of energy and removal efficiencies between micro and macro EDM. *CIRP Ann Manuf Technol* 61:187–190. <https://doi.org/10.1016/j.cirp.2012.03.006>
19. Joshi SN, Pande SS (2010) Technical paper. *J Manuf Process* 12(1):45–56. <https://doi.org/10.1016/j.jmapro.2010.02.001>
20. Zhang Y, Liu Y, Shen Y, Li Z, Ji R, Wang F (2013) A new method of investigation the characteristic of the heat flux of EDM plasma. *Procedia CIRP* 6:450–455. <https://doi.org/10.1016/j.procir.2013.03.086>
21. Shao B, Rajurkar KP, Wu M (2014) Study of micro-EDM electro-thermal models by finite element method. In: 9th international conference micromanufacturing (ICOMM 2014)

22. Murali MS, Yeo S-H (2005) Process simulation and residual stress estimation of micro-electrodischarge machining using finite element method. *Jpn J Appl Phys* 44:5254–5263
23. Jeswani ML (1979) Dimensional analysis of tool wear in electrical discharge machining. *Wear* 55:153–161
24. Van Dijk FS, Dutre WL (1974) Heat conduction model for the calculation of the volume of molten metal in electric discharges. *J Phys D Appl Phys* 7:899
25. Mohanty CP, Sahu J, Mahapatra SS (2013) Thermal-structural analysis of electrical discharge machining process. *Procedia Eng* 51(NUiCONE 2012):508–513. <https://doi.org/10.1016/j.proeng.2013.01.072>
26. Jithin S, Raut A, Bhandarkar UV, Joshi SS (2018) FE modeling for single spark in EDM considering plasma flushing efficiency. *Procedia Manuf* 26:617–628. <https://doi.org/10.1016/j.promfg.2018.07.072>
27. Mehta HN (2015) Modeling of electrical discharge machining process, vol 4, no 06, pp 153–156
28. Eubank PT, Patel MR, Barrufet MA, Bozkurt B (1993) Theoretical models of the electrical discharge machining process, III. The variable mass, cylindrical plasma model. *J Appl Phys* 73:7900
29. Gopal I, Rajurkar KP (1992) Artificial Neural Network approach in modelling of EDM process. *Intell Eng Syst Art Neural Netw* 2:845–850
30. Tsai K-M, Wang P-J (2001) Comparisons of neural network models on material removal rate in electrical discharge machining. *J Mater Process Technol* 17:111–124

# Structural, Optical and Magnetic Properties of Cobalt Ferrite Nanomaterials, Synthesized by a Green Technological Approach Using Lemon Juice



Shashank Bhushan Das, Vivek Kumar, Rakesh Kumar Singh, Nishant Kumar, Harendra Kumar Satyapal, and Atul Jyoti

## 1 Introduction

Ferrite nanomaterials are being used in various applications [1–5]. From a vital research view of Mathew, the nanostructured ferrites offer an exceptional system to study the magnetism at the nano level [1]. Cobalt ferrite offers enhanced coercivity, reasonable magnetization and huge magneto crystalline anisotropy [2]. These also exhibit superparamagnetic behaviour due to large crystalline anisotropy, if they are made significantly small in size [3]. Due to the coupling of electron at  $\text{Co}^{2+}$  lattice position, huge magnetic anisotropy is observed. In case of bulk  $\text{CoFe}_2\text{O}_4$ , cubic anisotropy dominates as the orbital contribution is not satisfied by the lattice [4].

The properties (electrical and magnetic) of bulk ferrite are highly dependent on grain size, porosity and dispersal of metal cations within the lattice sites [5]. Nanostructured cobalt ferrite exhibits very good properties (structural and magnetic) in comparison to the bulk [6]. The extraordinary magnetic behaviour in cobalt ferrites arises from surface spin disorder, reported in some recent investigations [7]. Amiri et al. prepared cobalt ferrite and its nanocomposite at different temperatures and investigated the magnetic behaviour of ferrite and proposed that the increased particle size may lead to improved magnetization [8]. Rajendran et al. examined the magnetic nature of  $\text{CoFe}_2\text{O}_4$  and concluded that structure and size strongly affect the magnetic properties [9]. Miao et al. studied the magnetic behaviour of plasma sprayed  $\text{CoFe}_2\text{O}_4$  and noticed a significant enhancement in the magnetic parameters like  $M_s$ ,  $H_c$  and others [10]. Ai and others discovered that magnetic separation is considered a quick and effective technique for separating magnetic particles [11]. Baldi et al. also studied the variation of magnetic properties

---

S. B. Das · V. Kumar · R. K. Singh (✉) · N. Kumar · H. K. Satyapal · A. Jyoti  
Aryabhatta Centre for Nanoscience and Nanotechnology, Aryabhatta Knowledge University,  
Patna 800001, India

of  $\text{CoFe}_2\text{O}_4$  materials with the controlled size and the surface state [12]. The lowering of magnetic saturation may be credited to the variation in spin-cycloidal magnetic moment as explained in previous research works [13]. The objective of the present research is to synthesize nanostructured cobalt ferrite by a green technological approach using metal cations ( $\text{Fe}^{3+}$ ,  $\text{Co}^{2+}$ ) and lemon juice precursors at different annealing temperatures and studied their structural, magnetic and optical properties.

## 2 Materials and Method

### 2.1 Method of Synthesis of $\text{CoFe}_2\text{O}_4$

To synthesize cobalt ferrite, Cobalt (II) Nitrate hexahydrate ( $\text{Co}(\text{NO}_3)_2 \cdot 6\text{H}_2\text{O}$ ), Sigma-Aldrich), Iron (III) Nitrate nonahydrate ( $\text{Fe}(\text{NO}_3)_3 \cdot 9\text{H}_2\text{O}$ , Merck) and fresh lemon juice was taken. Fresh Lemon juice contains highest percentage of hydrated citric acid among all citrus fruits. Hence, it is chosen to get maximum yield of  $\text{CoFe}_2\text{O}_4$  nanomaterials. The synthesis of  $\text{CoFe}_2\text{O}_4$  was performed via solution combustion route (sol-gel) using lemon juice as a source of citric acid. Cobalt nitrate ( $\text{Co}(\text{NO}_3)_2 \cdot 6\text{H}_2\text{O}$ ) and iron (III) nitrate ( $\text{Fe}(\text{NO}_3)_3 \cdot 9\text{H}_2\text{O}$ ) were taken in 1:2 molar ratio and mixed with deionized water till properly dissolved. After this, fresh lemon juice was poured into solution containing  $\text{Fe}^{3+}$  and  $\text{Co}^{2+}$  ions and pH was made 7 by adding 25%  $\text{NH}_3$  solution. The obtained solution was then continuously stirred at 100 °C to get viscous gel which was further dried in the oven. The obtained blackish material was heat treated between 400 and 750 °C to get cobalt ferrite nanomaterials. The flow chart of synthesis procedure is shown in Fig. 1.

### 2.2 Characterization

The heat-treated materials were further subjected to various characterizations like X-Ray diffraction, FTIR spectroscopy, UV-Vis spectroscopy, PL spectroscopy and Scanning electron microscopy and vibrating sample magnetometer (VSM). The phase formation of  $\text{CoFe}_2\text{O}_4$  was confirmed by XRD with  $\text{Cu-K}\alpha$  radiation ( $\lambda = 1.5405 \text{ \AA}$ ) (Make: Bruker, Germany). The molecular bonds were examined by FTIR spectroscopy (PerkinElmer, UK, model, make). Optical property examination was performed by double beam UV-Vis spectrophotometer (*LABTRONICS: LT-2200*) and PL spectroscopy (Make: Perkin Elmer, UK) for a better understanding of applications. The surface morphology was inspected using SEM (Make: Carl Zeiss Microscopy Ltd., UK). Magnetic measurements were recorded by VSM (Lakeshore, 7400).

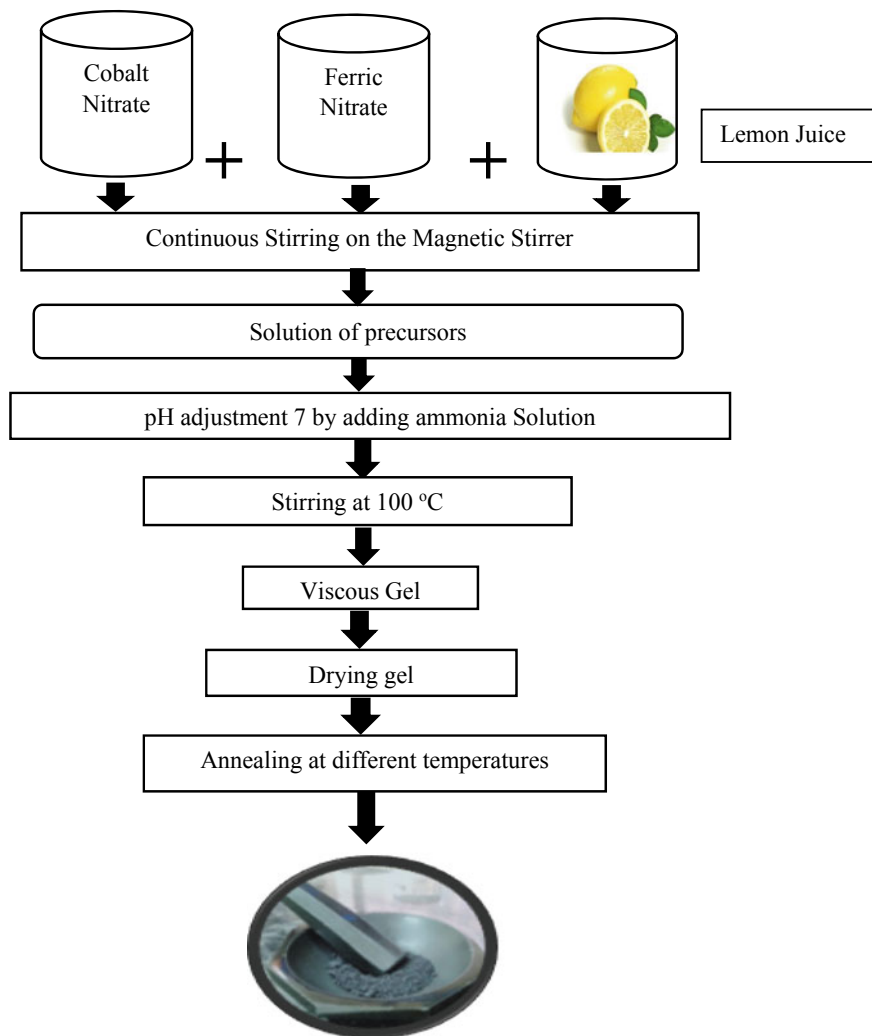


Fig. 1 Flow chart of synthesis process

## 3 Results and Discussion

### 3.1 Structural Analysis

#### 3.1.1 XRD Analysis

The phase identification of annealed material was executed by XRD. The XRD pattern of annealed cobalt ferrite are illustrated in Fig. 2. Figure 2a illustrates XRD



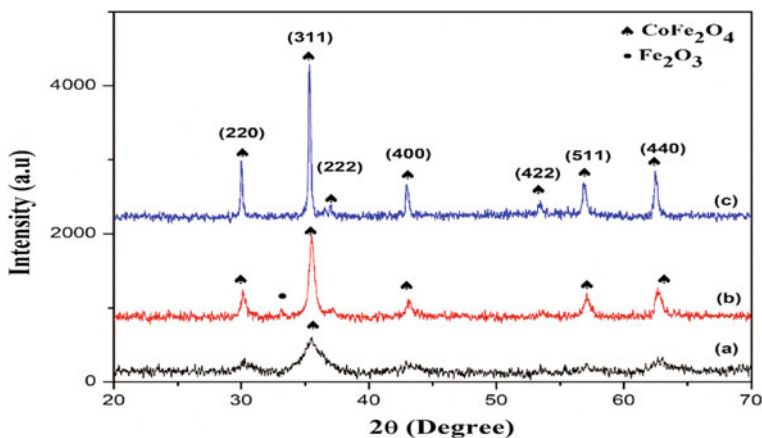
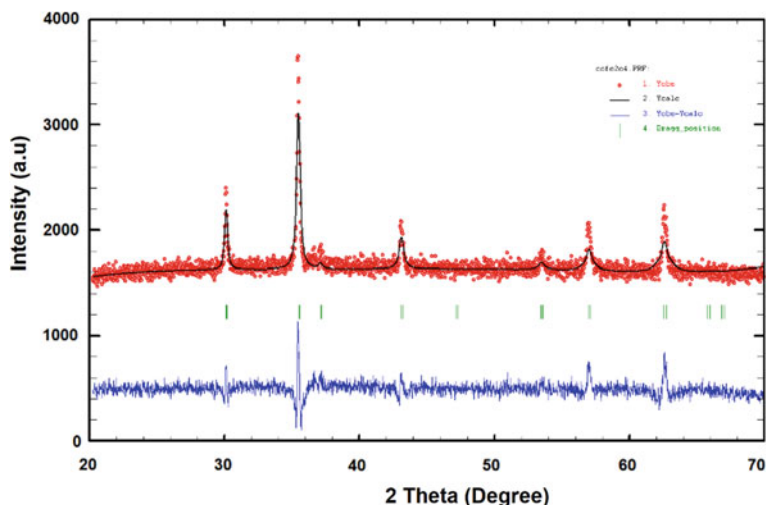


Fig. 2 XRD of annealed sample at **a** 400 °C for 1 h **b** 550 °C for 2 h **c** 750 °C for 3 h

pattern of material annealed at 400 °C for 1 h, were some of the peaks of CoFe<sub>2</sub>O<sub>4</sub> were detected. This indicated that phase formation of CoFe<sub>2</sub>O<sub>4</sub> started at 400 °C using lemon juice as precursor. Various crystallographic parameters like  $2\theta$  and  $d$ -value were noticed to be 35.53° and 2.5245 Å, respectively. The crystallographic structure of ceramics was identified as hexagonal with R-3 m space group having COD ID 1540973. In order to get complete phase formation and more crystallinity of cobalt ferrite, the annealing temperature was further increased. Figure 2b displays XRD spectra of heat-treated ceramics at 550 °C for 2 h. With gradual increase in annealing temperature, more crystalline peaks of CoFe<sub>2</sub>O<sub>4</sub> were observed along with some impurity phases of Fe<sub>2</sub>O<sub>3</sub> having crystallite size 17.34 nm. The XRD of CoFe<sub>2</sub>O<sub>4</sub> matched with COD ID 1533163. The impurity phases were further removed with rise in annealing temperature. Figure 2c demonstrates XRD pattern of sample annealed at 750 °C for 3 h where none of the impurity phases was observed. The structure changed from hexagonal to cubic structure having COD ID 1533163 with Fd-3 m space group. The  $d$  value and ( $hkl$ ) plane corresponding to highest intensity ( $2\theta = 35.49^\circ$ ) were noticed to be 2.5273 Å and (311), respectively. The lattice constants ( $a$ ) of cubic crystal system were evaluated by equation  $a = d[(h^2 + k^2 + l^2)]^{1/2}$  and found equal to 8.382 Å, which was near ideal values corresponding to COD ID 1533163. All experimental results clarify single phase formation of CoFe<sub>2</sub>O<sub>4</sub> with cubic crystal system has taken place. For proper peak refinement, we have used Rietveld analysis using FullProf software [14], which is displayed in Fig. 3. For calculating crystallite size, Scherrer's equation [15] was used, which is given as:

$$t = \frac{0.9\lambda}{\beta \cos \theta}$$



**Fig. 3** Rietveld refinement of  $\text{CoFe}_2\text{O}_4$  prepared at  $750\text{ }^\circ\text{C}$  for 3 h

**Table 1** XRD parameters of  $\text{CoFe}_2\text{O}_4$  prepared at  $750\text{ }^\circ\text{C}$  for 3 h

S. No.	$2\theta$ (Degree)	$d$ ( $\text{\AA}$ )	( $hkl$ )	Intensity ( $I/I_0$ )
1	30.13	2.9641	220	292.34
2	35.49	2.5273	311	1000.00
3	37.09	2.4219	222	63.23
4	43.13	2.0959	400	200.61
5	53.53	1.7104	422	82.54
6	57.04	1.6134	511	228.65
7	62.65	1.4817	440	341.20

where ' $t$ ' is the crystallite size and  $\beta$  is FWHM. All the corresponding  $2\theta$ ,  $d$ -values and ( $hkl$ ) planes are given in Table 1 in detail. Average crystallite size was calculated 41 nm approximately. The small crystallite size of prepared ceramics contributes towards some promising optical properties which have been explained in Sect. 3.4. Furthermore, to calculate crystallite size and strain we used Williamson-Hall plot as displayed in Fig. 4a, b respectively. The calculated size from W-H plot found in agreement with crystallite size obtained above, i.e.  $18 (\pm 1\text{ nm})$  and  $(38 \pm 1\text{ nm})$  for respective samples annealed at  $550$  and  $750\text{ }^\circ\text{C}$ . The value of strain was also evaluated, which increases from  $1.62 \times 10^{-3}$  to  $2.38 \times 10^{-3}$  shown in Table 2. This study relates that annealing temperature plays a vital role in structural characterization. Here, crystallite size, strain value and lattice constant are increased, which is according to earlier reported works [16]. Also, beauty of the method is eco-friendly.

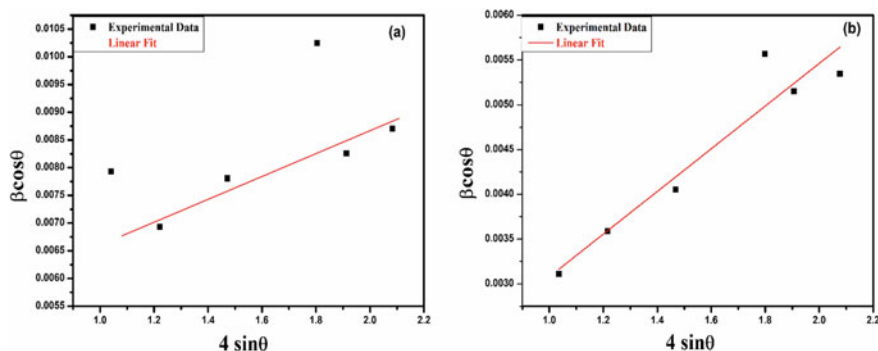


**Fig. 4** Williamson-Hall plot of  $\text{CoFe}_2\text{O}_4$  annealed at **a** 550 °C for 2 h **b** 750 °C for 3 h

**Table 2** Crystallographic parameters  $\text{CoFe}_2\text{O}_4$  annealed at 550 and 750 °C for 3 h

$\text{CoFe}_2\text{O}_4$	Crystallite size	Strain	Lattice constant (Å)
At 550 °C	18 ( $\pm 1$ ) nm	0.00162	8.3805
At 750 °C	38 ( $\pm 1$ ) nm	0.00238	8.382

### 3.1.2 Microstructure Analysis

Surface morphology of  $\text{CoFe}_2\text{O}_4$  was examined using SEM. We have chosen a sample prepared at 750 °C for microstructural analysis as it has highest crystallinity. The micrographs clearly indicate agglomerated and porous microstructures within cobalt ferrite in Fig. 5a–b. To estimate grain size of cobalt ferrite, histogram plot was drawn, which is depicted in Fig. 5c–d. Using corresponding histogram plot, the average grain size was evaluated 0.96  $\mu\text{m}$  approximately. The use of lemon juice as a precursor may contribute to enhanced porosity and agglomeration in present work [17]. Smaller and porous grains may contribute to some promising optical properties, which has been explained in optical properties measurement section.

## 3.2 FTIR Spectroscopy

Figure 6a–c represents FTIR spectra of  $\text{CoFe}_2\text{O}_4$  annealed at temperature 400°, 550° and 750 °C, respectively. All characteristic bands were recorded between 400 and 4000  $\text{cm}^{-1}$  and displayed in Table 3. The examination of molecular bonds reveal the presence of bands at 463  $\text{cm}^{-1}$ , 576  $\text{cm}^{-1}$ , 1104  $\text{cm}^{-1}$ , 1379  $\text{cm}^{-1}$ , 1639  $\text{cm}^{-1}$  and 3435  $\text{cm}^{-1}$ . The band at 463 and 576  $\text{cm}^{-1}$  is referred as Fe–O and Co–O stretching vibration, respectively. Fe–Co vibration band is present at 1104  $\text{cm}^{-1}$ . The symmetric vibration band near 1379  $\text{cm}^{-1}$  is associated with nitril

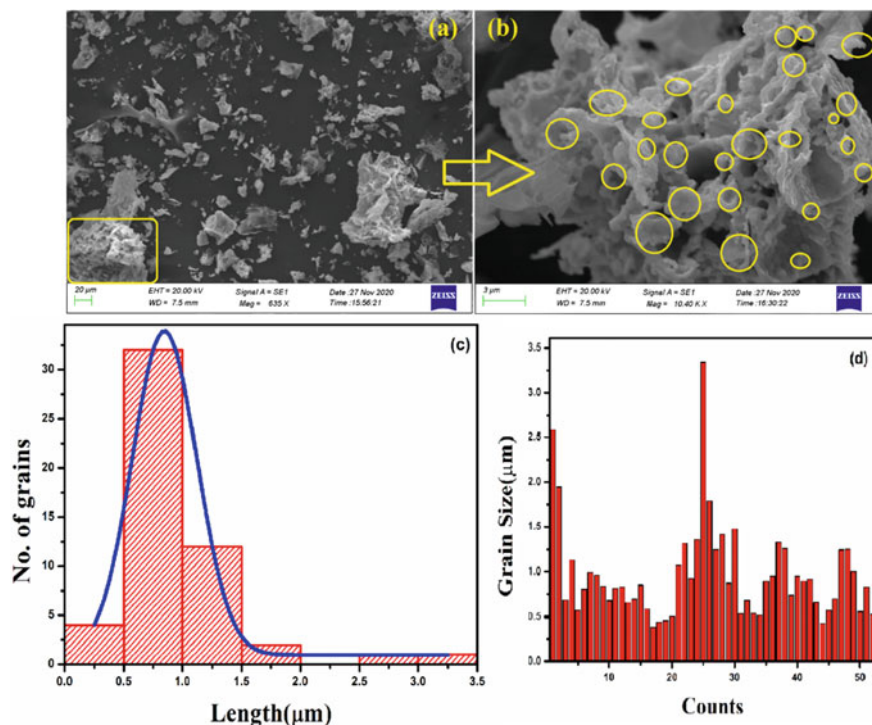


**Fig. 5** a–b SEM micrograph of  $\text{CoFe}_2\text{O}_4$  prepared at  $750^\circ\text{C}$  for 3 h and c–d grain size distribution for  $\text{CoFe}_2\text{O}_4$

groups ( $\text{NO}_3^{2-}$ ). The bands at  $1639\text{ cm}^{-1}$  and  $3435\text{ cm}^{-1}$  represent the vibrations (bending and stretching) of water molecules, respectively. No extra vibrations bands were detected in FTIR spectrum with usage of lemon as precursor. These results are according to earlier research works of  $\text{CoFe}_2\text{O}_4$  and confirm that pure phase formation of spinel cobalt ferrite has taken place [18, 19].

### 3.3 UV–Visible Spectroscopy

To study the absorption and band gap of cobalt ferrite, Uv–Vis spectroscopy of annealed sample was performed. The absorbance was studied between 300 and 500 nm wavelengths. Figure 7a illustrates the absorbance spectra of prepared ferrite at  $750^\circ\text{C}$ , which clearly indicates the prominent absorption near 325 nm. Band gap plays a significant role in defining electrical properties of nanomaterials. With the intention to evaluate these properties, band gap of  $\text{CoFe}_2\text{O}_4$  crystalline ceramic material was calculated by considering a direct allowed electronic transition. To

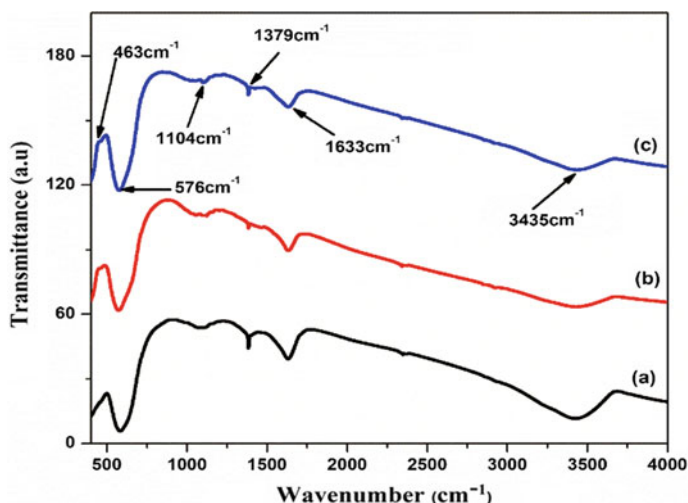


**Fig. 6** a–c FTIR spectra of cobalt ferrite at 400 °C for 1 h, 550 °C for 2 h and 750° for 3 h

**Table 3** FTIR vibration bands of prepared cobalt ferrite

Wavenumber (cm <sup>-1</sup> )	Vibration mode
463	Fe–O stretching
576	Co–O stretching
1104	Fe–Co vibration bond
1379	NO <sub>3</sub> <sup>2-</sup> symmetric vibration
1633	H <sub>2</sub> O bending vibration
3435	OH <sup>-</sup> stretching vibration

evaluate band gap ( $E_g$ ), Tauc equation  $\alpha h\nu = B(h\nu - E_g)^n$  was used, where  $\alpha$ ,  $h$ ,  $\nu$ ,  $B$ ,  $E_g$  and  $n$  represent absorption coefficient, Planck's constant, frequency, energy independent constant, band gap and index related to electronic transitions, respectively. For a direct allowed transition,  $n$  is taken to be 1/2. Considering  $n = 1/2$  in Tauc equation, plot of  $(\alpha h\nu)^2$  versus photo energy was obtained for  $\text{CoFe}_2\text{O}_4$  prepared at 750 °C as illustrated in Fig. 7b. The slope of this curve represents  $E_g$  of synthesized  $\text{CoFe}_2\text{O}_4$  which was found equal to 3.65 eV. The high band gap confirms the insulating behaviour of  $\text{CoFe}_2\text{O}_4$  nanomaterial. Uv-visible spectra of  $\text{CoFe}_2\text{O}_4$  prepared at 550 °C is been shown in Fig. 7c and corresponding  $E_g$  equal to 3.77 eV (Fig. 7d), possibly due to reduced size of ceramics at lower temperature as explained in Brus model [20]. The small size has already been confirmed in XRD analysis. Various research groups reported that  $E_g$  lies in between 1.8 and 2.5 eV [21, 22], but in this present research, high band gap was noticed as compared to other research, reported by some groups and this is to the best of our knowledge.

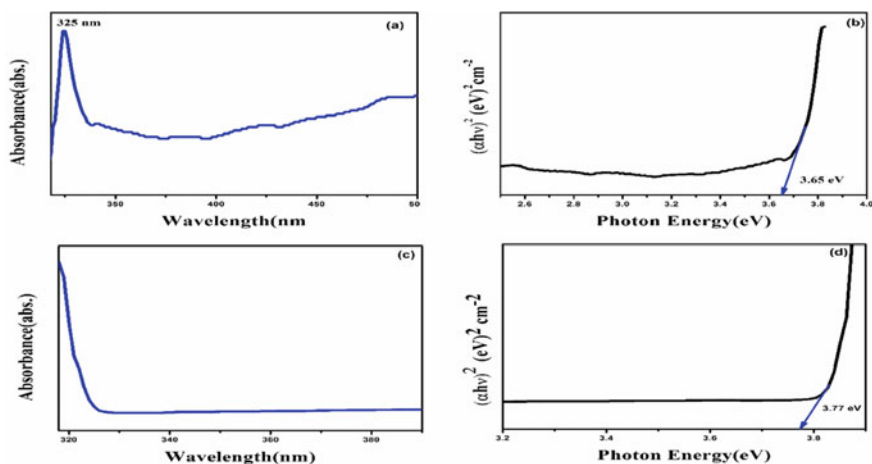


**Fig. 7 a–d** UV–Vis spectra and direct band gap of cobalt ferrite at 750 °C for 3 h and 550 °C for 2 h, respectively

### 3.4 PL Spectroscopy

The photoluminescence property of the cobalt ferrite was studied using PL spectrometer with excitation wavelength of 350 nm. Figure 8a–c represents PL spectra of treated sample at 400°, 550° and 750 °C, respectively. Here, emission peaks were noticed in visible range between 457 and 493 nm. It is quite evident from the plot that broad and intense peaks appeared for samples synthesized at 750 °C in comparison to other annealed samples in the present research work. The observed peaks in PL spectra clearly indicate strong blue emissions predominantly due to spinel structure of prepared material, which agrees with earlier research works. Here, existing broad bands are primarily due to charge transfer between octahedral sites and its surrounding oxygen atoms and also due to intra band gap defects (oxygen vacancies) [23].

### 3.5 Magnetic Measurements

Magnetic measurement was performed using VSM between –15 and 15 KOe. Effect of annealing on  $\text{CoFe}_2\text{O}_4$  nanomaterials were further studied. It has been observed from Fig. 9 that S-shaped curve is obtained indicating super paramagnetic behaviour. Furthermore, the magnetic parameters like saturation magnetization ( $M_s$ ),  $H_c$  (coercivity) and  $M_r$  (retentivity), etc. were calculated, which have been listed in Table 4. The saturation magnetization of  $\text{CoFe}_2\text{O}_4$  decreased from 400 to 750 °C as reported in earlier research works. With the increase in annealing

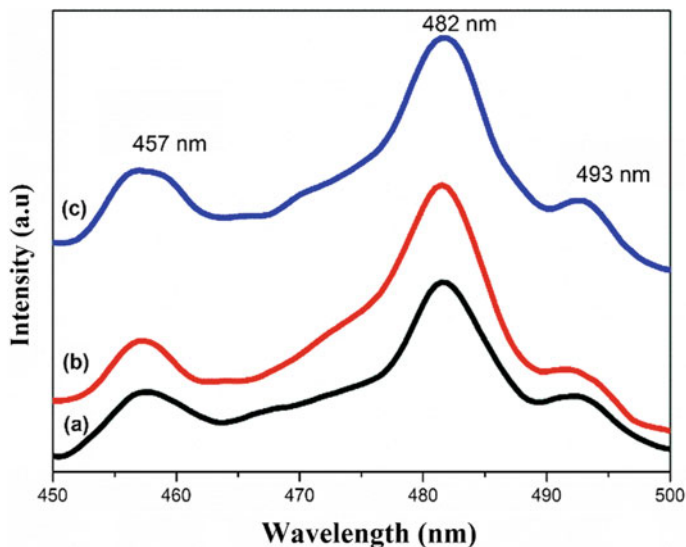


**Fig. 8** a–c PL spectra of cobalt ferrite at 400 °C for 1 h, 550 °C for 2 h and 750 °C for 3 h, respectively

temperature from 400 to 550 °C,  $M_s$  was found to increase, which might be due to the occurrence of  $\alpha$ - $\text{Fe}_2\text{O}_3$ . The enhancement of  $M_s$  may be credited to the strain created by the formation of  $\alpha$ -phase. Furthermore, the coercivity was noticed to increase with rise in annealing temperature. Coercivity ' $H_c$ ' depends on various different factors like micro strain, morphology, size distribution, magnetic domain structure, etc. Generally, we have seen that there is increase in  $M_s$  and decrease in coercivity, but finding in our case are different from earlier reported works [24].

High coercivity (2240 Oe) and high energy band gap (3.65 eV) are the important feature of this present research, which were not reported earlier to the best of our knowledge. This might be credited to generated strain and other structural parameters and lemon used as herbal ingredient. Thus, the materials can be used in magnetic recorders, microwave applications, etc.

## 4 Conclusions

Cobalt ferrite was successfully synthesized via green technological approach using lemon juice and metal nitrates as precursor materials between annealing temperatures 400–750 °C. XRD identified crystalline phase formation having cubic crystal structure with crystallite size 41 nm approximately. The lattice parameter of the corresponding crystal structure with Fd-3 m space group was calculated to be 8.382 Å. The molecular bending and stretching vibrations at  $463\text{ cm}^{-1}$ ,  $576\text{ cm}^{-1}$ ,

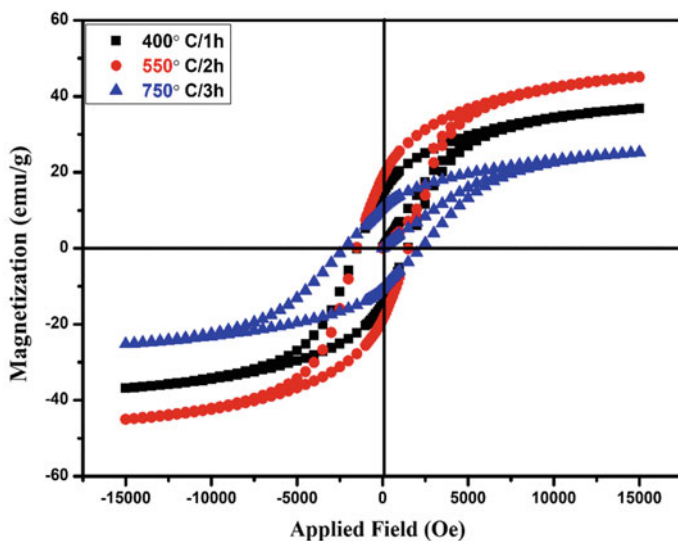


**Fig. 9** Magnetic measurement of cobalt ferrite

**Table 4** Magnetic parameters of cobalt ferrite

Magnetic parameters	At 400 °C for 1 h	At 550 °C for 2 h	At 750 °C for 3 h
Coercivity ( $H_c$ )/Oe	1525 Oe	1709 Oe	2240 Oe
Magnetization ( $M_s$ ) (emu/g)	37.35 emu/g	45.67 emu/g	25.25 emu/g

1104  $\text{cm}^{-1}$ , 1379  $\text{cm}^{-1}$ , 1633  $\text{cm}^{-1}$  and 3435  $\text{cm}^{-1}$  were identified by FTIR spectroscopy, which clearly indicates all characteristic bands of the concerned phase formation. Optical investigations with UV-Vis spectroscopy specified the absorbance at 325 nm. The direct band gap was also measured 3.65 eV considering corresponding absorbance by Tauc equation. A broad and strong emission between 457 and 493 nm was observed during photoluminescence studies. The blue emissions predominantly originated due to the charge transfer from regular octahedra to neighbouring oxygen atoms and also due to oxygen vacancies. Morphological characterization by SEM revealed agglomerated grain size distribution along with some porous microstructures. Grain size of SEM micrograph was calculated considering the histogram plot and found to be 0.96  $\mu\text{m}$ , approximately. Magnetic parameters were affected with the increase in annealing temperature. The coercivity was found to increase and the saturation magnetization was found to decrease. Thus, it may be concluded that, at 750 °C, the pure phase nanomaterial was synthesized having good electronic, optical and magnetic properties, which can be used in various electronic and magnetic industries. High coercivity (2240 Oe) and high energy band gap (3.65 eV) is the important feature of this present research, which were not reported earlier to the best of our knowledge. This might be credited to



generated strain and other structural parameters and lemon used as an herbal ingredient. Thus, the present study opens a new window for pure magnetic material, which can be produced with lemon juice as a chelating agent.

**Acknowledgements** Authors are grateful to Aryabhata Knowledge University, Patna and Dept. of Education under Govt. of Bihar for establishment and functioning of nanoscience and nanotechnology centre.

## References

1. Mathew DS, Juang RS (2007) An overview of the structure and magnetism of spinel ferrite nanoparticles and their synthesis in microemulsions. *Chem Eng J* 129:51–65
2. Veena Gopalan E, Joy PA, Al Omari IA et al (2009) On the structural, magnetic and electrical properties of sol–gel derived nanosized cobalt ferrite. *J Alloys Comp* 485:711–717
3. Koseoglu Y, Alan F, Tan M et al (2012) Low temperature hydrothermal synthesis and characterization of Mn doped cobalt ferrite nanoparticles. *Ceram Int* 38:3625–3634
4. Naik SR, Salker AV, Yusuf SM, Meena SS (2013) Influence of Co<sup>2+</sup> distribution and spin–orbit coupling on the resultant magnetic properties of spinel cobalt ferrite nanocrystals. *J Alloys Compd* 566:54–61
5. Jnaneshwara DM, Avadhani DN, Daruka Prasad B et al (2013) Electron paramagnetic resonance, magnetic and electrical properties of CoFe<sub>2</sub>O<sub>4</sub> nanoparticles. *J Magnet Mag Mater* 339:40–45
6. Sayed M, Gul M, Shah NS et al (2019) In-situ dual applications of ionic liquid coated Co<sup>2+</sup> and Fe<sup>3+</sup> co-doped TiO<sub>2</sub>: superior photocatalytic degradation of ofloxacin at pilot scale level and enhanced peroxidase like activity for calorimetric biosensing. *J Mol Liq* 282:275–285
7. Muscas G, Jovanović S, Vukomanovic M et al (2019) Zn-doped cobalt ferrite: tuning the interactions by chemical composition. *J Alloys Compd* 796:203–209
8. Amiri M, Salavati-Niasari M, Akbari A, Gholami T (2017) Removal of malachite green (a toxic dye) from water by cobalt ferrite silica magnetic nanocomposite: herbal and green sol-gel autocombustion synthesis. *Int J Hydrogen Energy* 42:24846–24860
9. Rajendran M, Pullar RC, Bhattacharya AK et al (2001) Magnetic properties of nanocrystalline CoFe<sub>2</sub>O<sub>4</sub> powders prepared at room temperature: variation with crystallite size. *J Magnet Mag Mater* 232:71–83
10. Miao Y, Zhu H, Gao P, Li L (2020) The effects of spraying power on microstructure, magnetic and dielectric properties of plasma sprayed cobalt ferrite coatings. *J Mat Res Tech* 9:14237–14243
11. Ai L, Huang H, Chen Z et al (2010) Activated carbon/CoFe<sub>2</sub>O<sub>4</sub> composites: facile synthesis, magnetic performance and their potential application for the removal of malachite green from water. *Chem Eng J* 156:243–249
12. Baldi G, Bonacchi D, Innocenti C et al (2007) Cobalt ferrite nanoparticles: the control of the particle size and surface state and their effects on magnetic properties. *J Magnet Mag Mater* 311:10–16
13. Sarkar K, Mukherjee S, Mukherjee S (2015) Structural, electrical and magnetic behaviour of undoped and nickel doped nanocrystalline bismuth ferrite by solution combustion route. *Proc App Ceram* 9:53–60
14. Kumar L, Kumar P, Narayan A, Kar M (2013) Rietveld analysis of XRD patterns of different sizes of nanocrystalline cobalt ferrite. *Int Nano Lett* 3:8
15. Mozaffari M, Amighian J, Darsheshdar E (2014) Magnetic and structural studies of nickel-substituted cobalt ferrite nanoparticles, synthesized by the sol–gel method. *J Magnet Mag Mater* 350:19–22

16. Sedlacik M, Pavlinek V, Peer P (2014) Tailoring the magnetic properties and magnetorheological behavior of spinel nanocrystalline cobalt ferrite by varying annealing temperature. *Petr Filip Dalton Trans* 43:6919–6924
17. Thi N, Loan T, Thi N et al (2019) CoFe<sub>2</sub>O<sub>4</sub> Nanomaterials: effect of annealing temperature on characterization, magnetic, photocatalytic, and photo-fenton properties. *MDPI Proc* 7:885
18. Prabhakaran T, Hemalatha J (2016) Combustion synthesis and characterization of cobalt ferrite nanoparticles. *Ceram Int* 42:14113–14120
19. Karthickraja D, Karthi S, Kumar GA et al (2019) Fabrication of core-shell CoFe<sub>2</sub>O<sub>4</sub>@HAp nanoparticles: a novel magnetic platform for biomedical applications. *New J Chem* 43:13584–13593
20. Azim M, Choudhry MA et al (2016) Structural and optical properties of cr-substituted co-ferrite synthesis by coprecipitation method. *Digest J Nanomaterial Bio structures* 11:953–962
21. Andhare DD, Patade SR, Kounsalye JS et al (2020) Effect of Zn doping on structural, magnetic and optical properties of cobalt ferrite nanoparticles synthesized via. Co-precipitation method. *Physica B Condens Matter* 583:412051
22. Nongjai R, Khan S, Asokan K et al (2012) Magnetic and electrical properties of In doped cobalt ferrite nanoparticles. *J Appl Phys* 112:084321
23. Paramasivan P, Venkatesh P (2016) A novel approach: hydrothermal method of fine stabilized superparamagnetics of cobalt ferrite (CoFe<sub>2</sub>O<sub>4</sub>) nanoparticles. *J Supercond Novel Magn* 29:2805–2811
24. Soibam I, Phanjoubam S, Prakash C (2009) Magnetic and Mössbauer studies of Ni substituted Li-Zn ferrite. *J Magnet Mag Mater* 321:2779–2782

# Automation in Inventory Management in MSME (Micro, Small, Medium Enterprises) Warehouse by Use of Robots



Meet Savla, Amar Pandhare, Shubham Gulunjkar, Pranav Pandit, and Prathamesh Dhawale

## 1 Introduction

Inventory management is arguably one of the important parts of any business which depends on the involvement of product fabricating, manufacturing, and selling, this is especially true for warehouses. Up to 60% of the budget is allotted towards the inventory of a business [1], thus inventory becomes a crucial aspect of a business. The more the efficiency of the inventory management system more the sales of the company, thus without a good inventory management system, a company will never be able to achieve its maximum potential performance [2]. Successful companies mainly focus on their inventories as in, the end raw materials as well as finished products to be stored and shipped from a warehouse on a given time frame so that further processes are carried out smoothly. Ideally, inventory management refers to the process of collecting material/components, storing them, and eventually handing them to the sales department when required, thus it is the process that ensures that the required item is obtained in the required time, in the required place, in the required quality and price [3, 4]. A company must consider the parameters such as the rate of obtaining the materials, material handling, the frequency of requirement of material/components, etc. [3]. These considerations of attributes decide whether a business will be profitable in long run or not.

Inventory management is always an evolving field as every industry has different sets of constantly changing demands and problems to be tackled over a period of time [5]. Regardless of the type of inventory management used, the basic sets of requirements remain the same. As a part of the supply chain, inventory management includes aspects such as controlling and overseeing purchases—from suppliers as well as customers—maintaining the storage of stock, controlling the amount of product for sale, and order fulfillment [6].

---

M. Savla (✉) · A. Pandhare · S. Gulunjkar · P. Pandit · P. Dhawale  
Sinhgad College of Engineering, Pune, India

Founders, entrepreneurs, and market leaders are now living in a world where small-to-medium scale businesses are trying to compete with the global conglomerates. In the case of India, a country with rising foreign investments of Amazon, IKEA, etc. is betting big on storage shades. It is high time for Micro, Small, and Medium Enterprises to step up their inventory management system to be able to sustain in this fast-changing business environment.

Large-scale companies already have adopted automated inventory management systems, the reason being the high demand, the requirement of precision, and the productivity improvement [6]. 37% of the Gross Domestic Product of India is contributed by the MSME sector, thus it is an integral part of the GDP. In spite of this, the sector is limited due to their longer production times leading to not being able to fulfill high demands thus eventually increasing costs. Automation in inventory management is considered to be extremely expensive with profitable results achievable after a certain number of years which is not sustainable for Micro, Small, and Medium scale enterprises. These industries depend heavily on humans and vast storage space which eventually leads to wastage of space, human error, excessive inventory, and loss in profit. Because of the new encouraging policies adopted by India after the 90s, even though the number of industries has surged warehouse industry in 'Micro, Small and Medium Enterprises' (MSME) has not seen a significant change from the 'Godown' stage with exceptions of ISO certified companies. These industries are now in need of inventory automation systems that will be easy to understand and will give return over their investments in less amount of time. This paper focuses on those industry's problems and will try to tackle them. This report comprises of overall design and considerations taken in the project of 'Automation in Micro, Small and Medium Enterprise warehouses by use of robots for inventory management'.

The solution proposed in this paper aims to eliminate the idle space present in the conventional inventory storage methods by using a custom altered rack arrangement, while an overhead 3-axis robot is used to access them. This not only increases the space efficiency but also reduces the loading-unloading time of the inventory with increased precision.

## 2 Methodology

Research starts with an aim to minimize difficulties faced by current warehouse industries in India. After careful observations, it is seen that most of the conventional warehouse management systems are seen to be safe but require most space as well as the workforce as that space goes on increasing [7]. Following shortcomings were seen in real-world warehouses and their management,

- Warehouses space mismanagement lead to an increase in cost
- Most of the warehouse space was being left out for access convenience and safety norms decided by different government bodies as well as private ones.

- A practical warehouse management system had humans as one of the main components, Human error could vary from organization to organization but its repercussions harm the overall organization.
- Current automated inventory solutions are far expensive and complex, which Micro, Small, and Medium Enterprises cannot bear to pay [8].

With an aim to find a solution following research is done.

## 2.1 Racks

As unused space is a liability for an organization [4], maximum space utilization is becoming an extensively important aspect of any investment strategy. Conventional racks need to be managed by machines like pallet cranes and forklifts. These machines require a moderate amount of space to operate and according to different standards space in between racks is defined for safety. While designing warehouses, parameters such as total dimensions of the space, structural constraints, the flow of material, and equipment are to be considered [9]. The warehouse designing process is intricate and tradeoffs are a part of it, thus priority is to be determined between maximum space utilization and maximum material accessibility. The rack is designed by considering two main important parameters maximum space utilization and maximum accessibility.

Assumptions given below are taken to design the following rack:

- All bins are having the same dimensions
- The area is taken such that 144 bins can be accommodated (36 bins \* 4 levels)
- External dimensions of rack are known
- The basic schematic layout is taken without clearances for a better understanding

First, a 2-dimensional layout of the rack is taken for comparative study; this gives us an idea about how much space we can actually save. We chose a  $6 \times 6$  layout for our top view as shown in Fig. 1.

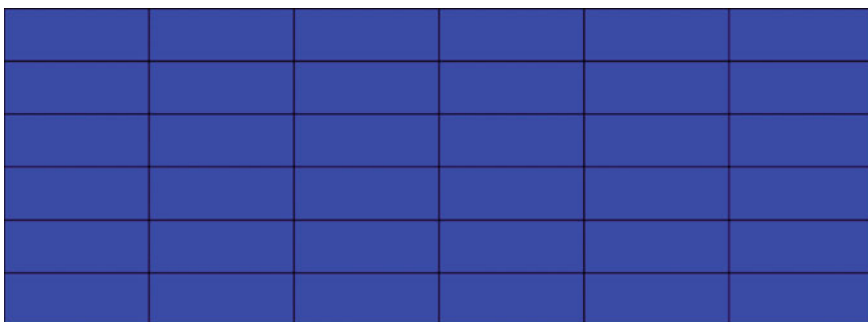


Fig. 1 Maximum utilization layout (top view)

This layout is aimed at fully utilizing the space for inventory storage, while it has the most capacity to store inventory there are some disadvantages of this layout. At a time, the robot is only able to access the bins on the top layer leading to a significant time and energy-delay to access lower bins, Since, if a lower bin is required to be accessed it first has to remove the preceding bins one at a time. This is the biggest disadvantage of the respective layout. Also, in the case of maintenance, it is very tedious and time consuming to access the bins.

This conventional layout as shown in Fig. 2 is most widely used in industries as it offers simplicity and less cost of operations. In this layout, the racks are arranged parallel to each other and a minimum space of two parallel bins stacked together is left for accessing the bins. The problem that arises here is that a minimum of 50% of the space is wasted due to the void left.

The comparative data of all 3 rack systems is displayed above in Table 1. This optimally designed rack arrangement overcomes the problem of not being able to specifically accessing lower bins by providing a void as denoted by the light blue color in Fig. 3, wherein the overhead 3 axis robot can access all bins as per command.

By referring to the layout in Fig. 3 we now take our step towards fully functional design. Aluminum extrusions are chosen because of their weight, strength, and availability [10–12]. The extrusion method of production makes it relatively cheaper than obtained by other processes, thus complex cross-sections having better rigidity can be used [13]. Different dimensions of rack are taken as per *IS: 1883–1983* [14], and recently released datasheet labeled 08–343 by a private organization named FM Global [15]. This made the rack design safe even in case of fire hazards. The final result will look as shown below (see Fig. 4).

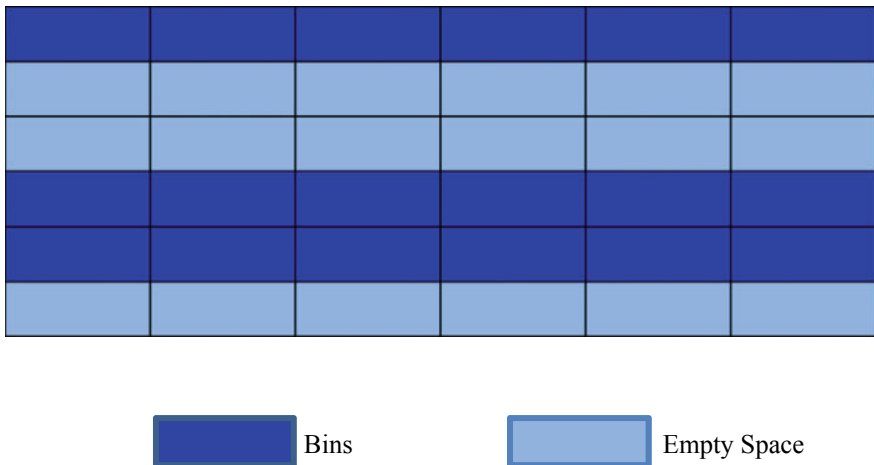
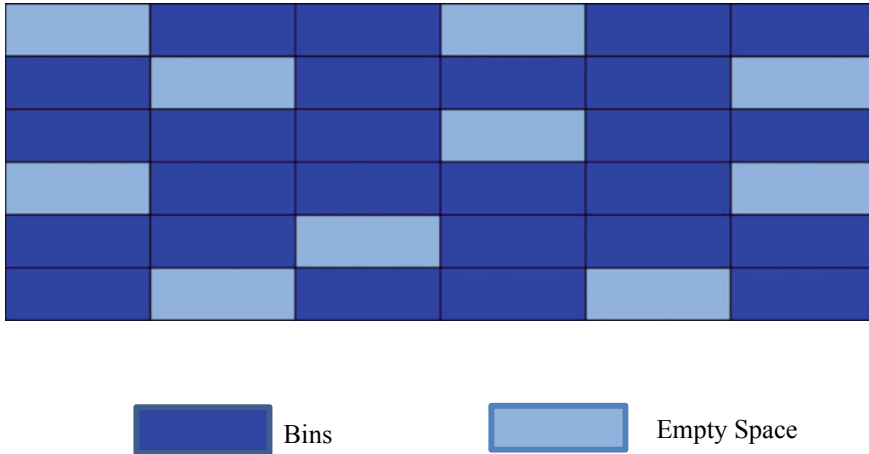


Fig. 2 Conventional rack layout (top view)

**Table 1** Summary of all 3 rack structures

Method	Total area (m <sup>2</sup> )	Useful area (m <sup>2</sup> )	Bins	Space efficiency (%)	Bin accessing efficiency (%)
Custom rack	2160	1560	26	72.3	100
Autostore	2160	2160	36	100	25
Conventional method	2160	1080	18	50	100

**Fig. 3** Custom rack layout (top view)

## 2.2 Robot

Robot process automation (RPA) is a technology in which the software acts as a mediator between the operator and the robot, making the interaction between man and machine possible [16], thus this technology is ideal for use.

The robot is designed with the aim to handle the bins present in the custom rack. With available dimensions of rack and space in between it to access bins, maximum external dimensions are fixed. In order to achieve maximum efficiency, apart from pick/place commands the robot must operate autonomously. It should locate itself and figure out the best path, for it the robot must continuously communicate with the computer on which the data is stored [7]. Highly efficient space utilizing rack uses multiple robots having complex algorithm and intricate design, a specialized skilled employee is desired to handle these kinds of tasks [17]. This inevitably leads to high initial investment and high recurring costs like employee payment, service, service parts. Return over investment for these systems is prolonged if stored material is not fast-moving and is not in demand. Micro, Small, and Medium

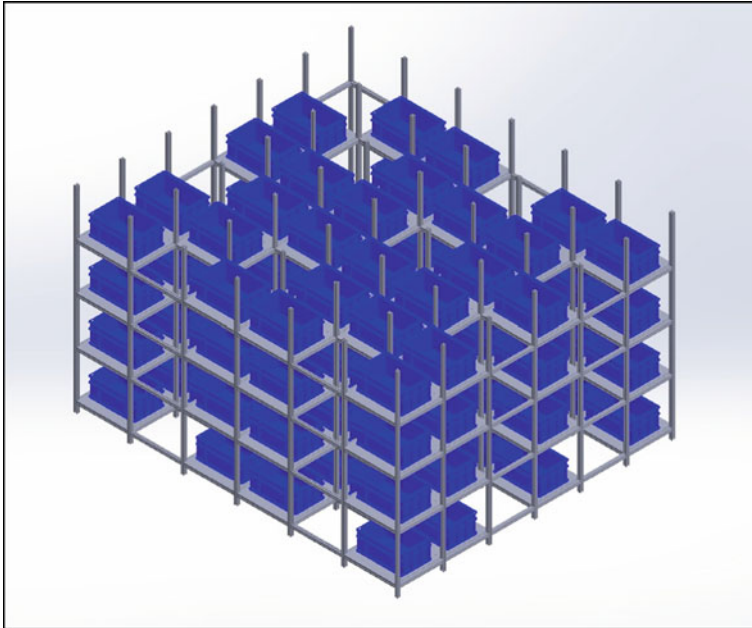


**Fig. 4** Isometric view of the designed rack system

Enterprises cannot afford to invest a high proportion of their capital into a system that cannot give a return in the least amount of time.

Aims given below are taken to design the following robot:

- Low manufacturing cost
- Ability to manufacture at a much faster rate
- Minimalistic design

With all available constraints, the external dimensions of the robot are fixed. A combination of servo motors and stepper motors is applied to the robot for easy programming and better results in terms of cost and precision. A retractable arm is first designed to access the bin and take it onto a fixed platform with respect to the robot. The Vertical (Z-axis) movement of the robot is achieved by the use of metal ropes and its operational basis is inspired by the movement of the hook of the Rope Hoist. Rotational movement of the retractable arm is achieved by the use of a spur gear mechanism where one spur gear is inserted in bearing and a second spur gear into the motor. Finally, movement of the robot in longitudinal (Y-axis) and lateral (X-axis) direction is achieved by taking inspiration of simple rope hoist design which moves on I beam. The final robot might look similar as shown in Fig. 5 and the overall integration of the rack and robot has been presented in Fig. 6.



**Fig. 5** Robot design  
(isometric view)

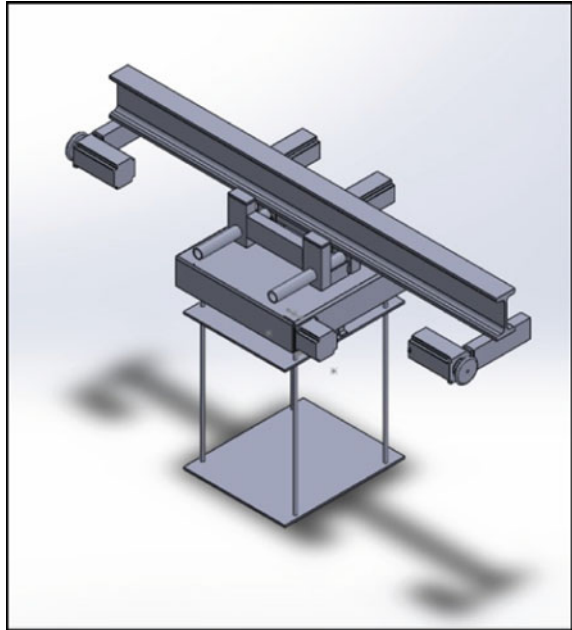
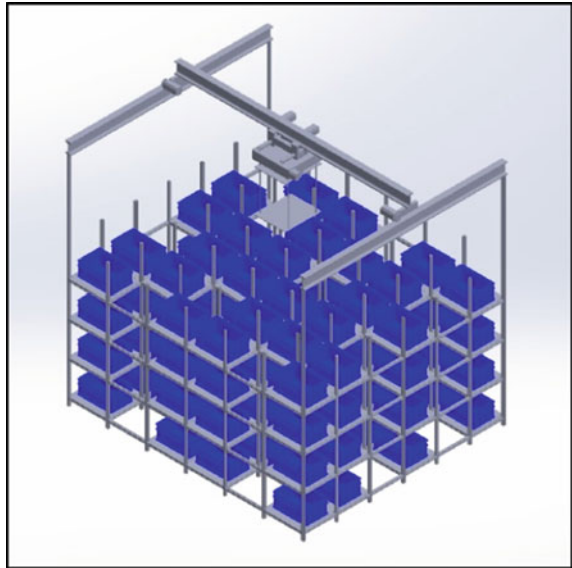


**Fig. 6** Robot mounted on the  
custom rack (isometric view)



### 2.3 Data Reading System

In order to have a track of every item like knowing its availability, quantities in which it is available, its location, the trend of the demand, it is vital to enter every data of that item in the MS-Excel sheet and have a more sophisticated and hassle-free track of the inventory in the warehouse [18]. This is the manual approach that requires the operator to feed the details of that product every time it comes in and goes out of the warehouse. This has proven to be extremely time consuming and there are increased possibilities of human errors that are bound to occur while entering all those long numbers that are uniquely assigned to each product [19, 20]. All these have an adverse effect on the business by the increased loss of stock, reduced customer satisfaction, increased lead times, human fatigue and it is subsequently reflected on the revenue of the company and reduced-order inflows [21].

So in order to counter this and ease the operation, there are two most renowned options available in the market namely RFID (radio frequency identification) and the barcode system. RFID is an accurate and dependable technology to record and manage inventory flow [20]. RFID tags contain important information regarding the product aiding the software in keeping track. RFID technology has some promising benefits but at the cost of high initial investment [22]. But the area of focus in this paper is on MSMEs, which are operating on a small scale as compared to some industry giants such as Walmart, Amazon, and Ikea. This research emphasizes emerging enterprises or those who have just established their business. One of the major factors for all these companies is the cost factor, which needs to be very tight as they are working on an individual level and simultaneously have to look at many other operational things. A comprehensive comparison has been done between the two technologies in Table 2.

**Table 2** Comparison between Barcode and RFID

S. No.	Parameters	Barcode	RFID
1.	Reading speed	Comparatively slow	Quick
2.	Accuracy in reading information	More as scans one item at a time	Less as more items are being scanned at a time
3.	Rate of reading	one at a time	Multiple products at a time
4.	Precision	Better	Not so reliable
5.	Data storing capacity	Less	Quite more (date of expiry, date of arrival, its history)
6.	Tag cost	Low	High (10X)
7.	Setup cost	low	High
8.	Auxiliary devices required for the functioning	Less (barcode printer, scanner, software to integrate)	More (RFID tags, printers, antennas, reader, software)
9.	Read and write data	Only read	Yes

No doubt RFID provides more features and is more dynamic and advanced than its counterpart, but the only negative point in this technology is the cost associated with it, not only its initial step cost but also its operational and maintenance cost [19, 23]. From the perspective of MSMEs operating on a low budget, the cost is the decisive aspect at every step of their business. For this very reason, a barcode system was chosen by keeping in mind the structure of MSMEs without having to compromise much on their functional requirements. This technology is best suited for these types of companies as they can extract the most out of it with minimal cost. Regardless of all this, this system is very reliable and fulfills the majority of their requirements. For barcode arrangements, the return on investment (ROI) is comparatively high. This allows MSMEs to have a very effective business model in this competitive world. Apart from its direct benefits, it also delivers indirect advantages like enhanced customer satisfaction and elevates working environments for the employees.

## ***2.4 Implementation***

A few of the major drawbacks of the existing inventory system are the human factor and the time taken by them to manually calculate the inventory. Considering these shortcomings, a new automated inventory management system has been developed by the authors [24]. The flow of incoming goods is explained in Fig. 7 and similarly, its outgoing flow is elaborated in Fig. 8. The whole system consisting of a robot, software, and an operator is integrated and works in harmony. The job of the operator has been reduced to the minimal as opposed to the conventional system, where they were solely responsible for managing those huge inventories. Now their task is to just scan the barcode attached to the product, feed into the computer the required items, and place the products into the bins. The entire process has been evolved to become less tiresome and carries out every step way smoothly. Instead of carrying the inventory once in a month or a year in the case of a manual system, this autonomous method facilitates taking the inventory any time when required that too in a few minutes or hours depending on the quantity being included [25]. Additionally, it allows for precise governing of the stock in hand reducing the possibilities of misplacing the materials.

The system is programmed in such a way that the product, which has arrived in the warehouse first, is the first one to go out, thereby ensuring that the product which has been manufactured first reaches the customer at the earliest.

Moreover, there have been made provisions for alarming the operator about the stock levels when falls below the preset limit. This KANBAN technique makes sure that optimum levels of stock are maintained in a way that customer satisfaction is at its peak [26]. It has been structured in such a manner that no excessive funds are infused in stocking up of the goods that are not much in demand and subsequently relieving that owner of that organization.

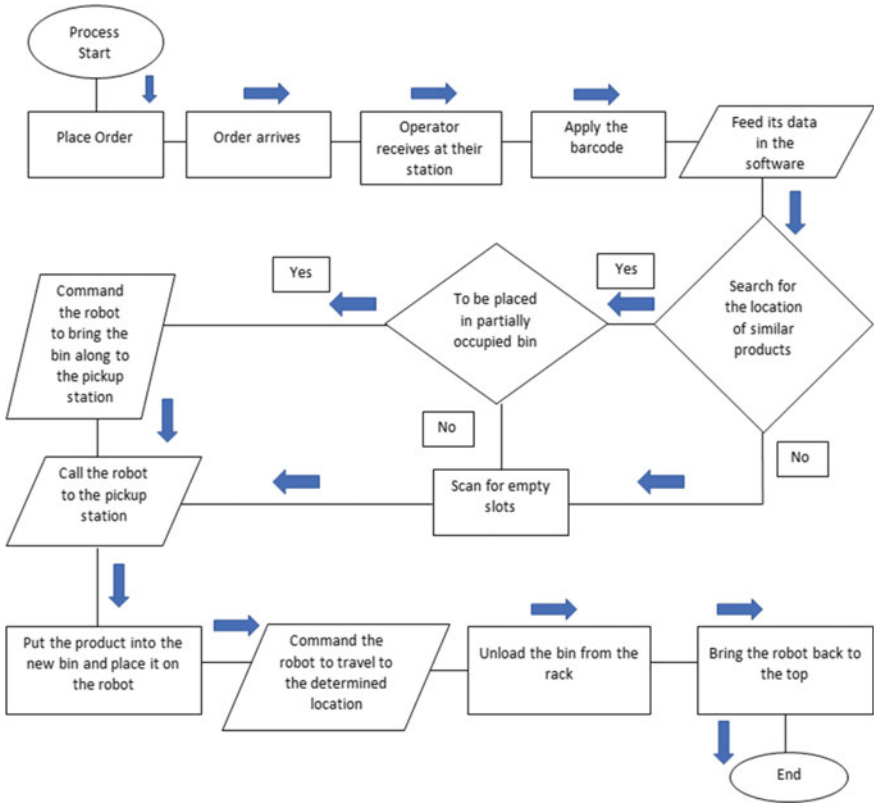


Fig. 7 Flow chart for loading the goods into the rack

### 3 Conclusion

With an accelerated surge in available competition, automation in inventory management in MSME warehouses by use of robots is required more than ever. A safe and efficient automated system in every aspect can be made for micro, small, medium enterprises.

As per the survey, MSME generally uses a human handled system for inventory management and conventional rack arrangements. This technique has flaws, which were—human error in managing the inventory, overstocking, human safety, poor space utilization, and cost of the inventory management department. These negatives were kept in mind and a new design was crafted.

22.3% increase in space utilization can be achieved with a new rack design which can be safe as per norms at the same time accessibility of a single robot can be increased up to 100%, this way FIFO and KANBAN concepts can be met for remarkable productivity.

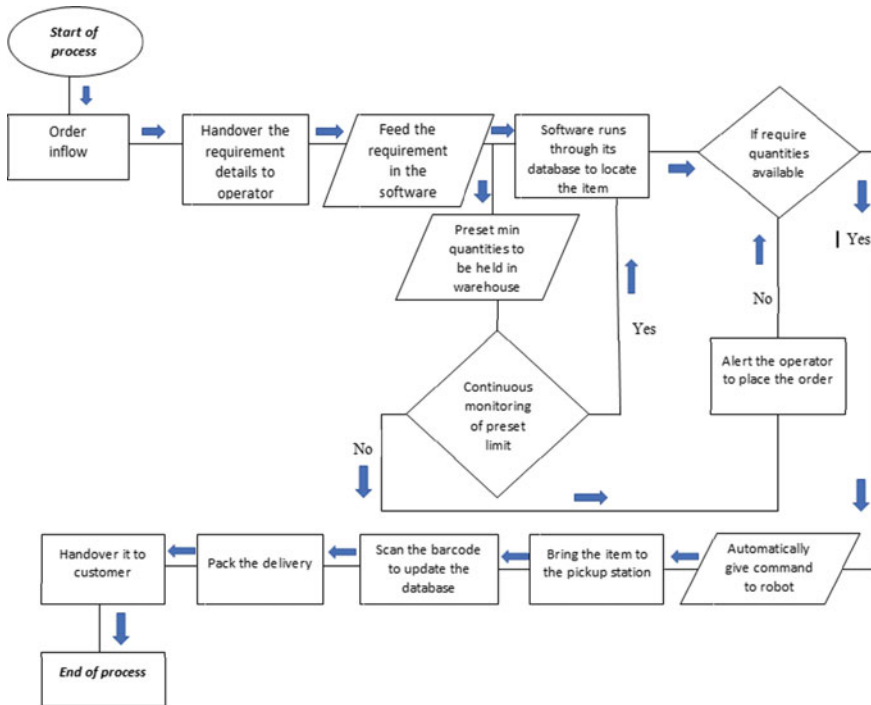


**Fig. 8** Flow chart for unloading of goods

This new version of the rack arrangement and the introduction of robots in the system make the inventory management process a lot more productive. Increased storage space from available warehouse space and reduction in error by use of the robot with help of bar code to store data will not only make the organization efficient in terms of cost from fixed assets but also the organization will be able to predict its next financial year inventory well in advance to reduce its working capital cycle.

## References

1. Carvalho H, Silva LH, Tavares JJPZS (2013) Automated planning applied in inventory management, vol. 6, no. PART 1. IFAC
2. Hübner A, Holzapfel A, Kuhn H (2015) Operations management in multi-channel retailing: an exploratory study. *Oper Manag Res* 8(3–4):84–100. <https://doi.org/10.1007/s12063-015-0101-9>
3. Panzuto NDS, Rodrigues PCC (2011) Analysis of inventory management in small business auto parts. In: 2011 4th international conference on logistics LOGISTIQUA'2011, no. May 2011, pp 186–191. <https://doi.org/10.1109/LOGISTIQUA.2011.5939424>

4. Kisperska-Moroń D (2003) Responsibilities for inventory decisions in polish manufacturing companies. *Int J Prod Econ* 81–82:129–139. [https://doi.org/10.1016/S0925-5273\(02\)00285-2](https://doi.org/10.1016/S0925-5273(02)00285-2)
5. Ding W (2013) Study of smart warehouse management system based on the IOT. *Adv Intell Syst Comput* 180 AISC 203–207. [https://doi.org/10.1007/978-3-642-31656-2\\_30](https://doi.org/10.1007/978-3-642-31656-2_30)
6. Gu J, Goetschalckx M, McGinnis LF (2010) Research on warehouse design and performance evaluation: a comprehensive review. *Eur J Oper Res* 203(3):539–549. <https://doi.org/10.1016/j.ejor.2009.07.031>
7. Mourtzis D, Samothrakis V, Zogopoulos V, Vlachou E (2019) Warehouse design and operation using augmented reality technology: a papermaking industry case study. *Procedia CIRP* 79:574–579. <https://doi.org/10.1016/j.procir.2019.02.097>
8. Carazas L, Barrios M, Nuñez V, Raymundo C, Dominguez F (2019) Management model logistic for the use of planning and inventory tools in a selling company of the automotive sector in Peru. *Adv Intell Syst Comput* 971:299–309. [https://doi.org/10.1007/978-3-030-20494-5\\_28](https://doi.org/10.1007/978-3-030-20494-5_28)
9. Shen H, Deng Q, Lao R, Wu S (2017) A case study of inventory management in a manufacturing company in China. *Nang Yan Bus J* 5(1):20–40. <https://doi.org/10.1515/nybj-2017-0003>
10. Types QAE aluminum extrusion types and parts selection aluminum extrusion tolerance data, p 69972
11. Minz SS, Rao PS (2020) Review paper on extrusion of Al-alloy series. *Int J Tech Innov Modern Eng Sci (IJTIMES)* December 2018
12. Schikorra M, Donati L, Tomesani L, Tekkaya AE (2007) Microstructure analysis of aluminum extrusion: grain size distribution in AA6060, AA6082 and AA7075 alloys. *J Mech Sci Technol* 21(10):1445–1451. <https://doi.org/10.1007/BF03177357>
13. Güler S, Karagülle H (2016) Finite element analysis of structures with extruded aluminum profiles having complex cross sections. *Lat Am J Solids Struct* 13(8):1499–1514. <https://doi.org/10.1590/1679-78252755>
14. Kisan M, Sangathan S, Nehru J, Pitroda SG (1983) Indian standard specification for metal shelving racks, third revision
15. FM global - Property loss preventive data sheets (2017), Capital POF, Sector M, Access TO, Skills E, To D, The B, Table of contents, list of figures, list of pictures
16. Atieh AM et al (2016) Performance improvement of inventory management system processes by an automated warehouse management system. *Procedia CIRP* 41:568–572. <https://doi.org/10.1016/j.procir.2015.12.122>
17. Nakayenga I (2011) Design and implementation of an automated inventory management system case study: Segofer technical services
18. Zhu X, Mukhopadhyay SK, Kurata H (2012) A review of RFID technology and its managerial applications in different industries. *J Eng Technol Manag JET-M* 29(1):152–167. <https://doi.org/10.1016/j.jengtecman.2011.09.011>
19. Alyahya S, Wang Q, Bennett N (2016) Application and integration of an RFID-enabled warehousing management system—a feasibility study. *J Ind Inf Integr* 4:15–25. <https://doi.org/10.1016/j.jii.2016.08.001>
20. Bagchi U, Guiffrida A, O'Neill L, Zeng A, Hayya J (2007) The effect of RFID on inventory management and control
21. Ngai EWT, Moon KKL, Riggins FJ, Yi CY (2008) RFID research: an academic literature review (1995-2005) and future research directions. *Int J Prod Econ* 112(2):510–520. <https://doi.org/10.1016/j.ijpe.2007.05.004>
22. Sarac A, Absi N, Dauzere-Pérès S (2010) A literature review on the impact of RFID technologies on supply chain management. *Int J Prod Econ* 128(1):77–95. <https://doi.org/10.1016/j.ijpe.2010.07.039>
23. Chande A, Dhekane S, Hemachandra N, Rangaraj N (2005) Perishable inventory management and dynamic pricing using RFID technology. *Sadhana Acad Proc Eng Sci* 30 (2–3):445–462. <https://doi.org/10.1007/BF02706255>

24. Metahri D, Hachemi K (2017) Automated storage and retrieval systems: a performances comparison between free-fall-flow-rack and classic flow-rack. In: 2017 6th international conference system control, ICSC 2017, no. March 2018, pp 589–594. <https://doi.org/10.1109/ICoSC.2017.7958654>
25. Anderson JR (2002) Automation of inventory management 2(4):2010–2013
26. Syntetos AA, Babai MZ, Davies J, Stephenson D (2010) Forecasting and stock control: a study in a wholesaling context. *Int J Prod Econ* 127(1):103–111. <https://doi.org/10.1016/j.ijpe.2010.05.001>

# A Review of the Mechanical Properties and Erosion Behavior of HVOF Sprayed Nanocomposite Coatings



Rajinder Kumar, Deepak Bhandari, and Khushdeep Goyal

## 1 Introduction

Energy plays a crucial role in the economic growth of a country and defining its standard of living. The demand for energy has been increasing at a very fast rate. The hydroelectric power plants highly contributed to the generation of power. Reports reveal that 66% of the world's feasible resources of hydroelectric power resources are undeveloped till now. Half of these potential resources lies only in the Asian countries [1]. In the world, India lies at the 7th position in hydroelectric power production. The consumption of power in India has been estimated to increase from 1107.8 TWh in 2016 to 1894.7 TWh in 2022 as per power sector report 2017 [2].

In hydroelectric power plants, material removal due to erosion from the turbine components cannot be stopped, but different types of coatings can be used to enhance the life of the materials used in the fabrication of turbine components. Major components of the hydro turbines, which are badly eroded are draft tube, facing plate, runner inlet, and outlet, shaft seal, guide vanes, nozzle, spear, and spiral casing. Figure 1 shows the components of hydro turbine affected due to erosion. Due to rise in the erodent particles in the river water, the problem of erosion becomes more critical during rainy season for the hydroelectric power plants located in the Himalayan region in India, which affect the power generation and economy [3]. Slurry erosion is a complex phenomenon, influenced by a number of factors, like impact velocity, weight of erodent particles, slurry concentration, average particle size of silt, impingement angle, contact time, and material properties.

---

R. Kumar (✉) · D. Bhandari  
Mechanical Engineering, Yadavindra College of Engineering, Talwandi Sabo, Punjab, India

K. Goyal  
Department of Mechanical Engineering, Punjabi University Patiala, Punjab, India



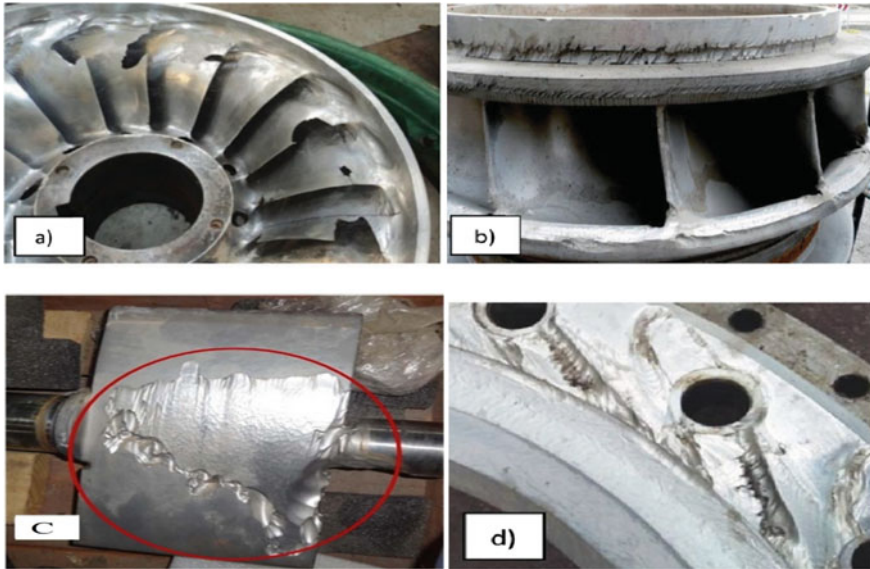


**Fig. 1** Hydro turbine components affected due to erosion (a) runner outlet (b) runner inlet (c) guide vane (d) facing plate [4]

Conventional steels used in the manufacturing of hydro turbine components are not able to overcome the problems occurred due to erosion in the hydroelectric power stations. To minimize erosion, suitable erosion-resistant coatings deposited by many advanced coating methods are mostly used. The studies of various authors highlighted that the problem of slurry erosion of hydro turbine components cannot be eliminated, but it can be reduced by using coated components of the hydro turbine. Many researchers compared the conventional coatings with nanostructured coatings and lots of improvements were observed in mechanical and microstructural properties of as-sprayed material as like increase in the hardness, lower the porosity and erosion rate, improved surface roughness, etc.

HVOF sprayed coatings are more popular due to high resistance to erosion, higher value of hardness, low porosity, and improved surface properties of the substrate materials [5, 6]. Till date, many researchers showed better results of the various micro and nano coating powders coated by HVOF technique [7]. By the addition of chromium to WC, coatings improve the resistance to erosion and wear. The erosion resistance of WC–10Co–4Cr coatings deposited with HVOF technique has been increased up to 50% than substrate stainless steel. The results of WC-based coatings mostly depend on the coating technique [8, 9]. Further, the composition of feedstock powders also plays a major role. Evaluation of the slurry erosion behavior of the hydro turbine material in actual working environment is a very complex phenomenon. Therefore, erosion testing of the substrate and as-sprayed materials can be performed on slurry erosion test rig under hydro accelerated environment by varying the operating parameters.

## 2 High-Velocity Oxy-Fuel (HVOF) Spray Coating Technique

Figure 2 represents an HVOF spraying process of coating. A mixture of fuel such as propane, propylene, hydrogen or a liquid fuel such as kerosene with oxygen/fuel ratio of 2.27 undergoes continuous combustion to provide a high-pressure jet of hot gas. The combustion chamber releases the hot gases into a nozzle to produce a spray with high speed. After combustion, coating powders like WC-10Co-4Cr, Cr<sub>3</sub>C<sub>2</sub>-NiCr, WC-10Co-4Cr + 10% YSZ, etc. are passed over the hot jet stream to obtain the semi molten state [10]. Nitrogen (N<sub>2</sub>) is used as carrier gas. The hot jet of the semi-solid particles strikes against the work piece and creates a layer of coating of varying thickness. The ratio of O/F has greater influence on hardness and roughness of coating. Fuel-rich mixture produces the coatings with less oxide. The shock waves have some influence on gas turbulence. Generally, the main result of the shock-turbulence interaction is the amplification of the velocity fluctuations. The major benefits of HVOF spraying process are that the coating layer has a very high density and sticks to the substrate material well. Figure 3 shows the SEM images of uncoated turbine steel, HVOF sprayed conventional coating and HVOF sprayed nanocomposite coating.

## 3 HVOF Sprayed Nanocomposite Coatings

The important findings of the various researchers on HVOF sprayed nanocomposite coatings have been presented in this section.

The HVOF spray coating technique was used to deposit the ceramic/polymer nanocomposite coatings by the author. Dense coatings with uniform particle distribution were obtained by optimizing the various spray parameters like design of

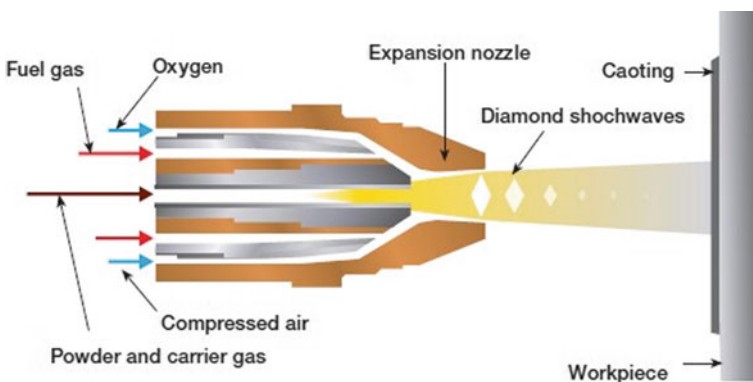
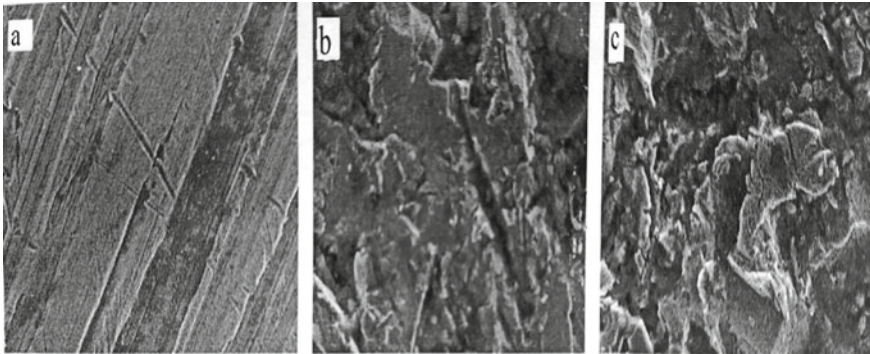


Fig. 2 Schematic diagram of HVOF spray coating [11]



**Fig. 3** SEM images of **a** uncoated CA6NM turbine steel **b** WC-10Co-4Cr conventional coating **c** WC-10Co-4Cr + 10%  $Y_2O_3/ZrO_2$  nanocomposite coating

nozzle, distance between nozzle and top surface of metal, oxygen-fuel ratio, and the powder feed position. It was observed that HVOF spray coating technique to deposit the polymer and nanoparticle ceramic-reinforced polymers performed better as compared to other spray coating techniques. Several thermal effects must be stabilized to attain perfect nanoparticle ceramic/polymer composite coatings using HVOF [12]. Stewart et al. compared the result of conventional and nanocomposite powders coated by HVOF thermal spraying process. The nanocomposite WC-Co resulted in improved wear resistance than the conventional material. For both the conventional and nanocomposite coatings, the wear rate with alumina particles was more in comparison to silica particles and resulted in low surface cracking and minimum material removal [13].

The sliding abrasion wear of  $Al_2O_3$ -SiC nanocomposite coatings deposited with HVOF and plasma spraying were analyzed by the researcher. The HVOF coatings showed excellent resistance to abrasive wear as compared with the plasma sprayed coatings and uncoated steel. The  $Al_2O_3$ -SiC nanocomposites coated with HVOF, showed higher fracture toughness. The HVOF coatings were worn relatively slowly by micro abrasion. The micro abrasion mechanism was reduced by SiC within the nanocomposite coatings [14]. Li et al. showed that hydroxyapatite/nano- $ZrO_2$  composite coatings were developed by using HVOF coating technique. SEM, TEM, XRD, and DSC were performed for microstructural characterization of the nanocomposite coatings. Results revealed that the roughness of nanosized zirconia particles was improved after the deposition of coatings by HVOF technique. XRD analysis highlighted the percentages of different phases present in the coatings [15]. Marple and Lima used HVOF technique to deposit the WC-12Co powder in which the WC phase was either in conventional form or was in the form of multimodal. The HVOF spray processes with a number of spray parameters were adopted to investigate the effect of in-flight particle characteristics on coating properties. The harder coating was obtained by using coating powder with nanosized WC phase. Due to higher deposition efficiency, multimodal feedstock is more useful [16].

The WC–Co coatings prepared with conventional micro and nano WC grains were compared by the author. The feedstock powder with nanoscale WC grains enhanced the wear resistance of the coatings. Coatings with nanoscale grains showed higher value of hardness and lower porosity. Due to micro-scale abrasion condition, rapid pullout of the hard phase was observed due to fine WC grains in the nanostructured material [17]. Turunen et al. developed the  $\text{Al}_2\text{O}_3$  and  $\text{Al}_2\text{O}_3$ –Ni nanocomposite coatings using HVOF process. Due to superior mechanical properties, nanocomposite materials have been recognized. The variation in mechanical and microstructural properties of the coatings were analyzed. It was observed that coatings of better quality can be obtained by the optimization of spray parameters. Increase in the hardness and wear resistance of the pure  $\text{Al}_2\text{O}_3$  coating were observed due to the addition of nano powders. Hardness and Fracture toughness were also improved by the reinforcement of Ni into alumina [18]. Lima et al. observed that  $\text{Al}_2\text{O}_3$ –13 wt%  $\text{TiO}_2$  coatings obtained by using micron and nanosized powders, would further improve the wear properties of the conventional coatings. Abrasion test was reported the enhanced wear resistance for the HVOF sprayed hybrid coating. The significant enhancement was obtained in wear resistance by using hybrid material [19]. Laha et al. analyzed the interfacial phenomena in plasma and HVOF sprayed hypereutectic Al–Si composite with MWCNT reinforcement theoretically and experimentally. The thickness of HVOF sprayed coatings as compared to plasma sprayed composite. Improved wettability of the molten MWCNT reinforced Al–Si alloy was obtained by the formation of b–SiC [20].

Gaona et al. deposited the hydroxyapatite (HA) blended nanosized titania ( $\text{TiO}_2$ ) powders on the Ti–6Al–4 V material with the help of HVOF coating technique. The tribological behavior and microstructural characteristics of the coated metal were examined. Minor improvement was found in the coatings due to poor mechanical properties of hydroxyapatite [21]. Baik et al. investigated the mechanical and surface properties of WC–Co nanocomposite coatings. The investigator used the Co surface layer to modify the porous spray-dried WC–Co nano powder. Huge amount of non-WC phases was observed in the microstructure of both as-sprayed WC–Co coatings. Coated surfaces exhibited the higher values of wear resistance and hardness [22]. The influence of nano WC–12Co powder reinforced into WC–10Co–4Cr were studied by the researcher. Wear and erosion test were conducted to examine the outcome of the reinforcement. The coatings were also examined by using scanning electron microscopy and X-ray diffraction technique to analyze the microstructural properties of the coatings. The hardness and erosion resistance of the coated samples were increased with the reinforcement of nano particles [23]. Wu et al. deposited nanostructured Ni60–TiB<sub>2</sub> composite coating on substrate steel by using HVOF spray coating technique and compared with conventional Ni60–TiB<sub>2</sub> composite coating. Nanostructured composite coatings showed excellent microstructural properties and improved wear resistance. The results revealed that the adhesive wear was mainly responsible for the wear of the nanocomposite coatings [24].

Movahedi examined the mechanical behavior and surface properties of the NiAl and NiAl–15 wt% ( $\text{Al}_2\text{O}_3$ –13%  $\text{TiO}_2$ ) nanocomposite coatings. SEM, TEM, and XRD techniques were used to examine the coatings. It has been observed that the microhardness and wear resistance were increased by using  $\text{Al}_2\text{O}_3$ –13%  $\text{TiO}_2$  nano powder as a reinforcement [25]. Mazaheri et al. deposited the Al 356– $\text{Al}_2\text{O}_3$  nanocomposite powder on Al alloy (A356-T6) with the help of HVOF thermal spraying technique. Al 356– $\text{Al}_2\text{O}_3$  powder was prepared by milling Al 356 powder and 5% micro and nano scaled alumina particles. Various mechanical tests were performed to characterize the composite coatings. Results revealed that mechanical properties like surface roughness, porosity, hardness, etc. were higher than substrate material. It was also found that the wear rates of nano and micro composite coatings were significantly less as compared with Al 356-T6 substrate material [26]. Yan et al. fabricated the nanostructured, bimodal, and multimodal WC–10Co4Cr coatings by using HVOF spray coating technique and evaluated the microstructural, mechanical, electrochemical properties, and slurry erosion resistance of the coatings. The multimodal coatings exhibited the lowest decarburization and high resistance to slurry erosion [27].

## 4 Discussion

Literature survey reveals that various investigations have been performed over the last many years to improve the surface properties and erosion resistance using HVOF sprayed nanocomposite coatings. It was observed that the HVOF sprayed nanocomposite coatings exhibit superior mechanical and microstructural properties as compared with conventional coatings [24]. It is observed from the different studies that the effect of micro and nano particles on the metal surface is quite different. The nano particles resist the penetration of erodent particles very effectively and are not easily cut out by the pin because of their small size, high hardness, and good bonding with the metal surface [16]. In recent years, the research activities on nanocomposite coatings have increased very extensively. In the field of thermal spray coatings, there has been a push to explore whether the potential benefits of nanocomposite coatings suggested by the various relationships can be realized and reflected in higher levels of performance. Investigations on the tribological behavior and performance of various nanocomposite coating compositions have produced a wide range of outcomes.

Significant improvement was observed in mechanical properties by the reinforcement of bioinert ceramics, such as yttria stabilized zirconia ( $\text{Y}_2\text{O}_3/\text{ZrO}_2$ ), alumina ( $\text{Al}_2\text{O}_3$ ) and titania ( $\text{TiO}_2$ ) into a hydroxyapatite (HA) matrix. However, mutual reaction between calcium phosphates (CP) and YSZ ( $\text{Y}_2\text{O}_3/\text{ZrO}_2$ ) seemed inevitable and phase transformation of zirconia invariably took place during HVOF coating deposition. This crystallographic transformation generated residual tensile stresses in the coating [15]. The nanostructured coatings attracted intense interest due to their improved mechanical properties. Basically, the decrease in particle size

**Table 1** Summary of performance characteristics of HVOF sprayed nanocomposite coatings

Substrate material	Nanocomposite material	Coating thickness (µm)	Hardness/microhardness (HV0.3)	Porosity (%)	Roughness (µm)	Fracture toughness (MPa m <sup>1/2</sup> )	Wear rate (mm <sup>3</sup> /Nm)	Application	References
Stainless steel	WC-12Co	215	1211 ± 43	0.79	4.9 ± 0.5		Low	Wear resistance	[13]
Plain carbon steel	Al <sub>2</sub> O <sub>3</sub> -SiC	150	1100 ± 150			High	Low	Wear resistance	[14]
Mild steel	WC-12Co	525	1020		5.2 ± 1.15		0.28 × 10 <sup>-6</sup>	Wear resistance	[17]
Carbon steel plates	Al <sub>2</sub> O <sub>3</sub> -Ni (2-10%)		1402			High		Sliding wear resistance	[18]
Low-carbon steel	Al <sub>2</sub> O <sub>3</sub> -13 wt% TiO <sub>2</sub>		808 ± 40	0.95				Erosion resistance	[19]
Ti-6Al-4 V	TiO <sub>2</sub> + 10-20 wt% (HA)	100-150	9.9 and 10.6 (Weibull modulus values)			High	Low	Erosion resistance	[21]
AISI 304 stainless steel	WC-12Co	400	1826 ± 49	1.4				Erosion resistance	[23]
carbon steel	Ni60-40 wt%TiB <sub>2</sub>	100-250	1102 ± 43	0.96 ± 0.18	2.8 ± 0.2	3.5 ± 0.2		Sliding wear	[24]
Mild steel	NiAl-15% (Al <sub>2</sub> O <sub>3</sub> -13 TiO <sub>2</sub> )		8.35	2.05 ± 0.12		7.12	0.78 ± 0.33 × 10 <sup>-5</sup>	Fracture toughness and wear resistance	[25]
A356-T6 Al alloy	Al <sub>2</sub> O <sub>3</sub>	210	138.4 ± 6.9				9.6	Wear resistance	[26]
AISI 304 stainless steel	WC-10Co-4Cr	300	1860 ± 40	0.57 ± 0.2	3.5 ± 0.8			Erosion resistance	[29]
AISI 304 stainless steel	MWCNTs with WC-10Co-4Cr		1665 ± 66	0.62 ± 0.22	2.54 ± 1.15	4.2 ± 0.9		Slurry erosion resistance	[30]

(continued)

**Table 1** (continued)

Substrate material	Nanocomposite material	Coating thickness ( $\mu\text{m}$ )	Hardness/microhardness (HV0.3)	Porosity (%)	Roughness ( $\mu\text{m}$ )	Fracture toughness ( $\text{MPa m}^{1/2}$ )	Wear rate ( $\text{mm}^3/\text{Nm}$ )	Application	References
Cast duplex stainless steel	WC grain reinforced WC-17NiCr	250	$7.42 \pm 1.06$	$0.69 \pm 0.18$		$6.39 \pm 0.88$	$0.37 \pm 0.06 \times 10^{-5}$	Erosion and sliding wear resistance	[31]
Stainless steel	Ni coated WC-120	394	$1214 \pm 25$	$0.5 \pm 0.1$	$3.1 \pm 0.3$			High-temperature resistance	[32]
Mild steel (ASTM A36)	TiO <sub>2</sub> , ZrO <sub>2</sub> and Al <sub>2</sub> O <sub>3</sub>	100–250	$0.80 \pm 0.21$	$6.2 \pm 2.1$			$1.9 \times 10^{-3}$	Sliding wear	[33]



of nanocomposite coatings enhances the strength and toughness of ceramics. In the recent studies on WC–Co nanocomposite coatings, it has been observed that the feedstock powder properties are responsible for the microstructure of the coatings. A porous feedstock powder produces a very dense coating but decarburization takes place at very high level due to higher degree of powder melting. In order to obtain the significant improvement in mechanical properties and wear resistance offered by WC–Co nanocomposites, it is essential to reduce the porosity and WC decomposition simultaneously [28]. Table 1 shows the summary of performance characteristics of HVOF sprayed nanocomposite coatings.

## 5 Conclusion

Erosion depends on several factors like materials of the hydro turbine, shape, and mineral contents of the erodent sand. The repair and maintenance impose huge loss of capital along with the premature failure of the hydro turbine components. HVOF sprayed nanocomposite coatings provide a protecting shield to the surface of the materials from erosion. It proves to be very effective technique to enhance the life of hydro turbine components. The existing data shows that the nanocomposite coatings prepared by HVOF spray coating technique showed improved tribological properties and high erosion resistance as compared with conventional coatings. Many researchers proved that surface roughness, porosity, and hardness of the coatings has improved significantly with the reinforcement of nanostructured particles like  $\text{Al}_2\text{O}_3$ ,  $\text{TiO}_2$ ,  $\text{Y}_2\text{O}_3$ , etc. There is still vast scope in the study of the performance of various nanostructured coatings by using HVOF spray coating technique. The size of the reinforcement powder in composite coating plays a crucial role in enhancing the strength of materials and it is worthwhile to use the nanometre grain size to improve the erosion resistance as compared to conventional coatings. The large number of mechanical and microstructural properties like porosity, surface roughness, hardness, wear resistance, erosion resistance and fracture toughness can be improved by using various nanocomposite combinations and optimization of process parameters. Some new techniques like laser cladding, tungsten inert gas cladding, and microwave processing with nanostructured and bimodal coatings have been suggested by some researchers to develop erosion-resistant coatings.

## References

1. Denhofer OE, Pichs MR, Sokona YP (2012) Renewable energy sources and climate change mitigation: special report of the intergovernmental panel on climate change. Cambridge University Press, New York
2. Miyam M (2018) Hydro power energy in India: a review. *Int J Pure App Res* 4(1):1–6



3. Mann BS (2000) High-energy particle impact wear resistance of hard coatings and their application in hydro turbines. *Wear* 237:140–146
4. Brekke H (2002) Design of hydraulic machinery working in sand laden water. Imperial College Press, London, pp 155–181
5. Javaheri V, Porter D, Kuokkala VT (2018) Slurry erosion of steel—review of tests, mechanisms and materials. *Wear* 408–409:248–273
6. Bukhaiti MA, Ahmed SM, Badran FMF, Emara KM (2007) Effect of impingement angle on slurry erosion behaviour and mechanisms of 1017 steel and high-chromium white cast iron. *Wear* 262:1187–1198
7. Kumar A, Sharma A, Goel SK (2016) Erosion behaviour of WC-10Co-4Cr coating on 23-8-N nitronic steel by HVOF thermal spraying. *App Surf Sci* 370:418–426
8. Ashby MF, Jones DRH (1986) An introduction to microstructures, processing and design. *Engineering materials*, vol 2. Pergamon Press, Oxford
9. Skuleva H, Malinobv S, Shac W, Basheer PAM (2005) Microstructural and mechanical properties of nickel-base plasma sprayed coatings on steel and cast-iron substrates. *Surf Coat Tech* 197:177–184
10. Thorpe M, Richter H (1992) A pragmatic analysis and comparison of HVOF processes. *J Therm Spray Technol* 1:161–170
11. Metco S (2013) An introduction to thermal spray, pp 4–10
12. Schadler LS, Laul KO, Smith RW, Petrovicova E (1997) Microstructure and mechanical properties of thermally sprayed silica/nylon nanocomposites. *J Therm Spray Technol* 6:475–485
13. Stewart D, Shipway P (1999) Abrasive wear behaviour of conventional and nanocomposite HVOF-sprayed WC-Co coatings. *Wear* 225:789–798
14. Dearnley PA, Panagopoulos K, Kern E, Weiss H (2003) Sliding abrasion wear assessment of Al<sub>2</sub>O<sub>3</sub>-SiC nanocomposite coatings. *Surf Eng* 19:373–378
15. Li H, Khor KA, Kumar R, Cheang P (2004) Characterization of hydroxyapatite/nano-zirconia composite coatings deposited by high velocity oxy-fuel (HVOF) spray process. *Surf Coatings Technol* 182:227–236
16. Marple BR, Lima RS (2005) Process temperature/velocity-hardness-wear relationships for high-velocity oxyfuel sprayed nanostructured and conventional cermet coatings. *J Therm Spray Technol* 14:67–76
17. Chen H, Xu C, Zhou Q, Hutchings IM, Shipway PH, Liu J (2005) Micro-scale abrasive wear behaviour of HVOF sprayed and laser-remelted conventional and nanostructured WC-Co coatings. *Wear* 258:333–338
18. Turunen E, Varis T, Gustafsson TW, Keskinen J (2006) Parameter optimization of HVOF sprayed nanostructured alumina and alumina—nickel composite coatings. *Surf Coatings Technol* 200:987–994
19. Lima RS, Moreau C, Marple BR (2007) HVOF-sprayed coatings engineered from mixtures of nanostructured and submicron Al<sub>2</sub>O<sub>3</sub>-TiO<sub>2</sub> powders: an enhanced wear performance. *J Therm Spray Technol* 16:866–872
20. Laha T, Kuchibhatla S, Seal S, Li W, Agarwal A (2007) Interfacial phenomena in thermally sprayed multiwalled carbon nanotube reinforced aluminum nanocomposite. *Elsevier* 55:1059–1066
21. Gaona M, Lima RS, Marple BR (2007) Nanostructured titania/hydroxyapatite composite coatings deposited by high velocity oxy-fuel (HVOF) spraying. *Elsevier* 458:141–149
22. Baik KH, Kim JH, Seong BG (2007) Improvements in hardness and wear resistance of thermally sprayed WC-Co nanocomposite coatings. *Mater Sci Eng* 448:846–849
23. Liu SL, Zheng XP, Geng GQ (2010) Influence of nano-WC-12Co powder addition in WC-10Co-4Cr AC-HVAF sprayed coatings on wear and erosion behaviour. *Elsevier* 269:362–367
24. Wu YS, Zeng DC, Liu ZW, Zhong XC (2011) Microstructure and sliding wear behavior of nanostructured Ni60-TiB<sub>2</sub> composite coating sprayed by HVOF technique. *Surf Coatings Technol* 206:1102–1108

25. Movahedi B (2013) Fracture toughness and wear behavior of NiAl-based nanocomposite HVOF coatings. *Surf Coatings Technol* 235
26. Mazaheri Y, Karimzadeh F, Enayati MH (2013) Development of Al356-Al<sub>2</sub>O<sub>3</sub> nanocomposite coatings by high velocity oxy-fuel technique. *J Mater Sci Technol* 29:813–820
27. Huang Y, Ding X, Yuan CQ, Yu ZK, Ding ZX (2020) Slurry erosion behaviour and mechanism of HVOF sprayed micro-nano structured WC-CoCr coatings in NaCl medium. *Trib Inter* 148
28. Sharma V, Kaur M, Bhandari S (2019) Micro and nano ceramic-metal composite coatings by thermal spray process to control slurry erosion in hydro turbine steel: an overview. *Eng Res Exp* 1(1):1–13
29. Thakur L, Arora N, Jayaganthan R, Sood R (2011) Applied surface science an investigation on erosion behavior of HVOF sprayed WC-CoCr coatings. *Appl Surf Sci* 258:1225–1234
30. Thakur L, Arora N (2016) A study of processing and slurry erosion behaviour of multi-walled carbon nanotubes modified HVOF sprayed nano-WC-10Co-4Cr coating. *Surf Coat Tech* 309:860–871
31. Asgari H, Saha G, Mohammadi M (2017) Tribological behavior of nanostructured high velocity oxy-fuel (HVOF) thermal sprayed WC-17NiCr coatings. *Ceram Int* 43:2123–2135
32. Jafari M, Enayati MH, Salehi M, Nahvi SM, Han JC, Park CG (2016) High temperature oxidation behaviour of micro/nanostructured WC-Co coatings deposited from Ni-coated powders using high velocity oxygen fuel spraying. *Surf Coatings Technol* 302:426–437
33. Limpichaipanit A, Banjongprasert C, Jaiban P, Jiansirisomboon S (2013) Fabrication and properties of thermal sprayed AlSi-based coatings from nanocomposite powders. *J Therm Spray Technol* 22:18–26

# Kitchen Waste Utilization Using Biogas Plant—Need of the Hour



Bhamre Hrishikesh, Shimpi Abhishek, and Gadhe Prakash

## 1 Introduction

According to the Food and Agriculture Organization (FAO) of the United Nation, the global volume of food wastage is estimated to be 1.6 billion tonnes of “primary product equivalents”, while the total wastage for the edible part of food is 1.3 billion tonnes [1]. The United Nations Development Programme states that 40% of total food production is wasted in India [2]. The estimated cost of food waste in India is US\$ 14 billion [3]. India has seen tremendous growth in terms of per capita income, infrastructure and population compared to previous decades. These factors resulted in the continuous growth of hotel industries and social gatherings, but along with that India is also facing the problem of food wastage on a mass level. To overcome this food wastage problem, one of the best solutions is the kitchen waste management which includes deploying the biogas plant.

### 1.1 History and Statistics of Biogas in India

In Indian Agricultural Research Institute (IARI), development of the first biogas plant took place and it was installed in 1946. In 1951, J. J. Patel built a digester with greater efficiency than the IARI model. It is used to produce 5.7 cubic metre biogas per day; he named it “Gramalaxmi gas plant”. Till 1963, India had 6000 biogas plants. But due to slow growth rate, India had only 6858 biogas plants at the end of 1974. Considering the increase in oil rates, it gave acceleration to the development of biogas plants, and at the end of March 1984, India had more than 2,50,000 biogas plants [4].

---

B. Hrishikesh · S. Abhishek (✉) · G. Prakash  
School of Mechanical Engineering, Dr Vishwanath Karad MIT World Peace University,  
Pune, Maharashtra, India

The global volume of micro-scale biogas digesters is around 50 million with 4.9 million in India [5]. The Tata Research Institute estimates that 12 million biogas systems can be installed in India while GATE, an alternative energy nongovernmental organization (NGO), estimates potential numbers of biogas plants that could be installed which is about 30 million household sizes and nearly 600,000 community-sized plants, one for each village [6].

Knol et al. (1978) concluded that anaerobic digestion would be a suitable process for the treatment of waste materials from the fruit and vegetable industry. Composition of carbohydrate-rich substrates inclined to be below per digestion by adding alkali, adjusting loading rate and concentration increases the effectiveness [7]. Banks et al. (2011) experimented on anaerobic digester which received food waste from the domestic kitchen. The mass balance was 90.4% (wet weight) and 95.7% (VS basis) allowing for the loss of volatile components [8].

In this study, the conclusion was that metal absorbs more sunlight and increases the temperature inside the digester in comparison to plastic made biogas plants and metal biogas plants were better in terms of biogas production and carbon credit [9]. Ariyanto et al. (2017) compared between landfill and biogas plant and the study was completed using life cycle assessment (LCA) to evaluate environmental impacts and daily processing costs. It concludes that wet waste should be utilized in a biogas plant rather than disposing it in landfill [10].

Pandey et al. (2017) have performed experiments to calculate the yield for anaerobic biogas production and methane percentage in the biogas using various kitchen wastes like spices. Analysis of the results shows various magnitudes of inhibition of the anaerobic digestion process of kitchen waste which have different spices [11]. Decker et al. (2018) have developed and tested a design approach for optimizing flame port geometry for household biogas-fired burners. Design results showed improvement in the efficiency of biogas burners [12].

Kougias et al. (2018) have summarized the current technological advances and present future perspectives related to the anaerobic digestion process for biogas production [13]. Shoar et al. (2019) have researched the effect of thermochemical pretreatment on the biogas production process from kitchen waste. The thermochemical pretreatment on kitchen waste increases biogas production [14].

Sindhu et al. (2019) have given the prospects and consequences of food waste management. In the various fields mentioned in the United Nations Sustainable Development goals such as social, economic and environmental concerns which are associated with food waste management and in the terms of greenhouse gases [15].

## ***1.2 Utilization of LPG***

LPG is utilized in 61% of India's total household [16]. According to the data by Petroleum Planning and Analysis Cell (PPAC), an arm of the Ministry of Petroleum and Natural Gas, LPG penetration stood at 98.1% as of 1 July 2020 [17]. Still, a

significant number of households in villages were using firewood, crop residue and chips for cooking. For such villages, biofuel can be a substitute fuel for LPG.

### 1.3 Comparative Study Between LPG and Biogas

Biogas is a type of biofuel which is safer than LPG as it has physical characteristics like low density and pressure compared to LPG. While LPG is stored at 14–17 bar pressure, biogas is generated at atmospheric pressure which leads to higher levels of safety. Burner efficiency for LPG is 65–70%, and for biogas, it is 50–55% [12, 18]. Usage of biogas instead of LPG is economical in long-term effect.

## 2 Principle of Biogas Plant

The biogas plant works on the principle of anaerobic digestion of waste to generate biogas. The anaerobic digestion occurs in three phases: hydrolysis of organic solids, acetic acid formation and biogas production. Biogas is an output of biomethanation of organic waste by anaerobic bacteria. The process of biomethanation involves breaking complex organic matter into simpler molecules, thereby releasing biogas. The digested material obtained in the form of slurry is organic manure to plants. Biogas is a mixture of methane, carbon dioxide, hydrogen sulphide, water and other compounds in traces [19]. Figure 1 shows a layout diagram of a floating drum biogas plant.

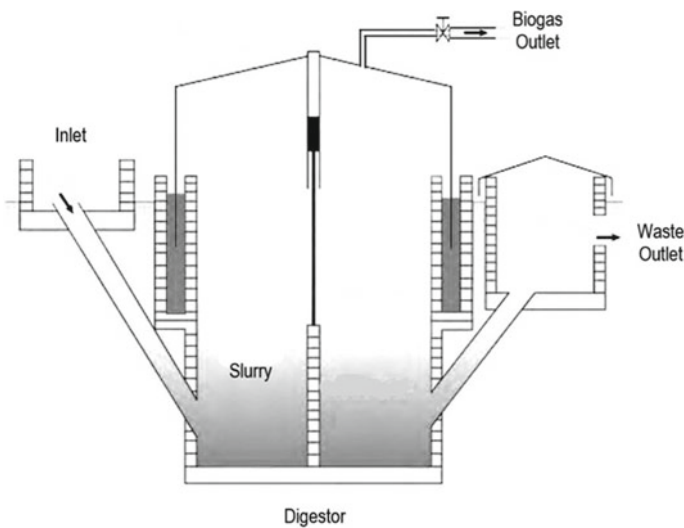


**Fig. 1** Floating drum biogas plant

### 3 Methodology

For determining biogas utilization from kitchen waste, certain factors need to be evaluated. Evaluation of biogas plant includes biogas output and the payback period of the biogas plant. To begin with a numerical and analytical calculation for biogas plants, it is important to understand the process of biogas generation.

In the initial step, food waste is collected. This waste is collected from kitchens, restaurants and community kitchens where food is prepared and consumed. Then, the wet waste is separated and mixed with water in a certain amount of percentage. Organic input material is mixed with water in a definite ratio for subsequent treatment by aerobic or anaerobic processes. The total amount of such mixed material is called the substrate amount.

The substrate has to be kept in the digester for a certain time period for the growth of microbes. This time period is called solid retention time (SRT). SRT depends on climatic conditions and mainly on temperature. It varies for different geographical areas. SRT has a significant role in microbial growth rate.

Also, volume of output biogas depends on total solids (TS) and volatile solid (VS) percentage in wet waste. TS and VS give an amount of slurry that can be transformed into biogas. Wet digesters have TS content below 16%, while dry reactors have TS content between 22 and 40% [20].

#### Total Solids (TS %)

It is the residual amount of solid content present in the sample. The residual amount of solid is collected after the presence of water in it is vaporized. Equation 1 computes total solids.

$$TS = \left( \frac{\text{final weight}}{\text{initial weight}} \right) \times 100 \quad (1)$$

#### Volatile Solids (VS %)

The organic matter in a sample is normally expressed as a percentage of the total solids which can easily transform from a solid phase to a vapour phase without going through a liquid phase.

#### Substrate Concentration (S)

Substrate concentration is the amount of substrate present that can be turned into a product.

Some terms are required for calculating total biogas production which includes organic loading rate (OLR), slurry amount and average biogas yield of vegetables. The OLR is computed by the below formula,

### Organic Loading Rate (OLR)

It is an amount of organic material per unit reactor volume, which is subjected to the anaerobic digester (AD) process in the reactor in a given unit time period. The unit is kg VS/m<sup>3</sup> per day. Equation 2 computes OLR.

$$\text{OLR} = \left( \frac{\text{substrate flow rate} \times \text{substrate concentration}}{\text{reactor volume}} \right) \quad (2)$$

Total biogas yield is a product of OLR, slurry amount and average biogas yield. Equation 3 computes total biogas output.

$$\text{Total Biogas Output (m}^3\text{)} = \text{OLR} \times \text{Average biogas yield} \times \text{slurry amount} \quad (3)$$

Figure 2 shows the step-by-step approach for the calculation of biogas output and payback period.

## 4 Analytical Methods and Calculation

Daily, a minimum fixed quantity of feedstock is necessary to run a biogas plant. This amount can vary according to the size of the reactor. As this paper is oriented towards high input values, it includes hotels, restaurants and community kitchens where minimum kitchen waste is generated above 50 kg per day. For the part of the calculation, input waste of 50 kg per day is taken. This waste is mixed and stirred with water in a 1:2 ratio. Equation 4 computes substrate flow rate per day

$$\begin{aligned} \text{Total wet waste per day} &= 50 \text{ kg} \\ \text{Substrate flow rate per day} &= 1 \text{ part of waste} + 2 \text{ parts of water} \\ &= 1 \times 50 + 2 \times 50 \\ &= 150 \text{ L (approximation of 1 L = 1 kg)} \\ &= 0.15 \frac{\text{m}^3}{\text{day}} \end{aligned} \quad (4)$$

The slurry is kept for certain days at the specific temperature and pressure to generate microbes. This time period is called solid retention time. The average temperature of India is between 32 and 40 °C. After analysing different papers, the optimum range of biogas production from kitchen waste is estimated to be 36 to 50 days for Indian temperature zone. Considering the required factors, SRT is taken as 43 days.

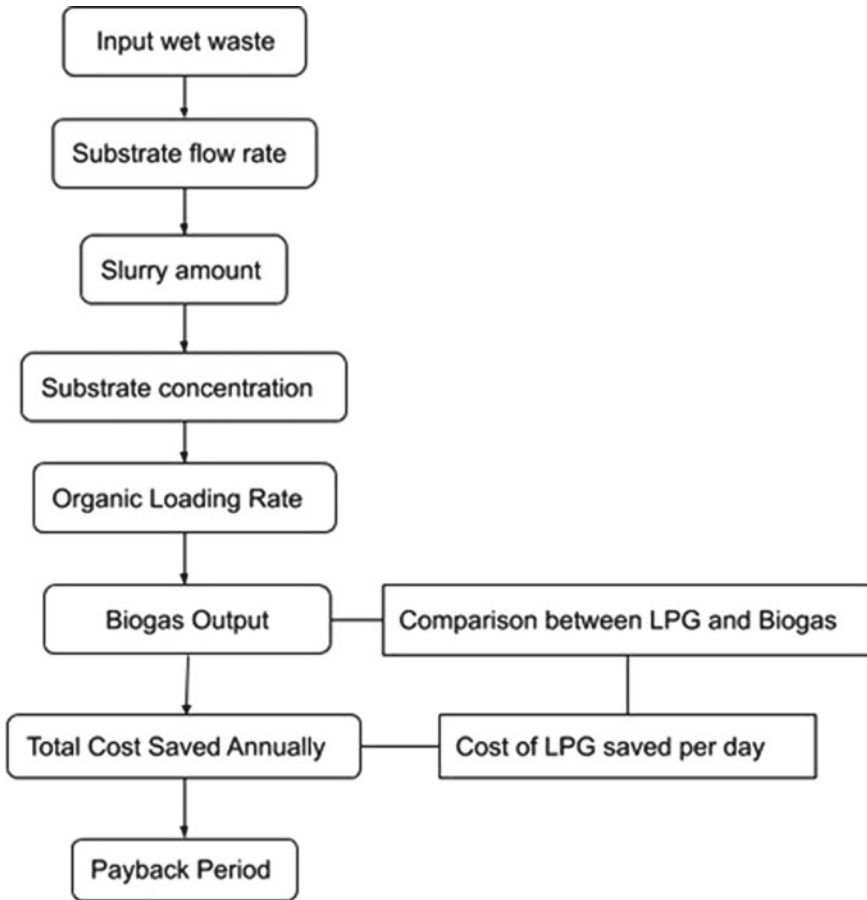


**Fig. 2** Steps for calculation of biogas output and payback period

To calculate slurry amount, substrate is placed in a biogas plant for 43 days. Equation 5 computes the slurry amount

$$\begin{aligned}
 \text{Slurry amount} &= \text{substrate flow rate per day} \times \text{solid retention time} \\
 \text{Slurry amount} &= 0.15 \times 43 \\
 \text{Slurry amount is } &6.45 \text{ m}^3
 \end{aligned}
 \tag{5}$$

Substrate concentration is calculated by the amount of volatile solid. For commercial food waste, TS and VS are considered to be 27.8% and 24.3%, respectively [8]. Therefore, VS is 87.4% of TS. Equation 6 computes substrate concentration.



*Substrate concentration*Step 1: *input wet waste*  $\times$  *TS*

$$\begin{aligned}
 &= 50 \times \frac{27.8}{100} \text{ kg of dry matter} \\
 &= 13.9 \text{ kg of dry matter} \\
 \text{VS of TS\%} &= \frac{24.3}{27.8} \times 100 \\
 \text{VS of TS\%} &= 87.4\%
 \end{aligned} \tag{6.1}$$

Step 2: *dry matter*  $\times$  *VS*

$$\begin{aligned}
 &= 13.9 \times \frac{87.4}{100} \left( \frac{\text{kg VS}}{150 \text{ L}} \text{ per day} \right) \\
 &= 12.14 \times \frac{1000}{150} \frac{\text{kg VS}}{\text{m}^3} \\
 &= 80.99 \frac{\text{kg VS}}{\text{m}^3}
 \end{aligned} \tag{6.2}$$

Therefore, substrate concentration is 80.99 kg VS/m<sup>3</sup>.

The organic loading rate (OLR) is a measure of the biological conversion capacity of the anaerobic digestion system. It represents the substrate quantity introduced into the reactor volume in a given time. Studies of anaerobic treatment of biowaste in developing countries, non-stirred AD systems and an OLR below 2 kg VS/m<sup>3</sup> reactor per day are recommended and considered suitable [21].

OLR is calculated by the following expression:

$$\begin{aligned}
 \text{OLR} &= \frac{\text{substrate flow rate} \times \text{substrate concentration}}{\text{reactor volume}} \\
 &= 0.15 \times \frac{80.99}{6.45} \\
 &= 1.883 \frac{\text{kg VS}}{\text{m}^3}
 \end{aligned} \tag{2}$$

The average biogas yield for vegetable is 0.44 m<sup>3</sup>/kg VS [7].

Total biogas yield is given by the following expression:

$$\begin{aligned}
 \text{Total Biogas Output (m}^3\text{)} &= \text{OLR} \times \text{Average biogas yield} \times \text{slurry amount} \\
 &= 1.883 \times 0.44 \times 6.45 \\
 &= 5.343 \text{ m}^3
 \end{aligned} \tag{3}$$

In India, the most preferred fuel for cooking is LPG. Therefore, this research tends to give biogas as a substitute fuel for LPG. The calorific values of LPG and biogas differ, so to compare heat content equivalent values are found.

$$\begin{aligned} \text{Calorific Value of LPG} &= 49789.6 \frac{\text{KJ}}{\text{kg}} \\ \text{Calorific Value of Biogas} &= 20920 \frac{\text{KJ}}{\text{m}^3} \end{aligned}$$

Therefore, by comparing calorific values, 1 m<sup>3</sup> biogas is found to be equivalent of 0.42 kg of LPG. Equation 7 compares the equivalent amount of biogas and LPG.

$$1 \text{ m}^3 \text{ biogas} = 0.42 \text{ kg of LPG} \quad (7)$$

LPG saved per day in terms of biogas is calculated as biogas output per day and in equivalence of LPG. Equation 8 gives the value of LPG saved per day.

$$\begin{aligned} \text{LPG saved per day} &= 0.42 \times \text{Biogas output} \\ &= 0.42 \times 5.343 \\ &= 2.244 \text{ kg} \end{aligned} \quad (8)$$

Equation 9 gives the amount of LPG saved annually.

$$\begin{aligned} \text{LPG saved annually} &= \text{LPG saved per day} \times 365 \text{ days} \\ &= 2.244 \times 365 \\ &= 819.06 \text{ kg} \end{aligned} \quad (9)$$

According to Indian Auto LPG Coalition, price for 1 L LPG is Rs. 38.954 as of 13 July 2020 [22].

1 kg LPG = 1.96 L LPG.

Cost of 1 kg LPG is Rs. 76.35.

Therefore, the cost of LPG saved per day is given by Eq. 10.

The cost of LPG saved per day is

$$\begin{aligned} \text{Total cost of LPG saved per day} &= 76.35 \times \text{LPG per day} \\ &= 76.35 \times 2.244 \text{ per day} \\ \text{LPG cost saved per day is} &= \text{Rs. } 171.3294 \end{aligned} \quad (10)$$

Equation 11 computes LPG cost saved annually.

$$\begin{aligned}
 \text{LPG cost saved annually} &= \text{Cost of LPG saved per day} \times 365 \\
 &= 171.3294 \times 365 \\
 &= \text{Rs. } 62535
 \end{aligned}
 \tag{11}$$

Therefore, annual saving for 50 kg input biogas plant is Rs. 62,535.

Installing the biogas plants is expensive, but required maintenance of biogas plants is low. Set-up cost for a biogas plant is a one-time investment which has high returns after a specific period. This specific period is termed as payback period for the biogas plant.

The payback period is given as time required to cover all expenses to set up the plant and maintenance cost. The installation cost of 50 kg input plant is Rs. 1.75 lakhs. Equation 12 computes payback period

$$\text{Payback Period} = \frac{\text{total investment}}{\text{annual saving}}
 \tag{12}$$

For 50 kg input, payback period is given as:

$$\begin{aligned}
 \text{Payback period} &= \frac{175,000}{62,535} \\
 &= 2.798 \text{ years}
 \end{aligned}$$

Hence, the payback period for a 50 kg input plant is 2.798 years.

Similar calculations are carried out for different inputs of wet waste as 50 kg/day, 100 kg/day, 150 kg/day, 200 kg/day, 500 kg/day, 750 kg/day and 1000 kg/day.

Table 1 shows theoretically calculated values which are interdependent for each step-in calculation. Calculations are given as per slots of input waste that are 50 kg/day, 100 kg/day, 150 kg/day, 200 kg/day, 500 kg/day, 750 kg/day and 1000 kg/day. Calculations for other slots are similar to 50 kg/day.

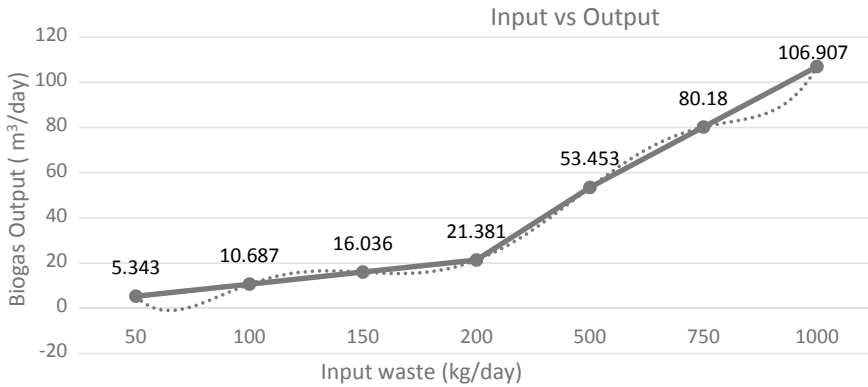
At MIT World Peace University, Pune, India, a biogas plant of capacity 750 kg of kitchen waste per day is installed and commissioned in November 2014. The total construction and installation cost of this biogas plant was Rs. 2,200,000. The cost of this biogas plant and the market survey on the cost of different biogas plants are considered as the reference for deciding the installation cost of the different capacities of the biogas plant.

## 5 Result and Discussion

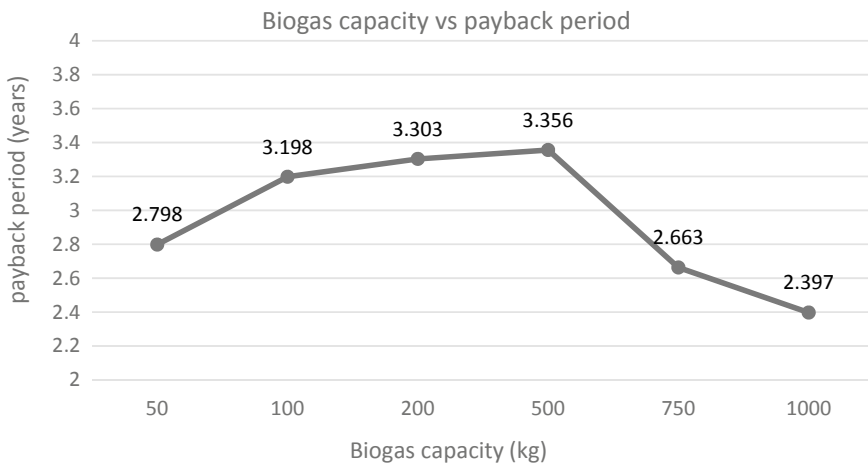
Different parameters such as input waste, biogas output, set-up cost and the payback period can be analysed through graphical methods.

**Table 1** Biogas output and payback period for a different kitchen waste input

Input (kg/day)	Substrate flow rate (litre)	slurry amount (m <sup>3</sup> )	Substrate concentration (kg VS/m <sup>3</sup> )	OLR (kg VS/m <sup>3</sup> day)	Biogas output per day (m <sup>3</sup> )	Volume of plant (m <sup>3</sup> )	LPG equivalent (kg)	Savings per day (Rs)	Set-up cost (Rs)	Payback period (years)
50	150	6.45	80.99	1.883	5.343	8.333	2.244	171.32	175,000	2.798
100	300	12.9	80.99	1.883	10.687	14.783	4.488	342.65	400,000	3.198
150	450	19.35	80.99	1.883	16.036	21.233	6.735	514.231	620,000	3.303
200	600	25.8	80.99	1.883	21.381	27.683	8.98	685.641	850,000	3.39
500	1500	64.5	80.99	1.883	53.453	66.383	22.45	1714.1	2,100,000	3.356
750	2250	96.75	80.99	1.883	80.18	98.63	33.67	2571.2	2,500,000	2.663
1000	3000	129	80.99	1.883	106.907	130.883	44.9	3428.2	3,000,000	2.397



**Fig. 3** Variation of the biogas output with input kitchen waste



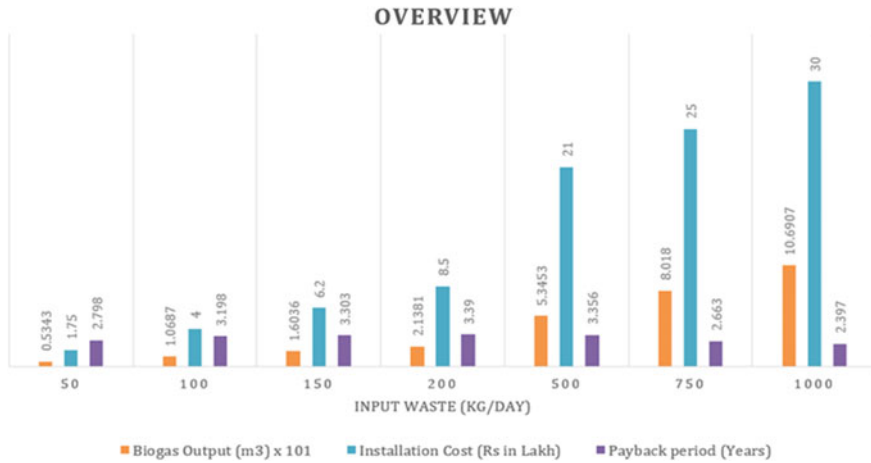
**Fig. 4** Variation of the payback period for a different biogas plant capacity

Figure 3 shows the variation of the biogas output with input kitchen waste.

Figure 4 shows the variation of the payback period for different capacities of biogas plants.

Figure 5 provides an overview of biogas yield, set-up cost and the payback period for different slots of input waste.

From the graph, it is observed that the biogas output is linearly varying with input waste in a ratio around 10:1. Based on the regression analysis from this graph, a correlation is developed which can provide the output of the biogas generated for different kitchen waste inputs.



**Fig. 5** Biogas output, installation cost and payback period for given input kitchen waste

This correlation is given in Eq. 13.

$$y = 0.2524x^6 - 6.0143x^5 + 55.986x^4 - 257.29x^3 + 609.38x^2 - 691.03x + 294.06 \tag{13}$$

where  $x$  = input waste to biogas plant (kg)

$$y = \text{Biogas output (m}^3\text{)}$$

It is observed in Fig. 4 that initially there is an increasing trend in the payback period from 50 to 500 kg of biogas plant capacity. This is because the plant cost also increases with the capacity of the biogas plant. But from 500 kg capacity, the graph shows the decline in the payback period. This is because with the increasing biogas plant capacity the biogas output also increases. So, it can be concluded that higher the capacity biogas plant less will be the payback period.

Figure 5 gives an overview of parameters like biogas output, installation cost and payback period for given input waste.

## 6 Conclusions

Kitchen waste can be utilized in a better way than to fill landfills. Using it in a biogas plant reduces operating cost for hotels and restaurants. For a comparative study of biogas plant between different installation costs according to input waste and payback period, different slots are created. It is observed that the input kitchen

waste feed and output biogas generation are in proportion around 10:1. Biogas yield increases with increase in input waste.

Also, payback period increases for small- to medium-scale biogas plants, i.e. less than 500 kg/day, whereas for large capacity of biogas plant above 500 kg/day the payback period reduced drastically. For small scale, biogas plant payback period is between 2.798 and 3.39 years and large-scale plant payback period is 3.35–2.397 years.

As the payback period for the capacity of 50–100 kg per day is between 2 and 4 years, the biogas plant can be proved to be cost-effective and economical for long-running businesses in the foodservice sector.

## References

1. Food and Agriculture Organization (2013) Food wastage footprint impact on natural resources. ISBN 978-92-5-107752-8. <http://www.fao.org/3/i3347e/i3347e.pdf>
2. National Academy of Agricultural. Saving the harvest: reducing the food loss and waste, Policy Brief No. 5. 2019. <http://naasindia.org/documents/Saving%20the%20Harvest.pdf>
3. Jehangir B (2018) Tackling the challenges of reducing and managing food waste in Mumbai restaurants. *Br Food J*
4. Kharbanda V, Qureshi M (1985) Biogas development in India and the PRC. *Int Assoc Energy Econ*
5. Jain S (2019) Global potential of biogas. World Biogas Association, June 2019
6. Baredar P, Khare V, Nema S (2020) Design and optimization of biogas energy systems. Academic Press
7. Knol W, Van der Most M, De Waart J (1978) Biogas production by anaerobic digestion of fruit and vegetable waste a preliminary study. *J Sci Food Agric*
8. Banks C, Chesshire M, Heavens S, Arnold R (2011) Anaerobic digestion of source segregated domestic food waste: performance assessment by mass and energy balance. *Bioresour Technol*
9. Agrahari R, Tiwari G (2013) the production of biogas using kitchen waste. *Int J Energy Sci*
10. Ariyanto T, Cahyono R, Vente A, Mattheij S, Millati RS, Taherzadeh M, Syamsiah S (2017) Utilization of fruit waste as biogas plant feed and its superiority compared to landfill. *Int J Technol* 8(8)
11. Sahu N, Sharma A, Mishra P, Chandrashekhara B, Sharma G, Kapley A, Pandey R (2017) Evaluation of biogas production potential of kitchen waste in the presence of spices. *Waste Manage* 70
12. Decker T, Baumgardner M, Prapas J, Bradley T (2018) A mixed computational and experimental approach to improved biogas burner flame port design. *Energy Sustain Dev* 44
13. Kougiaris P, Angelidaki I (2018) Biogas and its opportunities—a review. *Front Environ Sci Eng*
14. Shoar F, Abdi R, Najafi B, Ardabili S (2019) The effect of thermochemical pretreatment on biogas production efficiency from kitchen waste using a novel lab scale digester. *Renew Energy Focus* 28
15. Sindhu R, Gnansounou E, Rebello S, Binod P, Varjani S, Thakur I, Nair R, Pandey A (2019) Conversion of food and kitchen waste to value-added products. *J Environ Manage* 241
16. Petroleum Planning and Analysis Cell, Ministry of Petroleum and Natural Gas, Government of India (2016). <https://www.ppac.gov.in/WriteReadData/Reports/201710310449342512219/PrimarySurveyReportPPAC.pdf>

17. Petroleum Planning and Analysis Cell, Ministry of Petroleum and Natural Gas, Government of India (2020). <https://www.ppac.gov.in/WriteReadData/Reports/202009080228232396783WebVersionLPGProfile1.7.2020.pdf>
18. Surange J, Patil N, Rajput A (2014) Performance analysis of burners used in LPG cooking stove-a review. *Int J Innovative Res Sci Eng Technol* 3(4)
19. Subbarao S, Dhananjaya N (2015) Green economy via decentralized energy generation and waste management by a 60 kg/day Kitchen Waste Biogas Plant at Postal Training Centre, Mysore, India. *Micro perspective for decentralized energy supply* 2015
20. Ward A, Hobbs P, Holliman P, Jones D (2008) Optimization of the anaerobic digestion of agricultural resources. *Bioresour Technol*
21. Vogeli Y, Lohri C, Gallardo A, Diener S, Zurbrugg C (2018) Anaerobic digestion of biowaste in developing countries. *Ewag Swiss Fed Inst Aquat Sci Technol*
22. [https://www.globalpetrolprices.com/India/lpg\\_prices/](https://www.globalpetrolprices.com/India/lpg_prices/)



# Biosensor Based on One-Dimensional Photonic Crystal for Poliovirus Detection



Sapna Dinodiya and Anami Bhargava

## 1 Introduction

Poliovirus (PV) is a highly contagious disease that can affect the nervous system causing muscle weakness and paralysis. Early stage symptoms of PV are flu-like as headache, sore throat, fatigue, fever and pain in limbs. But after a week severe symptoms might appear that leads to paralysis in spinal cord, brainstem or both. The children under 5 years of age are more likely to be affected by polio. According to World Health Organisation (WHO), one in two hundred polio infections results in permanent paralysis [1]. In 5–10% of cases of paralysis, virus attack to muscles resulting in the failure of breathing and cause death. In 1988, a resolution of worldwide eradication of poliovirus was adopted by World Health Assembly. As a result, polio cases have decreased since 1988 but still three countries (Pakistan, Afghanistan and Nigeria) are suffering from this disease and have a risk to transmit the virus globally [1].

Polio may occur under the conditions of poor hygiene and less vaccination in overpopulated area [2]. The spread of PV is possible through water or foods or by direct contact with someone who is infected with virus. The virus is transmitted via the faecal oral rout through contaminated water. The surface water such as marine and recreational waters is contaminated by PV due to the discharge of untreated or improperly treated sewage [3]. The eradication of virus is very important for public health and economic growth of the country. The control of virus is necessary, especially in water used for drinking purpose. The frequent testing of water is required to prevent the risk of infection [4]. Polymerase chain reaction (PCR) and nucleic acid hybridisation are the most commonly used methods for the detection of different enteric viruses from water samples [5–7].

---

S. Dinodiya (✉)

Department of Physics, Govt. Women Polytechnic College, Bikaner 334001, India

A. Bhargava

Nanophysics Lab, Department of Physics, Govt. Dungar College, Bikaner 334001, India

© The Author(s), under exclusive license to Springer Nature Singapore Pte Ltd. 2022

303

P. Verma et al. (eds.), *Advancement in Materials, Manufacturing and Energy Engineering, Vol. I*, Lecture Notes in Mechanical Engineering,

[https://doi.org/10.1007/978-981-16-5371-1\\_26](https://doi.org/10.1007/978-981-16-5371-1_26)

Photonic crystals (PhCs) are emerging materials to use for sensing purpose due to its special optical properties of photonic band gap (PBG). The band gaps of photonic crystals can be changed by external perturbation like pressure, temperature, density and provide a basis for designing the different types of optical sensors. Photonic crystal sensor in comparison with conventional optical sensors is more efficient because of their inbuilt compactness, high sensitivity, high resolution and fast response. The biomolecules that can alter the refractive index of structure of the photonic crystal can be sensed by measuring optical properties like spectral pattern of transmitted power [8]. Several researchers have used photonic crystals to design optical biosensors such as blood glucose sensor [9], urea concentration sensor [10] and sensor for malaria diagnosis [11].

In this work, a one-dimensional (1D) PhC with a defect layer is proposed as a biosensor for the detection of poliovirus concentration in contaminated water samples. The advantage of 1-D photonic crystal is its simple layered structure, easy fabrication and good performance characteristics as a sensor [12]. As the refractive index of defect layer increases due to the concentration of poliovirus, the peak corresponding to the defect mode is shifted to higher wavelengths. Proposed structure can be useful in early detection of virus in water and to prevent transmission in humans.

## 2 Theoretical Model

1-D PhC of structure  $(AB)^N D (BA)^N$  is shown in Fig. 1 with  $4N + 1$  alternating layers of high refractive index material A, low refractive index material B and a single defect layer D between them. Transfer matrix method (TMM) is used for transmission spectrum [13–15].

Transfer matrix for whole structure can be written as

$$\begin{bmatrix} E_0 \\ H_0 \end{bmatrix} = M_1 M_2 \dots M_{2N} M_D \dots M_{4N} M_{4N+1} \begin{bmatrix} E_{4N+1} \\ H_{4N+1} \end{bmatrix} \tag{1}$$

$$\begin{bmatrix} E_0 \\ H_0 \end{bmatrix} = M \begin{bmatrix} E_{4N+1} \\ H_{4N+1} \end{bmatrix} \tag{2}$$

**Fig. 1** Schematic diagram of 1-D photonic crystal with defect



Transfer matrix  $M$  connects electric and magnetic fields of first and last ends of layers.

$$M = \prod_{j=1}^{4N+1} M_j = (M_A M_B)^N M_D (M_B M_A)^N = \begin{bmatrix} M_{11} & M_{12} \\ M_{21} & M_{22} \end{bmatrix} \tag{3}$$

Transfer matrix for  $j$ th layer is given as

$$M_j = \begin{bmatrix} \cos \delta_j & \frac{i \sin \delta_j}{\gamma_j} \\ i \gamma_j \sin \delta_j & \cos \delta_j \end{bmatrix} = \begin{bmatrix} m_{11} & m_{12} \\ m_{21} & m_{22} \end{bmatrix} \tag{4}$$

$\gamma_j = n_j \cos \alpha_j$  for TE polarisation

$\gamma_j = n_j / \cos \alpha_j$  for TM polarisation

$$\delta_j = \frac{2\pi}{\lambda} n_j d_j \cos \alpha_j \tag{5}$$

$n_j$  and  $d_j$  are refractive index and thickness of  $j$ th layer and  $\alpha_j$  is angle of refraction determined by angle of incidence by Snell's law.

Transmission coefficient for structure is given by

$$t = \frac{2\gamma_0}{\gamma_0 M_{11} + \gamma_0 \gamma_t M_{12} + M_{21} + \gamma_t M_{22}} \tag{6}$$

where  $\gamma_0$  and  $\gamma_t$  are related with first and last medium of structure.

Transmittance  $T$  is given as

$$T = \frac{\gamma_t}{\gamma_0} |t|^2 \tag{7}$$

### 3 Structure and Materials

The proposed biosensor is designed in the structure of  $(AB)^5D(BA)^5$ . Here, the materials of layer A and B are aluminium nitride (AlN) and air, respectively. The layer D is a defect layer that creates a defect state in PBG. This layer is filled with contaminated water. A shifting of transmission peak occurs with the change in concentration of poliovirus, due to the variation of refractive index of water. AlN is an interesting material with wide band gap (6.42 eV), stable crystal structure and good dielectric properties [16].

In this study, the value of specific refractive index increment of poliovirus is taken at a wavelength of 260 nm. At this wavelength, the value of extinction coefficient of AlN and the change of refractive index with wavelength are negligible [17].

The dispersion relation between refractive index and wavelength of AlN is given as [18]

$$n^2 - 1 = 2.1399 + \frac{1.3786\lambda^2}{\lambda^2 - 0.1715^2} + \frac{3.861\lambda^2}{\lambda^2 - 15.03^2} \quad (8)$$

Poliovirus is made of RNA genome and enclosed by protein shell [19]. Therefore, the refractive index of contaminated water is calculated by the refractive index of protein solution [20]. The refractive index of the water is related to concentration of virus as

$$n_{PV} = n_S + a \times C \quad (9)$$

where  $n_{PV}$  is refractive index of poliovirus solution,  $n_S$  is refractive index of pure water,  $a$  is specific refractive index of poliovirus taken as 0.174 ml/g [21], and  $C$  is concentration of virus in g/ml.

## 4 Results and Discussion

The transmission spectra of proposed structure are calculated using transfer matrix method. Here, the thickness of AlN layer and air is taken as 200 nm and 300 nm, respectively. The thickness of defect layer is taken as 1000 nm. The structure is designed such that the peak of transmission of defect layer is obtained around 260 nm [17]. The results of the simulation are shown in Table 1. The effective refractive index of the particles is a result of local polarisability of the atoms (water) and chemical groups (virus) due to the deformation of electron configuration about nuclei [22]. Table 1 shows the evolution of virus concentration (g/ml) with refractive index. The refractive index of the sample is found to increase linearly with the concentration of virus.

**Table 1** Simulation results at different concentration of poliovirus

Concentration of virus (g/ml)	Refractive index of water solution	Wavelength of defect mode (nm)	Quality factor
0	1.330	259.554	24649
0.005	1.33087	259.650	24495
0.010	1.33174	259.744	24343
0.015	1.33261	259.839	24148
0.020	1.33348	259.934	23957
0.025	1.33435	260.028	23768

Further, in PBG region corresponding to wavelength range 248–270 nm, only the wavelength of defect mode is allowed to propagate as shown in Fig. 2. It is observed that for pure water ( $n = 1.33$ ), transmission peak is obtained at 259.554 nm with good transmission coefficient ( $\sim 1$ ). As the concentration of poliovirus changes in water, the peak corresponding to the defect mode is shifted to higher wavelength as shown by Fig. 3.

An important parameter to characterise the sensor performance is sensitivity. The sensitivity of the 1-D PhC can be defined as the ratio of the change of wavelength of the transmission peak to the change in refractive index using the following equation [11, 23]

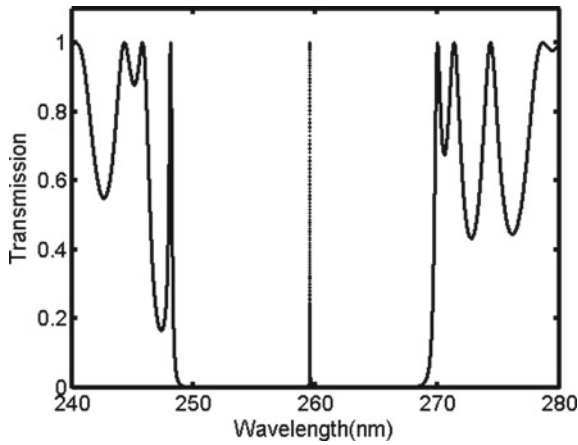


Fig. 2 Transmission spectra for pure water

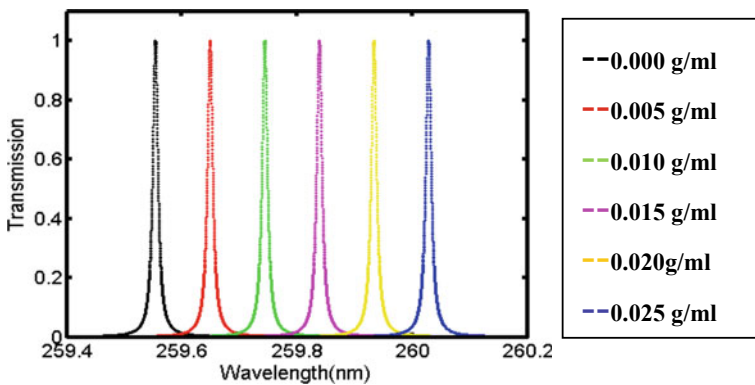


Fig. 3 Transmission spectra at different concentration of the poliovirus

$$S = \frac{\Delta\lambda}{\Delta n} \tag{10}$$

The proposed structure exhibits a sensitivity of about 110.340 nm per RIU.

The sensitivity increases with thickness of defect layer as shown in Table 2.

We can explain this behaviour using the relation,  $\delta = \frac{2\pi}{\lambda} nd \cos \alpha$  where  $\delta$ ,  $\lambda$ ,  $n$ ,  $d$  and  $\alpha$  are the phase shift, the wavelength, the refractive index, the thickness and angle of refraction, respectively. In terms of sensitivity, we find,  $\frac{d\lambda}{dn} = \frac{2\pi}{\delta} d \cos \alpha$ . For constant value of  $\delta$  and  $\alpha$ , sensitivity depends upon thickness, but for large value of thickness, it increases the time response of the sensor. Hence, the defect layer thickness is taken as 1000 nm.

Quality factor is another important performance index that defines the shape of resonant peaks and expressed as [24]

$$Q = \frac{\lambda}{FWHM} \tag{11}$$

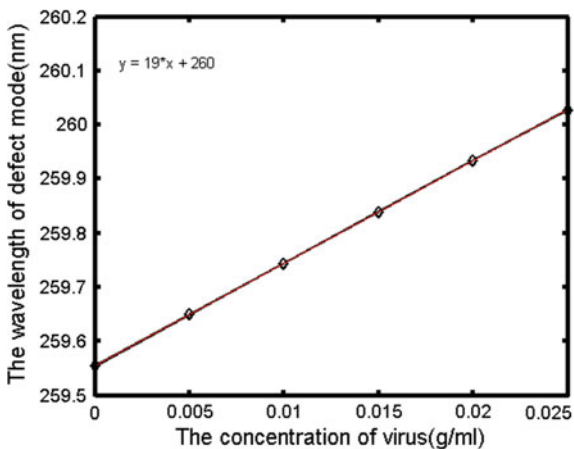
where  $\lambda$  is the resonant wavelength and FWHM is full width at half maximum. Table 1 exhibits a high  $Q$ -factor about 24,965 at 0.005 g/ml.

In Fig. 4, it is exhibited that wavelength of defect mode increases linearly with concentration of the virus. This property is used to estimate the working of the sensor. By fitting, sensitivity of proposed biosensor is obtained as 19 nm per (g/ml).

**Table 2** Thickness of defect and sensitivity

Thickness (nm)	Sensitivity (nm/RIU)
800	97.70
1000	110.34
1200	117.24

**Fig. 4** Concentration of virus with wavelength of defect mode



The device is found to be suitable to detect the poliovirus that has concentration more than 0.005 g/ml in water.

## 5 Conclusion

In this paper, a biosensor has been proposed to detect the concentration of poliovirus that is based on 1-D defective PhC. The defect layer is taken as contaminated water, and refractive index varies with the change in concentration of virus. The transmission spectra and performance of the proposed sensor are investigated using the transfer matrix method. Defect in 1-D PhC produces a transmission peak in photonic band gap. For pure water ( $n = 1.33$ ), transmission peak is obtained at 259.554 nm. A total wavelength shift of 0.474 nm is observed, as the concentration of poliovirus changes from 0 to 0.025 g/ml in water. It is found that the sensitivity increases with thickness of defect layer. The wavelength of defect mode is shifted linearly by the concentration of virus in water. The estimated parameters for the sensor are the sensitivity approximating to 110.34 nm per RIU and the quality factor of about  $2.4 \times 10^4$ .

## References

1. World Health Organisation. Poliomyelitis, Webpage. <https://www.who.int/news-room/fact-sheets/detail/poliomyelitis>. Last accessed 15 Jan 2021
2. Leveque N, Andreoletti L (2008) A novel mode of transmission for human enterovirus infection is swimming in contaminated seawater: implications in public health and in epidemiological surveillance. *Clin Infect Dis* 47:624–626
3. Dowdle WR, Birmingham ME (1997) Biological principles of poliovirus eradication. *J Infect Dis* 175:s286–s292
4. Rose JB, Gerba CP (1991) Use of risk assessment for development of microbial standards. *Water Sci Technol* 24(2):29–34
5. Enriquez CE, Abbaszadegan M, Pepper IL, Richardson KJ, Margolin AB, Gerba CP (1992) Poliovirus detection in water by cell culture and nucleic acid hybridization. In: Proceedings of the 16th biennial conference and exposition of the international association on water pollution research and control, pp 315–319, Washington
6. Atmar RL, Metcalf TG, Neill FH, Estes MK (1993) Detection of enteric viruses in oysters by using the polymerase chain reaction. *Appl Environ Microbiol* 59:631–635
7. Wilde J, Van R (1992) Detection of rotaviruses in the day care environment by reverse transcriptase polymerase chain reaction. *J Infect Dis* 166:507–511
8. Dinodiya S, Suthar B, Bhargava A (2018) Photonic crystal sensors: physics and applications. In: AIP conference proceedings, p 060016, Bikaner
9. Banerjee A (2019) Enhancement in sensitivity of blood glucose sensor by using 1D defect ternary photonic band gap structures. *J Opt* 48(2):262–265
10. Gharsallah Z, Najjar M, Suthar B, Janyani V (2018) High sensitivity and ultra-compact optical biosensor for detection of Urea concentration. *Opt Quant Electron* 50(6):249
11. Ankita, Suthar B, Bhargava A (2021) Biosensor application of one-dimensional photonic crystal for malaria diagnosis. *Plasmonics* 16(1):59–62

12. Suthar B, Bhargava A (2010) Improving the optical tuning and spectral efficiency in chalcogenide photonic quantum well structures. *J Ovonic Res* 6(3):117–123
13. Yeh P (1988) *Optical waves in layered media*. Wiley, New York
14. Suthar B, Nagar AK, Bhargava A (2009) Tuning the localized mode in point defect chalcogenide photonic crystal. *Chalcogenide Letters* 6(11):623–627
15. Barket O, Mamri B (2018) Numerical method for a one dimensional defective photonic crystal selective filters. *Electr Electron Technol Open Access J* 1(2):83–87
16. Fu X (2016) Aluminium nitride wide bandgap semiconductor and its basic characteristics. In: *Proceedings of the 6th international conference on electronic, mechanical information and management society*, pp 555–558, Shenyang
17. RPI ECSE. Material refractive index and extinction coefficient. [www.ecse.rpi.edu](http://www.ecse.rpi.edu). Last Accessed 15 Jan 2021
18. Pastrňák J, Roskocová L (1966) Refractive index measurements on AlN single crystals. *Physica Status Solidi B* 14(1)
19. Hogle JM (2002) Poliovirus Cell entry: common structural themes in viral cell entry pathways. *Ann Rev Microbiol* 56:677–702
20. Hand DB (1935) The refractivity of protien solutions. *J Biol Chem* 103:703–707
21. Charney J, Machlowitz R, Tytell AA, Sagin JF, Spicer DS (1961) The concentration and purification of poliomyelitis virus by the use of nucleic acid precipitation. *Virology* 16:269–280
22. Zhao H, Brown PH, Schuck P (2011) On the distribution of protien refractive index increments. *Biophys J* 100(9):2309–2317
23. Bagci F, Akaoglu B (2013) Enhancement of refractive index sensitivity in photonic crystal waveguide-based sensors by selective infiltration. *Acta Phys Pol A* 124:50–55
24. Olyae S, Seifouri M, Karami R, Bahabady AM (2019) Designing a high sensitivity hexagonal nano-cavity photonic crystal resonator for the purpose of seawater salinity sensing. *Optical Quan Electron* 51(4):97 1–9



# Assessment of Local River Sand Mould Property at Different Curing Temperatures



Jatin Sadarang, Ramesh Kumar Nayak<sup>ID</sup>, and Isham Panigrahi

## 1 Introduction

In recent years, the sand casting mail foundries are shifted from Western countries to India and other Asian countries due to the easy availability of manpower and raw materials. However, in India silica sand availability is decreasing gradually due to high production rate of sand casting products and huge civil construction and leads to increase in the cost of production of sand casting products.

Silica sand is readily available on the earth. High silica containing sand is available in some places like Allahabad in India, due to which foundry industries away from Allahabad have to pay the high transportation costs. Therefore, foundry engineers, researchers, and scientists are trying different materials in foundry applications.

Murthy et al. [1] use blast furnace slag in the sand mould for aluminium alloy casting. Thermal conductivity of blast furnace slag differs from silica sand mould, due to which change in casting microstructure occurs [2]. There are no defects observed in aluminium alloy casting made by blast furnace slag mould [3]. Ferrochrome slag mould has different thermal conductivity than silica sand [4, 5]. Waste steel industry powder reduces mould property. Therefore, it replaces only 20% silica sand from green sand mould [6]. Fly ash particles are smaller than silica sand particles [7], due to which mould permeability decreases [8].

Babata et al. [9] use Oyun River sand in mould and evaluate sand mould properties. The refractoriness of Oyun River sand is 1300 °C, which is suitable for aluminium alloy casting. Puri beach sand particles have an angular shape due to

---

J. Sadarang (✉) · I. Panigrahi  
School of Mechanical Engineering, KIIT Deemed To Be University,  
Bhubaneswar 754024, India

R. K. Nayak  
Department of Materials and Metallurgical Engineering, MANIT,  
Bhopal 462003, India

which green and dry strength of Puri beach sand mould is higher than Mahanadi River and mined sand mould [10]. Local river bed sand and silica sand have similar mould shear strength [11]. River Gurara bed sand's refractoriness is 1500 °C, suitable for light grey iron casting [12]. Local sand Ilorin and Ilesha can produce the non-ferrous sand casting [13]. Bala et al. [14] use Warri, Ethiopie and Ughelli river sand in green sand mould and evaluate physical and mechanical mould property. Warri, Ethiopie and Ughelli river sand have significant mould properties for foundry applications. The locally available sand shows suitability in a foundry application. Therefore, in the present investigation, locally available river sand was used as the principal mould material and evaluated mould property at different heating temperatures.

## 2 Materials and Method

### 2.1 Materials

River sand, bentonite clay, and coal dust were used to prepare sand mould samples. Bentonite clay and coal dust were procured from RSB Metaltech, Pvt. Ltd., Cuttack, India, and river bed sand were obtained from a local river near Bhopal, India. The physical appearance of river sand, bentonite clay, and coal dust is shown in Fig. 1.

### 2.2 Sample Preparation

Properly mixing of mould ingredients gives uniform mould property. The sand mould ingredients were mixed in sand muller having 5 kg capacity. Sand mould mixture having 83% river sand, 11% bentonite clay, and 5% coal dust and maintain 5% moisture in sand mould. The AFS standard sample was prepared by sand rammer. The moulding sand was compacted by applying three rammed strokes having 6.35 kg weight. The obtained sample having 50 mm height and diameter and is used to determine mould hardness, compressive and shear strength.



**Fig. 1** Physical appearance of **a** river sand, **b** bentonite clay, and **c** coal dust

### 2.3 Drying Procedure

Moisture in moulding sand increases the risk of gas defects in casting. River sand mould sample was heated at a different temperature (50, 100, 150 and 200 °C) to evaporate water and observe the effect of temperature on mould hardness, compressive and shear strength. River sand mould samples were heated for one hour in a hot air oven. Figure 2 shows a heating cycle of river sand mould.

### 2.4 Moisture Test

A rapid moisture teller was used to evaluate moisture per cent in moulding sand. The sand mould mixture of 6 g mixed with 12 g calcium carbide powder in moisture teller. The moisture present in the sand mould mixture reacts with calcium carbide and forms acetylene gas. The pressure created inside the moisture teller was obtained through a calibrated dial gauge in moisture percentage.

### 2.5 Mould Hardness

Mould hardness test is similar to Brinell hardness test [15]. In the present investigation, B scale mould hardness was used to determine river sand mould's hardness. The spring-loaded plunger was gradually pressed on the flat surface of sand mould samples. The resistance offered by sand mould was obtained from mould hardness dial gauge.

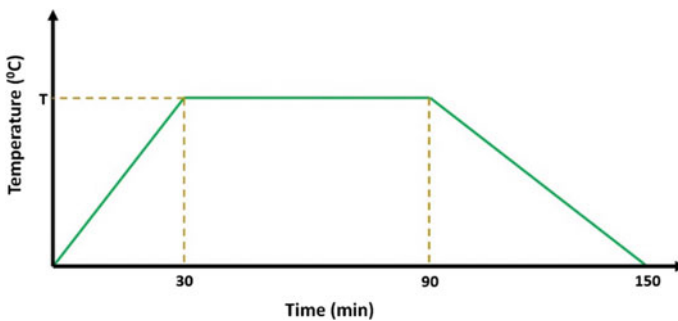


Fig. 2 Heating cycle

## 2.6 Mould Compressive and Shear Strength

River sand mould compressive and shear strength were obtained from a universal strength machine. The sand mould sample was axially compressed in universal strength machine. The compressive strength was obtained through an attached computer having USM software. The shear strength of sand mould was obtained by similar procedure. A shear gripper was used to apply shear force in sand mould sample.

## 3 Result and Discussion

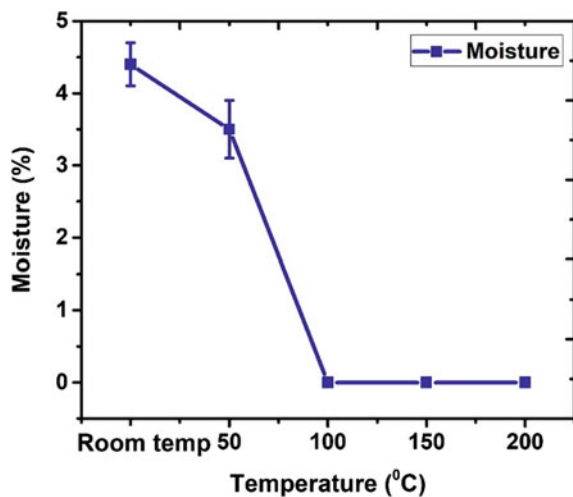
### 3.1 Moisture

Figure 3 shows the effect of temperature on moisture content in river sand mould. It is observed that there is no moisture present in moulding sand above 100 °C. Water evaporated at 100 °C, therefore, no water present in moulding sand, even in the centre portion of the river sand mould sample above 100 °C heating temperature.

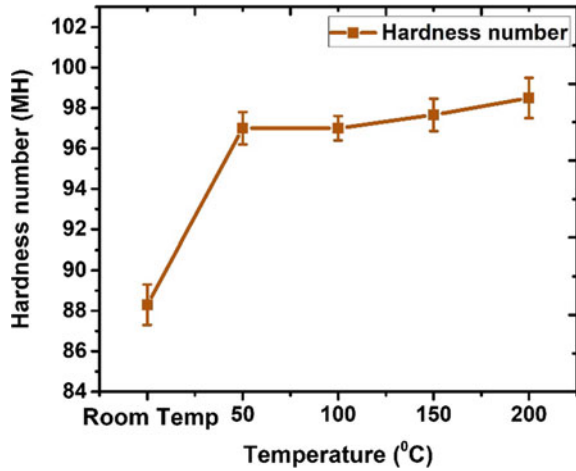
### 3.2 Mould Hardness

Figure 4 shows the effect of temperature on mould hardness. It is observed that mould hardness increases with increase in temperature. Moisture concentration decreases with increase in temperature. Moisture increases the plasticity and

**Fig. 3** Effect of temperature on moisture content in moulding sand



**Fig. 4** Effect of temperature on mould hardness

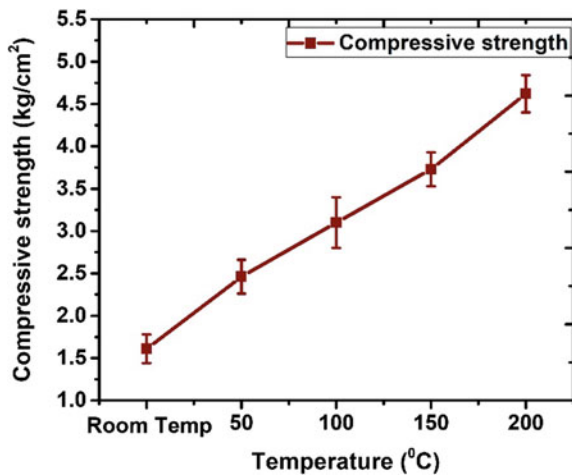


lubricant property of moulding sand [16]. Therefore, as the concentration of moisture reduces mould hardness increases. The maximum mould hardness (98.5 MH) of river sand mould was obtained at 200 °C.

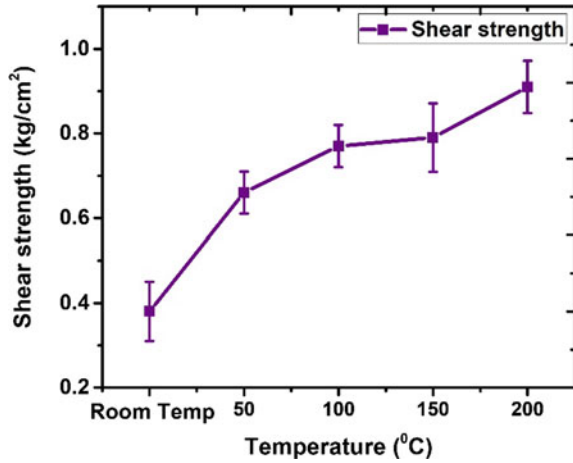
### 3.3 Mould Compressive Strength

Figure 5 shows the effect of temperature on compressive strength of river sand mould. It is observed that on increase in temperature mould compressive strength increases. Water and bentonite clay form a thin layer on sand particles responsible for mould strength by making cohesive bonds [17]. The water and bentonite clay

**Fig. 5** Effect of temperature on river sand mould compressive strength



**Fig. 6** Effect of temperature on river sand mould shear strength



mixture get harder as moisture gets evaporated. The maximum compressive strength (4.62 kg/cm<sup>2</sup>) was obtained at 200 °C.

### 3.4 Mould Shear Strength

Figure 6 shows the effect of temperature on shear strength of river sand mould. It is observed that on increase in temperature mould shear strength increases. Water and bentonite clay form thin layers on sand particles responsible for mould strength by making cohesive bonds [16]. The water and bentonite clay mixture get harder as moisture gets evaporated. The maximum shear strength (0.91 kg/cm<sup>2</sup>) was obtained at 200 °C.

## 4 Conclusion

Local river sand is used as a primary mould material. The AFS standard samples were prepared and evaluate the effect of temperature on mould hardness, compressive and shear strength. The following conclusion is drawn.

- Moisture percentage decreases on increase in heating temperature. There is no moisture present in the river sand mould sample above 100 °C.
- River sand mould hardness, compressive and shear strength increase with the increase in temperature.
- The mould hardness, compressive and shearing strength are 98.5 MH, 4.62 kg/cm<sup>2</sup> and 0.91 kg/cm<sup>2</sup> at 200 °C heating temperature.

**Acknowledgements** The authors would like to express their sincere thanks to the DST (AMT), for the financial support to carry out this work (Project No. DST/TDT/AMT/2017/173). Special thanks to RSB Metaltech, Pvt. Ltd., Cuttack, India, for their support as an industrial partner.

## References

1. Murthy IN, Arun Babu N, Babu Rao J (2018) Microstructure and mechanical properties of A356 alloy castings made in sand and granulated blast furnace slag moulds. *Mater Today Proc* 5:161–167. <https://doi.org/10.1016/j.matpr.2017.11.067>
2. Jinugu BR, Inampudi NM (2017) Microstructure, SDAS and mechanical properties of A356 alloy castings made in sand and granulated blast furnace slag moulds. *Arch Foundry Eng* 17. <https://doi.org/10.1515/afe-2017-0033>
3. Murthy IN, Rao JB (2018) Non destructive evaluation of A356 alloy castings made in sand and granulated blast furnace slag moulds. *Mater Today Proc* 5:168–174
4. Murthy IN, Rao JB (2017) Evaluation of the microstructure, secondary dendrite arm spacing, and mechanical properties of Al–Si alloy castings made in sand and Fe–Cr slag molds. *Int J Miner Metall Mater* 24:784–793. <https://doi.org/10.1007/s12613-017-1462-x>
5. Oloyede OR, Afolalu SA, Adelakun OJ, Abioye A, Adeoye AO (2020) Evaluation of structure-properties interdependence of commercial grey iron in silica & slag moulds. paper/ Evaluation-of-Structure-Properties-Interdependence-Oloyede-Afolalu/ 51553d847111687559071b5f9a2eea8bca340877. Last Accessed 10 Dec 2020
6. Karunakaran P (2012) Investigation of the properties of molding sand with waste powder from steel industry. *Eur J Sci Res* 77:5–11
7. Singh A (2018) Fly ash an alternative for molding. *Int J Res Appl Sci Eng Technol* 6:525–531. <https://doi.org/10.22214/ijraset.2018.1078>
8. Palaniappan J (2017) Study on Type C coal fly ash as an additive to molding sand for steel casting. *J Inst Eng India Ser D* 98:139–145. <https://doi.org/10.1007/s40033-016-0115-y>
9. Babata YS, Kabiru Suleiman A, Ambali I, Bello M (2019) Evaluation of the foundry properties of Oyun river (Ilorin) moulding sand. *Adeleke University J Eng Technol* 2:12–24
10. Sahoo PK, Pattnaik S, Sutar MK (2020) Investigation of the foundry properties of the locally available sands for metal casting. *SILICON*. <https://doi.org/10.1007/s12633-020-00677-x>
11. Sadarang J, Nayak RK, Panigrahi I (2020) Effect of binder and moisture content on compactibility and shear strength of river bed green sand mould. *Mater Today Proc*. <https://doi.org/10.1016/j.matpr.2020.08.640>
12. Ademoh NA, Ibrahim AO (2019) Determination of the suitability of river Gurara bed sand bonded with clay for foundry casting moulds. *Ind Eng Lett* 9:43–51
13. Aweda J, Jimoh Y (2009) Assessment of properties of natural moulding sands in Ilorin and Ilesha, Nigeria. *USEP J Res Inf Civ Eng* 6:68–77
14. Katsina C, Bala K, Reyazul H, Khan R (2013) Characterization of beach/river sand for foundry application. *Leonardo J Sci* 12:77–83
15. Rao PN (2013) Manufacturing technology. Tata McGraw-Hill Education
16. Shih T-S, Chang J-Y, Chang J-C (2001) Mould-metal movement in a horizontal sand mould. *Int J Cast Met Res* 14:43–52. <https://doi.org/10.1080/13640461.2001.11819424>
17. Heine RW, Loper CR, Rosenthal PC (1967) Principles of metal casting. Tata McGraw-Hill Education

# Microstructure and Interfacial Characterization Near Grain Boundary of Al<sub>2</sub>O<sub>3</sub>/SiC Reinforced AA 6061 Semi-solid Squeeze Cast Composite



Nitin Srivastava and Mohd Anas

## 1 Introduction

A heterogeneous solid consisting of two or more different materials that are metallurgically or mechanically bonded together forms a composite material. It is noteworthy that in the components retain their identity in the composite, and interfaces are formed between the materials. The composite materials exhibit superior mechanical properties which are not possible with the individual materials. The composites normally consist of a matrix material and reinforcements which might be of particulate or fibre form. Whilst in fibre composites thin fibres which may be continuous or discontinuous are imbedded in the matrix, the particulate composites consist of discrete particles of one material surrounded by matrix of other material. The different varieties of reinforcements which may be natural or synthetic have been a topic of interest amongst researchers [1, 2]. Metal matrix composites are the ones having matrix material as metal which describe a metal concerned and its alloy. Aluminium matrix composites (AMC's) are the group of materials which are in major demand nowadays since they exhibit superior mechanical properties of high strength, light weight, low coefficient of thermal expansion and excellent friction as well as wear resistance properties [3–5]. The areas of application of aluminium matrix composites are very specific in nature such as aerospace, automobile and military weapons. The automobile industry specially has been benefitted much in recent times due to high strength to weight ratio [6–8].

---

N. Srivastava (✉)

Department of Mechanical Engineering, PSIT Kanpur, Kanpur, Uttar Pradesh 209305, India

N. Srivastava · M. Anas

Department of Mechanical Engineering, Integral University, Lucknow, Uttar Pradesh 226021, India



Different types of processing techniques are applied for the fabrication of AMC's which are classified as solid-state processing, semi-solid processing and liquid processing. In recent times, importance for semi-solid casting has been well accepted amongst various processing routes for aluminium alloys. Further, this process has been emerged as an advanced metal processing route for the composites and components by the use of consolidated stirring and squeeze actions. Here, process utilizes aluminium slurry and multiple nano-size fine powder as reinforcement for similar aluminium base alloys. The process is a simple way to reduce porosity of the cast composite by the advantage of reinforcements inside the cavities with increased density. The key of semi-solid process is dendrite-free slurry with the solid being present as non-agglomerated, fine and spherical particles formation for improved mechanical properties. For the manufacturing processes of Al alloy, semi-solid metal casting is considered as important and effective for useful mechanical and metallurgical properties in the context of product requirement and competitiveness. One of the significant aspects of semi-solid metal processing is the manipulation of the solidification process in a positive and effective manner with the help of external means for achievement of desirable microstructure. Squeeze casting is one such method to produce metal matrix composites by forcing liquid under pressure into the mould. It is the methodology applied in which rapid solidification of semi-solid metal under high pressure takes place and the pressure is applied directly until solidification is completed ensuring refined microstructure and reduction of porosities. The production of components from the semi-solid metal slurries combined with squeeze casting is found to be very attractive for the aluminium industry due to following reasons.

- Integration of slurry making and component shaping operation into one single-step process.
- The slurry making operation is quite efficient.
- The process is capable of providing a microstructure comprising fine and spherical particles distributed uniformly in a liquid matrix.
- The controlled process suggests efficient processing routes for the composite regarding net shape components.

In AMC's, the reinforcements have a primary function of carrying most of the applied load where the reinforcements and matrix bind together. Further the external loads are transmitted and distributed to individual reinforcements [9–11]. Proper wetting and cavity filling are exhibited by microstructural and interfacial characterization which is the focus area of this paper. Wetting between the reinforcements and Al alloy metal matrix and incorporation of reinforcements in the cavities is an important condition in generating a satisfactory bond which allows the distribution and transfer of load from matrix to reinforcements without failure [12–16]. Further fracture analysis is also done to study the mode of fracture.

## 2 Materials and Methods

For the preparation of dual slurry, primary matrix material considered is AA 6061 alloy available commercially in form of chill bricks (Composition in Table 1). Whilst AA 6061 in fine powdered form was considered to be secondary material.  $Al_2O_3$  and SiC were considered to be reinforcement agents of sizes ( $Al_2O_3$ , 120 mesh, Loba Chemi. Pvt. Ltd.) in powder form and (SiC, 220 mesh, Loba Chemi. Pvt. Ltd.)

Powdered form of AA 6061 was mixed with the reinforcements mechanically via ball milling process for a ball to material weight ratio of 10:1. It was observed that the reinforcements and powder AA 6061 were embedded into each other. Primary slurry was prepared by heating the AA 6061 alloy above its liquidus temperature (680 °C) in a crucible in an open furnace up to the range of 750–760 °C to ensure proper liquid melt.

Figure 1 demonstrates the experimental set up for the preparation of the dual-slurry cast composite aided by squeeze casting. The secondary slurry of AA6061 powder and the reinforcements were heated in another crucible and stirred with A-10 tool steel rod for proper dispersion of reinforcements into liquid. The temperatures were measured with the help of a thermocouple attached with a digital data taker. The fabrication of composite was carried out by a consolidated effect of primary slurry and reinforcement slurry. The stand with a height adjuster was provided to facilitate smooth functioning. The two slurries were poured in a die the material of which was tool steel and inside surface was chrome coated for proper and smooth finish. A uniform mix was observed due to liquid–liquid dispersion. As the temperature of mix went down, the liquidus temperature converted into semi-solid slurry in the temperature zone of nearly 600 °C pressure was applied with the help of UTM for squeeze casting for different combinations as per Table 2. The process of pouring of dual slurry in a die and squeeze casting is demonstrated in Fig. 1b, c, respectively.

## 3 Microstructure of the Cast Composite

### 3.1 Interface of the $Al_2O_3$ -SiC with the Matrix

Microstructural observations by the processing effect and reinforcement incorporation have been made according to Fig. 2. It is clear from the figures that

**Table 1** Chemical composition for AA 6061 alloy by wt

Element	Cu	Mg	Si	Fe	Mn	Ni	Zn	Pb	Cr	Al
Chemical composition (weight %)	0.042	0.693	0.404	0.529	0.021	0.004	0.097	0.058	0.017	97.97

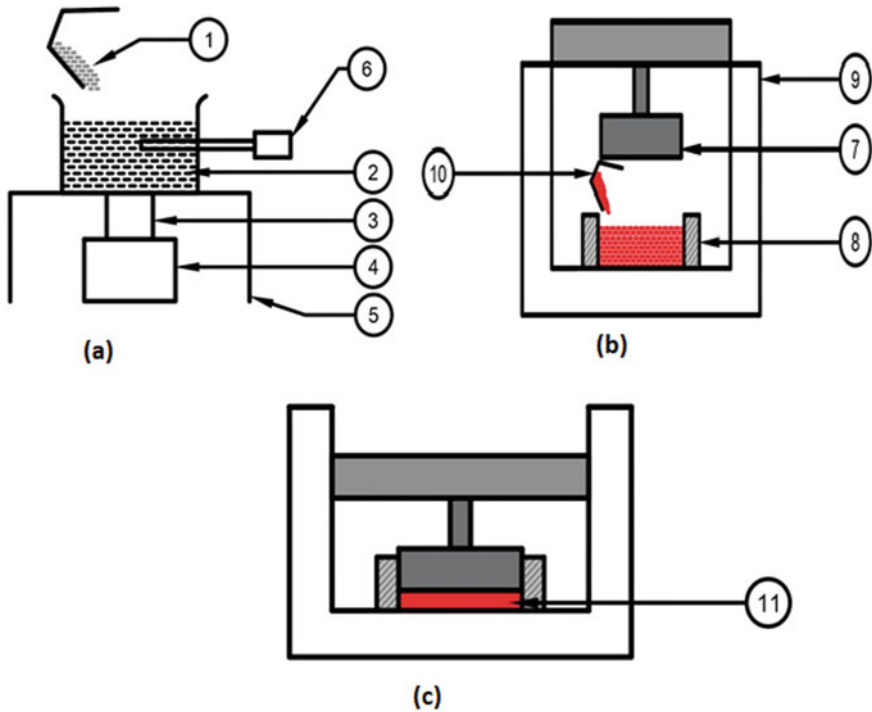


**Fig. 1** Processing route for composite fabrication **a** experimental set up **b** pouring of dual slurry in die **c** squeeze casting. (1) Melt primary slurry of AA6061 (2) Reinforcement slurry (3) open mould (4) Height adjuster (5) Stand (6) Digital data taker (7) Punch (8) Die (9) UTM (10) dual slurry (11) Cast composite

**Table 2** Percentage weight of alloy and reinforcements

Materials and combinations	AA 6061 bricks (%)	AA6061 powder (%)	Al <sub>2</sub> O <sub>3</sub> nanoparticles (%)	SiC nanoparticles (%)	AA 6061 (%)	Al <sub>2</sub> O <sub>3</sub> (%)	SiC (%)
Procedure and outcome	Primary slurry by melting	Secondary slurry by ball milling and melting			Dual slurry		
Combination 1	100	nil	nil	nil	nil	nil	nil
Combination 2	50	44	4	2	94	4	2
Combination 3	50	44	3	3	94	3	3
Combination 4	50	44	2	4	94	2	4

reinforcements are incorporated, and their distribution is different according to their share weightage as Al<sub>2</sub>O<sub>3</sub> is observed in white phases, whilst SiC is observed by dark grey phases.

In Fig. 2b, alumina particles are distributed inside the cavities conforming their solid phase incorporation, whilst spreading of SiC is seen over the matrix [17, 18].

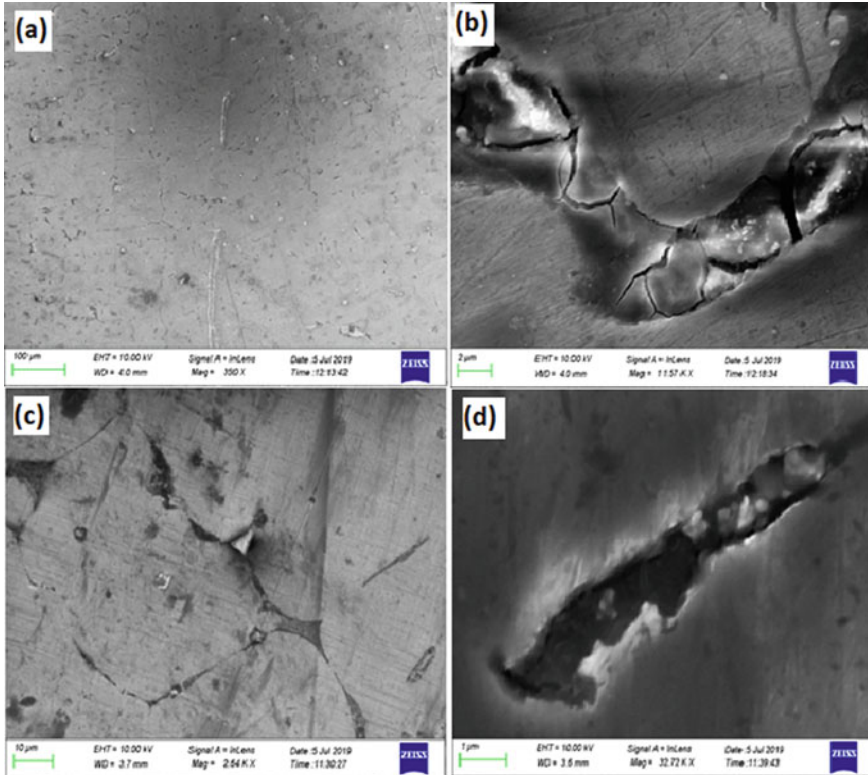


**Fig. 2** FESEM images for **a** as cast AA6061, **b** 4% Al<sub>2</sub>O<sub>3</sub> + 2% SiC cast composite **c** 3% Al<sub>2</sub>O<sub>3</sub> + 3% SiC cast composite, **d** 2% Al<sub>2</sub>O<sub>3</sub> + 4% SiC cast composite

The above effect is obtained due to mismatch of specific weight of added reinforcements. Further it represents incomplete recrystallization of alumina particles which is obvious since melting temperature of the alumina particles is higher [19–21]. In Fig. 2c, equal distribution of Al<sub>2</sub>O<sub>3</sub> and SiC is observed. Also, near the alumina particles hot cracks are seen which were not observed in Fig. 2b. Further the pattern of distribution of alumina is observed to be same inside cavities. It is noteworthy that reinforcement particle distribution is missing in Fig. 2a (As cast). Figure 2d represents dominating the presence of SiC due to higher weightage in comparison with Al<sub>2</sub>O<sub>3</sub>, and it is obvious that incorporation of SiC along and nearby cavities is higher. Also, a clear observation is made that small cavities are filled with micro size alumina particles less than 20 μm, whilst circular patches of SiC conform the ball milling effect of SiC and alumina [22, 23]. It was predicted that during the ball milling SiC reduces in size which is a clear observation from the microstructural images. Due to reduced size of SiC, it is easily dispersed with primary aluminium melt which otherwise was not possible with alumina particle.

### 3.2 Interface of the SiC with the Matrix

According to share weightage of  $\text{Al}_2\text{O}_3$  and SiC, the presence of well-distributed SiC particles acts as a deterrent to freely growing aluminium grains. With the enhanced number of interspread SiC particles, a great number of nucleation sites is developed thus ensuring formation of finer grains taking place due to enhanced grain refinement.

A predominant presence of SiC particulates with minor dendritic structure of Al particles with several pores has been observed in images as shown in Fig. 3. This is the effect of uneven solidification in the presence of SiC due to mismatch solidification rate and some healing effect of the pores size ball milled particulates which are settled over the available space. It is also clear by the cast microstructure images. An effect of squeeze action with incomplete crystallization provides more healing effect during the solidification. This is observed in form of dark grey

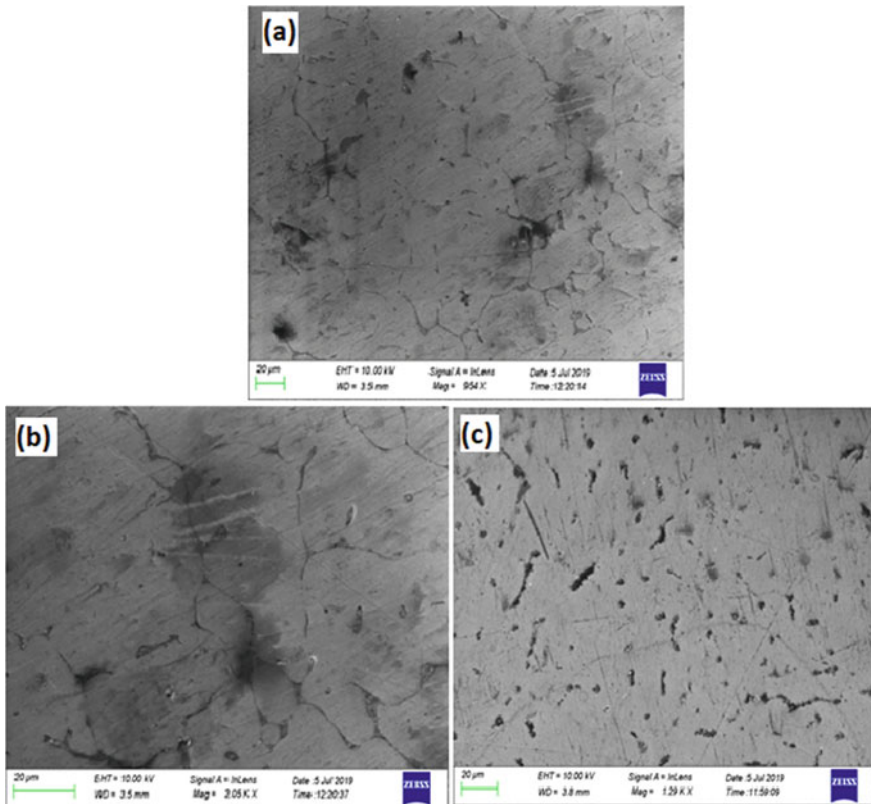


**Fig. 3** a FESEM images for 4%  $\text{Al}_2\text{O}_3$  + 2% SiC cast composite b FESEM images for 3%  $\text{Al}_2\text{O}_3$  + 3% SiC c 2%  $\text{Al}_2\text{O}_3$  + 4% SiC cast composite

patches and spots on all the microstructures [24, 25]. In fact these are the particulates highly brittle in nature which works in two distinct ways as first being a solidification occurs in a primary condition which depends on the inserted powder particles. As here, size of powder particles is so small that solidification rate increases rapidly. This appears initially for the reinforcement particulates. Secondly, solidification rate is affected by the primary matrix metal. As it is well known that a huge difference of temperature which increases the rate of heat transfer in the medium which is higher for the SiC and environment.

### ***3.3 Interface of the $Al_2O_3$ with the Matrix***

In the present work for the reinforcement modified squeeze cast composite near grain boundary, interface layer formation is observed where semi-solid micro eutectics of  $Al_2O_3$  can be identified.

Spherical grains of flower type are seen the cause of which is liquid–solid dispersion between the matrix and reinforcement slurry. The interfacial structures of 2, 3 and 4%  $Al_2O_3$  are clearly different from each other as in Fig. 4. With the increasing percentage of  $Al_2O_3$ , it is observed accumulation of  $Al_2O_3$  particles become denser and are more spread near the grain boundary [26, 27]. Also,  $Al_2O_3$  particles at places are conjugated to each other. It can be inferred that interface layers are affected due to melting temperature and weight of  $Al_2O_3$  under pouring temperature. The images of higher magnification also confirm to above discussed phenomenon.

## **4 Mechanical Characteristics**

Evaluation of tensile property for  $Al_2O_3/SiC$  modified AA6061 has been done according to tensile strength. The ultimate tensile stress of unmodified and modified cast composite was measured with the help of universal testing machine (UTM) by unidirectional stress with a rate of 0.2 mm/min. The curves obtained for tensile strength for 3%  $Al_2O_3$  + 3% SiC exhibit best improvement (310.43 Mpa) over unmodified cast alloy (216.66 Mpa) (see Fig. 5) which is an improvement of 43.2% in the tensile strength of the modified cast composite with respect to as cast composite.

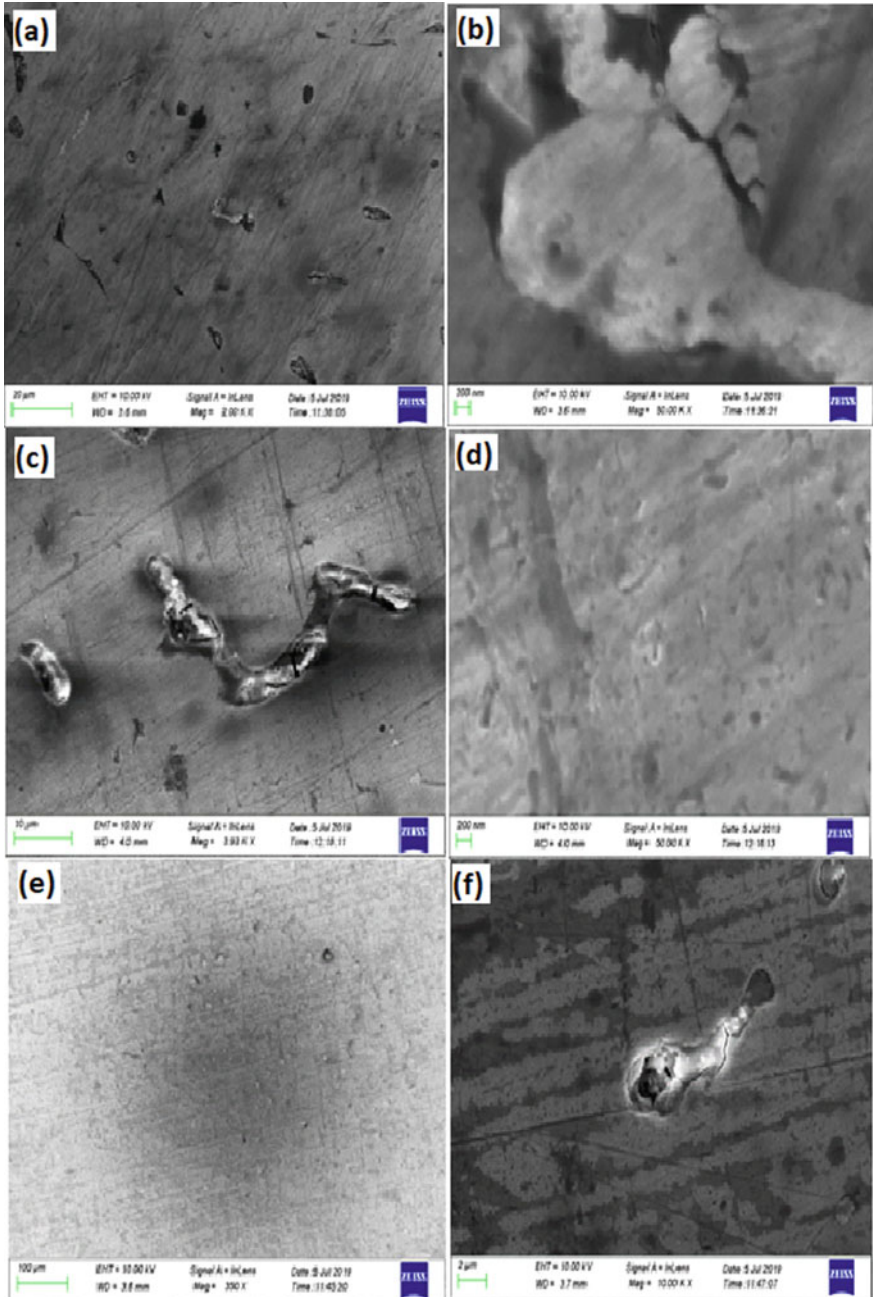


**Fig. 4** FESEM images for **a, b** 4%  $\text{Al}_2\text{O}_3$  + 2% SiC cast composite for different magnifications, **c, d** 3%  $\text{Al}_2\text{O}_3$  + 3% SiC cast composite for different magnifications, **e, f** 2%  $\text{Al}_2\text{O}_3$  + 4% SiC cast composite for different magnifications



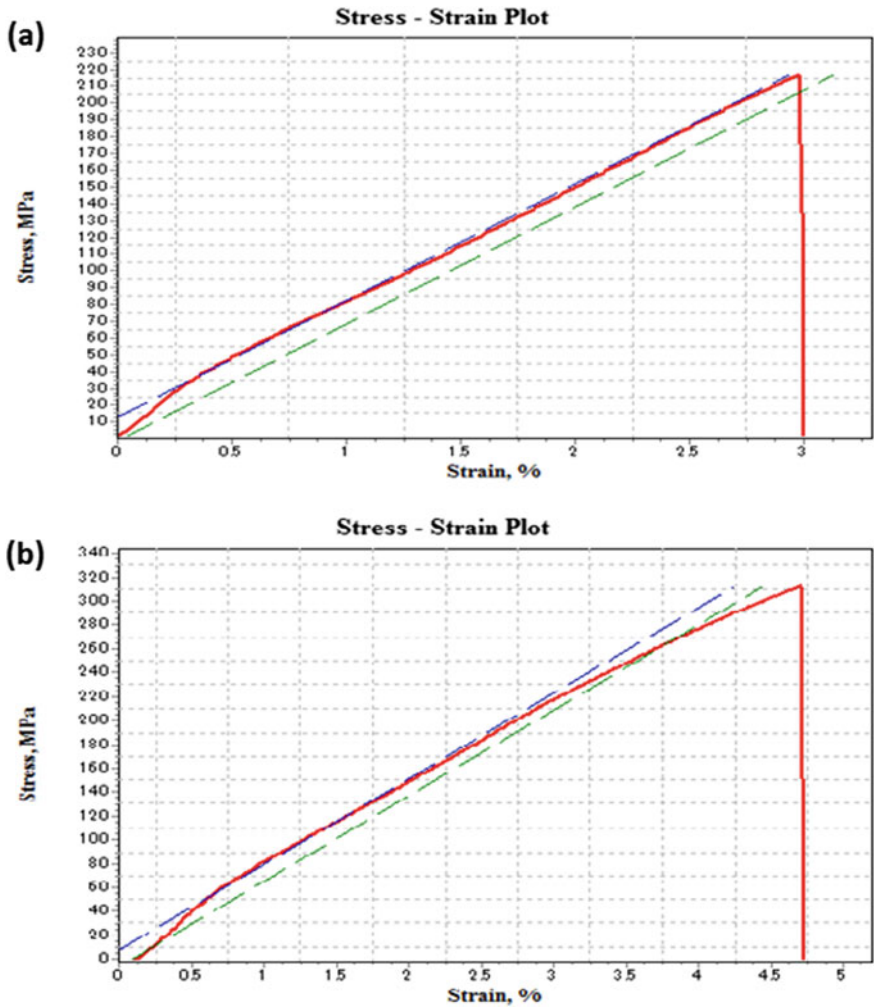


**Fig. 5** Typical engineering stress–strain plot for **a** as cast AA6061, **b** 3% Al<sub>2</sub>O<sub>3</sub> + 3% SiC cast composite

## 5 Fracture Analysis

Figure 6a, b represents the fractured surfaces for the combination of 3% Al<sub>2</sub>O<sub>3</sub> + 3% SiC at different magnifications which is dominated by ductile behaviour in the presence of SiC. Several cavities and patches are observed which is possible when particles are plugged out from one surface to another. At this stage, shear fracture is little bit low as compared to the ductile fracture due to the absence of brittle particulates. In figure b, big patches in form of dimples confirm the ductile



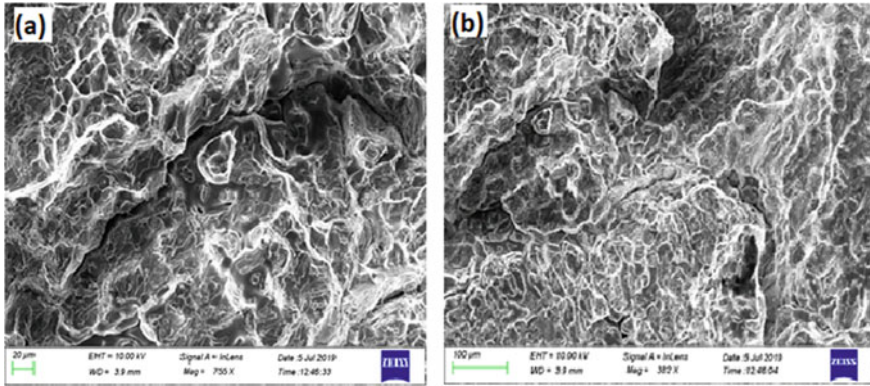


**Fig. 6** a, b FESEM images for 3%  $\text{Al}_2\text{O}_3$  + 3% SiC cast composite for different magnifications

behaviour of the material. This also affects the properties but failure is totally different and depending on the fractured surface behaviour.

This phenomenon is again reflected on the dimples due to availability of microcracks as shown in figure a by wavy white phases which totally confirms that here a combination of ductile and brittle fracture takes place on particles, matrix and its interfaces. From the fractured surfaces, it can be concluded that this is possible due to the effect of interfacial particulates cracking on which strain energy consumes to the cracking phenomenon during a sudden drop in the effective cross-sectional area of the sample. Generally, this is variable and mostly dependent on the matrix material. Sometimes, this is also affected by the reinforcement particulates in the composite which alters the crack propagation path. If this is forwarded towards the longitudinal direction, then value of the impact strength increases and near the plastic zone brittle fracture takes place, whilst the elastic zone behaviour of fracture is ductile in nature. Moreover, on the interfaces mostly brittle fracture takes place due to the availability of oxide formation therefore stress required in the fracture can be divided into three parts as

- Ductile fracture related to the matrix at its interfaces with SiC
- Brittle fracture related to the  $\text{Al}_2\text{O}_3$  as well as its interfaces with matrix and SiC
- Stress required to crack the particulates, formation of voids, fracture in longitudinal direction as well as the shear mode.

Above all are the interrelated parameters and totally independent which is highly influenced by the individual properties of matrix and reinforcements. Nonetheless, various grooves also appear on the fractured surfaces due to ejection of several particles from the matrix in all cases.

## 6 Conclusions

- AA6061 alloy composite fabricated by multiple reinforcement is cast with improved morphology and successfully processed through semi-solid casting route with the help of squeeze pressure. The squeeze action leads to reduction of volume inside cavities and improvement in morphology
- It is observed from microstructural evaluation that reinforcement led to reduction in volume inside the cavities by alumina along with distribution and dispersion of SiC owing to their specific gravity. It could also be concluded that the cavities and cracks are filled by the reinforced particles
- Subsequent pressurized treatment under moderate temperature improved the wetting characteristics of reinforcement as well as refining of the microstructure.
- Major improvement in tensile strength is obtained with best results for 3% Al<sub>2</sub>O<sub>3</sub> + 3% SiC. Fracture analysis depicts load bearing by reinforcements transferred due to tensile loading. The nature of fracture observed was the combination of ductile and brittle fracture.

**Acknowledgements** Authors are thankful to the lab staff of Workshop, Integral University Lucknow & PSIT Kanpur as well as Mr. Abhilash Bajpai, Centre of Nano-sciences IIT Kanpur for their assistance during the experimental work.

## References

1. Chiba R, Yoshimura M (2015) Solid-state recycling of aluminium alloy swarf into c-channel by hot extrusion. *J Manuf Processes* 17:1–8
2. Sood M, Dwivedi G (2018) Effect of fibre treatment on flexural properties of natural fibre reinforced composites: a review *Egypt J Petrol* 27(4):775–783
3. Haase M, Khalifa NB, Tekkaya AB, Misiolek WZ (2012) Improving mechanical properties of chip-based aluminum extrudates by integrated extrusion and equal channel angular pressing. *Mater Sci Eng A* 539:194–204
4. Gronostajski J, Marciniak H, Matuszak A (2000) New methods of aluminium and aluminium-alloy chips recycling. *J Mater Process Technol* 106(1–3):34–39
5. Canyook R, Wannasin J, Wisuthmethangkul S, Flemings MC (2012) Characterization of the microstructure evolution of a semi-solid metal slurry during the early stages. *Acta Mater* 60(8):3501–3510
6. Seo Y-H, Kang C-G (1995) The effect of applied pressure on particle-dispersion characteristics and mechanical properties in melt stirring squeeze-cast SiCp/Al composites. *J Mater Process Technol* 370–379
7. Beoort O, Long S, Cayron C, Kuebler J, Buat P-A (2007) Alloying effects on microstructure and mechanical properties of high-volume fraction SiC-particle reinforced Al-MMCs made by squeeze casting infiltration. *Compos Sci Technol* 67:737–745
8. Li R-X, Rond-de Li (2003) Effect of specific pressure on microstructure and mechanical properties of G U C L present state of investigation and application of zinc and zinc alloy. *Nonferrous Alloy* 55(4):45–47

9. Rao AKP (2014) Understanding the evolution of the microstructure in melt-conditioned direct-chill cast Al alloys. *Mater Manuf Processes* 29:848–852
10. Wang H (2005) Semi-solid structure formation and semi-solid casting. *J Mater Sci Technol* 21:65–71
11. Birol Y (2004) The effect of homogenization practice on the microstructure of AA6063 billets. *J Mater Process Technol* 148:250–258
12. Pech-Canul MI, Katz RN et al (2000) Optimum parameters for wetting silicon carbide by aluminum alloys. *Metall Mater Trans* 31(A):565–573
13. Srinivasan A, Pillai UTS (2005) Microstructure and mechanical properties of Si and Sb added AZ91 magnesium alloy. *Metall Mater Trans A* 36A:2235–2243
14. Mabuchi M et al (1996) Tensile strength, ductility and fracture of magnesium-silicon alloys. *J Mater Sci* 31:1529–1535
15. Easton MA, Schiffel A, Yao J-Y, Kaufmann H (2006) Grain refinement of Mg–Al(–Mn) alloys by SiC additions. *Scripta Mater* 55(4):379–382
16. Guangyin Y et al (2003) Microstructure and mechanical properties of Mg/Zn/Si-based alloys. *Mater Sci Eng A* 357:314–320
17. Agarwal M, Srivastava R (2016) Influence of solid fraction casting on microstructure of aluminium alloy 6061. *Mater Manuf Processes* 31(15):1958–1967
18. Yu Y et al (2015) Effects of coating contents on the interfacial reaction and tensile properties of  $\text{Al}_2\text{O}_3$  coated-Al18B4O33w/Al-Mg matrix composite. *Mater Charact* 107:327–333
19. Zhou M, Hu H, Li N, Lo J (2005) Microstructure and tensile properties of squeeze cast magnesium alloy AM50. *J Mater Eng Perform* 14:539–545
20. Liu Y, Yang C, Chen W, Zhu D, Li Y (2014) Effects of particle size and properties on the microstructures, mechanical properties, and fracture mechanisms of 7075Al hybrid composites prepared by squeeze casting. *J Mater Sci* 49:7855–7863
21. Zhao Z, Chen Q, Tang Z, Wang Y, Ning H (2010) Microstructure evolution and mechanical properties of  $\text{Al}_2\text{O}_3/\text{AZ91D}$  magnesium matrix composites fabricated by squeeze casting. *J Mater Sci* 45:3419–3425
22. Ruirui W, Zheng Y, Qishu L (2017) Microstructure and mechanical properties of 7075 Al alloy based composites with  $\text{Al}_2\text{O}_3$  nanoparticles. *Int J Cast Met Res*
23. Chen X-H, Yan H (2015) Effect of nanoparticle  $\text{Al}_2\text{O}_3$  addition on microstructure and mechanical properties of 7075 alloy. *Int J Cast Met Res*
24. Sukumaran K, Ravikumar KK, Pillai SGK, Rajan TPD, Ravi M, Pillai RM, Pai BC (2008) Studies on squeeze casting of Al 2124 alloy and 2124–10% SiCp metal matrix composite. *Mater Sci Eng A* 235–241
25. Shabani MO, Baghani A, Khorram A, Heydari F (2020) Evaluation of fracture mechanisms in Al-Si metal matrix nanocomposites produced by three methods of gravity sand casting, squeeze casting and compo casting in semi-solid state. *SILICON* 12:2977–2987
26. Agarwal M, Singh A, Srivastava R (2018) Influence of powder-chip based reinforcement on tensile properties and fracture behaviors of LM6 aluminium alloy. *Trans Indian Inst Met* 71 (5):1091–1098
27. Ahmed SI, Mkhoyan KA, Youssef KM (2020) The activation of deformation mechanisms for improved tensile properties in nanocrystalline aluminium. *Mater Sci Eng A* 777:139069

# Utilization of Stone-dust in Sand Mould Casting Process



Jatin Sadarang, Ramesh Kumar Nayak<sup>ID</sup>, and Isham Panigrahi

## 1 Introduction

Sand mould contains silica sand as the main mould ingredient. Silica sand has high thermal stability and readily available. A typical sand mould contains 85–95% silica sand, 0.5–2% coal dust, 5–10% bentonite clay, and 2–5% moisture [1]. High silica content sand was extracted from river beds, which creates pollution in the nearby area. Therefore, researchers and scientists are trying to use different waste materials in sand mould applications. Slag is a waste material produces from iron and steel plants. The mould prepared with ferrochrome slag has high moulding property than silica sand mould [2]. Ferrochrome slag mould has high thermal conductivity, so less casting cooling time is reduced compared to conventional sand mould [3]. Casting obtains from ferrochrome slag mould possesses high mechanical properties than sand casting [4]. The sand mould property increases on the increase in the blast furnace slag [5]. Agricultural waste groundnut shell ash has a similar chemical composition to silica sand and can be used in non-ferrous casting [6]. Aluminium industry waste material red mud can partially be used in green sand mould [7]. The particle size of fly ash is smaller than silica sand; therefore, only 15% of fly ash can be used in green sand mould [8]. Local river sand has similar shear strength to silica sand mould [9]. The mechanical properties of extrusion compounded and injection moulded short GF and CF reinforced polypropylene composites and reported that the fibre efficiency factors reduced on increase of fibre content, and these were lower for CFRPs as compared to GFRPs. An increase in fibre vol.% caused substantial reduction of fibre length in the FRPs. Strength and stiffness of compression moulded short CF reinforced polypropylene composites increased with fibre

---

J. Sadarang · I. Panigrahi  
School of Mechanical Engineering, KIIT Deemed to be University, Bhubaneswar 754024,  
India

R. K. Nayak (✉)  
Department of Materials and Metallurgical Engineering, MANIT, Bhopal 462003, India

content and fibre length. Increase in fibre content caused a rise in density, hardness and impact strength of the CFRPs, whereas increase in fibre length caused increase of their thermal stability. Flexural strength was also maximum (250.23 MPa) for the CFRP samples. Increase in fibre concentration up to a certain limit enhanced rapidly the composite strength, beyond which it slowed down. It was because of the more air inclusions in the composites containing higher fraction of fibres.

Stone crushing plants produce stone dust as waste material. The produced stone dust has fine as well as coarse particles. The fine particles of stone dust flow in the air cause air pollution [9], reduce soil fertility, and cause skin problems [10]. The construction industry uses waste stone dust in concrete [11–13] and mortar [14] but unable to utilize it fully. In the present investigation, waste stone dust used as the primary mould material. The samples were heated at different temperatures and evaluate the effect of mould property.

## 2 Materials and Method

### 2.1 Material

The mould samples were prepared with stone dust, bentonite clay, and coal dust. Bentonite clay and coal dust were procured from RSB Metaltech Pvt. Ltd, Cuttack India, and stone dust procured from the nearest stone crushing plant in Bhopal. The physical appearance of stone crush, bentonite clay, and coal dust is reported in Fig. 1.

### 2.2 Sample Preparation

Stone dust mould was prepared with 83% stone dust, 11.3% bentonite clay, and 5% coal dust. Mould ingredients were mixed with a laboratory size sand muller. The moisture content in mould is maintained at 5%. Sand rammer was used to prepare American foundry society (AFS) cylindrical sample of 50 mm height and diameter. The sample was filled in specimen tube and applied three rammed strokes with 6.35 kg weight and 50 mm falling height. The prepared AFS sample was used to evaluate mould hardness, compressive, and shear strength.



**Fig. 1** Physical appearance of **a** stone dust, **b** bentonite clay, and **c** coal dust

### 2.3 Drying Procedure

Stone dust AFS samples were heated in a hot air oven for one hour and allow to cool. Moisture present in the mould gets evaporated on heating. While pouring molten metal into the mould cavity, less gas formation occurs, which reduces the risk of gas defects in casting. The stone dust samples were heated at different temperatures and evaluate mould hardness, compressive, and shear strength. The heating cycle of the stone dust mould sample was shown in Fig. 2. The stone dust mould samples were placed in a hot air oven at room temperature. The specimen was heated at the desired temperature  $T$  (50, 100, 150, and 200 °C) for 1 h. The samples cooled at normal room temperature for one hour and evaluate mould hardness, moisture %, compressive and shear strength.

### 2.4 Moisture Test

Moisture present in moulding sand was determined with rapid moisture teller equipment. The moisture teller's pressure chamber was filled with 6 g mould sample and 12 g calcium carbide powder and mixed it properly. The moisture present in mould sample reacts with calcium carbide powder and forms acetylene gas. Pressure increases inside the moisture teller and sense by a calibrated dial gauge, which shows the percentage of water/moisture present in moulding sand.

### 2.5 Mould Hardness

Mould hardness of stone dust mould was measured by B scale mould hardness gauge. Mould hardness is similar to the Brinell hardness test [15]. A spring-loaded

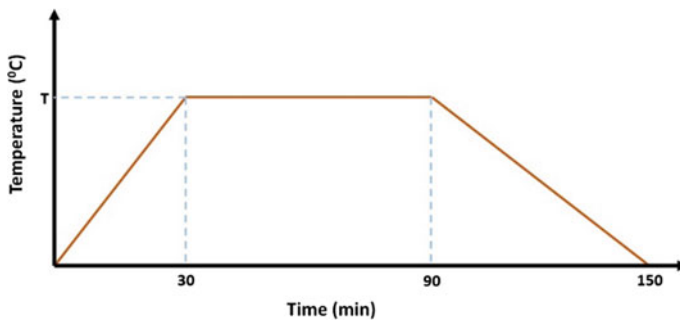


Fig. 2 A heating cycle of stone dust mould samples

plunger is gradually pressed on the stone dust mould sample's flat surface and obtained hardness value through dial gauge.

## 2.6 Mould Compressive and Shear Strength

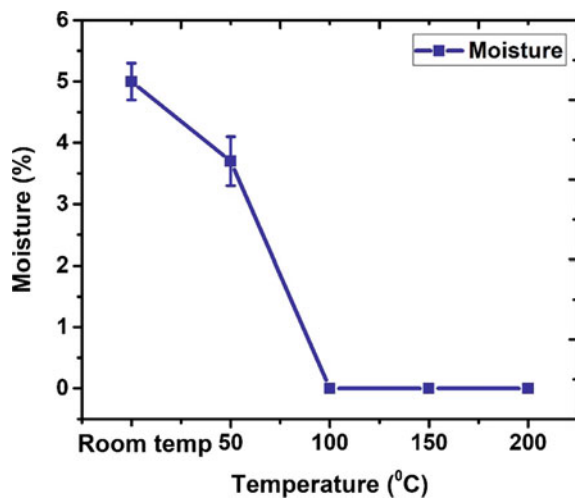
A universal strength machine was used to evaluate the compressive and shear strength of stone dust mould samples. The samples were placed between compressive and shear grippers to determine compressive and shear strength, respectively. The axial compressive load was gradually applied to the sample and obtained sample strength through the attached computer. The similar procedure is followed to determine shear strength.

## 3 Result and Discussion

### 3.1 Moisture

Moisture in moulding sand increases the risk of gas defects in casting. The effect of heating temperature on moisture content is shown in Fig. 3. It is observed that on the increase in temperature, moisture gets evaporated from stone dust mould. There is no moisture present in mould sample above 100 °C. Water evaporates at 100 °C. Therefore, there is no moisture present in mould, even in the centre of the mould sample.

**Fig. 3** Effect of temperature on moisture %



### 3.2 Mould Hardness

The effect of temperature on mould hardness is shown in Fig. 4. It is observed that mould hardness increases on increase in temperature up to 100 °C. Further increase in temperature cause no change in mould hardness. Moisture in moulding sand increases the plasticity and lubricant property of mould [16]. Therefore, as the concentration of moisture decreases on heating mould hardness increases. The maximum mould hardness (98 MH) of stone dust mould was obtained at 100 °C.

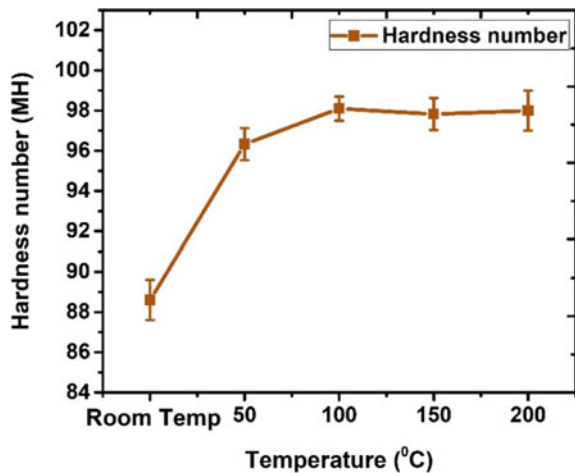
### 3.3 Mould Compressive Strength

The effect of temperature on compressive strength is shown in Fig. 5. It is observed that mould compressive strength increases on increase in temperature up to 100 °C. Further increase in temperature decreases mould compressive strength. Bentonite clay and moisture mixture forms a gel, which makes a thin layer around the sand particle. The gel gets hard on the evaporation of moisture. Therefore, on the increase in temperature, compressive strength of mould increases. The maximum compressive strength (3.40 kg/cm<sup>2</sup>) of stone dust mould was obtained at 100 °C.

### 3.4 Mould Shear Strength

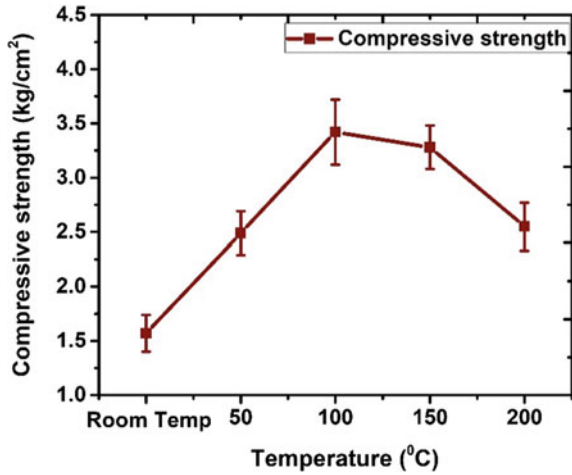
The effect of temperature on shear strength is shown in Fig. 6. It is observed that mould shear strength increases on increase in temperature up to 100 °C. Further increase in temperature decreases mould shear strength. Bentonite clay and

Fig. 4 Effect of temperature on mould hardness

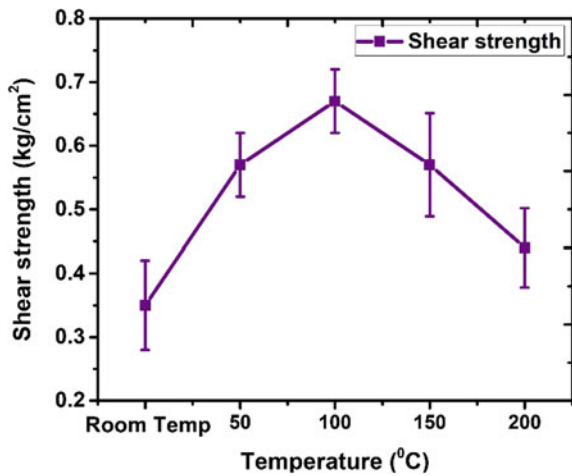




**Fig. 5** Effect of temperature on mould compressive strength



**Fig. 6** Effect of temperature on mould shear strength



moisture mixture form a gel, which makes a thin layer around the sand particle. The gel gets hard on the evaporation of moisture. Therefore, on increase in temperature, shear strength of mould increases. The maximum shear strength (0.67 kg/cm<sup>2</sup>) of stone dust mould was obtained at 100 °C.

#### 4 Conclusion

The mould samples were prepared with stone dust and evaluate the effect of temperature on mould hardness, compressive, and shear strength. The following conclusion was drawn.

- The concentration of moisture decreases on increase in the temperature of mould. There is no moisture present in mould sample above 100 °C.
- The compressive and shear strength first increases with temperature, and after achieving an optimum value, it decreases.
- Stone dust mould heated at 100 °C have 98 mould hardness, 3.40 kg/cm<sup>2</sup> compressive strength, and 0.67 kg/cm<sup>2</sup> shear strength.

**Acknowledgements** The authors would like to express their sincere thanks to the Advanced Manufacturing Technology program of the Department of Science & Technology, Govt. of India, for the financial support to carry out this work (Grant no. DST/TDT/AMT/2017/173). Special thanks to RSB Metaltech, Pvt. Ltd, Cuttack, India, for their support as an industrial partner to develop alternate source to commercial-grade silica sand for Indian foundry industries.

## References

1. Paluszkiwicz C, Holtzer M, Bobrowski A (2008) FTIR analysis of bentonite in moulding sands. *J Mol Struct* 880:109–114. <https://doi.org/10.1016/j.molstruc.2008.01.028>
2. Murthy IN, Babu NA, Rao JB (2016) High carbon ferro chrome slag-alternative mould material for foundry industry. *Proc Environ Sci* 35:597–609
3. Murthy IN, Rao JB (2017) Molding and casting behavior of ferro chrome slag as a mold material in ferrous and non-ferrous foundry industries. *Mater Manuf Process* 32:507–516. <https://doi.org/10.1080/10426914.2016.1257796>
4. Inampudi NM, Jinugu BR (2016) Ferro chrome slag: an alternative mould material in ferrous and non-ferrous foundries. *Int J Metalcast* 11. <https://doi.org/10.1007/s40962-016-0103-x>
5. Narasimha Murthy I, Arun Babu N, Babu Rao J (2018) Microstructure and mechanical properties of A356 alloy castings made in sand and granulated blast furnace slag moulds. *Mater Today: Proc* 5:161–167. <https://doi.org/10.1016/j.matpr.2017.11.067>
6. Okonji PC, Nwobi-Okoye CC, Atanmo PN (2018) Experimental study of the feasibility of using groundnut shell ash and ant hill powder in foundry application. *J Chin Adv Mater Soc* 6:270–281. <https://doi.org/10.1080/22243682.2018.1461576>
7. Jústiz-Smith N, Buchanan VE, Oliver G (2006) The potential application of red mud in the production of castings. *Mater Sci Eng A* 420:250–253. <https://doi.org/10.1016/j.msea.2006.01.038>
8. Srinivasa Rao P, Birru AK (2017) Effect of mechanical properties with addition of molasses and flyash in green sandmoulding. *Mater Today: Proc* 4:1186–1192. <https://doi.org/10.1016/j.matpr.2017.01.136>
9. Sadarang J, Nayak RK, Panigrahi I (2020) Effect of binder and moisture content on compactibility and shear strength of river bed green sand mould. *Mater Today: Proc*. <https://doi.org/10.1016/j.matpr.2020.08.640>
10. Sheikh A, Rana SVS, Pal A (2011) Environmental health assessment of stone crushers in and around Jhansi, U. P., India. *J Ecophysiol Occup Health* 11:107–115. <https://doi.org/10.18311/jeoh/2011/2255>
11. Muhit IB, Raihan MT, Nuruzzaman MD (2014) Determination of mortar strength using stone dust as a partially replaced material for cement and sand. *Adv Concrete Constr* 2(4):249–559. <https://doi.org/10.12989/2014.2.4.249>
12. Verma SK (2018) Study the effect of stone dust as partial replacement of sand adding steel fibre. *Inter J Sci Eng Develop Res* 3(8):160–164
13. Gupta L, Suresh G (2018) Determination of indirect tensile strength of bituminous concrete mix prepared using stone dust and cement as filler materials. In: Struble L, Tebaldi G

- (eds) *Materials for sustainable infrastructure*. Springer International Publishing, Cham, pp 249–261. [https://doi.org/10.1007/978-3-319-61633-9\\_16](https://doi.org/10.1007/978-3-319-61633-9_16)
14. Rajput SPS, Chauhan MS (2014) Suitability of crushed stone dust as fine aggregate in mortars. *Int J Emerg Technol Adv Eng* 4(3):87–89
  15. Rao PN (2013) *Manufacturing technology*. Tata McGraw-Hill Education
  16. Shih T-S, Chang J-Y, Chang J-C (2001) Mould-metal movement in a horizontal sand mould. *Int J Cast Met Res* 14:43–52. <https://doi.org/10.1080/13640461.2001.11819424>

# Effect of Fe-Cr Mold Temperature on Mold Hardness, Compressive and Shear Strength



Jatin Sadarang, Ramesh Kumar Nayak , and Isham Panigrahi

## 1 Introduction

Silica sand is a natural material that is readily available on earth. Silica sand has high refractory due to which foundries are continuously used in mould making. Consumption and cost of silica sand increase as it is used as a raw material in various industrial applications. Therefore, foundry engineers, researchers and scientists are trying to use different mould materials to increase mould strength and replace silica sand. Sing [1] use fly ash in a sand mould and evaluate the physical and mechanical properties. Fly ash has fine and spherical particles [2], due to which mould permeability, tensile and compressive strength decrease on the increase in the concentration of fly ash [3]. The combination of 2.25% molasses and 15% fly ash in moulding sand gives desired mould green and dry compressive strength [4]. Groundnut shell ash has 79% SiO<sub>2</sub> and can be used in sand mould for non-ferrous casting [5]. Smith et al. [6] use red mud in sand mould and observe red mud can partially replace silica sand. Iron filler has no significant effect on sand mould property [7]. The river sand particles are similar to mined sand, and there is not much difference between river sand and mined sand mould property [8]. River sand mould has similar compactibility and shear strength to silica sand mould [9].

Slag is a waste material generated from iron and steel plants. Around 11.8 million tons of blast furnace slag are generated [10], which is dumped in a large area. Construction industries use slag as a raw material in cement [11–13], ceramics [14] and bricks [15] but unable to utilize it fully. Rao and Murthy [16] use blast furnace slag in the Fe-Si casting process. The thermal conductivity of blast furnace slag is higher than silica sand; therefore the cooling time of casting decreases [17].

---

J. Sadarang · I. Panigrahi  
School of Mechanical Engineering, KIIT Deemed To Be University,  
Bhubaneswar 754024, India

R. K. Nayak (✉)  
Department of Materials and Metallurgical Engineering, MANIT, Bhopal 462003, India

Casting has no surface defects and having good mechanical property than silica sand mould [18]. Ferrochrome slag is also a waste material generated from the steel plant. CO<sub>2</sub> mould prepared with ferrochrome slag has similar mould property and casting finish [19]. The thermal conductivity of ferrochrome slag is higher than silica sand, due to which casting cooling time decreases [20]. The mechanical property of moulding sand is maximum at 60-grain fineness number with 2.4% binder having 4 h curing time. That dry compressive strength increases as moisture percentage increases but maximum green compressive strength is obtained at 5% moisture content in sand base mould. Molasses and fly ash in sand mould to improve green sand dry compressive strength. They observed that green and dry compressive strength increases with 2.25% molasses and 15% fly ash. Therefore, in the present investigation, Fe-Cr slag is used as an alternative mould material in place of silica sand. The moisture present in the sand mould may lead to creating gas defects in casting. The samples were heated at different temperatures for one hour to remove water from the mould and evaluated the effect of heating temperature on Fe-Cr slag mould hardness, compressive and sharing strength.

## 2 Materials and method

### 2.1 Materials

Fe-Cr Slag, bentonite clay and coal dust were used to prepare mould samples. Bentonite clay and coal dust were procured from RSB Metaltech, Pvt. Ltd, Cuttack, India, and Fe-Cr slag was collected from a ferro-steel plant, Jajpur, Odisha, India. The physical appearance of Fe-Cr slag, bentonite clay and coal dust is shown in Fig. 1.

### 2.2 Sample Preparation

The mould samples were prepared with 83% Fe-Cr slag, 12% bentonite clay and 5% coal dust. A laboratory muller was used to properly mixing of slag mould aggregates. The moisture content of 5% was maintained in mould mixture.



**Fig. 1** Physical appearance of **a** slag, **b** bentonite clay and **c** coal dust

American Foundry Society (AFS) standard specimen were prepared with a sand rammer. The moulding sand was compact by three rammed strokes having 6.35 kg weight and 50 mm falling height. The obtained sample was having 50 mm in height and diameter.

### 2.3 Heating Procedure

Green sand mould contains water that evaporates while pouring molten metal into the mould cavity. Evaporated water may cause a gas defect in casting. Therefore in the present investigation, moulding samples were heated at different temperatures (50, 100, 150 and 200 °C) for 1 h and evaluate moisture content, hardness, dry compressive and shear strength of Fe-Cr slag mould. Figure 2 shows the heating cycle of Fe-Cr slag mould samples.

### 2.4 Moisture Test

A portable moisture teller equipment was used to determine moisture content in Fe-Cr slag mould samples. The slag mould sample of 6 g was mixed with 12 g calcium carbide powder in the moisture teller's pressure chamber. Moisture present in the mould sample reacts with calcium carbide and forms acetylene gas, which increases pressure inside the pressure chamber. The calibrated dial gauge shows the percentage of water present in the mould sample.

### 2.5 Mould Hardness

The mould hardness test is similar to the Brinell hardness test [21]. A mould hardness test gauge was used to measure the hardness of Fe-Cr slag mold samples.

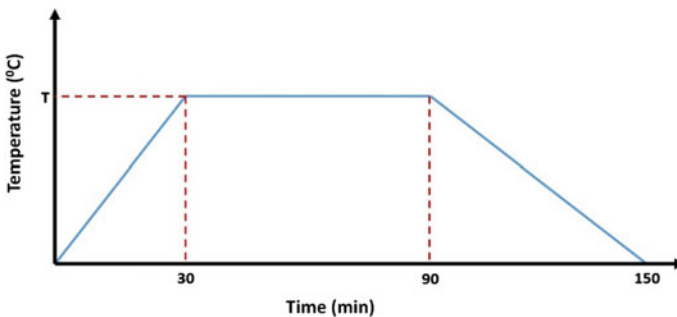


Fig. 2 Heating curve of Fe-Cr slag mould sample

The spring-loaded plunger was gradually pressed on a flat surface of mould sample [22]. The resistance offered by the sample was shown in a calibrated dial gauge.

## 2.6 Mould Compressive and Shear Strength

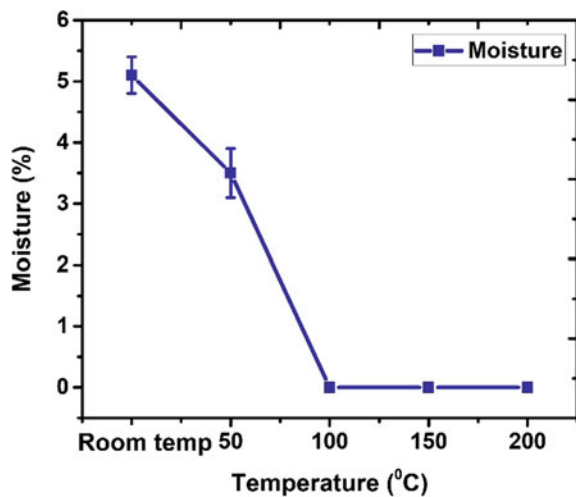
A universal strength machine (USM) was used to evaluate dry compressive and shear strength. AFS standard sample was placed between the compressive gripper of USM and applied axial compressive load. The computer attached with the machine shows the maximum compressive strength of samples. An average of three samples was taken. A shear gripper was used to evaluate shear strength and followed similar procedure.

## 3 Result and Discussion

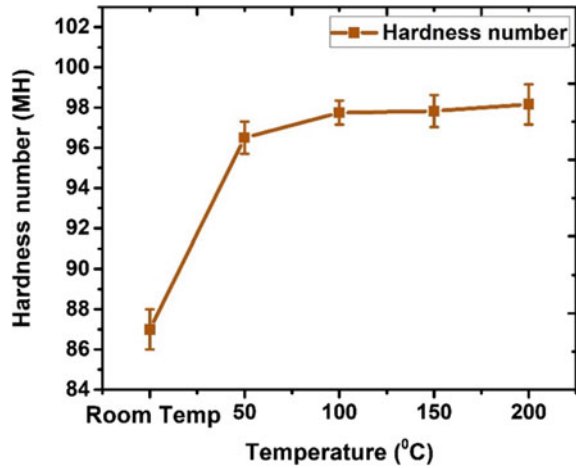
### 3.1 Moisture

Figure 3 shows the effect of temperature on moisture content in Fe-Cr slag mould. It is observed that increasing temperature moisture % decreases. Water evaporates at 100 °C. Therefore, the percentage of moisture decreases on heating, and there is no moisture present in Fe-Cr slag mould sample above 100 °C. The risk of gas defects in casting is minimized due to no moisture present in mould.

**Fig. 3** Effect of temperature on moisture content



**Fig. 4** Effect of temperature on mould hardness



### 3.2 Mould Hardness

Figure 4 shows the effect of temperature on mould hardness. It is observed that mould hardness increases up to 100 °C; further increasing temperature, there is no change in mould hardness. Moisture in moulding sand increases the plasticity and lubricant property of mould [23]. Therefore, mould hardness increases as the concentration of moisture decreases. The maximum mould hardness (99 MH) was obtained at 200 °C.

### 3.3 Mould Compressive Strength

Figure 5 shows the effect of temperature on compressive strength. It is observed that mould compressive strength increases on the increase in temperature up to 100 °C; further, increase in temperature compressive strength decreases. The bentonite clay creates a thin layer on sand particles in the presence of moisture and is also responsible for plasticity and lubrication [24]. The moisture gets evaporated on heating, due to which bentonite layer gets hard so that compressive strength of Fe-Cr slag mould increases. The maximum compressive strength (6.0 kg/cm<sup>2</sup>) is obtained at 100 °C temperature.

### 3.4 Mould Shear Strength

Figure 6 shows the effect of temperature on shear strength. It is observed that shear strength increases on the increase in temperature up to 150 °C; further increase in



**Fig. 5** Effect of temperature on compressive strength

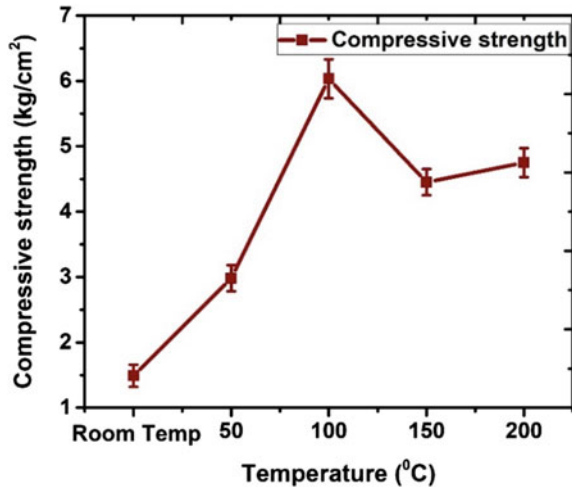
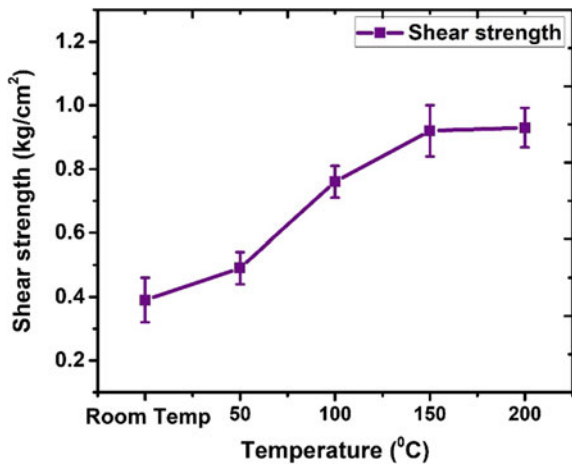


**Fig. 6** Effect of temperature on shear strength



temperature, there is no change in shear strength. The bentonite clay creates a thin layer on sand particles in the presence of moisture and is also responsible for plasticity and lubrication [24]. The moisture gets evaporated on heating, due to which bentonite layer gets hard so that shear strength of Fe-Cr slag mould increases. The maximum shear strength (0.92 kg/cm<sup>2</sup>) is obtained at 150 °C temperature.

## 4 Conclusion

In the present investigation, Fe-Cr slag is used as a primary mould material. The effect of temperature on mould hardness, compressive and shear strength was studied. The following conclusion is drawn from the present investigation.

- The moisture content in the moulding sand decreases with the increase in temperature. Moisture is completely evaporated from Fe-Cr slag sampl at 100 ° C.
- The compressive strength increases up to 100 °C and then decreases. The high compressive strength of the Fe-Cr slag mould was obtained at 100 °C of heating temperature.
- At temperature 100 °C, values of mould hardness, compressive and shear strength are 98, 6.0 kg/cm<sup>2</sup> and 0.76 kg/cm<sup>2</sup>, respectively.

**Acknowledgements** The authors would like to express their sincere thanks to the Advanced Manufacturing Technology program of the Department of Science & Technology, Govt. of India, for the financial support to carry out this work (Grant no. DST/TDT/AMT/2017/173). Special thanks to RSB Metaltech, Pvt. Ltd, Cuttack, India, for their support as an industrial partner to develop alternate source to commercial-grade silica sand for Indian foundry industries.

## References

1. Singh A (2018) Fly ash an alternative for molding. *Int J Res Applied Sci Eng Technol* 6:525–531. <https://doi.org/10.22214/ijraset.2018.1078>
2. Karunakaran P, Jegadheesan C, Dhanapal P, Sengottuvel P (2014) Sugar industry fly ash: an additive for molding sand to make aluminium castings. *Russ J Non-ferrous Metals* 55:247–253. <https://doi.org/10.3103/S1067821214030079>
3. Palaniappan J (2017) Study on type C coal fly ash as an additive to molding sand for steel casting. *J Inst Eng India Ser D* 98:139–145. <https://doi.org/10.1007/s40033-016-0115-y>
4. Srinivasa Rao P, Birru AK (2017) Effect of mechanical properties with addition of molasses and flyash in green sandmoulding. *Mater Today: Proc* 4:1186–1192. <https://doi.org/10.1016/j.matpr.2017.01.136>
5. Okonji PC, Nwobi-Okoye CC, Atanmo PN (2018) Experimental study of the feasibility of using groundnut shell ash and ant hill powder in foundry application. *J Chin Adv Mater Soc* 6:270–281. <https://doi.org/10.1080/22243682.2018.1461576>
6. Jústiz-Smith N, Buchanan VE, Oliver G (2006) The potential application of red mud in the production of castings. *Mater Sci Eng A* 420:250–253. <https://doi.org/10.1016/j.msea.2006.01.038>
7. Adedayo AV (2010) Effects of addition of iron (Fe) filings to green moulding sand on the microstructure of grey cast iron. *J Braz Soc Mech Sci Eng* 32:171–175. <https://doi.org/10.1590/S1678-58782010000200011>
8. Sahoo PK, Pattnaik S, Sutar MK (2020) Investigation of the foundry properties of the locally available sands for metal casting. *SILICON*. <https://doi.org/10.1007/s12633-020-00677-x>
9. Sadarang J, Nayak RK, Panigrahi I (2020) Effect of binder and moisture content on compactibility and shear strength of river bed green sand mould. *Mater Today: Proc*. <https://doi.org/10.1016/j.matpr.2020.08.640>
10. Al-Jabri K, Shoukry H, Khalil Ibrahim S, Nasir S, Hassan HF (2018) Reuse of waste ferrochrome slag in the production of mortar with improved thermal and mechanical performance. *J Mater Civ Eng* 30:04018152. [https://doi.org/10.1061/\(ASCE\)MT.1943-5533.0002345](https://doi.org/10.1061/(ASCE)MT.1943-5533.0002345)
11. Das B, Prakash S, Reddy PSR, Misra VN (2007) An overview of utilization of slag and sludge from steel industries. *Resour Conserv Recycl* 50:40–57. <https://doi.org/10.1016/j.resconrec.2006.05.008>

12. Kumar S, Kumar R, Bandopadhyay A, Alex TC, Kumar BR, Das SK, Mehrotra SP (2008) Mechanical activation of granulated blast furnace slag and its effect on the properties and structure of portland slag cement. *Cement Concr Compos* 30:679–685
13. Mostafa NY, El-Hemaly SAS, Al-Wakeel EI, El-Korashy SA, Brown PW (2001) Characterization and evaluation of the hydraulic activity of water-cooled slag and air-cooled slag. *Cem Concr Res* 31:899–904. [https://doi.org/10.1016/S0008-8846\(01\)00497-5](https://doi.org/10.1016/S0008-8846(01)00497-5)
14. Fredericci C, Zanotto ED, Ziemath EC (2000) Crystallization mechanism and properties of a blast furnace slag glass. *J Non-Cryst Solids* 273:64–75. [https://doi.org/10.1016/S0022-3093\(00\)00145-9](https://doi.org/10.1016/S0022-3093(00)00145-9)
15. Sadek DM (2014) Effect of cooling technique of blast furnace slag on the thermal behavior of solid cement bricks. *J Clean Prod* 79:134–141. <https://doi.org/10.1016/j.jclepro.2014.05.033>
16. Rao JB, Murthy IN (2018) Properties of silica sand and GBF slag moulds practiced by Nishiyama process. *Int J Cast Met Res* 31:360–372. <https://doi.org/10.1080/13640461.2018.1495862>
17. Narasimha Murthy I, Arun Babu N, Babu Rao J (2018) Microstructure and mechanical properties of A356 alloy castings made in sand and granulated blast furnace slag moulds. *Mater Today: Proc* 5:161–167. <https://doi.org/10.1016/j.matpr.2017.11.067>
18. Murthy IN, Rao JB (2018) Non destructive evaluation of a356 alloy castings made in sand and granulated blast furnace slag moulds. *Mater Today: Proc* 5:168–174
19. Murthy IN, Rao JB (2017) Evaluation of the microstructure, secondary dendrite arm spacing, and mechanical properties of Al–Si alloy castings made in sand and Fe–Cr slag molds. *Int J Miner Metall Mater* 24:784–793. <https://doi.org/10.1007/s12613-017-1462-x>
20. Inampudi NM, Jinugu BR (2016) Ferro chrome slag: an alternative mould material in ferrous and non-ferrous foundries. *Int J Metalcast* 11. <https://doi.org/10.1007/s40962-016-0103-x>
21. Rao PN (2013) *Manufacturing technology*. Tata McGraw-Hill Education
22. Siddharth VS, Rao DS, Murthy BVR (2020) Investigations on the suitability of banana peel powder as an alternative additive in synthetic green sand moulding system. *Int J Cast Met Res* 0:1–6. <https://doi.org/10.1080/13640461.2020.1796294>
23. Shih T-S, Chang J-Y, Chang J-C (2001) Mould-metal movement in a horizontal sand mould. *Int J Cast Met Res* 14:43–52. <https://doi.org/10.1080/13640461.2001.11819424>
24. Heine RW, Loper CR, Rosenthal PC (1967) *Principles of metal casting*. Tata McGraw-Hill Education

# A Comprehensive Study on Electrical and Electronic Waste Management



V. Iswarya and T. Yuvaraj

## Nomenclature

GDP	Gross domestic product
E-Waste	Electronic waste
WEEE	Waste electrical and electronic equipment
EPR	Extended producer responsibility
DNA	Deoxyribonucleic acid

## 1 Introduction

E-waste can be termed as scrap from different electrical appliances, devices, or gadgets, disposed of once its ability to serve its purpose concludes. This waste is a mixture of many types of materials, including different metals, semiconductors, ceramics, and thermoplastics. The initial process of electronic waste management includes the removal of refurbishable components like printed circuit boards and cathode ray tubes which are not damaged and can be sold to the consumers of second-handed devices. Then, the dead equipment is organized and separated to further treat, sell and dispose of the residues. The recovery and recycling happen continuously to extract the metal as much as possible and to economically support the process [1].

Electronic devices and gadgets play a major role in our lives, in education, job, business, and many. Changing gadget immediately after every sudation of a new version happens widely among people, and the thought about impacts after disposing of the old gadgets is lessening. The growth in using electronic devices has increased ten times in the last decade due to lifestyle changes. The production and usage of electrical and electronic material could not be limited as it contributes more to urbanization and economic growth. In industrialized countries, the most

---

V. Iswarya · T. Yuvaraj (✉)

Department of EEE, Saveetha School of Engineering, Saveetha Institute of Medical and Technical Sciences, Saveetha University, Chennai, India

dangerous threat is the electronic waste stream. It is estimated that the global E-waste generation would be increasing by 52.2 million tons by 2021. And it may increase by about 38% by 2030, according to the report of 2019. Normally, E-waste contains about 40% of metals with a small quantity of precious metals, 30% of plastics, and 30% of refractory oxides. Only 5.7% of electronic waste is recycled in India, and only 1.5% of the total scrap is reclaimed by formal recyclers. India, being the world's largest waste importing country, needs safe methods to recycle waste and to do it in formal sectors. Hazardous material when reacts with water or incinerated can pollute the surrounding affecting animals and other living beings [2].

Generally, electrical and electronic waste can be categorized into three divisions, namely white goods, brown goods, and grey goods. White goods include large home appliances such as air-conditioners, refrigerators, and they are less toxic and easily recyclable. Brown goods are consumer goods like television and radio, it has a bit of toxicity due to the presence of dyeing chemicals. Technological electronics like mobile phones and laptops come under grey goods, which have high toxicity and are complicated to recycle [3].

## 2 Materials in E-Waste

Electrical and electronic wastes contain many materials, both toxic and non-toxic, which include plastics, metals, and refractory oxides in the ratio of 30:40:30 [3]. Metals used in devices have different properties, for an instance, E-waste contains precious metals. The approximate percentage of every metal in the complete waste of electrical and electronic equipment is shown in Table 1 [4].

**Table 1** Composition of E-waste

Components	Percentage (%)
Plastics	30
Refractory oxides	30
Copper	20
Iron	8
Lead	2
Tin	4
Gold	0.2
Silver	0.1
Aluminum	2
Zinc	1
Palladium	0.01
Nickel	2
Other toxic metals	1

The other toxic and radioactive metals in electronic waste include arsenic, barium, beryllium, chromium, mercury, cadmium, and other persistent organic pollutants like polybrominated diphenyl ethers, polychlorinated biphenyls, polychlorinated dibenzo-p-dioxins and dibenzofurans, and polycyclic aromatic hydrocarbons. These chemicals while treated without required safety measures could cause a lot of health disorders, short-term exposure to these chemicals may cause skin lesions, skin patches, and liver diseases. Long-term exposure leads to immune system damage, issues with the reproductive system, and even cause cancer [1].

### 3 Materials in E-Waste

The sources of waste electrical and electronic equipment are home, hospitals, and offices. E-waste from home includes gadgets and other household and kitchen appliances. Bio-medical instruments such as electrocardiography scanner, computed tomography scanner, incubator, and other testing instruments are the wastes from hospitals. Offices have a lot to do with electronics which includes computers, air-conditioners, printers, etc.

In the last decade, the number of household appliances in a normal household has increased tremendously. The appliance involves both personalized and common devices. Every person has individual mobile phones, and the usage of temperature conditioning appliances has become common in houses. The average composition of household appliances and devices in India is in the proportion as shown in Fig. 1.

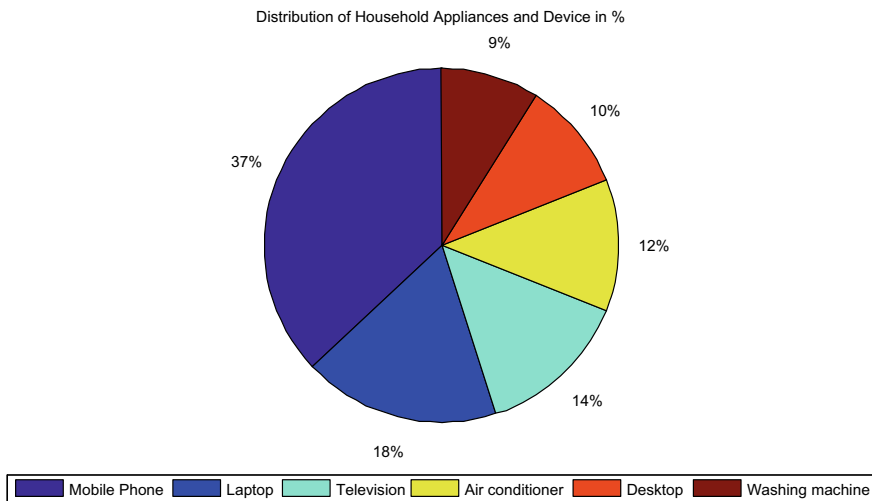
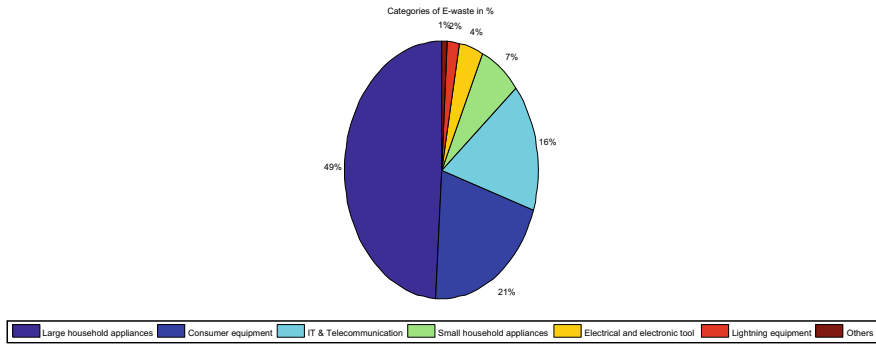


Fig. 1 Distribution of household appliances and devices



**Fig. 2** Categories of E-waste

In a broader approach, the generation of E-waste from different sources can be proportioned below (see Fig. 2).

## 4 Effects of E-Waste

### 4.1 Effects on Human Health

The effects on human health while the material are mistreated.

- Arsenic, a human carcinogen, affects the production of red blood cells and white blood cells, causes allergic reactions, dermatitis, vomiting, and cardiac malfunctioning.
- Beryllium roots lung damage, chronic beryllium diseases, and also carcinogenic.
- Chromium is a human carcinogen and a strong allergic reactant and causes damage in kidney and liver, ulcer, bronchitis, and even DNA damage.
- Exposure to lead may result in impairment of the nervous system, circulatory system, and endocrine system. It also disturbs brain development and kidney functioning.
- Mercury is carcinogenic, and it increases the risk of cardiac arrest, blood pressure, chronic disease in the brain, kidney, and lungs, fetal damage, and lack of muscle movement coordination.
- Exposure to copper may cause eye irritation, headache, vomiting, diarrhea, and higher exposure cause liver and kidney problems.
- Zinc exposure causes a lot of skin diseases.
- Nickel is a human carcinogen and results in allergic reactions, asthma, chronic bronchitis, and other lung problems [3].

## ***4.2 Effects of E-Waste on Environment***

Electronic waste releases toxic heavy metals while disintegrating. This emission of chemical diffuses into the soil and have harmful effects on the plant and tree. The diffused chemicals in the soil get into the groundwater and water bodies during precipitation or runoff. The polluted water in-take of humans or animals can travel to the longer terms with the food web and even cause the extinction of certain species of animals or plants. Burning or heating the E-waste may release toxic gaseous and other greenhouse gases, polluting the air and its effect lasts long on the atmosphere causing climatic changes and ozone depletion [5].

## ***4.3 Informal Recycling***

The informal sector plays a major role in waste recycling in India, as about 95% of electronic waste is managed by informal recyclers. They used manual and primitive methods to treat, segregate, and dismantle the waste which has evil effects on both people and surrounding. The workers in informal sectors are usually children, and they were not instructed any safety measures or methods to handle the electrical and electronic equipment given to them. The first step of informal recycling is manual dismantling with their bare hand using hammers and screwdrivers, to open the device however they can. This entire process of dismantling is done in open areas without appropriate conditions. The second step, heating the circuit boards and cables with open grills to separate the metals present which emit toxic smoke, affects the recycler as they have no safety helmet or masks, and affects the atmosphere due to the lack of closed protective conditions. In the third step, the remaining precious plated metals are extracted by acid leaching which results in hazardous emissions due to the reaction between different metals and acid. The fourth step is to melt and merge the obtained similar metals and plastics, making it ready to sell as a raw material for different purposes. Then, the extracted materials are reused and refurbished if possible. The other leftover materials are open incinerated or disposed of in landfills or by river banks [6].

## ***4.4 Flaws of Informal Recycling Sectors***

Open incineration of E-waste directly contaminates the air by the toxic emissions and land by the combusted residues and indirectly affects the water bodies by wet deposition of the emissions and groundwater by penetrating the soil in different means.

Acid leaching pollutes air, water, and soil directly through hydrochloric acid and nitric acid fumes, and dumping of acid solution.



Heating and melting in open space leave gaseous and particulate emissions to the atmosphere, then the migration of these particulate pollutants pollutes soil and water [7].

## 5 Process Involved in Formal Recycling

### 5.1 *Extended Producer Responsibility (EPR)*

Extended producer responsibility is a take-back system designed as that the producer/seller takes the responsibility of the electrical and electronic equipment which they have produced/sold to a consumer, at the end of the product life at the postconsumer stage. This system of EPR is widely used in many European countries [8].

### 5.2 *Product Stewardship*

The product stewardship system is a shared responsibility concept, where every stakeholder including the producer, seller, consumer, etc. takes the responsibility of the product to be disposed of and treated safely, considering the environmental obstacles. Product stewardship is introduced as the recycling costs make the system uneconomical.

**Disposal of remaining scrap.** Remaining harmless scrap like paper, cardboard can be sent to landfills and other treatment yards, where other metal can be incinerated with a proper incinerator in appropriate closed conditions. A detailed comparison of formal and informal E-waste management is given in Table 2 [9].

## 6 Duties of a Consumer

As a commoner, every individual has the rights to live as they wish, but that does not mean one can be lethargic while using or disposing of a property that he/she own. Any product which is manufactured must be used till the product is dead or expired. And those expired products must be reused or recycled to the best, and the rest must be disposed of properly. This applies to every waste and especially E-waste.

Upgrading to the latest model gadgets is getting increase which makes the reliable gadget which is already in use, become scrap. In this case, a consumer must re-evaluate the need for a new device and must try to extend the life of the device. And if the up-gradation is necessary, then the old gadget can be given for reuse as a

**Table 2** Formal and informal recycling sectors

Formal sector	Informal sector
Laborers are provided with enough knowledge to handle the dead electronics with care, and safety suits are provided concerning their health	Laborers are not educated about safety measures and precautions, and they are allowed to handle the electronics with bare hands without safety suits
Requires high capital as an investment to properly organize the recycling plant with necessary machinery	Low capital investment is adequate, as they do not need proper conditions or space for recycling
Recovered metal is used as a raw material for manufacturing new electrical equipment	The metals that are recovered are sold to scrap dealers or ornament makers
It is mandatory to employ professionals to check the quality of the materials and to approve it	No professionals are involved in the entire process of recycling
No middle man or scavenging is involved	Involves middle man and scavenging
Hazardous wastes are vigilantly disposed of	Hazardous wastes are disposed to waterways or other places in contact with people
Does not bother environmental health much	Leaves a terrible impact on environmental health

whole gadget or this can be handed over to a formal sector for recycling or refurbishing. Reselling the undamaged parts of a device to apply in any other device has a huge market. These refurbishments can reduce waste products and also reduce the extraction of new resources from nature.

When it comes to recycling, it is very important that to whom we hand over it. If we consumers throw E-waste together with other solid waste, then this waste has a chance to reach go to a scrap yard and the E-waste will be separated, this will be collected by rag pickers or any other informal recyclers, the remaining unnoticed electronic scraps are headed to the landfill. Dumping E-waste to landfill has many risks which include incineration polluting the air with hazardous oxides from it, runoff, and migration of pollutants to water bodies and also has long-term effects on people who are exposed to those pollutants.

We have several formal sectors to collect our E-waste on our doorstep and the only responsibility of a consumer is to collect the WEEE in our household, for neighbors too if possible, later this E-waste can be handed to formal recyclers [10].

## 7 Discussion

Due to many inevitable ins and outs like sudden growth in information technology and communication, reduction in price due to the usage of non-degradable materials, and condensed lifecycle of products, the waste from electrical and electronic equipment is generated in tons. Collection and disposal of electronic waste have many guidelines which are hardly followed ending up in the distraction of health of

human and environment. Take-back systems can be an effective method to collect the old appliances, due to the orderly maintained data on the waste generation and neat collection of the equipment. The efficiency of recycling is dependent on the collection method.

Indolent behavior of the user to dispose of the electronic waste together with other wet or dry solid waste is the major reason for mismanagement in waste from electrical and electronic equipment. Disposal of electronic waste together with wet waste may result in rusting or corroding of the components inside the device, which affects the quality of the metal while reuse. Hence, the door-step take-back collection system by the producer, which involves dealers and collection centers would be the best method of disposing of E-waste.

In the process of breaking down the electric component, the workers involved in dismantling must be educated about the safety measures, since this process needs some manual or semi-manual work such as separation of directly usable parts of the devices or the segregation of parts that contain hazardous material. Then, the final disposal of the residues after the extraction of resources needs much attention because those residues may pollute the environmental health in every aspect. Increase in illegal import of waste from other developed countries without considering the international and national legislation demands for setting up more E-waste recycling units.

## 8 Conclusion

India being the major generator and importer of electrical and electronic waste in the world, needs a lot of care in storing, handling, and managing those electronic parts. So, it is always better to reuse the device or device components directly as much as possible, instead of recycling them. Disposal issues can be resolved by announcing government policies and subsidies to both producer and consumer sides. Meanwhile, the life expectancy of electronic devices is reducing gradually and so it is very important to develop more formal sectors for recycling. The Gross Domestic Product (GDP) and the quantity of electronic waste are proportional as this waste is composed of gold, silver, copper, etc. That is why the management of E-waste is otherwise known as urban mining. Among all these positives, due to the complexity of E-waste, it has recycling challenges. The hazardous material in electronics is more vulnerable to react with the component at any state. Ignoring the effects of hazardous waste, completely is not realistic, but the dosage and the intensity of its consequence on the environment can be mitigated. It is mandatory to concentrate more on the health concern of the workers, who are in direct contact with the waste and the people with indirect exposure to electronic waste residues. The adverse distraction of the environment is also connected with the health of the animals and human beings, dependent on the environment. While the waste or its excess is dumped in the landfill, the chemicals in it are cared to the groundwater by infiltration, or to the waterways by runoff. People consuming, this contaminated

water have a high chance of getting several serious diseases. On the other hand, the gases escaping from the components in the dead appliances contaminate the air we breathe.

## References

1. Garlapati VK (2016) E-waste in India and developed countries: management, recycling business and biotechnological initiatives. *Renew Sustain Energy Rev* 54:874–881
2. Aboughaly M, Gabbar HA (2020) Recent technologies in electronic waste management. Springer, Berlin, pp 63–80
3. Samuel M, Chidambaram R, Needhidasan S (2014) Electronic waste—an emerging threat to the environment of urban India. *Environ Health Sci Eng* 12:1–9
4. Jaibee S (2015) Review on current status of waste electric and electronic product in Malaysia. *Appl Mech Mater* 898–907
5. Ismail H, Hanafiah MM (2020) A review of sustainable e-waste generation and management: present and future perspectives. *J Environ Manage* 264:110495
6. Holuszko M, Espinosa DC, Kumar A (2017) E-waste: an overview on generation, collection, legislation and recycling practices. *Resour Conserv Recycl* 122:32–42
7. Perkins DN, Drisse MN, Nxele T, Sly PD (2014) E-waste: a global hazard. *Ann Global Health* 80(4):286–295
8. Kiddee P (2013) Electronic waste management approaches: an overview. *Waste Manage* 1237–1250
9. Leung AO (2019) Environmental contamination and health effects due to e-waste recycling. *Electr Waste Manage Treat Technol* 335–362
10. Mohd S, Kaushal VK (2018) E-waste management in India: current practices and challenges. ResearchGate

# Investigating the Effect of Annealing Temperature on Structural, Luminescence, and Magnetic Properties of Nickel and Zinc Aluminate



Sampurnanand, Nishant Kumar, Rakesh Kumar Singh, Atul Jyoti, and Vikash Kumar

## 1 Introduction

Spinal structured aluminate is a compound containing aluminum and oxygen with more electropositive elements that is a salt of the hypothetical aluminic acid. It is broadly used in water purification, manufacture of zeolites, ceramics, petrochemical industry, and photocatalysts due to its thermal resistance, electronics, and optical properties [1–6]. Generally, the spinal structure is formulated as  $A^{2+}B_2^{3+}O_4$  in which A and B are known as divalent and trivalent metal ions. Spinal structure may be classified as  $A^{2+}$  occupy eight tetrahedral holes,  $B^{3+}$  occupy four octahedral holes, and the anions are arranged in a cubic close packed lattice which belongs to fd-3 m space group [7–9]. Zinc aluminates ( $ZnAl_2O_4$ ) are well-known luminescent materials emitting in the visible region when doped with suitable activators such as rare earth and transition metal ions [10, 11]. Zinc aluminates have high thermal stability, high mechanical resistance, hydrophobicity, and magnificent optical properties; due to this ability, they may be used as a ceramic, electro-conductive material, and catalyst [5, 12]. Nickel aluminate ( $NiAl_2O_4$ ) has received attention as a catalyst solid support due to its stability, strong resistance to acids and alkalis, and high melting point [13]. Nickel aluminates are one of the most important aluminates materials used in many applications such as magnetic materials, catalysts, pigments, sensors, and refractory materials [14–17]. Spinal metal aluminates can be synthesized by various methods such as co-precipitation, combustion, hydrothermal, micro-emulsions, electrodeposition, solid-state reactions, and sol–gel methods [18–22]. Generally, nanosized metal aluminates are synthesized by solid-state

---

Sampurnanand · N. Kumar · R. K. Singh (✉) · A. Jyoti  
School of Engineering and Technology, Aryabhata Centre for NanoScience  
and Nanotechnology, Aryabhata Knowledge University, Patna 800001, India

V. Kumar  
Department of Mechanical Engineering, Maulana Azad National Institute of Technology  
(MANIT), Bhopal, India

reaction, but the main disadvantage of this method is using a high temperature of more than 1000 °C [23, 24]. Due to this high temperature, product is obtained with low surface area, heterogeneous, and lack of morphology control [25]. The sol–gel approach is an effective and low temperature technique that allows the stoichiometric control of the products chemical composition and produces homogeneous materials [26]. Sol–gel is a facile way to synthesize nanoparticles from aqueous salt solution by the addition of a base under inert atmosphere at room temperature or at elevated temperature [27]. The significance of the sol–gel process as compared to other methods is that it includes the ability to maintain a high degree of purity, high homogeneity, and high surface area at low temperature [28].

In the present work, pure phase nickel and zinc aluminate material has been synthesized using sol–gel method and effect of annealing on structural parameters like (crystallite size, lattice strain etc.) luminescence and magnetic properties. To the best of my knowledge very few research finding are available on optical properties of aluminate and its annealing effect.

## 2 Experimental

### 2.1 Materials

All the compositions of  $\text{NiAl}_2\text{O}_4$  and  $\text{ZnAl}_2\text{O}_4$  nanoparticles were prepared from Merck Germany GR grade chemicals viz  $\text{Ni}(\text{NO}_3)_2 \cdot 6\text{H}_2\text{O}$ ,  $\text{Zn}(\text{NO}_3)_2 \cdot 6\text{H}_2\text{O}$ ,  $\text{Al}(\text{NO}_3)_3 \cdot 9\text{H}_2\text{O}$ , and aqueous  $\text{NH}_3$  (Merck India, 30%). The chemicals obtained were used as received without any further purification.

### 2.2 Synthesis of $\text{NiAl}_2\text{O}_4$ and $\text{ZnAl}_2\text{O}_4$ Nanoparticles

#### 2.2.1 Synthesis of $\text{NiAl}_2\text{O}_4$ Nanoparticles

In the present study, Ni aluminate nanoparticles have been synthesized using suitable precursors by the sol–gel method. Nickel nitrate, (99% assay), aluminum nitrate (99.9% assay), and citric acid (99% assay) as a chelating agent were used for synthesis of  $\text{NiAl}_2\text{O}_4$  nanoparticles. Schematic diagram of preparation method of nickel aluminate is shown in Fig. 1a. Nickel nitrate (290.79 gm/mole), aluminum nitrate (750.26 gm/mole), and citric acid (768.48 gm/mole) were taken after weighing. Firstly, nickel nitrate is mixed in deionized water which is 20 ml, and then, aluminum nitrate in another beaker separately mixed with deionized water. All three chemicals are mixed in one beaker and shifting of pH with the help of ammonia ( $\text{NH}_3$ ) at pH 7. Then, it was put on magnetic stirrer for 4–5 h at 80 rpm for preparing a homogenous mixture. The solution obtained was then evaporated at

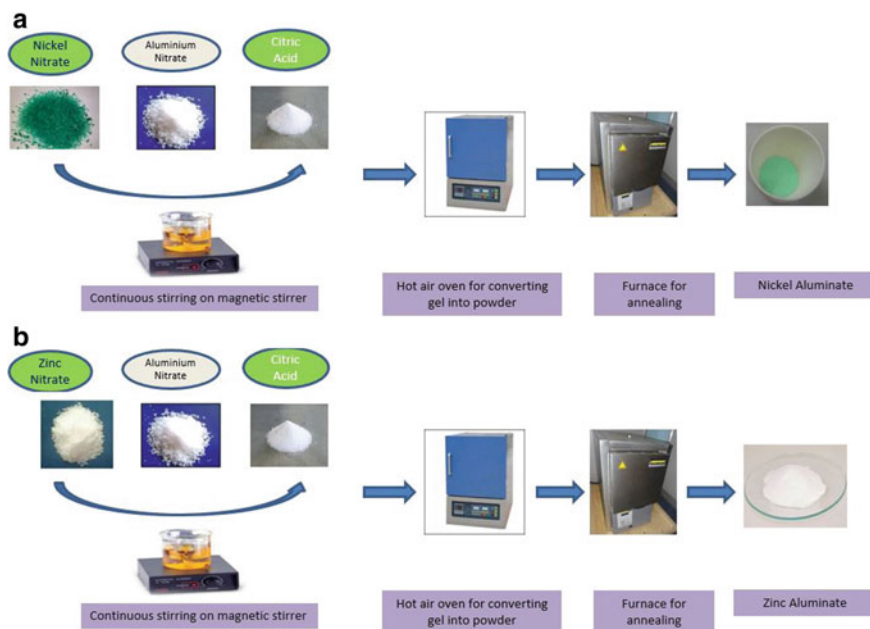


**Fig. 1** **a** Schematic diagram of nickel aluminate. **b** Schematic diagram of zinc aluminate

80 °C to get a gel. Then, gel was dried in an oven and obtained nickel aluminate powder. Finally, nickel aluminate was annealed at 650, 750, and 850 °C for 2 h in muffle furnace (Nabertherm, Germany).

### 2.2.2 Synthesis of $\text{ZnAl}_2\text{O}_4$ Nanoparticles

In case of Zinc aluminate, zinc nitrate (99.9% assay) 297.47 mol/gm, aluminum nitrate (99.9% assay) 750.26 mol/gm, and citric acid (99% assay) 768.48 gm/mole were used for synthesis. Schematic diagram of synthesis method of zinc aluminate is shown in Fig. 1b. Zinc nitrate is mixed in 20 ml deionized water in a beaker, and aluminum nitrate is mixed with 20 ml deionized water in another beaker. All three chemicals are mixed and shift the pH value with the help of ammonia ( $\text{NH}_3$ ) at pH 7. Afterword similar process was used as used in synthesis of nickel aluminate. The precise measurement of the properties of the synthesized material has the utmost importance in the field of research. In the present study, the synthesized samples were characterized by modern sophisticated instruments namely XRD, VSM, and PL in order to reveal the physical properties.

### 3 Results and Discussion

#### 3.1 X-Ray Diffraction Measurement

X-ray diffraction pattern of powder  $\text{ZnAl}_2\text{O}_4$  has been obtained using a Bruker D8 X-ray diffractometer as shown in Fig. 2a. The crystallite size of the prepared  $\text{ZnAl}_2\text{O}_4$  particles was calculated applying Scherer's Eq. (1), particularly to the peak having highest intense value at angular location  $2\theta = 36.75^\circ$  (Fig. 2a). Powder X-ray diffraction graph reveals that all samples were of single phase cubic in nature possessing spinel structure [29]. The crystalline size calculated using Scherer's equation given below [30].

$$d = \frac{0.9\lambda}{B \cdot \cos\theta} \quad (1)$$

In which  $d$  represents the average crystallite size,  $\lambda$  is the wavelength of X-ray,  $B$  is the peak width at half-maximum height, 0.9 is known as shape factor, and  $\theta$  is for Bragg's incident angle. The crystalline size obtained was 18 nm, 28 nm, and 30 nm for annealing temperatures of 650 °C, 750 °C, and 850 °C, respectively. It concludes that crystallinity size of  $\text{ZnAl}_2\text{O}_4$  particles increases with annealing temperature. All the diffraction peaks were found to be perfectly at  $2\theta$  positions ( $31.2^\circ$ ), ( $36.75^\circ$ ), ( $44.7^\circ$ ), ( $59.3^\circ$ ), and ( $65.3^\circ$ ) which signifies to (220), (311), (400), (511), and (440) crystallographic planes, respectively, which are in agreement with the reported values. This indicates that the complete formation of  $\text{ZnAl}_2\text{O}_4$  spinel phase with reference that zinc aluminate is a cubic crystal system spinel structure (JCPDS file no. 98-007-5098) of  $\text{Fd}3\text{m}$  space group. Moreover, absence of any extra peaks reveals impurities which were negligible in the synthesized sample.

For the same three different annealing temperatures of 650, 750, and 850 °C, XRD patterns of nickel aluminate are shown in Fig. 2b. The sample consisted of moderate crystalline  $\text{NiAl}_2\text{O}_4$  particles being present as a single phase. But degree of crystallinity is quite different from that of zinc aluminate. Although both the materials were prepared with same thermodynamic parameters and utilizing same chemical based citrate precursor method, result shows that nucleation and growth mechanism of both Zn aluminate and Ni aluminate crystal is different. The thermal analysis measurement is required for better understanding of thermal decomposition. This is our future work. Further, the XRD spectrum contains desirable five signature peaks in coincidence with the standard data of the cubic spinel Ni aluminate phase (JCPDS card No. 98-007-2075). The peaks of the prepared solid powders were referred to the crystal plane of spinel nickel aluminate, which planes having miller indices {220}, {311}, {400}, {511}, and {440} as shown in Fig. 2b. The nickel aluminate crystals possess spinel form and have got space group  $\text{Fd}3\text{m}$ . Average crystallite size was calculated using Scherer's formula and was found to be 8 nm, 12 nm, and 14 nm, respectively. The lattice parameter ( $a$ ) is calculated from the peak with highest intensity {311} using the following equation [30]



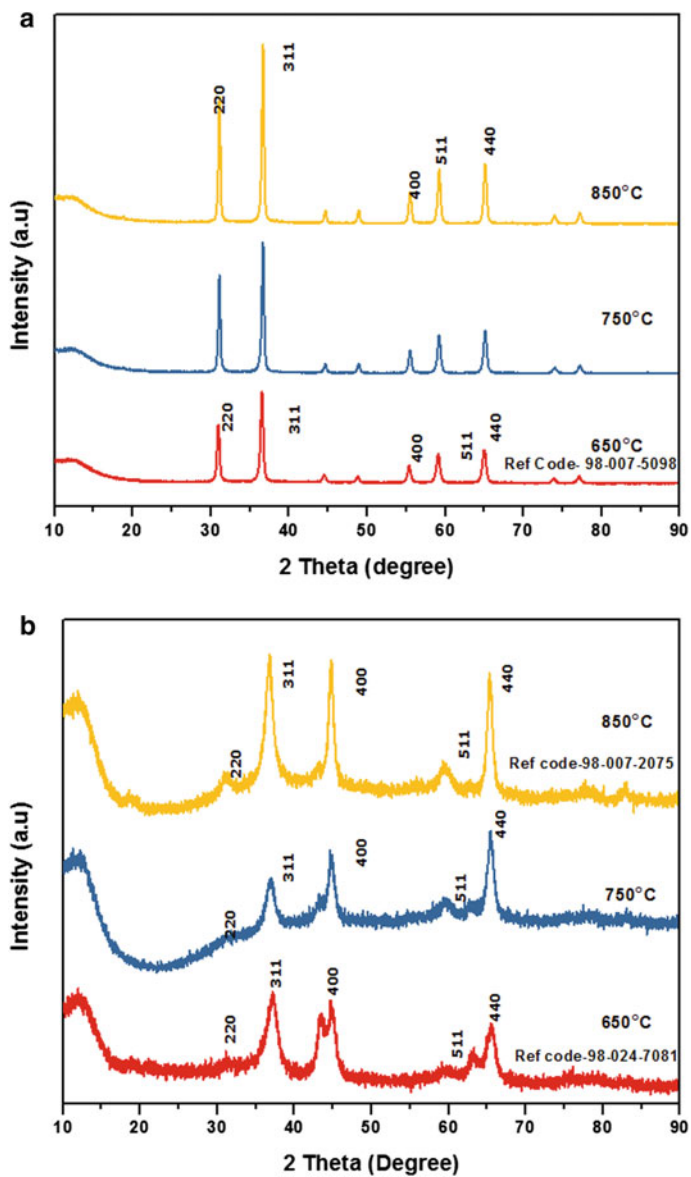


**Fig. 2** a XRD spectra of ZnAl<sub>2</sub>O<sub>4</sub> at various annealing temperatures. b XRD spectra of NiAl<sub>2</sub>O<sub>4</sub> at various annealing temperatures

**Table 1 (a-b)** Lattice parameters for ZnAl<sub>2</sub>O<sub>4</sub> and NiAl<sub>2</sub>O<sub>4</sub>

Nickel aluminate (annealed at)	d-spacing (Å)	Angular position (2θ) in degree	Lattice constant (Å)	Cell volume (cm <sup>3</sup> )
650 °C	2.4245	37.050	8.0410	519.912
750 °C	2.4259	37.026	8.0460	520.882
850 °C	2.4277	36.998	8.0520	522.049
Zinc aluminate (annealed at)	d-spacing (Å)	Angular position (2θ) in degree	Lattice constant (Å)	Cell volume (cm <sup>3</sup> )
650 °C	2.4244	36.823	8.0890	529.278
750 °C	2.4419	36.775	8.0990	531.244
850 °C	2.4567	36.443	8.1010	531.637

$$a = d [(h^2 + k^2 + l^2)]^{1/2} \quad (2)$$

where  $h$ ,  $k$ , and  $l$  denote miller indices,  $d$  is used for the distance between crystallographic planes, and 'a' is lattice parameter. The structural parameters were evaluated like  $d$ -spacing, lattice constant, and cell parameters which are being shown in Table 1a–b.

### 3.2 Magnetic Measurement and Discussion

Magnetic properties were characterized by using vibrating sample magnetometer (Lake Shore, USA). M-H curves were characterized in the range of magnetic field  $\pm 20$  kOe. Figure 3a shows M-H curves for the NiAl<sub>2</sub>O<sub>4</sub> particles at room temperature. It is observed that saturation magnetization ( $M_s$ ) is not attained even in the high magnetic field of 20 kOe. The same trend is observed for all three samples. The M-H curve declares the magnetization behavior of NiAl<sub>2</sub>O<sub>4</sub> particles that are paramagnetic at room temperature. From Table 2, it is clear that coercivity and retentivity increase regularly with increase in annealing temperature, while saturation magnetization is approximately steady with slight variation in the values. This is due to crystallite size, broken exchange bond, and the increases in annealing temperature. As the particle size increases, the magnetization increases. Similar behavior was also reported [31].

M-H curve of zinc aluminate for the same three annealing temperatures such as 650, 750, and 850 °C is depicted in Fig. 3b. The magnetic behavior of zinc aluminate samples was investigated by magnetic field between  $\pm 20$  kOe. M-H curves are showing diamagnetic behavior of zinc aluminate. Coercivity values do not follow a regular pattern, while magnetization values increase smoothly. The coercivity ( $H_c$ ), magnetization ( $M_s$ ), and retentivity ( $M_r$ ) have been enlisted in Table 3. The maximum coercivity was found 909.86 G for nickel aluminates.

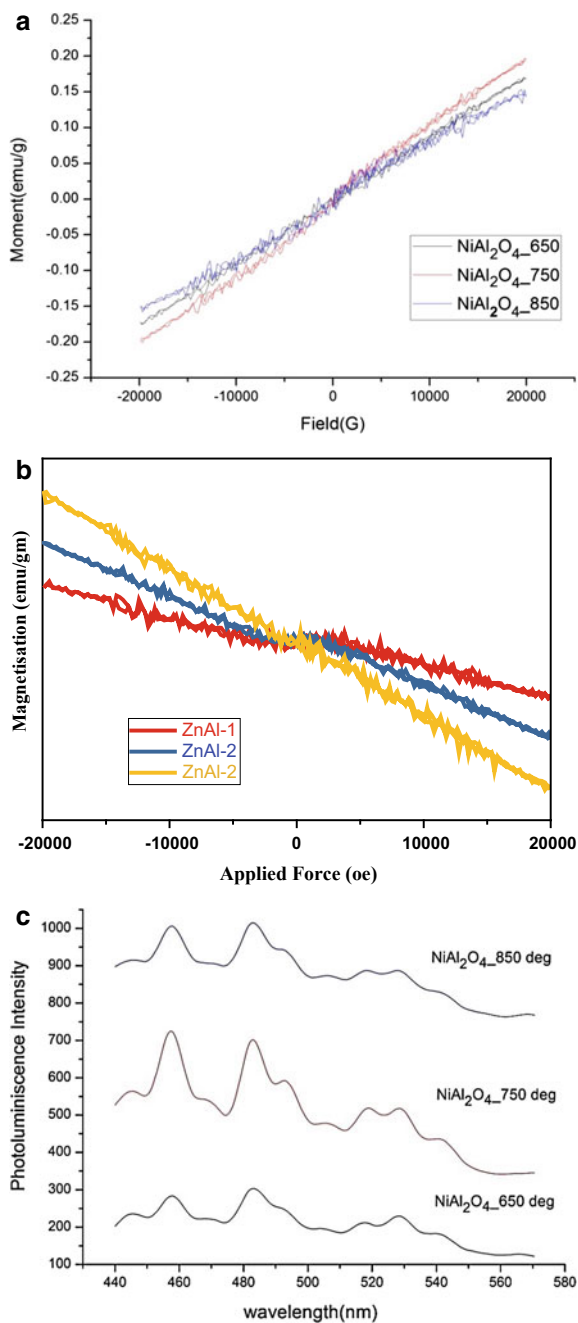


**Fig. 3** **a** M-H curve of  $\text{NiAl}_2\text{O}_4$  for three different annealing temperatures. **b** M-H curve of  $\text{ZnAl}_2\text{O}_4$  for three different annealing temperatures. **c** Photoluminescence spectra of  $\text{NiAl}_2\text{O}_4$ . **d** Photoluminescence spectra of  $\text{ZnAl}_2\text{O}_4$

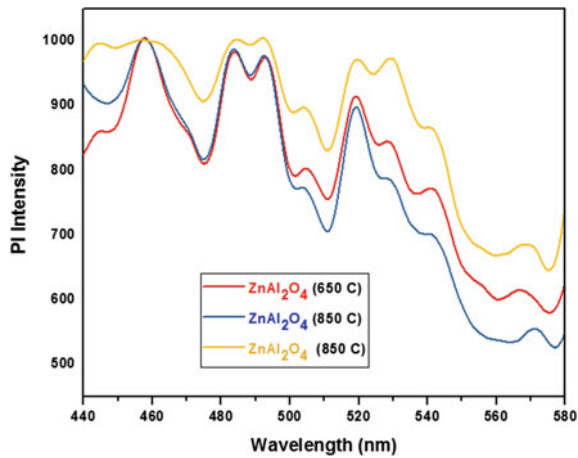


Fig. 3 (continued)

**Table 2** Magnetic parameters of nickel aluminate

Magnetic parameters	Nickel aluminate at 650 °C	Nickel aluminate at 750 °C	Nickel aluminate at 850 °C
Coercivity ( $H_c$ ) Oe	104.41G	208G	909.86G
Magnetization (Ms) (emu/gm)	0.17338	0.1984	0.1522
Retentivity (Mr) (emu/gm)	$3.3063 \times 10^{-3}$	$8.396 \times 10^{-4}$	$6.926 \times 10^{-4}$

**Table 3** Magnetic parameters of zinc aluminate

Magnetic parameters	Zinc aluminate at 650 °C	Zinc aluminate at 750 °C	Zinc aluminate at 850 °C
Coercivity ( $H_c$ ) Oe	109.76G	29.759G	264.08G
Magnetization (Ms) (emu/gm)	0.0972	0.1620	0.2473
Retentivity (Mr) (emu/gm)	$2.7146 \times 10^{-3}$	$3.9744 \times 10^{-3}$	$4.0578 \times 10^{-4}$

### 3.3 Photoluminescence Measurement

In order to understand the fluorescence mechanism of the prepared  $ZnAl_2O_4$  and  $NiAl_2O_4$  samples, schematic band diagram best examples the excitation phenomenon as well as emission for the system. PL spectra for  $NiAl_2O_4$  and  $ZnAl_2O_4$  were excited by 200 nm wavelength resulted in an intense blue emission using Perkin Elmer photoluminescence spectroscopy. In the wavelength window of (420–580) nm, the reflected optical spectrum was obtained for aluminates as shown in Fig. 3c, d. The PL spectrum of the both nickel aluminate and zinc aluminate samples annealed at different temperatures are in visible range. In nickel aluminate

sample annealed at 750 °C, PL peaks intensity are sharp and higher compared to sample annealed at 850 and 650 °C. On the other hand, in nickel aluminates, all the emissions peaks are in visible range.

But the peak intensities are not prominent. This may be due to size dependent properties. Further study needed the actual mechanism of this phenomenon. This is our future plan. Most interesting things is that emission are in visible range, which may be useful for various applications [32, 33]. The emission peaks near 480, 519, and 530 nm (known as red shift) might be due to oxygen vacancies. This is called green emission. It is obvious that PL emission is getting shifted with the change in particle size and shape, which supports the results of XRD data suggesting average crystallize size as 8 nm, 12 nm, and 14 nm, respectively. Such PL emission was also reported [34].

## 4 Conclusion

The nanosized zinc and nickel aluminate nanoparticles were synthesized using low-cost citrate precursor method. The XRD study confirmed that pure phase nickel and zinc aluminate nanoparticles are formed having space group Fd3m. The PL measure measurement shows that the material shows both blue and green emissions this might be due to the oxygen vacancies and defects created in the nanomaterials. These materials will show good photocatalytic and optoelectronic properties and can be used in varied applications. Similarly, the material shows decrease in saturation magnetization and corresponding increase in coercivity showing the size dependency on magnetic properties.

**Acknowledgements** The authors would like to extend their sincere appreciation to the Aryabhata Knowledge University Patna, and Dept. Of Education, Govt. of Bihar for their well established scientific laboratory, as all the characterization were done in their laboratories

## References

1. Busca G, Lorenzelli V, Escribano VS, Guidetti R (1991) *J Catal* 131:167
2. Michel CR, Rivera J, Martinez AH, Aranda MS (2008) *J Electrochem Soc* 155:263
3. Cavalcante PMT, Dondi M, Guarini G, Raimondo M, Baldi G *Dyes Pigments* 80(209):226
4. Dhak D, Pramanik P (2006) *J Am Ceram Soc* 89:1014
5. Tzing WS, Tuan WH (1996) *J Mater Sci Lett* 15:1395–1396
6. Bouropoulos N, Tsiaoussis I, Pouloupoulos P, Roditis P, Baskoutas S (2008) *Mater Lett* 62:3533–3535
7. Khaledi AG, Afshar S, Jahromi HS (2012) *Mater Chem Phys* 135:855–862
8. Liang Z, Guang-Fu J, Feng Z, Zi-Zheng G (2011) *Chin Phys B* 20:047102–047107
9. Sickafus KE, Wills JM, Grimes NW (1999) *J Am Ceram Soc* 82:3279–3292
10. Salavati-Niasari M, Davar F (2009) *Mater Lett* 63:441–443
11. Gao X, Li X, Yu W (2005) *J Phys Chem B* 109:1155–1161

12. Roesky R, Weiguny J, Bestgen H, Dingerdissen U (1999) *Appl. Catal A:Gen.* 176:213–220
13. Dussault L, Dupin JC, Guimon C, Monthieux M, Latorre N, Ubieta T, Romeo E (2007) *J Catal* 251:223–232
14. Li W, Li J, Guo J (2003) *J Eur Ceram Soc* 23:2289–2295
15. Platero EE, Arean CO, Parra JB (1999) *Res Chem Intermed* 25:187
16. Melo DMA, Cunha JD, Fernandes JDG, Bernardi MI, Melo MAF, Martinelli AE (2003) *Mater Res Bull* 38:1559–1564
17. Shaheen WM (2002) *Thermochim Acta* 385:105–116
18. Valenzuela MA, Jacobs JP, Bosch P, Reijne S, Zapata B, Brongersma HH (1997) *Appl Catal A: Gen* 148:315–324
19. Zawadzki M, Wrzyszczyk J (2000) *Mater Res Bull* 35:109–114
20. Chen Z, Shi E, Zheng Y, Li W, Wu N, Zhong W (2002) *Mater Lett* 56:601–605
21. Adak AK, Pathak A, Pramanik P (1998) *J Mater Sci Lett* 17:559–561
22. Phani AR, Passacantando M, Santucci S (2001) *Mater Chem Phys* 68:66–71
23. Hong W-S, De Jonghe LC, Yang X, Rahaman MN (1995) *J Am Ceram Soc* 78:3217–3224
24. van der Laag NJ, Snel MD, Magusin PCMM, de With G (2004) *J Eur Ceram Soc* 24:2417–2424
25. Wei X, Chen D (2006) *Mater Lett* 60:823–827
26. Duan X, Yuan D, Wang X, Xu H (2005) *J. Sol-Gel Sc. & Tech.* 35:221–224
27. Kumar RT, Selvam NCS, Ragupathi C, Kennedy LJ, Vijaya JJ (2012) *Powd. Tech.* 224:147–154
28. Khaledi AG, Afshar S, Jahromi HS (2012) *Mat. Chem. & Phys.* 135:855–862
29. Bragg WH (1915) *Phil Mag* 30:305–315
30. Scherrer P (1918) Bestimmung der Grösse und der inneren Struktur von Kolloidteilchen mittels Röntgenstrahlen, *Nachrichten von der Gesellschaft der Wissenschaften, Göttingen*, pp 98–100
31. Singh RK, Yadav A, Narayan A, Chandra M, Verma RK (2012) *J Therm Anal Calorim* 107:205–210
32. Raghupathi C, Juditya Vijya J, John Kennedy L (2014) *Mat Sci Engg B* 184:18–25
33. Jung M, Kim S, Ju S (2011) *Opt Mat* 33:280–283
34. Suresh K, Sampath CF, James J (1998) *of Ameri. Ceram. Soci.* 81:649–654

# Review of Battery Technologies Available for Promoting Electric Mobility in Urban India



Rahul Tiwari, Umang Patel, and Atmagya Raj

## 1 Introduction

Urban revolution has transformed the face of Indian cities in the last couple of decades. These cities with an unprecedented population growth and migration have created a surge in the travel demand which have resulted in exponential increase in personal vehicles. Today, India is one of the thriving economies in the world, but its increasing reliance on private vehicles is one of the major concerns for the deteriorating air quality and increased dependency on crude oil leading to higher export bills. While there have been advances in technology to make the country safer and facilitate the lives of everyone, still rising environmental concerns and growing need for sustainable mobility solutions have posed significant economic and social challenges for the country [1]. Therefore, the challenge of technological innovation is growing over time as society continues to build and grow better ways to live and improve lives.

The particular aspect of saving the earth from various environmental threats has led the automotive industry to take various initiatives to prevent environmental degradation, particularly air pollution. Therefore, automobile manufacturers have launched environmentally friendly vehicles to tackle this problem. Other than protecting the environment, sustainable mobility solutions also aim for economic development which requires sound trade-offs and thus calls for green mobility solutions. The recent technological advancement and government policies in the field of automotive industry and pollution control have led to reduction in fuel emissions and thereby enhance the environmental conditions.

Electric vehicles are considered to be one of the best options, triggering the introduction of innovations for electric mobility or e-mobility. The idea of electric mobility is not recent. Reportedly, as early as 15 or so years ago, e-mobility

---

R. Tiwari (✉) · U. Patel · A. Raj

Department of Architecture and Planning, Maulana Azad National Institute of Technology (MANIT), Bhopal, India

innovations began to take root in the automotive industry. In simple terms, e-mobility refers to the development of electric or electronic power trains, cars, bikes or any other vehicle that moves away from the conventional fossil fuel and oil automotive technology. This covers technological alternatives such as battery electric vehicles, hybrid electric vehicles and hydrogen fuel cell vehicles [2].

The key purpose of e-mobility is to manufacture vehicles that are more environmentally sustainable and efficient and thus fulfil current legislative standards imposed by policymakers and other law-setting bodies. The widespread use of electric vehicles (EVs) for personal mobility is likely to make improvements in battery technology possible, as they are seen as one of the solutions for reducing global greenhouse gas (GHG) emissions, improving air quality, reducing reliance on crude oil and increasing energy security [3].

## 2 Literature Review

Over the decades, progress in production of electric vehicles and innovation in battery technology have been revamped at a rapid pace. This era of limited natural resources such as combustion fuels like oil and coal and also the ongoing environmental concerns have led the society to shift focus onto sustainable mobility. Out of all the options, electric vehicles pose a great power to ameliorate environmental conditions. For production of electric vehicles, batteries play an inextricable role as it stores electricity and provides it to the motor [4]. Further, these batteries used in EVs are known as traction batteries for electric vehicle batteries (EVB). These are usually rechargeable (secondary) batteries, mainly used in road locomotives, trucks and mechanical handling equipment. Examples of major traction batteries are the lead-acid battery, the nickel–cadmium battery (Ni–Cd), the nickel-metal hydride battery (NiMH) and the lithium ion [4]. According to electric vehicle index, countries like China, the United States of America and Germany are in the forefront of transition to electric mobility. India being a developing nation still lags behind in the race to green mobility solutions when compared with developed nations. However, as the battery technology is a crucial part of the electric vehicle industry, different battery technologies for electric vehicles have been elaborated in the further section.

## 3 Lead-Acid Batteries

The world's first rechargeable traction battery was developed about 160 years ago by Gaston Planté, which was later enhanced and the practical version of the battery came into existence in 1886 [4]. Over the years, the battery's strength and power have been enhanced by better utilization of lead grid lattice for better implementation. These batteries convert chemical energy into electrical energy by employing



lead oxide as positive electrode, spongy lead as negative electrode and sulphuric acid as electrolyte; furthermore, it has several types like flooded, sealed and gel type. This technology is primarily used in electric motors, submarines and power generation for sump pumps. Lead-acid batteries provide optimal function at 25 °C as high temperature shortens longevity. Also, due to its wide availability and low cost, it continues to make a huge contribution to the automotive sector. Its ability to supply high surge currents and large power to weight ratio are some of the attractive attributes of the battery. However, the downside is that they have a short life cycle, low power density and heavy weight.

### **3.1 Lithium-Ion Batteries**

Rechargeable lithium-ion batteries came into existence in the 1990s with the substantial advantage over the other battery systems due to its lightweight, high energy density and the ability to recharge. It is one of the most widely recognized innovations in the modern electrochemical industry. Lithium-ion batteries are fast growing, most promising and widely used battery technology in the field of e-mobility. In a conventional Li-ion battery, carbon serves as anode and metal oxide as cathode while electrolyte is a lithium salt in an organic solvent. It shows potential for yet higher capacities and high specific energy. This increases the mileage to three times that of lead-acid battery resulting in coverage of larger travel distance. This technology is primarily applied in the automotive industry on account of its added benefits such as low self-discharge, low maintenance, long-life cycle, high energy capacity and high performance. Other than electric vehicles, Li-ion batteries are also used in portable electronics and aerospace applications. However, the battery exhibits a few drawbacks which include high manufacturing cost, ageing and the requirement for protection circuit. As the output of new technology, inventions and solutions continues to advance, lithium-ion batteries are highly likely to contribute more to established markets and people's lives [2]. There are three main variants of Li-ion batteries, as detailed further.

#### **3.1.1 NMC (Lithium Manganese Cobalt Oxide)**

NMC batteries exhibit good overall performance by virtue of its attributes such as high specific energy, high power and low self-heating rate. Graphite is employed as an anode while  $\text{LiNiMnCoO}_2$  as cathode. Further, the battery is widely used as power tools, e-bikes and other electric power-train because of its relatively low costs and light weight. The downside of the battery is that it requires 6 h of charging time for the regular use of EVs and the restriction on the ambient temperature, which should not be more than 40° for the battery's proper functioning. However, the standard battery discharge rate is 2 h, and it holds up to 80% depth of discharge (DoD) while lasting up to 2500 charging cycles.

### 3.1.2 LTO (Lithium Titanate)

LTO batteries demonstrate greater prospective than NMC batteries as major drawbacks have been solved by the advancement in the batteries. The reduction in charging time and resistance to ambient temperature (45°) are the most prominent qualities of the battery technology. Also, it can last up to 10,000 life cycles and thus tend to be used for home energy storage, transportation, solar powered lighting, etc. However, the major drawbacks include 3–4 times higher costs than the NMC, low particular energy and high weight.

### 3.1.3 LFP (Lithium Phosphate)

LFP batteries are one of the safest batteries as it shows great potential to handle high temperature with minimum degradation. Between the NMC and the LTO batteries, the LFP batteries hold an intermediate position as temperature tolerance is higher, but lower than LTO and more effective load and unload ability. Also, it experiences a lower rate of capacity loss with great calendar life.

### 3.1.4 Nickel-Metal Hydride Battery

Nickel–metal hydride is one of most readily available rechargeable batteries which bear nickel hydroxide as a positive electrode, titanium or nickel as a negative electrode. Electrolyte solutions are alkaline solutions, usually potassium hydroxide. These batteries are immune to a wide temperature range, mild toxins and long life cycles also they are recyclable. However, they suffer from lower self-discharge, lower capacity due to voltage depression and no function in case of devices operating on primary alkaline chemistry, a comparison of the available technologies is as detailed in Fig. 1.

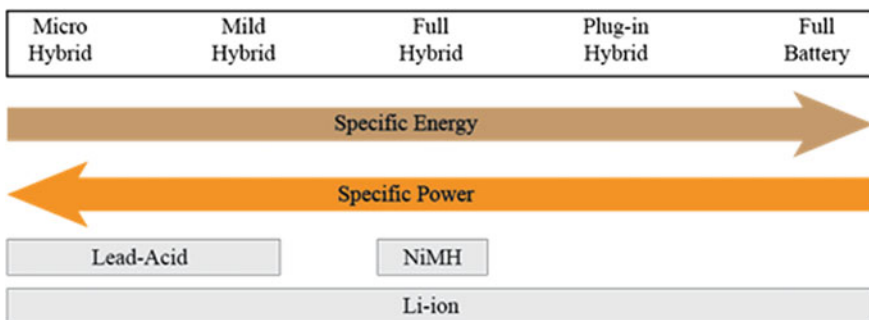


Fig. 1 Battery requirements depending on vehicle class and battery technology

### **3.2 Nickel–Cadmium Batteries**

Nickel–Cadmium batteries consist of nickel and cadmium species which serve as the positive and negative electrodes, as well as alkali solution being the electrolyte. It is a well-established technology which has been in operation since 1950 due to its low maintenance requirement and a long-life cycle of more than 3500. The Ni–Cd battery has low internal resistance, but a high degree of discharge period at a very short time. Its efficiency during service requires a high charging rate at a very fast cycle. A major concern about nickel–cadmium batteries is the toxicity and thus environmental inefficiency of cadmium [5].

### **3.3 Zebra Battery Technology**

The ‘ZEBRA’ (zero emissions batteries research activity) battery is a limited-volume sodium nickel–chloride battery manufactured in Switzerland for EV applications. The technology was first developed during the 1970s and 1980s in South Africa [6]. It is a well-tested technology available in a variety of EV formats, manifesting maintenance-free operation. Zebra cells deliver 7–8 times higher cycle life than lead-acid and low resistance failure of cells so that sequence of linked strings containing failed cells will continue to function. Also, this technology showcases some other benefits such as robust nature, potentially inexpensive, ambient temperature, no gassing, no self-discharge and easy charge estimation. (Charge Ah in = discharge Ah out). However, it takes 12–15 h for the battery to thaw out after freezing and also shows 90 W energy loss while not in use, which acts as a major disadvantage [7].

### **3.4 Nickel-Zinc Batteries**

Ni-Zn battery technology is one of the alternatives for rechargeable batteries which have shown great potential in high-drain applications and power tools. It is known for its relatively low costs compared to other Ni-based chemistries and high energy to mass ratio. The chemical properties of the battery are quite similar to nickel–metal hydride as zinc and nickel hydroxide serve as negative and positive electrodes, respectively, in the presence of an alkaline electrolyte (potassium hydroxide, KOH). The battery shows very low levels of toxicity and hence do not possess threat to the climate. Other positive characteristics include its non-flammable nature, quick recharge, high discharge rates while preserving thermal stability and easily recyclable while preserving physical and chemical properties [8]. However, commercialization remains problematic due to short-circuit issues, life-cycle issues and gas recombination in a sealed cell.

## 4 Comparison

The development and revolution of battery technology from old centuries to latest battery technology have been observed all over the world. The parameters such as specific capacity, energy density, particular capacity, weight and size have improved along the evolution based on the transition from lead-acid battery to lithium-ion battery. Therefore, to understand and compare the basic characteristics of various battery typologies, Table 1 has been formulated.

There are various battery technologies present in the current modern world. Out of which, six widely used battery types have been tabulated and compared in Table 1 [9] on the basis of various parameters necessary for the best output in electric vehicles. The most promising candidate amongst the above-mentioned batteries applicable to EVs is lithium-ion battery. It excels mostly in every parameter and hence is considered the best option for the production of new generation EVs. Lithium-ion batteries are superior in terms of high energy efficiency and power density, allowing them to be built lighter and smaller in weight and scale, respectively, when compared to other types of batteries, such as lead-acid batteries, nickel–cadmium (Ni–Cd) batteries and nickel–metal hydride (Ni–MH) batteries. Other advantages of lithium-ion batteries include a wide operating temperature range, fast charging capability, no memory effects, a relatively long-life cycle and a low self-discharge rate. Desired attributes of EV batteries include: high energy density, power density, cycle life, safety and low cost. ZEBRA battery technology also shows great potential, but 90 W of energy loss can be observed when not in use. New cell chemistry is being developed to make batteries smaller, lighter and hold enough energy so that traditional vehicles can compete with EVs. Currently, lithium-ion batteries are the most common and most favourable battery technology that can closely meet the United States Advanced Battery Consortium (USABC) minimum criteria for the commercialization of EVs.

## 5 Indian Context

In India, the percentage of urbanized areas along with urban population is rising at a faster rate, thereby leading to derived demand for travel for different purposes. Increasing transportation mobility may lead to rise in problems like traffic congestion, air pollution, accidents, etc. Therefore, solution to these problems results in a major transformation of India's transportation system through various government initiatives and schemes at national and state levels. These government initiatives and schemes include National Electric Mobility Mission Plan (NEMMP) 2020, Faster Adoption and Manufacturing of Electrical vehicles (FAME), Smart city mission, etc. These schemes and policies energize elective modular alternatives move to electric vehicles and improvement of public transport, road infrastructure, etc. [10]. The government operates and manages public transit and road networks,

**Table 1** Specific battery parameters for electric vehicles (rough estimations on cell level)

Battery type	Specific energy (Wh kg <sup>-1</sup> )	Specific power (W kg <sup>-1</sup> )	Cycle life	Efficiency (%)	Self-discharge % per month	Operating temperature	Nominal voltage (V)
Lead-acid	35	150	400	80	3–5%	–20–60 °C	2
Nickel– cadmium	50	400	1500	70	20%	–20–45 °C	1.2
Nickel–Metal– hydride	90	300	1000	75	30%	–20–60 °C	1.25
Nickel–zinc	75	500	500	70	20%	–30–75 °C	1.65
ZEBRA (Na/ NiCl <sub>2</sub> )	160 cell 90 battery	150	2000	90	Only thermal self-discharge	Internal operating temperature (270–350 °C)	2.67
Lithium-ion	200	400	1500	93	2–3%	–20–60 °C	3.6

while last-mile connectivity is typically managed, controlled and supported by government agencies, while private individuals play a more important role in last-mile connectivity.

Electric vehicles (EVs) are increasingly being taken into consideration because of the maximum logical alternative in the direction of reducing local air pollution. In current instances, EV innovation has sufficiently developed and is being advanced in accordance with zero tailpipe discharge. These forthcoming advances are turning into a brilliant option for customary fuel vehicles in India. The public government programs, plans and policies are the most grounded drive to shift into electric modes [10]. Electric vehicles are estimated to have 35–45% lower emissions compared to traditional IC engines, as predicted by the International Energy Agency. The adoption of electric vehicles could lead to a successful reduction of pollution and health problems. Depending on the specifications and viability of the city, e-rickshaws, e-autos, mini electric buses, etc. For comparison of growth of electric vehicles in India, Fig. 2 depicts the data of automobiles sales against the sale of electric vehicles in Fig. 3 [11].

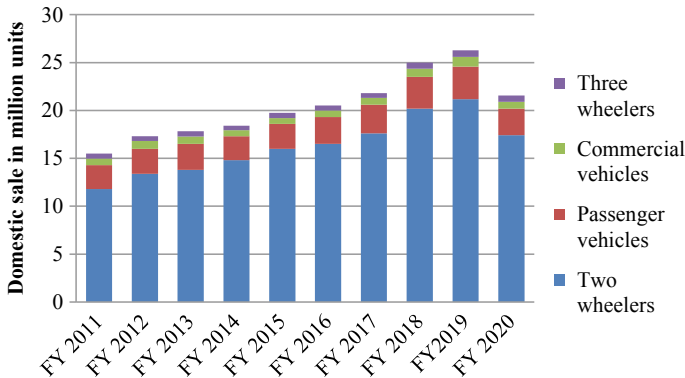


Fig. 2 Sales of automobiles India FY 2011–2020

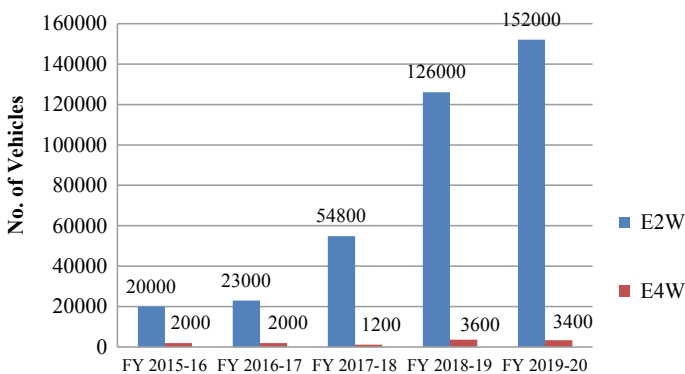


Fig. 3 EVs sale trend in India

The FAME initiative was introduced in 2015 and has resulted in raising the share of electric two-wheelers and four-wheelers in the automobile market in India. In the financial year 2019–20, the EV industry delivered 152,000 electric two-wheelers and 3400 electric four-wheelers. Electric vehicle sales in India rose by 20% in 2019–2020, largely led by rising two-wheeler sales as per the Society of Electric Vehicle Manufactures. In January 2020, the Department of Heavy Industries, under the second phase of the FAME India initiative, approved 2636 electric vehicle charging stations in 62 cities across 24 states and union territories [11].

### ***5.1 Upcoming Energy Technology and Innovation Enables “Make in India”***

Research and development on energy can be a good enabler of India’s energy policy goals which also leads to wider national agendas such as the ‘Make in India’ manufacturing initiative. Through this programme, the government is working with multinational companies to produce solar PV, lithium batteries, solar charging facilities and other advanced technologies in India. Innovation and specific policy support for India has been significant in driving the growth of energy technologies. In a wide variety of energy technology fields, including cooling, electric mobility, smart grids and innovative bio-fuels, the government is reinforcing its research efforts [12].

### ***5.2 Battery Cells, Packs and Materials***

India needs a minimum of 10 GWh of cells by 2022, which will have to be extended to 50 GWh by 2025. Therefore, in India, manufacturing these cells will be promoted [12]. Therefore, manufacturing of these cells will be encouraged in India. It is necessary for manufacturers to work upon the different parameters such as energy density, efficiency, safety, etc. so that their batteries are the world’s best. In order to protect the components used in lithium-ion batteries, including lithium, cobalt, nickel, manganese and graphite, India will need a strategy. Our first job will be to search for these commodities within India while at the same time allowing or promoting strategic investments for these materials in foreign mines. Setting up the lithium-ion battery recycling industry will perhaps be the most critical task. Strict criteria for the recycling of any lithium-ion battery used in electric vehicles, cell phones or laptops should be enforced in India. In order to allow zero emissions at all recycling facilities, it would promote the import of used lithium-ion recycled batteries with stringent environmental criteria [12].

### **5.3 *Last-Mile Connectivity and Rural Transport***

Today, some Indian cities have metros as public transportation services while other cities have bus services. Autos/rickshaws provide connectivity in cities which have metro/bus facilities. The early up gradation of cars to electric vehicles by means of lithium-ion batteries would provide a significant sustainable transportation system for countless individuals in cities. Today, three-wheelers are the main transport in towns, for dropping the people to bus stops on motorways or railway stations. It is possible to quickly transform them over to electric, giving pollution-free vehicles in villages. Specifications should ensure that these vehicles are not an annoyance for all users of public roadways. Further, job opportunities in rural areas can be created by operating various battery-charging and swapping outlets in larger villages. Smaller transport vehicles are mostly responsible for the transportation of freight in rural areas and for transport linking agriculture to towns (like tempos, rickshaws, and autos). These vehicles are appropriate for substitution by EVs [12].

## **6 Conclusion**

Electrical mobility is the most feasible approach to accomplish pollution-free environment which is crucial for the sustainable development of the world. EVs have high possibilities of embracing a healthier and eco-friendly transportation system, thereby preventing global warming caused by fossil fuel dependent on the traditional technologies. In EV applications, the battery plays the most important role. This paper gives an overview of various EV battery innovations, impacts and approaching course of progress. Based on the comparison of various batteries, the lithium-ion battery has the best performance amongst different batteries in terms of its efficiency and travel distance. However, there are at present a couple of developing batteries which utilize diverse anode, cathode and electrolyte separator that might upgrade the performance of the batteries by increasing the parameters such as heat capacity, lifecycle sustainability. Therefore, a shift of transportation sector from ICE motors to EVs in India will require a lot of planning, research work and development. Government policies like FAME (faster adoption and manufacturing of electric vehicles) and few other policies which promote the manufacturing of electric and hybrid vehicle technology should be revised and upgraded on a regular basis to keep in pace with the development, while focussing on improving the energy-efficiency of EVs.




## References

1. Pranavant MS, Garg A (2019) Recharging India's electric vehicle ambition. Deloitte
2. Ahmed F, Okoro F (2018) Li-ion batteries for electric mobility
3. Faria R, Pedro M, Rita G, Pedro M, Fausto F, Joaquim D, de Almeida AT (2014) Primary and secondary use of electric mobility batteries from a life cycle perspective. *J Power Sources* 262:169–177
4. Chian TY, Wei WLJ, Ze ELM, Ren LZ, Ping YE, Abu Bakar NZ, Faizal M, Sivakumar S (2019) A Review on Recent Progress of Batteries for Electric Vehicles. *Int J Appl Eng Res* 14 (24):4441–4461
5. Wilber T, Thompson FJ, Olabi A (2020) Classification of energy storage materials. In: Reference module in materials science and materials engineering
6. Battery technologies. *Meridian Int Res* (2005)
7. O'sullivan TM, Bingham CM, Clark RE (2006) Zebra battery technologies for all electric smart car. In: International symposium on power electronics, electrical drives, automation and motion, 2006. SPEEDAM 2006, p 243. IEEE
8. Fetcenko M, Koch J, Zelinsky M (2015) Nickel–metal hydride and nickel–zinc batteries for hybrid electric vehicles and battery electric vehicles. In: *Advances in battery technologies for electric vehicles*, pp. 103–126. Woodhead Publishing
9. Iclodean C, Varga B, Burnete N, Cimerdean D, Jurchiş B (2017) Comparison of different battery types for electric vehicles. In: *IOP conference series: materials science and engineering*, vol 252, no. 1, p 012058. IOP Publishing
10. Shandilya N, Saini V, Ghorpade AR (2018) E-rickshaw deployment in Indian cities-Handbook (Supporting Sustainable Mobility under Smart.“ Regulation 91
11. Society of manufacturers of electric vehicles. EV sales scenario
12. Aayog NITI, Juyal S, Sanjeevi H, Saxena A, Sharma S, Singh A (2018) Zero emission vehicles (ZEVs): towards a policy framework. NITI Aayog, Government of India, New Delhi, India

# Application of Combined Compromise Solution Method for Material Selection



Farheen Jahan, Manoj Soni, Aasiya Parveen ,  
and Mohammad Waseem

## 1 Introduction

Choosing the appropriate material for making products for specific applications has always been a challenging task for the materials engineers and production managers as the material's attributes significantly contribute to the successful functioning of the product. The material selection represents an MCDM problem where the decision maker has to select the relevant material based on simultaneous maximization of some of the criteria/attributes and minimization of the remaining ones. An MCDM problem can be effectively and efficiently solved with the help of MCDM methods and that is why literature reveals that for investigating material selection problems of distinct engineering applications researchers have employed different MCDM methods. Rathod et al. [1] analyzed the two MCDM methods: TOPSIS and fuzzy logic approach method to select the proper phase change material (PCM) to check the effectiveness of these methods. It is found that the TOPSIS method is preferred where performance ratings are precise. Chauhan et al. [2] investigate the relative ranking of the soft and hard magnetic materials by using the VIKOR and TOPSIS technique. Girudha et al. [3] also uses fuzzy VIKOR technique to select the optimal material for instrument panel used in an electric car. Bahraminasab et al. [4] and Cavallini et al. [5] used the comprehensive ranking technique to select the ideal material for the specific applications. In another study done by Chatterjee et al. [6], two MCDM methods are used to solve the material selection problem: VIKOR and ELECTRE (Elimination and Et Choice Translating

---

F. Jahan (✉) · M. Soni · A. Parveen  
Department of Mechanical and Automation Engineering, Indira Gandhi Delhi Technical  
University for Women, New Delhi, India  
e-mail: [lncs@springer.com](mailto:lncs@springer.com)

M. Waseem  
Department of Mechanical Engineering, Jamia Millia Islamia, New Delhi, India

Reality). In addition to these methods, preference ranking tools are other kinds of MCDM methods.

Chatterjee et al. [7] and Peng et al. [8] investigate the material selection problem by using the preference ranking method: PROMETHEE. Several MCDM methods involve quite complex computational procedure, and therefore, researchers have been striving to develop relatively simpler methods. One such simple MCDM method has recently been developed by which is known as combined compromise solution (CoCoSo) technique for solving MCDM [9].

The objective of this paper is to ascertain the utility and potentiality of the CoCoSo method through its application on two illustrative examples related to the material selection problems which have already been determined by researchers using various methods. Other sections of this paper are arranged in the following way: Sect. 2 defines the CoCoSo method. Section 3 shows the application of the CoCoSo method on two illustrative examples, and Sect. 4 provides the conclusion of the present study.

## 2 Combined Compromise Solution (CoCoSo) Method

This method depends on the relative distance of alternative from the ideal one which gives compromised solution of alternatives ranking. This method comprises the five steps as follows:

### Step 1:

Select the available alternatives  $Q_i$  ( $i = 1, 2, 3, \dots, m$ ) and decision criteria  $R_j$  ( $j = 1, 2, 3, 4, \dots, n$ ).

### Step 2:

Formulate decision matrix  $R$  by arranging alternatives in the row and decision criteria in the column as given in Eq. (1).

$$R = [R_{ij}]_{m \times n} = \begin{bmatrix} R_{11} & R_{12} & \cdots & R_{1j} & \cdots & R_{1n} \\ R_{21} & R_{22} & \cdots & \cdots & \cdots & R_{2n} \\ \cdots & \cdots & \cdots & \cdots & \cdots & \cdots \\ R_{i1} & \cdots & \cdots & R_{ij} & \cdots & R_{in} \\ \cdots & \cdots & \cdots & \cdots & \cdots & \cdots \\ R_{m1} & \cdots & \cdots & R_{mj} & \cdots & R_{mn} \end{bmatrix} \quad (1)$$

where  $i = 1, 2, \dots, m$ ;  $j = 1, 2, \dots, n$

where  $R_{ij}$  represents  $i$ th alternative performance value on  $j$ th criterion,  $m$  defines the alternatives, and  $n$  defines the number of criteria.

**Step 3:**

Normalize the performance value of alternatives for favorable and non-favorable criteria using Eqs. (2) and (3), respectively.

$$N_{ij} = \frac{R_{ij} - \min R_{ij}}{\max R_{ij} - \min R_{ij}} \quad \text{for favourable criteria} \tag{2}$$

$$N_{ij} = \frac{\max R_{ij} - R_{ij}}{\max R_{ij} - \min R_{ij}} \quad \text{for non-favourable criteria} \tag{3}$$

where  $N_{ij}$  = Normalized performance value of alternatives based on criteria.

Determine weighted comparability sequence ( $WS_i$ ) and power weight of comparability sequence ( $PS_i$ ) using Eqs. (4) and (5), respectively.

$$WS_i = \sum_j^n w_j R_{ij} \tag{4}$$

$$PS_i = \sum_j^n (R_{ij})^{w_j} \tag{5}$$

**Step 4:**

Based on  $WS_i$  and  $PS_i$  values, three appraisal score strategies are employed for ranking of alternatives which are calculated using Eqs. (6), (7), and (8), respectively.

$$k_{ia} = \frac{PS_i + WS_i}{\sum_{i=1}^m (PS_i + WS_i)} \tag{6}$$

$$k_{ib} = \frac{WS_i}{\min WS_i} + \frac{PS_i}{\min PS_i} \tag{7}$$

$$k_{ic} = \frac{\mu WS_i + (1 - \mu) PS_i}{\mu \max WS_i + (1 - \mu) \max PS_i} \tag{8}$$

where  $\mu = 0.5$  is usually chosen by decision-maker, ranking can be done based on the  $k_{ia}$ ,  $k_{ib}$ ,  $k_{ic}$  (larger k acquires good rank preference), but it is recommended that ranking obtained through all the three appraisal score should be in highest agreement with each other.

**Step 5:**

Determine the value of  $K_i$  using Eq. (9). Rank the alternatives based on  $K_i$ , and the alternative which is having the highest value of  $K_i$  will acquire the first rank followed by others with decreasing  $K_i$ .

$$K_i = (k_{i1}k_{i2}k_{i3})^{1/3} + \frac{(k_{i1} + k_{i2} + k_{i3})}{3} \quad (9)$$

### 3 Illustrative Examples

The CoCoSo method is applied in the following two illustrative examples related to material selection.

#### 3.1 Cryogenic Storage Tank

The performance of the storage tank depends upon the material properties. To enhance its performance, the material should have good weldability and processability, low coefficient of thermal expansion and thermal conductivity, low density and specific heat, and high toughness and stiffness. Manshadi et al. [10] investigated the issue for the selection of appropriate material for the cryogenic storage tanks which were used for the transportation of liquid nitrogen safely [11]. The seven material properties were taken as selecting criteria, i.e., J1 (Toughness index), J2 (yield strength), J3 (Young's Modulus of Elasticity), J4 (density), J5 (thermal expansion coefficient), J6 (thermal conductivity), and J7 (specific heat) [12], and seven optional materials, i.e., Al2026-T6(E1), Al5052-O (E2), SS301-FH(E3), SS310-3AH(E4), Ti-6Al-4V(E5), Inconel 718(E6), 70Cu-30Zn(E7), were taken. Out of these materials, the best alternative was chosen for the design of the cryogenic storage tank. Among these seven decision criteria, J1, J2, J3 are the valuable criteria while J4, J5, J6, J7 are the non-valuable criteria. The decision matrix is given in Table 1.

**Table 1** Comparison of different materials for cryogenic tanks based on their mechanical properties (Manshadi et al. [10])

S. no.	Materials	J1	J2 in MPa	J3 in GPa	J4 in gm/cm <sup>3</sup>	J5 (10 <sup>-6</sup> /°C)	J6 (cal/s/cm/°C)	J7 (cal/gm/°C)
1	E1	75.5	420	74.2	2.8	21.4	0.37	0.16
2	E2	95	91	70	2.68	22.1	0.33	0.16
3	E3	770	1365	189	7.9	16.9	0.04	0.08
4	E4	187	1120	210	7.9	14.4	0.03	0.08
5	E5	179	875	112	4.43	9.4	0.016	0.09
6	E6	239	1190	217	8.51	11.5	0.31	0.07
7	E7	273	200	112	8.53	19.9	0.29	0.06

**Table 2** Normalized decision matrix for storage tank material selection

Weight	0.28	0.14	0.05	0.24	0.19	0.05	0.05
Material	J1	J2	J3	J4	J5	J6	J7
E1	0	0.258242	0.028571429	0.979487179	0.05511811	0	0
E2	0.028078	0	0	1	0	0.112994	0
E3	1	1	0.80952381	0.107692308	0.409448819	0.932203	0.8
E4	0.160547	0.807692	0.952380952	0.107692308	0.606299213	0.960452	0.8
E5	0.149028	0.615385	0.285714286	0.700854701	1	1	0.7
E6	0.235421	0.862637	1	0.003418803	0.834645669	0.169492	0.9
E7	0.284377	0.085557	0.285714286	0	0.173228346	0.225989	1

**Table 3** Ranking of alternative material for cryogenic storage tank

Material	Rank
E1	6
E2	7
E3	1
E4	3
E5	2
E6	4
E7	5

**Table 4** Comparison of ranking

Material	Rank	
	CoCoSo	Digital logic method (Manshadi et al. [10])
E1	6	6
E2	7	7
E3	1	1
E4	3	3
E5	2	2
E6	4	4
E7	5	5

The normalized decision matrix is formulated using Eqs. (2) and (3) which is given in Table 2. The first row of Table 2 shows the weights of the criteria which are taken from Manshadi et al. [10].

The ultimate ranking of the alternative materials is found following the steps of CoCoSo method, represented in Table 3. The comparison of ranking results achieved from different methods is illustrated in Table 4.

It is evident from Table 4 that CoCoSo produces the same rank of the materials as that of the digital logic method used by Manshadi et al. [10]. From the analysis, it is predicted that the stainless steel 301, followed by titanium alloy, Inconel 718, stainless steel 310, aluminum alloy, and brass would have the best performance. Thus, CoCoSo method is quite effective for material selection problem.

### 3.2 Light Load Wagon Wall

In this study, CoCoCo method will be applied for the light load wagon wall material selection. Only changes were made in the wagon wall to reduce the light. For this, the material should have low density, high specific stiffness, good corrosion, and wear resistance. Findik et al. [13] in his work produced the wagon wall materials in plate-shape, and the design is done by using performance indices to enhance strength and stiffness as  $E^{1/3}/\rho$  and  $\sigma_f^{1/2}/\rho$  as suggested by Ashby in ASM Metals Handbook [14]. Figures 1 and 2 show the different materials as per the performance indices. For finding the best suitable material to design the light load wagon walls, Findik et al. [13] recognized B1 (aluminum), B2 (aluminum alloys), B3 (low carbon steel), B4 (titanium alloys), B5 (nickel alloys), B6 (zinc alloys), and B7(copper alloys) as the comparable materials and five decision criteria, i.e., C1 (material density), C2 (specific stiffness), C3 (corrosion resistance), C4 (wear resistance), and C5 (cost of the material) [12, 15]. C1 and C5 are non-valuable criteria, while the other three are valuable criteria. Table 5 illustrates the initial decision matrix.

The normalized decision matrix is formulated with the help of Eqs. (2) and (3). Table 6 illustrates the matrix. The first row of Table 6 shows the weight of the criteria which has been taken from Findik et al. [13].

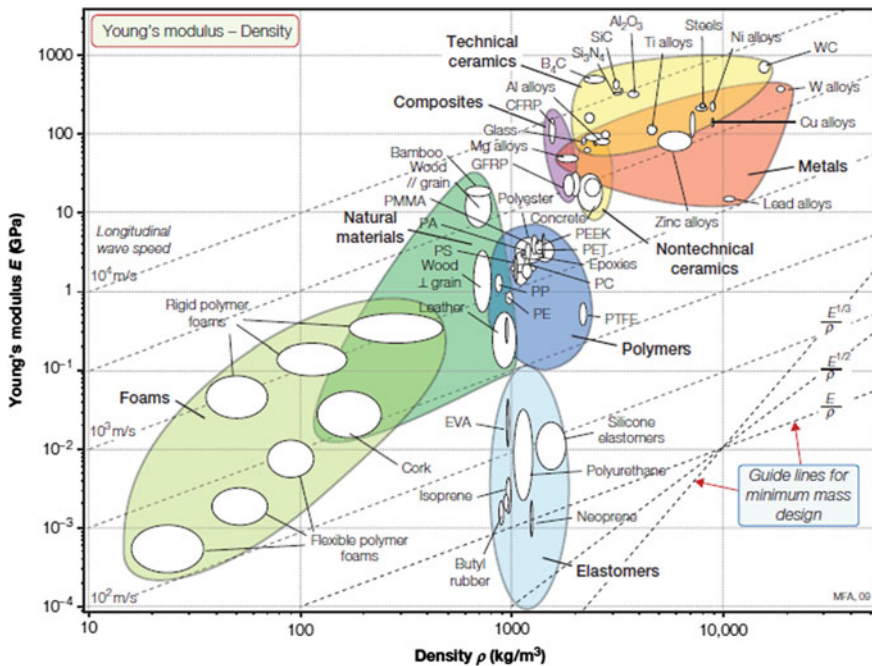


Fig. 1 Young's modulus  $E$  plotted against density  $\rho$  (Taken from [14])

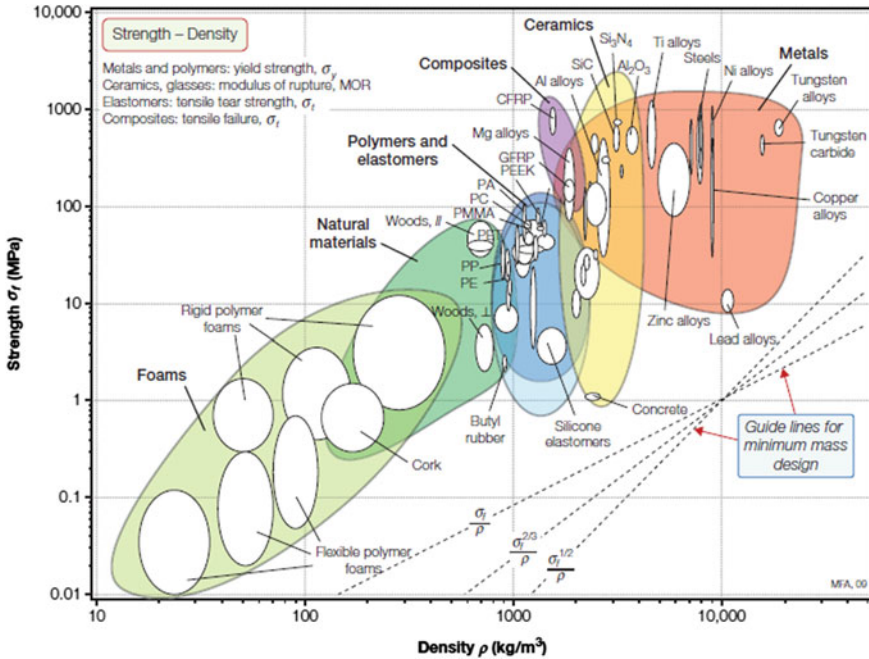


Fig. 2 Strength  $\sigma_f$  plotted against density  $\rho$  (Taken from [14])

Table 5 Comparison of different materials for light load wagon wall material based on their mechanical properties (Findik and Turan [13])

Sl. no.	Material	C1	C2	C3	C4	C5
1	B1	2700	0.03	4	3	2.32
2	B2	2700	0.03	4	3	2.3
3	B3	7900	0.03	3	5	0.85
4	B4	4500	0.02	5	3	13
5	B5	8900	0.02	5	4	6
6	B6	6000	0.02	3	1	2.2
7	B7	8930	0.02	5	5	2.3

Table 6 Normalized decision matrix for wagon wall material selection

Weight	0.4	0.1	0.1	0.1	0.3
Material	C1	C2	C3	C4	C5
B1	1	0	0.5	0.5	0.879012
B2	1	0	0.5	0.5	0.880658
B3	0.165329	0	1	0	1
B4	0.711075	1	0	0.5	0
B5	0.004815	1	0	0.25	0.576132
B6	0.470305	1	1	1	0.888889
B7	0	1	0	0	0.880658



**Table 7** Ranking of alternative material for light load wagon wall

Material	Rank
B1	3
B2	2
B3	6
B4	4
B5	5
B6	1
B7	7

**Table 8** Comparison of ranking results for wagon wall materials

Material	Rank	
	CoCoSo	Weighted property index method
B1	2	2
B2	1	1
B3	3	3
B4	5	4
B5	6	7
B6	7	6
B7	4	5

The ultimate ranking of the alternative materials is found following the steps of CoCoSo method which is represented in Table 7.

Table 8 shows the comparison of ranking results for the wagon wall materials obtained from different methods.

It is quite a clear Table 8 that CoCoSo produces approximately the same rank of the materials as that of the Weighted Property Index Method [13]. Thus, CoCoSo method is quite effective in solving material selection problem.

## 4 Conclusion

Selection of proper material is significantly important because the mechanical behavior of the product in the given application depends on the material's properties/attributes. Material selection is a challenging task and to accomplish these decision makers use MCDM methods. However, many researchers have used MCDM techniques for choosing the most appropriate material.

This paper demonstrated the application of a newly developed MCDM method called combined compromise solution (CoCoSo) method for cracking the material selection problem through two illustrative examples. In the case of cryogenic storage tank, results are matched with the existing methods. In another case for selecting material for light wagon wall, Al alloys are considered. It has been found

that the final ranking of the alternative materials derived by the CoCoSo method is almost equivalent to that of other methods, and thus, it produces results at par with other MCDM methods.

**Acknowledgements** This work is not supported by any funding agency or project.

## References

1. Rathod MK, Kanzaria HV (2011) A methodological concept for phase change material selection based on multiple criteria decision analysis with and without fuzzy environment. *Mater Des* 32(6):3578–3585
2. Chauhan A, Vaish R (2012) Magnetic material selection using multiple attribute decision making approach. *Mater Des* 36:1–5
3. Jeya Girubha R, Vinodh S (2012) Application of fuzzy VIKOR and environmental impact analysis for material selection of an automotive component. *Mater Des* 37:478–486
4. Bahraminasab M, Jahan A (2011) Material selection for femoral component of total knee replacement using comprehensive VIKOR. *Mater Des* 32(8–9):4471–4477
5. Cavallini C, Giorgetti A, Citti P, Nicolaie F (2013) Integral aided method for material selection based on quality function deployment and comprehensive VIKOR algorithm. *Mater Des* 47:27–34
6. Chatterjee P, Athawale VM, Chakraborty S (2009) Selection of materials using compromise ranking and outranking methods. *Mater Des* 30(10):4043–4053
7. Chatterjee P, Chakraborty S (2012) Material selection using preferential ranking methods. *Mater Des* 35:384–393
8. Peng AH, Xiao XM (2013) Material selection using PROMETHEE combined with analytic network process under hybrid environment. *Mater Des* 47:643–652
9. Yazdani M, Wen Z, Liao H, Banaitis A, Turskis Z (2019) A grey combined compromise solution (Cocoso-G) method for supplier selection in construction management. *J Civ Eng Manag* 25(8):858–874
10. Dehghan-Manshadi B, Mahmudi H, Abedian A, Mahmudi R (2007) A novel method for materials selection in mechanical design: combination of non-linear normalization and a modified digital logic method. *Mater Des* 28(1):8–15
11. Rao RV (2007) *Decision making in the manufacturing environment*. Springer, London
12. Chakraborty S, Chatterjee P (2013) Selection of materials using multi-criteria decision-making methods with minimum data. *Decis Sci Lett* 2(3):135–148
13. Findik F, Turan K (2012) Materials selection for lighter wagon design with a weighted property index method. *Mater Des* 37:470–477
14. Ashby MF (2011) *Material property charts*. In: *Materials selection in mechanical design*. Elsevier, pp 57–96
15. Karande P, Gauri SK, Chakraborty S (2013) Applications of utility concept and desirability function for materials selection. *Mater Des* 45:349–358

# Analysis of Performance and Emission Parameters in Direct Injection Diesel Engine by Using Biodiesel Blended with Additives



Mamuni Arya, Akshaya Kumar Rout, and Samiran Samanta

## 1 Introduction

Energy is very essential and important resource for a country's economic and social growth. The increasing demand of transportation sectors, industrials sectors, and research sectors are possible due to the growth of population in the world, which is a major factor of energy crisis [1]. Maximum energy is available from petroleum fuels, but due to the redundancy of petroleum fuel and the adverse effect of the engine emission to the environment, there are so many researches going on for alternative fuels. The most possible alternative fuels for internal combustion engines are biodiesel which is a clean burning fuel. According to the International Energy Agency, biodiesels are the best option to fulfill the world's energy demand up to 32% by 2050 [2]. Biodiesels are formed from plants product, so it has low toxicity and contains almost very less quantity sulfur. According to technical and environmental benefit, biodiesel have higher combustion efficiency, lower percentage sulfur content, higher cetane number, higher biodegradability, higher flash point, and lubricity property as compared with the petroleum fuel, so biodiesel is a best alternative in the transportation sectors [3]. Generally, combining vegetable oil with methanol in presence of sodium hydroxide produces biodiesel which can be used as an engine fuel [4]. Biodiesels are produced from plant products like sugarcane, corn, jatropha, canola, neemseeds, karanja, etc. [5]. From the survey, it was found that the descending order of oxidation stability index of vegetable oils are as follows—castor > mahua > neem > karanja [6]. In compression ignition (C.I.) engine, biodiesels are used neat or blended with diesel in different percentage in volume based without any engine modifications because biodiesel mixes with diesel properly without any chemical imbalance. Using biodiesel in C.I. engines produces less smoke, particulate matter (PM), carbon monoxide (CO), and unburned

---

M. Arya (✉) · A. K. Rout · Samiran Samanta  
Department of Mechanical Engineering, KIIT Deemed to be University,  
Bhubaneswar, Odisha 751024, India

hydrocarbon (HC) emissions that are produced as compared with the combustion of diesel [7]. Addition of 10% of eucalyptus biodiesel with diesel was found to be superior quality to control the air pollution, but the engine performance was lesser than the diesel fuel [8]. But the biodiesels are having less calorific value, more viscosity, higher density, higher pour point, less cold flow property, and less volatility, and hence, brake specific fuel consumption (BSFC) gets higher, brake thermal efficiency (BTE) becomes lower, and  $\text{NO}_x$ ,  $\text{CO}_2$  emissions generate more, and exhaust gas temperature (EGT) also gets more compared with diesel. From the investigation, it shows that the addition of alcohols and little additives with biodiesel may produce less exhaust emissions and also overcome some of the above-mentioned features [9]. According to the survey of Dwivedi and Sharma, the cold flow properties such as pour point and cloud point of biodiesel are the major cause of solidification of fuel which occurs blockages in fuel filter lines [10]. To overcome those demerits of using only biodiesel with diesel, different types of additives have been added and the research work are also carried out.

There are very less research articles related to the *Argemone* biodiesel blended with diesel. There has been a lot research on biodiesel blended with diesel and DMC additives to operate the compression ignition engine. However, there are no literatures available by using *A. mexicana* biodiesel blended with diesel and DMC additives to operate the C.I. engine, and analysis of engine performances and emission characteristics of these blends is also not available.

In this work, the *A. mexicana* biodiesel was prepared by transesterification process from *A. mexicana* crude oil. The work was carried out in a direct injection dual fuel compression ignition engine by using non-edible biodiesel that is *A. mexicana* blended with diesel and very little amount of di-methyl carbonate. Di-methyl carbonate is colorless and easily available additives in market. So, DMC is used as an additive with the biodiesel blended with diesel. Initially, the engine is run by using biodiesel blended with diesel like B25 (25% biodiesel and 75% diesel), B45 (45% biodiesel and 65% diesel), and B65 (65% biodiesel and 35% diesel) and by taking 20% load to 100% load. The engine parameters like brake thermal efficiency, brake specific fuel consumption, and exhaust gas temperature are obtained. In the meantime, the emission parameters like  $\text{CO}_2$ , unburned HC, and  $\text{NO}_x$  are also measured by using exhaust gas analyzer. The fuel blends are B25 + 2.5%DMC, B45 + 5%DMC, and B65 + 7.5% DMC. Both the engine performance parameters and engine emission parameters were obtained and compared with the fuel without additives.

## 2 Materials Used

### 2.1 *Argemone Mexicana Biodiesel Preparations*

The *A. mexicana* seeds are round and small exactly look like mustard seed, but *Argemone* oils are not edible oil which is available in rural area. So *A. mexicana* crude oil was purchased from rural local supplier in Bhubaneswar, Odisha, India.

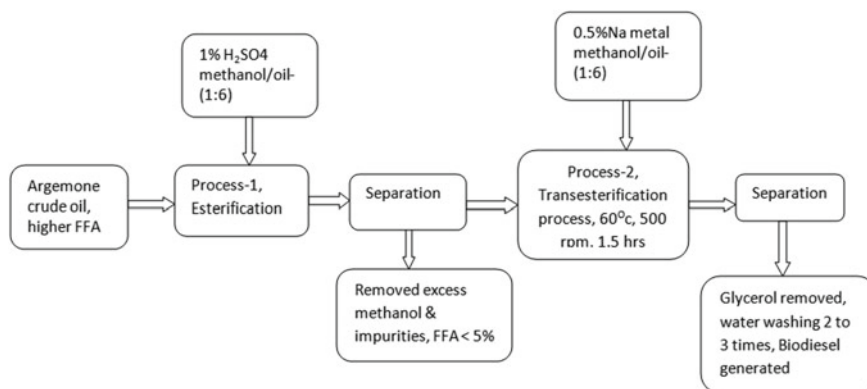


**Fig. 1** Schematic layout of biodiesel preparation method

Biodiesel was prepared from *Argemone* seed oil by transesterification followed by esterification process. The *A. mexicana* crude oil's free fatty acid (FFA) value was found to be 19.5 which were very high and to reduce the FFA value, esterification process was carried out. Initially, the crude oil was degummed by mixing 250 ml of phosphoric acid in 1lit. of preheat crude oil and heated at a temp of 60 °C for one hour on a magnetic stirrer and after that 0.1% aqueous sodium hydroxide (NaOH) solution was added and kept one day in a beaker to settle [11]. After that the oil was ready for esterification process where the oil heated at a temperature of 65 °C for 3 h by adding 200 ml methanol and 20 ml sulfuric acid. The FFA value was found less than 2 after separation of oil, and then, the oil was ready for esterification process to find out the final biodiesel. For removing the alcohol, transesterification process was adopted where 200 ml of methanol and 8gm of potassium hydroxide (KOH) mixed in the preheated oil. By doing water washing, the final *A. mexicana* biodiesel was ready to use in compression ignition engine [12]. Figure 1 shows the schematic layout of the biodiesel preparation.

## 2.2 Di-methyl Carbonate (DMC) as an Additive

Many studies found that ethanol, *n*-butanol, diethyl ether, and oxygenated fuels are used as additives because the mix of diesel, biodiesel, and additives are considered as best alternative petroleum fuels [13]. The effects of additives such as di-methyl ether (oxygenated fuel) using with *A. mexicana* biodiesel at different engine operating condition were found dramatically improved in engine performances and emission performances. From maximum studies, it clears that the fuel properties consist of diesel–biodiesel additive blends having almost the same properties of diesel [14]. In this experiment, di-methyl carbonate (DMC) is used as an additive in *A. mexicana* biodiesel blend with diesel, and the engine performance parameters

and emission parameters are evaluated. DMC is a good fuel additive because of its excellent physical and chemical properties. It is a colorless, flammable organic liquid composing formula  $C_3H_6O_3$  having less toxic. By using DMC, the properties of fuel such as cetane number, density, viscosity, volatility, flash point, and calorific value changed which affect the performances and emissions in a better way [15]. Very less percentage of DMC are used in the fuel which does not affect the fuel economy. DMC was purchased from chemical store in Bhubaneswar.

### 2.3 Preparation of Fuel Blends

Fuel was prepared by blending the diesel with biodiesel in different percentages like B25 (25% biodiesel), B45 (45% biodiesel), and B65 (65% biodiesel) and run the engine after checking the properties of the blended fuel. Again, another set of fuel was prepared such as B25 + 2.5%DMC, B45 + 5%DMC, and B65 + 7.5%DMC and determined the engine performance and emission parameters by using in direct injection diesel engine after checking the properties of the fuel [16]. The properties of diesel fuel, *A. mexicana* biodiesel, DMC, and B25, B45, B65 are given in Table 1.

All the prepared fuel samples have been kept for one hour before doing experiment for checking of phase separation. It was found that all the blended fuels were stable under atmospheric conditions without any phase separation issues. Some physical and chemical blended oil samples were tested according to standard testing procedure. The physical and chemical properties have been shown nearly equal to the properties of diesel that was possible by adding DMC as an additive. The calorific values and the kinematic viscosity values have been found lower than the biodiesel and diesel blends fuel [17]. The value of cetane number of all the DMC blended fuels was nearly equal to the diesel fuel, and these makes ready to use for an engine application.

**Table 1** Fuel properties

Fuel properties	Units	Diesel	Biodiesel	DMC	B25	B45	B65
Flash point	°C	53	169	65	88	114	131
Kinematic viscosity at (40 °C)	Cst	2.30	5.06	0.62	4.1	4.33	4.61
Density	Kg/m <sup>3</sup>	823	869	1065	845	851	860
Calorific value	KJ/kg	42,600	41,450	1578	42,503	42,240	41,910
Cetane number	–	46	50	36	52	56	58
Oxygen content	Wt.%	0	11	53.27	5	7	8

Fuel samples are:

1. Sample-1: Diesel.
2. Sample-2: *A. mexicana* Biodiesel.
3. Sample-3: B25 (Diesel 75% + Biodiesel 25%).
4. Sample-4: B45 (Diesel 55% + Biodiesel 45%).
5. Sample-5: B65 (Diesel 35% + Biodiesel 65%).
6. Sample-6: B25 + 2.5%DMC (Diesel 72.5% + Biodiesel 25% + 2.5%DMC).
7. Sample-7: B45 + 5%DMC (Diesel 50% + Biodiesel 45% + 5%DMC).
8. Sample-8: B65 + 7.5%DMC (Diesel 27.5% + Biodiesel 65% + 7.5%DMC).

### 3 Experimental Setup

The effects of DMC on direct injection diesel engine performance by using diesel–biodiesel additive blends mode were experimented in a four strokes, single cylinder, and water cooled engine. The engine specifications are listed in Table 2. Engine was coupled with eddy current dynamometer along with load controller for varying the engine loads at constant speed condition. Intake air flow rate was measured by the help of a standard air tank attached with a manometer device. Estimation of engine fuel consumption was determined by noting the time taken for 100 cc of fuel consumption through standard burette assembly. The exhaust emissions like carbon monoxide (CO), hydrocarbon (HC), carbon dioxide (CO<sub>2</sub>), and nitrogen oxides (NO<sub>x</sub>) were measured by using AVL 444 N gas analyzer in ppm and also in percentage. A K-type thermocouple was utilized for deciphering the exhaust gas temperature. A computer along with Engine Soft LV was connected to measure the engine performance and combustion performance value according to the varying

**Table 2** Engine specifications of experimental setup

Model name	Kirloskar/TV1
No. of cylinder	1
No. of stroke	4
Rated power (Kw)	3.5 Kw
Cylinder diameter (mm)	87.5
Stroke length (mm)	110
Speed (rpm)	1500
Connecting rod length	234
Orifice diameter (mm)	20
Dynamometer arm length (mm)	185
Cooling type	Water
Swept volume (cc)	66,105
Injection pressure (bar)	240
Compression ratio	17.5:1

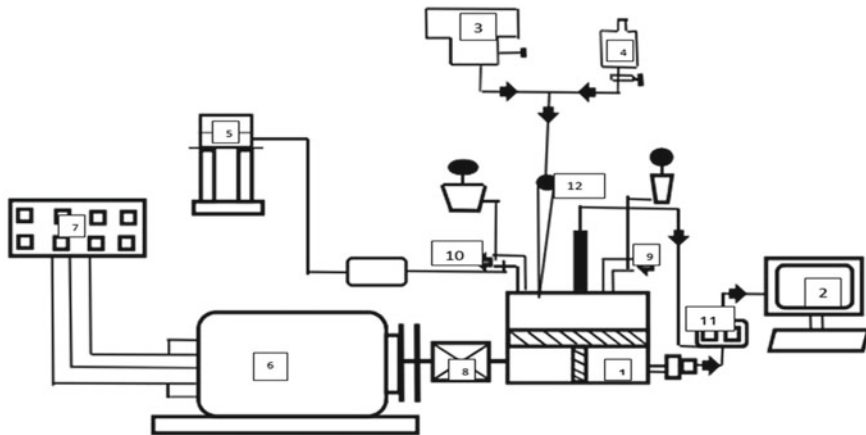
**Table 3** Uncertainties of engine of various quantities

Instruments	Accuracy	Uncertainty (%)
U-tube manometer	±2 mm	±2.0
Engine speed	±15 rpm	±0.12
Exhaust gas temperature	±3 °C	±0.2
Dynamometer load cell	±60gm	±0.022
Standard burette system	±0.2 cc	±1.5
CO emission	±0.002%	±0.1
HC emission	±11 ppm	±0.3
NO <sub>x</sub> emission	±12 ppm	±0.1

load conditions. The data of cylinder pressure, temperature, engine speed, and manometer reading were checked in computer display and tally with the engine panel for all the fuel samples. Fuel samples were tested for four times, and the average values were taken for analytical purpose.

These experiments data had some little errors due to accuracy of the equipment, engine adjustment, natural conditions, and so on. The uncertainty percentages and accuracy of various quantities were evaluated based on square root method which is given in Table 3.

The experimental setup of direct injection C.I. engine is shown in Fig. 2 with labeling. In this schematic layout, all the connections of engines with fuel pipes and exhaust gas analyzer are shown clearly.



- 1-Engine      2-Computer      3-Fuel tank      4-Biodiesel      5-Exhaust gas analyzer
- 6-Eddy current dynamometer      7-Dynamometer controller      8-Coupling
- 9-Air intake      10-Exhaust      11-Combustion data acquisition system      12-Fuel injector

**Fig. 2** Schematic layout of direct injection C.I. engine



## 4 Results and Discussion

In this work, the fuel blends were prepared by diesel, *A. mexicana* biodiesel, and additives. The experiments were performed by using the above fuel blends in direct injection diesel engine test rig at 20, 40, 60, 80, and 100% load conditions. The engine performances such as brake thermal efficiency, brake specific fuel consumption, and exhaust gas temperature were determined and analyzed by plotting the graphs. The emission characteristics like HC, CO, NO<sub>x</sub> were also determined by using those fuel blends and compared by plotting graphs. As per the outcomes, it has been analyzed that by using DMC in fuel blend performed better engine performances and less exhaust emissions as compared with using only diesel or using biodiesel, diesel blends.

### 4.1 Engine Performance Characteristics

#### 4.1.1 Brake Thermal Efficiency (BTE)

Brake thermal efficiency stated as a break power of a heat engine as a work of thermal energy input from the fuel. BTE is used to evaluate how well chemical energy from a fuel converts mechanical energy by an engine. BTE depends on fuel utilization. The all-blended fuels followed the same procedure to determine BTE during the experiments at 20, 40, 60, 80, and 100% load, which are represented in Fig. 3. For diesel at constant engine speed, the value of BTE for 80% load was the lowest as compared with the other fuels. It was shown from the results that by using DMC as an additive the values of BTE was maximum at 60% load in B25 + 2.5% fuel blend. Addition of 65% biodiesel in diesel in B65 blend, the value of BTE was the lowest value at 20% engine load condition. After addition of additives in *A. mexicana* biodiesel and diesel fuel blends, the value of BTE was increased in all load conditions. At 80% load, the value of BTE was maximum in case in B45 + 5.0% blended fuel. But at the same time, if the percentage of DMC and biodiesel increased, the value of BTE were decreased almost all load conditions in B65 + 7.5% fuel blend.

#### 4.1.2 Brake Specific Fuel Consumption (BSFC)

Brake specific fuel consumption is a parameter which shows the efficiency of a C.I. engine that burns fuel and produce rotational power to shaft. So BSFC can be stated as the ratio of rate of fuel consumption and shaft power produced from the engine. Figure 4 shows the values of BSFC for all fuel blends at various load conditions. The value of BSFC at 100% load conditions for fuel B65 + 7.5%DMC was maximum from the experiment, whereas for diesel fuel and B25 fuel, the BSFC

**Fig. 3** Variations of BTE with loads for fuel samples

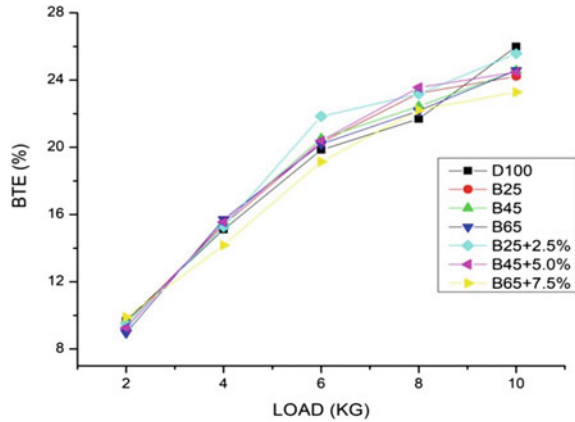
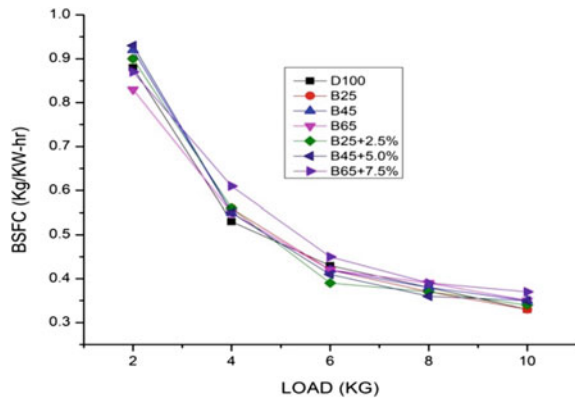


**Fig. 4** Variations of BSFC with loads in all fuel samples

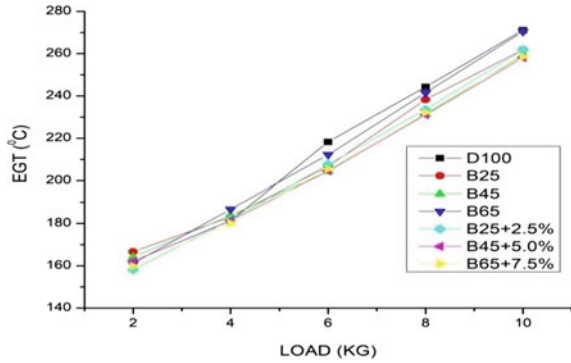


values were lower than the other fuel. The range of BSFC values for full load conditions was 0.33 to 0.37 kg/KWh for all fuel blends. From Fig. 4, it was clearly shown that by adding of DMC as an additive, the BSFC value was improved, and in the addition of 7.5% DMC in B65 blend, the BSFC values were maximum for all load conditions. But only the addition of biodiesel with diesel found less BSFC value for B65 fuel at 20% load conditions.

### 4.1.3 Exhaust Gas Temperature

Exhaust gas temperatures in C.I. engine vary with engine load and speed. In this paper, speed was taken as constant, so high loads results the highest temperature which was shown in Fig. 5.

**Fig. 5** Variations of EGT with loads in all fuel blends



At full load case, the EGT was maximum for diesel fuel and B65 fuel. From the experiments, it was shown that by the addition of DMC the values of EGT were reduced in all load conditions. The values of EGT range were 158 °C to 167 °C at 20% load conditions. At low load condition, the EGT values were very nearly equal in all blends of fuels. In this experiment, the EGT value was minimum in B45 + 5% DMC fuel blend at full load conditions.

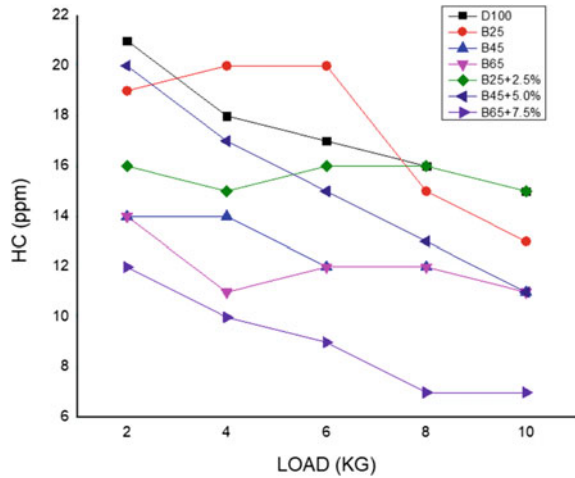
## 4.2 Emission Analysis

In this experiment, emission characteristics of engine were analyzed by AVL gas analyzer at the time of running in all fuel blend at all load conditions. The emissions like HC, CO, NO<sub>x</sub> were analyzed, and details were listed below [18].

### 4.2.1 Hydrocarbon (HC) Emissions

The HC emissions are mostly affected by air–fuel ratios, fuel properties, and fuel injection system. Due to incomplete combustion inside the combustion chamber, unburned HC emissions are produced. In this experiment, the variations of HC emissions for all fuel blends at different load conditions are shown in Fig. 6. The highest HC emission for diesel was 21 ppm for B25, 14 ppm for B45, 14 ppm for B65, 17 ppm for B25 + 2.5%, 20 ppm for B45 + 5%, and 12 ppm for B65 + 7.5%. Addition of DMC as an additive in biodiesel found less HC emissions, and it means higher cetane number gave complete combustion. So, the HC emissions of B65 + 7.5%DMC was lower as compared to other fuel blends at all load conditions. From this experiment, it was shown that by the addition of biodiesel with diesel, HC emissions were produced less at all load conditions.

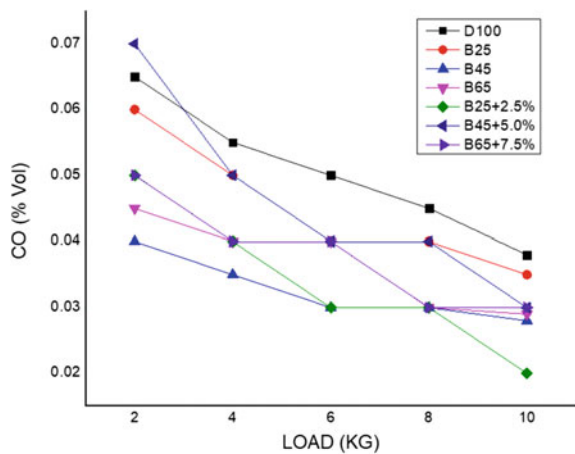
**Fig. 6** Variations of HC with loads for the fuel samples



### 4.2.2 Carbon Monoxide (CO) Emissions

At the time of combustion if the air supply is not sufficient at low temperature, carbon monoxide gas is produced. So, CO emissions are produced in the exhaust due to incomplete combustion of fuel. Variations of CO emissions with respect to loads are shown in Fig. 7. When the engine running by diesel, CO emissions generated were maximum except low load conditions. The CO emissions were less than diesel fuel at all engine loads for the concentrations of 2.5, 5, and 7.5% of DMC with biodiesel and diesel fuel. By the addition of 25% biodiesel with the diesel there were very less variation in CO emissions all load conditions. CO emissions were lowered in the addition of biodiesel and DMC in the blended fuel.

**Fig. 7** Variations of CO emissions with loads for fuel samples

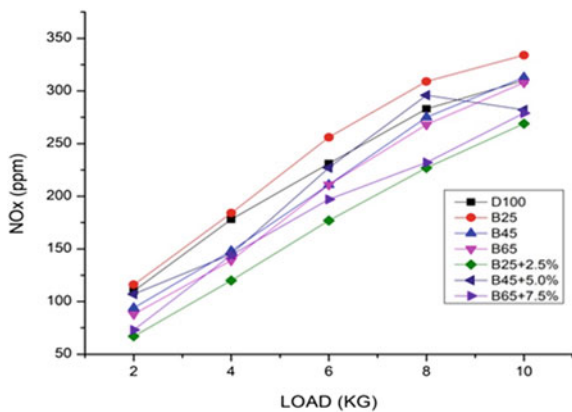


This was possible by the effects of higher oxygen content and cetane number in the blend. Due to the presence of DMC and biodiesel, the combustion process was speed up and reduces the CO emission.

### 4.2.3 Nitrogen Oxides (NO<sub>x</sub>) Emissions

The nitrogen oxides emissions in exhaust gases are generated due to the presence of oxygen in the fuel and the maximum temperature inside the cylinder. The generation of NO<sub>x</sub> was increased as the amount of oxygen increased. Cylinder geometry, compression ratio, inlet air temperature and pressure, and chemical properties of fuel are also factoring of formation of NO<sub>x</sub> emissions. Variations of NO<sub>x</sub> emissions with respect to load for all fuel blends are shown in Fig. 8. By running B25 fuel in engine, the NO<sub>x</sub> emissions generated were the highest emission as compared form the other fuel blends at all load conditions. The range of NO<sub>x</sub> emission from 20 to 100% load for diesel were 109 ppm to 309 ppm, for B25 emissions vary from 116 to 334 ppm, for B45 NO<sub>x</sub> vary from 94 to 313 ppm, for B65 it vary from 88 ppm to 308, for B25 + 2.5%DMC emissions vary from 67 to 269, for B45 + 5%DMC NO<sub>x</sub> vary from 107 to 282 ppm, and for B65 + 7.5%DMC emission vary from 73 to 279 ppm, respectively. By addition of DMC in biodiesel and diesel fuel blends, it was found that the NO<sub>x</sub> generations were less compared with the other fuel blends. When the engine was running by using the fuel blend B25 + 7.5%DMC, the lowest amount of exhaust NO<sub>x</sub> gas was generated at all load conditions. At the same time, if only 25% biodiesel was used in the diesel fuel, the NO<sub>x</sub> gas produced the highest amount as compared with the other fuel blends at all load conditions. It means by the addition of DMC with the biodiesel, and the fuel blends become more stable.

**Fig. 8** Variations of NO<sub>x</sub> with respect to load for all fuel blends



## 5 Conclusions

A direct injection CI engine was running using fuel of diesel, biodiesel, and blended diesel–biodiesel DMC (oxygenated additive) in this experiment. Engine performances and emission characteristics of all fuel samples had been studied, and results were analyzed by comparing with the diesel fuel sample. The conclusions of this experimental study are summarized as follows.

*A. mexicana* biodiesel was prepared by transesterification process by following esterification process from crude *Argemone* oil in laboratory by doing different methods which was discussed in this paper. These fuel blends had lower brake thermal efficiency compared to diesel. The brake thermal efficiency increased by using the fuel B25 + 2.5%DMC at 6 kg load compare with the other blended fuel. The BTE had decreased by using the fuel B65 + 7.5%DMC at all load conditions compare with other fuel blends. BSFC values were increased by using biodiesel blended with diesel as compared with only diesel. However, the fuel B25 + 2.5% DMC results lower brake specific fuel consumptions at 6 kg load even than ordinary diesel fuel. The value of EGT decreased with all blends of fuel at 6 kg and 8 kg load when comparison with only diesel fuel. By using B25 + 2.5%DMC fuel, the CO and NO<sub>x</sub> emission produced lesser as compared with other fuel blend. Significant reduction in HC emissions were observed for all fuel blends compared with only diesel fuel.

In this experimental work, it can be concluded that the fuel blends of diesel-*A. mexicana* biodiesel DMC are the most promising alternative fuels for a compression ignition engine for appreciable reduction in exhaust emissions and increment in engine performance compared to only diesel fuel without major modifications of engine.

## References

1. Jayed MH, Masjuki HH, Kalam MA, Mahlia TMI, Husnawan M, Liaquat AM (2011) Prospects of dedicated biodiesel engine vehicles in Malaysia and Indonesia. *Renew Sustain Energy Revol* 15:220–235
2. Ministry of Petroleum and Natural Gas Authority PBY, Delhi (2018) The gazette of India: extraordinary, Part 1-Section 1, National policy on biofuels, pp 1–23
3. Nayaka SK (2014) Experimental investigation on performance and emission characteristics of a diesel engine fuelled with mahua biodiesel using additive. *Energy Procedia* 54:569–579
4. Dwivedi G, Jain S, Sharma MP (2011) Impact analysis of biodiesel on engine performance—a review. *Renew Sustain Energy Rev* 15:4633–4641
5. How HG, Masjuki HH, Kalam MA, Teoh YH (2014) Engine performance, emission and combustion characteristics of a common-rail diesel engine fuelled with bioethanol as a fuel additive in coconut oil biodiesel blends. *Energy Procedia* 61:1655–1659
6. Dwivedi G, Sharma MP (2014) Potential and limitation of straight vegetable oils as engine fuel—an Indian perspective. *Renew Sustain Energy Rev* 33:316–322

7. Devarajan Y, Beemkumar N, Ganesan S, Arunkumar T (2020) An experimental study on the influence of an oxygenated additive in diesel engine fuelled with neat papaya seed biodiesel/diesel blends. *Fuel* 268:117254
8. Verma P, Sharma MP, Dwivedi G (2016) Potential use of eucalyptus biodiesel in compressed ignition engine. *Egypt J Petrol* 25:91–95
9. Singh M, Sandhu SS (2020) Performance, emission and combustion characteristics of multi-cylinder CRDI engine fueled with *argemone* biodiesel/diesel blends. *Fuel* 265:117024
10. Dwivedi G, Sharma MP (2014) Impact of cold flow properties of biodiesel on engine performance. *Renew Sustain Energy Rev* 31:650–656
11. Pramanik P, Das P, Kim PJ (2012) Preparation of biofuel from *argemone* seed oil by an alternative cost-effective technique. *Fuel* 91:81–86
12. Kumar R, Singh M (2019) Experimental investigation of performance and emission characteristics of DI CI engine with dual biodiesel blends of Mexicana *Argemone* and *Mahua*. *Mater Today: Proc* 16:321–328
13. Yuvarajan D (2018) Experimental evaluation of combustion, emission and performance of research diesel engine fuelled di-methyl-carbonate and biodiesel blends. *Atmos Poll Res* 10(3)
14. Parida MK, Joardar H, Rout AK, Routaray I, Mishra BP (2017) Multiple response optimizations to improve performance and reduce emissions of *Argemone Mexicana* biodiesel-diesel blends in a VCR engine. *Appl Therm Eng* 8(3):181–188
15. Rathore V, Tyagi S, Newalkar B, Badoni RP (2014) *Jatropha* and *Karanja* oil derived DMC–biodiesel synthesis: a kinetics study. *Fuel* 140:597–608
16. Anwar M, Rasul MG, Ashwath N (2019) The synergistic effects of oxygenated additives on papaya biodiesel binary and ternary blends. *Fuel* 256:115980
17. Nanthagopal K, Ashok B, Garnepudi RS, Tarun KR, Dhinesh B (2019) Investigation on diethyl ether as an additive with *Calophyllum Inophyllum* biodiesel for CI engine application. *Energy Convers Manage* 179:104–113
18. Yesilyurt MK, Aydin M (2020) Experimental investigation on the performance, combustion and exhaust emission characteristics of a compression-ignition engine fueled with cottonseed oil biodiesel/diethyl ether/diesel fuel blends. *Energy Convers Manage* 205:112355

# Femur Bone Implant Plate Design Analysis Under Varying Fracture Conditions



Nilesh Tipan, Ajay Pandey, and Girish Chandra

## 1 Introduction

The femur bone is the most proximal bone in human beings that plays a prominent role in daily activities like walking, running and jumping [1, 2]. In human anatomy, femur is the longest and largest bone, but it is strong enough only for compressive loads [3]. The femur is responsible for supporting the highest percentage of body weight during normal exercise. The femur body is long, thin and almost cylindrical in structure. Bone fracture of femur is one of the most common traumas. Femoral fractures are quite problematic and responsible for significant orthopedic trauma because they are the strongest, longest and heaviest bones in the human body [4, 5]. Femoral shaft fractures in human beings occur frequently due to high-power collisions that are typical of road accidents, fall from a height, gunshot wounds, etc. A relatively low-intensity accident, such as fall from standing position, can also create a femoral fracture in an old person with weak bones [6].

There are three fracture regions in a femur bone fracture: the top/neck of the bone (near the pelvis), the primary shaft of the bone or the lower end near the knee. Injury happens when a high-force blow hits the thigh bone [7]. This can be due to the frame weight of the person or a collision with an object [8].

Femur fractures vary greatly, depending on the force that causes the break. The items of bone could line up properly (stable fracture) or be out of alignment (displaced fracture). The skin around the fracture could be intact (closed fracture), or the bone could puncture the skin (open fracture) [9]. Femur fractures are categorized depending on the specific fracture location (distal, center or proximal) and/or the fracture pattern (crosswise, lengthwise or concentrated toward the middle).

---

N. Tipan (✉) · A. Pandey · G. Chandra  
Department of Mechanical Engineering, Maulana Azad National Institute of Technology,  
Bhopal, Madhya Pradesh 462003, India



Bone tissue, unlike most body tissues, has the remarkable capacity to regenerate itself [10–12]. If a fractured bone can be held correctly, it may regenerate the tissue and regain most of its authentic strength [13, 14]. For intense fractures, bone plates are surgically implanted to preserve the bone at its vicinity. The design of implant plates is largely influenced by the choice of the material and its biocompatibility [15–17]. The bone plate needs to be sufficiently strong to support the weight generally transferred onto the bone, even as the bone heals. The plate ought to have additional stiffness to support the bone to which it is attached. The implant must be non-toxic and non-inflammatory [18–20].

The stiffness of the bone plate is important from the viewpoint of protection from stress generated due to stiffness differential. Strain defense is the phenomenon, wherein the implant bears maximum burden typically placed on the bone [21]. This is favorable while the bone is vulnerable. This is essentially because when the bone heals and regains power, there might be a loss in bone mass and strength is regained if the bone plate does, now, not allow the bone to carry growing load [22].

## 2 Materials and Methodology

### 2.1 Material Selection

Orthopedic applications have conventionally employed metallic alloys, like stainless steel (SS316L), titanium alloy (Ti6Al4V) and cobalt–chromium (Co–Cr) to make different elements of implants, namely the screws, plates, nails, etc. The common mechanical properties of these biomaterials and cortical bone are listed in Table 1. These are considered throughout this work. These biomaterials are observed biocompatible under physiological environments and possess adequate mechanical strength and properties.

**Table 1** Mechanical properties of cortical bone and conventionally used metallic alloys

Element	Density (Kg/m <sup>3</sup> )	Young's modulus (Gpa)	Poisson's ratio	Ultimate tensile strength (Mpa)	Ultimate compressive strength (Mpa)
Cortical bone	1750	16.7	0.3	43.44 ± 3.62	115.29 ± 12.94
SS316L	7750	193	0.31	485	570
CoCr alloy	8500	210	0.34	960	560
Ti6A14V	4512	119	0.37	1200	1080

## 2.2 Design of Plate and Assembly

In osteosynthesis, most fracture cases may be cured using different types of plates, namely the straight plate, cobra head plate, tabular plate, reconstruction plate, etc., and corresponding screws with buttress threads. These implants are generally made up of metallic alloys listed above. In this analysis, three different designs of plates and respective screws have been prepared with these three different biomaterials having been taken for each design, and analysis has been carried out with commonly occurring loading and boundary conditions for the fracture of femur bone as shown in Fig. 1. These designs have been successfully configured in assembly with the femoral fractured bone structure and screws with the help of computational design approaches.

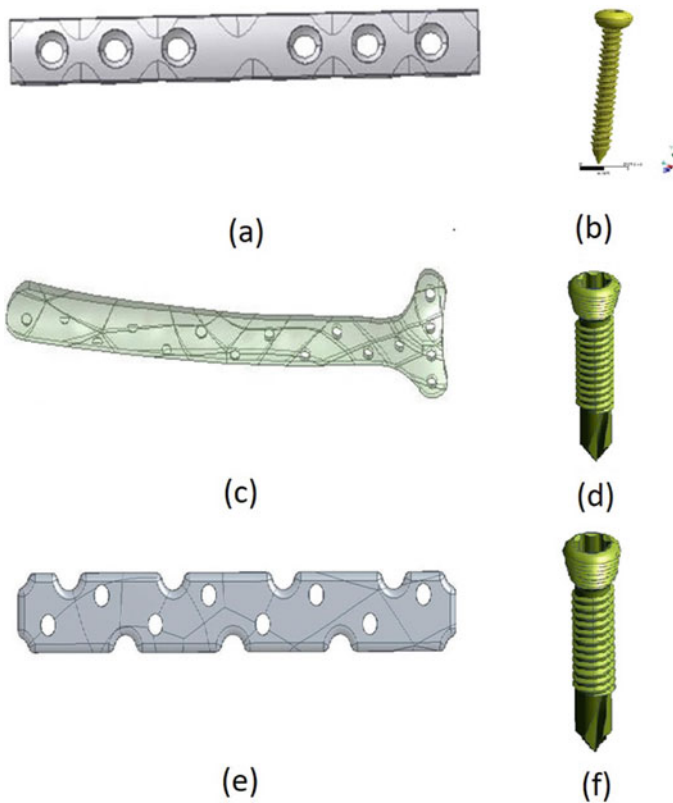


**Fig. 1** Plates and screws for different design, **a** and **b** shows implant plate and screw, respectively, for Design-1 which will be used for all material combinations (i.e., stainless steel alloy, titanium alloy and chromium–cobalt alloy), **c** and **d** shows implant plate and screw, respectively, for Design-2 which will be used for all material combinations, **e** and **f** shows implant plate and screw, respectively, for Design-3 which will be used for all material combinations

### **2.3 Meshing**

The finite element analysis reduces the degrees of freedom from infinite to finite with the help of meshing or discretization. The analysis accuracy and duration depend on the mesh size and orientation. For an optimum analysis using FEM, the implant assembly has been divided into many elements and nodes and calculations carried out at a limited number of points. The results have been extrapolated to arrive at results for the entire domain. All three designs of implant plate are shown in Fig. 2, with meshed geometry, which contains adaptive size and tetrahedral-structured elements. The mesh details for these designs are listed in Table 2.

### **2.4 Assumptions and Boundary Conditions**

The designs of plate with assembled fractured femur have been assumed to be homogeneous in materials properties. Meshes are tetrahedral structured and adaptive in sizing for all three designs. Any structure can be tested only with specified boundary and loading conditions. In this case, a fixed support is provided at the lower part of the femur bone in such a manner that it can deform or move in all possible directions or exhibit multi-degree of freedom behavior, except the vertical downward translation. The load acting on the femur is applied on the upper part of vertically oriented femur bone with a value of  $\sim 750$  N based on maximum average weight of human beings. For dynamic and fatigue analysis, transient structural loading is selected for the second analysis, and auto-step time of 0.1 s for each step is set. Nonlinear controls are set as default or program controlled, and the output results are noted as stresses, deformation, etc.

## **3 Results**

According to input loading and boundary conditions, deformation, generated stress and fatigue performance of the three implant plate designs for the three materials under consideration have been observed and analyzed. The output results are listed below.

### **3.1 Total Deformation**

The comparative analysis for all three designs is shown in Fig. 3, in terms of total deformation. It can be observed that the total deformation in case of Design-1 for SS316L varies from the minimum to moderate under the permissible range. This is

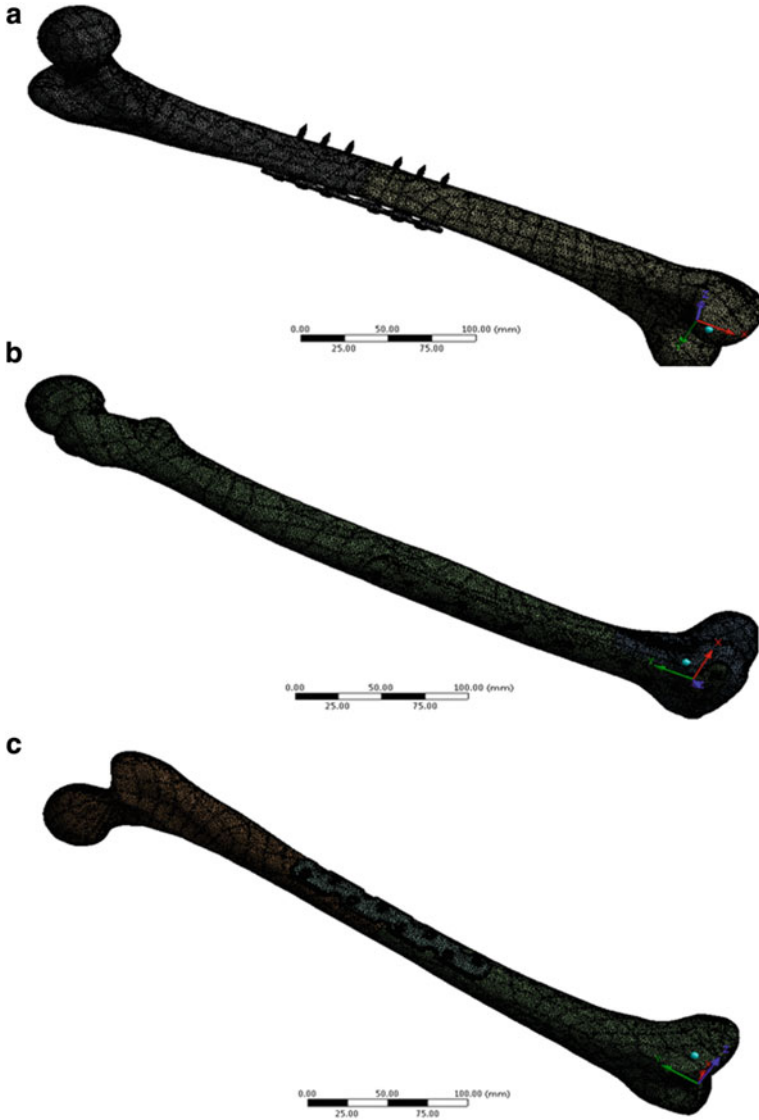


**Fig. 2** Meshing of **a** plate Design-1, **b** plate Design-2 and **c** plate Design-3 with femur bone fracture

**Table 2** Meshing details of three different plates assembled with respective fractured positions of femur bone

Design of plate with femur	Numbers of nodes	Number of elements
Design-1	938,820	569,821
Design-2	1,060,797	628,480
Design-3	1,393,335	866,696

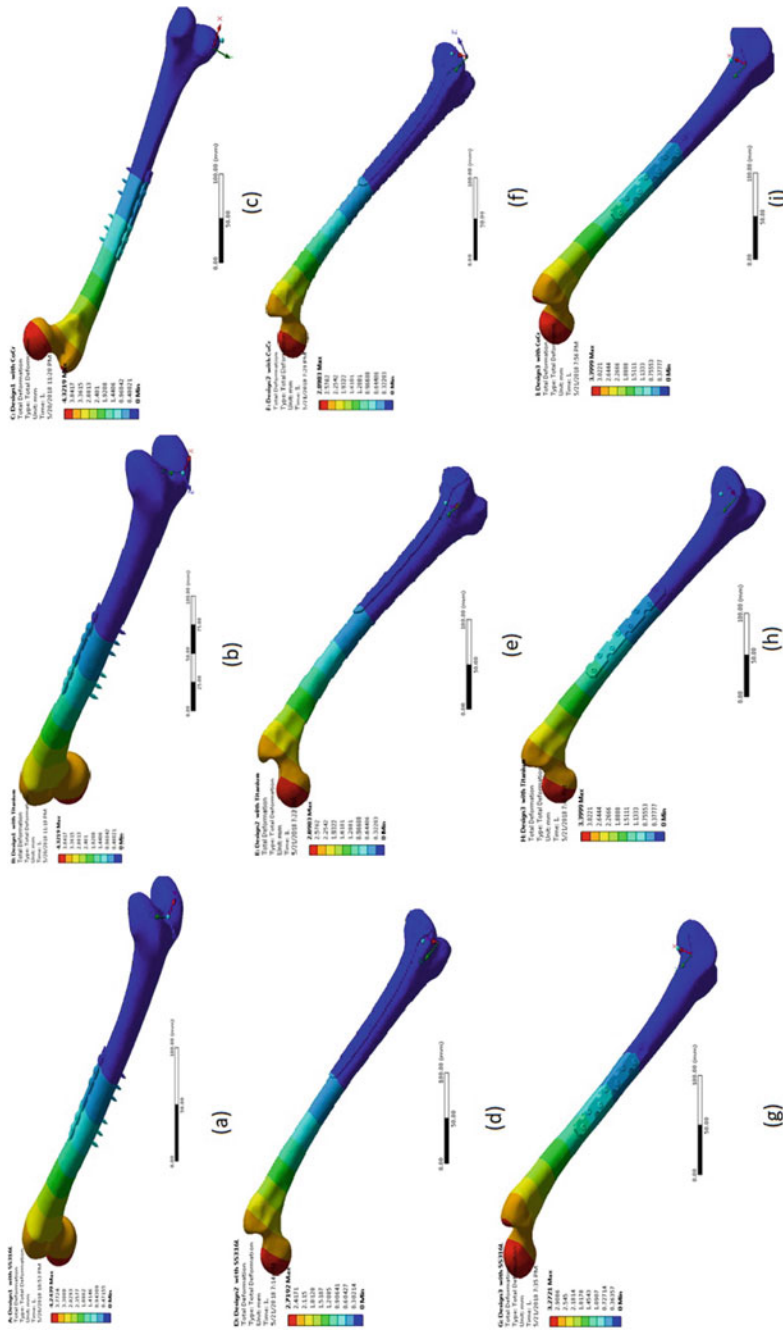


**Fig. 3** Total deformation of three designs of plate with corresponding material, i.e., **a** Design-1 with stainless steel alloy **b** Design-1 with titanium alloy **c** Design-1 with CoCr alloy **d** Design-2 with stainless steel alloy **e** Design-2 with titanium alloy **f** Design-2 with CoCr alloy **g** Design-3 with stainless steel alloy **h** Design-3 with titanium alloy **i** Design-3 with CoCr alloy

shown by dark blue and light blue colors. From Design-1 with titanium alloy, it can be observed that total deformation for the implant plate lies between the minimum to moderate but is inclined toward the moderate while being still under the permissible range. This is again shown by dark blue and light blue colors. From Design-1 with CoCr alloy, it can be observed that total deformation for the implant plate is inclined even more toward the moderate value in the permissible range and is shown by light blue colors.

From Design-2 with SS316L, it can be observed that total deformation is between the minimum to a moderate value but more inclined toward the minimum value which is under permissible range and is shown by dark blue and light blue colors. From Design-2 with titanium alloy, it can be observed that total deformation for the implant plate is between the minimum to a moderate value but more toward the minimum value which is under permissible range and is shown by dark blue and light blue colors. From Design-2 with CoCr alloy, it can be observed that the total deformation for the implant plate is toward the minimum value which is under permissible range and is shown by dark blue color.

From Design-3 with SS316L, it can be observed that total deformation for the implant plate varies from minimum to moderate value but is more toward the moderate value which is under permissible range and is shown by dark blue and light blue colors. From Design-3 with titanium alloy, it can be observed that total deformation for the implant plate is between the minimum to moderate value but more toward a moderate value which is under permissible range and is shown by dark blue and light blue colors. From Design-3 with CoCr alloy, it can be observed that total deformation for the implant plate is more toward a moderate value which is under permissible range and is shown by light blue color.

After performing analysis on femur bone plate using different materials and different designs, the final results obtained are shown in Table 3.

In Design-1, total deformation using different materials follows similar patterns. In Design-2, total deformation values for chromium–cobalt alloy follow a different pattern but follows a similar kind of pattern for titanium alloy and stainless steel alloy. In Design-3, values for chromium–cobalt alloy follow a different pattern, but for titanium alloy and stainless steel alloy, a similar kind of pattern is observed.

### ***3.2 Maximum Equivalent Stress***

The comparative analysis for all three designs is shown in Fig. 4, in terms of maximum equivalent stress.

It can be seen that from Design-1 with SS316L alloy, it can be observed that maximum equivalent stress for the implant plate is toward the minimum value which is under permissible range and is shown by dark blue color. From Design-1 with titanium alloy, it can be observed that maximum equivalent stress for the implant plate is toward the minimum value which is under permissible range and is shown by dark blue color. From Design-1 with CoCr alloy, it can be observed that

**Table 3** Total deformation

Time	Design-1 SS316L	Design-1 Titanium alloy	Design-1 CoCr alloy	Design-2 SS316L	Design-2 Titanium alloy	Design-2 CoCr alloy	Design-3 SS316L	Design-3 Titanium alloy	Design-3 CoCr alloy
0.1	0.42241	0.43009	0.43009	0.27204	0.28993	0.28993	0.32723	0.34	0.34
0.2	0.84482	0.86019	0.86019	0.54401	0.57977	0.57977	0.65444	0.67999	0.67999
0.3	1.2672	1.2903	1.2903	0.81617	0.86981	0.86981	0.98165	1.02	1.02
0.4	1.6896	1.7204	1.7204	1.0882	1.1597	1.1597	1.3089	1.36	1.36
0.5	2.112	2.1513	2.1513	1.3602	1.45	1.45	1.6361	1.7	1.7
0.6	2.5351	2.583	2.583	1.6317	1.7397	1.7397	1.9633	2.0399	2.0399
0.7	2.959	3.0152	3.0152	1.9034	2.0293	2.0293	2.2905	2.3799	2.3799
0.8	3.3838	3.4482	3.4482	2.1752	2.3187	2.3187	2.6177	2.7199	2.7199
0.9	3.8114	3.8884	3.8884	2.447	2.6086	2.6086	2.9449	3.0599	3.0599
1	4.2439	4.3219	4.3219	2.7192	2.8983	2.8983	3.2721	3.3999	3.3999

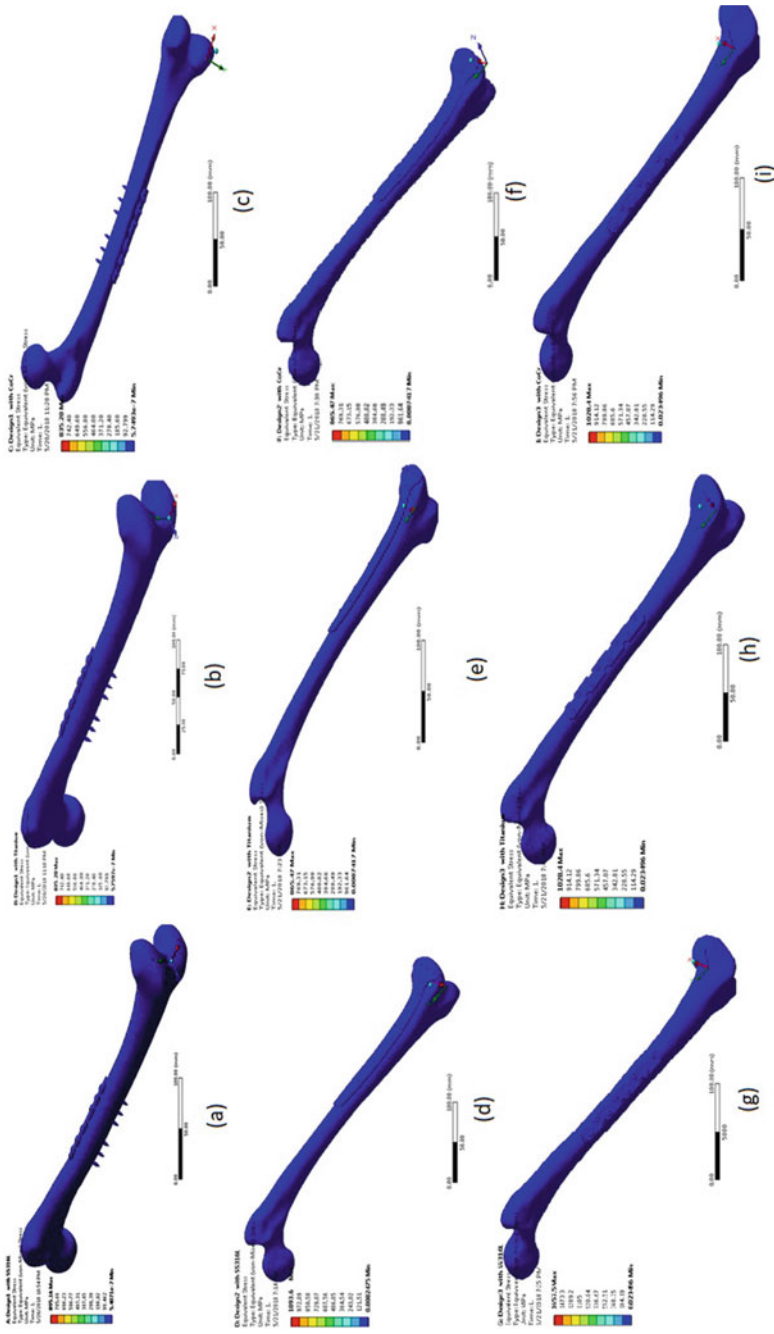


**Fig. 4** Maximum equivalent stress of three designs of plate with its correspondingly used materials, i.e., **a** Design-1 with stainless steel alloy **b** Design-1 with titanium alloy **c** Design-1 with CoCr alloy **d** Design-2 with stainless steel alloy **e** Design-2 with titanium alloy **f** Design-2 with CoCr alloy **g** Design-3 with stainless steel alloy **h** Design-3 with titanium alloy **i** Design-3 with CoCr alloy



maximum equivalent stress on implant plate is toward the minimum value which is under permissible range and is shown by dark blue color.

From Design-2 with SS316L alloy, it can be observed that maximum equivalent stress is toward the minimum value which is under permissible range and is shown by dark blue color. From Design-2 with titanium alloy, it can be observed that the maximum equivalent stress for the implant plate is toward the minimum value which is under permissible range and is shown by dark blue color. From Design-2 with CoCr alloy, it can be observed that the maximum equivalent stress for the implant plate is inclined toward the minimum value which is under permissible range and is shown by dark blue color.

From Design-3 with SS316L alloy, it can be observed that maximum equivalent stress for the implant plate is toward the minimum value which is under permissible range and is shown by dark blue color. From Design-3 with titanium alloy, it can be observed that the maximum equivalent stress for the implant plate is toward the minimum value which is under permissible range and is shown by dark blue color. From Design-3 with CoCr alloy, it can be observed that maximum equivalent stress for the implant plate is toward the minimum value which is under permissible range and is shown by dark blue color.

After performing analysis on femur bone plate using different materials and different designs, the final results obtained are shown in Table 4.

In Design-1, the maximum equivalent stress using different materials follows similar patterns. In Design-2, maximum equivalent stress values for chromium–cobalt alloy follow different patterns but for titanium alloy and stainless steel alloy follow similar kind of pattern. In Design-3, values of maximum equivalent stress for chromium cobalt follow a different pattern, but for titanium alloy and stainless steel alloy, a similar kind of pattern is observed.

### ***3.3 Maximum Principal Stress***

The comparative analysis for all three designs is shown in Fig. 5, in terms of maximum principal stress. It can be seen that from Design-1 with SS316L alloy, it can be observed that maximum principal stress for the implant plate is between the minimum to moderate value which is under permissible range and is shown by light blue color. From Design-1 with titanium alloy, it can be observed that the maximum principal stress for the implant plate is between the minimum and moderate which is under permissible range and is shown by light blue color. From Design-1 with CoCr alloy, it can be observed that the maximum principal stress for the implant plate is between the minimum to moderate which is under permissible range and is shown by light blue color.

From Design-2 with SS316L alloy, it can be observed that the maximum principal stress for the implant plate is between the moderate and the maximum value but inclined more toward the maximum value which is shown by dark yellow color. From Design-2 with titanium alloy, it can be observed that the maximum

**Table 4** Maximum equivalent stress

Time	Design-1 SS316L	Design-1 Titanium alloy	Design-1 CoCr alloy	Design-2 SS316L	Design-2 Titanium alloy	Design-2 CoCr alloy	Design-3 SS316L	Design-3 Titanium alloy	Design-3 CoCr alloy
0.1	153.02	135.92	135.92	70.613	50.012	50.012	162.71	100.43	100.43
0.2	305.17	271.41	271.41	1558	1091.8	1091.8	328.9	203.54	203.54
0.3	457.32	406.9	406.9	27,089	20,427	20,427	494.81	306.5	306.5
0.4	609.49	542.4	542.4	57,658	43,536	43,536	660.77	409.51	409.51
0.5	761.66	14,142	14,142	43,903	38,442	38,442	826.78	512.56	512.56
0.6	15,503	23,186	23,186	44,353	45,117	45,117	992.84	615.65	615.65
0.7	24,896	24,408	24,408	1.04E+05	52,292	52,292	1158.9	718.78	718.78
0.8	58,199	84,057	84,057	84,341	52,315	52,315	1325.1	821.95	821.95
0.9	89,408	83,450	83,450	94,305	84,082	84,082	1491.3	925.15	925.15
1	89,516	83,520	83,520	1.09E+05	86,547	86,547	1657.5	1028.4	1028.4

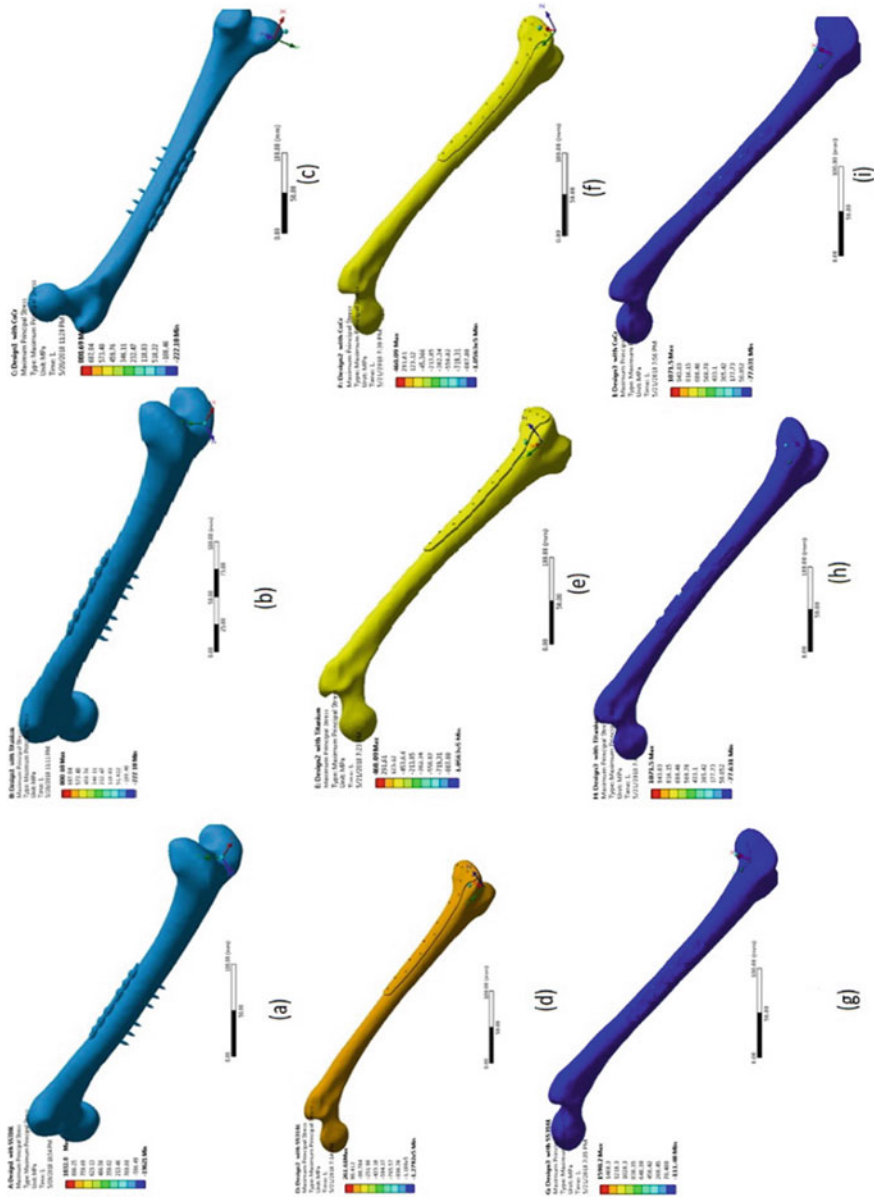


**Fig. 5** Maximum principal stress of three designs of plate with its correspondingly used materials, i.e., **a** Design-1 with stainless steel alloy **b** Design-1 with titanium alloy **c** Design-1 with CoCr alloy **d** Design-2 with stainless steel alloy **e** Design-2 with titanium alloy **f** Design-2 with CoCr alloy **g** Design-3 with stainless steel alloy **h** Design-3 with titanium alloy **i** Design-3 with CoCr alloy

principal stress for the implant plate is between the moderate and the maximum value but inclined more toward the maximum value which is shown by dark yellow color. From Design-2 with CoCr alloy, it can be observed that the maximum principal stress for the implant plate is between a moderate and the maximum value but inclined more toward the maximum value which is shown by dark yellow color.

From Design-3 with SS316L alloy, it can be observed that the maximum principal stress for the implant plate is inclined more toward the minimum value which is under permissible range and is shown by dark blue color. From Design-3 with titanium alloy, it can be observed that the maximum principal stress for the implant plate is inclined more toward the minimum value which is under permissible range and is shown by dark blue color. From Design-3 with CoCr alloy, it can be observed that the maximum principal stress for the implant plate is more toward the minimum value which is under permissible range and is shown by dark blue color.

After performing analysis on femur bone plate using different materials and different designs, the final results obtained are shown in Table 5.

In Design-1, the maximum principal stress using different material follows a similar kind of pattern. In Design-2, the maximum principal stress values for chromium–cobalt alloys follow a different pattern but for titanium alloy and stainless steel alloy follow similar kind of pattern. In Design-3, the maximum principal stress values for chromium–cobalt alloy follow a different pattern, but for titanium alloy and stainless steel alloy, a similar kind of pattern is observed.

### ***3.4 Fatigue Performance***

From Design-1 with SS316L alloy, it can be observed that fatigue performance for an implant plate is more inclined toward the maximum which is shown by dark blue and light blue colors. From Design-1 with titanium alloy, it can be observed that fatigue performance for an implant plate is more toward the maximum which is shown by dark blue and light blue colors. From Design-1 with CoCr alloy, it can be observed that the fatigue performance for the implant plate is variable and at different points on the plate different colors can be observed.

From Design-2 with SS316L alloy, it can be observed that fatigue performance is inclined more toward the maximum which is shown by dark blue and light blue colors. From Design-2 with titanium alloy, it can be observed that fatigue performance for an implant plate is more toward the maximum which is shown by dark blue and light blue colors. From Design-2 with CoCr alloy, it can be observed that fatigue performance for the implant plate is more toward the maximum which is shown by dark blue and light blue colors.

From Design-3 with SS316L alloy, it can be observed that fatigue performance for the implant plate is more toward the maximum which is shown by dark blue and light blue colors. From Design-3 with titanium alloy, it can be observed that fatigue performance for the implant plate is more toward the maximum which is shown by

**Table 5** Maximum principal stress

Time	Design-1 SS316L	Design-1 Titanium alloy	Design-1 CoCr alloy	Design-2 SS316L	Design-2 Titanium alloy	Design-2 CoCr alloy	Design-3 SS316L	Design-3 Titanium alloy	Design-3 CoCr alloy
0.1	105.75	99,468	99,468	93,821	67,998	67,998	149.26	98,979	98,979
0.2	240.38	228.91	228.91	648.58	461.46	461.46	311.08	207.58	207.58
0.3	374.8	359.23	359.23	663.09	477.03	477.03	471.91	315.53	315.53
0.4	509.88	490.1	490.1	1741.3	11,321	11,321	632.72	423.45	423.45
0.5	644.99	19,667	19,667	10,935	15,669	15,669	793.56	531.4	531.4
0.6	20,892	33,856	33,856	14,643	21,775	21,775	954.44	639.37	639.37
0.7	36,723	29,565	29,565	65,677	33,273	33,273	1115.3	747.37	747.37
0.8	40,913	70,517	70,517	25,362	33,692	33,692	1276.3	855.4	855.4
0.9	78,315	83,031	83,031	283.64	40,259	40,259	1437.2	963.44	963.44
1	1.03E+05	80,069	80,069	261.61	46,009	46,009	1598.2	1071.5	1071.5

dark blue color. From Design-3 with CoCr alloy, it can be observed that fatigue performance for the implant plate is more toward the maximum which is shown in Fig. 6 by dark blue color.

## 4 Discussion

The current work involves transient structural analysis on femur bone implant made up of different plates, screws and biomaterials. Conventionally used biomaterials such as stainless steel (SS316L) alloy, Ti alloy (grade-II Ti6A14V) and CoCr alloy are used for all the three assemblies (Design-1, Design-2 and Design-3). All the assemblies are analyzed by finite element method employing transient structural analysis (a tool on ANSYS).

After performing analyses for Design-1 with different biomaterials, total deformation is observed as 4.2439 mm for SS316L and 4.3219 mm for both the alloys (Ti6A14V and CoCr alloy). Similarly, equivalent stress for Design-1 is observed as 895.16 MPa for SS316L and 835.2 MPa for both the alloys (Ti6A14V and CoCr alloy). Also, maximum principal stress for Design-1 is observed as 1032.8 MPa for SS316L and 800.69 MPa for both the alloys (Ti6A14V and CoCr alloy).

After performing analyses for Design-2 with different biomaterials, total deformation is observed as 2.7192 mm for SS316L and 2.8983 mm for both the alloys (Ti6A14V and CoCr alloy). Similarly, equivalent stress for Design-2 is observed as 1093.6 MPa for SS316L and 865.47 MPa for both the alloys (Ti6A14V and CoCr alloy). Also, maximum principal stress for Design-2 is observed as 261.61 MPa for SS316L and 460.09 MPa for both the alloys (Ti6A14V and CoCr alloy).

After performing analyses for Design-3 with different biomaterials, total deformation is observed as 3.2721 mm for SS316L and 3.3999 mm for both the alloys (Ti6A14V and CoCr alloy). Similarly, equivalent stress for Design-2 is observed as 1657.5 MPa for SS316L and 1028.4 MPa for both the alloys (Ti6A14V and CoCr alloy). Also, maximum principal stress for Design-2 is observed as 1598.2 MPa for SS316L and 1071.5 MPa for both the alloys (Ti6A14V and CoCr alloy).

Based on these observations, a comparison of analyzed data is shown in Fig. 7 which describes the output parametric values vis-a-vis applied input parametric values employing FEM.

## 5 Conclusion

An implant is one of the most frequently employed medical devices for critical fracture fixation of bones. It consists of the implant plate, screws, etc., and each one of these elements has a specific role to play. It is a fair assumption that an implant plate designed to bear axial compressive load and required to support the longest bone (Femur) will be strong enough to support all other bones in the human body.

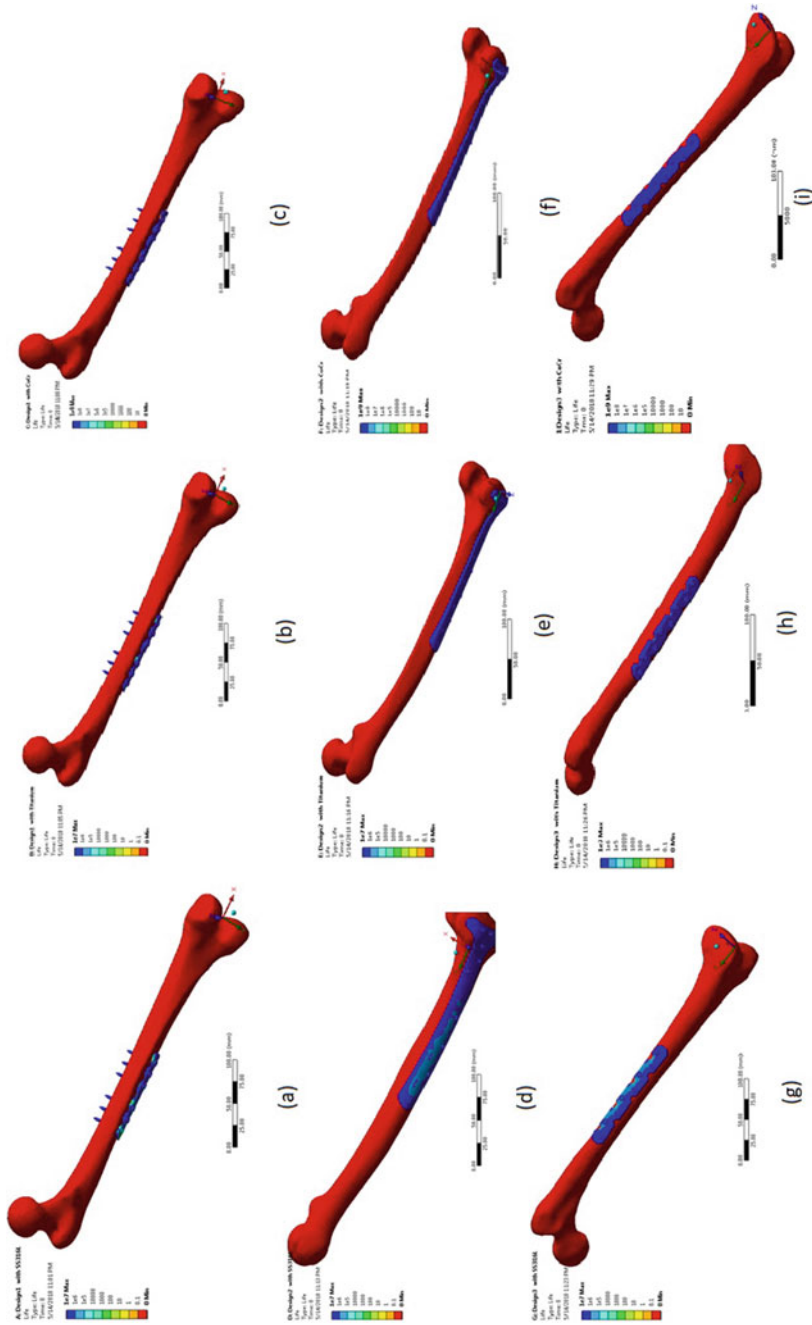


**Fig. 6** Fatigue performance of three designs of plate with its correspondingly used materials, i.e., **a** Design-1 with stainless steel alloy **b** Design-1 with titanium alloy **c** Design-1 with CoCr alloy **d** Design-2 with stainless steel alloy **e** Design-2 with titanium alloy **f** Design-2 with CoCr alloy **g** Design-3 with stainless steel alloy **h** Design-3 with titanium alloy **i** Design-3 with CoCr alloy

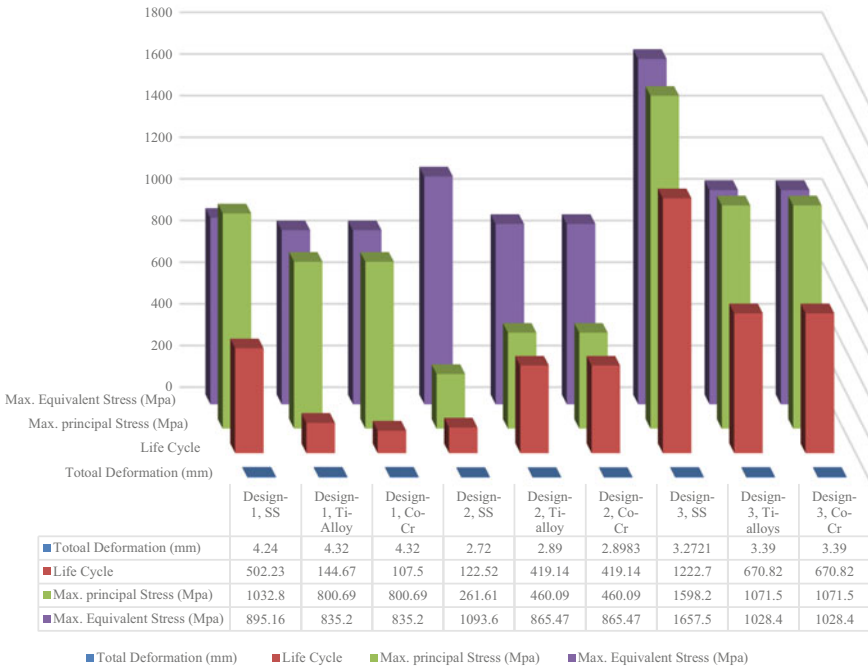


**Fig. 7** Comparatively analyzed data for three design assemblies with each biomaterial

This computational analysis has focused on different designs and different materials for the implant plate subjected to dynamic loading. Structural and fatigue behaviors have been analyzed for the minor single crack in the middle of the femur bone shaft. It is basically observed that out of all materials considered, titanium alloy grade-II has the lowest value of equivalent stress, deformation and maximum principal stress for similar loading conditions. It is precisely because of this that this alloy becomes the preferable choice as it offers good strength, load sustainability and corrosion resistance. Implant plates are immensely useful for orthopedic patients that require appropriate healing of bone over a period of time. However, they may require removal after fulfilling their intended purpose, and this necessitates a secondary surgery. There is tremendous future research potential scope in this area, with adequate focus on the material used, use of biodegradable materials, exhaustive design by incorporating a number of design parameters, some of which may not be getting used at this point, as also analysis relying on implant dissolution rate, rate of corrosion, effect of operating environment, etc.



## References

1. Chandra G, Pandey A, Pandey S (2020) Design of a biodegradable plate for femoral shaft fracture fixation. *Med Eng Phys* 81:86–96. <https://doi.org/10.1016/j.medengphy.2020.05.010>
2. Chandra G, Pandey A (2020) Biodegradable bone implants in orthopedic applications: a review. *Biocybern Biomed Eng* 40(2):596–610. <https://doi.org/10.1016/j.bbe.2020.02.003>
3. Parashar SK, Sharma JK (2016) A review on application of finite element modelling in bone biomechanics. *Perspect Sci* 8:696–698. <https://doi.org/10.1016/j.pisc.2016.06.062>
4. Prakash C, Singh S, Verma K, Sidhu SS, Singh S (2018) Synthesis and characterization of Mg–Zn–Mn–HA composite by spark plasma sintering process for orthopedic applications. *Vacuum* 155(May):578–584. <https://doi.org/10.1016/j.vacuum.2018.06.063>
5. Satapathy PK, Sahoo B, Panda LN, Das S (2018) Finite element analysis of functionally graded bone plate at femur bone fracture site. *IOP Conf Ser Mater Sci Eng* 330(1). <https://doi.org/10.1088/1757-899X/330/1/012027>
6. Kadam AG, Pawar SA, Abhang SA (2017) A review on finite element analysis of different biomaterials used in orthopedic implantation. *Int Res J Eng Technol* 4(4):2192–2195. Available <https://www.irjet.net/archives/V4/i4/IRJET-V4I4559.pdf>
7. Xie G, Takada H, Kanetaka H (2016) Development of high performance MgFe alloy as potential biodegradable materials. *Mater Sci Eng A* 671:48–53. <https://doi.org/10.1016/j.msea.2016.06.051>
8. Naidubabu Y, Mohana Rao G, Rajasekhar K, Ratna Sunil B (2017) Design and simulation of polymethyl methacrylate-titanium composite bone fixing plates using finite element analysis: optimizing the composition to minimize the stress shielding effect. *Proc Inst Mech Eng Part C J Mech Eng Sci* 231(23):4402–4412. <https://doi.org/10.1177/0954406216668550>
9. Dhanopia A, Bhargava M (2017) Finite element analysis of human fractured femur bone implantation with PMMA thermoplastic prosthetic plate. *Procedia Eng* 173:1658–1665. <https://doi.org/10.1016/j.proeng.2016.12.190>
10. Phillips ATM, Villette CC, Modenese L (2015) Femoral bone mesoscale structural architecture prediction using musculoskeletal and finite element modelling. *Int Biomech* 2 (1):43–61. <https://doi.org/10.1080/23335432.2015.1017609>
11. Ali W, Mehboob A, Han MG, Chang SH (2019) Effect of fluoride coating on degradation behaviour of unidirectional Mg/PLA biodegradable composite for load-bearing bone implant application. *Compos Part A Appl Sci Manuf* 124. <https://doi.org/10.1016/j.compositesa.2019.05.032>
12. Sanchez AHM, Luthringer BJC, Feyerabend F, Willumeit R (2015) Mg and Mg alloys: how comparable are in vitro and in vivo corrosion rates? A review. *Acta Biomater* 13:16–31. <https://doi.org/10.1016/j.actbio.2014.11.048>
13. Qasim M et al (2016) Patient-specific finite element estimated femur strength as a predictor of the risk of hip fracture: the effect of methodological determinants. *Osteoporos Int* 27(9):2815–2822. <https://doi.org/10.1007/s00198-016-3597-4>
14. Chandra G, Pandey A (2020) Preparation strategies for Mg-alloys for biodegradable orthopaedic implants and other biomedical applications: a review. *IRBM* 1:1–21. <https://doi.org/10.1016/j.irbm.2020.06.003>
15. Zheng YF, Gu XN, Witte F (2014) Biodegradable metals. *Mater Sci Eng R Reports* 77:1–34. <https://doi.org/10.1016/j.mser.2014.01.001>
16. Gu X et al (2018) In vitro and in vivo studies on as-extruded Mg—5.25wt.%Zn—0.6wt.%Ca alloy as biodegradable metal. *Sci China Mater* 61(4):619–628. <https://doi.org/10.1007/s40843-017-9205-x>
17. Yao H, Wen J, Xiong Y, Lu Y, Ren F, Cao W (2018) Extrusion temperature impacts on biometallic Mg–2.0Zn–0.5Zr–3.0Gd (wt%) solid-solution alloy. *J Alloys Compd* 739:468–480. <https://doi.org/10.1016/j.jallcom.2017.12.225>
18. Zakiuddin KS, Khan IA, Hinge RA (2016) Review paper on biomechanical analysis of human femur. *Int J Innov Res Sci Eng* 2:356–363

19. Zhang S et al (2010) Research on an Mg–Zn alloy as a degradable biomaterial. *Acta Biomater* 6(2):626–640. <https://doi.org/10.1016/j.actbio.2009.06.028>
20. Razzaghi M, Kasiri-Asgarani M, Bakhsheshi-Rad HR, Ghayour H (2020) Microstructure, mechanical properties, and in-vitro biocompatibility of nano-NiTi reinforced Mg–3Zn–0.5Ag alloy: prepared by mechanical alloying for implant applications. *Compos Part B Eng* 190:107947. <https://doi.org/10.1016/j.compositesb.2020.107947>
21. Vignoli LL, Kenedi PP (2016) Bone anisotropy—analytical and finite element analysis. *Lat Am J Solids Struct* 13(1):51–72. <https://doi.org/10.1590/1679-78251814>
22. Sheikh MS, Ganorkar AP (2015) Optimization of femoral intramedullary nailing using finite element analysis. 2(4):123–125

# Study of Electrical and Mechanical Parameters of Electromagnetic Railgun



Shreyas Maitreya, Ritwik Mishra, Ayush Vatsa, and Amit Ojha

## 1 Introduction

As shown in Fig. 1, an electromagnetic railgun consists of two extremely long parallel rails with a small sliding armature in between them connected to a pulsed power supply (Fig. 2) [1, 2]. The armature acts as the projectile, and the rails act as the barrel of the gun. From now on, the terms armature and projectile and the terms rails and barrel will be used interchangeably in the entire paper until and unless specified. The aim of this paper is to present a detailed analysis of the electrical and mechanical parameters of a railgun, and further, this paper makes an attempt to propose suitable modifications to the conventional designs of railguns to improve their deployability and reliability in military and civilian applications.

The block diagram highlighting the working of a typical railgun is given below in Fig. 3.

## 2 Comparison of Electromagnetic Railgun with Conventional Weaponry

Conventional weapons and warheads use chemical propellants and explosives to reach and destroy their targets whereas an electromagnetic railgun destroys its targets purely by the means of the kinetic energy possessed by the projectile which is several orders of magnitude greater than that possessed by the conventional weapons and warheads. Table 1 shows a comparison of the destructive energy that is available on target between conventional weaponry and electromagnetic railguns.

---

S. Maitreya · R. Mishra · A. Vatsa · A. Ojha (✉)

Department of Electrical Engineering, Maulana Azad National Institute of Technology, Madhya Pradesh, Bhopal 462003, India

© The Author(s), under exclusive license to Springer Nature Singapore Pte Ltd. 2022

P. Verma et al. (eds.), *Advancement in Materials, Manufacturing and Energy Engineering, Vol. 1*, Lecture Notes in Mechanical Engineering,

[https://doi.org/10.1007/978-981-16-5371-1\\_37](https://doi.org/10.1007/978-981-16-5371-1_37)

**Fig. 1** Overview of electromagnetic railgun

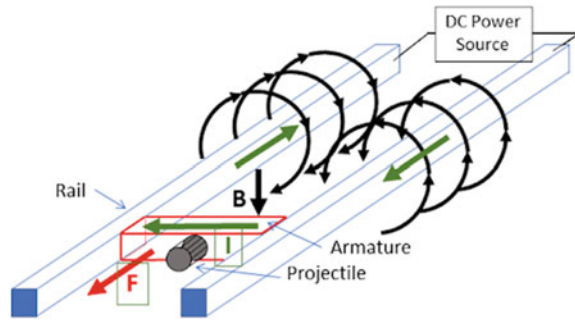


**Fig. 2** Setup of electromagnetic railgun

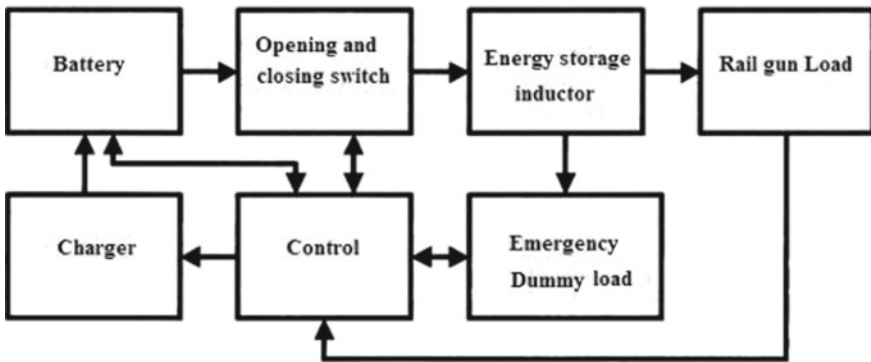
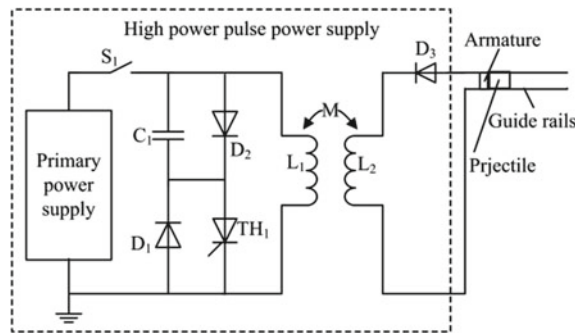


**Fig. 3** Block diagram of electromagnetic railgun

From Table 1, it can be concluded that a railgun has the advantage of superior range and destructive energy available on target. Further, operational cost of an electromagnetic railgun is roughly just less than 10% of the operational cost of conventional weaponry, i.e. the cost of an 18" railgun projectile is just US\$25,000 whereas the cost of a missile of equivalent range and destructive power ranges between US\$500,000 to US\$1.5million. The projectiles of a railgun can be stored

**Table 1** Comparison of railgun with conventional weaponry

S. No	Weapon	Energy available on target (MJ)	Size (inches)	Total flight time (minutes)	Range (km)	Weight (propellant + warhead)	Warhead
1	Extended range guided munition (ERGM)	7	60	6	116.67	50 kg + 18.14 kg	Explosive
2	Long range land attack projectile	14	88	6	185.2	117.93 kg + 40.82 kg	Explosive
3	EM railgun	17	30	6	407.44	20 kg + 1.36 kg	Non-explosive

and transported anywhere with minimum risk of premature explosion or misfiring as the warhead which is normally carried by a railgun is non-explosive in nature, and there are little or no combustible propellants involved.

### 3 Derivation of Force, Acceleration and Speed of Projectile

The mathematical expressions pertaining to the electrical and mechanical parameters of a railgun are based on the following assumptions;

1. The size of the projectile is negligible in comparison to that of the rails.
2. The resistance and inductance per unit length of the rails are uniform.
3. The voltage applied across the entire railgun assembly is constant.
4. The formation and effect of plasma arc is ignored.

The force acting on the projectile of the railgun is given by,

$$\mathbf{F} = \frac{\lambda(i(t))^2}{2} \quad (1)$$

Here,  $\lambda$  is the inductance per unit length of the rails,  $i(t)$  is the current through the entire railgun assembly as a function of time. If the mass of the projectile is 'm', then its acceleration 'a' is given by,

$$a = \frac{dv}{dt} = \frac{\lambda(i(t))^2}{2m} \quad (2)$$

On integrating (2), the expression for the speed of the projectile can be derived;

$$V(t) = V_0 + \int_0^T \frac{\lambda(i(t))^2}{2m} dt \quad (3)$$

where  $V_0$  is the speed of the projectile at time  $t = 0$ , and  $T$  is the total time for which the projectile is within the railgun assembly. Assuming that the projectile starts from rest,  $V_0 = 0$ , therefore

$$V(t) = \int_0^T \frac{\lambda(i(t))^2}{2m} dt \quad (4)$$

Upon integrating (3), the position of the projectile in the barrel of the railgun as a function of time can be determined

$$X(t) = X_0 + \iint_0^T \frac{\lambda(i(t))^2}{2m} dt \tag{5}$$

Now, using (5), the expressions for inductance ( $L(x)$ ) and resistance ( $R(x)$ ) can be derived as a function of time

$$R(x) = R_0 + \rho X(t) \tag{6}$$

$$L(x) = L_0 + \lambda X(t) \tag{7}$$

Upon substituting the value of  $X(t)$  from (5) in (6) and (7), the expressions for inductance and resistance as functions of time.

$$\therefore R(t) = R_0 + \rho \iint_0^T \frac{\lambda(i(t))^2}{2m} dt \tag{8}$$

$$\therefore L(t) = L_0 + \lambda \iint_0^T \frac{\lambda(i(t))^2}{2m} dt \tag{9}$$

### 4 Equivalent Circuit and Electrical Behaviour of Electromagnetic Railgun

As shown in Fig. 4, the equivalent circuit of an electromagnetic railgun can [3] be represented as a time varying resistance and inductance in series which are connected to a pulsed power supply capable of withstanding extremely high temperatures.

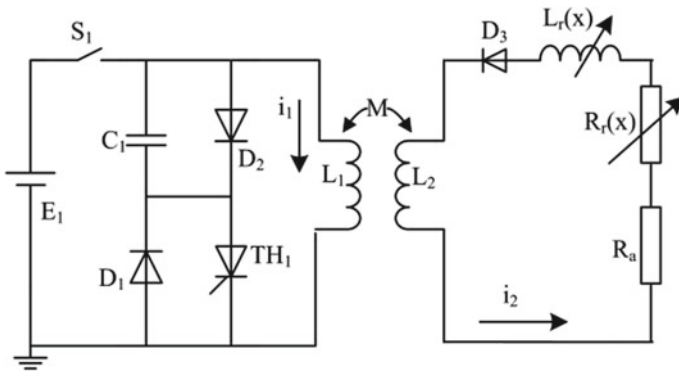


Fig. 4 Practical equivalent circuit of electromagnetic railgun

The 1:1 transformer is present to protect the railgun assembly from voltage/current impulses. The transient and steady state equations can be derived from the following steps [4],

- The inductor  $L_1$  is charged by the voltage source  $E_1$  once the source  $S_1$ .

$$E_1 = i_1 R_{s1} + L_1 \frac{di_1}{dt} \quad (10)$$

$$i_1 = \frac{E_1 - i_1 R_{s1}}{L_1} \quad (11)$$

- $S_1$  is switched off and thyristor  $TH_1$  is turned on and  $L_1$  is discharged and the capacitor  $C_1$  is charged.

$$L_1 \frac{di_1}{dt} + M \frac{di_2}{dt} + u_c = 0 \quad (12)$$

$$i_1 = C_1 \frac{dU_c}{dt} \quad (13)$$

On secondary side,

$$[L_2 + L_r] \frac{di_2}{dt} + M \frac{di_1}{dt} + \left[ \frac{dL_r}{dt} + R_r(x) + R_a \right] i_2 \quad (14)$$

$$\frac{dL_r(x)}{dt} = \frac{dL_r}{dx} \frac{dx}{dt} = \lambda v \quad (15)$$

$$[L_2 + \lambda x] \frac{di_2}{dt} + M \frac{di_1}{dt} + (\lambda v + \rho x + R_a) i_2 \quad (16)$$

$$\frac{di_1}{dt} = \frac{-(L_2 + \lambda x)}{(L_2 + \lambda x)L_2 - M^2} U_c + \frac{M(\lambda v + \rho x + R_a)}{(L_2 + \lambda x)L_2 - M^2} \quad (17)$$

$$\frac{di_2}{dt} = \frac{-M}{(L_2 + \lambda x)L_2 - M^2} U_c - \frac{L_1(\lambda v + \rho x + R_a)}{(L_2 + \lambda x)L_2 - M^2} \quad (18)$$

$$\frac{dU_c}{dt} = \frac{i_1}{C_1} \quad (19)$$

$$\therefore L \frac{di_1}{dt} + M \frac{di_2}{dt} = 0 \quad (20)$$

$$(L_2 + \lambda x) \frac{di_2}{dt} + M \frac{di_1}{dt} + (\lambda x + \rho x + R_a) i_2 = 0 \quad (21)$$



$$\frac{di_1}{dt} = \frac{M(\lambda v + \rho x + R_a)}{(L_2 + \lambda x)L_1 - M^2} i_2 \tag{22}$$

$$\frac{di_2}{dt} = - \frac{L_2(\lambda v + \rho x + R_a)}{(L_2 + \lambda x)L_2 - M^2} i_2 \tag{23}$$

## 5 Derivation of Mechanical Parameters of Electromagnetic Railgun

From the above equations for position, speed and acceleration can be used to derive the following parameters,

Friction and friction losses.

Air resistance and work done against air resistance.

$$\mu_k N = \text{Force due to friction}$$

N apparent normal reaction between rails and armature.

N mg-force of repulsion between rails.

$$F = \mu_k \left( mg - \mu(i(t))^2 \frac{1}{4\pi d} \right)$$

$\mu_k$  Coefficient of kinetic friction between rails and armature

$\therefore$  Work done against friction =  $fl$  ( $l$  = length of rails)

$$Ef = \mu_k \left( mg - \mu(i(t))^2 \frac{1}{4\pi d} \right) \times (t)$$

$$\text{Air resistance} = \eta A \frac{dv}{dx}$$

where  $\eta$  = coefficient of viscosity of air,  $A$  = area of cross section of projectile.

$$\text{Acceleration } a = \frac{dv}{dt} = V(t) \frac{dv}{dx} = \frac{\lambda(i(t))^2}{2m} \tag{24}$$

$$\frac{dv}{dx} = \lambda \frac{(i_2(t))^2}{2mV(t)} \tag{25}$$

$$\therefore \text{force due to air resistance} = F_a = \eta A \lambda \frac{(i_2(t))^2}{2mV(t)} \tag{26}$$

Energy lost in overcoming air resistance is given by the following expression,

$$E_a = F_a l = \eta A \lambda \frac{(i_2(t))^2}{2mV(t)} l \quad (27)$$

From the above expressions, the efficiency [5] of a railgun can be derived. Theoretically, a railgun can be viewed as a series R-L circuit which typically has a theoretical efficiency of 50% which is much higher than that of conventional weaponry.

### 5.1 Simulation of Electromagnetic Railgun

The entire setup was developed as per the block diagram shown in Figs. 3 and 4 and the parameters chosen are shown in Table 2. The simulation was run for a total period of 2s, and the results are discussed in the next section.

## 6 Results and Discussion

From Fig. 5, it can be seen that the acceleration of the projectile is of several orders of magnitude higher than that of a conventional weapon. This gives the railgun a superior destructive power over a simple chemical driven artillery gun.

Figure 6 further highlights the sheer destructive power of the gun which is due to the extremely high muzzle velocity of the projectile, i.e. 50,000 m/s. Equations (1)–(23) give a clear picture of the variation of current and voltage with respect to time. In case of multiple pulsed power supply units connected in parallel, the currents can be added as per Kirchhoff's current law.

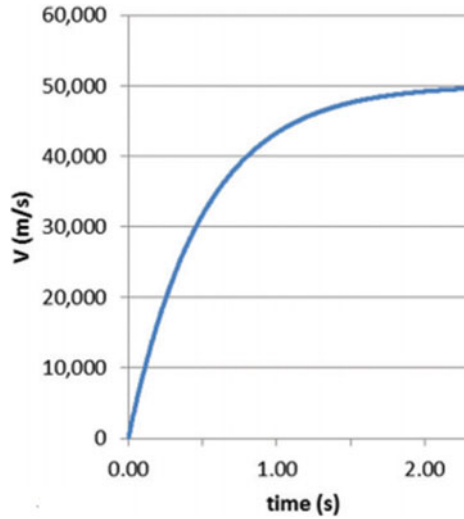
From Figs. 5, 6 and from Table 2, the following can be concluded [6].

- The projectile continues to accelerate until the electromagnetic force acting on it is balanced by the force of friction acting on it and the force due to air resistance acting on it.

**Table 2** Parameters used in simulation of railgun

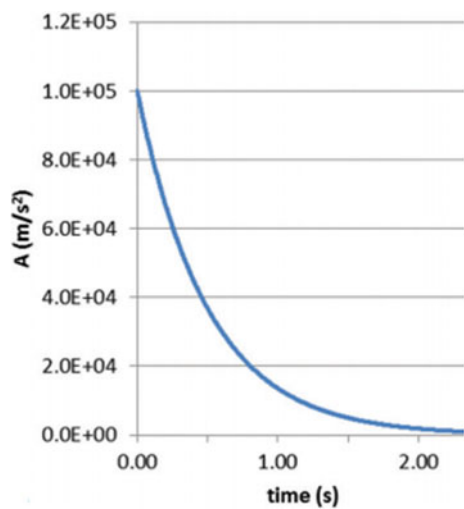
S. No	Parameter	Value
1	Transformer ratio	1:1
2	Capacitance	15.6F
3	Supply voltage	450 V (DC)
3	Mass of projectile	0.6318 gm
4	Energy at firing	0.789750 MJ
5	Energy supplied	1.5765 MJ

**Fig. 5** Speed-time graph for electromagnetic railgun



- Initially, the force acting on the projectile is extremely high which is obvious due to the extremely large starting current flowing through the entire railgun assembly that thereby produces an extremely strong magnetic field in between the rails.
- The extremely large starting current in the railgun which results in extremely powerful magnetic fields which can result in extremely strong repulsive forces on the rails which can cause them to bend and flex repeatedly due to the huge bending moments developed because of the huge repulsive forces. This will eventually lead to elastic fatigue of the rails which will lead to catastrophic

**Fig. 6** Acceleration-time graph of electromagnetic railgun



failure of the entire railgun assemble at some point of time. This also limits the number of shots per minute that can be fired by the railgun.

## 7 Proposed Improvements to Design of Railgun

The above limitations of a railgun are extremely difficult to overcome and require an extremely high degree of advancement in the field of metallurgy and material science. A certain degree of mitigation can be achieved for this problem by using the following means,

- As shown in Fig. 7, division of the entire rail into smaller sub rails in order to reduce the overall bending moment acting on the entire railgun assembly as shown in the figure given below.
- Lubrication of the projectile, rail assembly with graphite in order to minimise frictional losses and heating due to friction [7, 8].
- Use of a rapid cooling system which uses free expansion of gas in order to rapidly cool the interior of the railgun assembly as shown in the block diagram below (Fig. 8).
- Use of hybrid propulsion systems, i.e. a mix of electromagnetic and chemical propulsion in order to propel the projectile towards the target that is intended to be destroyed [9].
- Use of multiple smaller railgun modules attached in parallel and alternatingly firing them in order to achieve a higher number of shots per minute.

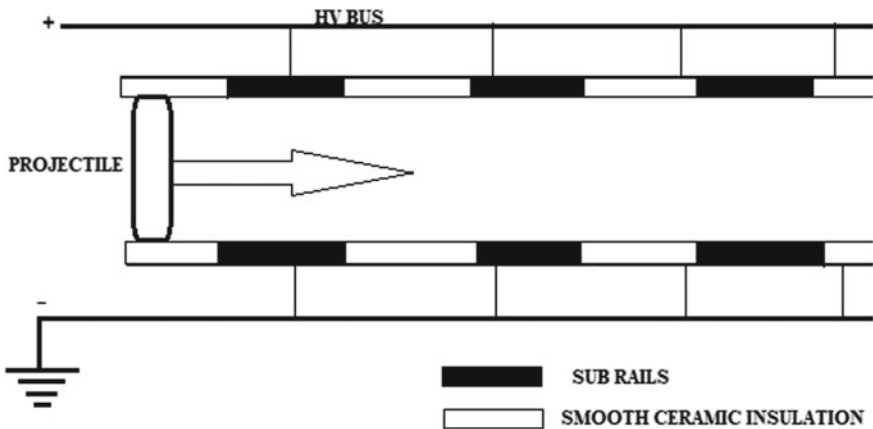
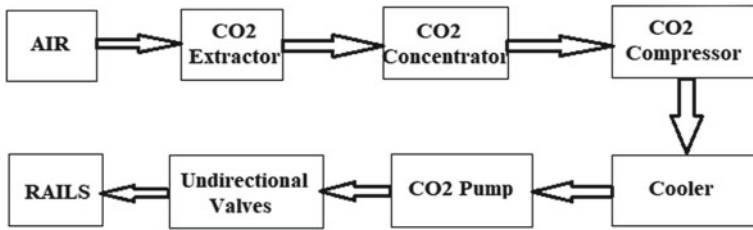


Fig. 7 Modified design of railgun barrel (proposed not verified)



**Fig. 8** Cooling system for railgun barrel (proposed not verified)

## 8 Conclusions

From the above study, it can be concluded that there is still a requirement of significant advancements in the field of material science in order to achieve a firing rate of a several hundred shots per minute for a railgun. Materials such as tungsten and tungsten carbide have been used, but these materials are also only capable of sustaining a few dozen shots per minute. Further, the improvements mentioned above are yet to be tested for their practicality and deployability for military applications.

Railguns, though considerably superior to conventional weapons both in terms of cost and destructive power, but still they are quite far away from reaching either military or civilian deployment in the current era.

The improvements mentioned in Sect. 7 can only overcome the limitations of a railgun to a certain extent the real improvement will come only from advancements in material science and technology which is still quite far-fetched in the current day and age.

## References

1. Rashleigh SC, Marshall RA (1978) Electromagnetic acceleration of macroparticles to high velocities. *J Appl Phys* 49(4):2540–2542
2. Hundertmark S, Liebfried O (2017) Power supply options for a naval railgun, 18 Sept 2017 [Online]. Available: <https://arxiv.org/pdf/1709.05901.pdf>. Accessed 18 Mar 2020
3. Dreizin YA (1996) Electromagnetic launcher with advanced rail and barrel design. United States of America Patent US5483863A, 16 Jan 1996
4. Tataka SG, Daniel KJ, Ghosh AA, Tokekar KP, Rao KR, Khan II (1994) Modelling and simulation of a railgun powered by a capacitor bank. *Defence Sci J* 44(2):131–137
5. Li Z, Li H, Zhang X, Zhang C, Liu S, Lu T (2018) Modeling and simulation of railgun system driven by multiple HTSPPT modules. *IEEE Trans Plasma Sci*
6. Brahmhatt NS (2018) Design and optimization of an electromagnetic railgun. Open access master's report, Houghton
7. Talake SG, Daniel KJ, Rao KR, Ghosh AA, Khan II (1994) Railgun. *Def Sci J* 44(3):257–262

8. Peterson D, Weeks D, Zowarka R, Cook R, Weldon W (1986) Testing of a high performance precision bore gun. In: 3rd symposium on electromagnetic launch technology, Austin
9. Gully J (1991) Power supply technology for electric guns. *IEEE Trans Magn* 27(1):329–334

# Performance Analysis of Optimal Designed Photovoltaic/Diesel Generator-Based Hybrid Energy System Coupled to Utility Grid



Anurag Chauhan, Ashish Srivastava, Mohd Tauseef Khan, Altaf Alam, and Subho Upadhyay

## 1 Introduction

Sustainable development has gained more importance in recent times due to adverse impacts of utilization of conventional resources (coal, oil, gas, etc.). Solar photovoltaic power, biomass power and wind turbine power integrated with diesel generator has been recognized as a viable option in place of conventional sources to meet the rapidly increasing demand. Also, use of renewable sources does not emit carbon emission in the environment. Renewable energy sources can be developed in both grid environment and/or stand-alone mode. Therefore, such hybrid system is very efficient to fulfil the energy demand of isolated areas [1–5].

Suresh et al. [6] minimized the net present cost of hybrid system consisted of solar PV array, wind turbines, biomass, biogas, battery and fuel cell. They used genetic algorithm to estimate the value of cost of energy, carbon emission and unmet load. Four combinations were considered and compared based on cost. They have also performed the sensitivity analysis for the varying values of fuel prices and wind speed. Mokhtara et al. [7] suggested a demand side management for a solar/diesel/batter based system to meet the demand of a building. Further, they reduced the cost of system using PSO algorithm. They compared the results of cost of energy and carbon emission with and without demand side management.

---

A. Chauhan (✉) · A. Srivastava · M. T. Khan · A. Alam  
Department of Electrical Engineering, Rajkiya Engineering College, Banda,  
Uttar Pradesh 210201, India  
e-mail: [anurag@recbanda.ac.in](mailto:anurag@recbanda.ac.in)

S. Upadhyay  
Department of Electrical Engineering, Dayalbagh Educational Institute, Agra,  
Uttar Pradesh 282005, India

Zhang et al. [8] optimized a PV and wind turbine-based hybrid system with battery and hydrogen storage using global mixed integer linear programming. They found that fuel cell-based hydrogen storage for hybrid system offered promising results for high load conditions compared to battery storage. Alshammari and Asumadu [9] used harmony search algorithm and Jaya and PSO algorithm to determine the sizes of hybrid system comprised of PV array, biomass, wind turbines and battery bank. They considered four decision variables in size optimization such as number of PV modules, size of biomass generator, size of battery bank and number of wind turbines. They observed that harmony search algorithm converges at faster rate compared to Jaya and PSO algorithm.

Murugaperumal et al. [10] performed the forecasting of the load demand of a district which consisted of domestic, commercial, agricultural and institutional sector. They investigated load following, cycle charging and combined strategies in order to optimize PV–wind–biomass–battery-based system using HOMER software. Taheri and Zahedi [11] designed a novel hybrid system consisted of solar still distiller, parabolic trough collector, trans-esterified conversion reactor along with ground source heat pump and microalgal culture pond. They also used cooling water layer along with vacuum method in passive solar still distiller.

Many studies have been conducted on the size optimization of isolated hybrid system. However, few researchers investigated the hybrid system with utility grid. Also most of the authors have not investigated the performance indicators of the hybrid system components. This paper presents an optimal design of grid connected PV/Diesel generator-based hybrid system. Mathematical modelling is discussed in the Sect. 3. Further, formulation of objective function and operational constraints is given in Sect. 4. Finally, developed hybrid system model has been simulated to get the best optimal size of each system component.

## 2 Hybrid System Configuration

A PV/Diesel generator-based hybrid system coupled to utility grid has been considered in the paper as displayed in Fig. 1. This hybrid system is planned to meet the electrical energy demand of three hostels of the institute Rajkiya Engineering College Banda of India. Output of PV array is linked to DC bus, while output of diesel generator is connected to AC bus. Available utility grid is also integrated in the considered system to make energy balance at each time interval. When excess generation is available, surplus power is sold to utility grid. At any instant, when demand exceeds combined generation of PV array and diesel generator, shortage power is taken from the utility grid. Bidirectional converter has also been used in the system in order to convert AC to DC and vice-versa.



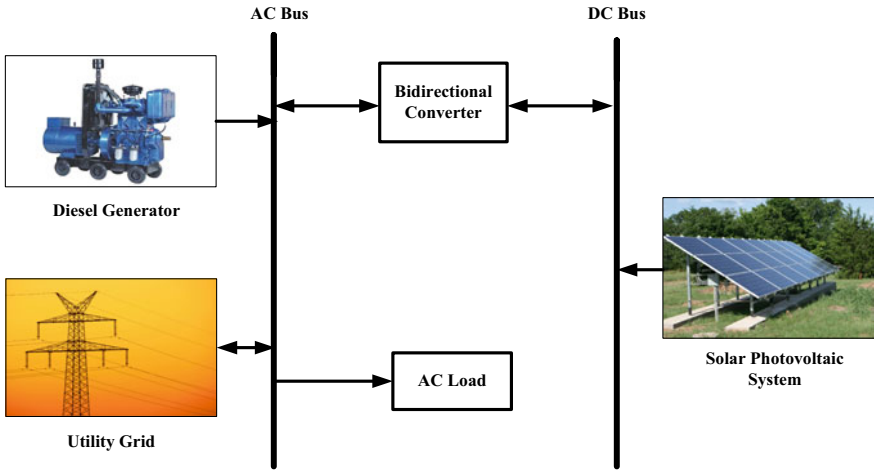


Fig. 1 Schematic of PV/diesel generator-based hybrid system coupled to utility grid

### 3 Mathematical Modelling

Modelling is an important step before optimization as it gives the static and dynamic characteristics of the component. It relates the output of the system component in the terms of many variables. Mathematical model of the each component of hybrid system is explained as below:

#### 3.1 Model of PV Array

The electrical power output of solar photovoltaic array is a function of solar radiation and PV cell temperature. Hourly output can be estimated as [2]:

$$P_{PV}(t) = P_{PV,Rated} f_{PV} \left[ \frac{\beta(t)}{\beta_{STC}} \right] [1 + \alpha_P (T_{cell}(t) - T_{cell,STC})] \quad (1)$$

where  $P_{PV}$  is the PV array output,  $P_{PV,Rated}$  is panel rated capacity (kW),  $f_{PV}$  is derating factor of panel,  $\beta$  is solar radiation ( $\text{kW}/\text{m}^2$ ),  $\beta_{STC}$  is solar radiation at standard test conditions,  $\alpha_P$  is the temperature coefficient of power ( $\%/^{\circ}\text{C}$ ),  $T_{cell}$  is PV cell temperature and  $T_{cell,STC}$  is the panel cell temperature at STC ( $25^{\circ}\text{C}$ ).

### 3.2 Model of Diesel Generator

Diesel generator (DG) is operated to serve the demand of area during the peak hours. Power output of DG is the function of rated power output ( $P_{DG,gen}$ ) and time step ( $\Delta t$ ). Model of hourly output can be modelled by Eq. (2) as [3]:

$$P_{DG}(t) = P_{DG,gen}(t) \times \Delta t \quad (2)$$

### 3.3 Model of Utility Grid

Grid is incorporated in the considered hybrid configuration which is typically works in two different modes. In the first mode, grid supplies deficit power to the load demand when demand surpasses generation of solar panels and generator. Mathematical model can be explained as:

$$P_{GP}(t) = P_{Demand}(t) - [P_{PV}(t) \times \eta_{Con} + P_{DG}(t)] \quad (3)$$

where  $P_{GP}$  is electricity purchased from the utility grid,  $P_{Demand}$  is hourly electrical energy demand and  $\eta_{Con}$  is efficiency of converter.

Under the situation when electricity generation from the sources is greater than the electrical demand, the additional generation is transferred to the grid. Mathematically, selling of electricity to grid ( $P_{GS}$ ) is modelled by Eq. (4) as:

$$P_{GS}(t) = [P_{PV}(t) \times \eta_{Conv} + P_{DG}(t)] - P_{Demand}(t) \quad (4)$$

## 4 Objective Function

Minimization of cost of energy generation from the hybrid system is the taken as the objective function. It is the function of total annualized cost and energy served. Objective function is modelled by using Eq. (5) as:

$$COE = \frac{\text{Annualized Cost of System}}{\text{Energy Served}} \quad (5)$$

Annualized cost is the addition of capital costs, maintenance costs and replacement costs. It is dependent upon the different costs of system components and capital recovery factor (CRF). It is calculated as:

$$\text{Annualized Cost} = CRF \times [C_{PV} + C_{DG} + C_{Grid,Purchase} - C_{Grid,Sell} + C_{Con}] \quad (6)$$

where  $C_{PV}$  is cost of solar PV array,  $C_{DG}$  is cost of diesel generator,  $C_{Grid,Purchase}$  is the cost of electricity purchase from the grid,  $C_{Grid,Sale}$  is the revenue generated by selling electricity to the grid and  $C_{Conv}$  is the converter cost.

Value of CRF is determined as follows [12]:

$$CRF = \frac{d(1+d)^{n_{life}}}{(1+d)^{n_{life}}-1} \quad (7)$$

where  $d$  is discount rate and  $n_{life}$  is lifetime of the project.

## 5 Operational Algorithm

HOMER provides a time-based simulation of a hybrid system. It takes many inputs such as solar radiation, wind speed, hourly electrical energy demand and thermal demand. Also, economic data such as capital cost, replacement cost and maintenance cost are also required before simulation. Further, HOMER makes several combinations of components based on the data inserted by the designer. Further, it simulates each combination in order to optimize the system cost while fulfilling constraints imposed by the modeller. Finally, it gives the most optimal combination which meets the demand at lowest cost [12]. Step-wise working procedure of HOMER software is given as follows [13]:

- Step 1: Enter the technical data such as load demand, solar radiation, battery and converter.
- Step 2: Enter the economic data of diesel generator, solar PV array, converter and battery.
- Step 3: Enter user constraint
- Step 4: Start simulation to optimize the cost under user-defined constraint
- Step 5: Obtain the optimization results.

## 6 Results and Discussions

Data inputs are required for the performance analysis of PV/DG-based hybrid energy system coupled to grid. Further, these data inputs are used for the analysis of the considered system using HOMER software. Various results related to size optimization, break-up of net present cost, monthly generation of different sources, etc. are discussed in the chapter.

### 6.1 Data Inputs Used

Various data inputs such as data of solar radiation, solar PV array cost, DG cost, fuel price, grid purchase price, grid sale price, efficiency curve of DG and cost of converter.

#### 6.1.1 Data of Solar Radiation

The daily solar radiation of each month for the area has been taken as depicted in Fig. 2. Highest daily solar radiation has been measured in month of May as 7.047 kWh/m<sup>2</sup>, while lowest daily solar radiation is recorded during December as 4.079 kWh/m<sup>2</sup>. The daily annual average solar radiation is estimated to be as 5.26 kWh/m<sup>2</sup>.

#### 6.1.2 Cost of PV Array

The capital cost of 1 kW of solar panels is taken as 857 \$. Replacement cost and O & M cost of solar PV panels are taken as 857 \$/kW and 25 \$/kW, respectively, as given in Table 1. Lifetime of 25 years, derating factor of 80% and slope angle of 25.28° were considered during the analysis.

#### 6.1.3 Cost of DG

The capital cost of 1 kW DG is considered as 570 \$. Replacement cost and O & M cost of DG are taken as 540 \$/kW and 0.015 \$/h, respectively, as given in Table 1. Efficiency curve of DG is shown in Fig. 3. The intercept coefficient and slope of the

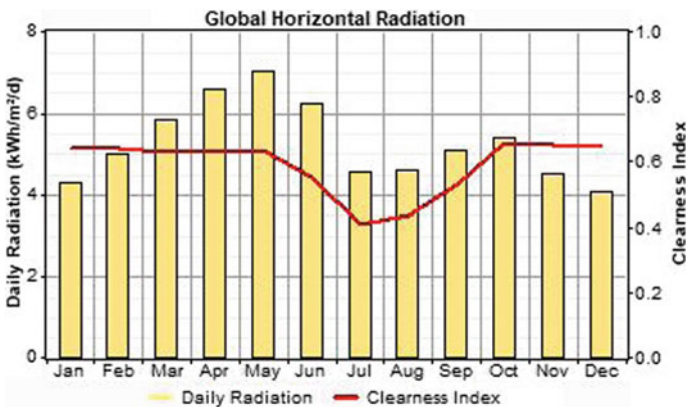


Fig. 2 Month wise daily solar radiation

**Table 1** Economic data of sources and system components

S. No	Source/system component	Capital cost (\$/kW)	Replacement cost (\$/kW)	Operation and maintenance cost
1	Solar photovoltaic panel	857	857	25 \$/year
2	DG	570	540	0.015 \$/h
3	Converter	40	40	1 \$/year

curve are 0.08 L/h/kW rated and 0.25 L/h/kW output. Price of 1 L diesel fuel for DG is taken as 1 \$. Carbon content and sulphur content in the fuel are as 88% and 0.33%, respectively.

### 6.1.4 Hourly Load Demand of the Area

Three boy’s hostels of the institute Rajkiya Engineering College Banda are considered as the study area for the project. Appliances such as LED lamp, ceiling fan, LED TV, refrigerator, insect killer machines, water cooler and geyser loads were accounted during demand estimation. Based on the hourly consumption of appliances, hourly electrical demand of the considered area is calculated which is depicted in Fig. 4. Load demand of each hour of the area is estimated as 872 kWh. The lowest and highest hourly load of the area is found as 8.160 kW and 73.116 kW, respectively. In the study, uniform load profile has been considered throughout the year.

### 6.1.5 Interest Rate and Project Lifetime

Project life time of 25 years has been considered in the paper during simulation. Interest rate to estimate CRF is taken as 6%. Capacity shortage of 0% is considered as power reliability constraint.

**Fig. 3** Efficiency curve of diesel generator

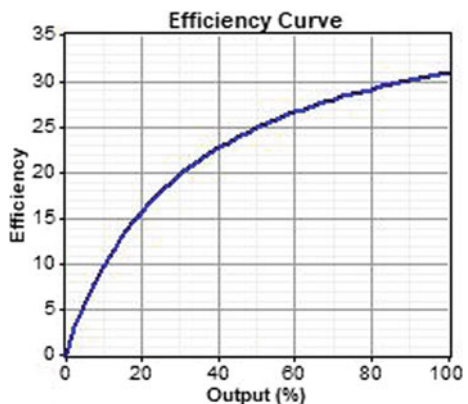
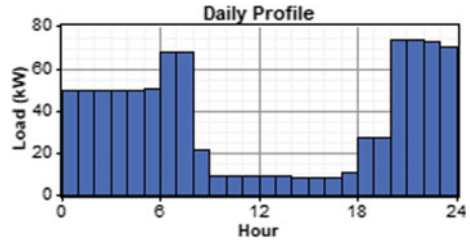


**Fig. 4** Hourly demand of the area taken



### 6.1.6 Grid Purchase Price and Grid Sale Price

The tariff of electricity purchase from the grid and tariff for selling the electricity to grid are taken as 0.121 \$/kWh.

### 6.1.7 Converter Cost

The capital cost of 1 kW converter is considered as 40\$. Replacement cost and O & M cost of converter are taken as 40 \$/kW and 1 \$/year, respectively as given in Table 1. Converter lifetime of 15 years, and efficiency of 90% haven been taken during the analysis.

## 6.2 Results and Discussions

Best optimal configuration and cost of energy of the hybrid system has been obtained by using HOMER. Results such as optimum configuration, monthly average electricity generation, break-up of total NPC and technical details of PV array, utility gird and DG have been discussed in detail as follows:

### 6.2.1 Optimum Configuration of Hybrid System

The hybrid system with input data base is simulated and optimized to attain the reliability of power supply as 100%. Based on simulation of 365 days considering each hour as unit step, various system configurations are attained and the details are described in Table 2. It has been analysed that the best configuration offers the lowest COE as 0.127 \$/kWh. Sizes of this configuration are found as DG: 31 kW, solar PV panels: 180 kW<sub>p</sub> and converter: 148 kW. Further, this system needs electricity purchase of 230,429 kWh/year grid to supply the system demand. Moreover, annual spare electricity of 222,837 kWh is also generated by the system that is sold to the grid. The NPC is calculated as 518,756 \$.

**Table 2** Optimum configuration of hybrid system

S. No	Solar PV panels (kW <sub>p</sub> )	DG (kW)	Converter (kW)	Grid purchase (kWh per year)	Total NPC (\$)	COE (\$/kWh)
1	180	31	148	230,429	518,756	0.127
2	180	32	145	229,778	518,780	0.128
3	170	32	140	230,234	533,225	0.131
4	160	32	140	230,719	548,173	0.135
5	150	32	140	231,288	563,405	0.138
6	150	34	140	230,155	563,534	0.139
7	144	33	140	231,343	578,590	0.142

### 6.2.2 Component Wise Electricity Generation

Component wise electricity generation and percentage share in total system generation are presented in Figs. 5 and 6, respectively. Share of solar photovoltaic panels in total system generation is maximum as 53% (3,02,647 kWh per year). Part of grid purchase and DG are estimated to be as 40% (2,30,429 kWh per year) and diesel generator 7% (38,451 kWh per year), respectively.

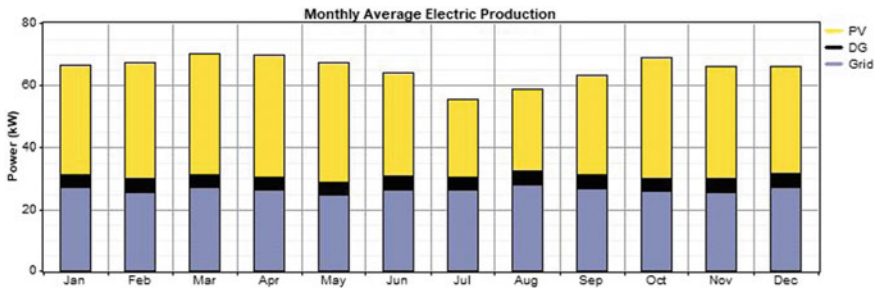
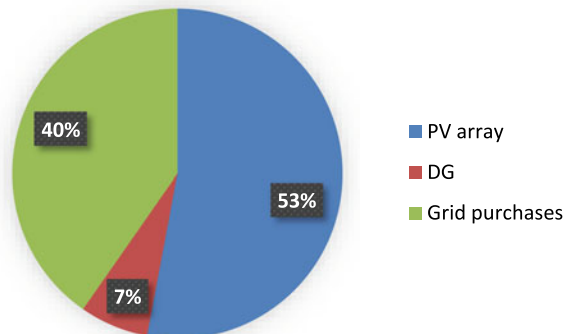


**Fig. 5** Component wise monthly average electricity generation

**Fig. 6** Component wise percentage share in total generation



### 6.2.3 Component Wise Part in Total Net Present Cost

Component wise part in total NPC of the system is shown in Fig. 7. It has been observed that PV array has the highest contribution in total NPC which accounts 2,11,785 \$ followed by DG with 1,96,466 \$ and grid with 1,00,683 \$. Converter has the minimum share of 9822 \$ in the total NPC. Percentage wise share of each component in the total NPC is as follows: PV array with 41%, DG with 38%, grid with 19% and converter with 2%.

### 6.2.4 Break-up of Total NPC

The NPC of the optimum configuration is \$5,18,756. Major break-up of the total NPC of the system is given in Table 3. It has been observed that in the total NPC, the part of the capital cost of different components is maximum as 1,77,850 \$. The contribution of maintenance cost, replacement cost and fuel cost of different components in the total NPC are 1,67,015 \$, 1,67,015 \$ and 8349 \$, respectively.

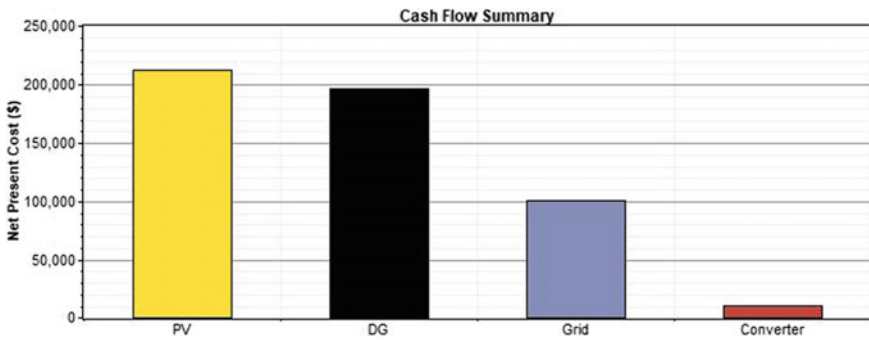


Fig. 7 Component wise share in total NPC

Table 3 Break-up of total NPC

S. No	Component	Capital (\$)	Replacement (\$)	O&M (\$)	Fuel (\$)	Salvage (\$)	Total (\$)
1	PV	1,54,260	0	57,525	0	0	2,11,785
2	DG	17,670	5879	8,274	1,67,015	-2,371	1,96,466
3	Grid	0	0	1,00,683	0	0	1,00,683
4	Converter	5,920	2470	1,892	0	-460	9822
<b>System</b>		1,77,850	8349	1,68,374	1,67,015	-2,831	5,18,756



### 6.2.5 Performance Indicators of DG

Various performance indicators of diesel generator is given in Table 4. The value of important performance indicators are as follows: rated power output as 31 kW, hours of operation as 1392 h/year, number of starts as 727 starts/year, capacity factor as 14%, specific fuel consumption as 0.34 L/kWh and electricity production as 38,451 kWh/year.

### 6.2.6 Performance Indicators of PV Array

Various performance indicators of solar PV array are given in Table 5. The value of important performance indicators are as follows: rated capacity as 180 kW<sub>p</sub>, capacity factor as 19% and total production as 3,02,647 kWh/year.

### 6.2.7 Performance Indicators of Grid

Various performance indicators of grid are given in Table 6. It has been found that the total energy purchased and total energy sold in a year are 2,30,429 and 2,22,837 kWh, respectively. The highest energy of 20,621 kWh has been purchased during the month of August, and the lowest energy of 17,149 is purchased in the month of February. Whereas, the highest energy of 21,688 kWh has been sold to grid in the month of March, and the lowest energy of 12,625 kWh is sold to grid in the month of July.

**Table 4** Performance indicators of DG

S. No	Indicator	Quantity
1	Total operating hours in a year	1392
2	Total start operation in a year	727
3	Lifetime of operation in year	18
4	Capacity factor in %	14
5	Fixed generation cost in \$/h	3.61
6	Marginal generation cost	0.25
7	Annual generation of electricity in kWh/year	38,451
8	Average power output in kW	27.6
9	Minimum power output in kW	14
10	Peak power output in kW	31
11	Annual consumption of diesel in litre per year	13,065
12	Specific consumption of diesel in litre per kWh	0.34
13	Fuel energy input in kWh per year	1,28,560
14	Average efficiency in %	29.9

**Table 5** Performance indicators of solar PV array

S. No	Quantity	Quantity
1	Rated power output in kW <sub>p</sub>	180
2	Average power output in kW	35
3	Daily average power output in kWh	829
4	Capacity factor in %	19
5	Annual energy generation in kWh	3,02,647
6	Lowest power delivered in kW	0
7	Peak power delivered in kW	177
8	Penetration of PV array in %	95.1
9	Annual operating hours	4375

**Table 6** Performance indicators of grid

S. No	Month of a year	Energy Purchased from grid (kWh)	Energy transferred to grid (kWh)	Total net purchases (kWh)
1	January	20,009	19,919	90
2	February	17,149	19,246	-2097
3	March	20,046	21,688	-1643
4	April	18,850	20,935	-2085
5	May	18,386	21,026	-2640
6	June	18,972	16,953	2019
7	July	19,423	12,625	6798
8	August	20,621	13,503	7118
9	September	19,172	16,674	2498
10	October	19,269	21,447	-2178
11	November	18,359	19,422	-1063
12	December	20,173	19,398	776
<b>Annual</b>		<b>2,30,429</b>	<b>2,22,837</b>	<b>7592</b>

## 7 Conclusions

In the paper, performance analysis of optimal configuration of hybrid system coupled to grid has been carried out. Grid connected hybrid energy system comprised of solar PV array and DG which meets the electrical demand of an area. After hourly-based iterative simulation for a year, the most optimum configuration has been selected that meets the demand at minimum COE. The COE of the hybrid energy system is calculated as \$ 0.127 per kWh. Optimal configuration of hybrid system contains 180 kW<sub>p</sub> sized solar PV array, 31 kW rated diesel generator and 148 kW rated converter. Annual energy purchased from the utility grid has been estimated as 2,30,429 kWh, whereas annual selling of electricity to utility grid is calculated as 2,22,837 kWh. In future, study on incentives on the utilization of renewable energy from the government can be carried out.

## References

1. Das M, Singh MAK, Biswas A (2019) Techno-economic optimization of an off-grid hybrid renewable energy system using metaheuristic optimization approaches—case of a radio transmitter station in India. *Energy Convers Manage* 185:339–352
2. Verma S et al (2020) Solar PV powered water pumping system—a review. *Mater Today Proc* xxx. <https://doi.org/10.1016/j.matpr.2020.09.434>
3. Chauhan A, Upadhyay S, Srivastav A, Khan MT (2020) An intelligent load management technique for remotely located areas powered by grid connected solar/diesel generator based system. In: 2020 International conference on power electronics & IoT applications in renewable energy and its control (PARC), pp 320–324
4. Chauhan A Modeling and simulation of a sustainable hybrid energy system under changing power reliability index at user end. In: Modeling and simulation based analysis in reliability engineering. CRC Press, pp 215–232
5. Upadhyay S, Chauhan A (2020) Design of power distribution network for an isolated hybrid energy system located in a hilly area. In: 2020 International conference on power electronics & IoT applications in renewable energy and its control (PARC), pp 252–256
6. Suresh V, Muralidhar M, Kiranmayi R (2020) Modelling and optimization of an off-grid hybrid renewable energy system for electrification in a rural areas. *Energy Rep* 6:594–604
7. Mokhtara C, Negrou B, Bouferrouk A, Yao Y, Settou N, Ramadan M (2020) Integrated supply–demand energy management for optimal design of off grid hybrid renewable energy systems for residential electrification in arid climates. *Energy Convers Manage* 221:113192, 1–18
8. Zhang Z, Hua QS, Sun L, Liu Q (2020) Life cycle optimization of renewable energy systems configuration with hybrid battery/hydrogen storage: a comparative study. *J Energy Storage* 30(101470):1–9
9. Alshammari N, Asumadu J (2020) Optimum unit sizing of hybrid renewable energy system utilizing harmony search, Jaya and particle swarm optimization algorithms. *Sustain Urban Areas* 60(102255):1–11
10. Murugaperumal K, Srinivasn S, Satya Prasad GRKD (2020) Optimum design of hybrid renewable energy system through load forecasting and different operating strategies for rural electrification. *Sustain Energy Technol Assess* 37:100613, 1–17
11. Taheri P, Zahedi AR (2020) Techno-economic analysis of a renewable quadruple hybrid system for efficient water/biofuel production. *Sol Energy* 211:1053–1069
12. Baruah A, Basu M, Deeshank Amuley D (2021) Modeling of an autonomous hybrid renewable energy system for electrification of a township: a case study for Sikkim, India. *Renew Sustain Energy Rev* 135(110158):1–21
13. El-houari H, Allouhi A, Rehman S, Buker MS, Kousksou T, Jamil A, El Amrani B (2020) Feasibility evaluation of a hybrid renewable power generation system for sustainable electricity supply in a Moroccan remote site. *J Clean Prod* 277:123534

# Effective Control of Response of a Reinforced Concrete Building Under Seismic Loads Using Tuned Liquid Damper



Mukul Srivastava, Shailja Bawa, and Ujjwal Sharma

## 1 Introduction

Seismic tremor is a natural phenomenon related to the vicious oscillation of the ground. They are vibrations of the earth's surface brought about by unexpected developments of the earth's crust generally because of tectonic movements. Since seismic forces are arbitrary, the building devices must be sharpened to examine the building or structures below the action of these forces. Skyscraper structures are delicate against lateral loads produced because of wind and earthquake forces. To control the death toll and property, different techniques such as the shear wall, bracings, base isolation, and dampers can be adopted. This research aims to determine the best earthquake-resistant construction strategy by utilizing a water tank as a damping device in a high-rise structure. TLD is a modern technique. The study focusses to unravel the best earthquake-resistant design technique by installing the reinforced concrete tank on the terrace of the building, and by varying the water level, the optimum depth ratio is estimated and finding out the best tuning of the tank which can resist the dynamic vibrations.

The first installation took place at Nagasaki Airport Tower Nagasaki Japan, which is 42 m high. Reference [1] in 1987, a temporary implementation was done to check the efficacy of TLDs in minimizing structural vibration. He found with the use of 25 vessels of TLD, there was a reduction in the amplitude of vibration by 44% while the reduction in RMS displacement was approximately 35%. Fluid tanks are utilized to decrease the aerodynamic forces, specifically the torque component which causes unsteadiness during the development of long-range span bridges [2, 3]. Reference [1] Installed 1400 TLD filled with water and floating polyethylene

---

U. Sharma  
RAMA University, Kanpur, Uttar Pradesh 209217, India

M. Srivastava (✉) · S. Bawa  
Dr. B.R. Ambedkar National Institute of Technology, Jalandhar, Punjab 144011, India

particles on Tokyo Airport Tower of height 77.6 m to improvise the energy loss and to verify the TLD behaviour under various wind phenomenon. The cylindrical-shaped containers with radii of 0.3 m and 0.0625 m, respectively, were placed in six layers above steel consoles. The overall mass of the TLD was about 3.5% of the present modal mass, and its frequency increased to 0.74 Hz. This analysis revealed a decline in the root mean square (RMS) acceleration by almost 60% at a top speed by 25 m/s. Reference [4] mounted the tuned sloshing damper (TSD) on two actual high steel towers which were subjected to wind, i.e. on Nagasaki airport (42 m high) and Marine tower (101 m high) of Yokohama to enhance the serviceability of the towers and found the displacement became nearly half upon the installation of TSD. Reference [5] performed experiments to find the properties of TLDs with rectangular, circular, and annular tanks. The tanks were filled with liquids differing in viscosities along with varying amplitude and frequency which were exposed to harmonic base excitation. Using the TMD equivalence, the parameters for TLD were calibrated by using experimental results [6]. Numerical experiments have been performed to explore the impact of simultaneous usage of liquid dampers adjusted to various frequencies in a multi-degree-freedom system. The findings suggest that the usage of dampers calibrated to multiple vibration modes of the system is advantageous. In [7] prolonged the idea for dissipating the tsunami wave energy by providing a sloped-bottom tank. Results showed that the sloshing related with a sloped-bottom base TLD and contrasted it with a box-shaped TLD. 300 sloped bottom base TLD was considered and identified to act as a softening spring against a box-shaped TLD that acts as a hardening spring. The sloped-bottom base TLD was found to be particularly effective when tuned slightly above the system's natural frequency. However, they had an issue relating to the sloping bottom base of the TLD because moment with high magnitude developed at the TLD base. Reference [8] studied a 2-D finite element analysis. This study was done to understand the dynamic analysis of a rectangular tank filled with liquid with baffles. The work is based on the concepts of linear water wave theory and the velocity potential formulation. The liquid slosh frequencies in the rectangular tank were determined with and without baffles. It was assumed the tank baffle framework was rigid. The slosh frequencies were calculated at different positions and dimensions of the baffle. The response of sloshes was studied when subjected to steady-state sinusoidal base excitation. Reference [9] performed a shake table test to determine the characteristics of TLD (rectangular and circular) and TLCD water sloshing. Analysis of different dynamic parameters like energy dissipation, base shear, and height of the wave, etc. were performed and reported that the TLCD was more effective over to TLD for controlling the oscillation. Reference [10] work includes finite element modelling, analysis, and experimental verification of two-storied buildings to inspect the natural frequencies followed by the mode shapes on ANSYS workbench. Damping of the structure reduces the water level inside the tank which gives a boost in the liquid sloshing, wave development, and breaking reduces since the entire mass of water is not contributing in the sloshing motion. By incorporating TLD on structure, dampness increases with mass ratio and found TLD as an effective damper for controlling the vibration. Reference [11] performed

experimental and analytical analysis. In experimental work, a prototype reduced to one-sixth scale having three bays and four storeys with a water tank kept on the top floor and constructed monolithically, and a 4-storey RC frame structure was analysed and designed on ETABS. They used various mass ratios 0, 1, 2, 2.5, and 3% and suggested it as an effective damping device to mitigate the seismic response, and also, there is no time lag. It was shown that the corresponding response acceleration decreased twice when the mass ratio ranged between 2 and 2.5%, while the response deflection decreased by 1.8 times. The researcher also proved that the concrete demand is increasing day by day as a best suitable material [12, 13]. Reference [14] conducted an experimental comparison on a scaled three-storey steel structure by three different passive dampers which consist of a tuned liquid column damper (TLCD), TMD, and TLD. Reference [15] the efficacy of a liquid column vibration absorber (LCVA) and TLCD under optimal design is studied in this paper in the suppression of structural rotational motions during excitation of white noise. The implications of diverging from the ideal configuration under white noise and the influence of the excitation strength are also discussed. For a structure with a damper, the analytical model is first developed. The non-linear regulation of the liquid column's relative motion equation is linearized, and the issue is assessed in the frequency zone. The way for finding the optimum estimate for the tuning ratio  $f$  and the coefficient of head loss coefficient  $\xi$  are studied and implemented taking into account the complications caused by the previous non-linear type of the governing equations. Through an extensive parametric study, controlled LCVA and TLCD output with optimum values of  $f$  and  $\xi$  is investigated numerically. At last, the consequences of  $f$ ,  $\xi$ , and the severity of the excitation are addressed. The position of the damper in relation to the rotational axis plays an important role in determining the reduction of the rotational vibration, and that LCVA is more flexible in relation to its location in relation to the structure by choosing the vertical to horizontal tube segment area correctly. Reference [16] the value of optimum frequency can be estimated on the basis of results of static and harmonic analysis. Reference [17] examined the effectiveness of installation of a water tank and a rooftop frame as a passive TMD and discussed the behaviour of structure by incorporating a water tank as a TMD using a non-linear time history model to minimize the structural responses in full and half-tank form in ETABS. The base shear value decreased by almost 15%, and the displacement value decreased by an average of 14% when using a TLD. Reference [18] performed numerous tests to investigate the system's dynamic actions when exposed to free vibration by linking accelerometers with the TLD-TMD device located. The research was performed both experimentally and using the SAP 2000 system. An accelerometer connection is used to vibrate a building model with and without a damper unit and a time-acceleration plot was achieved using the LabVIEW. In the experimental study, the natural frequency and mode form of the system matched the findings obtained from the program and claimed that damper is able to adjust the frequency. In the analytical approach (SAP 2000), a 30-storied structure with and without damper was modelled and the time history research was performed on specific stiffness ranging from 500 to 4500 KNm, and after conducting a normal

mode analysis of the system with TMD-TLD tanks, upon performing the normal mode study of the system by means of TMD-TLD tanks, the structural frequency improved with the rise in stiffness values, rendering it less susceptible to seismic forces, and the optimal natural frequency of 3500 KNm was determined. Reference [19] in this analysis, a 25-storey and 78 m tall irregular RC building have been considered. Analysis and modelling of the frames were done on FEAST. They performed a comparative analysis of TLDs relating to the various mass ratios varying from 0.5 to 3.5% and found at a mass ratio of 1.5% to be the most ideal situation for systemic damping and economics.

## 1.1 TLD

The TLD comprises of a tank which is filled with liquid. Like a TMD, it indirectly damps the structure thus raising the response. Energy losses take place by a number of mechanisms: the viscous motion of the fluid, the breaking of the flow, the mixing of the free surface with beads, as well as the structure and roughness of the wall of the container. However, unlike a TMD, a TSD uses a transfer function which is amplitude dependent based that is incorporated through non-linear sloshing and breaking of liquid.

Applying TLDs to diminish the structural vibration in the structural building started in the mid-1980s by [20] who gave the idea for the utilization of a rectangular-shaped container filled with two immiscible fluids to narrow down the dynamic responses. [4, 21, 22] were likewise among the first to propose the utilization of dampers using fluid movement for building. The fundamental idea on which this damper works depends on the sloshing of fluids for which these are now and then termed as tuned sloshing damper (TSDs).

TSDs are a commonly rectangular or circular type shaped tank and are placed on the top floor as per building type and the purpose of vibration control.

For externally excited low-magnitude vibration, shallow water shows an enormous damping effect. However, it is a real challenge to analyse the system for under an external excited vibration of high magnitude. The sloshing of water inside the tank shows non-linear behaviour due to the deepwater [21, 22]. At the point when frequency of the tank movement is near one of the normal frequencies of tank liquid, a huge sloshing amplitude can be observed. If the two frequencies get equalled, resonance will happen. Tuning the TLD's fundamental sloshing frequency to the structure's natural frequency usually induces a considerable amount of sloshing and wave breakage at the resonant frequencies of the integrated TLD-structure device which dissipates substantial amount of energy [23].

## 2 Proposed Algorithm

### 2.1 TLD Behaviour

TLD normally comprises a tank filled partially with fluid (generally water), often rectangular or circular. The fluid carried in a TLD behaves as the secondary mass and gravity imparts the spring force. Tuning of TLD is made in such a manner so that the fundamental frequency of TLD is nearly equivalent to the natural frequency of the structure on which TLD is installed so that it can lessen the dynamic response.

Most of the energy loss in TSDs is due to wave activity, and it may be expanded with the application of lattice screens and unevenness of the wall. TSDs can be introduced as huge tanks (usually from 1 to 4) or in a few little units that can be introduced as a progression of stacks. Designing a TLD for the non-linear response is still a big challenge. TLD may be categorized as either shallow, intermediate, or deep water according to the depth ratio. In shallow water, a large proportion of fluid takes part in the sloshing motion ( $d_{TL} = L_{TL}$  less than 0.1) ( $d_{TL}$  = liquid depth and  $L_{TL}$  = length of the tank), and it uses breaking of wave as the essential component for energy loss. Commonly, numerous tanks are required to meet the required mass and the behaviour of a shallow-water TLD.

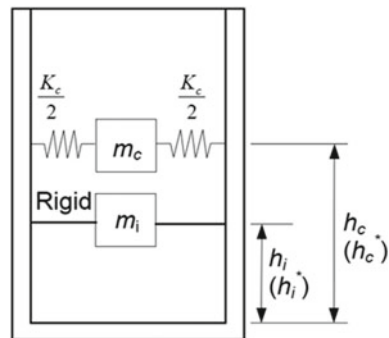
### 2.2 Methodology

A TLD is represented as a spring dashpot model system (Fig. 1).

where

$h_c^*$  = Convective mass height above the tank wall bottom (without taking into account the base pressure).

**Fig. 1** Spring-mass analogy for TLD





$h_i^*$  = Impulsive mass height above the tank wall bottom (without taking into account the base pressure).

$m_c$  = Convective mass of liquid.

$m_i$  = Impulsive mass of liquid.

$K_c$  = spring stiffness for the convective mode.

**Depth ratio ( $d_r$ ):** Ratio of tank depth to tank length in the direction of sloshing. The proportion of convective mass to the impulsive mass of water is contrarily identified with the depth ratio.

### 2.3 TLD Modelling

The TLD is modelled by the water requirement of the people in the building. Here, the TLD is displayed as a spring-mass framework as indicated in IS1893 section 2. The design curves present in the IS code is utilized for design purposes. As the lateral forces strike the liquid-containing tank with a free top, the wall of tank and fluid are exposed to horizontal acceleration. The fluid in the bottom of the tank serves as a rigid mass that is rigidly bounded to the wall of the tank, and this mass is referred to as an impulsive fluid mass that accelerates along the tank wall and creates hydrodynamic pressure on the wall along with the tank base. The top portion of the fluid mass experiences a sloshing movement; this mass is termed as convective fluid mass, and it applies convective hydrodynamic pressure on the tank wall and base. In this manner, fluid mass gets distributed into two parts, i.e. impulsive and convective mass. In the spring-mass model of a tank-fluid framework, these two fluid masses are illustrated in Fig. 1 [24]. Figure 2 illustrates the qualitative distribution of impulsive and convective hydrodynamic pressure on the wall and base of the tank respectively [25]. The tank capacity is maintained same with all depth ratios, and the necessary water levels are carried out according to its tank size. The study is carried out on four depth ratios of 0.2%, 0.3%, 0.4%, and 0.5%, respectively. As TLD is designed in a square-shaped tank so, only unidirectional analysis is necessary, and hence only the sloshing action will counteract the lateral forces (Tables 1, 2 and 3).

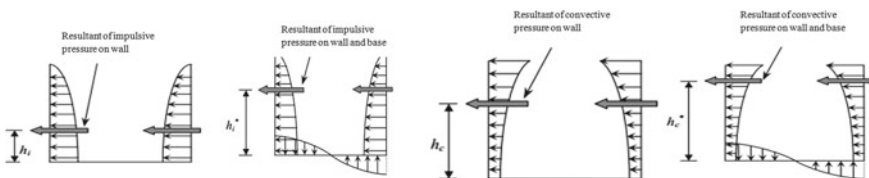


**Fig. 2** Qualitative explanation of the application of hydrodynamic pressure on the tank wall and base

**Table 1** Modelling structure description and detailing

Description	Detailing
Number of floors	G + 15 + 1 basement
Number of flats on each floor	6
Number of members in a family	6 (assumed)
Water demand per capita	150 L per capita per day (assumed)
Capacity of the tank	86.4 m <sup>3</sup>
Thickness of tank wall	150 mm (assumed)

**Table 2** TLD parameters for 0.2% of depth ratio

Parameters	Values
Total weight of liquid (KN)	847.584
Mass of water (kg)	86,400
Height of the water tank (H) (m)	2.1133412
Maximum sloshing wave height ( $d_{max}$ ) (m)	0.601436
$m_c$ (KN)	625,893.9
$h_i^*$ (m)	3.085422
$m_i$ (KN)	195,679
$h_c^*$ (m)	4.360091
$k_c$ (N-m)	146,147.5

Assuming the initial depth ratio ( $h/L$ ) as 0.2%

$$\frac{m_c}{m} = 0.738445 \quad \frac{m_i}{m} = 0.230867 \quad \frac{h_i^*}{h} = 2.040751$$

$$\frac{h_c^*}{h} = 2.883839 \quad \frac{k_c h}{mg} = 0.260695.$$

The above values can be calculated from Fig. 3 of IS 1893:2002 part 2, or it can be calculated by using the formula suggested by [25].

As the convective height ( $h_c^*$ ) of water is higher than the height of the water tank ( $H$ ), the new height of the tank should be higher than the convective height.

So, the final height of the tank

$$(H') = h_c^* + d_{max} = 4.961527 \tag{1}$$

The sloshing height is added so that the water does not spill out of the tank, and sloshing height also acts as a freeboard for the tank.

Similarly, the parameters for other depth ratios are given in Table 3.

By using the above parameters, the tank is modelled. Tank wall comprises of concrete with M25 grade, and two different linear link elements should be defined: one for the impulsive mass and the second one for convective mass.

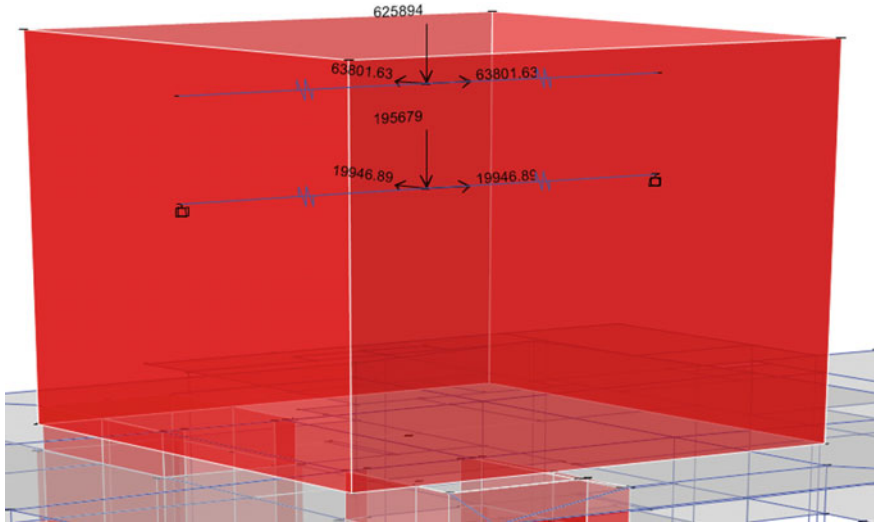


**Fig. 3** Representation of joint forces and joint mass in TLD with 0.2% of depth ratio

**Table 3** Parameters for TLD at different depth ratios

Parameters	Depth ratios			
	0.20%	0.30%	0.40%	0.50%
Water level ( $h$ ) (m)	1.511905	1.981156	2.4	2.784953
Length of tank c/c ( $L'$ ) (m)	7.709526	6.753854	6.15	5.719907
Height of tank ( $H'$ ) (m)	4.961527	3.508997	2.87736	3.228095
$m_i$ (KN)	195,679	291,800	381,317.7	459,658.6
$m_c$ (KN)	625,893.9	551,108.5	476,704.7	411,096.7
$h_i^*$ (m)	3.085422	2.629662	2.367332	2.219528
$h_c^*$ (m)	4.360091	2.983595	2.515384	2.390292
$k_c$ (N-m)	146,147.5	194,559.5	213,629.9	213,926.5

Joint mass is allocated with values  $m_c$  and  $m_i$  in the X and Y direction, and the joint force is allocated with values  $m_c$  and  $m_i$  in Z direction as shown in Fig. 3. Plan of building is shown in Fig. 4a, and its 3D view is shown in Fig. 4b (Table 4).

### 3 Experiment Results

ESA and THA have been performed in ETABS software. El Centro 1940-05-19 earthquake of PGA (peak ground acceleration) 0.348 g in the Imperial Valley in Southern California is used for THA.

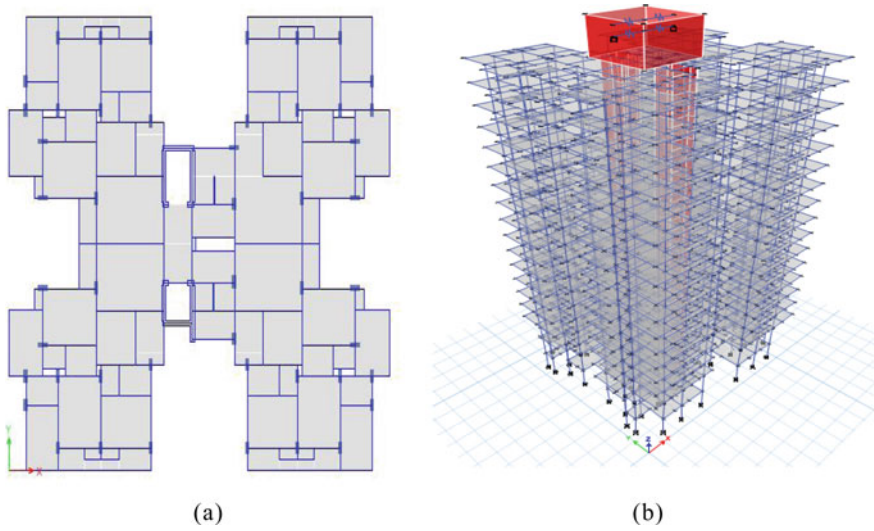


**Fig. 4** a Plan of the building under consideration, b 3-D View of the Structure with TLD

### 3.1 Base Shear

Figure 5 shows that the setting up of the TLD at the top floor diminishes the base shear in a significant amount around 44% in the X direction and 49% in the Y direction for all depth ratios.

### 3.2 Maximum Storey Displacements

Figure 6 analysis by ESA shows that the coupling of TLD at the terrace shows a significant reduction with all depth, and TLD with depth ratios of 0.3 and 0.5% showing the maximum reduction in ranging from 44 to 100%; however, by THA analysis, TLD with 0.2% of depth ratio raises the storey displacement abruptly by more than 380% as compared to the structure without TLD as shown in Fig. 7, while TLD with depth ratios of 0.3%, 0.4%, and 0.5% shows almost same reduction ranging from 59 to 69%, respectively.

### 3.3 Storey Drift

As from Fig. 8, analysis by the ESA approach structure without TLD crosses the permissible limit for some floor as per IS 1893 part 1, but with the introduction of

**Table 4** Description of building under consideration

Serial number	Building description									
1	Number of storeys	G + 15 and 1 Basement								
2	Height of the building	55.43 m								
3	Plan area of the building	26.66 m × 23.42 m								
4	Type of soil	Medium soil								
5	Seismic Zone	IV								
6	Response reduction factor	5								
7	Importance factor	1								
8	Thickness of slab	150 mm								
9	Shear wall thickness for lift core	300 mm								
10	Grade of concrete for shear wall	M25								
11	Size of beam	<table border="1"> <tr> <td>Storey 1 to terrace</td> <td>230 mm × 450 mm</td> </tr> <tr> <td>Basement to ground storey</td> <td>230 mm × 850 mm (outer beams)</td> </tr> <tr> <td>Basement to ground storey</td> <td>230 mm × 550 mm (for interior beam with span &lt; 3 m)</td> </tr> <tr> <td>Basement to ground storey</td> <td>300 mm × 550 mm (for interior beam with span &gt; 3 m)</td> </tr> </table>	Storey 1 to terrace	230 mm × 450 mm	Basement to ground storey	230 mm × 850 mm (outer beams)	Basement to ground storey	230 mm × 550 mm (for interior beam with span < 3 m)	Basement to ground storey	300 mm × 550 mm (for interior beam with span > 3 m)
Storey 1 to terrace	230 mm × 450 mm									
Basement to ground storey	230 mm × 850 mm (outer beams)									
Basement to ground storey	230 mm × 550 mm (for interior beam with span < 3 m)									
Basement to ground storey	300 mm × 550 mm (for interior beam with span > 3 m)									
12	Grade of concrete for beam	M25								
13	Size of Column	<table border="1"> <tr> <td>Basement to storey 1</td> <td>400 mm × 750 mm 750 mm × 400 mm</td> </tr> <tr> <td>Storey 2 to terrace</td> <td>300 mm × 750 mm 750 mm × 300 mm</td> </tr> </table>	Basement to storey 1	400 mm × 750 mm 750 mm × 400 mm	Storey 2 to terrace	300 mm × 750 mm 750 mm × 300 mm				
Basement to storey 1	400 mm × 750 mm 750 mm × 400 mm									
Storey 2 to terrace	300 mm × 750 mm 750 mm × 300 mm									
14	Grade of concrete for column	M35								
15	Grade of steel	Fe500								
16	Damping ratio	5%								
17	Thickness of slab	150 mm								
18	Shear wall thickness for lift core	300 mm								
19	Grade of concrete for shear wall	M25								

TLD on terrace, storey drift narrows down and are within the permissible limit; however, by THA analysis, TLD with a depth ratio of 0.2% abruptly raises the storey drift as compared to the normal structure though the storey drift is in the permissible limit still it raises the storey drift in a very huge amount as compared to the normal structure ranging from 280 to 5476% (see Fig. 9) which is an undesirable effect.

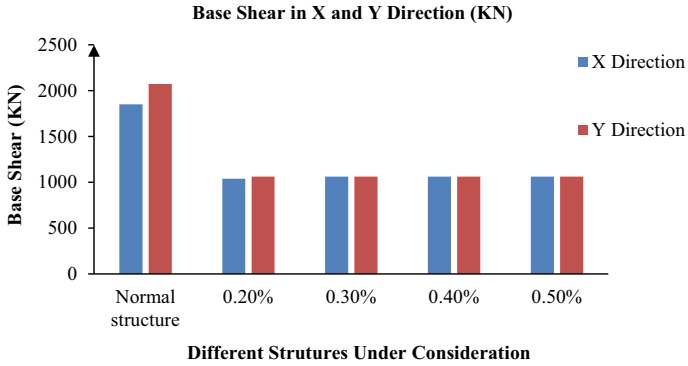


Fig. 5 Variation of base shear in X and Y direction

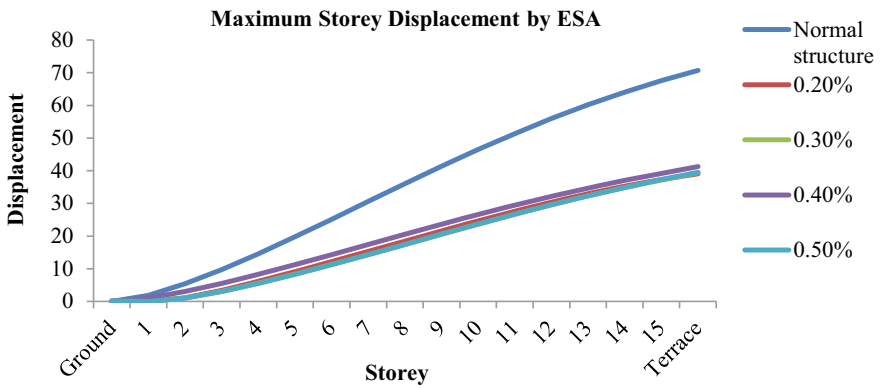


Fig. 6 Plot of storey displacement by equivalent static analysis

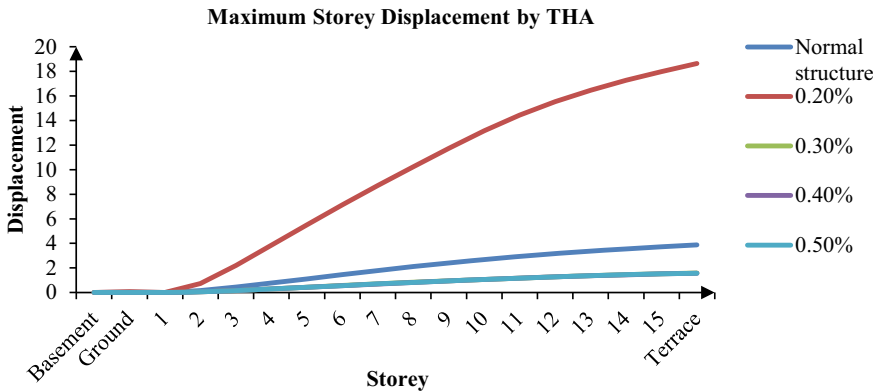


Fig. 7 Plot of storey displacement by time history analysis

### 3.4 Spectral Displacement

To compare the spectral displacement of all the arrangements, displacements of each arrangement at 5% of critical damping are taken into account. From Fig. 10, it is observed that spectral displacement of TLD with a depth ratio of 0.2% is drastically greater than the normal structure which is an unappealing result. TLD with other depth ratios is less than the normal structure. Hence, TLD with 0.3%, 0.4%, and 0.5% of depth ratios decreases the spectral displacement in notable amount.

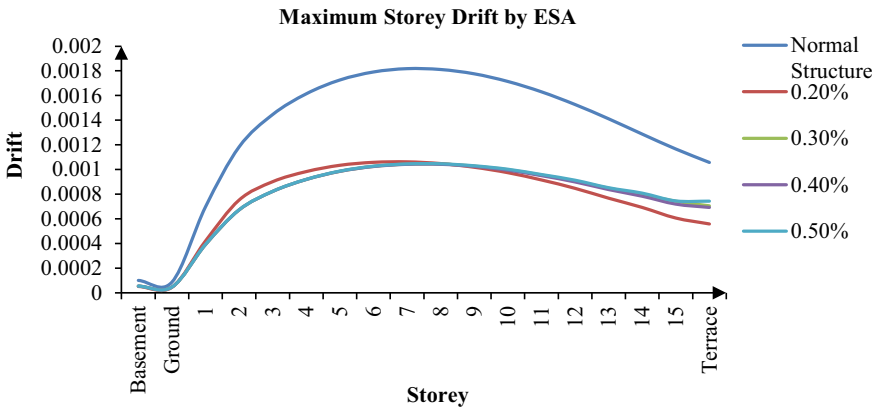


Fig. 8 Plot of storey drift by equivalent static analysis

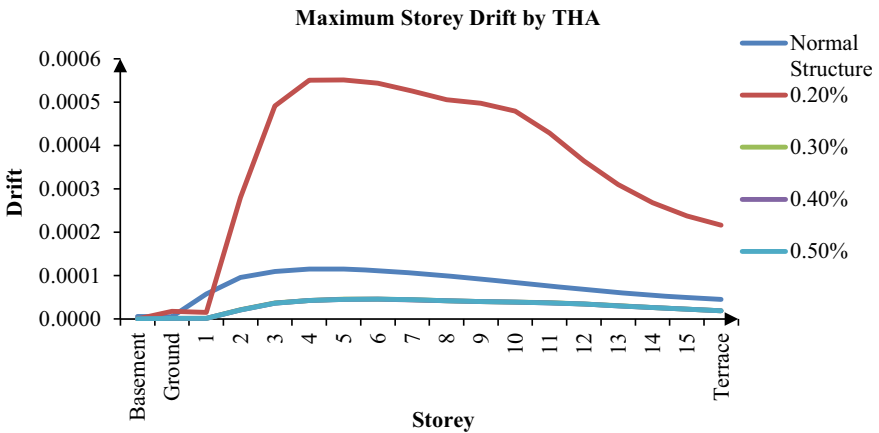


Fig. 9 Plot of storey drift by time history analysis

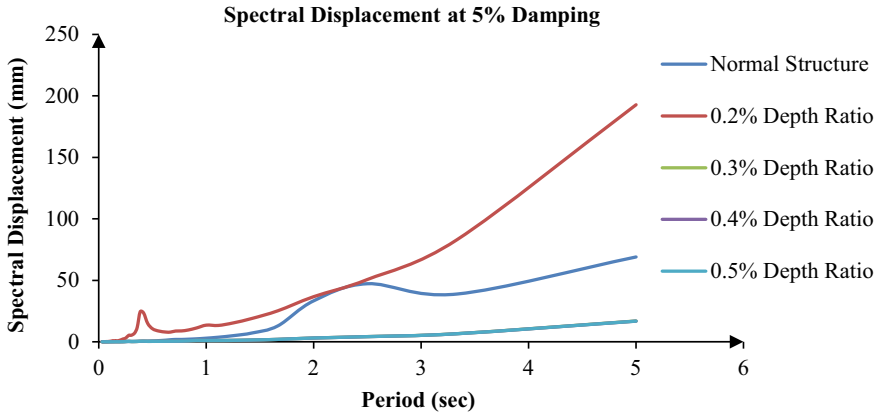


Fig. 10 Comparison of spectral displacement of different models at 5% of critical damping

### 3.5 Spectral Acceleration

To compare the spectral acceleration of all the arrangements, accelerations of each arrangement at 5% of critical damping are taken into account. From Fig. 11, it is observed that spectral acceleration of TLD with a depth ratio of 0.2% is too high than the normal structure which is an unappealing result. Hence, 0.2% depth ratio is not an optimum depth ratio while TLD with other depth ratios have a very small difference between them and are also less than the normal structure, so they can be used as a damper.

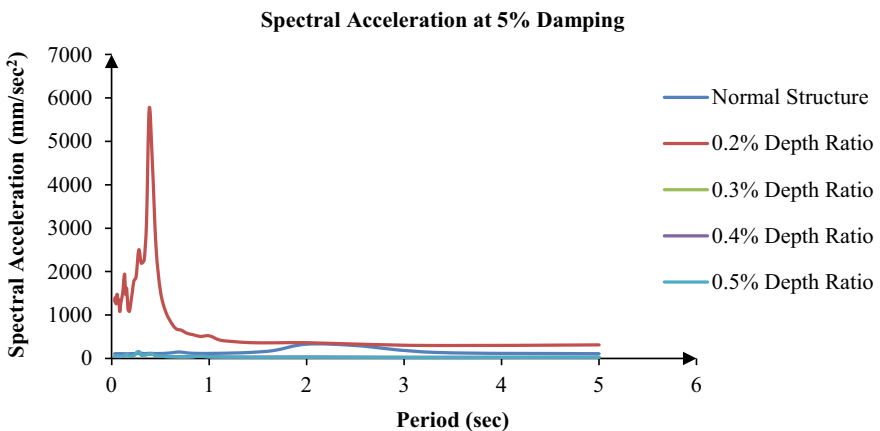


Fig. 11 Comparison of spectral acceleration of different models at 5% of critical damping



## 4 Result Analysis

On comparing the analytical results with the predicted results, the variation between the results is minimal.

## 5 Conclusion

Installing the TLD on the terrace, the seismic efficiency of the structure has been significantly improved. ESA method shows that installation of TLD narrows down the base shear, maximum storey displacement, and storey drift in a significant amount with all the depth ratios. But by THA analysis, TLD with 0.2% of depth ratio abruptly increases the above parameters. The spectral displacement and spectral acceleration with 0.3, 0.4, and 0.5% of depth ratios at critical damping of 5% found to be reduced in a significant amount as compared to the normal structure. While with a 0.2% of depth ratio, these parameters increases significantly as compared to the normal structure. TLD performed very well in almost every aspect. So TLD with 0.3–0.5% of depth ratio can be opted as the optimum depth ratio for the normal structure. TLD with a 0.2% depth ratio should never be recommended for the normal structure; otherwise, it will cause an adverse effect on structural integrity. The static approach received higher displacement values than the dynamic method, so dynamic analysis for high-rise structures should be executed to achieve reliable results.

## 6 Future Scope

This research can be extended to study the behaviour of TLD of different shapes interconnected with each other. TLD combinations with different passive dampers can also be used for the study, and this study can also be performed on an irregular structure.

## References

1. Tamura Y, Fujii K, Ohtsuki T, Wakahara T, Kohsaka R (1995) Effectiveness of tuned liquid dampers under wind excitation. *Eng Struct* 17:609–621. [https://doi.org/10.1016/0141-0296\(95\)00031-2](https://doi.org/10.1016/0141-0296(95)00031-2)
2. Hoang N, Fujino Y, Warnitchai P (2008) Optimal tuned mass damper for seismic applications and practical design formulas. *Eng Struct* 30:707–715. <https://doi.org/10.1016/j.engstruct.2007.05.007>
3. Ueda T, Nakagaki R, Koshida K (1992) Suppression of wind-induced vibration by dynamic dampers in tower-like structures. *J Wind Eng Ind Aerodyn* 43:1907–1918. [https://doi.org/10.1016/0167-6105\(92\)90611-D](https://doi.org/10.1016/0167-6105(92)90611-D)

4. Fujii K, Tamura Y, Sato T (1990) Wind induced vibration of tower and practical applications. *J Wind Eng Ind Aerodyn* 33:263–272
5. Sun LM, Fujino Y, Chaiseri P, Pacheco BM (1995) The properties of tuned liquid dampers using a TMD analogy. *Earthq Eng Struct Dyn* 24:967–976. <https://doi.org/10.1002/eqe.4290240704>
6. Koh CG, Mahatma S, Wang CM (1995) Reduction of structural vibrations by multiple-mode liquid dampers. *Eng Struct* 17:122–128. [https://doi.org/10.1016/0141-0296\(95\)92643-M](https://doi.org/10.1016/0141-0296(95)92643-M)
7. Gardarsson S, Yeh H, Reed D (2001) Behavior of sloped-bottom tuned liquid dampers. *J Eng Mech.* [https://doi.org/10.1061/\(asce\)0733-9399\(2001\)127:3\(266\)](https://doi.org/10.1061/(asce)0733-9399(2001)127:3(266))
8. Biswal KC, Bhattacharyya SK, Sinha PK (2003) Free-vibration analysis of liquid-filled tank with baffles. *J Sound Vib* 259:177–192. <https://doi.org/10.1006/jsvi.2002.5087>
9. Kim YM, You KP, Cho JE, Hong DP (2006) The vibration performance experiment of tuned liquid damper and tuned liquid column damper. *J Mech Sci Technol* 20:795–805. <https://doi.org/10.1007/BF02915943>
10. Kartha RV, Ritzy R (2015) Tuned liquid damper to control earthquake response in a multi-storied building frame. *Int J Eng Res Appl* 5:49–56. [www.ijera.com](http://www.ijera.com)
11. Ahmad MJ, Khan QZ, Ali SM (2016) Use of water tank as tuned liquid damper (TLD) for reinforced concrete (RC) structures. *Arab J Sci Eng* 41:4953–4965. <https://doi.org/10.1007/s13369-016-2188-1>
12. Sharma U, Gupta N, Saxena KK (2020) Static and harmonic analysis of a fiber reinforced polymer guyed segment. *Mater Today Proc.* <https://doi.org/10.1016/j.matpr.2020.06.211>
13. Gupta N (2019) Sustainability of Brick Kiln dust as a partial replacement to cement in different grades of concrete. *Int J Res Appl Sci Eng Technol.* <https://doi.org/10.22214/ijraset.2019.4058>
14. Bigdeli Y, Kim D (2016) Damping effects of the passive control devices on structural vibration control: TMD, TLC and TLCD for varying total masses. *KSCE J Civ Eng* 20:301–308. <https://doi.org/10.1007/s12205-015-0365-5>
15. Ruiz RO, Taflanidis AA, Lopez-Garcia D (2016) Characterization and design of tuned liquid dampers with floating roof considering arbitrary tank cross-sections. *J Sound Vib* 368:36–54. <https://doi.org/10.1016/j.jsv.2016.01.014>
16. Yadav S (2019) Static and harmonic analysis of a fiber reinforced polymer guyed segment. *Int J Res Appl Sci Eng Technol.* <https://doi.org/10.22214/ijraset.2019.4118>
17. Manjusha M, Saathappan V (2017) Analytical investigation of water tank as tuned mass damper using etabs 2015:1622–1624
18. Jacob NV, Mariyam Varkey M, Michael J, Reji NM, Philip EV, Mathew EA (2018) Study of combined action of coupled tuned liquid and mass damper on earthquake response of buildings. *Int Res J Eng Technol* 5:755–762. [www.irjet.net](http://www.irjet.net)
19. Varkichan NT, Sandeep TN, Engineering TS, Ernakulam S (2019) Effective control of response of a building under wind vibration using tuned liquid dampers 5248–5253
20. Bauer HF (1984) Oscillations of immiscible liquids in a rectangular container: a new damper for excited structures. *J Sound Vib* 93:117–133. [https://doi.org/10.1016/0022-460X\(84\)90354-7](https://doi.org/10.1016/0022-460X(84)90354-7)
21. Modi VJ, Welt F (1988) Damping of wind induced oscillations through liquid sloshing. *J Wind Eng Ind Aerodyn* 30:85–94. [https://doi.org/10.1016/0167-6105\(88\)90074-8](https://doi.org/10.1016/0167-6105(88)90074-8)
22. Kareem A (1990) Reduction of wind induced motion utilizing a tuned sloshing damper. *J Wind Eng Ind Aerodyn* 36:725–737. [https://doi.org/10.1016/0167-6105\(90\)90070-S](https://doi.org/10.1016/0167-6105(90)90070-S)
23. Shang CY, Zhao JC (2008) Periods and energy dissipations of a novel TLD rectangular tank with angle-adjustable baffles. *J. Shanghai Jiaotong Univ* 13 E 139–144. <https://doi.org/10.1007/s12204-008-0139-z>
24. F.C. Only, Indian Standard, 1893 (2006)
25. Jaiswal OR, Jain SK (2005) Modified proposed provisions for aseismic design of liquid storage tanks : Part II commentary and examples. 32:297–310

# A Review on Tribo-Mechanical Behaviour and Corrosion Performance of AA8000 Based Composites



Rajesh Sharma , Mohan K. Pradhan , and Pankaj Jain 

## 1 Introduction

At present in worldwide, there is a rise of demand for the advanced materials so as to get desired properties. Composite materials are those materials which are made from two or more chemically different constituents combined macroscopically to yield a useful material. According to the matrix material, there are primarily three types of composites: polymer matrix composites, metal matrix composites and ceramic matrix composites [1]. Aluminium metal matrix composites (AMMCs) are the materials in which aluminium metal is used as matrix material reinforced with other materials [2]. Reinforcement may be in continuous and discontinuous form, i.e., whiskers, particulates, fibres.

Without affecting ductility, nanosized reinforcements will greatly boost mechanical strength, creep resistance at high temperatures, improved machinability and greater fatigue life. Improvement in the properties of composites is attributed to the hardening mechanism, particle size, uniform distribution, inter particle spacing and thermal stability at high temperature [3, 4]. Fabrication method adopted in manufacturing any composite plays an important role in determining the ultimate properties of the composite. Stir casting and powder metallurgy, which are used also in commercial applications, are the most common process used in the production of AMCS.

Because of their strong physical and chemical properties, such as formability, corrosion, lightweight, and also because it is possible to control the microstructural composition of the alloy by means of specific thermal and mechanical treatments, the aluminium alloy 8xxx series has found wider application in the construction and

---

R. Sharma (✉) · P. Jain  
University Institute of Technology, RGPV, Bhopal, India  
e-mail: [pankaj@rgtu.net](mailto:pankaj@rgtu.net)

M. K. Pradhan  
Maulana Azad National Institute of Technology, Bhopal 462003, India

**Table 1** Chemical composition of series 8xxx aluminium alloys

Author	Alloy	Fe	Si	Mn	Zn	Cu	Ti	Cr	Mg	Other	Li	Al
Shankar et al. [6]	8011	1.0	0.9	0.2	0.1	0.1	0.08	0.05	0.05	–	–	Bal
Moldovan et al. [7]	8006	1.2 2.0	Max 0.4	0.3 1.0	Max. 0.1	Max. 0.3	–	–	Max. 0.1	Max. 0.05		Bal
Guo et al. [8]	8030	0.67	0.047	–	0.001	0.25	–	–	0.001	0.001	–	Bal
Patil et al. [9]	8081	0.70	0.70	–	0.1	0.005	0.7– 1.3	–	–	–	–	Bal
Markovina et al. [10]	8090	0.05	0.02	0.001	–	1.32	–	–	0.65	–	2.37	Bal
Smyraka et al. [11]	8176	0.25– 0.45	0.1	–	0.05	0.04	–	–	0.04– 0.12	0.03	–	Bal

automotive industries [5]. From the literature review, it has been found that most work has been devoted towards 6xxx series and 7xxx series aluminium matrix composites. Besides this, aluminium alloys of the 8xxx series were not commonly used by researchers for the production of composites. Present work aims to find potential applications for 8006, 8009, 8011, 8030, 8081, 8090, 8091, 8176 aluminium alloy. The chemical composition of 8xxx series aluminium alloys is given in Table 1.

## 2 Review Literature

The objective of this paper is to review the reinforcement particles on tribo-mechanical behaviour and corrosion response and the effect of the manufacturing method on aluminium matrix composites, as experienced by various researchers.

### 2.1 Mechanical Properties

There have been comprehensive studies by researchers related to the mechanical properties of aluminium hybrid metal matrix composites. From the literature, it has been exhibited that the mechanical properties of the composites are enhanced with a higher percentage of reinforcement content and also that the mechanical properties of composites depend on the type, weight %, size of reinforcement and also the method of fabrication. Mechanical properties' viz. tensile strength, compressive strength, hardness, toughness, fatigue life, resistance to corrosion, wear resistance and machinability are greatly improved by reinforcement. Additionally, it has been reported that the aforementioned properties further enhance, if there is a hybridization of the reinforcement. The mechanical properties of AA8011 based metal matrix composites are summarized in Table 2, and for AA8xxx other than AA8011, composites reported in the literature are depicted in Table 3.

**Table 2** Mechanical properties of AA8011 based metal matrix composites

Authors Alloy/composite Vol./wt%, particle size	Methods	Result with maximum percentage reinforcement
Fayomi et al. [12] AA8011/ nano-ZrB <sub>2</sub> + Si <sub>3</sub> N <sub>4</sub> Up to 20% in a step of 5	Mechanical test (UTS, YS, hardness)	With 20% composite has better strengthening mechanism & excellent yield propagation
Fayomi et al. [13] AA8011/ nano-Si <sub>3</sub> N <sub>4</sub> up to 20% in a step of 5	Mechanical Test (UTS, YS, Hardness)	AA8011-20% UTS:185.8, YS:144.95 MPa Hardness: 55.86
Fayomi et al. [14] AA8011 nano-ZrB <sub>2</sub> 0–20 wt%	Mechanical test (UTS, YS, hardness)	UTS: 221.6(Max. at 20%) YS: 172.87 MPa Hardness: 66.62
Fayomi et al. [15] AA8011 ZrB <sub>2</sub> – Si <sub>3</sub> N <sub>4</sub> 0–20 wt%, 40– 50 nm	Mechanical test (UTS, YS, hardness)	Mechanical strength of AA8011 –20 wt% composite is superior to those of the 5, 10 and 15 wt%
Vembu et al. [16] AA8011 SiC-15%/ 23μ	Effect of ageing behaviour on mechanical properties	Peak-aged condition 5 h at 170 C TS:257, YS:226, 65 HN
Chandrasekar et al. [17] AA8011 TiC,WC, B <sub>4</sub> C,ZrC 8 wt% each, 44μ	Mechanical test (Vickers hardness, UTM)	Max.8wt%(B <sub>4</sub> C) HV 131, UTS 430Mpa
Cui et al. [18]	Cryogenic rolled for six passes & then annealed	TS, YS, Hardness are all improved TS: 202 MPa, 65HV
Harshavardhan et al. [19] AA8011 Rmp 4-16wt% Particle size average 90μ	Mechanical test (fracture toughness) Maximum load and K <sub>1c</sub> for 16%Rmp SENB CT/SENB specimen	12%Rmp CT specimen Pmax-2.745 kN, K <sub>1c</sub> -18.492 Pmax-3.539 kN, K <sub>1c</sub> -15.721
Rao et al. [20] AA8011 Rmp 4–20 wt% 90,120,180μ	Mechanical test (TS, CS & hardness)	TS increased by 24.45% at Al. 14 wt% Rmp90 HN Al 20 wt%Rmp180 CS-14 wt% Rmp90
Anil et al. [21] AA8011 GRp 2–8%	Mechanical test (TS, CS, hardness)	Max. with 8 wt% TS: 160.09Mpa,CS:78.50 Mpa 34.87 BHN
Kandan et al. [22] AA8011 B <sub>4</sub> C/ Al <sub>2</sub> O <sub>3</sub>	Mechanical test (TS, CS & microhardness)	Achieved maximum strength at 5% B <sub>4</sub> C/ 5% Al <sub>2</sub> O <sub>3</sub>

(continued)

**Table 2** (continued)

Authors Alloy/composite Vol./wt%, particle size	Methods	Result with maximum percentage reinforcement
Karthikkumar et al. [23] AA8011 B4C < 10 $\mu$ 3 wt% RMp 150 $\mu$ 3 wt%	Mechanical test (TS, CS & microhardness)	TS 77.024 MPa, CS 76.877 MPa YS 59.973 Mpa, 45.4 HV
Shankar et al. [6] AA8011 GRp 2– 8%, 50 $\mu$	Mechanical Test (%Elongation, HN)	Max(8%wt) TS: 190.54 MPa % 2.6, 86 HN
Yakubu et al. [5] AA8011, Fe	Mechanical Test (TS & Charpy impact)	Improvement in the mechanical properties
Vembu et al. [24] AA8011, 15%SiC	Heat treatment optimization for tensile properties	Max. TS of 265 MPa & microhardness of 67.17
Shivanand and Santhosh [25] AA8011, E-glass/ fly-ash	Mechanical test (tensile & compression test)	Increases with the weight percentages
Rahimi et al. [26] AA8011	Water wettability, surface roughness & frost formation	High contact angle 78°
Reddy et al. [27] AA8011	Tensile exp. at 150 & 450° with different condition	Higher temp. showed lower YS and lower TS, more strain ductile when increasing temp

## 2.2 Tribological Properties

Wear is a process of extracting material from one or both of two solid surfaces when during sliding or rolling under the action of the load, their surfaces have solid contact. The wear behaviour of synthetic ceramic materials and industrial waste reinforced into AA8000 series-based metal matrix composites has been examined by numerous analysts. In this paper, an attempt has been made to provide a succinct overview of how the wear characteristics of different Al MMCs and the reasons behind the wear patterns found on the composite surfaces are influenced by factors such as applied load, reinforcement particles and sliding speed. Tribological properties include wear resistance, specific wear rate and friction coefficient produced during wear testing. Table 4 exhibits the tribological properties of the AA8000 composite. The strengthening of hard particles in the matrix has increased the wear resistance of composites.

**Table 3** Mechanical properties reported for AA8006, 8009, 8030, 8081, 8090, 8091, 8176 composites in the literature

Author/materials/ reinforcement size & wt%	Testing method	Mechanical properties changing with maximum % reinforcement
Pazman et al. [28] AA8006	Influence of heat treatments & mechanical strengthening technologies	Achieved better strength and toughness
Shuai et al. [29] AA8176	ECAP (at room temp. and elevated temp.)	YS: 178 MPa
Guo et al. [8] AA8030-GNP Graphene-0.5 wt %, 20 $\mu$	Ultimate tensile strength Yield strength	With 0.5 wt% GNPs achieved an enhancement in YS (37.5%) & UTS (62.9%)
Abass et al. [30] AA8090	Influence of annealing on TS and fatigue strength	Lower
Natrayan et al. [31] AA8030 GNP 5– 20 wt%, 32 $\mu$	Hardness, tensile strength flexural strength	10wt% graphene
Khodabakhshi et al. [32] AA8006 B4C-10% vol, 34 nm	Hardness tester	205.4 HV
Patil et al. [9] AA8081 B4C 0– 6%, 80–90 $\mu$	Vickers microhardness UTS	MAX-B4C(6wt%)-108.3 VHN TS: 220Mpa
Moldovan et al. [7] AA8006	Metallographic analysis electron microscopy	Sheet contains fine particles and foil has uniform distribution
Markovina et al. [10] AA8090T3, Li	Shot peening	Improved fatigue strength
Missori and Sili [33] AA8090, Li, 5% Mg, GTAW	Tensile strength Ductility	Reduced
Orrhede et al. [34] AA8091, 0–15% SiC, 1–10 $\mu$	Elastic constant Thermal expansion	Model developed to predict elastic constant and thermal expansion
Zhu et al. [35] AA8009 SiC 14.5 vol% 30–50 nm	Creep strain rate Activation energy Stress exponents	lower by two order magnitude 200 kJ/mol similar
Salazar et al. [36] AA8176	Influence of heat treatment annealing time	Ductility more and grain size increases

**Table 4** Tribological properties

Authors Name Alloy/Composite Reinforcement size & wt%	Fabrication/ apparatus/ DOE	Control factors (load, speed, time, wt%)	Result (for max. load/wt%): wear rate/coefficient of friction
Magibalan et al. [37] AA8011	Stir casting, Pin-On-Disc RSM, ANOVA	5, 10, 15 N 1.5, 3, 4.5 m/s 5,10, 15 min	For load 15 N, $t = 15$ min, $v = 4.5$ m/s Wear loss = $17.96 \times 10^{-3}$ g For load 15 N, $t = 5$ min, $v = 1.5$ m/s Wear loss = $2.54000 \times 10^{-3}$ g
Fayomi et al. [13] AA8011-nano $\text{Si}_3\text{N}_4$ 40–50 nm, up to 20% step of 5	Stir casting	20, 30, 40 N 60 s	For load 40 N, 20% $\text{Si}_3\text{N}_4$ , Wear rate = 0.056 g/min Coefficient of friction ( $\mu$ ) = 0.126
Fayomi et al. [38] AA8011-nano-ZrB <sub>2</sub> 40–50 nm, range 5– 20% step of 5	Stir casting	20, 30, 40 N	For load 40, 20% nano-ZrB <sub>2</sub> Wear rate = $3.32 \times 10^{-3}$ mm <sup>3</sup> /m Coefficient of friction = 0.117
Fayomi et al. [39] AA8011- $\text{Si}_3\text{N}_4$ Range 0–20%	Stir casting Universal Tribometer	20, 30, 40 N	With 20 wt%, to have lowest wear rate and lowest COF
Kalaiyarasan and Sundaram [40] 8090/ $\text{Al}_2\text{O}_3 + \text{B}_4\text{C}$	Stir casting Pin-On-Disc	10, 20, 30, 40 N	Reinforcement media help to attain better wear resistance
Fayomi et al. [41] AA8011-ZrB <sub>2</sub> + $\text{Si}_3\text{N}_4$ 40–50 nm, range 0– 20 wt% step of 5	Stir casting Pin-On-Disc	20, 30, 40 N	For load 40 N, 20% ZrB <sub>2</sub> + $\text{Si}_3\text{N}_4$ Wear rate = $3.74 \times 10^{-3}$ mm <sup>3</sup> /m Coefficient of friction = 0.12
Shankar et al. [42] AA8011-Gr Grp 0–8%, 45 $\mu\text{m}$	Stir casting, 3- body abrasive Taguchi, ANOVA	10, 20, 30 kgs 10, 20, 30 min 0, 4, 8 wt%	For load 20 kg, 8% Grp, 30 min Minimum wear rat = $0.102 \times 10^{-3}$ mm <sup>3</sup> /m

### 2.3 Corrosion Properties

Corrosion is a significant problem in the failure of aluminium alloy systems. Usually, the corrosion of metals depends on the composition and microstructure. If the material responds to the environment, corrosion weakens the material. Corrosion results in the weakening of the material's mechanical properties and eventually the material's failure. Designers take many safety measures to protect the materials from corrosion, but corrosion failures remain a major problem. The corrosion properties of the AA8011 composite are given in Table 5.



**Table 5** Corrosion properties

Authors Alloy/ composite	Reinforcement (Max.%)	Medium	Corrosion rate/corrosion resistance
Mishra et al. [43] AA8011	–	3.5, 4.0, 4.5, 5.0% NaCl	Maximum amount of surface degradation at 5%NaCl
Fayomi et al. [44] AA8011/ nano-ZrB <sub>2</sub>	20%wt	3.65% NaCl	Lowest corrosion rate 0.5017 mm/year High resistance 7831.7Ω
Fayomi et al. [45] AA8011/ nano-Si <sub>3</sub> N <sub>4</sub>	20%wt	3.65% NaCl	Lowest corrosion rate 0.7585 mm/year
Fayomi and Popoola [38] AA8011/ nano-ZrB <sub>2</sub>	20%wt	0.5 M H <sub>2</sub> SO <sub>4</sub>	Lowest corrosion rate 0.9974 mm/year
Karthikeyan and Jinu [46] AA8011/TiC/ Grp	20%TiC + 2% Grp		Lowest corrosion rate and increase in 83.9% corrosion resistance

### 3 Industrial Application of Aluminium Matrix Composites

Aluminium metal matrix composites have numerous applications in automobile, aerospace, rockets, missiles, sports, transportation, infrastructure, biomedical, agricultural equipment, computer, healthcare and other industries due to their lightweight, high strength-to-weight ratio, corrosion resistance and workability. Various applications of metal matrix composites based on AA8000 are listed in Table 6.

**Table 6** Application of various AA8000 based metal matrix composites

Authors	Alloy, composites	Application
Mishra [43]	8011	Heat exchanger fins for use in air conditioners, refrigerators, automobiles
Moldovan et al. [7]	8006, 8011 8018	Thin sheets and foils, packing Microelectronics industry
Fayomi et al. [41]	8011	Transportation, construction and the building
Magibalan et al. [47]	8011	Disc brake plate
Kalaiyarasan et al. [40]	8090	Automotive parts

## 4 Conclusion

This paper presents a review of the literature associated with the advance and trends in the fabrication process and application of alloys of 8000 series for usage in the automobile industry, packing, microelectronics industry, etc. AA8000 properties are improved by the addition of nanosized reinforcement through a fabrication process to enhance the tribo-mechanical performance and corrosion resistance. The following conclusions can be taken from the analysis presented:

- The reported work shows that the strength of the composite is improved by a decrease in particle size and an improvement in the percentage addition of reinforcement.
- The wear rate increases with an increase in applied load, but decreases with ceramic particles being added.
- The corrosion rate decreases with an increase in the reinforcement percentage, but the corrosion rate increases with an increase in the concentration of mediums.
- Stir casting method is the most used and economical fabrication method for metal matrix composites.

## References

1. Surappa M (2003) Aluminium matrix composites: challenges and opportunities. *Sadhana* 28 (1–2):319–334
2. Mechanical properties. <https://mechanicalc.com/reference/mechanicalproperties-of-materials>.
3. Choi S-M, Awaji H (2005) Nanocomposites—a new material design concept. *Sci Technol Adv Mater* 6(1):2–10
4. Cao G, Kobliska J, Konishi H, Li X (2008) Tensile properties and microstructure of sic nanoparticle-reinforced mg-4zn alloy fabricated by ultrasonic cavitation—based solidification processing. *Metall Mater Trans A* 39(4):880–886
5. Yakubu O, Usman I, Aliyu A, Emmanuel O (2016) Influence of iron content and plastic deformation on the mechanical properties of 8011-type Al-Fe-Si alloy. *Niger J Technol* 35 (1):122–128
6. Shankar BL, Anil K, Karabasappagol PJ (2016) A study on effect of graphite particles on tensile, hardness and machinability of aluminium 8011 matrix material. In: IOP conference series. materials science and engineering (online), vol 149
7. Moldovan P, Popescu G, Miculescu F (2004) Microscopic study regarding the microstructure evolution of the 8006 alloy in the plastic deformation process. *J Mater Process Technol* 153:408–415
8. Guo Y, Yi D, Liu H, Wang B, Jiang B, Wang H (2020) Mechanical properties and conductivity of graphene/Al-8030 composites with directional distribution of graphene. *J Mater Sci* 55(8):3314–3328
9. Patil KL, Ali M, Nagral M (2014) Studies on al8081-b4c metal matrix composites fabricated by stir casting method. *Int J Modern Eng Res* 4(7):1–4
10. Markovina R, Blagojevic B, Vlaskovic F (2009) Bending fatigue behaviour of shotpeened al-li 8090t3 thin plates. *Kovov'e materi'aly* 47(2):115–120

11. Smyrak B, Knych T, Mamala A, Uliasz P, Jablon'ski M (2011) A study of a new generation of multi-functional aluminium alloys for the power industry. *Mater Sci Forum* 690:439–442, Trans Tech Publ
12. Fayomi J, Popoola A, Popoola O (2020) Hybrid effect of zrb<sub>2</sub>+ si<sub>3</sub>n<sub>4</sub> on the microstructure and mechanical properties of aa8011 for service life improvement. *Mater Sci Forum* 975:171–175 Trans Tech Publ
13. Fayomi J, Popoola A, Popoola O, Oladijo O, Fayomi O (2020) Understanding the microstructural evolution, mechanical properties, and tribological behavior of aa8011-reinforced nano-si<sub>3</sub>n<sub>4</sub> for automobile application. *Int J Adv Manuf Technol* 1–10
14. Fayomi J, Popoola A, Popoola O, Fayomi O (2019) Influence of zirconium diboride (ZrB<sub>2</sub>) on the physio-mechanical behavior of aa8011 alloy base. *J Phys: Conf Ser* 1378:032044, IOP Publishing
15. Fayomi J, Popoola A, Oladijo O, Popoola O, Fayomi O (2019) Experimental study of zrb<sub>2</sub>-si<sub>3</sub>n<sub>4</sub> on the microstructure, mechanical and electrical properties of high grade aa8011 metal matrix composites. *J Alloy Compd* 790:610–615
16. Vembu V et al (2019) Aging behaviours of 8011 al and 8011 al/15% sicp composites. *J Miner Mater Characterization Eng* 7(05):221
17. Chandrasekar P, Natarajan S, Ramkumar K (2019) Influence of carbide reinforcements on accumulative roll bonded al 8011 composites. *Mater Manuf Processes* 34(8):889–897
18. Cui J, Chen L, Li Y, Liu J, Xie J (2019) Effects of annealing treatment on mechanical properties of 8011 aluminum alloy after cryogenic rolling. *Metal Res Technol* 116(2):219
19. Harshavardhan R, Anil K, Rao KS (2018) Evaluation of fracture toughness of red mud reinforced aluminium matrix composite. *Mater Today: Proc* 5(11):24854–24861
20. Rao KS, Anil K, Girisha K et al (2017) Effect of particle size on mechanical properties of al-rmp metal matrix composites. *Mater Today: Proc* 4(10):11154–11157
21. Anil K, Vikas M, Shanmukha Teja B, Sreenivas Rao K (2017) Effect of cutting parameters on surface finish and machinability of graphite reinforced al-8011 matrix composite. In: IOP conference series: materials science and engineering, vol 191, p 012025
22. Kandan R, Kumar D, Sudharssanam M, Venkadesan A, Badrinath R (2017) Investigation of mechanical properties on newly formulated hybrid composite aluminium 8011 reinforced with b<sub>4</sub>c and al<sub>2</sub>o<sub>3</sub> by stir casting method. *Int J Sci Res Dev* 5:962–965
23. Karthikkumar C, Baranirajan R, Premnauth I, Manimaran P (2016) Investigations on mechanical properties of al 8011 reinforced with micro b<sub>4</sub>c/red mud by stir casting method. *Int J Eng Res Gen Sci* 4:405–412
24. Vembu V, Ganesan G (2015) Heat treatment optimization for tensile properties of 8011 al/15% sicp metal matrix composite using response surface methodology. *Defence Technol* 11(4):390–395
25. Shivanand YADH, Santhosh Kumar S (2015) Investigation on mechanical properties of e-glass and flyash reinforced al 8011 based hybrid composites. *Int J Mech Eng Technol* 4(6)
26. Rahimi M, Fojan P, Gurevich L, Afshari A (2015) Aluminium alloy 8011: Surface characteristics. *Appl Mech Mater* 719:29–37, Trans Tech Publ
27. Reddy DM, Lakshmi AA, ul Haq A (2019) Experimental taguchi approach and gray–taguchi optimization on mechanical properties of aluminum 8011 alloy sheet under uniaxial tensile loads. *Mater Today: Proc* 19:366–371
28. Pazman J, Feher K, Gonda V, Vero B (2020) Effect of the homogenization and cold deformation on the mechanical performance of al8006 aluminium alloy. In: IOP conference series: materials science and engineering, vol 903, p 012039, IOP Publishing
29. Shuai G, Li Z, Zhang D, Tong Y, Li L (2020) The mechanical property and electrical conductivity evolution of al–fe alloy between room temperature and elevated temperature. *Vacuum* 183:109813
30. Abass M, Mahmud F, Alali M, Abood A (2019) The effect of annealing and anisotropic behaviour on tensile and fatigue properties of aa8090. *Arch Mater Sci Eng* 99(1/2)

31. Natrayan L, Yogeshwaran S, Yuvaraj L, Kumar MS (2019) Effect of graphene reinforcement on mechanical and microstructure behavior of aa8030/graphene composites fabricated by stir casting technique. In: AIP conference proceedings, vol 2166, p 020012. AIP Publishing LLC
32. Khodabakhshi F, Gerlich A, Worswick M (2018) Fabrication and characterization of a high strength ultra-fine grained metal-matrix aa8006-b4c layered nanocomposite by a novel accumulative fold-forging (aff) process. *Mater Des* 157:211–226
33. Missori S, Sili A (2002) Mechanical and microstructural properties of 8090 al-li alloy welded joints. *Metal Sci Technol* 20(2)
34. Orrhede M, Tolani R, Salama K (1996) Elastic constants and thermal expansion of aluminum-sic metal-matrix composites. *Res Nondestr Eval* 8(1):23–37
35. Zhu S, Peng L, Ma Z, Bi J, Wang F, Wang Z (1996) High temperature creep behavior of sic whisker-reinforced alfevsi composite. *Mater Sci Eng A* 215(1–2):120–124
36. Salazar L, Matute K, Sidorovas L Evaluation of the influence of annealing time on the mechanical, electrical and microstructural properties of aluminium alloy aa-8176
37. Magibalan S, Kumar PS, Balan A, Shivasankaran N, Sankar S, Prabu M, Saravanan S (2020) Wear loss of stir cast aluminium alloy 8011. *Mater Today: Proc* 21:762–765
38. Fayomi J, Popoola A (2020) The assessment of the microstructural modification, corrosion response, and tribological behavior of aa8011 reinforced nano-zrb. *J Bio- Tribo-Corrosion* 6 (79):79
39. Fayomi J, Popoola A, Popoola O, Oladijo O (2020) Effect of silicon nitride (si<sub>3</sub>n<sub>4</sub>) addition on the mechanical and tribological performance of Al–Fe–Si alloy (aa8011). *Mater Sci Forum*, 982, 34–38, Trans Tech Publ
40. Kalaiyaranan A, Sundaram S (2020) Tribological investigation of 8090 al alloy metal matrix composite. *Tierarztl Prax* 40:394–405
41. Fayomi J, Popoola A, Popoola O, Oladijo O, Fayomi O (2019) Tribological and microstructural investigation of hybrid aa8011/zrb<sub>2</sub>-si<sub>3</sub>n<sub>4</sub> nanomaterials for service life improvement. *Results Phys* 14: 102469
42. Shankar BL, Nagaraj P, Anil K (2017) Optimization of wear behaviour of aa8011gr composite using taguchi technique. *Mater Today: Proc* 4(10):10739–10745
43. Mishra R (2020) Study the effect of pre-corrosion on mechanical properties and fatigue life of aluminum alloy 8011. *Mater Today: Proc* 25:602–609
44. Fayomi J, Popoola A, Popoola O, Fayomi O, Ajenifuja E (2020) Response evaluation of aa8011 with nano zrb<sub>2</sub> inclusion for multifunctional applications: considering its thermal, electrical, and corrosion properties. *J Alloys Compounds* 157197
45. Fayomi J, Popoola A, Popoola O, Fayomi O (2020) The appraisal of the thermal properties, electrical response, and corrosion resistance performance of aa8011 reinforced nano si<sub>3</sub>n<sub>4</sub> for automobile application. *J Alloys Compounds* 850:156679
46. Karthikeyan A, Jinu G (2019) Investigation on mechanical and corrosion behaviour of aa8011 reinforced with tic and graphite hybrid composites. *Mater Res Express* 6(10):1065b5
47. Magibalan S, Senthilkumar P, Senthilkumar C, Prabu M (2019) Tribological behaviour of aluminium alloy 8011. *Indian J Eng Mater Sci* 26(5):43–50

# Plasma Processing of Carbon Dioxide



Kali Charan Sabat , Archana Singh, and Satyabrata Das

## 1 Introduction

With the advent of modern society's development, the uses of metals and alloys are increasing day by day. The extraction of metals and alloys from ores involves carbon in one form or other, producing carbon dioxide, which is detrimental to the environment. For example, steel being the largest consumed alloy by modern society, each ton of steel produced emits approximately 1.8 tons of CO<sub>2</sub> to the atmosphere [1]. The current steel production is 1869 million tons (MT), with an estimated emission of 3364 MT of CO<sub>2</sub> per year. The steel industry's emission alone constitutes only 6.7 pct of the total CO<sub>2</sub> emission [1]. Recently, there have been significant successful efforts for reducing CO<sub>2</sub> by replacing carbon by hydrogen plasma (HP) [1]. The total estimated global emission of CO<sub>2</sub> is 50209 MT. This high amount of CO<sub>2</sub> is pushing the world to several environmental climate changes. Due to the ecological changes, the world is facing several disasters such as: (i) the ecosystem is moving toward destruction, (ii) the glaciers are shrinking, (iii) biodiversity is being lost, (iv) the levels of the sea are rising, (v) heatwaves are being generated, and (vi) there is a massive loss in economy. Overall, the global CO<sub>2</sub> emission is a massive threat to the current society and future. Despite efforts to decrease CO<sub>2</sub> emission, there is little chance of eliminating the emission of CO<sub>2</sub> to the atmosphere, but there is tremendous scope for converting CO<sub>2</sub> to liquid fuels and other chemicals. This approach of converting waste to wealth is helpful for sustainable development. If the global emission of CO<sub>2</sub> which is 50209 MT per year can be utilized, it will generate huge wealth for development. Also, it supports the green economy concept. The utilization of CO<sub>2</sub>

---

K. C. Sabat (✉) · S. Das  
Maulana Azad National Institute of Technology, MANIT, Bhopal 462003, India

A. Singh  
CSIR—Advanced Materials and Processes Research Institute, Bhopal 462026, India

© The Author(s), under exclusive license to Springer Nature Singapore Pte Ltd. 2022  
P. Verma et al. (eds.), *Advancement in Materials, Manufacturing and Energy Engineering, Vol. I*, Lecture Notes in Mechanical Engineering,  
[https://doi.org/10.1007/978-981-16-5371-1\\_41](https://doi.org/10.1007/978-981-16-5371-1_41)

helps in maintaining a zero discharge principle, which is becoming mandatory day by day by the environmental regulations imposed on industries. Therefore, there has been growing interest from industries to convert  $\text{CO}_2$  to valuable products. Several traditional methods, such as electrochemical, solar, thermochemical, biochemical, and photochemical, have been investigated.

However, in recent years, the approach of conversion based on non-thermal plasma is gaining importance. Microwave non-thermal hydrogen ( $\text{H}_2$ ) plasmas have been successfully used for the production of iron from the iron oxide/ore [1, 2], production of copper from copper oxide, production of cobalt from cobalt oxide, and production of alloys [3–5] from oxide mixtures. Several approaches have been investigated concerning plasma utilization for converting  $\text{CO}_2$  to valuable products and liquid fuels, for example, splitting  $\text{CO}_2$  to carbon monoxide ( $\text{CO}$ ) and oxygen ( $\text{O}_2$ ), reforming methane ( $\text{CH}_4$ ), reaction with  $\text{H}_2$  or water ( $\text{H}_2\text{O}$ ) to produce valuable chemical products like formic acid, methanol, formaldehyde, etc., [6]. Although there is enormous potential for the plasma processing of carbon dioxide, it has not yet reached the significant limelight. Therefore, the fundamentals of plasma have been discussed first, followed by their applications to the processing of  $\text{CO}_2$ .

## 2 Plasma Fundamentals

Although plasmas are the fourth state of matter, they are nothing but excited gases. Gas molecules are always associated with nucleus–nucleus, nucleus–electron, electron–electron interactions. There exists various attraction and repulsions between these species. In other words, gas molecules are always associated with some electromagnetic interactions. Therefore, when energy is given to gas molecules by electrons or electromagnetic waves, the gas molecules' polarity interacts with the electromagnetic waves associated with electrons or electromagnetic waves. Due to this energy, the gas molecules get rovibrationally excited, followed by dissociation and then ionization. In these states, the gases are called plasmas. Plasmas are divided into two types, (i) high-pressure plasma or thermal plasma and (ii) low-pressure plasma or non-thermal plasma. The difference between these two plasmas is reported in Fig. 1.

### 2.1 Thermal Plasmas

Thermal plasmas refer to the plasmas where heavy species' temperature (i.e., molecules, atoms, ions, etc.) and electrons' temperature are equal, i.e., they are in thermal equilibrium. Physically, at first, the electrons get heated up by absorbing energy from direct current (DC), alternative current (AC), radiofrequency (RF), microwave (MW), or any other electromagnetic wave (EM). These excited/heated

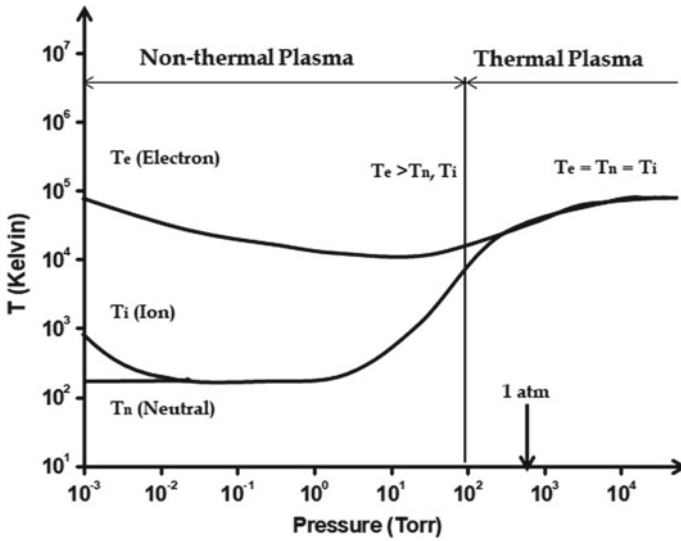


**Fig. 1** Difference between thermal and non-thermal plasma

electrons transfer the energy to heavy particles due to the high collision rates arising from high pressure. This gives rise to a property called local thermodynamic equilibrium (LTE), where all the temperatures (i.e., translational temperatures of heavy particles and electrons, vibrational and rotational temperatures of heavy species and electrons, equilibrium temperature of the chemical reaction) are equal at the given position. Figure 1 shows the thermal plasmas at pressures above 0.1 atm. Further, the thermal plasmas are two types: (i) transferred arc plasma and (ii) non-transferred arc plasma. These two types of plasmas are primarily used for many metallurgical processing routes, plasma spraying, cutting, arc furnaces, waste treatment, reduction of metal oxides, etc.

## 2.2 Non-Thermal Plasmas

Non-thermal plasmas are plasmas where the heavy species and electrons are not in thermal equilibrium. They are also called non-equilibrium plasma or cold plasma. They are called cold plasma because they can be touched in a finger. They occur at low pressure, as shown in Fig. 1. In non-thermal or cold plasmas, although the electrons absorb energy from DC, AC, RF, MW, EM, etc., in the same manner as thermal plasma, the electrons are unable to transfer power to heavy species due to less number of collisions because of low pressure. Hence, the electron temperature remains higher than the temperature of heavy species. This temperature difference is observed in all non-thermal plasmas. Non-thermal plasmas can also be produced at

atmospheric pressure by ensuring the lifetime of plasma very short. The short time does not permit the heavy particles to absorb energy from the electrons. Therefore, thermal equilibrium does not occur. Thus, in non-thermal plasmas, the electron temperature remains higher than the temperature of heavy species, as shown in Fig. 1. As shown in Fig. 1, non-thermal plasmas are characterized by several temperatures, i.e., electron temperature ( $T_e$ ), vibrational temperature ( $T_v$ ), rotational temperature ( $T_r$ ), ion temperature ( $T_i$ ), and gas temperature ( $T_g$ ); typically,  $T_e > T_v > T_r \approx T_i \approx T_g$  [1]. In many non-thermal plasmas,  $T_e$  can attain 11,600 K while keeping the  $T_g$  at room temperature, hence can be touched in the finger. Non-thermal plasma has already been used for several purposes such as thin-film deposition, etching of semi-conductor, ozone production, gas cleaning, modification of surface properties of plastics, plasma displays, etc. The current investigation reports the  $\text{CO}_2$  treatment by non-thermal plasma.

Although the non-thermal plasma indicates high electron temperature, sometimes to take advantage of both electron temperature and heavy species' temperature (i.e., molecules, atoms, ions, etc.), moderate pressures are used. Moderate pressure incorporates high electron temperature, which gives rise to rovibrationally excited molecules. These rovibrationally excited molecules possess higher energy due to the energy stored in rotation and vibration of molecules, which increase the stored energy of the reactants, thereby decreasing the activation energy of the reaction. Moderate pressure also leads to increased collisions between the electrons and heavy species, giving rise to high gas temperature, directly related to chemical kinetics. However, rather than gas temperature, high electron temperature due to vibrational excitation of  $\text{CO}_2$  is essential for dissociation of  $\text{CO}_2$  and producing excited  $\text{CO}_2$  molecules, which make the production of chemicals/fuels from  $\text{CO}_2$  easier and faster [7]. Therefore, in comparison with thermal plasma, cold plasma has more potential for  $\text{CO}_2$  conversion and energy efficiency. Thus, the advantages of low-pressure non-thermal plasma have been discussed in this review.

The advantages of cold plasma have already been used by Sabat et al. [1–5] to reduce metal oxides and their mixtures for production of metals and alloys, respectively. Sabat et al. produced cold microwave hydrogen plasma (HP) using a simple microwave setup (similar to the domestic microwave) shown in Fig. 2. The microwave plasma reactor incorporates a power supply up to 6000 W at  $2.45 \times 10^9$  Hz microwave generator to produce HP of high power densities. The high-frequency microwaves interact with the polarity provided by  $\text{H}_2$  molecules inside the microwave oven to produce HP. The lump/pellet sample was placed on a sample holder made of molybdenum, placed at the reaction chamber's center. Plasma was generated at the center, covering the sample. The controlling factors of the plasma were the microwave power and  $\text{H}_2$  flow rate. These controlling factors were kept constant and monitored throughout the experiments. Also, temperature and pressure were monitored throughout the reduction studies. The reduction studies were carried out for different time periods till the reduction goes to completion. The percentage reductions for each period were estimated from the weight loss measurements by digital weighing balance with accuracy  $0.1 \times 10^{-6}$  kg. Using this microwave setup, Sabat et al. reported the production of iron from hematite

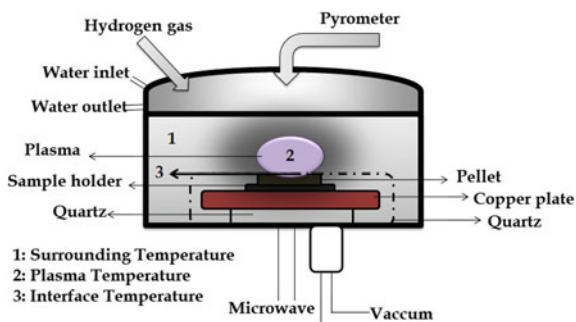


( $\text{Fe}_2\text{O}_3$ ) [1], copper from copper oxide ( $\text{CuO}$ ), cobalt from cobalt oxide ( $\text{Co}_3\text{O}_4$ ), and alloys like iron–cobalt alloy [5], copper–nickel ( $\text{CuNi}$ ) alloy [3], magnetic copper–cobalt ( $\text{CuCo}$ ) alloy [4], etc., from the reduction of metal oxide mixtures. In these experiments, Sabat et al. could reduce lumps/pellets of size up to 15 mm, using microwave power in the range of 600–1500 W and  $\text{H}_2$  flow rate in the range of 70–500 sccm. The power ranges used in their investigations were below the power range required in domestic microwave ovens, generally used for cooking foods. Also, the sizes of the pellets were up to 15 mm. This size opened up the possibility of mass-scale industrial production of metals and alloys from their oxides/ores by industrial processes (e.g., reduction roasting) using HP.

Apart from microwave, this concept of HP reduction of metal oxides can be utilized industrially by generating HP by other means such as DC, AC, RF, or any other EM. These different studies of obtaining metals by cold HP reduction of  $\text{Fe}_2\text{O}_3$  and other metal oxides have been reviewed extensively in earlier publications [1, 2].

The importance of discussing here the reduction of metal oxides by HP is the following: (i) Sabat et al. [1–5] carried out the reduction studies in solid state. The atoms are so closely arranged in solid state that there is minimal space available for the HP to penetrate and reach the HP–metal oxide reduction interface. Still, the diffusion of plasma species through these voids in the solid state is faster, and the plasma species of HP can diffuse to 15 mm inside the solid. For the reduction to proceed, the plasma species has to diffuse through the formed product layer (i.e., metal) to the HP–metal oxide interface for the reduction to take place. The HP–metal oxide reduction reactions are heterogeneous and chemically controlled. Therefore, the reduction rate is dependent on the interfacial area. The product layer’s presence limits the reduction interfacial area between HP–metal oxide, limiting the reaction rate. However, when  $\text{CO}_2$  is used as plasma, the reactions mostly occur between  $\text{CO}_2$  plasma and another gas (e.g.,  $\text{CH}_4$ ,  $\text{H}_2$ , etc.) or liquid (e.g.,  $\text{H}_2\text{O}$ ). The reaction between  $\text{CO}_2$  plasma and other gas is homogeneous. There is no obstruction for the movement of  $\text{CO}_2$  plasma to the reaction interface, like the obstruction caused to HP by product during the reduction of metal oxides by HP. This easier interaction in the homogeneous state increases the reaction kinetics. Thereby, the reaction between  $\text{CO}_2$  and the other reactant becomes more comfortable and faster.

**Fig. 2** Microwave HP setup used by Sabat et al. [1–5]



Similarly, the reaction between CO<sub>2</sub> plasma and liquid (H<sub>2</sub>O) is easier. Therefore, the use of MW plasmas for CO<sub>2</sub> splitting, dry reforming of CH<sub>4</sub>, photosynthesis of H<sub>2</sub>O and reaction with H<sub>2</sub>, etc., is cited in Table 1. Also, (ii) CO<sub>2</sub> possesses more polarity than H<sub>2</sub>. An electromagnetic wave produces the plasma. This is because all electromagnetic waves have an electric field and magnetic field associated with them. The interaction of the electric field and magnetic field produces some polarity in the electromagnetic wave. This polarity gives energy to the electrons, which easily interact with high polarity molecules than low polarity molecules. CO<sub>2</sub> being higher polarity than H<sub>2</sub>, the interaction of plasma producing electromagnetic wave and CO<sub>2</sub> is easier and faster than H<sub>2</sub>. Therefore, there is a vast research scope in creating CO<sub>2</sub> plasma to examine the possibility of producing chemicals or fuels from CO<sub>2</sub>.

### Advantages of Non-thermal plasma processing of CO<sub>2</sub>

The non-thermal plasma treatment of CO<sub>2</sub> has several advantages in comparison with thermal plasmas. They are:

1. It can be simply produced by passing CO<sub>2</sub> gas between the electrodes (positive and negative) or by inserting electrodes in a gas chamber. The potential difference between the two electrodes gives rise to electron flow, which collides with CO<sub>2</sub> molecules, to produce CO<sub>2</sub> plasma.
2. The collision of electrons while moving to positive electrodes transfer their energy to CO<sub>2</sub> gas molecules. This produces rovibrational excited CO<sub>2</sub> molecules followed by dissociation and ionization. This process creates radicals, which quickly form new compounds.
3. The stored energy in CO<sub>2</sub> due to the excited species increases the energy of the reactants. It decreases the activation energy of the chemical reactions associated with CO<sub>2</sub>, thereby causing the reactions easier and faster.
4. The non-thermal plasmas of CO<sub>2</sub> can be produced quickly by various means, for example, DC, AC, RF, MW, EM, etc.

**Table 1** Different applications of non-thermal plasma for processing of CO<sub>2</sub>

Types of plasma	Applications	Latest references
Microwave plasma	CO <sub>2</sub> splitting	[9–17]
	Dry reforming of CH <sub>4</sub>	[18]
	Photosynthesis of H <sub>2</sub> O	[10, 19–22]
	Reaction with H <sub>2</sub>	[10, 23]
Dielectric barrier discharge	CO <sub>2</sub> splitting	[24]
	Dry reforming of CH <sub>4</sub>	[25]
	Photosynthesis of H <sub>2</sub> O	[26, 27]
	Reaction with H <sub>2</sub>	[28, 29]
Gliding arc discharge	CO <sub>2</sub> splitting	[30, 31]
	Dry reforming of CH <sub>4</sub>	[32, 33]
	Photosynthesis of H <sub>2</sub> O	[34, 35]

5. More than 95% of total non-thermal discharge energy at  $T_e \approx 1\text{--}2$  eV can be transferred from plasma electrons to induce molecular vibration and rotation, thereby stored in rovibrationally excited molecules.
6. Once rovibrationally excited  $\text{CO}_2$  molecules store the non-thermal energy, the endothermic reactions for chemical conversion to other chemicals and liquid fuels are enhanced [1, 2].
7. The extra internal energy stored by rovibrationally excited  $\text{CO}_2$  molecules transfers into translational energy of products [2, 7, 8].
8.  $\text{CO}_2$  can maintain vibrational energy without relaxation for a long duration, which helps store a high amount of energy, which can be utilized for chemical reactions of  $\text{CO}_2$  to produce chemicals or liquid fuels [2].
9. Non-thermal  $\text{CO}_2$  plasma can be activated even at low temperatures.
10.  $\text{CO}_2$  plasma production does not require any external heater to heat the entire  $\text{CO}_2$  inside the reactor for the chemical reaction to take place. Instead, the chemical reactions are initiated by localized heating by EM waves.
11.  $\text{CO}_2$  plasma does not require any volumetric heating. This eliminates heat loss from the reaction chamber and costs.
12. The setups are very movable, flexible, or a turn-key process. It can be switched on or off at any moment instantly.
13. It can be used as a storage of energy from wind or sunlight by converting the renewable energies to chemical form, also being able to withstand an irregular supply of power.
14. Non-thermal plasma-based conversion of  $\text{CO}_2$  can store electrical energy in a desirable chemical form, which can be utilized as per the market needs.
15. Low investments and can be easily scaled from W to MW.
16. Possess extreme scalability starting from small devices to large devices.
17. The application's scalability and flexibility make it useful for different applications, including the carbon capture and storage application.

### 3 Developments So Far

There are several options for the plasma treatment of  $\text{CO}_2$  in several types of plasma reactors. The options include but not limited to:

- (a) Splitting of  $\text{CO}_2$  to CO and  $\text{O}_2$
- (b) Producing value-added chemicals along with fuels by reaction with hydrogen carrying gases. Examples are dry reforming of  $\text{CH}_4$ , artificial photosynthesis of  $\text{H}_2\text{O}$ , hydrogenation (reaction with  $\text{H}_2$ ), production of  $\text{CH}_3\text{OH}$ , syngas, formaldehyde, and formic acid, etc.,

As mentioned earlier, the plasma treatment of  $\text{CO}_2$  has been carried out by many types of plasmas. Still, depending on their efficiency in plasma treatment for  $\text{CO}_2$  splitting and production of chemicals/fuels, they are mainly divided into

(i) microwave, (ii) dielectric barrier discharge, and (iii) gliding arc discharge. Applications of these plasmas for different plasma treatment of  $\text{CO}_2$  are given in Table 1.

## 4 Conclusions

Keeping in view the environmental problems faced by the emission of  $\text{CO}_2$ , plasma processing of  $\text{CO}_2$  has vast potential for the future. To make it understandable, we have given a brief introduction to the basic concepts of plasma, including thermal and non-thermal plasma. Out of these two plasmas, non-thermal plasma possesses the immense potential to convert  $\text{CO}_2$  to value-added products and fuels. Therefore, the advantages of non-thermal plasmas have been discussed. The most important areas for non-thermal  $\text{CO}_2$  plasma in the context of industrial applications and up-scalability are microwave, dielectric barrier discharge, and gliding arc. These processes' detailed applications have been cited to bring attention to the researchers and readers. More emphasis has been given to the microwave  $\text{CO}_2$  plasma. Overall, non-thermal plasmas have vast potential for effective utilization of  $\text{CO}_2$  to convert to value-added products and fuels by various processes like  $\text{CO}_2$  dissociation, dry reforming of  $\text{CH}_4$ , hydrogenation of  $\text{CO}_2$ , artificial photosynthesis of water, etc.

## References

1. Sabat KC, Murphy AB (2017) Hydrogen plasma processing of iron ore. *Metall Mater Trans B Process Metall Mater Process Sci* 48:1561–1594
2. Sabat KC, Rajput P, Paramguru RK, Bhoi B, Mishra BK (2014) Reduction of oxide minerals by hydrogen plasma: an overview. *Plasma Chem Plasma Process* 34:1–23
3. Sabat KC, Paramguru RK, Mishra BK (2018) Formation of copper-nickel alloy from their oxide mixtures through reduction by low-temperature hydrogen plasma. *Plasma Chem Plasma Process* 38:621–635
4. Sabat KC (2019) Formation of CuCo alloy from their oxide mixtures through reduction by low-temperature hydrogen plasma. *Plasma Chem Plasma Process* 39:1071–1086
5. Sabat KC, Paramguru RK, Mishra BK (2017) Reduction of oxide mixtures of ( $\text{Fe}_2\text{O}_3 + \text{CuO}$ ) and ( $\text{Fe}_2\text{O}_3 + \text{Co}_3\text{O}_4$ ) by low-temperature hydrogen plasma. *Plasma Chem Plasma Process* 37:979–995
6. Fridman A (2008) *Plasma Chem* 9780521847
7. Fridman AA, Kennedy LA (2004) *Plasma physics and engineering*
8. Rajput P, Sabat KC, Paramguru RK, Bhoi B, Mishra BK (2014) Direct reduction of iron in low temperature hydrogen plasma. *Ironmak Steelmak* 41:721–731
9. Chen G, Godfroid T, Britun N, Georgieva V, Delplancke-Ogletree MP, Snyders R (2017) Plasma-catalytic conversion of  $\text{CO}_2$  and  $\text{CO}_2/\text{H}_2\text{O}$  in a surface-wave sustained microwave discharge. *Appl Catal B Environ* 214:114–125
10. Chen G, Britun N, Godfroid T, Georgieva V, Snyders R, Delplancke-Ogletree M-P (2017) An overview of  $\text{CO}_2$  conversion in a microwave discharge: the role of plasma-catalysis. *J Phys D Appl Phys* 50:84001

11. Huang Q, Zhang D, Wang D, Liu K, Kleyn AW (2017) Carbon dioxide dissociation in non-thermal radiofrequency and microwave plasma. *J Phys D Appl Phys* 50:294001
12. Mitsingas CM, Rajasegar R, Hammack S, Do H, Lee T (2016) High energy efficiency plasma conversion of CO<sub>2</sub> at atmospheric pressure using a direct-coupled microwave plasma system. *IEEE Trans Plasma Sci* 44:651–656
13. Berthelot A, Bogaerts A (2017) Modeling of CO<sub>2</sub> splitting in a microwave plasma: how to improve the conversion and energy efficiency. *J Phys Chem C* 121:8236–8251
14. Silva T, Britun N, Godfroid T, Snyders R (2014) Optical characterization of a microwave pulsed discharge used for dissociation of CO<sub>2</sub>. *Plasma Sources Sci Technol* 23
15. Bongers W, Bouwmeester H, Wolf B, Peeters F, Welzel S, van den Bekerom D, den Harder N, Goede A, Graswinckel M, Groen PW, Kopecki J, Leins M, van Rooij G, Schulz A, Walker M, van de Sanden R (2017) Plasma-driven dissociation of CO<sub>2</sub> for fuel synthesis. *Plasma Process Polym* 14
16. den Harder N, van den Bekerom DCM, Al RS, Graswinckel MF, Palomares JM, Peeters FJJ, Ponduri S, Minea T, Bongers WA, van de Sanden MCM (2017) Homogeneous CO<sub>2</sub> conversion by microwave plasma: wave propagation and diagnostics. *Plasma Process Polym* 14:1600120
17. van den Bekerom DCM, Linares JMP, Verreycken T, Van Veldhuizen EM, Nijdam S, Berden G, Bongers WA, Van De Sanden MCM, van Rooij GJ (2019) The importance of thermal dissociation in CO<sub>2</sub> microwave discharges investigated by power pulsing and rotational Raman scattering. *Plasma Sources Sci Technol* 28:55015
18. Zhang J-Q, Yang Y-J, Zhang J-S, Liu Q (2002) Study on the conversion of CH<sub>4</sub> and CO<sub>2</sub> using a pulsed microwave plasma under atmospheric pressure. *ACTA Chim Sin Ed* 60:1973–1980
19. Ihara T, Kiboku M, Iriyama Y (1994) Plasma reduction of CO<sub>2</sub> with H<sub>2</sub>O for the formation of organic compounds. *Bull Chem Soc Jpn* 67:312–314
20. Ihara T, Ouro T, Ochiai T, Kiboku M, Iriyama Y (1996) Formation of methanol by microwave-plasma reduction of CO<sub>2</sub> with H<sub>2</sub>O. *Bull Chem Soc Jpn* 69:241–244
21. Chen G, Silva T, Georgieva V, Godfroid T, Britun N, Snyders R, Delplancke-Ogletree MP (2015) Simultaneous dissociation of CO<sub>2</sub> and H<sub>2</sub>O to syngas in a surface-wave microwave discharge. *Int J Hydrogen Energy* 40:3789–3796
22. Hayashi N, Yamakawa T, Baba S (2006) Effect of additive gases on synthesis of organic compounds from carbon dioxide using non-thermal plasma produced by atmospheric surface discharges. *Vacuum* 80:1299–1304
23. de la Fuente JF, Moreno SH, Stankiewicz AI, Stefanidis GD (2016) A new methodology for the reduction of vibrational kinetics in non-equilibrium microwave plasma: application to CO<sub>2</sub> dissociation. *React Chem Eng* 1:540–554
24. Sun SR, Wang HX, Mei DH, Tu X, Bogaerts A (2017) CO<sub>2</sub> conversion in a gliding arc plasma: performance improvement based on chemical reaction modeling. *J CO<sub>2</sub> Util* 17:220–34
25. Devid E, Zhang D, Wang D, Ronda-Lloret M, Huang Q, Rothenberg G, Shiju NR, Kleyn AW (2020) Dry reforming of methane under mild conditions using radio frequency Plasma. *Energy Technol* 8
26. Snoeckx R, Ozkan A, Reniers F, Bogaerts A (2017) The quest for value-added products from carbon dioxide and water in a dielectric barrier discharge: a chemical kinetics study. *Chemsuschem* 10:409–424
27. Snoeckx R, Bogaerts A (2017) Plasma technology—a novel solution for CO<sub>2</sub> conversion? *Chem Soc Rev* 46:5805–5863
28. De Bie C, Van Dijk J, Bogaerts A (2016) CO<sub>2</sub> hydrogenation in a dielectric barrier discharge plasma revealed. *J Phys Chem C* 120:25210–25224
29. Chen G, Britun N, Godfroid T, Georgieva V, Snyders R, Delplancke-Ogletree MP (2017) An overview of CO<sub>2</sub> conversion in a microwave discharge: the role of plasma-catalysis. *J Phys D Appl Phys* 50:084001

30. Li L, Zhang H, Li X, Kong X, Xu R, Tay K, Tu X (2019) Plasma-assisted CO<sub>2</sub> conversion in a gliding arc discharge: Improving performance by optimizing the reactor design. *J CO<sub>2</sub> Util* 29:296–303
31. Li L, Zhang H, Li X, Huang J, Kong X, Xu R, Tu X (2020) Magnetically enhanced gliding arc discharge for CO<sub>2</sub> activation. *J CO<sub>2</sub> Util* 35:28–37
32. Tu X, Whitehead JC (2014) Plasma dry reforming of methane in an atmospheric pressure AC gliding arc discharge: Co-generation of syngas and carbon nanomaterials. *Int J Hydrogen Energy* 39:9658–9669
33. Mei D, Zhu X, He Y-L, Yan JD, Tu X (2014) Plasma-assisted conversion of CO<sub>2</sub> in a dielectric barrier discharge reactor: understanding the effect of packing materials. *Plasma Sources Sci Technol* 24:15011
34. Indarto A, Choi JW, Lee H, Song HK (2006) Effect of additive gases on methane conversion using gliding arc discharge. *Energy* 31:2986–2995
35. Nunnally T, Gutsol K, Rabinovich A, Fridman A, Gutsol A, Kemoun A (2011) Dissociation of CO<sub>2</sub> in a low current gliding arc plasmatron. *J Phys D Appl Phys* 44(27):274009

# Metal-Inorganic Nickel Complexes-Derived Nanostructured Nickel Oxide as an Efficient Water Oxidation Catalyst



Kamlesh, Deepika Tawar, Kali Charan Sabat, and Archana Singh

## 1 Introduction

The oxygen evolution reaction (OER) is a critical reaction that plays a significant role in several energy technologies, like hydrogen evolution reaction (HER), fuel cell, metal-air batteries, etc. Water oxidation reaction (i.e.  $2\text{H}_2\text{O} \rightarrow \text{O}_2 + 4\text{H}^+ + 4\text{e}^-$ ) is a four-electron transfer process; the overall reaction is kinetically hindered and always operates at energy input higher than the thermodynamically calculated potentials [1–7]. Among different applications, Water oxidation reaction for hydrogen production by electrolysis of water is a promising method for a green future. Water splitting combines two steps, process one is oxygen evolution reaction (OER):  $2\text{H}_2\text{O} \rightarrow \text{O}_2 + 4\text{H}^+ + 4\text{e}^-$ , and the other is hydrogen evolution reaction (HER):  $2\text{H}^+ + 2\text{e}^- \rightarrow \text{H}_2$  [5, 8–11]. The OER occurs at the anode side, where O–H bond dissociation and O–O bond formation takes place. It is multiple protons and electron transfer process, and therefore not a kinetically favourable process [5, 8, 12]. OER is facilitated by using a catalyst modified anode. Among different available oxides, Ru and Ir oxides can be the most effective and commonly used OER electrocatalysts. However, Ru and Ir are expensive and available in a limited amount, thus not useful for large-scale production [4, 5, 12, 13]. A variety of OER catalysts depends on natural available 3d transition metals, including Mn, Fe, Co, Ni, and their complexes have been studied [5, 8, 12–18].

---

Kamlesh · D. Tawar · A. Singh (✉)

Academy of Scientific & Innovative Research (AcSIR), Ghaziabad 201002, India

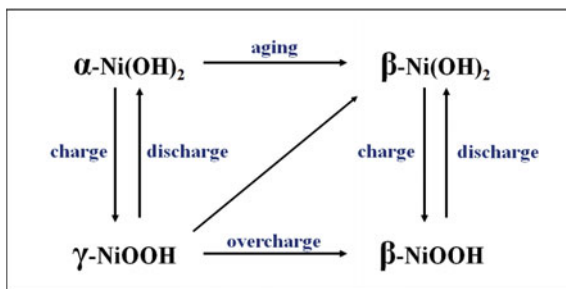
Kamlesh · D. Tawar · A. Singh

CSIR—Advanced Material and Processes Research Institute, Bhopal 462026, India

K. C. Sabat

Maulana Azad National Institute of Technology, MANIT, Bhopal 462003, India

**Fig. 1** Bode's diagram representing the relation between nickel hydroxide and oxyhydroxide



Among first-row transition series metals, Ni is one of the most effective, low-cost, and ninth highest available element on the earth's crust. It has shown excellent properties for the oxidation of water, and therefore, has received attention as oxygen evolution catalysts. Ni redox chemistry can be well understood using Bode's diagram (Fig. 1) that shows that under different experimental conditions, four phases of nickel hydroxides, namely  $\alpha$ -Ni(OH)<sub>2</sub>,  $\beta$ -Ni(OH)<sub>2</sub>,  $\beta$ -NiOOH, and  $\gamma$ -NiOOH exist [1, 5, 7, 19–21]. Various researchers have proposed an OER mechanism for Ni-based electrocatalysts, but which is the active phase of nickel oxide/hydroxide is still not very well understood. Among different phases, either  $\beta$ -Ni(OOH) or  $\gamma$ -NiOOH is reported to be the active oxygen evolution reaction catalyst [3, 22, 23]. Therefore, the origin of the OER activity in Ni-based catalysts is still debatable for the scientific community.

In addition, the attempt has been made to improve the catalytic efficiency of Ni-based catalysts by the production of nanostructured oxides as well as by doping. By designing nanostructures, the intrinsic activity will be significantly increased via enhancing the surface area of the catalyst, which increases their active sites for the water oxidation reaction. Nanostructured nickel hydroxide has been synthesized using different methods. Among them, hydrothermal is one of the most explored processes, whereby changing experimental parameters, different nanostructures can be synthesized. In the present work, metal-inorganic complexes have been used as nickel precursors to synthesize nanostructured nickel hydroxide, which has been shown as an efficient water oxidation catalyst. For metal-inorganic complex [Ni(NH<sub>3</sub>)<sub>6</sub>]<sup>2+</sup> has been used. It has been demonstrated under similar experimental conditions using presynthesized complex Ni(NO<sub>3</sub>)<sub>2</sub>, result in metal hydroxide with the same lattice structure but with different morphology. It was also reported that former metal precursor in the form of the complex also outperforms as oxygen evolution catalyst. The studies will be necessary to synthesize nanostructured metal hydroxide for various applications further; therefore, the current research has been carried.



## 2 Experimental

### 2.1 Materials

All chemical reagents, nickel nitrate hexahydrate;  $\text{Ni}(\text{NO}_3)_2 \cdot 6\text{H}_2\text{O}$ , ammonia;  $\text{NH}_3$ , sodium hydroxide;  $\text{NaOH}$ , ethanol;  $\text{C}_2\text{H}_5\text{OH}$ , Nafion solution 5% were purchased from SRL Pvt. Ltd. India and used without further purification. The distilled water was obtained using an ECO-STILL Mark—2000, single-phase system, used for synthesis and chemical apparatus washing.

### 2.2 Synthesis $\beta\text{-Ni}(\text{OH})_2$ Nanoparticles

Nanoparticles of  $\beta\text{-Ni}(\text{OH})_2$  were synthesized via various Ni(II) complexes, in which  $[\text{Ni}(\text{NH}_3)_6]^{2+}$  is first prepared by coprecipitation methods described below:

**Synthesis of  $[\text{Ni}(\text{NH}_3)_6]^{2+}$ :** Nickel nitrate hexahydrate (6 gm) was dissolved in water not be greater than 10 ml and then added 20 ml of ammonia and 15 ml of ethanol while keeping the reaction in an ice bath. The precipitate was filtered and dried at room temperature.

**Hydrothermal synthesis:** The synthesis was carried out in a 100 ml hydrothermal cell at 170 °C for 24 h. After the reaction, the residue so obtained was washed thoroughly and then dried at room temperature and used for characterization and to study the water oxidation reaction. The hydrothermal synthesis reaction conditions were similar for all the samples except the precursor, mentioned below. On the basis of precursor used, two types of nickel hydroxides are abbreviated as  $\beta\text{-Ni}(\text{OH})_2\text{-NO}_3$ , and  $\beta\text{-Ni}(\text{OH})_2\text{-NH}_3$ .

**Synthesis of  $\beta\text{-Ni}(\text{OH})_2\text{-NO}_3$ :** 0.2 M nickel nitrate is taken in which 46 ml of 50% concentrated ammonia solution added. The pH of this solution was adjusted to 13 by the addition of  $\text{NaOH}$  pallets. The solution was then transferred to the autoclave for the synthesis reaction.

**Synthesis of  $\beta\text{-Ni}(\text{OH})_2\text{-NH}_3$ :** 0.2 M nickel precursor ( $[\text{Ni}(\text{NH}_3)_6]^{2+}$  complex is taken in 46 ml of solution. pH was adjusted to 13 by the addition of sodium hydroxide pallets.

### 2.3 Material Characterization

The morphological investigation and imaging of nanoparticles were taken on a high-resolution scanning electron microscope (HRSEM) using Carl Zeiss Ultra Plus instrument. Brunauer–Emmett–Teller (BET) model Smart SORB 92/93 is utilized to measure the surface area of the samples. X-ray diffraction (PXRD) patterns were

recorded using a Bruker AXS with Cu K $\alpha$  radiation wavelength of 1.54 Å with a 2 $\theta$  range of 20 to 80°.

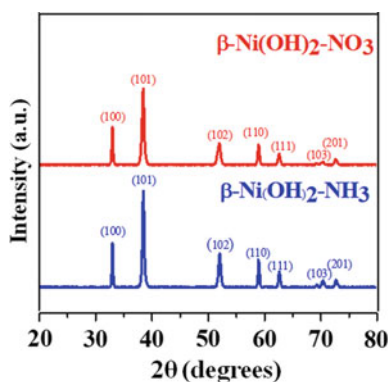
**Electrochemical Studies:** Linear sweep voltammograms (LSV) and Nyquist plot using electrochemical impedance spectroscopy (EIS) were performed using CH Instruments (Model No. CHI 604C) at pH 14 into a standard electrochemical cell, where 3 mm glassy carbon (surface area 0.071 cm<sup>2</sup>) was taken as a working electrode, and Pt wire and Ag/AgCl (saturated with KCl) were taken as an auxiliary electrode and a reference electrode, respectively. All the experiments were carried out at atmospheric oxygen and room temperature. The reported applied potential is converted into reversible hydrogen electrode (RHE) via following equation;  $E(\text{RHE}) = E(\text{Ag}/\text{AgCl}) + E^0(\text{Ag}/\text{AgCl}) + 0.059 \cdot \text{pH}$ , where  $E(\text{Ag}/\text{AgCl})$  is indicating the working electrode potential,  $E^0(\text{Ag}/\text{AgCl})$  is the theoretical potential for saturated Ag/AgCl with respect to standard hydrogen electrode. EIS was done at the applied potential of 1.72 V versus RHE and the frequency range between 1 and 10<sup>5</sup> Hz.

**Water Oxidation Studies:** LSVs were performed using a modified glassy carbon working electrode. First, 5 mg of nanoparticles of the catalyst was dispersed in a solution of 1 mL of 3:1 v/v water/ethanol (or isopropyl alcohol) and 20 mL of Nafion solution (5 wt. %). Then, the mixture was ultrasonicated for 20 min. 4  $\mu\text{L}$  of ink was drop cast onto the glassy carbon working electrode and dried it at room temperature and then at 120 °C for 10 min.

### 3 Results and Discussion

X-ray diffraction (XRD) patterns of  $\beta\text{-Ni}(\text{OH})_2$  nanoparticles synthesized by two different Ni(II) complexes are shown in Fig. 2. XRD pattern confirmed the formation of pure hexagonal phase  $\beta\text{-Ni}(\text{OH})_2$  and was well indexed with JCPDS card number (140,117), and the structures are defined in space group P-3m1 (164). The typical diffraction patterns for 2 $\theta$  values are 33.0, 38.5, 59.0, and 62.7 that

**Fig. 2** X-ray diffraction pattern of synthesized nanoparticles,  $\beta\text{-Ni}(\text{OH})_2\text{-NO}_3$  (red) and  $\beta\text{-Ni}(\text{OH})_2\text{-NH}_3$  (blue)



correspond to the planes of (100), (101), (110), and (111), respectively. The calculated lattice parameters values for samples are 0.3125 Å for a, and b and 0.4648 Å for c which is in well accordance to standard  $\beta$ -Ni(OH)<sub>2</sub>. As shown in the XRD pattern, the diffraction peak of (101) is the strongest in all the diffraction peaks. Also, no other characteristic peaks were observed; confirming the formation of pure phase of the sample. The results show that different precursors led to the formation of the same phase of nickel hydroxide.

The morphology of the sample as determined by scanning electron morphology is shown in Fig. 3a, b. As can be observed in Fig. 3, the metal precursors taken for the synthesis of nickel hydroxide has a significant impact on the morphology of the samples obtained. On using  $\text{-NH}_3$  separately along with nickel nitrate and on using  $[\text{Ni}(\text{NH}_3)_6]^{2+}$  forms nanoparticles; however, for sample, lots of agglomerated structure can be observed. The particle sizes for both of the samples were found to be between 20 and 50 nm. These results show that by using predefined metal complexes, well-defined nanostructures are produced. Brunauer–Emmett–Teller (BET) was utilized to measure the surface area of the samples. The obtained results are shown in Table 1, and it can be seen that among all samples,  $\beta$ -Ni(OH)<sub>2</sub>-NH<sub>3</sub> possess the highest specific surface area of 59.916 m<sup>-2</sup> g.

The electrocatalytic behaviour of the nanomaterials for the oxygen evolution rate was tested in 1 M NaOH. The LSV plot of differently synthesized nanomaterials are shown in Fig. 4a. As per Fig. 4b,  $\beta$ -Ni(OH)<sub>2</sub>-NH<sub>3</sub> shows the lowest overpotential of 370 mV at a current density of 10 mA/cm<sup>2</sup> compared to  $\beta$ -Ni(OH)<sub>2</sub>-NO<sub>3</sub>, which offers an overpotential of 570 mV to achieve a similar current density. Electrochemical impedance spectroscopy (EIS) was performed to determine the charge transfer resistance for the developed electrode material. The Nyquist plot for

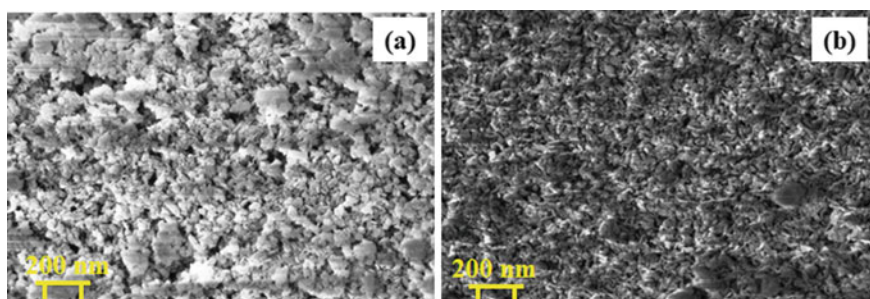


**Fig. 3** FESEM of **a**  $\beta$ -Ni(OH)<sub>2</sub>-NO<sub>3</sub>-200 nm, **b**  $\beta$ -Ni(OH)<sub>2</sub>-NH<sub>3</sub>-200 nm nanoparticles

**Table 1** Different parameters obtained for various samples

Parameters	Overpotential (mV) at current density 10 mAcm <sup>-2</sup>	R <sub>ct</sub> (KΩ)	BET Specific surface area (m <sup>-2</sup> g)
$\beta$ -Ni(OH) <sub>2</sub> -NO <sub>3</sub>	570	4.02	37.186
$\beta$ -Ni(OH) <sub>2</sub> -NH <sub>3</sub>	370	0.68	59.916

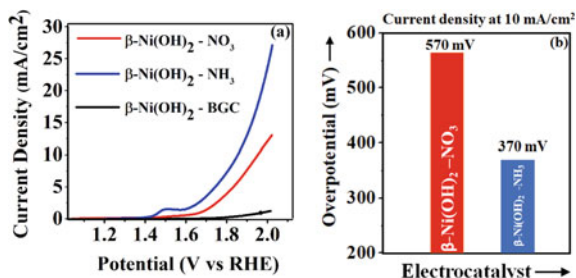


**Fig. 4** a LSV curve for OER for a glassy carbon electrode (black) and modified glassy carbon with  $\beta$ -Ni(OH) $_2$  nanoparticles (red and blue) in 1 M NaOH electrolyte with scan rate 100 mVs $^{-1}$ , b representing the overpotentials of  $\beta$ -Ni(OH) $_2$  nanoparticles at current density 10 mAcm $^{-2}$

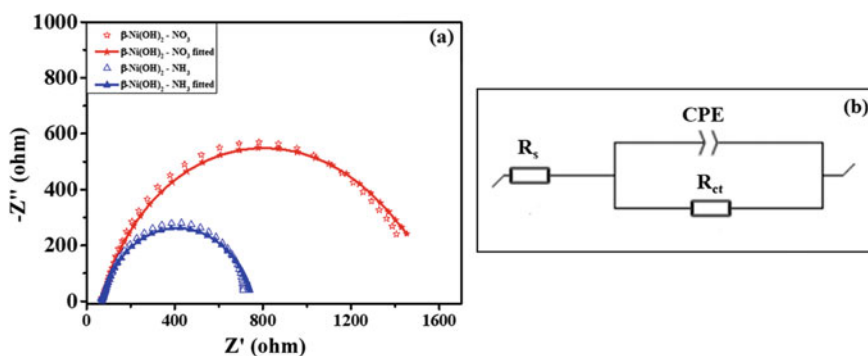


**Fig. 5** a Nyquist plot of catalyst modified glassy carbon working electrode at applied potential 1.72 V versus RHE in 1 M NaOH (raw data represented by unfilled symbols whereas the fitted data are the solid lines with filled symbols) and the scan frequency range between 10 $^5$  and 1 Hz, b representing the insert equivalent circuit model

the samples is drawn between  $-Z''$  imaginary vs.  $Z'$  real axis in the frequency region of 10 $^5$ –1 Hz at potential 1.72 V and is shown in Fig. 5a. Figure 5b shows the best fitted equivalent circuit of the Nyquist graph using Autolab software. Derived charge transfer resistance  $R_{ct}$  from the equivalent circuit indicates that  $\beta$ -Ni(OH) $_2$ -NH $_3$  gives a minimum value of 0.68 K $\Omega$  compared to other samples and facilitates the best charge transfer.

In all samples, using metal-inorganic complexes as a precursor for the synthesis of nickel hydroxide resulted in the formation of metal hydroxide with higher activity compared to the hydroxides obtained from using metal salt, under exactly similar experimental conditions. This may be attributed to the higher solubility of the metal complexes in the reaction medium. Also, it may be possible that during the formation of metal hydroxide, presynthesized metal complexes might have resulted in slow and controlled release of metal ions that leads to the formation of

well-defined structures with good morphology, higher surface area, and minimum charge transfer resistance. These factors resulted in higher activity for the  $\beta$ -Ni(OH)<sub>2</sub>-NH<sub>3</sub> compared to  $\beta$ -Ni(OH)<sub>2</sub>-NO<sub>3</sub>.

## 4 Conclusions

In the current investigation, nickel hydroxide has been synthesized using nickel inorganic complexes Ni(NO<sub>3</sub>)<sub>2</sub>·6H<sub>2</sub>O and [Ni(NH<sub>3</sub>)<sub>6</sub>]<sup>2+</sup> as efficient precursors under hydrothermal conditions.  $\beta$ -Ni(OH)<sub>2</sub>-NH<sub>3</sub> metal hydroxides obtained from [Ni(NH<sub>3</sub>)<sub>6</sub>]<sup>2+</sup> precursors achieved the lowest overpotential of 370 mV at a current density of 10 mAcm<sup>-2</sup> as compared to  $\beta$ -Ni(OH)<sub>2</sub>-NO<sub>3</sub>. Results were also confirmed with other characterization methods. The Nyquist graph of  $\beta$ -Ni(OH)<sub>2</sub>-NH<sub>3</sub> gives a minimum value of 0.68 K $\Omega$  compared to other samples and facilitates the best charge transfer. Scanning electron microscopy confirms the morphology that the  $\beta$ -Ni(OH)<sub>2</sub>-NH<sub>3</sub> has the lowest average particle size of about 20–50 nm and maximum specific surface area of 59.916 m<sup>-2</sup> g. Considering all these parameters, it is further concluded that  $\beta$ -Ni(OH)<sub>2</sub>-NH<sub>3</sub> shows better electrocatalytic activity. These findings will be necessary for the design of future catalysts for the water oxidation reaction.

**Acknowledgements** The authors acknowledge the facility support from Director CSIR-AMPRI, Bhopal. Mr. Kamlesh acknowledges the financial support from the CSIR-UGC (JRF).

## References

1. Chen Y, Rui K, Zhu J, Dou SX, Sun W (2019) Recent progress on nickel-based oxide/(Oxy) hydroxide electrocatalysts for the oxygen evolution reaction. *Chem A European J* 25:703–713
2. Cirone J, Ahmed SR, Wood PC, Chen A (2019) Green synthesis and electrochemical study of cobalt/graphene quantum dots for efficient water splitting. *J Phys Chem C* 1(23):9183–9191
3. Jin Y, Huang S, Yue X, Du H, Shen PK (2018) Mo- and Fe-modified Ni(OH)<sub>2</sub>/NiOOH nanosheets as highly active and stable electrocatalysts for oxygen evolution reaction. *ACS Catal* 8:2359–2363
4. Kuo C-H, Mosa IM, Poyraz AS, Biswas S, El-Sawy AM, Song W, Luo Z, Chen S-Y, Rusling JF, He J, Suib SL (2015) Robust mesoporous manganese oxide catalysts for water oxidation. *ACS Catal* 5:1693–1699
5. Schäfer H, Sadaf S, Walder L, Kuepper K, Dinklage S, Wollschläger J, Schneider L, Steinhart M, Hardege J, Daum D (2015) Stainless steel made to rust: a robust water-splitting catalyst with benchmark characteristics. *Energy Environ Sci* 8:2685–2697
6. Tahmasebi S, Jahangiri S, Mosey N, Jerkiewicz G, Mark A, Cheng S, Botton G, Baranton S, Coutanceau C (2020) Remarkably stable nickel hydroxide nanoparticles for miniaturized electrochemical energy storage. *ACS Appl Energy Mater*
7. Trafela Š, Zavašnik J, Šturm S, Rožman KŽ (2019) Formation of a Ni(OH)<sub>2</sub>/NiOOH active redox couple on nickel nanowires for formaldehyde detection in alkaline media. *Electrochim Acta* 309:346–353

8. Singh A, Hocking RK, Chang SLY, George BM, Fehr M, Lips K, Schnegg A, Spiccia L (2013) Water oxidation catalysis by nanoparticulate manganese oxide thin films: probing the effect of the manganese precursors. *Chem Mater* 25:1098–1108
9. Du X, Fu J, Zhang X (2018) NiCo<sub>2</sub>O<sub>4</sub>@NiMoO<sub>4</sub> supported on nickel foam for electrocatalytic water splitting. *ChemCatChem* 10:5533–5540
10. Kalamaras CM, Efstathiou AM (2013) Hydrogen production technologies: current state and future developments. *Conf Papers Energy* 690627
11. Shi Z, Wang X, Ge J, Liu C, Xing W (2020) Fundamental understanding of the acidic oxygen evolution reaction: mechanism study and state-of-the-art catalysts. *Nanoscale* 12:13249–13275
12. Gao M, Sheng W, Zhuang Z, Fang Q, Gu S, Jiang J, Yan Y (2014) Efficient water oxidation using nanostructured  $\alpha$ -nickel-hydroxide as an electrocatalyst. *J Am Chem Soc* 136:7077–7084
13. Maitra U, Naidu BS, Govindaraj A, Rao CNR (2013) Importance of trivalency and the  $e_{g1}$  configuration in the photocatalytic oxidation of water by Mn and Co oxides. *Proc Natl Acad Sci* 110:11704–11707
14. Chowdhury DR, Spiccia L, Amritphale SS, Paul A, Singh A (2016) A robust iron oxyhydroxide water oxidation catalyst operating under near neutral and alkaline conditions. *J Mater Chem A* 4:3655–3660
15. Koza JA, He Z, Miller AS, Switzer JA (2012) Electrodeposition of crystalline Co<sub>3</sub>O<sub>4</sub>—a catalyst for the oxygen evolution reaction. *Chem Mater* 24:3567–3573
16. Singh A, Fekete M, Gengenbach T, Simonov AN, Hocking RK, Chang SLY, Rothmann M, Powar S, Fu D, Hu Z, Wu Q, Cheng Y-B, Bach U, Spiccia L (2015) Catalytic activity and impedance behavior of screen-printed nickel oxide as efficient water oxidation catalysts. *ChemSuschem* 8:4266–4274
17. Surendranath Y, Dincă M, Nocera DG (2009) Electrolyte-dependent electrosynthesis and activity of cobalt-based water oxidation catalysts. *J Am Chem Soc* 131:2615–2620
18. Zhou F, Izgorodin A, Hocking RK, Spiccia L, MacFarlane DR (2012) Electrodeposited MnOx films from ionic liquid for electrocatalytic water oxidation. *Adv Energy Mater* 2:1013–1021
19. Bode H, Dehmelt K, Witte J (1996) Zur kenntnis der nickelhoxidielektrode—I.Über das nickel (II)-hydroxidhydrat. *Electrochimica Acta* 11:1079–1087
20. Chen Y, Rui K, Zhu J, Dou SX, Sun W (2019) Recent progress on nickel-based oxide/(Oxy) hydroxide electrocatalysts for the oxygen evolution reaction. *Chem Eur J* 25:703–713
21. Ahghari MR, Soltaninejad V, Maleki A (2020) Synthesis of nickel nanoparticles by a green and convenient method as a magnetic mirror with antibacterial activities. *Sci Rep* 10:12627
22. Bediako DK, Lassalle-Kaiser B, Surendranath Y, Yano J, Yachandra VK, Nocera DG (2012) Structure-activity correlations in a nickel-borate oxygen evolution catalyst. *J Am Chem Soc* 134:6801–6809
23. Ash B, Nalajala VS, Popuri AK, Subbaiah T, Minakshi M (2020) Perspectives on nickel hydroxide electrodes suitable for rechargeable batteries: electrolytic vs Chemical Synthesis Routes. *Nanomaterials* 10:1878

# Synthesis and Morphological Study of Ethylene Diamine-Based Nickel Oxide Flower-Like Nanostructure



Deepika Tawar, Kamlesh Goyre, Diksha Choudhary,  
Kali Charan Sabat, and Archana Singh

## 1 Introduction

Nanoparticles are atomic clusters of size between 1 and 100 nm. Typically, nanoparticle's physiochemical properties such as texture, shape, size, and composition, solid or hollow interiors, are different than their bulk materials [1, 2]. The surface properties of materials depend on their large surface-to-volume ratio [3]. Various approaches have been reported to synthesize nanoparticles so far, like radiolytic reduction, polyol process, microemulsion, and alcohol reduction. Recently, nanoparticles' production of various metals and alloys by the hydrogen plasma reduction metal oxides was reported [4–12]. Among the different synthesized metal nanoparticles, synthesized Ni, Fe, Co [4, 12], and Cu [8, 10] nanoparticles attracted attention because they have useful application as conductive and magnetic materials, and can act as a catalyst. But the formation of such nanostructures is comparatively challenging because they get oxidized easily [13]. For the synthesis of nanostructures, two types of approaches are used. The top-down approach includes mechanical devices, ball-mills, etc., and other is the bottom-up approach, which includes growth from the atomic-scale or the reduction of precursors described for nanoparticles of metals and alloys [4–12]. Bottom-up approaches are more favorable as it is suitable for desirable size nanoparticles synthesis. The hydrothermal approach is a better choice among the different synthesis methods, although reaction in the hydrothermal method may take longer times from a few hours up to days. Due to this, in hydrothermal processing,

---

D. Tawar · K. Goyre · A. Singh (✉)

Academy of Scientific & Innovative Research (AcSIR), Ghaziabad 201002, India  
e-mail: [archanasingh@ampri.res.in](mailto:archanasingh@ampri.res.in)

D. Tawar · K. Goyre · D. Choudhary · A. Singh

CSIR–Advanced Material and Processes Research Institute, Bhopal 462026, India

K. C. Sabat

Maulana Azad National Institute of Technology, MANIT, Bhopal 462003, India

microwave technology controls the different experimental parameters like time and temperature which conversely reduces the time up to a few minutes.

Preparation of nanostructures through ultrasonication provides the advantage of better uniform distribution of the developed nanoparticles and provides a thermally stable and pure phase. Nanoparticles synthesis by sonochemistry was previously reported in the literature and structures obtained like nanorods, nanosheets, etc., have the advantages of both the building blocks particles and assemblies. The other fact is that the building blocks particles with high specific surface area provide more effective contact of the electrolyte with the active material, enhancing the structure's utilization rate. The mechanical properties of these assemblies create better stability and practical synthesis. The properties of nanomaterials depend on the size of the structure; therefore, substantial efforts are in progress to synthesize nanostructures in a controlled condition. Similarly, controlled crystallization is also a better method for nanomaterial development because it can produce well-structured particles at the nanoscale.

Nickel hydroxide is generally used for positive electrodes as active material in Ni-based alkaline rechargeable batteries. To understand the reaction time's effect, morphology is systematically studied to further rationalize the structural configuration. How the morphology is an effective parameter and can change the electrochemical performance were also studied. The literature presented that the 3D flower-like  $\beta$ -Ni(OH)<sub>2</sub> electrode revealed a higher specific capacitance. The excellent capacitance of the  $\beta$ -Ni(OH)<sub>2</sub> was developed as a 3D flower-like structure. Due to this, the surface area of the structure was increased, and a shorter conduction length was developed for electrolytic ions. Two polymorphs of nickel hydroxide were demonstrated as  $\alpha$ -Ni(OH)<sub>2</sub> and  $\beta$ -Ni(OH)<sub>2</sub>. The alpha phase represents a theoretically higher electrochemical capacity [14, 15] because it is a metastable phase that during synthesis changed to a beta phase in alkali media [10]. As previously reported, ethylene diamine is a good complexing agent [3, 13]. NiCl<sub>2</sub>·2H<sub>2</sub>O combines with deionized water and forms an intermediate product hydrated nickel cation [Ni(H<sub>2</sub>O)<sub>6</sub>]<sup>2+</sup> in solution. The replacement rate of the bound water in developed nickel complexes depends well on the ligands coordinated to the nickel. Also, the water exchange rate through amine increased with the number of nitrogen which is coordinated to the nickel.

Bodes diagram shows four phases of nickel hydroxides as  $\alpha$ -Ni(OH)<sub>2</sub>,  $\beta$ -NiOOH,  $\beta$ -Ni(OH)<sub>2</sub>, and  $\gamma$ -NiOOH. Literatures proposed  $\alpha$ -Ni(OH)<sub>2</sub> and represented as Ni(OH)<sub>1.5</sub>(NO<sub>3</sub>)<sub>0.5</sub>·0.5H<sub>2</sub>O. A perfect Ni(OH)<sub>2</sub> structure appears through  $\beta$ -Ni(OH)<sub>2</sub>, without any intercalated species. Different nanostructures were observed like marigold, flower-like structure, spherical, and honeycomb with different combinations of precursors. Some of the well-proven structures are discussed here. The structure of nickel hydroxide depends on the adopted method of synthesis. Basically, nickel hydroxide is insoluble in water. In earlier experiments, researchers had added nickel precursor and the ethylene diamine separately or used the nickel precursor, and then, the ammonia is added separately. Hydrothermal can be applied to the synthesis of material, which is not stable at high temperatures. The composition and the morphological parameter of nanomaterials can be organized



with the hydrothermal method [14]. Bernard et al. treated  $\alpha$ -Ni(OH)<sub>2</sub> by aging and formed  $\beta$ -Ni(OH)<sub>2</sub> as a final product where they observed texture and structural properties. They also demonstrated that the formed structure is stable and do not act as a mixture of both. With XRD diffraction, it was seen that the structure of  $\alpha$ -Ni(OH)<sub>2</sub> is disordered, and on the other hand,  $\beta$ -Ni(OH)<sub>2</sub> is well crystallized, and with the aging time, the peaks for (101 and 102) diffraction plane become narrower. Size of the  $\beta$ -Ni(OH)<sub>2</sub> increases with the aging time observed by TEM, which shows that the small needle-shaped  $\alpha$ -phase becomes transformed into  $\beta$ -phase, which is an overall crystalline structure [16]. Sac-Epee et al. reported the phase transformation of  $\gamma$ -NiOOH to form  $\beta$ -Ni(OH)<sub>2</sub> phase due to direct reduction of  $\gamma$ (III) to  $\beta$ (II). The transformation occurred at 0.8 V at the overvoltage of 400 mV. In this transformation process, the particle size during the oxidation retained and  $\gamma$ (III) particles with pseudo-hexagonal platelets set on the 001 planes. They showed the texture difference with TEM and SEM that the  $\beta$  and  $\alpha$  phases have a parallel and well-arranged NiO<sub>2</sub> layer whose inter-sheet distance is 4.6 Å, but  $\gamma$ -layers is showing defects in the inter-sheet distance which varies between 6.75 and 7.3 Å [17]. In 2006, Xiaomin et al. synthesized  $\beta$ -Ni(OH)<sub>2</sub> flower-like structure through a reaction of nickel dimethylglyoximate and NaOH in a solution. The structure consisted of integrated flake-like petals and formed by precursor Ni(dm<sub>g</sub>)<sub>2</sub>. It is observed that the complexing agent of dimethylglyoxime, with alkaline forms a flower-like structure, and it also depends on the temperature. They also tested electrochemical properties of flower-like structure in alkali battery, which showed a discharge capacity of 259 mAh g<sup>-1</sup> which was very good compared to the particulate powder sample. XRD observations showed hexagonal structure without any impurity. Field emission scanning electron microscope (FESEM) showed a uniform sphere of diameter 2–3 μm where the flake-like structures of length 0.5–1.5 μm as a subunit are interconnected and formed a flower-like structure [18]. Yuanyuan et al. developed a flower-like Ni(OH)<sub>2</sub> nanostructure with ethylene diamine in NiCl<sub>2</sub> aqueous solution through hydrothermal reaction, which consisted of ultrathin nanosheets in the range of nanometers. These nanosheets were grown in (001) planes. It showed that the specific surface area is a favorable factor as a material of positive electrode for alkaline batteries utilized in the catalysts, sensors, and electrochromic devices. Specific surface area is well understood as the accessible area of the solid surface per unit mass of the material. It can be calculated as  $S_0 = 2S/m$ , where  $m$  is mass and  $S$  is the structure's surface area [19]. It is observed from the flower-like structure that ethylene diamine is worked as a good complexing agent. Patil et al. prepared a honeycomb-shaped  $\beta$ -Ni(OH)<sub>2</sub> thin films with the chemical bath deposition process. It is centered on thermal decomposition of the ammonia-complexed nickel ions at a temperature of 333 K. SEM images confirmed a less crystalline macroporous and well-interconnected covered honeycomb-shaped morphology. The nanoparticles and nanorod morphologies provide a high specific surface area and porous structure, and provide a better structural foundation results in the form of enhanced specific capacitance. It shows a specific capacitance of  $398 \times 103 \text{ Fkg}^{-1}$  and shows its applicability as better electrode material in electrochemical capacitors [20]. Xiao et al. developed a solvothermal method based on

oleylamine and synthesize nickel hydroxide nanostructure. They obtained flower-like spheres of  $\alpha$ -Ni(OH)<sub>2</sub> and hexagonal sheets of  $\beta$ -Ni(OH)<sub>2</sub> during the synthesis by tuning the water volume. The morphology of the  $\alpha$ -Ni(OH)<sub>2</sub> and  $\beta$ -Ni(OH)<sub>2</sub> were examined to confirm their sphere and nanosheet structure, respectively. Spheres and sheets of NiO were also achieved by direct thermal decomposition of nickel hydroxides [21]. Seth et al. synthesized a nanomaterial-like  $\beta$ -Ni(OH)<sub>2</sub> coating on commercial cotton fabric with the one-pot hydrothermal process. It can separate both lights and heavy oils from the mixture of oil–water with separation efficiency up to 99%.  $\beta$ -Ni(OH)<sub>2</sub> coated fabric presented a significant bacterial reduction in the polluted water. It is fabricated by an economical process and is useful for hassle-free separation of oil–water mixtures. Also, this coated fabric shows a noteworthy electrical conductivity [22].

In, our experiment  $[\text{Ni}(\text{en})_3]^{2+}$  complex is used as a precursor that resulted in improved morphology compared to the material obtained using nickel salt and ethylene diamine precursor. We synthesized  $\beta$ -Ni(OH)<sub>2</sub> flower-like nanostructure using Ni(II) complexes through one-pot hydrothermal method. The morphology and composition of nanomaterials can be controlled with the hydrothermal method.

## 2 Experimental

### 2.1 Materials

All chemical reagents, in which nickel nitrate hexahydrate; Ni(NO<sub>3</sub>)<sub>2</sub>·6H<sub>2</sub>O, ammonia, ethylene diamine (en); H<sub>2</sub>NCH<sub>2</sub>CH<sub>2</sub>NH<sub>2</sub>, sodium hydroxide; NaOH, ethanol; C<sub>2</sub>H<sub>5</sub>OH, were purchased from SRL Pvt. Ltd. India and used as it is. The distilled water was obtained using an ECO-STILL Mark—2000, a single-phase system, used for synthesis and chemical apparatus washing.

### 2.2 Synthesis of $\beta$ -Ni(OH)<sub>2</sub>

Nickel hydroxide nanoparticles were synthesized with Ni(NO<sub>3</sub>)<sub>2</sub>·6H<sub>2</sub>O and  $[\text{Ni}(\text{en})_3]^{2+}$  complexes precursor. We use  $[\text{Ni}(\text{en})_3]^{2+}$  precursor and nickel salt along with ethylene diamine precursor in the separate synthesis process.  $[\text{Ni}(\text{en})_2]^{2+}$  was first prepared by coprecipitation methods as described below:

**Synthesis of  $[\text{Ni}(\text{en})_2]^{2+}$  complex** Nickel nitrate hexahydrate (6 gm) was first dissolved in water (3 ml) in a beaker with stirring at room temperature. After that, the solution was cooled in ice, and ethylene diamine (5.6 ml) was added, and then, cool ethanol (15 ml) was added to the solution, so that the precipitates were formed. After cooling the precipitates settle down, which is then filtered and dried at room temperature.

**Hydrothermal synthesis:** This is carried out in a 100 ml hydrothermal cell at a temperature of 170 °C for 24 h. Obtained precipitate after reaction was washed thoroughly and then dried at room temperature. Based on the used precursor, two different metal hydroxide nanostructures are abbreviated as  $\beta$ -Ni(OH)<sub>2</sub>-A and  $\beta$ -Ni(OH)<sub>2</sub>-B.

**Synthesis of  $\beta$ -Ni(OH)<sub>2</sub>-A:** 0.2 M nickel nitrate is taken and added 43.5 ml H<sub>2</sub>O. In this solution, 2.5 ml ethylene diamine is added, and the pH was adjusted to 13. Afterward, the solution was put in an autoclave at a temperature of 170 °C for 24 h and then rinse with water and dried at room temperature.

**Synthesis of  $\beta$ -Ni(OH)<sub>2</sub>-B:** 0.2 M [Ni(en)<sub>3</sub>]<sup>2+</sup> complex is taken and added 46 ml 1 M NaOH solution. In this process, pH was adjusted to 13. Put this solution in an autoclave at the temperature of 170 °C for 24 h. Then, cool the autoclave, rinse with water, and dry it at room temperature.

## 2.3 Characterization

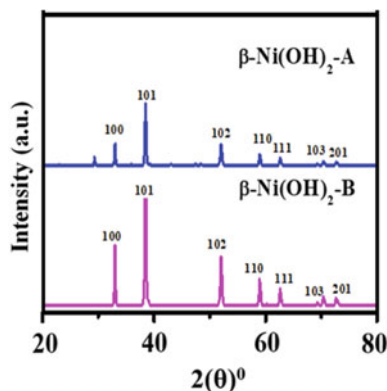
The X-ray diffraction (XRD) pattern was recorded via a Bruker AXS with Cu K $\alpha$  radiation wavelength of 1.54 Å with a  $2\theta$  range of 20°–80°. The morphological investigation and imaging of nanoparticles were taken on a high-resolution scanning electron microscope (HRSEM) using the Carl Zeiss Ultra Plus instrument. The hydrodynamic size of different  $\beta$ -Ni(OH)<sub>2</sub> nanoparticles was determined via Beckman coulter S/N 133,210 particle size analyzer.

## 3 Results and Discussion

### 3.1 X-ray Diffraction

XRD patterns of  $\beta$ -Ni(OH)<sub>2</sub> nanoparticles synthesized with two different precursors are shown in Fig. 1. XRD pattern confirms the formation of pure hexagonal phase  $\beta$ -Ni(OH)<sub>2</sub>. The peaks were well indexed with standard value (JCPDS 14-0117), and the structures are defined in space group P-3m1 (164) [23]. The characteristic diffraction patterns were observed at  $2\theta = 33.0, 38.5, 59.0,$  and  $62.7$  corresponding to the planes of (100), (101), (110), and (111), respectively. The calculated lattice constants for prepared samples are to be  $a = b = 0.3125$  nm and  $c = 0.4648$  nm. It is observed that they are close to the standard values of  $\beta$ -Ni(OH)<sub>2</sub>. The XRD pattern shows that the diffraction peak of (101) is the strongest in all the diffraction peaks. Also, it is observed that no other peaks were observed confirming the pure phase formation for the sample.

**Fig. 1** X-ray diffraction pattern of synthesized  $\beta$ -Ni(OH)<sub>2</sub> nanoparticles



### 3.2 Morphological Study

The morphology of the prepared sample as determined by a scanning electron microscope is shown in Fig. 2. Figure 2a, b shows FESEM image of  $\beta$ -Ni(OH)<sub>2</sub>-A at 1  $\mu$ m and 200 nm, respectively. Figure 2c, d represents  $\beta$ -Ni(OH)<sub>2</sub>-B at 1  $\mu$ m and 200 nm, respectively. As can be seen that, the metal precursors taken for the formation of nickel hydroxide have a significant impact on the morphology of the developed samples. On using ethylene diamine separately and along with nickel nitrate, [Ni(en)<sub>3</sub>]<sup>2+</sup> complex formed. It is seen that for  $\beta$ -Ni(OH)<sub>2</sub>, the agglomerated structure is observed. SEM image of  $\beta$ -Ni(OH)<sub>2</sub>-A shows a sheet-like structure of size 5.2  $\mu$ m and for  $\beta$ -Ni(OH)<sub>2</sub>-B shows a flower-like structure of size 3.7  $\mu$ m because in these structures the particles are assembled as a group and form a congregated structure of size in the range of micrometer. Using -en ligand both with the metal salt or complexed with the nickel results in the agglomerated structure; however, in the latter case, the formed flower-like structure is very well defined with uniform size [24]. These flowers are made of nanoplates-like structures. Results show that by using predefined metal complexes, well-defined nanostructures are produced.

### 3.3 Dynamic Light Scattering (DLS)

To determine the hydrodynamic sizes or particle size distribution of different  $\beta$ -Ni(OH)<sub>2</sub> nanoparticles, each of the synthesized material was dispersed in an aqueous medium and sonicated. The formed colloidal solution was left for one minute under equilibrium. DLS experiment of aqueous colloidal solution was performed for estimation of the particle size in the liquid phase. Figure 3a, b represents dynamic light scattering for particle size distribution for  $\beta$ -Ni(OH)<sub>2</sub>-A and  $\beta$ -Ni(OH)<sub>2</sub>-B, respectively. Figure 3 shows that particle size distribution of  $\beta$ -Ni(OH)<sub>2</sub>-A is higher than the particles of  $\beta$ -Ni(OH)<sub>2</sub>-B.

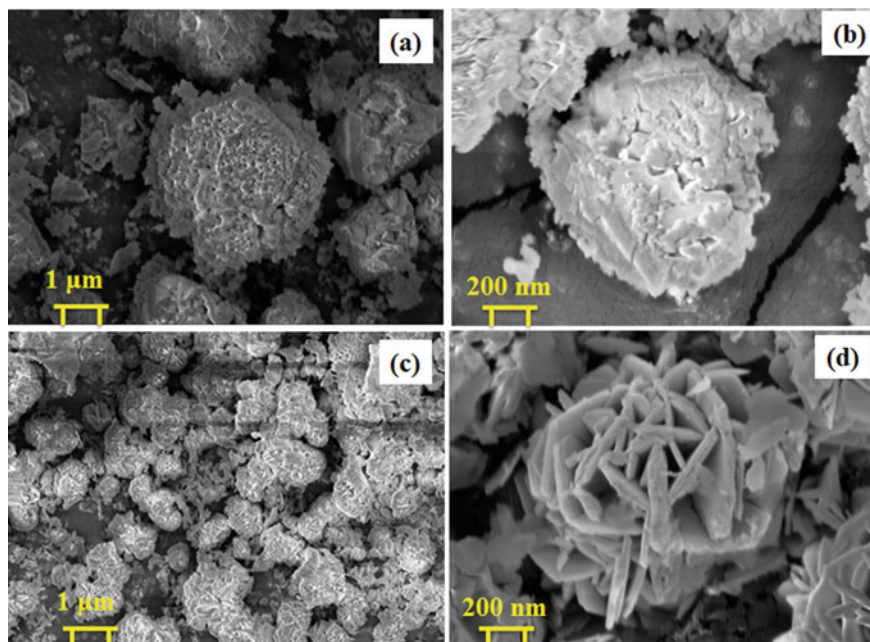


Fig. 2 FESEM image of **a**  $\beta$ -Ni(OH)<sub>2</sub>-A at 1  $\mu$ m and **b** 200 nm, **c**  $\beta$ -Ni(OH)<sub>2</sub>-B at 1  $\mu$ m and **d** 200 nm

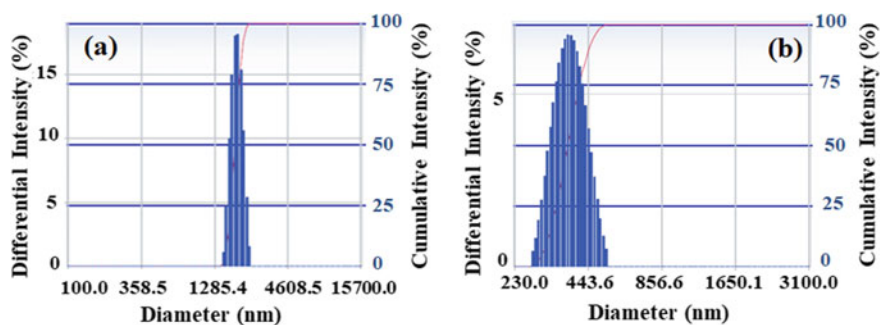


Fig. 3 Dynamic light scattering for particle size distribution for **a**  $\beta$ -Ni(OH)<sub>2</sub>-A and **b**  $\beta$ -Ni(OH)<sub>2</sub>-B

## 4 Conclusions

In this work, nickel hydroxide is synthesized using nickel inorganic complex  $[\text{Ni}(\text{en})_3]^{2+}$  and metal salt along with ethylene diamine precursor as two different precursors under hydrothermal conditions. With this approach, the materials' morphology is improved with nickel ethylene diamine complex compared to the

material obtained using nickel salt along with ethylene diamine precursor. SEM image of  $\beta$ -Ni(OH)<sub>2</sub>-A showed a sheet-like structure of size 5.2  $\mu\text{m}$ , and  $\beta$ -Ni(OH)<sub>2</sub>-B showed a flower-like structure of size 3.7  $\mu\text{m}$ . Using a mixture of –en ligand and the metal salt precursor for the synthesis of nickel hydroxide, lots of agglomerated structure were found. In contrast, on using predefined [Ni(en)<sub>3</sub>]<sup>2+</sup> complex, a very well-defined flower-like structure was found. These findings will be important for the design of nanomaterials with well-defined morphology.

**Acknowledgements** Authors would like to acknowledge Director CSIR-AMPRI, and AcSIR, Bhopal, India to provide facility to carry out research work.

**Conflict of Interest** The authors declare that there is no conflict of interest.

## References

1. Din MI, Aneela R (2016) Recent advances in the synthesis and stabilization of nickel and nickel oxide nanoparticles: a green adeptness Int J Anal Chem
2. De Oliveira PF, Torresi RM, Emmerling F, Camargo PH (2020) Challenges and opportunities in the bottom-up mechanochemical synthesis of noble metal nanoparticles. J Mater Chem A 8 (32):16114–16141
3. Ahghari MR, Soltaninejad V, Maleki A (2020) Synthesis of nickel nanoparticles by a green and convenient method as a magnetic mirror with antibacterial activities. Sci Rep 10(1):1–10
4. Sabat KC, Paramguru RK, Mishra BK (2017) Reduction of oxide mixtures of (Fe<sub>2</sub>O<sub>3</sub> + CuO) and (Fe<sub>2</sub>O<sub>3</sub> + Co<sub>3</sub>O<sub>4</sub>) by low-temperature hydrogen plasma. Plasma Chem Plasma Process 37 (4):979–995
5. Sabat KC (2019) Hydrogen plasma-thermodynamics. J Phys: Conf Ser vol 1172(1):12086 (IOP Publishing)
6. Sabat KC, Rajput P, Paramguru RK, Bhoi B, Mishra BK (2014) Reduction of oxide minerals by hydrogen plasma: an overview. Plasma Chem Plasma Process 34(1):1–23
7. Sabat, K. C., Iron production by hydrogen plasma. International Conference on Applied Physics, Power and Material Science vol 1172 (Institute of Physics Publishing), 1–5 (2019).
8. Sabat KC (2019) Formation of CuCo alloy from their oxide mixtures through reduction by low-temperature hydrogen plasma. Plasma Chem Plasma Process 39(4):1071–1086
9. Sabat KC, Murphy AB (2017) Hydrogen plasma processing of iron ore metall. Mater Trans B Process Metall Mater Process Sci 48(3):1561–1594
10. Sabat KC, Paramguru RK, Mishra BK (2016) Reduction of copper oxide by low-temperature hydrogen plasma. Plasma Chem Plasma Process 36(4):1111–1124
11. Sabat KC, Paramguru RK, Mishra BK (2018) Formation of copper-nickel alloy from their oxide mixtures through reduction by low-temperature hydrogen plasma. Plasma Chem Plasma Process 38(3):621–635
12. Sabat KC, Paramguru RK, Pradhan S, Mishra BK (2015) Reduction of cobalt oxide (Co<sub>3</sub>O<sub>4</sub>) by low temperature hydrogen plasma. Plasma Chem Plasma Process 35(2):387–399
13. Chen DH, Hsieh CH (2002) Synthesis of nickel nanoparticles in aqueous cationic surfactant solutions. J Mater Chem 12(8):2412–2415
14. Gan YX, Jayatissa AH, Yu Z, Chen X, Li M (2020) Hydrothermal synthesis of nanomaterials. J Nanomater

15. Hall DS, Lockwood DJ, Bock C, MacDougall BR (2015) Nickel hydroxides and related materials: a review of their structures, synthesis and properties. *Proc R Soc A Math Phys Eng Sci* 471:2174
16. Bernard MC, Bernard P, Keddam M, Senyariç S, Takenouti H (1996) Characterization of new nickel hydroxides during the transformation of  $\alpha$  Ni(OH)<sub>2</sub> to  $\beta$  Ni(OH)<sub>2</sub> by ageing. *Electrochim Acta* 41(1):91–93
17. SacÉpée N, Palacin MR, Delahaye VA, Chabre Y, Tara JM (1998) Evidence for direct  $\gamma$ -NiOOH $\leftrightarrow$   $\beta$ -Ni(OH)<sub>2</sub> transitions during electrochemical cycling of the nickel hydroxide. *Electrode J Electrochem Soc* 145(5):1434
18. Ni X, Zhao Q, Zhang Y, Song J, Zheng H, Yang K (2006) Large scale synthesis and electrochemical characterization of hierarchical  $\beta$ -Ni(OH)<sub>2</sub> flowers. *Solid State Sci* 8(11):1312–1317
19. Luo Y, Duan G, Li G (2007) Synthesis and characterization of flower-like  $\beta$ -Ni(OH)<sub>2</sub> nanoarchitectures. *J Solid State Chem* 180(7):2149–2153
20. Patil UM, Gurav KV, Fulari VJ, Lokhande CD, Joo OS (2009) Characterization of honeycomb-like “ $\beta$ -Ni(OH)<sub>2</sub>” thin films synthesized by chemical bath deposition method and their supercapacitor application. *J Power Sources* 188(1):338–342
21. Liang X, Xiao J, Gou Y, Chen B (2011) Synthesis and catalysis properties of NiO flower-like spheres and nanosheets: Water-induced phase transformation of nickel hydroxides. *J Mater Res* 26(24):3091–3097
22. Seth M, Jana S (2021) Fabrication and multifunctional properties of marigold-like nanostructured  $\beta$ -Ni(OH)<sub>2</sub> coated cotton fabric. *Cellulose* 39:1–22
23. Xia J, Wang Q, Wei M, Chen L, Liu N, Fan S, Wu H (2021) In situ grown NiIn<sub>2</sub>S<sub>4</sub> nanosheets as counter electrode for bifacial quasi-solid-state dye-sensitized solar cells. *J Mater Sci* 56(3):2372–2384
24. Lv B, Liu Z, Ding R, Wu D, Xu Y (2013) Fast production of  $\beta$ -Ni(OH)<sub>2</sub> nanostructures with (001) and (100) plane exposure and their electrochemical properties. *J Mater Chem A* 1(18):5695–5699

# Automated Real-Time Transformer Health Monitoring System Using the Internet of Things (IoT)



P. Venkat Subramanian, Venkatesh Boddapati, and S. Arul Daniel

## 1 Introduction

The distribution transformer is a vital element in any power transmission system. Hence, if the transformer's health is not monitored with due importance, it can lead to many quandaries that may cause a huge loss in time, power, infrastructure, and money. The transformers health is affected by several factors involving the windings, insulation, core, and transformer oil. However, the most influential parameters that affect the health of a transformer are the voltage, current, and winding temperature of the transformer [1]. Thus, measuring these parameters could give a good analysis of the transformer's health [2]. The operating conditions are generally determined by the loading of the transformer and the losses involved in the transmission line. This affects the transformer temperature, eventually disturbing the transformer's health [3]. Since we cannot predict the transients and sudden disturbances (sag, swell, etc.) in a power system, we need to monitor the transformer continuously to obtain real-time data and warn the engineer if there is a need for intervention [4, 5]. Presently, monitoring is done by an engineer on-site. This is highly unreliable as the engineer may not always be available and hence there is a possibility that major faults and surges go undetected [1]. Hence, it is necessary to build a monitoring system that is reliable, detects faults quicker than the existing model and to analyze real-time data concerning the transformer and provide adequate reports to the data center in time, so that appropriate precautions are taken to prevent adversities. The life of a transformer is dependent on its health. The healthier the transformer, the longer the transformer can be put into use [6].

This article aims at using Internet of things to solve this problem. The analyzed data is used to alert the engineer in case the data is abnormal, and an automated feedback system will sense if the temperature of the transformer is high and

---

P. V. Subramanian · V. Boddapati (✉) · S. A. Daniel  
National Institute of Technology, Tiruchirappalli 620015, India  
e-mail: [venkateshb.eee@bmsce.ac.in](mailto:venkateshb.eee@bmsce.ac.in)



accordingly increase the capacity of the cooling mechanism. Overall, the IoT-based monitoring system helps identify problems before they occur hence allowing us to arrange for methods to reduce the effects of the fault, thus manuscript clicks here to view linked references improving the health and performance. The article compares the proposed model with the existing model and compares the results to provide a reasonable conclusion. Various sources and papers were thoroughly studied and analyzed, and the inspirations and observations drawn are listed below. This article identifies and attempts to overcome the drawbacks of each model proposed. Mariprasath et al. [7] suggested a thermal imaging-based technique to monitor the temperature of a transformer. From the thermal images, the major hotspots are found out and are cooled accordingly using the cooling mechanism. However, this method can be expensive and sophisticated. The authors in [8] and [9] suggested a GSM-based technique. GSM is independent of the distance between the data center and the transformer; thus, it is more reliable during network interruptions and is also faster than conventional communication methods. Thus, it is fair to employ it in an IoT-based system. In the papers [2, 3], sensors that track each parameter—voltage, current, and temperature and send the data to the microcontroller, which sends the data to the data center via the Internet, were used. This system is highly reliable and effective. In [5] and [10], a localized mobile embedded prototype was proposed. This tracks the load current, transformer potential, transformer oil temperature, and levels and displays the parameters' values. The system also employs a GSM module and a microcontroller to carry out the data transfer and alert the engineer using an SMS. Srivastava et al. [2] had simulated a laboratory model of the proposed IoT-based display system. Another laboratory model was proposed in [11], where an integrated GSM module was also used for data transfer, and the results were claimed to be promising. Hasan et al. [9] had simulated the working of an IoT-based transformer and recorded the transformer life, comparing it against the present transformer model's lifetime, plotting the obtained results.

### ***1.1 GPRS Technology Used***

GPRS stands for general packet radio service. The technology uses cellular networks to transfer data via a packet-switching technology. The speed of GPRS ranges from 150 to 300 kbps. The GPRS technology is used here to send and receive voice and data simultaneously. The GPRS is synonymous to the Internet, offering mobility, reliability, and localization [13].

### ***1.2 Transformer Health Parameters***

**Transformer voltage.** The voltage of a transformer is prone to variations in a power system. Harmonics in the power system can cause disturbances to the

transformer due to continuously varying voltage. The health of a transformer reduces with frequent swells, sags, and overvoltages. Thus, monitoring the voltage of the transformer using a voltage sensor is crucial.

**Transformer current.** The current of a transformer is instrumental in determining the losses present. High current can lead to increased losses in the transformer and reduction in the transformer life and power quality of the power system. The current of the transformer is measured using a current transformer or current sensor.

**Winding temperature.** The temperature of the windings plays a major role in determining the lifetime of a transformer. Increase in winding temperature for a significantly long time can damage the windings and its insulation, causing the transformer to even fail. A temperature-dependent resistor is used to measure the temperature and accordingly give an analog output.

**Transformer oil level.** The oil of the transformer is used as an insulating material used in the safe functioning of a transformer. It is tested in regular intervals using various chemical tests to ensure that it is fit for use in the transformer. The temperature of the oil also gives a measure about the general health of the transformer and its performance.

## 2 Proposed IoT-Based Model

### 2.1 Block Diagram

A block diagram depicting the model that is to be used for invigilating the transformer is represented by Fig. 1. We need to note that the design comprises of two major parts (i) the hardware and (ii) the software sections. The two are integrated to perform seamlessly, complementing each other.

### 2.2 Hardware

**Voltage sensor.** A potential transformer is employed to serve as a voltage sensor. An analog voltage proportional and corresponding to the transformer voltage is recorded and sent to the ADC and then to the microcontroller.

**Current sensor.** A current transformer is used as a current sensor where it measures the current flowing through the transformer and steps it down to an analog value that can be processed by a microcontroller. The values stored in the database of the current sensors can be later used for different analysis. If the current exceeds a particular value, the circuit trips to prevent permanent damage.

**Temperature sensors (LM-35).** The temperature sensors measure the temperature of the windings, the insulations, and the transformer oil and pass it to the

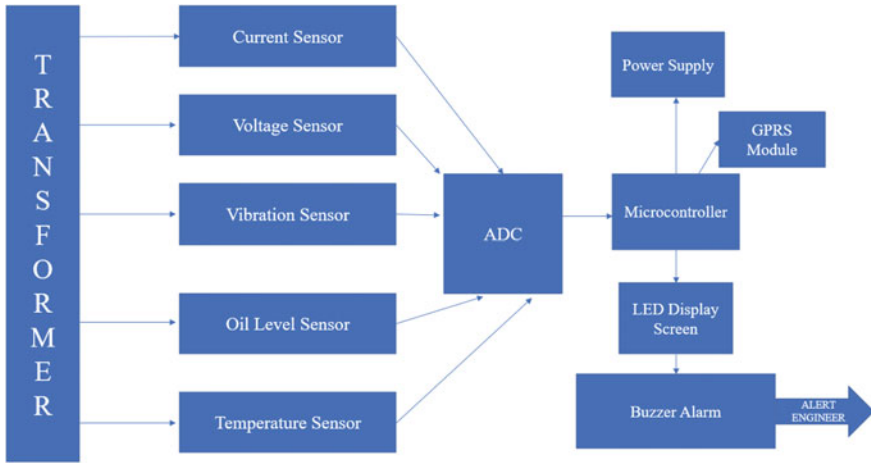


**Fig. 1** Block diagram of proposed real-time health monitoring system

analog-to-digital converter (ADC) where they are converted to digital data. The LM series temperature sensors are the most reliable and accurate integrated circuit sensors in the market due to the fact that the output voltage is directly proportional to the Celsius scale. The LM-35 sensors do not require external regulation as they deliver a precision of  $\pm 1/4^{\circ}\text{C}$  at room temperature.

**Oil-level sensor.** The oil levels of a transformer determine the longevity of the transformer. The oil samples are to be regularly taken and analyzed chemically to determine the health of the transformer. The level of oil present in the transformer is critical as it determines the insulating properties of the transformer during its function. So a floating device is used to measure the level of oil in the transformer during its day-to-day functioning [10].

**NodeMCU.** It is an open-source Internet of things platform consisting of a Wi-Fi development board of 24 GHz. The NodeMCU is a combined unit and all the resources are present in the development board. The main advantage of using NodeMCU is its compatibility with modern tools such as node.js, which helps achieve the best results in the fastest time.

**GPRS module.** The GSM module has the capability to send an SMS or a message to the engineer who is off-site using mobile data as the means of communication. The module has the capability to receive, delete, store, and write messages simultaneously.

**Microcontroller.** A capable and powerful microcontroller such as the PIC 18F4550 is used as a control mechanism. The microcontroller analyzes the digital signals that arrive from the analog-to-digital converters (ADCs) and accordingly warn the engineer via the GSM/GPRS module.

## 2.3 Software

**NodeMCU software.** The NodeMCU software plays a critical role in coding the control unit of the microcontroller. The IDE is preferred due to its speed, reliability, and universal presence.

**Database management system.** A database that records the transformer data is required for the engineer to refer to the previous data to get an idea about the condition of the transformer. The engineer cannot monitor the transformer constantly. Thus, the previous data is stored in the database to be updated on the Web page regularly.

**Application development.** Communication between the transformer and the engineer is implemented through the Web page. A basic language like HTML is enough to design a simple Web page that will track all the parameters consistently and display the information in a neat user interface.

## 3 Impact on Transformer Life—Case Study

The transformer failure can impact the power system drastically. Such failures reduce the lifetime of a transformer as the windings and other components are permanently damaged. However, most of these damages can be prevented if the engineer predicts the failure before it happens. With the intervention of IoT, this can be made possible. Figure 2 shows the primary causes of failure in a distribution transformer. We can see that the leading causes of failure are insulation failure and winding failure. Insulation failure mainly occurs due to the overheating of the windings. Winding failure is primarily due to persistent overvoltages and faults in the transformer and due to heating of the windings.

Using the present real-time monitoring system using IoT, the engineer can foresee these errors and failures before the failure occurs, thus preventing the failures from happening. Majority of the failures are due to overheating, oil contamination, and overloading. Since oil levels are also monitored in the proposed mechanism, a significant number of failures are reduced. The health of a transformer is influenced by the number of failures it faces throughout its lifetime. If a transformer is prone to many failures, it reduces the lifetime of the transformer by a large amount. Bringing in automation into the picture reduces the scope for these failures and thus increases the life and health of the transformer.

The proposed model was tested in a laboratory, and the results obtained were recorded. Over the long run, the smart model was successfully able to prevent a large number of unprecedented failures as the engineer was able to identify the root cause of the problem and resolve it in due time.

Bringing in automation into the picture has proven to be very useful as the cooling mechanism does not require to operate in maximum capacity when there is significantly low load. This saves energy and cost of operation. The elimination of

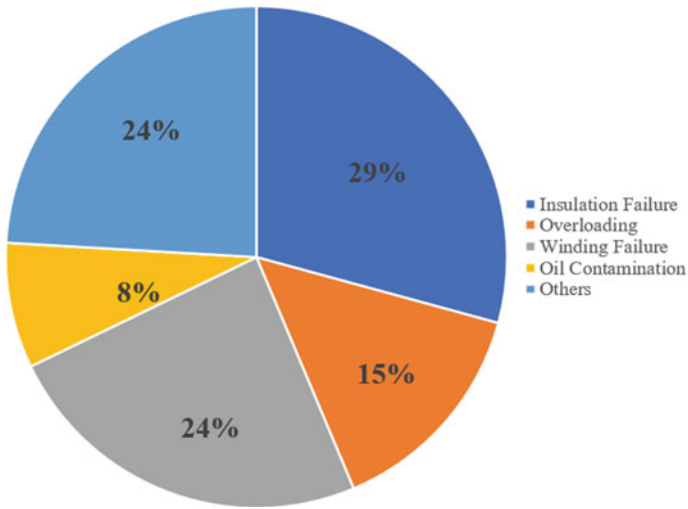


Fig. 2 Pie chart depicting the causes of transformer failure [12]

the human factor in the equation has resulted in a more reliable system, as the feedback system operates itself to nullify the disturbances caused. The proposed model's results are shown from MPLAB in Fig. 3 where the existing cumulative lifetime of a transformer is compared to that of the proposed model, with results obtained from [9, 12, 14–20].

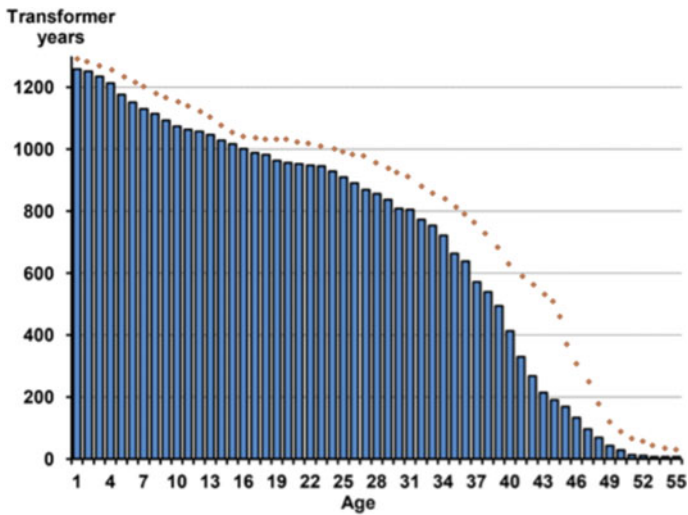


Fig. 3 Graph comparing lifetime of existing transformer [9] with proposed model

The average lifespan of a transformer is increased considerably by 5–6 years as observed from the graph plotted above. Moreover, significant amount of energy, effort, and cost are saved by employing automated mechanisms to control the transformer parameters.

## 4 Conclusions

The real-time health monitoring system using Internet of things as proposed by this article is being designated as the energy efficient and cost-effective alternative to the existing model, where the monitoring is done manually. The model eliminates the scope for human error and automates the process thereby making the system more reliable and freer from faults and errors. By tracking critical transformer health parameters such as the voltage, current, temperature, and oil level continuously with time, we can prevent the transformer from encountering frequent failures, thus improving the overall health of the transformer, subsequently its lifetime. The parameters are tracked using appropriate sensors which transmit real-time data to the microcontroller which sends an alert to the engineer who is not on-site via GSM as an SMS or through the Internet. Although the proposed system poses certain risks such as cyberattacks, establishing a secure cybersecurity system to implement the model will prove very useful on the long run, saving significant costs and energy. The system uses a cloud-based database management system and displays the real-time health parameters through a Web-based application; thus, the data is accessible remotely to the engineer.

## 5 Future Scope

The system is a breakthrough in integrating the transformer with the new advents of the Internet and seamless microcontroller systems. In future models of the same, the system can also incorporate GPS and other technologies to automate tasks based on the weather, temperature, and condition of the location. The security in such cases must be of a very high standard and must be tested in frequent intervals of time. It is impractical to replace all the existing transformer systems with the new IoT-based transformers as it will incur huge costs and may cause significant interruptions in the respective power systems. Hence, the proposed model can be implemented in the transformers that are constructed in the future. With the implementation of smart grids and microgrids gaining popularity in the energy sector, smart transformers are the next breakthrough in the field of power systems research.

## References

1. Bengtsson C (1996) Status and trends in transformer monitoring. *IEEE Trans Power Delivery* 11(3)
2. Srivastava D, Tripathi MM (2018) Transformer health monitoring system using internet of things. In: 2018 2nd IEEE international conference on power electronics, intelligent control and energy systems (ICPEICES), Delhi, India, pp 903–908. <https://doi.org/10.1109/ICPEICES.2018.88>
3. Chan WL, So ATP, Lai LL (1999) Internet based transmission substation monitoring. *IEEE Trans Power Syst* 14(1):293–298. <https://doi.org/10.1109/59.744546>
4. Marques AP, de Jesus Ribeiro C, Azevedo CHB et al (2014) Power transformer disruptions—a case study. *IEEE Electr Insul Magaz* 30(2):17–21
5. Couto M, Peças Lopes JA, Moreira CL (2019) Control strategies for multi microgrids islanding operation through smart transformers. *Electr Power Syst Res* 174, 105866, ISSN 0378-7796. <https://doi.org/10.1016/j.epsr.2019.105866>
6. Liebfried T (1998) Online monitors keep transformers in service. *IEEE Comput Appl Power* 36–42
7. Mariprasath T, Kirubakaran V (2018) A real time study on condition monitoring of distribution transformer using thermal imager. *Infrared Phys Technol* 90:78–86. <https://doi.org/10.1016/j.infrared.2018.02.009>
8. Sujatha MS, Kumar MV (2011) On-line monitoring and analysis of faults in transmission and distribution lines using gsm technique. *J Theor Appl Inf Technol* 33(2), ISSN: 1992-8645, E-ISSN: 1817-3195
9. Hasan WKA, Alraddad A, Ashour A, Ran Y, Alkelsh MA, Ajele RAM (2019) Design and implementation smart transformer based on IoT. In: 2019 International conference on computing, electronics and communications engineering (iCCECE), London, United Kingdom, pp 16–21. <https://doi.org/10.1109/iCCECE46942.2019.8941980>
10. Hussain M, Salman M, Rohit Subhan A, Khalid H, Zaidi SSH (2018) Condition based health monitoring of transformers. In: 2018 International conference on computing, mathematics and engineering technologies (iCoMET) 10.1109
11. Nelson AA, Jaiswal GC, Ballal MS, Tutakne DR (2014) Remote condition monitoring system for distribution transformer. 978-1-4799-5141-3/14/\$31.00 ©IEEE
12. Singh J, Singh S (2016) Transformer failure analysis: reasons and methods. *Int J Eng Res Technol* (IJERT), ISSN: 2278–0181
13. Mao H (2010) Research of wireless monitoring system in power distribution transformer station based on GPRS, vol 5, IEEE, 978-1-4244-5586-7/10/\$26.00
14. Jayanth KG, Boddapati V, Geetha RS (2018) Comparative study between three-leg and four-leg current-source inverter for solar PV application. In: Proceedings of the 2018 international conference on power, instrumentation, control and computing (PICC), Thrissur, India, 18–20 January 2018. <https://doi.org/10.1109/PICC.2018.8384793>
15. Boddapati V, Sathesh Kumar T, Prakash N et al. Current droop control of parallel inverters in an autonomous microgrid. *Mater Today: Proc.* <https://doi.org/10.1016/j.matpr.2020.09.496>
16. Boddapati V, Arul Daniel S (2020) Performance analysis and investigations of grid-connected solar power park in Kurnool, South India. *Energy Sustain Dev* 55:161–69. <https://doi.org/10.1016/j.esd.2020.02.001>
17. Munjer MA, Sheikh MRI, Alim MA, Boddapati V, Musaib MA (2018) Minimization of THD for multilevel converters with triangular injection approach. In: 2018 3rd international conference for convergence in technology (I2CT), Pune, pp 1–4. <https://doi.org/10.1109/I2CT.2018.8529750>
18. Boddapati V, Ram Nandikatti AS (2020) Salient features of the national power grid and its management during an emergency: a case study in India. *Energy Sustain Dev* 59:170–179. <https://doi.org/10.1016/j.esd.2020.10.010>

19. Suresh Babu V, Ravi Kumar M, Boddapati V. Design and control of a DC microgrid by using a modern predictive controller. Mater Today: Proc. <https://doi.org/10.1016/j.matpr.2020.10.115>
20. Munjer MA, Boddapati V, Sheikh MRI, Alim MA (2020) Materials today : proceedings application of modified triangular injection technique on MMC to decrease ARM current Upper arm. Mater Today Proc 1–6. <https://doi.org/10.1016/j.matpr.2020.12.054>



# A Comprehensive Study on Adaptive MPPT Control Techniques for Efficient Power Generation



Pushpendra Dangi, Amit Ojha, Shiv Pratap Singh, Suresh Kr. Gawre, Sangharsh Meshram, and Arvind Mittal

## 1 Introduction

The renewable energy sources are playing a critical role in supplying and meeting the present energy requirements of the world. Among these energy sources, solar photovoltaic (PV)-based energy is playing the biggest role as it is omnipresent, available all the day. The application of PV-based generation is low cost and pollution-free source of energy and hence can be taken into account to fulfil the energy needs of residential, horticulture, health sectors, etc. Due to various constraints of technicalities, we are unable to utilize the total energy of the sun. The photovoltaic cells of type crystalline-silicon modules have efficiency of 14–16% and the high quality design accounts for attaining an efficiency of 17–21%. We also have to consider that solar energy harnessed array/module in real time is comparatively low due to the dynamic nature of solar insolation. The energy generation is tracked to get maximum power and directed towards maximum power point. This converter techniques make use of PV-energy as an input and output is the storage or external load connected to it. These MPPT converters also make photovoltaic uncontrolled DC power to a regulated power supply. A lot of MPPT techniques used to run PV-modules on maximum possible power with their respective pros and cons. The efficiency of the particular technique depends on the ability of its tracking in instantaneously changing weather conditions like shading, wind velocity and angle of solar insolation. So, depending on their nature of tracking these techniques are classified classical MPPT, intelligence MPPT and optimization MPPT.

For classical MPPT [1, 2], the techniques include incremental conductance (InC), perturb and observe (P&O), variable step size (P&O), etc. The above named

---

P. Dangi · A. Ojha (✉) · S. P. Singh · S. Kr. Gawre · S. Meshram  
Department of Electrical Engineering MANIT, Bhopal, India

A. Mittal  
Energy Centre MANIT, Bhopal, India

techniques are easy to implement and very effective for unvarying irradiation circumstances as the PV will produce only one GMPP in these conditions. But these algorithms suffer from MPP oscillations and hence results in loss of power. Artificial neural network (ANN), fuzzy logic control (FLC), Fibonacci series-based MPPT, sliding mode control (SMC) and Gauss–Newton approach-based MPPT are included in intelligence-based techniques [1, 3]. These techniques are suitable for dynamic conditions. But these techniques suffer from big data processing and huge control-circuit complexity for the purpose of training of the system. These techniques are emerging rapidly because of their intelligence in tracking maximum power point because of straightaway and rapid updating the searching range. Optimization-based techniques [1, 4] include grey wolf optimization (GWO), particle swarm optimization (PSO), cuckoo search CS-based, artificial bee colony (ABC) and ant colony optimization (ACO). These techniques can search true maximum power point in dynamic weather conditions and with lesser steady-state oscillations. The implementation of these is also easier with the help of low-cost microcontrollers. GWO can search for optimum point of working at a faster as if like wolf continuously searching for its prey and require fewer temperature and voltage sensors than classical ones. In this comprehensive study, pros, cons and performance of MPPT techniques are compared based on their control strategy, stability, tracking rate, efficiency and complexity. The ultimate objective is to present the ongoing advanced made in MPPT techniques. Thus, the rest of this paper is organized as follows. In Sect. 2, it talks about the different method used for optimization with their experimental data. Section 3 consists of a table which compares all the method used and gives an easy way to compare them. Moreover, some important conclusions can be found in Sect. 4.

## 2 PV MPPT Techniques

### 2.1 *Perturb and Observe MPPT Technique*

Perturbation and observation MPPT method of optimization [5–12] is one of the MPPT techniques mostly used as it is considered among easiest one too. Basic principle depends upon trial and error method in reaching MPP. It calculates and compares power at two points in P–V curve and thereafter equate voltage value at two points and update it thereafter on power voltage curve in order to search for maximum power point (MPP). Power comparison equation is stated as:

$$DP = P(K) - P(K - 1)$$

Using flowchart of P&O method and above equation incremental of duty ratio changes as,

If  $DP$  is positive, then  $D$  remains the same but if  $DP$  is negative then direction of  $D$  reverses (Fig. 1).

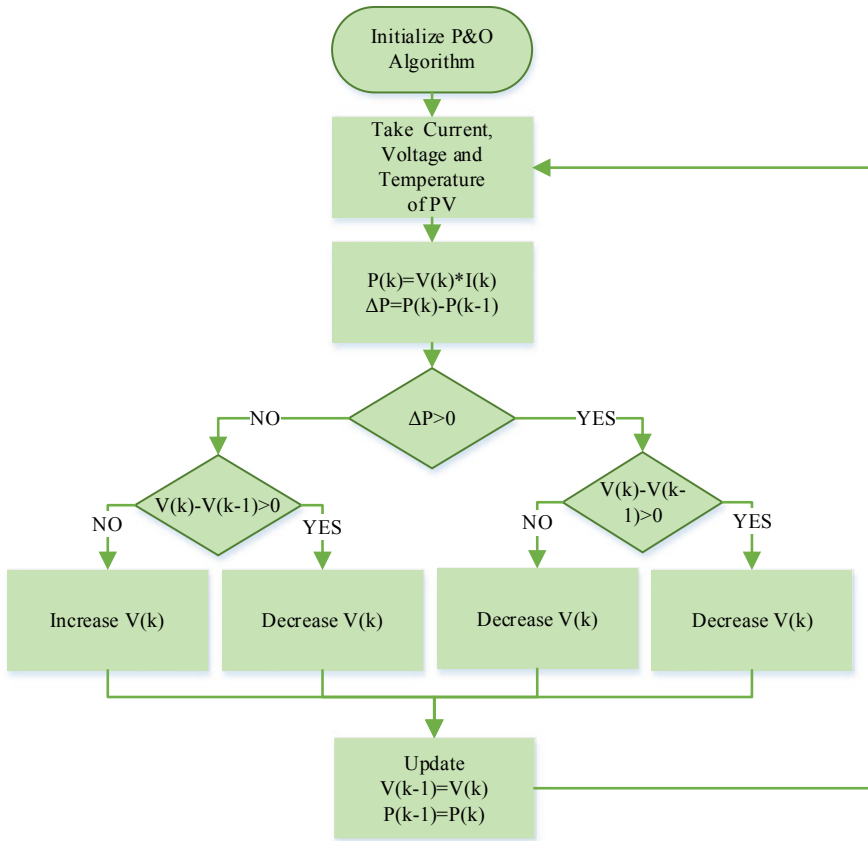


**Fig. 1** P&O algorithm flowchart

It is found that tracking time (MPP reaching time) is 2.5 s, with tracking efficiency of 97.6%.

## 2.2 Artificial Neural Network MPPT Technique (ANN)

ANN-based MPPT [13–19] is one of the most widely used machine techniques for multiple applications [20–22], due to its innate nature of learning by training and biological nature of neurons.

It is shown by nodes and edges which are equivalent to neurons and synapses resp [23] (Figs. 2 and 3).

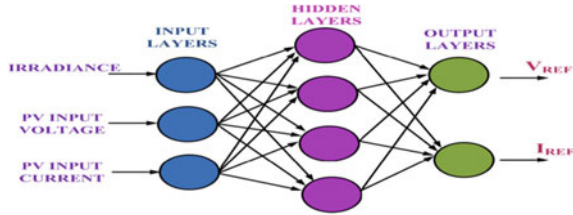


Fig. 2 ANN-based MPPT structure

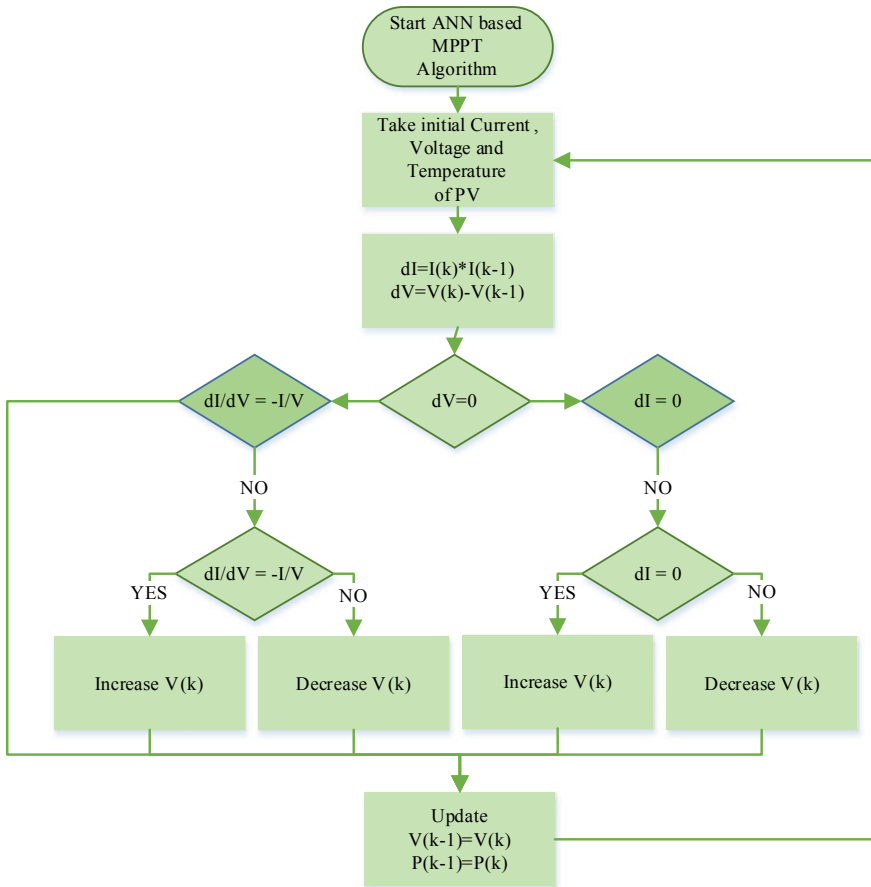


Fig. 3 ANN algorithm flowchart

### Steps to create ANN

To create an ANN, first step is data collection followed by ANN structure selection followed by ANN training with final step as ANN testing.

### ANN training

It adjusts the parameters in order to optimize the output from ANN tool. In training, it may use solar irradiance and temperature as raw data and then adjust parameters accordingly to get optimum output.

Corresponding to irradiance and temperature level [23–26], the response time for the sudden change of irradiance is 0.04 s which provides us good tracking speed.

## 2.3 Particle Swarm Optimization (PSO)-Based MPPT Technique

This technique [20–23] uses swarm intelligence in order to reach maximum power point. Intelligence shown by mutual behaviour of self-disciplined insects represents swarm intelligence. It is inspired from collective behaviour in societies in nature, like movement of fish birds and bees. In a swarm every member movement is inspired by its surrounding space. The unexplored region is searched based on swarm member's velocity stochastic factor. Here, each particle matches its position and trajectory with neighbouring particle position and trajectory, therefore the position of particle  $P_{\text{best}}$  is affected by best arrangement found by every particle in whole population  $G_{\text{best}}$  and is inspired by every particle location and the superior particle in a region inspires the individual particle path and location.

Updation of position of a particle

$$L_i^{k+1} = L_i^k + \Psi_i^{k+1}$$

$L_i$  is particle position and  $\Psi_i$  is the velocity part.

Velocity is find out as

$$\Psi_i^{k+1} = M\psi_i^k + z_1 O_1 [P_{\text{best}} - L_i^k] + z_2 O_2 [G_{\text{best}} - L_i^k]$$

Inertia weight is shown by  $M$ ,  $z_1$  and  $z_2$  are the accelerating, best position of individual molecule is represented by  $O_1$ ,  $O_2$ , and  $G_{\text{best}}$  is the best position of molecule in whole population (Fig. 4).

Intelligent swarm satisfies the following rules:

- Space and time consumption problem should be easily overcome by it.
- Pros and Cons of a solution should be easily visible to it.

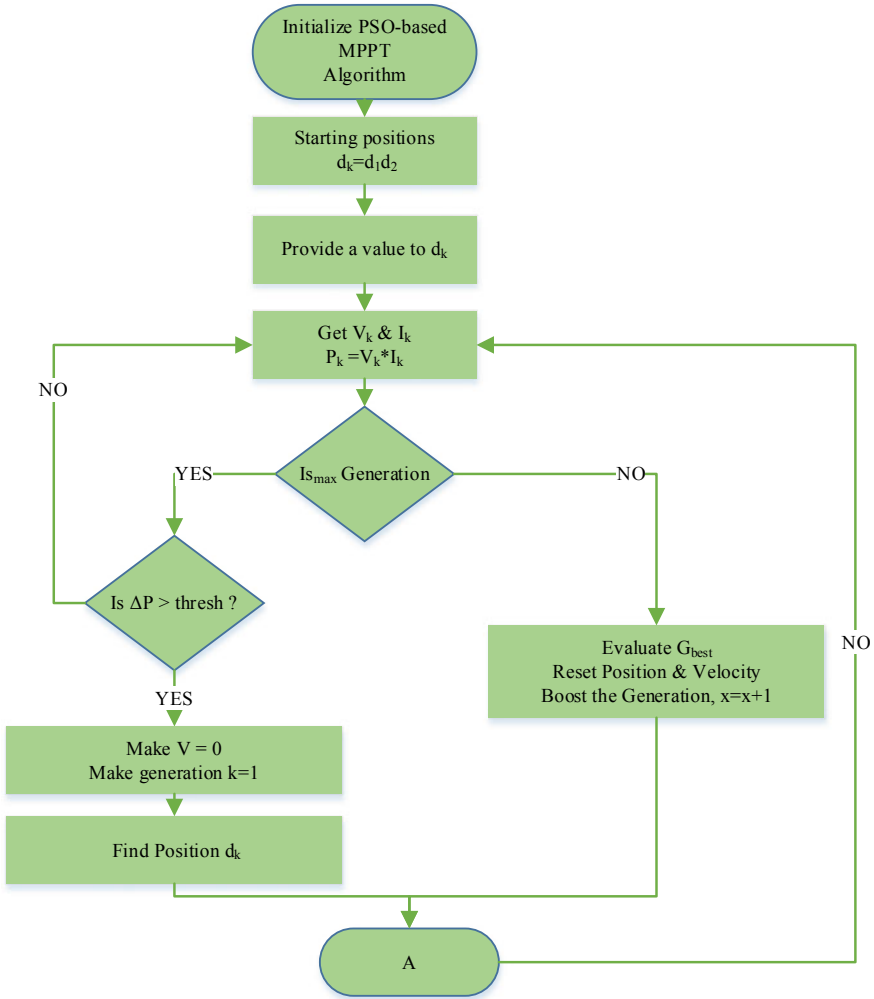


Fig. 4 Flowchart of PSO algorithm

- In case of change in surrounding condition swarm way of reaching optimal solution must not change.
- In case of sudden change of environmental condition it should alter its way when it is worth.

Fundamental strategy is shown in flowchart, and here, GMPP can be reached without any problem.

Abdulkadir et al. [25] show that time taken to reach MPP is 2 s and with PSO INC cascaded methodology it only took 1 s to reach MPP.

Badis et al. [23], by cascading PSO and GA complexity can be decreased.

## 2.4 *Ant Colony Optimization (ACO)-Based MPPT Technique*

Algorithm used in ACO [20–23] is of probabilistic nature inspired by food searching of ants [22]. Steps involved for the solution construction in ACO consist of:

### 1. Initialization

Initial values of parameters are set. These parameter are no. of ants, speed convergence constant, etc. More ants correspond to easier solution with lower convergence speed. Fewer ants correspond to better convergence speed, with more probability of getting trapped in local MPP. Size of solution archive should be greater or equal to dimension of the problem.

### 2. New solution

Probability density function of Gaussian kernel is used for finding new solution.

### 3. Ranking and archive updating $k$ .

Newly generated solution is added to original solution in archive.  $K$  superior solution is kept out of the  $NP + K$  ranked solutions.

### 4. Searching is stopped when termination condition is satisfied, i.e. (Fig. 5),

$$\text{Mod}[V_{\text{ref}}(k) - V_{\text{ref}}(k - 1)] < \xi$$

## 3 Result and Discussion

See Table 1.

## 4 Conclusion

In this comprehensive study, four techniques for tracking maximum power point are reviewed in such a way, so that it can boost the efficiency and instantaneous power output of solar PV system. This review contains thorough explanation of working processes along with the process flowchart representation for each MPPT method. With the help of above four MPPT techniques, all the classifications are covered, i.e. P&O belongs to classical MPPT techniques, ANN-based method belongs to intelligence-based techniques, and PSO & ACO are from optimization-based techniques depending upon the tracking algorithm utilized to track maximum power point.

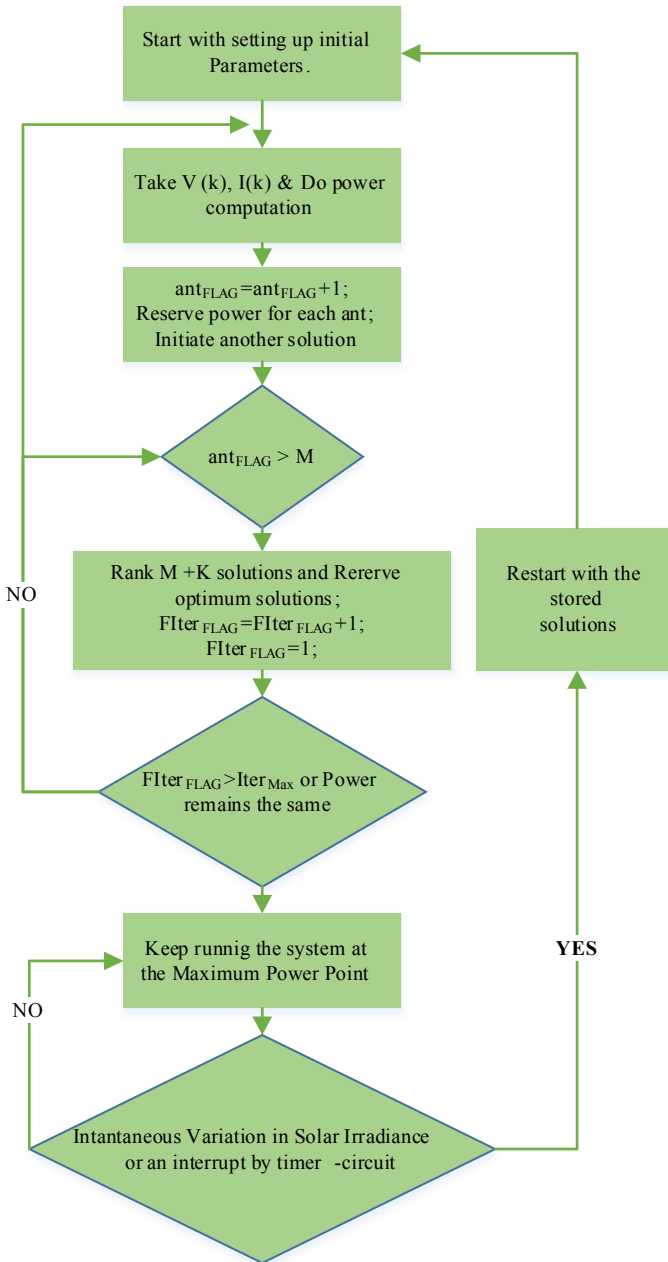


Fig. 5 ACO algorithm flowchart



**Table 1** Summary of analysis

Technique	Sampling rate	Tracking speed	Tracking accuracy	SP	Complexity	Parameter tuning	Periodic tuning	Stability	A/D	Percentage efficiency	Cost
P&O	Low	Slow	Medium	V&C	Simple	No	No	No	A, D	97.6	Low
ANN-based MPPT	High	High	High	V&C	Complex	Yes	Yes	Very stable	D	96	High
PSO-based MPPT	High	Medium	Medium	V&C	Medium		No	Stable	D	98	High
ACO-based MPPT	Medium	Medium	Medium	V	Medium		Yes	Stable	D	99.29	Medium

Some basic parameters knowledge is helpful in order to use a particular MPPT technique. So, design aspects like complexity of algorithm, microcontrollers used, tracking speed, stability and control parameter are also taken into consideration. In the table, advantages and disadvantages of these techniques are also discussed. At last we can say that all classical algorithms, i.e. P&O, have high reliability for unvarying irradiation with less algorithmic complexity and low tracking. Intelligent techniques, i.e. ANN-based MPPT, are superior method for getting best result in diverse irradiation conditions with high speed of tracking, detecting and storing enormous information and data. Moreover, optimization-based MPPT methods are suitable with any system without any prior information about the solar (PV) panel parameters. To conclude, this study will help to pick the valuable MPPT control that is best suitable for a specific application in industries, residential, health sectors, etc.

**Acknowledgements** This work is ostensibly supported by SERB-DST, Government of India, and authors are thankful to SERB-DST for funding the project titled “Performance Investigation of Grid Connected Micro Multilevel Inverter Based Solar Photovoltaic System” SERB sanction no. EMR/2017/004604. Also authors are extremely thankful to Director, Maulana Azad National Institute of Technology, Bhopal for extending all supports for the implementation of the project.

## References

1. de Brito MAG, Galotto L, Sampaio LP et al (2013) Evaluation of the main MPPT techniques for photovoltaic applications. *IEEE Trans Ind Electron* 60(3):1156–1167
2. Manickam C, Raman GP, Raman GR, Ganesan SI, Chilakapati N (2017) Fireworks enriched P&O algorithm for GMPP and detection of partial shading in PV systems. *IEEE Trans Power Electron* 32(6):4432–4443
3. Manickam C, Raman GR, Raman GP, Ganesan SI, Nagamani C (2016) A hybrid algorithm for tracking of GMPP based on P&O and PSO with reduced power oscillation in string inverters. *IEEE Trans Industr Electron* 63(10):6097–6106
4. Ahmed J, Salam Z (2016) A modified P&O maximum power point tracking method with reduced steady-state oscillation and improved tracking efficiency. *IEEE Trans Sustain Energy* 7(4):1506–1515
5. Sundareswaran K, Vigneshkumar V, Sankar P, Simon SP, Srinivasa Rao Nayak P, Palani S (2016) Development of an improved P&O algorithm assisted through a colony of foraging ants for MPPT in PV System. *IEEE Trans Ind Inf* 12(1):187–200
6. Sher HA, Murtaza AF, Noman A, Addoweesh KE, Al-Haddad K, Chiaberge M (2015) A new sensorless hybrid MPPT algorithm based on fractional short-circuit current measurement and P&O MPPT. *IEEE Trans Sustain Energy* 6(4):1426–1434
7. Elgendy MA, Zahawi B, Atkinson DJ (2015) Operating characteristics of the P&O algorithm at high perturbation frequencies for standalone PV systems. *IEEE Trans Energy Convers* 30(1):189–198
8. Kota VR, Bhukya MN (2019) A novel global MPP tracking scheme based on shading pattern identification using artificial neural networks for photovoltaic power generation during partial shaded condition. *IET Renew Power Gener* 13(10):1647–1659
9. Elobaid LM, Abdelsalam AK, Zakzouk EE (2015) Artificial neural network-based photovoltaic maximum power point tracking techniques: a survey. *IET Renew Power Gener* 9(8):1043–1063

10. Karatepe SE, Hiyama T (2009) Artificial neural network-polar coordinated fuzzy controller based maximum power point tracking control under partially shaded conditions. *IET Renew Power Gener* 3(2):239–253
11. Giraud F, Salameh ZM (1999) Analysis of the effects of a passing cloud on a grid-interactive photovoltaic system with battery storage using neural networks. *IEEE Trans Energy Convers* 14(4):1572–1577
12. Gopalakrishnan SK, Kinattungal S, Simon SP, Ark Kumar K (2020) Enhanced energy harvesting from shaded PV systems using an improved particle swarm optimization. *IET Renew Power Gener* 14(9):1471–1480
13. Motamarri R, Nagu B (2020) GMPPT by using PSO based on Lévy flight for photovoltaic system under partial shading conditions. *IET Renew Power Gener* 14(7):1143–1155
14. Priyadarshi N, Padmanaban S, Holm-Nielsen JB, Blaabjerg F, Bhaskar MS (2020) An experimental estimation of hybrid ANFIS–PSO-based MPPT for PV grid integration under fluctuating sun irradiance. *IEEE Syst J* 14(1):1218–1229
15. Li H, Yang D, Su W, Lü J, Yu X (2019) An overall distribution particle swarm optimization MPPT algorithm for photovoltaic system under partial shading. *IEEE Trans Industr Electron* 66(1):265–275
16. Abdullah MA, Al-Hadhrani T, Tan CW, Yatim AH (2018) Towards green energy for smart cities: particle swarm optimization based MPPT approach. *IEEE Access* 6:58427–58438
17. Kumar S, Pal NS (2017) Ant colony optimization for less power consumption and fast charging of battery in solar grid system. In: 2017 4th IEEE Uttar Pradesh section international conference on electrical, computer and electronics (UPCON), Mathura, pp 244–249
18. Sahoo SK, Balamurugan M, Anurag S, Kumar R, Priya V (2017) Maximum power point tracking for PV panels using ant colony optimization. In: 2017 Innovations in power and advanced computing technologies (i-PACT), Vellore, pp 1–4
19. Ma Y, Zhou X, Gao Z, Bai Y (2017) Summary of the novel MPPT (maximum power point tracking) algorithm based on few intelligent algorithms specialized on tracking the GMPP (global maximum power point) for photovoltaic systems under partially shaded conditions. In: 2017 IEEE international conference on mechatronics and automation (ICMA), Takamatsu, pp 311–315
20. Jiang LL, Maskell DL (2014) A uniform implementation scheme for evolutionary optimization algorithms and the experimental implementation of an ACO based MPPT for PV systems under partial shading. In: 2014 IEEE symposium on computational intelligence applications in smart grid (CIASG), Orlando, FL, pp 1–8
21. Pandey A, Srivastava S (2019) Perturb & observe MPPT technique used for PV system under different environmental conditions. *Int Res J Eng Technol (IRJET)* 6(4):2829–2835
22. Karami N, Moubayed N, Outbib R (2017) General review and classification of different MPPT techniques. *Renew Sustain Energy Rev* 68(1):1–18
23. Bahgat ABG, Helwa NH, Ahmad GE et al (2005) Maximum power point tracking controller for PV systems using neural networks. *Renew Energy* 30(8):1257–1268
24. Agarwal NK, Sadhu PK, Chakraborty S (2019) MPPT based PMSG wind turbine system using sliding model control (SMC) and artificial neural network (ANN) based regression analysis. *IETE J Res* 1–9
25. Abdulkadir M, Yatim AHM et al (2014) Hybrid maximum power point tracking technique based on pso and incremental conductance. In: IEEE conference on energy conversion (CENCON), Johor Bahru, pp 271–276
26. Badis A, Mansouri MN, Sakly A et al (2016) PSO and GA-based maximum power point tracking for partially shaded photovoltaic systems. In: 2016 7th IEEE international renewable energy congress (IREC), Hammamet, Tunisia, pp 1–6

# Preliminary Design and Flow Analysis of Domestic Chimney for Water Boiling Using Finite Volume Analysis



Faraz Ahmad, Shubham Pal, Viveksheel Yadav, and Vimlesh Bijalwan

## 1 Introduction

We are aware of this fact that with passage of every second demand for the energy increases and it is also very necessary to fulfill this demand. This demand is generally met through nonrenewable sources of energy. There are some serious threats related to these sources of energy like they are depleting with time and have bad effects on environment and health. In order to avoid this problem, it is required to make an alternate way out of these nonrenewable sources of energy. Domestic chimney is one of the methods which can be used as alternate sources of nonrenewable energy. In domestic chimney, large amount of heat is lost as waste heat to the surrounding when combustion of fuel and air takes place inside the chimney. Here, our main purpose is to extract this waste heat from the chimney as useful heat. The best method to recover this waste heat from chimney is to make it as double pipe heat exchanger as shown in Fig. 1. Heat exchanger is simply a device which allows two fluids to exchange heat between them without allowing them to mix.

In the present study, chimney body acts an inner cylinder, and the other cylinder is placed outside the chimney which acts as outer cylinder or pipe of double pipe heat exchanger as shown in Fig. 1. When the combustion of flue and air takes place, inner cylinder gets heated up, and at the same time, water is allowed to flow through the space between the cylinders. As a result of which hot gases will exchange its heat with water and this water will get heated up.

Furthermore, this heated water can be used for various useful purposes. Figure 1 shows that the flow arrangement of hot gases and water is counter flow, so that maximum heat transfer can be obtained.

There has been lot of work done on this topic of recovering or exchanging heat between the two fluids with the help of heat exchanger. Sharma et al. [1] studied maximizing heat transfer through fins using CFD. They analyzed heat transfer and

---

F. Ahmad (✉) · S. Pal · V. Yadav · V. Bijalwan  
Dev Bhoomi Institute of Technology, Dehradun, India

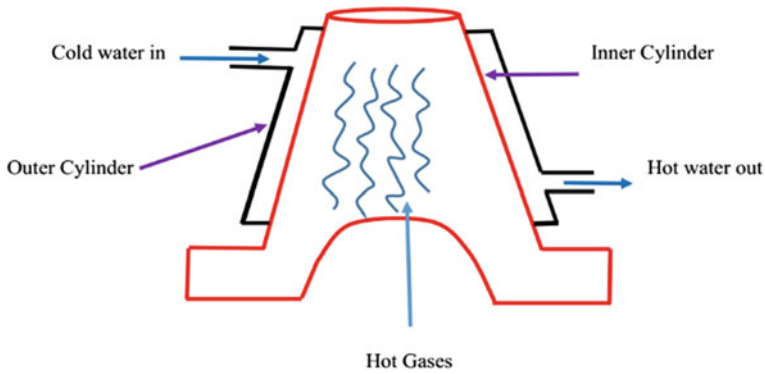


**Fig. 1** Double pipe heat exchanger-type domestic chimney

air flow for automobile engine. They have considered three different types of pin fins for their analysis. In their results, it was found that at higher pressure drop values circular fins and drop-shaped fins offer highest performance. Hatami et al. [2] analyzed the heat exchanger at the place gasoline engine exhaust. Furthermore, different fin dimensions have been analyzed, and the result concludes that heat recovery can be improved by using fins at specified distance and of specified dimensions. Didwania et al. [3] carried out CFD analysis on two types of fins circular and rectangular. Based on the study, it was found that circular fins give the maximum heat transfer as compared to rectangular fin. Ereke et al. [4] studied the effect of different fin geometry, on pressure drop and heat transfer. Furthermore, it was found that high heat transfer and pressure drop is achieved with high fin height as increasing the surface area. Ambreen et al. [5] studied effect on thermal performance by varying fin shape. They carried their investigation on three fin configurations: hexagonal, circular, and square. Their results show that circular fins give highest thermal performance followed by hexagonal and square fins. His study concludes that for circular fin 44% enhancement in Nusselt number can be achieved. Fan et al. [6] carried out investigation on critical temperature and maximum heat transfer rate in boiling for circular-finned tubes. It was found that varying the parameters like height, width, and pitch can increase the heat transfer rate. In their results, they found that heat transfer rate and critical temperature increase by adding a circular fin. Cheng et al. [7] carried experimental study on shell and tube heat exchanger, and they carried out their experiment with and without circular fins. Their results conclude that circular fins improve heat transfer. Reddy et al. [8] carried out CFD analysis for helically coiled tube in tube heat exchanger. In their results, it was found that by adding semicircular plates in annulus region turbulence increases, as heat transfer enhances between two fluids.

## 2 Material Properties and CAD Model

Material used for chimney body fins and outer cylinder is austenitic stainless steel. Flue gases pass through the inner chimney which was taken as first fluid and water was taken as secondary fluid. Austenitic stainless steel is one of the most common types of steel used for thermal application with less corrosion resistance. It contains about 16% chromium, 6% nickel, and low level of carbon. It provides high resistance temperature, so it is widely used for applications like furnaces, jet engines, etc. Here, austenitic stainless steel 330 is being used. Tables 1, 2, and 3 show the properties of austenitic stainless steel 330, flue gas, and water, respectively.

CAD model for domestic chimney (Fig. 2) was designed in Catia V5 and analyzed by Ansys 16.0. In order to increase the heat transfer, circular fins have been installed on the outer side of inner cylinder and on the inner side of outer cylinder. Fins increase the surface area as a result of which maximum heat transfer

**Table 1** Mechanical property of austenitic stainless steel

Properties	Value
Density	8 g/cm <sup>3</sup>
Thermal conductivity	13 W/mk
Melting point	1149–1177 °C
Yield tensile strength	260 MPa
Ultimate tensile strength	550 MPa
Hardness	139 Brinell, 80 Rockwell
Elastic modulus at room temperature	197 GPa

**Table 2** Properties of flue gas at 600 °C

Properties	Value
Specific heat	1.214 kJ/kg.k
Density	0.405 kg/m <sup>3</sup>
Viscosity	37.9 Ns/m <sup>3</sup>

**Table 3** Properties of water

Properties	Value
Specific heat at °C	4.1796 kJ/kg.k
Boiling point	100 °C
Thermal conductivity	0.608 W/m.k
Viscosity at 25 °C	0.889 Ns/m <sup>3</sup>
Enthalpy of vaporization, 100 °C	2257.7 kJ/kg
Enthalpy of fusion, 0 °C	333.84 kJ/kg
Enthalpy of fusion, 0 °C	72 N/m

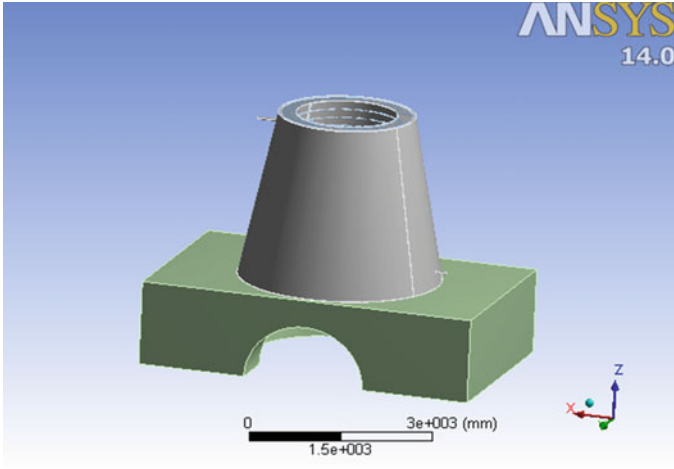


**Fig. 2** CAD model

can be achieved. To increase the heat transfer rate, fins are installed in such a manner that they create turbulence flow as shown in Fig. 3.

The height of the chimney is 3048 mm. The outer and inner diameters for the base of chimney are 2772 mm and 3372 mm, respectively. The outer and inner diameters of upper side of chimney are as 2859 mm and 1659 mm, respectively. Figure 3 shows the sectional view of the chimney, where water will flow in counter manner. Furthermore, fins are arranged in such a way that they will create turbulence for water flow as a result of which heat transfer will take place more effectively. Figure 4 shows the mesh mode of considered chimney. The meshing was done in fine mode with 100 relevance settings, and it contains 7,743,165 numbers of node and 9,862,594 numbers of element.

### 3 Flow Simulation and Results

CAD model was imported to Ansys workbench, and two types of analysis were performed using CFX analysis. CFX is a flow simulation module of Ansys which provides the result of multiphysics domain [9]. In first analysis, air at a temperature of 600 °C was supplied in the chimney from bottom to top which gives its temperature to inner surrounding cylinder. The outlet boundary condition, inlet boundary condition, and temperature distribution in this case are shown in Figs. 5, 6, and 7, respectively. It was concluded that maximum temperature will be at the bottom of chimney and will start decreasing as we move in upward direction. Second analysis was done on chimney with fins installed on both cylinders. Temperature applied to chimney was 600 °C as shown in Fig. 8 and water

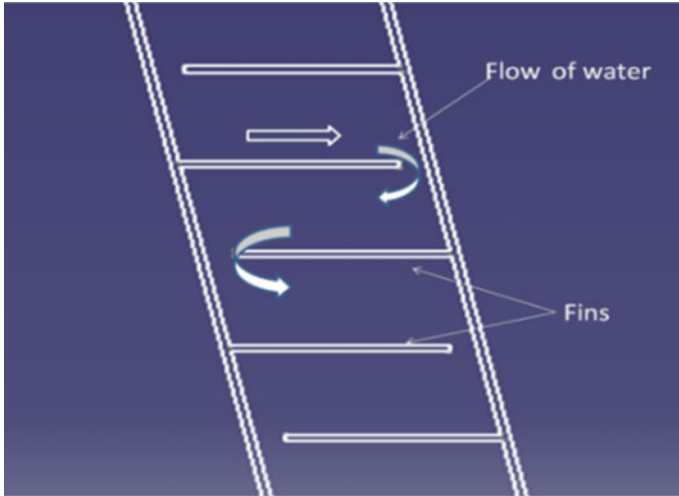


Fig. 3 Front view of fins

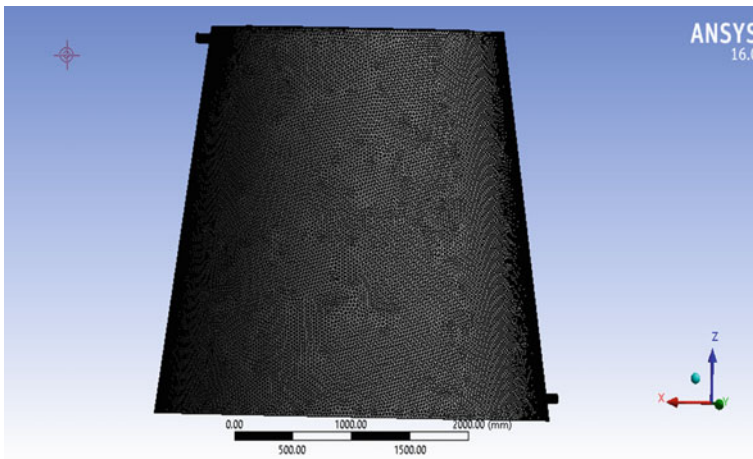
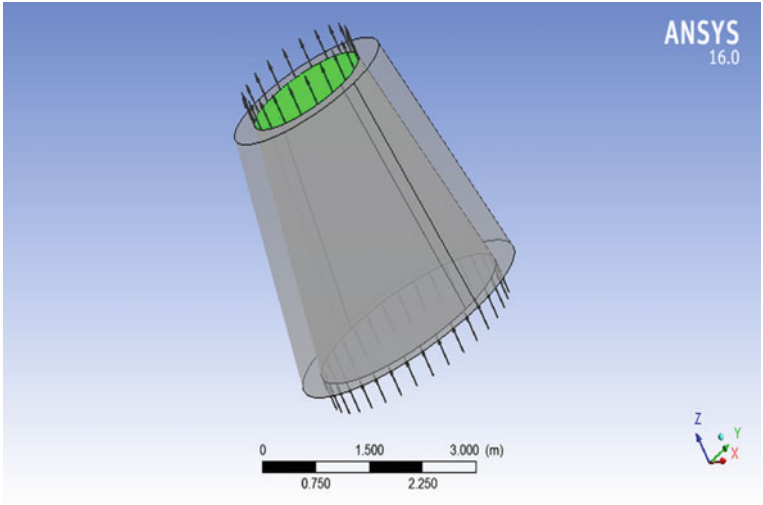


Fig. 4 Mesh model

(Temperature 25 °C) flowed from top to bottom in counter flow manner at a flow rate of 0.1 kg/s.

Figures 9 and 10 show the outlet and inlet boundary condition of water. The simulation result gives the temperature variation from inlet to outlet due to the cylinder wall temperature, which can be seen in Fig. 11. It was found that temperature of water starts increasing as it moves from top to bottom of chimney. From the above results, we found that the temperature of water at outlet was 594 °C after





**Fig. 5** Outlet boundary condition for flue gases

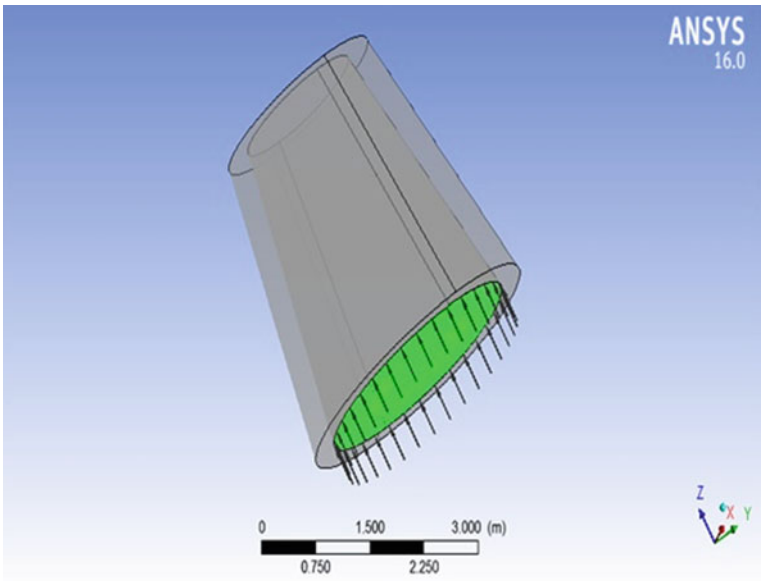


**Fig. 6** Inlet boundary condition for flue gases

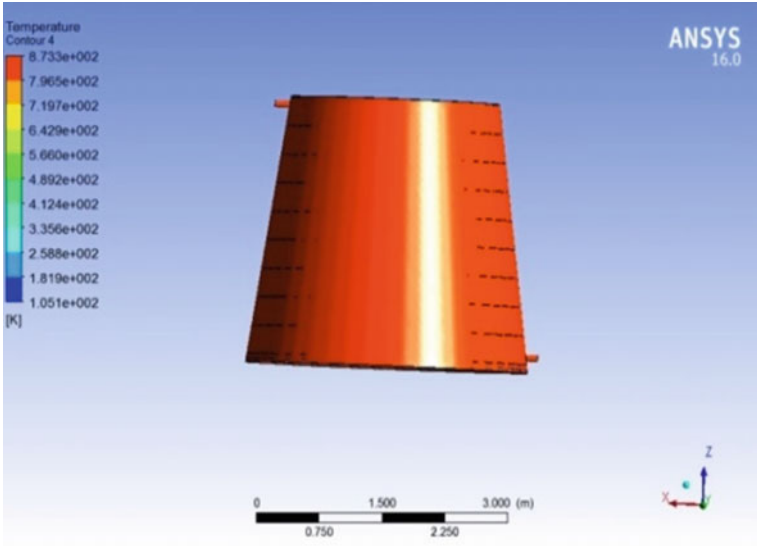


Fig. 7 Temperature distribution for chimney wall

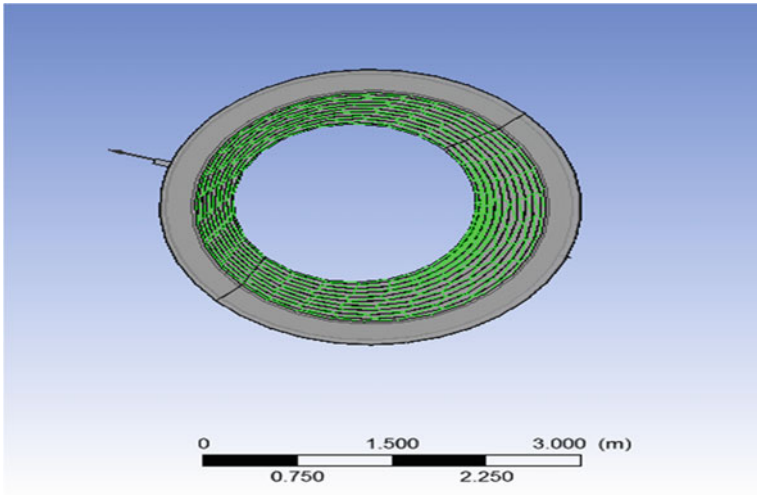
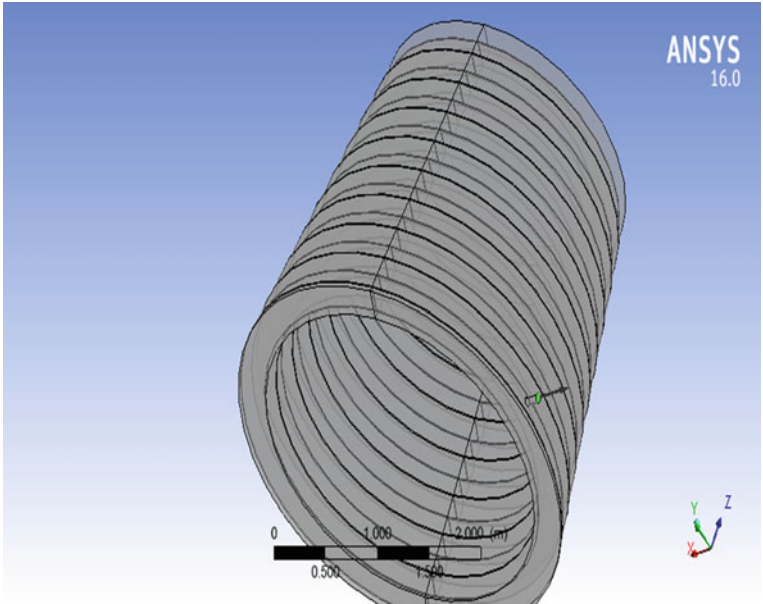
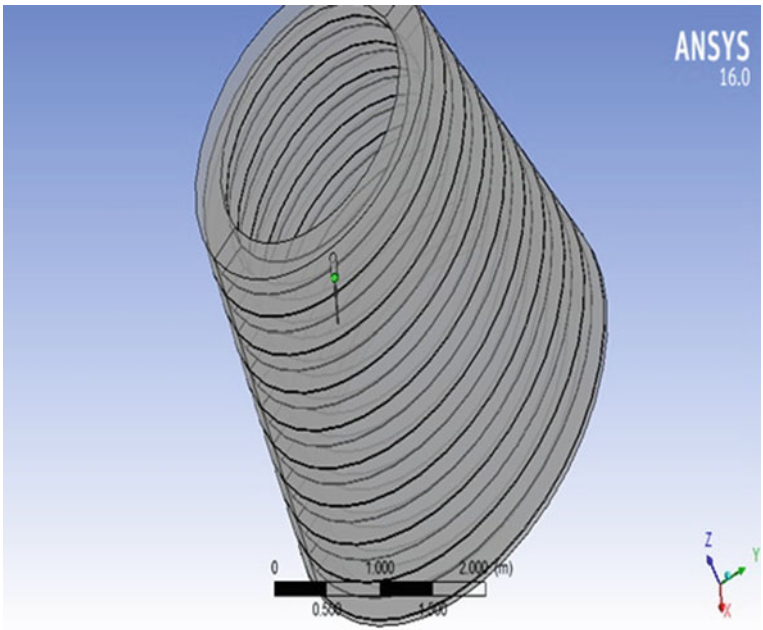


Fig. 8 Applied temperature of 600 °C at inner cylinder



**Fig. 9** Outlet boundary condition for water



**Fig. 10** Inlet boundary condition for water

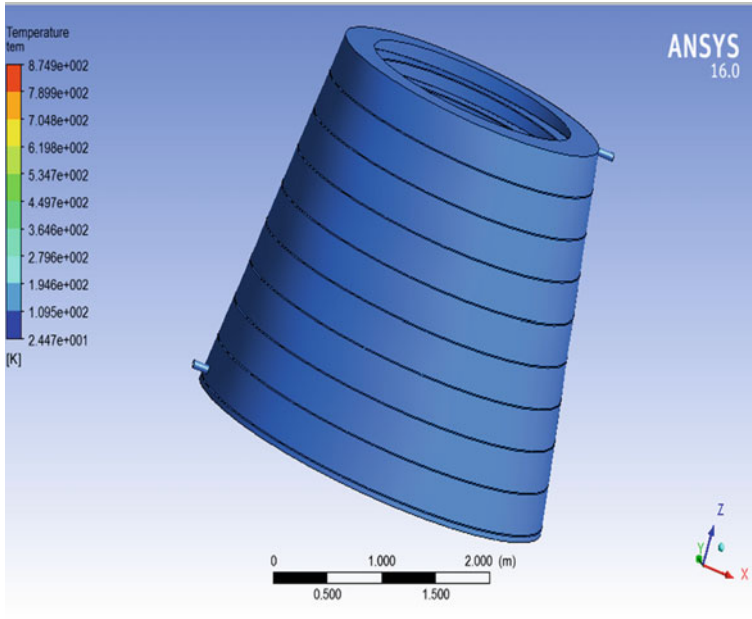


Fig. 11 Temperature distribution for water

10 min. The present study is limited to minimum flow rate, and if water flow rate from top to bottom is high, there will be a drop in temperature.

#### 4 Conclusions

In present study, CAD model of domestic chimney was designed and analyzed by flow simulation. Two types of analysis were performed in Ansys 16.0. In first case, air at a temperature of 600 °C is supplied to the chimney body and the temperature distribution for wall was obtained and it was found that maximum temperature is on the bottom of chimney wall. In second analysis, water at a temperature of 25 °C was allowed to flow between the two cylinders and a temperature of 600 °C was supplied from the base of chimney. The temperature of water at the outlet was measured after 10 min, and it was found that after 10 min the temperature of water at outlet was 594 °C. The present study helps the researchers in analyzing the flow behavior in heat exchanger-type domestic chimney. Furthermore, in future heat exchanger-type domestic chimney can be used as alternate sources of nonrenewable energy.

## References

1. Kumar SS, Sharma V (2013) Maximising the heat transfer through fins using CFD as a tool. *Int J Recent Adv Mech Eng (IJMECH)* 2:13–28
2. Hatami M, Ganji DD, Gorji-Bandpy M (2014) CFD simulation and optimization of ICES exhaust heat recovery using different coolants and fin dimensions in heat exchanger. *Neural Comput Appl* 25(7–8):2079–2090
3. Didwania M, Gopal Krishan R (2013) Study and analysis of heat transfer through two different shape fins using CFD tool. *Int J IT, Eng Appl Sci Res (IJIEASR)*, 2(4):13–20
4. Ereǵ A, Özerdem B, Bilir L, Ilken Z (2005) Effect of geometrical parameters on heat transfer and pressure drop characteristics of plate fin and tube heat exchangers. *Appl Therm Eng* 25 (14–15):2421–2431
5. Ambreen T, Kim MH (2018) Effect of fin shape on the thermal performance of nanofluid-cooled micro pin-fin heat sinks. *Int J Heat Mass Transf* 126:245–256
6. Fan CC, Liaw SP (1999) Computation of boiling water on circular finned tubes. *Int Commun Heat Mass Transfer* 26(3):379–388
7. Cheng H, Luo T, Yu J, Yang X, Liu Y, Gu Z, Jin L (2018) Experimental study of a shell-and-tube phase change heat exchanger unit with/without circular fins. *Energy Procedia* 152:990–996
8. Reddy KVK, Kumar BSP, Gugulothu R, Anuja K, Rao PV (2017) CFD analysis of a helically coiled tube in tube heat exchanger. *Mater Today Proc* 4(2):2341–2349
9. Ahmad F, Kumar A, Kanwar K, Patil PP (2016) CFX, static structural analysis of tractor exhaust system based on FEA. In: *CAD/CAM, robotics and factories of the future*, pp 159–172. Springer, New Delhi

# Revivification of Spent Lubricating Oil by Ecofriendly Extraction Flocculation Method



Sayantana Sarkar , Deepshikha Datta, K. S. Deepak , and Bimal Das

## 1 Introduction

Lubricating oil are viscous petroleum products used prevalently in automobiles and machineries [1]. The ultimate purpose of an engine lubricant is to reduce the friction between the engine's metal component, corrosion, and heat transfer. The hydrocarbons used in mineral lubricants are a complex arrangement of paraffins and aromatic compounds. A homogeneous hydrocarbon molecule consists of non-conventional synthetic base fluids, such as phosphate esters, polyalkylene glycols, polyisobutenes, and silicone oils [2]. Lubricating oil plays an imperative role in preventing excess temperature buildup on an engine's surface [3]. When performing these tasks to a long extent, lube oil losses its properties [3] due to the formation of oxidative products like organic acids, unsaturates, mercaptans, asphaltenes, and condensed aromatics. Alkyl hydro peroxide (ROOH), alcohols (ROH), aldehydes [RCHO], ketones ( $R - RC = O$ ), and formation of diketones [ $RCO (CH_2)_x COR'$ ] at low temperature [4]. When the temperature is high primary and secondary oxidation phases occurred.

Further increase in temperature produces a secondary oxidation phase resulting from polycondensation, and polymerization reaction of high molecular weight leads to form sludge (comprises degraded additives, contaminations, and carbonaceous particles) [4]. These products make the used oil very ineffective for further use [5]. Used lubricating oil contains a complex mixture of recovered base oil, polymeric additives, water, extraneous contaminants, light hydrocarbons, metals, and carbonaceous particles [6]. Metal particles often contaminate the lubricant due to the

---

S. Sarkar · K. S. Deepak · B. Das (✉)

Department of Chemical Engineering, National Institute of Technology, Durgapur 713209, India

e-mail: [bimal.das@che.nitdgp.ac.in](mailto:bimal.das@che.nitdgp.ac.in)

D. Datta

Department of Chemical Engineering, GMR Institute of Technology, Rajam 532127, India

© The Author(s), under exclusive license to Springer Nature Singapore Pte Ltd. 2022

535

P. Verma et al. (eds.), *Advancement in Materials, Manufacturing and Energy*

*Engineering, Vol. I*, Lecture Notes in Mechanical Engineering,

[https://doi.org/10.1007/978-981-16-5371-1\\_47](https://doi.org/10.1007/978-981-16-5371-1_47)

wear of the metallic engine surface [7]. The compounds that are formed by  $\text{NO}_x$  and  $\text{SO}_x$  due to dissociation and subsequent oxidation of the  $\text{N}_2$  present in the inlet air and the sulfur content in the gasoline, as well as other products, affecting the efficiency of lubricants. Both oxides are subsequently combined with the water present in the lubricant, creating acids that drastically modify the oil's properties by increasing its pH and making it corrosive [8]. Waste lubricating oil is a harmful environmental contaminant released into the atmosphere when a car engine lubricant is converted and disposed of in water drains, open vacant plots, and farmlands [9]. Misallocation of waste lubricating oil harms the environment and human health [10]. Numerous techniques have been proposed for recycling of used lubricating oil, which are reprocessing, reclamation, and re-refining [6, 11, 12]. The most promising method for recycling used lubricating oil is re-refining [11]. Re-refined oil is used with a range of methods such as chemical treatment (acid and clay) [6, 13], physical treatment by distillation and evaporation of thin-film and solvent extraction [14]. These methods have distinct yield, qualities of the product are less, and construction and operating costs are higher. After the treatment with chemicals, it creates environmental issues. Therefore, solvent extraction was suggested as an option [15]. Treatment with solvent extraction followed by adsorption has received considerable attention in recent years because it overcomes the problems associated with chemical treatment-related acid sludge [14], and this is the most attractive technology. By distillation, the solvent could be retrieved [16]. Various scientific studies have been carried out in the recent past by researchers in re-refining waste lubricating oil using extraction flocculation technology and adsorption [17–20]. The current study aimed to achieve the maximum percentage of recovered oil yield to achieve the best quality recovered oil conforming to quality parameters of fresh oil utilizing suitable solvent and flocculant. Various effects of operating parameters of experimentation, such as refining time, refining temperature, solvent-to-waste oil ratio on the percentage of recovered oil, and the physicochemical properties of recovered lubricating base oil, are studied to figure out the best possible result in regeneration of base oil suitable for further use. Regeneratable base oil has been obtained with two different solvents, such as methyl ethyl ketone and 2-propanol and monoethanolamine as a flocculant and tested for different physicochemical properties, and results were compared with virgin lubricating oil.

## 2 Experimental Work

### 2.1 Material and Methods

Two extracting solvents, such as methyl ethyl ketone and 2-propanol and flocculating agents (monoethanolamine), are used for the extraction flocculation process.

Used lubricating engine oil was collected first from the vehicle service station of NIT, Durgapur. The collected oil was allowed to settle under gravity for five days to

remove metal scrapings, dust, dirt, etc. Subsequently, by dehydration, the oil was heated to 120 °C to remove light hydrocarbons and water. After completion of the dehydration process, the mixture of pre-treated used lubricating oil and solvent (methyl ethyl ketone and 2-propanol) (mass ratio ranging from 1:1 to 5:1) along with flocculant concentration of 2 g/kg of solvent was agitated properly to ensure uniformity in the solution in a magnetic stirrer with the rpm of 340 for 60 min. The mixtures were then poured into an oak ridge centrifuge tube and centrifuge for 10 min with the rpm of 7500 to settle down the sludge. After this solvent extraction process, the solvent was separated from the mixture of a solution by atmospheric distillation setup and weighed the recovered oil. Finally, to remove the dark brown color of the recovered oil (which might result as the oil is overheated in direct contact with the heated glass plate), adsorption is carried out activated bentonite clay. The lubricating oil retrieved was then blended into a beaker with a fixed quantity of 20% of the activated bentonite clay. The mixture is then agitated vigorously for 4 h. After that, the oil extracted was separated by centrifugation from the adsorbent mixture. A schematic diagram of the extraction flocculation process, along with adsorption, is shown in Fig. 1, whereas the pictorial representation of used oil, recovered oil with 2-Propanol, and recovered oil with MEK is in Fig. 2a-c, respectively.

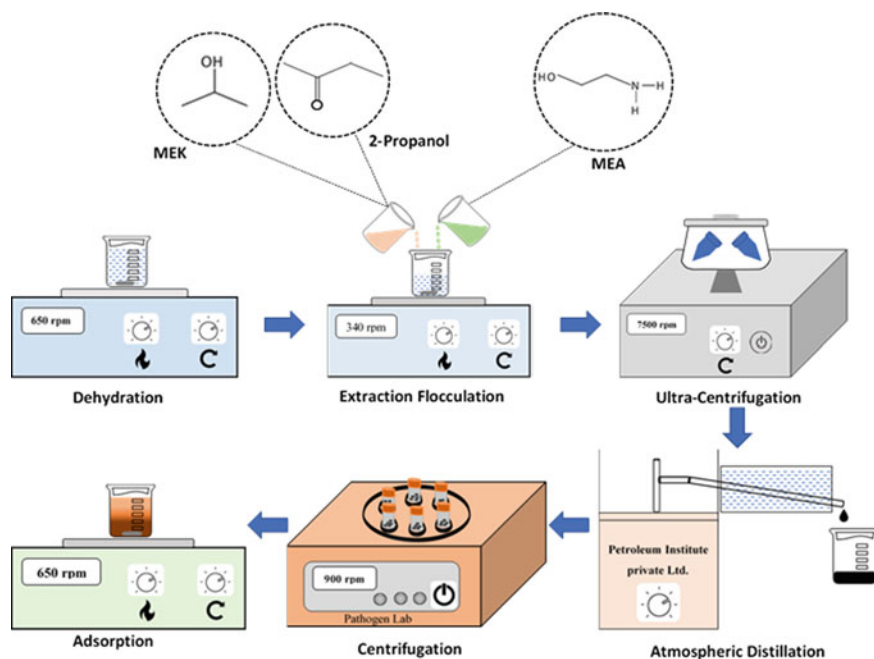


Fig. 1 Process flow diagram of extraction flocculation technique



## 2.2 Preparation of Activated Bentonite Clay as Adsorbent

Bentonite clay is purchased from Loba Chemie Pvt Ltd, rinsed with distilled water to remove debris, and oven-dried at 100 °C until all moisture content is removed. 30 g of bentonite clay is added to 100 ml of 2 M H<sub>2</sub>SO<sub>4</sub> solution. The mixture was agitated vigorously for 24 h at room temperature. After that solution is put into a Whatman filter paper and washed until excess acids are removed (filtrate pH = neutral) and placed in a glass plate and oven-dried at 80 °C for 24 h. A schematic diagram of activation of bentonite clay is shown in Fig. 3.

## 3 Result and Discussion

### 3.1 Effect of Factors Responsible for Maximizing the Percentage of Yield of Recovered Oil

Based on the statement given, several factors such as refining time, refining temperature, and solvent-to-waste oil ratio are investigated to maximize base oil percentage recovery.

**Effect of refining time on percentage of yield.** A group of experiments has been conducted to determine the mixing time for the system to get balance. Figure 4 shows that as the refining time upsurges, extraction yield increases until a constant value is reached. When compare the yield of recovered oil with 2-propanol, it can be seen that methyl ethyl ketone gave the highest yield to the tune of 97%, whereas 2-propanol solvent gave only 94% yield. It can be inferred from the above statement that the solvent takes long enough to dissolve the base oil

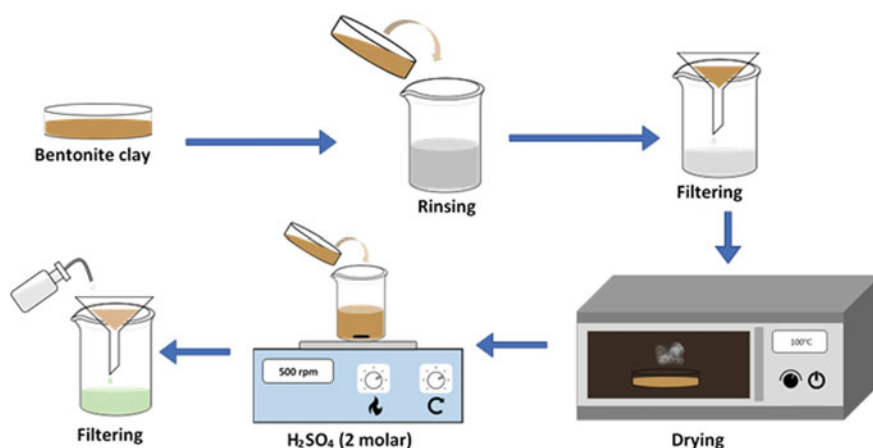


Fig. 2 a Used oil, b recovered oil with 2-propanol and c recovered oil with methyl ethyl ketone

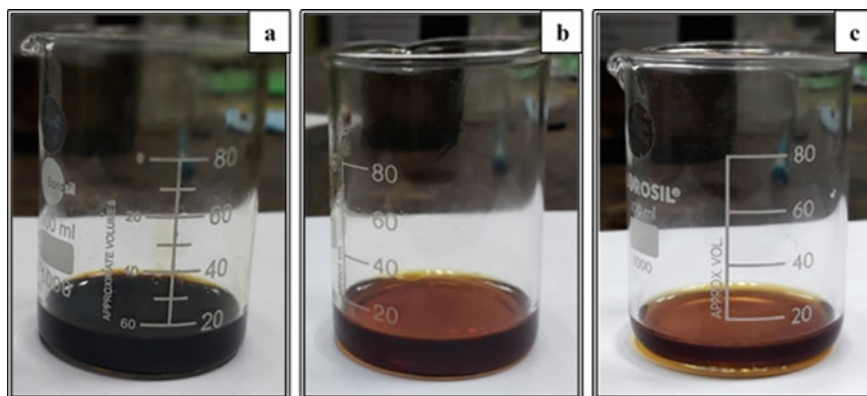


Fig. 3 Process flow diagram of activation of bentonite clay

contained in waste oil [21]. Alongside the other factor may be attributed that it should allow to neutralize the charge and form a hydrogen bond to break the stabilization. Evaluation of the extraction yield with refining time greatly depends on the consideration of the solvent. Due to the longer chain present in methyl ethyl ketone, percentage yields are more compared to 2-propanol.

**Effect of refining temperature on the percentage of yield.** Experimentation was carried out at various refining temperature performed with methyl ethyl ketone

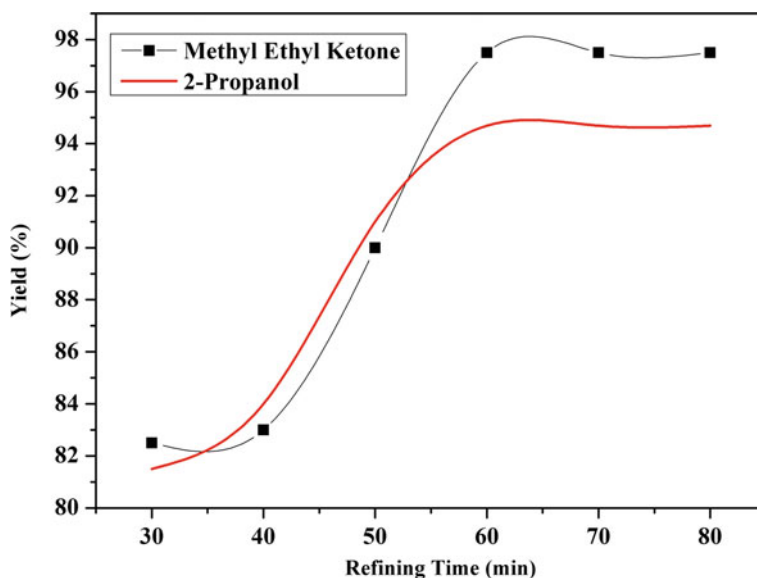


Fig. 4 Effect of refining time on the yield of recovered oil

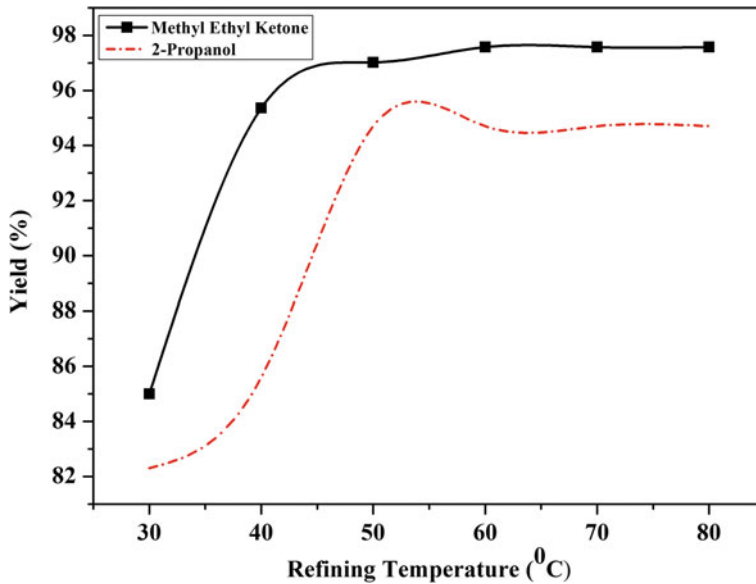


Fig. 5 Effect of refining temperature on yield of recovered oil

and from 30 to 80 °C, refining time of 60 min, solvent-to-spent oil ratio 3:1 g/g, and flocculant concentration of 2 g/kg of solvent. As shown in Fig. 5, when there is an increment of refining temperature, the amount of reclaimed oil increases. Comparing with MEK and 2-propanol, base oil dissolved in methyl ethyl ketone from 85 to 97%. The reason behind this is due to two factors involved:

- The viscosity of organic solvent is decreased as the refining temperature rises, resulting in further oil dissolution in the solvent.
- On the other hand, an increase in temperature increases the solubility of base oil in the extraction solvent. At optimum temperature, there is maximum removal of sludge and minimum oil loss for maximization of yield.

**Effect of solvent-to-waste oil ratio on a percentage of yield.** The effect of solvent-to-waste oil ratio on the percentage yield for a system comprises two individual extracting solvents, such as 2-propanol and methyl ethyl ketone, as shown in Fig. 6. Figure 6 shows that as the solvent-to-waste oil ratio increases, extraction yield increases up to a point where it attains equilibrium. When the solvent-to-oil ratio is small, the solvent is saturated and does not dissolve all the base oil present in waste oil. If the solvent-to-waste oil ratio increases up to a point, it ensures that more oil gets dissolve into the solvent and less oil is left in the sludge [22]. Another aspect can be due to the fact that the overall mutual solubility of the oil in the solvent increases as the solvent oil proportion increases [23]. Figure 6 shows that methyl ethyl ketone contributes better results in yield to the tune of 97% compared to 2-propanol, which gives 94% yield. This can be endorsed by the fact

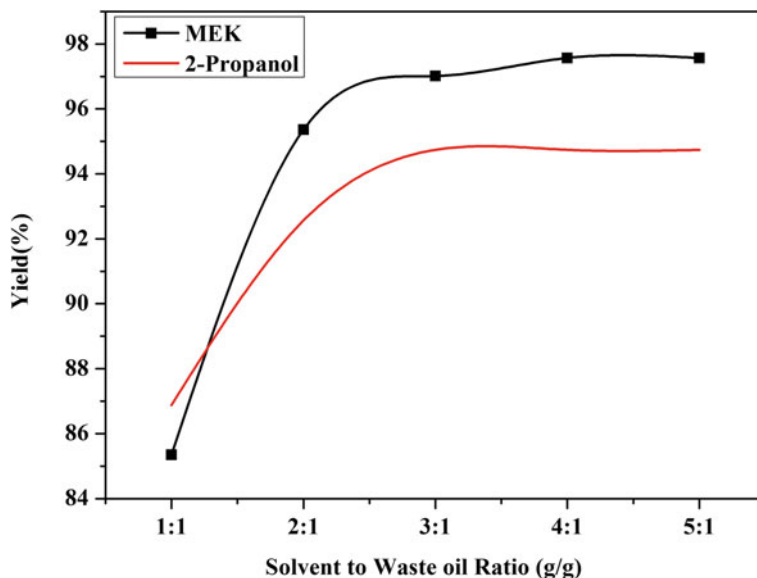


Fig. 6 Effect of solvent-to-waste oil ratio on yield of recovered oil

that as the chain length of carbon atoms in the solvent and polarity decreases, its ability to eliminate the sludge increases [18]. Thus, percentage yield is more with methyl ethyl ketone. Here in current investigations, solubility parameters play an important role in maximizing the recovered oil yield percentage. According to Hildebrand solubility theory, when the difference between the solubility parameter of solvent ( $\delta_1$ ) and polyisobutylene (polyolefin that is used for additives) ( $\delta_2$ ) are low, miscibility of solvent to oil is high [24]. Extraction efficiency can also be adequately justified in terms of the relation between solubility and the carbon chain size. The higher the chain length of the carbon atom, the solubility is higher and more yield can be obtained [24].

### 3.2 FTIR Analysis of Fresh, Used, and Recovered Lubricating Oil Using Two Different Solvent and Flocculant

FTIR analysis has been performed to investigate the functional group, bond, and structure of fresh, waste, and regenerated lubricating oil. Details of peaks, bond, functional group, and structure of bond present in the fresh, waste, and recovered lubricating oil (treated two different solvents and flocculants) are shown in Table 1. From FTIR analysis (Spectrum Two PerkinElmer, USA), the peaks are classified into two categories, viz. (i) main peaks and (ii) undesirable peaks. The main peaks

**Table 1** FTIR analysis of virgin, used and recovered lubricating oil using two different solvents

Type of oil	Peaks (Cm <sup>-1</sup> )	Bond	Functional group	Structure of bond
Fresh lubricating oil	2951	(C–H)	Alkanes	Stretch
	2920	(C–H)	Alkanes	Stretch
	2850	(C–H)	Alkanes	Stretch
	1463	(C–H)	Alkanes	Bend
	1373	(C–H)	Alkanes	Stretch
	2730	H– C = O: C–H	Aldehydes	Stretch
Waste lubricating oil	1700	C = O	Beta-unsaturated aldehydes, ketones, carbonyl compound	Stretch
	1175	C–O	Alcohol, Carboxylic acids, ethers, esters	Stretch
		C–N	Aliphatic amine	Stretch
	730	C–H	Aromatics	Out of plane
	820	C–H	Aromatics	Out of plane
Regenerated oil treated by (MEK)	2973.24	C-H	Alkane	Stretch
	2780.34	H– C = O: C–H	Aldehyde	Stretch
	1375.90	C–H	CH <sub>3</sub> (Methane)	Out of plane bending
	1155.82	C–O	Alcohols, carboxylic acid, esters	Stretch
	965.64	C–H	Aromatics	Bending
	813.673	= C– H	Alkanes	Bending
Regenerated oil treated by (2-Propanol)	2953	C–H	Alkanes	Stretch
	1463	C–H	Alkanes	Stretch
	1373	C–H	Alkanes	Rock
	814	= C– H	Alkanes	Bending
	1608	N–H	Amine (Primary)	Bending
	971	= C– H	Alkanes	Bending

are 2951 cm<sup>-1</sup>, 2920 cm<sup>-1</sup>, 2850 cm<sup>-1</sup>, 1463 cm<sup>-1</sup>, 1373 cm<sup>-1</sup>, which is due to the paraffinic compound in the fresh oil (Fig. 7). Undesirable peaks are depicted by 2730 cm<sup>-1</sup>, 1700 cm<sup>-1</sup>, 1175 cm<sup>-1</sup>, 820 cm<sup>-1</sup>, and 730 cm<sup>-1</sup>, which indicates oxidation products such as alcohols (R'CH<sub>2</sub>OH), ketones (R'COCH<sub>3</sub>), the

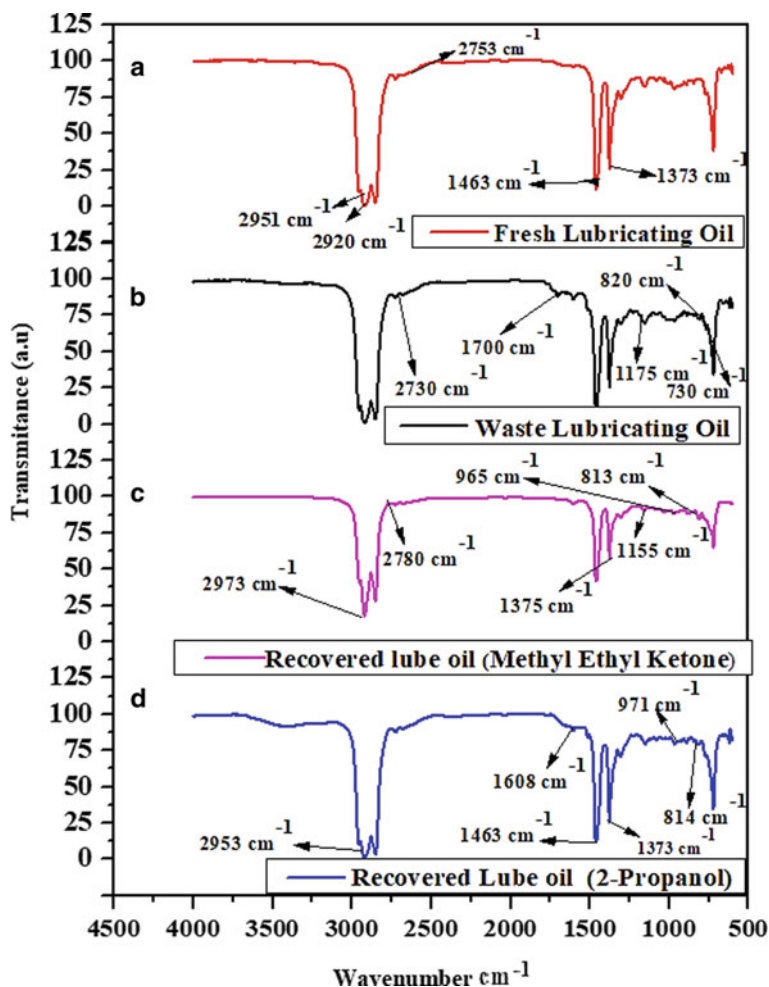


**Fig. 7** FTIR analysis of fresh lubricating oil, used lubricating oil, and recovered lubricating oil while treating with methyl ethyl ketone, recovered lubricating oil while treating with 2-propanol

carboxylic acid ( $R'COOH$ ), aldehydes ( $R'CHO$ ), carbonyl compound, aromatics, ether, and esters in the waste oil (Fig. 7). During the treatment by 2-propanol and MEA, it is observed that the solvent and flocculating agent do not remove all contaminants, such as oxidative products, aromatics, characterized by peaks of 2953, 1608, 1463, 1373, 971, 814  $cm^{-1}$  (Fig. 7). It is also observed that aldehydes, alcohol, and carboxylic acid, and a small amount of aromatics are still present in the recovered oil, affecting the percentage of yield (94%) and the quality of regenerated oil. However, all contaminants and oxidative products have been removed during the treatment of waste oil with methyl ethyl ketone and MEA, leaving the base oil components like saturated alkanes, primary amine characterized by the peaks

2973.24  $\text{cm}^{-1}$ , 2780.34  $\text{cm}^{-1}$ , 1375.90  $\text{cm}^{-1}$ , 1155.82  $\text{cm}^{-1}$ , 965.64  $\text{cm}^{-1}$ , 813.67  $\text{cm}^{-1}$  (Fig. 7). The flashpoint improvement in the regenerated oil is mainly attributed to eliminating aromatics represented by peaks of 820  $\text{cm}^{-1}$ , 730  $\text{cm}^{-1}$ , and oxidative products represented by 1175  $\text{cm}^{-1}$ , 1700  $\text{cm}^{-1}$  from waste oil after treatment (Fig. 7).

### 3.3 Comparison of Properties of Recovered Lubricating Oil

The oil recovered in this process using the optimum conditions of different variables such as refining time—60 min, refining temperature—48 °C, solvent-to-waste oil ratio—3:1, and flocculant MEA dosage—2 g/kg of solvent for 2-propanol and refining time—60 min, refining temperature—50 °C, solvent-to-waste oil ratio—7:1, and flocculant MEA concentration—2 g/kg of solvent for methyl ethyl ketone. Table 2 displays the physicochemical properties of fresh lubricating oil used and recovered lubricating oil. The flash point is 240 °C for fresh lubricating oil and 180 °C for used lubricating oil. The reduction in flash point value may result from the presence of light ends in the oil. In essence, oil breaks down into parts, including some light ends, after combustion and oxidation at high temperatures in the combustion engine [3]. The flashpoint of recovered lube oil using methyl ethyl ketone solvent is 203 °C, and that of using 2-propanol is 189 °C. Improvement of

**Table 2** Physicochemical properties of fresh, used, and recovered oil with two different solvents

Sl No	Properties	Designation	Units	Fresh oil	Used oil	Recovered oil (MEK)	Recovered oil (2-Propanol)
1	Kinematic viscosity @ 40°C	ASTM D-445	cSt	164.67	115.38	163.25	158.58
2	Kinematic viscosity @ 100°C	ASTM D-445	cSt	18.75	14.30	16.56	15.59
3	Viscosity index	ASTM D-2270	—	183.60	118.10	180.36	179.12
4	Specific gravity	ASTM D-1298	—	0.85	0.887	0.859	0.849
5	Flash point	ASTM D-93	°C	240	180	203	189
6	Pour point	ASTM D-97	°C	−27	−35	−12	−11
7	TAN	ASTM D-664	mg KOH/g oil	—	2	0.89	0.58
8	Ash content	ASTM D-482	wt.%	0.35	0.95	0.3	0.28

the flashpoint indicates that extracted oil is free of solvent, carbonaceous particles, and fuels [17]. Table 2 shows that the specific gravity of used oil is higher than that of fresh and refined oil. The specific gravity of fresh oil is 0.85, and that of used oil is 0.887, whereas the specific gravity of recovered oil, when treated with methyl ethyl ketone, is 0.859 and 0.849 when treated with and 2-propanol. The specific gravity of contaminated oil could be lower or higher than that of virgin/fresh lubricating oil, depending on the type of contaminant present in the used oil. If the used oil were contaminated due to fuel dilution, then its specific gravity would be lower. If the used oil were contaminated due to water originating from fuel combustion in the engine and accidental contamination rain, the specific gravity would be higher than that of fresh lubricating oil or refined oil [3]. From the result obtained, the pour point of used oil is high compared to fresh oil. This is because of the degradation of additives in the lube oil. Pour point will vary widely depending on the base oil, the source of lube oil, and the refining method, especially if dewaxing has been done [25]. The pour point of recovered oil is  $-12\text{ }^{\circ}\text{C}$  while treated with methyl ethyl ketone. The viscosity shows that used lube oil has lost most of the viscosity due to oxidation and contamination. The kinematic viscosity of used oil @ $40\text{ }^{\circ}\text{C}$  and @ $100\text{ }^{\circ}\text{C}$  are 115.38cSt and 14.30cSt, respectively. The kinematic viscosity of recovered oil @ $40\text{ }^{\circ}\text{C}$  and @ $100\text{ }^{\circ}\text{C}$  are 163.38 cSt and 16.56 cSt, respectively, when treated with MEK and 158.58 cSt, 15.59 cSt, respectively, while the used oil is treated with 2-propanol. It is evident that kinematic viscosity @ $40\text{ }^{\circ}\text{C}$  and @ $100\text{ }^{\circ}\text{C}$  increases with the increase in the solvent-to-waste oil ratio compared to use oil. This indicates that solvent precipitates out non-metallic polymeric material, which improves kinematic viscosity. Methyl ethyl ketone has the best performance to remove those additives. Ash content in the recovered oil shows a reduction of metallic impurities. The ash content of recovered oil is 0.3 while treated with methyl ethyl ketone and 0.28 while treated with 2-propanol. The total acid number of recovered oil also gets reduced, indicating that organic and inorganic acids, esters, phenolic compounds, lactones, and resins have separated satisfactorily due to the treatment of extraction flocculation. The acid number of recovered oil is reduced from 2.0 to 0.89 while treated with and from 2.0 to 0.58 while treated with 2-propanol.

## 4 Conclusion

In this modern era, it is evident that massive pollution occurs in the environment due to industrial and automobile growth over the years. It necessitates ensuring the stability and sustainability of the environment and preserving natural resources. The extraction flocculation technique to refine waste oil seems to be more relevant and appropriate among other methods for protecting environmental hazards and converting the waste to a valuable energy product. Following conclusions can be derived a posteriori.



- The addition of MEA in the solvent oil mixture of waste oil improves the capability to remove the sludge from the waste oils effectively.
- Considering the technical and economic aspects, the best set of operating parameters for extraction flocculation technique is
  - Refining time: 60 min,
  - Refining temperature: 48 °C,
  - Solvent-to-waste oil ratio: 3:1, and
  - Flocculant concentration: 2 g/kg solvent.
- On a comparison between methyl ethyl ketone and 2-propanol in terms of yield obtained of recovered lube oil, MEK exhibits more yield (97%) than 2-propanol. From the result obtained, it can be seen that methyl ethyl ketone is the most promising solvent in removing the sludge and reducing oil loss and thereby improving the percentage recovery of lubricating oil than 2-propanol.
- Further, through the experimentation of the recovered oil's physicochemical properties and the result obtained, it is observed that with MEK as a solvent, the properties of recovered base oil are in close proximity with the virgin lubricating oil, which can be reused with the addition of proper additives.

## 5 Limitation and Future Scope of the Study

The biopolymer flocculant is a potent choice in the field of re-refining, which has been left unexplored. Moreover, a comprehensive exploration of the sludge generated in various cases needs to be carried out to narrow out the potential applications.

The capabilities associated with natural bio-coagulants are untapped and would be incorporated in the extended work. Further, entwined effects of functional groups like hydroxyl and amine in compounds like chitosan facilitate improvised sludge removal due to the high efficiency of flocculation. The comparative assessment of parameters like percentage oil loss and percentage sludge removal using single and composite solvents could have a catalytic effect in this field.

## References

1. Usman M, Saqib S, Zubair SWH, Irshad M, Kazmi AH, Noor A, Zaman HU, Nasir Z, Ijaz Malik MA (2020) Experimental assessment of regenerated lube oil in spark-ignition engine for sustainable environment. *Adv Mech Eng* 12(7)
2. Torbacke M, Rudolphi AK, Kassfeldt E (2014) *Lubricants: introduction to properties and performance*, 1st edn. John Wiley & sons, United Kingdom
3. Udonne JD (2011) A comparative study of recycling of used lubrication oils using distillation, acid and activated charcoal with clay methods. *J Petrol Gas Eng* 2(2):12–19

4. Owang F, Mattsson H, Pedersen J (2004) Investigation of oxidation of a mineral and a synthetic engine oil. *Thermochim Acta* 413(1-2):241-248
5. Hsu YL, Liu CC (2011) Evaluation and selection of regeneration of waste lubricating oil technology. *Environ Monit Assess* 176(1):197-212
6. Kamal A, Khan F (2009) Effect of extraction and adsorption on re-refining of used lubricating oil. *Oil Gas Sci Technol Revue de l'IFP* 64(2):191-197
7. Zhang J, Dong Q (2018) Lubrication performance analysis of crankshaft bush in compressor. *Eng Fail Anal* 90:277-289
8. Temitayo O, Jacob S, James O (2018) Investigation of Co and So<sub>2</sub> from acid clay treatment of used lubricating oil. In: *IOP conference series: materials science and engineering*, pp 012052. IOP Publishing, United Kingdom
9. Cavalcanti TG, de Souza AF, Ferreira GF, Dias DSB, Severino LS, Morais JPS, de Sousa KA, Vasconcelos U (2019) Use of agro-industrial waste in the removal of phenanthrene and pyrene by microbial consortia in soil. *Waste Biomass Valorization* 10(1):205-214
10. Pinheiro CT, Pais RF, Quina MJ, Gando-Ferreira LM (2018) Regeneration of waste lubricant oil with distinct properties by extraction-flocculation using green solvents. *J Clean Prod* 200:578-587
11. Durrani HA, Panhwar MI, Kazi RA (2012) Determining an efficient solvent extraction parameters for re-refining of waste lubricating oils. *Mehran Uni Res J Eng Technol* 31(2):265-270
12. Josiah PN, Ikiensikimana SS (2010) The effect of desludging and adsorption ratios on the recovery of low pour fuel oil (LPFO) from spent engine oil. *Chem Eng Res Bull* 14(1):25-28
13. Abdel-jabbar NM, Al Zubaidy EAH, Mehrvar M (2010) Waste lubricating oil treatment by adsorption process using different adsorbents. *World Acad Sci, Eng Technol* 62:9-12
14. Durrani HA, Panhwar MI, Kazi RA (2011) Re-refining of waste lubricating oil by solvent extraction. *Mehran Univ Res J Eng Technol* 30(2):237-246
15. Ogbeide SO (2010) An investigation to the recycling of spent engine oil. *J Eng Sci Technol Rev* 3(1):32-35
16. Bhaskar T, Uddin MA, Muto A, Sakata Y, Omura Y, Kimura K, Kawakami Y (2004) Recycling of waste lubricant oil into chemical feedstock or fuel oil over supported iron oxide catalysts. *Fuel* 83(1):9-15
17. Mohammed RR, Ibrahim IAR, Taha AH, McKay G (2013) Waste lubricating oil treatment by extraction and adsorption. *Chem Eng J* 220:343-351
18. Osman DI, Attia SK, Taman AR (2018) Recycling of used engine oil by different solvent. *Egypt J Pet* 27(2):221-225
19. Zgheib N, Takache H (2020) Recycling of used lubricating oil by solvent extraction: experimental results, Aspen Plus simulation and feasibility study. *Clean Technol Environ Policy* 1-12
20. Adewole BZ, Olojede JO, Owolabi HA, Obisesan OR (2019) Characterization and suitability of reclaimed automotive lubricating oils reprocessed by solvent extraction technology. *Recycling* 4(3):31
21. Yang X, Chen L, Xiang S, Li L, Xia D (2013) Regeneration of waste lubricant oil by extraction-flocculation composite refining. *Ind Eng Chem Res* 52(36):12763-12770
22. Raza H, Omar Q, Awan JA (2016) Regeneration of contaminated lubricating oil by solvent extraction. In: *6th symposium in engineering science*, pp 4393-4397. Science International, Lahore
23. Elbashir NO, Al-zahrani SM, Mutalib MIA, Abasaheed AE (2002) A method of predicting effective solvent extraction parameters for recycling of used lubricating oils. *Chem Eng Process* 41(19):765-769
24. Filho JLA, Moura LGM, Ramos ACS (2010) Liquid-liquid extraction and adsorption on solid surfaces applied to used lubricant oils recovery. *Braz J Chem Eng* 27(4):687-697
25. Awaja F (2006) *Design aspects of used lubricating oil re-refining*, 1st edn. Elsevier, Netherlands

# Effect of Sintering Temperature on the Microstructure and Properties of the Copper Synthesized by Powder Metallurgy Route



Manish Dixit  and Rajeev Srivastava 

## 1 Introduction

The Cu is extensively used in electrical power transmission and heat sink applications because of its good corrosion resistance, superior electrical, and thermal conductivity [1–3]. The synthesis of the Cu was accomplished by the powder metallurgy route. It comprises the three key processes: milling; compaction; and sintering [2, 3]. Milling is a process of mechanical alloying of the different powder constituents. It reduces the particle size and improves the dispersion homogeneity. Then, milled powder was consolidated in a dedicated compaction die. In compaction process, the Cu powder was compacted in a die and punch assembly to prepare a green compact. The green compact was associated with poor mechanical bonds which cause poor mechanical strength. Therefore, the compaction process was subsequently followed by the sintering which converts these poor mechanical bonds into the strong metallic bonds. The preferable sintering should be between the 0.75 to 0.85 of the melting point temperature [1, 3].

Alexander et al. [4] performed a detailed investigation of the sintering behavior of the Cu. The sintering of the Cu takes place by the diffusion of the Cu atoms, which governs by the different diffusion mechanism for different sintering temperature range. For low temperatures, the diffusion of the Cu atoms mainly governs by the viscous flow diffusion because of the quasi-viscous behavior of the Cu. However, plastic flow and evaporation–condensation diffusion mechanism also significantly influence the diffusion at low-temperature diffusion. The intimately bonded Cu particles initiate the neck formation by increasing the temperature and develop metallic bonds. The sintering of the Cu depicts the shrinkage behavior at a higher temperature, which attribute to the volume diffusion. In this, material flow from the grain boundary to the near pores and voids and grain boundary act as a

---

M. Dixit (✉) · R. Srivastava

Department of Mechanical Engineering, Motilal Nehru National Institute of Technology  
Allahabad, Prayagraj, UP 211004, India

© The Author(s), under exclusive license to Springer Nature Singapore Pte Ltd. 2022

549

P. Verma et al. (eds.), *Advancement in Materials, Manufacturing and Energy Engineering, Vol. I*, Lecture Notes in Mechanical Engineering,

[https://doi.org/10.1007/978-981-16-5371-1\\_48](https://doi.org/10.1007/978-981-16-5371-1_48)

material source. The shrinkage depends on the rate of volume diffusion and stops as grain boundaries disappeared. However, viscous flow and plastic flow diffusion also influence the shrinkage behavior of the Cu.

Kuczynski [5] develops the mathematical model of the different diffusion mechanisms and investigates the phenomenon of the interface adhesion of the two particles. It also illustrates the influence of the different parameters involve in the interaction of the metallic particle for different diffusion mechanism and also determine the surface diffusion coefficient for the Cu. Sintering below the melting point does not follow the thermodynamic equilibrium and dominated by the volume diffusion at a higher temperature. Rockland [6] also investigated the influence of the particle size on the sintering mechanism and performed the comparative study of the “exponential method” with theoretical rate exponent (Kuczynski) method. In general, volume diffusion is the dominant diffusion mechanism for the Cu above 900 °C at the sintering temperature. For the particle size 50–300 μm range, surface diffusion mechanism leads the interface adhesion, whereas volume diffusion leads to the densification of Cu. However, surface diffusion and grain boundary diffusion are dominated over the volume diffusion for particle size below 400 μm and 1 μm, respectively.

Ngai et al. [7] reported the effect of sintering temperature (750–1070 °C) on density and hardness of the Cu–Ti<sub>3</sub>SiC<sub>2</sub> composites. They observe the improvement in the interface adhesion and mechanical properties with increasing the sintering temperature. Rajkumar et al. [8] performed the comparative study of microwave sintering and conventional sintering on the mechanical and tribological properties of the Cu-graphite composite. They reported the superior interface adhesion and densification for microwave sintering over conventional sintering. It significantly improves the mechanical and tribological properties of the Cu-graphite. Padmavathi et al. [9] and Sethi [10] reported the negative densification parameter for the Cu-Sn composite, which causes expansion in the specification size by conventional sintering, whereas microwave sintering causes shrinkage because of uniform diffusion of the Cu atom. Naveen Kumar et al. [11] review the effect of compacting pressure and sintering temperature on the microstructure and properties of the Cu. They also suggest the high sintering temperature for better mechanical properties.

Therefore, literature survey indicates that the sintering temperature and sintering technique have a great impact on the microstructure and properties of the Cu. In the present work, the microstructure and properties of the Cu were determined at different temperatures of the different sintering temperatures of 700, 800, 900, and 1000 °C. The present studies provide a preliminary analysis to select the extrusion ratio for the Cu-based metal matrix composite.

## 2 Material and Methods

The present study employed the electrolytic Cu of 40 microns and 99.9% purity from Sarda Industrial Enterprises Jaipur. Initially, Cu powder was preheated at 120 °C for 1h to eliminate the moisture content. The preheated Cu powder was mechanically milled for the 1h in a planetary ball mill. The milling process was performed with hardened steel balls of 10 mm diameter rotating at 300 rpm. Then, milled Cu powder was compacted in dedicated compaction die at a compaction pressure of 700 MPa to prepare the green compact. The synthesis details are given in our previous article [3]. The sintering of the compacted Cu was performed at the different sintering temperatures of 700, 800, 900, and 1000 °C. Field emission scanning electron microscopy (FESEM) and X-ray diffraction (XRD) were employed to observe the surface morphology and phase formation, respectively. At least, five specimens were tested to determine the mechanical properties, including density and micro-hardness. The specimen's preparation details are given in our previous article [2].

## 3 Results and Discussion

### 3.1 Microstructure Analysis

Figure 1 shows the morphology of the sintered surface of the Cu for different sintering temperatures including 700, 800, 900, and 1000 °C. Figure 1a shows the morphology of the as-obtained dendritic Cu powder. Figure 1b shows the micrograph of the Cu sintered at 700 °C. It shows the pores on the Cu surface, which confirms the viscous flow and plastic flow diffusion mechanism during sintering [4, 5]. It also depicts the rugged surface with poor surface integrity. It may refer to the absence of the volume diffusion at low sintering temperatures. Figure 1c displays the micrograph of Cu sintered at 800 °C. It depicts that the pores and voids are almost disappeared with an increase in the sintering temperature. It shows the presence of volume diffusion during sintering. However, micrographs depict the very few micro-pores which indicate the low rate of volume diffusion. It depicts the relative better surface integrity, which refers to the proper diffusion of the Cu atoms [5, 6].

Figure 1d shows the micrograph of the Cu sintered at 900 °C. The micrograph depicts the absence of micro-pores indicate the proper volume diffusion at an elevated temperature of 900 °C. The proper volume diffusion improves the surface adhesion and results in excellent surface integrity with the presence of grain boundary. It also confirms proper diffusion with adequate volume diffusion rate. At higher temperature, grain boundaries act as a material source, the metal Cu flow from the grain boundary and diffuse to pores and voids present near to the grains. It significantly eliminates the pore and voids from the Cu surface. Therefore, the

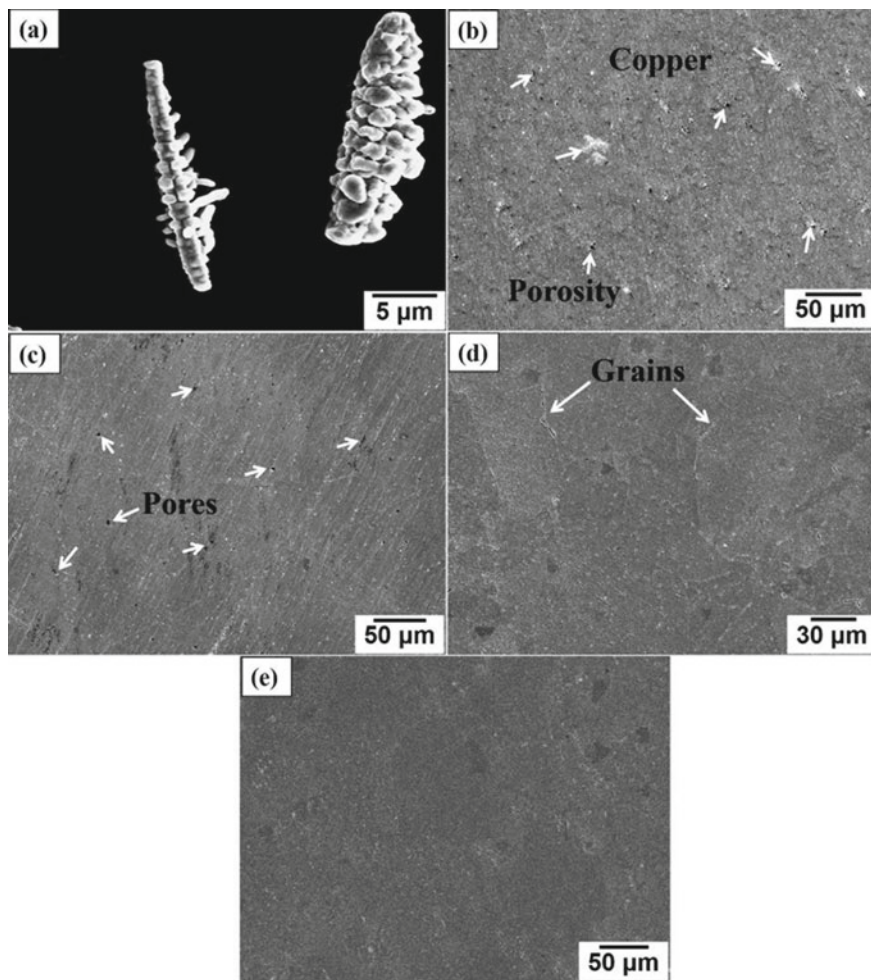


**Fig. 1** FESEM micrograph of **a** as-obtained dendritic Cu powder, **b** Cu sintered at 700 °C, **c** Cu sintered at 800 °C, **d** Cu sintered at 900 °C, **e** Cu sintered at 1000 °C

specimen also confirms the shrinkage in the size of the Cu, which indicates the true sintering at 900 °C [1, 6].

Figure 1e shows the microstructure image of the Cu sintered at 1000 °C. It presents superior surface integrity with no visual micro-pores on the sintered surface. It confirms the domination of surface diffusion and volume diffusion at an elevated temperature of 1000 °C.

The surface diffusion strengthens the densification of the Cu, whereas volume diffusion enhances the interface adhesion [5, 6]. The microstructure depicts that the grains are disappeared which confirms the no shrinkage of the Cu [1, 4]. The micrograph confirms the superior microstructure of Cu sintered at 1000 °C.

### 3.2 X-Ray Diffraction (XRD) Study

Figure 2 shows the XRD pattern of the Cu sintered at 700, 800, 900, and 1000 °C. The interlayer spacing of the sintered Cu was calculated by Bragg's equation ( $d = n\lambda/2\sin\theta$ ), where  $\theta$  is the angle of incident rays,  $\lambda$  is the wavelength of the incident electrons,  $d$  is the lattice spacing. XRD pattern depicts the high-intensity peaks of Cu at the  $2\theta$  angle of  $43.21 \pm 0.04^\circ$ ,  $50.30 \pm 0.06^\circ$ , and  $73.98 \pm 0.4^\circ$ , which corresponds to the lattice spacing 2.092, 1.812, and 1.28 Å, respectively. These lattices spacing refer to the (111), (200), and (220) planes of the face-centered cubic (fcc) structure of the Cu atom. The XRD survey depicts sharp peaks of Cu, which confirms the polycrystalline structure [1, 2].

XRD pattern confirms very low-intensity peaks of the  $\text{Cu}_2\text{O}$  which indicate the involvement of atmospheric air with Cu at elevated temperature. Figure 2 illustrates that the intensity of the Cu peaks slightly decreases with increasing the sintering temperature. It also indicates the more interaction of Cu with atmospheric oxygen, which leads to the formation of copper oxide [2, 3].

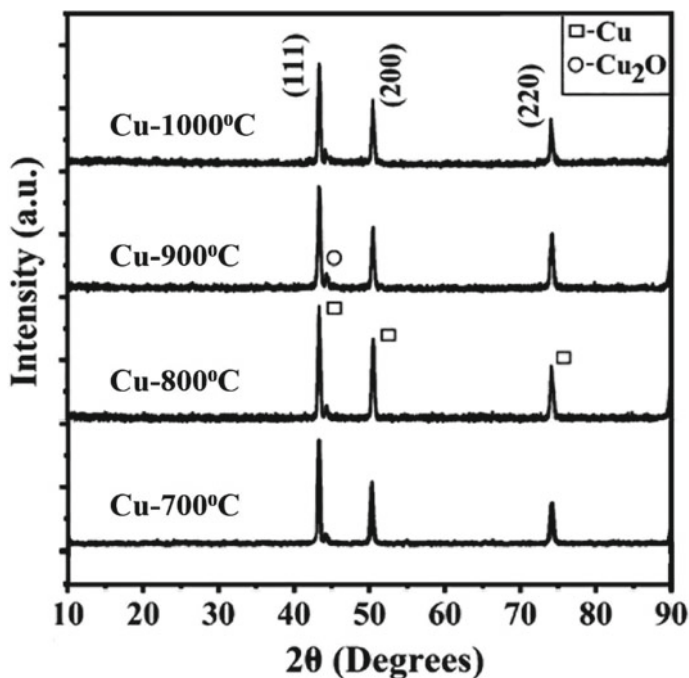


Fig. 2 XRD pattern of Cu sintered at 700, 800, 900, and 1000 °C

### 3.3 Density

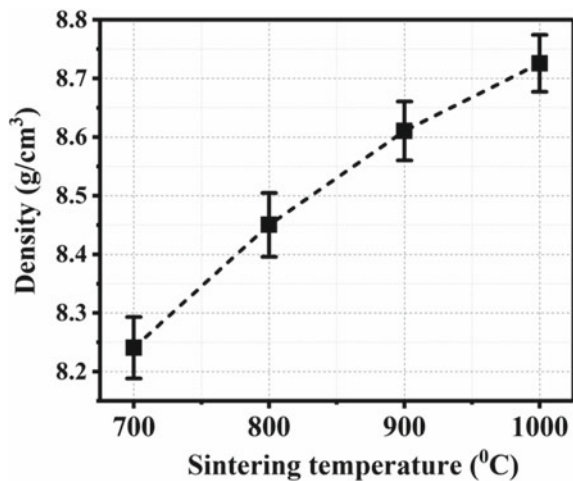
Figure 3 shows the density of the Cu for different sintering temperatures. The density of the sintered Cu specimens was determined by the Archimedes principle, and at least, five measurements were taken for each sintering temperature.

The density depends on the interface adhesion, surface integrity, and presence of pores and voids. It shows that density increases with increasing temperature and exhibits the maximum value of sintered density  $8.73 \text{ g/cm}^3$  for the  $1000 \text{ }^\circ\text{C}$ , which is 5.61% higher than that of sintering at  $700 \text{ }^\circ\text{C}$  [1, 3]. It may refer to the high rate of volume and surface diffusion, which significantly improve the surface adhesion and densification of Cu at high temperature. The volume diffusion considerably eliminates micro-pores from the Cu surface [4]. Whereas, viscous flow of the Cu atoms is the governing diffusion mechanism at low temperature, which leads to poor surface integrity and interface adhesion at low sintering temperature. It causes low density at low sintering temperature. Table 1 gives the density data of the Cu for different sintering temperatures.

### 3.4 Hardness

Figure 4 shows micro-hardness of the Cu for different sintering temperature including 700, 800, 900, and  $1000 \text{ }^\circ\text{C}$ . The hardness of the specimen depends on the interface adhesion, presence of porosity content, surface integrity, and point of indication. In the hardness test, indentation was performed by the diamond ball on the desired surface, which plastically deforms the surface.

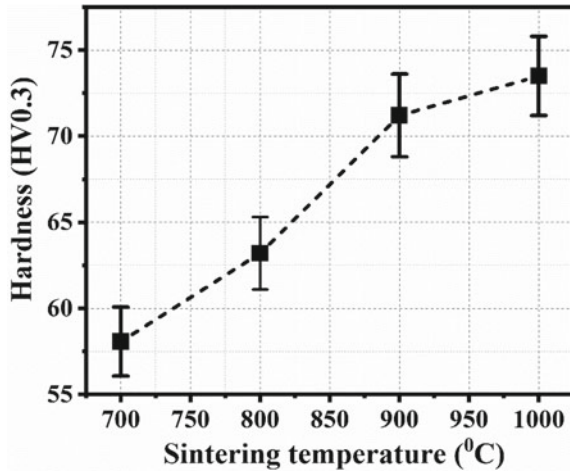
**Fig. 3** The density of Cu sintered at 700, 800, 900, and  $1000 \text{ }^\circ\text{C}$





**Table 1** Properties of the Cu at different sintering temperature

Sintering temperature	Density (g/cm <sup>3</sup> )	Micro-hardness (HV)
Cu-700 °C	8.24 ± 0.052	58.08 ± 2
Cu-800 °C	8.45 ± 0.054	63.20 ± 2.1
Cu-900 °C	8.61 ± 0.050	71.21 ± 2.4
Cu-1000 °C	8.73 ± 0.049	73.50 ± 2.3

**Fig. 4** Hardness of Cu sintered at 700, 800, 900, and 1000 °C

The strong interface adhesion and surface integrity cause high resistance against the plastic deformation of the material surface which increases the hardness. General trend in Fig. 4 depicts the increase in the hardness of the Cu with increasing the sintering temperature. Hardness depicts its lowest value ( $58.08 \pm 2$  HV) for the Cu, sintered at 700°C which refers to poor surface integrity and pores [1, 7]. However, the hardness increases with increasing the sintering temperature and obtained its maximum value of  $73.50 \pm 2.3$  HV for 1000 °C sintering temperature, 20.98% higher than that of 700 °C sintering temperature [1, 2].

It refers to the proper volume and surface diffusion of the Cu atom at an elevated temperature of 1000° C which eliminates the micro-pores and develops strong interfacial adhesion and surface integrity. Table 1 shows the hardness of the Cu for different sintering temperature.

## 4 Conclusion

The specimens of the Cu were successfully prepared by the conventional powder metallurgy route for different sintering temperature of 700, 800, 900, and 1000 °C. The study employed the Field emission scanning electron microscopy (FESEM)

and X-ray diffraction (XRD) technique to characterize the surface morphology and phase formation. It also investigates the influence of sintering temperature on the mechanical properties, including density and micro-hardness of the sintered Cu.

The metallographic observations indicate the poor surface adhesion, surface integrity, and the presence of pores on the Cu surface at a low sintering temperature of 700 °C. It may refer to low diffusion rate and domination of viscous flow and plastic flow diffusion mechanism at low sintering temperature. The micrograph depicts the improvement in the microstructure of the Cu with increasing the sintering temperature which shows the superior interface adhesion and surface integrity for the Cu sintered at 1000 °C. It corresponds to the high diffusion rate caused by the volume and surface diffusion at high sintering temperatures. It significantly eliminates the pores and improves surface adhesion and densification. The general trend depicts the increase in the density and hardness with an increase in the sintering temperature. The maximum value of sintered density and micro-hardness is obtained as 8.73 g/cm<sup>3</sup> and 73.50 HV, respectively, for 1000 °C, 5.61% and 20.98% higher than that of Cu at 700 °C sintering temperature.

The improvement in the microstructure and properties of the Cu refers to the superior surface integrity and interface adhesion of the Cu cause by the proper diffusion of the Cu atom.

## References

1. Samal CP, Parihar JS, Chaira D (2013) The effect of milling and sintering techniques on mechanical properties of Cu-graphite metal matrix composite prepared by powder metallurgy route. *J Alloy Compd* 569:95–101. <https://doi.org/10.1016/j.jall-com.2013.03.122>
2. Dixit M, Srivastava R (2019) The effect of copper granules on interfacial bonding and properties of the copper-graphite composite prepared by flake powder metallurgy. *Adv Powder Technol* 30:3067–3078. <https://doi.org/10.1016/j.appt.2019.09.013>
3. Dixit M, Srivastava RK (2018) Effect of compaction pressure on microstructure, density and hardness of Copper prepared by Powder Metallurgy route. *IOP Conf Ser Mater Sci Eng* 377. <https://doi.org/10.1088/1757-899X/377/1/012209>
4. Alexander BH (1967) The mechanism of sintering of copper. *Acta Metall* 5(1967):666–677. [https://doi.org/10.1016/0001-6160\(57\)90113-X](https://doi.org/10.1016/0001-6160(57)90113-X)
5. Kuczynski GC (1990) Self-diffusion in sintering of metallic particles. *Trans AIME* 85 (1949):169–78. Reprinted 509–527. [https://link.springer.com/chapter/https://doi.org/10.1007/978-94-009-0741-6\\_33](https://link.springer.com/chapter/https://doi.org/10.1007/978-94-009-0741-6_33)
6. Rocklandt JGR (1967) The determination of the mechanism of sintering. *Acta Metall* 15:277–286. [https://doi.org/10.1016/0001-6160\(67\)90203-9](https://doi.org/10.1016/0001-6160(67)90203-9)
7. Ngai TL, Zheng W, Li Y (2013) Effect of sintering temperature on the preparation of Cu–Ti<sub>3</sub>SiC<sub>2</sub> metal matrix composite. *Prog Nat Sci Mater Int* 23:70–76. <https://doi.org/10.1016/j.pnsc.2013.01.011>
8. Rajkumar K, Aravindan S (2010) Tribological performance of microwave heat treated copper—graphite composites. *Tribol Lett* 37:131–139. <https://doi.org/10.1007/s11249-009-9499-2>
9. Padmavathi C, Upadhyaya A, Agrawal D (2011) Effect of microwave and conventional heating on sintering behavior and properties of Al–Mg–Si–Cu alloy. *Mater Chem Phys* 130:449–457. <https://doi.org/10.1016/j.matchemphys.2011.07.008>

10. Sethi DAG, Uppadhyay A (2003) Microwave sintering of premixed and pre-alloyed Cu–12Sn bronze. *Sci Sinter* 35:49–65
11. Kumar N, Bharti A, Dixit M, Nigam A (2020) Effect of powder metallurgy process and its parameters on the mechanical and electrical properties of copper-based materials: literature review. *Powder Metall Metal Ceram* 590. <https://doi.org/10.1007/s11106-020-00174-1>

# Assessment of the Chambal River Quality at Kota Metropolis Through the Drinking Water Quality Index and Irrigation Water Quality Index



Kuldeep, Sohil Sisodiya, and Anil K. Mathur

## 1 Introduction

Potable water is essentially required to survive human beings, and hence, it is listed in sustainable development goals [1]. Approximately, 165 billion liters of water are consumed daily in India. The presence of contaminants in water for such quantity and such characteristics possess potential risks to human health known as water pollution. As per the recent WHO report, 70% of diseases can be introduced in the human body through water [2]. Even 20% of cancers are connected to water pollution [3]. Water quality is generally influenced by geology, hydrogeology, rock-water interactions, evaporation, mineral dissolution, precipitation, weathering, industrial effluents, cultivation/irrigation, chemical fertilizers, and mostly human-made activities [4]. Various impurities from human activities such as industry and agriculture degrade water quality, making it useless for a stated purpose [5].

Kota Metropolis is a district of Rajasthan state (India). It is globally reckoned as an industrial and educational city with more than 2 million population [6]. The city is primarily dependent on the Chambal River to fulfill all water demands for all purposes. It also holds great spiritual and cultural significance. This research paper reveals Chambal River water's hydro-chemical properties and its nature for drinking and irrigation purposes in the Kota district, Rajasthan (India). The measure of water quality used for irrigation and drinking is essential to estimate its long-term usage to increase productivity. WQI and IWQI are the most widely used rating tools to indicate water quality for drinking and agricultural use.

---

Kuldeep · S. Sisodiya (✉) · A. K. Mathur  
Department of Civil Engineering, UD, RTU, Kota, Rajasthan 324010, India  
e-mail: [ssisodiya.npiu.ce@rtu.ac.in](mailto:ssisodiya.npiu.ce@rtu.ac.in)

© The Author(s), under exclusive license to Springer Nature Singapore Pte Ltd. 2022  
P. Verma et al. (eds.), *Advancement in Materials, Manufacturing and Energy Engineering, Vol. 1*, Lecture Notes in Mechanical Engineering,  
[https://doi.org/10.1007/978-981-16-5371-1\\_49](https://doi.org/10.1007/978-981-16-5371-1_49)

559

## 2 Study Area and Research Methodology

Kota metropolis is located in the southeast of Rajasthan state (India), globally famous for its educational institutes and industrial units. The urban population was 11,76,604 as per India’s census, 2011 [7, 8]. The river water completes almost all the city’s water demand for drinking, irrigation, commercial, and industrial

**Table 1** GPS coordinates for the selected sampling locations

Location code	Latitude	Longitude	Sampling points	Sampling position	Flow direction
S-1	25.15122	75.80984	Akelgarh	Upstream	Southeast of Rajasthan
S-2	25.26765	75.95587	Rangpur	Downstream	

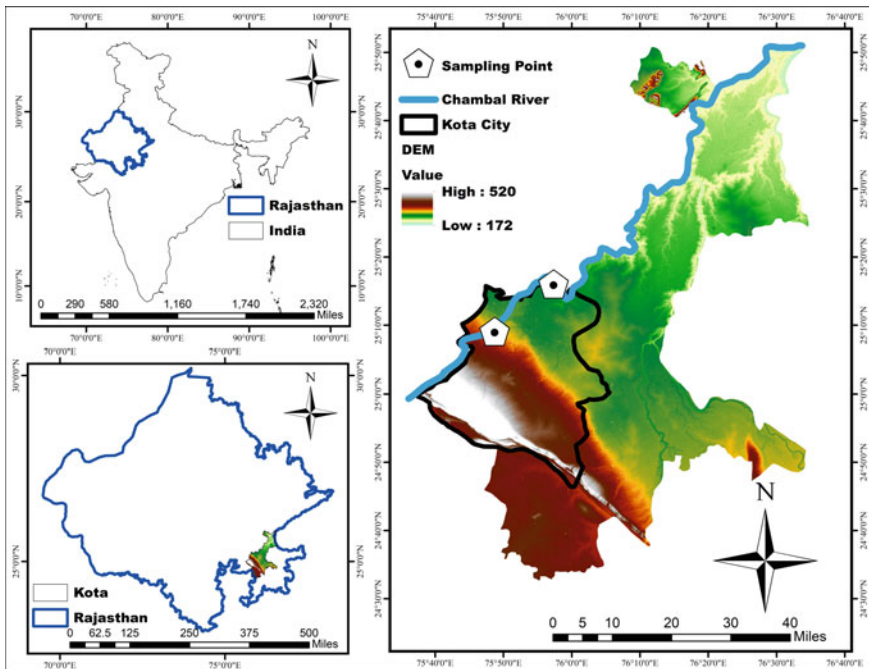


**Fig. 1** Sampling locations demonstration in the Kota metropolis

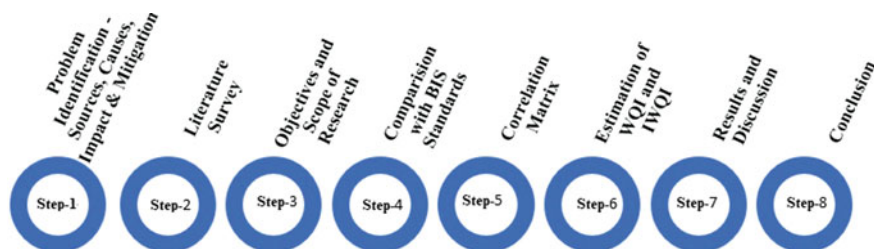


**Fig. 2** Study work methodology

activities. Two sampling points are selected to assess river water quality: first at Akelgarh in the upstream of the Chambal River, and second at Rangpur in the downstream of the Chambal River. Monitoring sites are mentioned in Table 1 and presented in Fig. 1. The methodology adopted in this study is shown in Fig. 2.

### 3 Observation

The study period selected for study was one year from January 01, 2019 to December 31, 2019. The seasonal mean, the highest and the lowest value, and standard deviation for summer, rainy, and winter seasons from the laboratory testing of samples for Akelgarh (S-1) are shown in Tables 2, 3, and 4, respectively. On the same basis (Table 5), seasonal observations for Rangpur (S-2) are presented in Tables 6, 7, and 8, respectively. The annual mean, highest and lowest values, and standard deviation for S-1 and S-2 are listed in Tables 5 and 9. The monitored data is obtained from RSPCB, and MS Excel software is used to prepare the required dataset for further calculation to calculate WQI and IWQI.

**Table 2** The mean, highest, lowest, and standard deviation for summer season at S-1

Parameter	Seasonal mean	Highest	Lowest	Standard deviation
Ammonia (mg/l)	0.46	0.48	0.44	0.03
BOD (mg/l)	1.40	1.65	1.14	0.36
Boron (mg/l)	0.23	0.25	0.21	0.03
COD (mg/l)	14.79	20.85	8.73	8.57
Calcium (mg/l)	26.40	27.20	25.60	1.13
Chloride (mg/l)	58.00	64.00	52.00	8.49
Conductivity ( $\mu$ mho/cm)	360.00	420.00	300.00	84.85
Dissolved oxygen (mg/l)	5.44	5.51	5.36	0.11
Fecal coliform (MPN/100 ml)	7.00	7.00	7.00	0.00
Fluoride (mg/l)	0.87	0.90	0.84	0.04

(continued)

**Table 2** (continued)

Parameter	Seasonal mean	Highest	Lowest	Standard deviation
Magnesium as Mg (mg/l)	7.81	11.71	3.90	5.52
Nitrate (mg/l)	1.80	1.84	1.76	0.06
pH	7.93	8.00	7.85	0.11
Phosphate (mg/l)	0.15	0.20	0.10	0.07
Potassium (mg/l)	2.30	2.70	1.90	0.57
Sodium (mg/l)	40.50	43.00	38.00	3.54
Sulfate (mg/l)	38.00	41.00	35.00	4.24
Temperature (°C)	28.50	32.00	25.00	4.95
Bi-carbonate alkalinity (mg/l)	102.00	104.00	100.00	2.83
Total coliform (MPN/100 ml)	20.00	20.00	20.00	0.00
Total dissolved solids (mg/l)	313.00	318.00	308.00	7.07
Total hardness (mg/l)	98.00	112.00	84.00	19.80
Turbidity (JTU/NTU)	1.10	1.30	0.90	0.28

**Table 3** The mean, highest, lowest, and standard deviation for rainy season at S-1

Parameter	Mean	Highest	Lowest	S.D.
Ammonia (mg/l)	0.46	0.48	0.44	0.03
BOD (mg/l)	0.88	0.90	0.85	0.04
Boron (mg/l)	0.23	0.24	0.21	0.02
COD (mg/l)	6.03	7.92	4.13	2.68
Calcium (mg/l)	18.40	19.20	17.60	1.13
Chloride (mg/l)	40.00	48.00	32.00	11.31
Conductivity (µmho/cm)	260.00	290.00	230.00	42.43
Dissolved oxygen (mg/l)	5.71	5.80	5.62	0.13
Fecal coliform (MPN/100 ml)	15.50	20.00	11.00	6.36
Fluoride (mg/l)	0.82	0.84	0.80	0.03
Magnesium as Mg (mg/l)	5.37	6.83	3.90	2.07
Nitrate (mg/l)	1.71	1.76	1.66	0.07
pH	7.96	8.08	7.84	0.17
Phosphate (mg/l)	0.10	0.10	0.10	0.00
Potassium (mg/l)	1.40	1.50	1.30	0.14
Sodium (mg/l)	30.50	33.00	28.00	3.54
Sulfate (mg/l)	33.00	35.50	30.50	3.54
Temperature (°C)	25.00	26.00	24.00	1.41
Bi-carbonate alkalinity (mg/l)	42.00	44.00	40.00	2.83
Total coliform (MPN/100 ml)	28.00	28.00	28.00	0.00
Total dissolved solids (mg/l)	195.00	212.00	178.00	24.04
Total hardness (mg/l)	68.00	72.00	64.00	5.66
Turbidity (JTU/NTU)	11.70	22.60	0.80	15.41

**Table 4** The mean, highest, lowest, and standard deviation for winter season at S-1

Parameter	Mean	Highest	Lowest	S.D.
Ammonia (mg/l)	0.49	0.54	0.44	0.05
BOD (mg/l)	1.02	1.79	0.56	0.67
Boron (mg/l)	0.25	0.31	0.19	0.06
COD (mg/l)	8.42	12.15	5.60	3.37
Calcium (mg/l)	20.80	24.00	16.00	4.23
Chloride (mg/l)	54.67	68.00	32.00	19.73
Conductivity ( $\mu$ mho/cm)	330.00	350.00	300.00	26.46
Dissolved oxygen (mg/l)	5.97	6.11	5.70	0.24
Fecal coliform (MPN/100 ml)	10.33	20.00	4.00	8.50
Fluoride (mg/l)	0.85	0.90	0.80	0.05
Magnesium as Mg (mg/l)	10.09	10.74	8.78	1.13
Nitrate (mg/l)	1.83	2.00	1.66	0.17
pH	7.80	7.98	7.60	0.19
Phosphate (mg/l)	0.10	0.10	0.10	0.00
Potassium (mg/l)	1.03	1.20	0.90	0.15
Sodium (mg/l)	40.67	50.00	26.00	12.86
Sulfate (mg/l)	40.17	42.00	38.50	1.76
Temperature ( $^{\circ}$ C)	20.00	20.00	20.00	0.00
Bi-carbonate alkalinity (mg/l)	77.33	96.00	44.00	28.94
Total coliform (MPN/100 ml)	19.67	28.00	11.00	8.50
Total dissolved solids (mg/l)	215.33	236.00	198.00	19.22
Total hardness (mg/l)	93.33	104.00	76.00	15.14
Turbidity (JTU/NTU)	1.00	1.10	0.90	0.10

**Table 5** The mean, highest, lowest, and standard deviation for whole year at S-1

Parameter	Mean	Highest	Lowest	S.D.
Ammonia (mg/l)	0.47	0.54	0.44	0.04
BOD (mg/l)	1.08	1.79	0.19	0.47
Boron (mg/l)	0.24	0.31	0.19	0.04
COD (mg/l)	9.56	20.85	4.13	5.58
Calcium (mg/l)	21.71	27.20	16.00	4.22
Chloride (mg/l)	51.43	68.00	32.00	15.04
Conductivity ( $\mu$ mho/cm)	318.57	420.00	5.36	59.28
Dissolved oxygen (mg/l)	5.74	6.11	4.00	0.29
Fecal coliform (MPN/100 ml)	10.86	20.00	0.80	6.57
Fluoride (mg/l)	0.85	0.90	0.80	0.04
Magnesium as Mg (mg/l)	8.09	11.71	1.66	3.27
Nitrate (mg/l)	1.79	2.00	1.66	0.12
pH	7.88	8.08	0.10	0.16

(continued)



**Table 5** (continued)

Parameter	Mean	Highest	Lowest	S.D.
Phosphate (mg/l)	0.11	0.20	0.10	0.04
Potassium (mg/l)	1.50	2.70	0.90	0.62
Sodium (mg/l)	37.71	50.00	26.00	9.14
Sulfate (mg/l)	37.50	42.00	20.00	4.06
Temperature (°C)	23.86	32.00	20.00	4.41
Bi-carbonate alkalinity (mg/l)	74.29	104.00	11.00	29.83
Total coliform (MPN/100 ml)	22.14	28.00	11.00	6.34
Total dissolved solids (mg/l)	237.43	318.00	64.00	54.55
Total hardness (mg/l)	87.43	112.00	0.80	18.10
Turbidity (JTU/NTU)	4.09	22.60	0.80	8.17

**Table 6** The mean, highest, lowest, and standard deviation for summer season at S-2

Parameter	Mean	Highest	Lowest	S.D.
Ammonia (mg/l)	0.73	0.84	0.54	0.13
BOD (mg/l)	2.79	3.33	2.35	0.46
Boron (mg/l)	0.27	0.31	0.23	0.03
COD (mg/l)	26.18	31.78	19.83	6.03
Calcium (mg/l)	36.80	40.00	35.20	2.26
Chloride (mg/l)	113.00	164.00	84.00	35.38
Conductivity (µmho/cm)	710.00	780.00	660.00	55.98
Dissolved oxygen (mg/l)	4.07	4.75	3.76	0.46
Fecal coliform (MPN/100 ml)	43.25	75.00	20.00	22.98
Fluoride (mg/l)	0.91	0.96	0.84	0.05
Magnesium as Mg (mg/l)	17.81	21.47	9.76	5.43
Nitrate (mg/l)	2.71	3.04	2.36	0.28
pH	8.40	8.48	8.32	0.07
Phosphate (mg/l)	0.18	0.20	0.10	0.05
Potassium (mg/l)	4.05	5.10	1.70	1.59
Sodium (mg/l)	67.00	71.00	63.00	3.27
Sulfate (mg/l)	65.75	106.50	35.50	32.20
Temperature (°C)	29.00	32.00	26.00	2.94
Bi-carbonate alkalinity (mg/l)	158.00	168.00	148.00	8.33
Total coliform (MPN/100 ml)	150.00	210.00	120.00	42.43
Total dissolved solids (mg/l)	520.50	576.00	468.00	48.62
Total hardness (mg/l)	165.00	180.00	140.00	17.40
Turbidity (JTU/NTU)	4.13	4.50	3.90	0.26

**Table 7** The mean, highest, lowest, and standard deviation for rainy season at S-2

Parameter	Mean	Highest	Lowest	S.D.
Ammonia (mg/l)	0.82	0.94	0.72	0.09
BOD (mg/l)	1.66	2.86	1.10	0.81
Boron (mg/l)	0.25	0.27	0.24	0.01
COD (mg/l)	7.65	11.98	5.78	2.92
Calcium (mg/l)	24.00	36.80	19.20	8.57
Chloride (mg/l)	63.00	88.00	48.00	18.00
Conductivity ( $\mu$ mho/cm)	415.00	630.00	310.00	147.31
Dissolved oxygen (mg/l)	5.82	6.80	4.45	1.01
Fecal coliform (MPN/100 ml)	84.75	150.00	39.00	46.69
Fluoride (mg/l)	0.84	0.90	0.80	0.04
Magnesium as Mg (mg/l)	8.54	13.66	4.88	3.77
Nitrate (mg/l)	2.00	2.10	1.84	0.11
pH	8.18	8.53	7.93	0.25
Phosphate (mg/l)	0.20	0.30	0.10	0.08
Potassium (mg/l)	3.05	4.40	2.10	0.99
Sodium (mg/l)	39.25	57.00	29.00	12.39
Sulfate (mg/l)	60.25	82.00	49.00	15.56
Temperature ( $^{\circ}$ C)	26.50	32.00	24.00	3.79
Bi-carbonate alkalinity (mg/l)	68.00	124.00	48.00	37.38
Total coliform (MPN/100 ml)	297.50	460.00	120.00	188.04
Total dissolved solids (mg/l)	305.50	464.00	234.00	108.28
Total hardness (mg/l)	95.00	148.00	72.00	35.68
Turbidity (JTU/NTU)	15.63	28.30	1.60	14.41

**Table 8** The mean, highest, lowest, and standard deviation for winter season at S-2

Parameter	Mean	Highest	Lowest	S.D.
Ammonia (mg/l)	0.72	0.94	0.58	0.17
BOD (mg/l)	1.76	2.44	0.90	0.64
Boron (mg/l)	0.27	0.31	0.23	0.03
COD (mg/l)	14.97	20.80	6.80	5.88
Calcium (mg/l)	27.60	35.20	20.80	7.88
Chloride (mg/l)	102.00	156.00	60.00	43.02
Conductivity ( $\mu$ mho/cm)	530.00	640.00	370.00	114.02
Dissolved oxygen (mg/l)	6.35	6.50	6.30	0.10
Fecal coliform (MPN/100 ml)	132.25	240.00	64.00	81.36
Fluoride (mg/l)	0.84	0.90	0.80	0.04
Magnesium as Mg (mg/l)	13.18	16.59	9.76	3.43
Nitrate (mg/l)	2.08	2.20	1.82	0.18
pH	8.20	8.36	7.99	0.15

(continued)

**Table 8** (continued)

Parameter	Mean	Highest	Lowest	S.D.
Phosphate (mg/l)	0.23	0.50	0.10	0.19
Potassium (mg/l)	2.15	3.30	1.20	0.97
Sodium (mg/l)	48.50	63.00	33.00	12.69
Sulfate (mg/l)	78.50	95.00	57.00	15.80
Temperature (°C)	21.00	25.00	18.00	3.16
Bi-carbonate alkalinity (mg/l)	102.00	152.00	52.00	53.32
Total coliform (MPN/100 ml)	335.00	460.00	210.00	144.34
Total dissolved solids (mg/l)	349.00	432.00	266.00	67.81
Total hardness (mg/l)	123.00	156.00	92.00	33.68
Turbidity (JTU/NTU)	3.08	4.10	1.90	1.14

**Table 9** The mean, highest, lowest, and standard deviation for the whole year at S-2

Ammonia (mg/l)	Mean	Highest	Lowest	S.D.
BOD (mg/l)	0.75	0.94	0.54	0.13
Boron (mg/l)	2.07	3.33	0.90	0.79
COD (mg/l)	0.26	0.31	0.23	0.03
Calcium (mg/l)	16.27	31.78	5.78	9.22
Chloride (mg/l)	29.47	40.00	19.20	8.37
Conductivity (µmho/cm)	92.67	164.00	48.00	37.90
Dissolved oxygen (mg/l)	551.67	780.00	310.00	162.47
Fecal coliform (MPN/100 ml)	5.41	6.80	3.76	1.17
Fluoride (mg/l)	86.75	240.00	20.00	63.14
Magnesium as Mg (mg/l)	0.86	0.96	0.80	0.05
Nitrate (mg/l)	13.18	21.47	4.88	5.54
pH	2.26	3.04	1.82	0.38
Phosphate (mg/l)	8.26	8.53	7.93	0.19
Potassium (mg/l)	0.20	0.50	0.10	0.11
Sodium (mg/l)	3.08	5.10	1.20	1.37
Sulfate (mg/l)	51.58	71.00	29.00	15.29
Temperature (°C)	68.17	106.50	35.50	21.93
Bi-carbonate alkalinity (mg/l)	25.50	32.00	18.00	4.60
Total coliform (MPN/100 ml)	109.33	168.00	48.00	51.74
Total dissolved solids (mg/l)	260.83	460.00	120.00	150.90
Total hardness (mg/l)	391.67	576.00	234.00	120.39
Turbidity (JTU/NTU)	127.67	180.00	72.00	40.52
Ammonia (mg/l)	7.61	28.30	1.60	9.60

## 4 Result and Discussion

### 4.1 Correlation Matrix

The correlation matrix was developed with MATLAB software for all parameters of Station 1 and Station 2. It is created to understand the interrelationship between monitored parameters. It is found that the correlation matrix for S-1 (Fig. 3) shows less correlation between all parameters than the correlation matrix for S-2 (Fig. 4), i.e., as the concentration of pollutants increases, the correlation between them also improved.

### 4.2 Water Quality Index

The WQI for S-1 and S-2 is estimated with the help of observed data. The step-by-step procedure to calculate WQI is as follows [9]:

1. Assign weight ( $W_i$ ) to all parameters based upon their importance. The topmost weight assigned is 5, and the lowermost being 1. Relative Weights ( $RW_i$ ) is calculated with the help of  $RW_i = \frac{W_i}{\sum_i W_{ii}}$ .
2. Quality Rating Scale ( $q_i$ ) is computed as:  $q_i = \frac{e_i - v_i}{b_i - v_i} * 100$ .  
Where the base value is  $v_i$  for each parameter under monitoring (0 for all variables except for DO (14) and pH (7)),  $e_i$  are the values observed experimentally, and  $b_i$  is the standard value recommended in IS 10500.
3. Sub Index ( $SI_i$ ) is computed for each variable as:  $SI_i = RW_i * q_i$ .
4. Finally, the water quality index for potable water is computed as:  $WQI = \sum_i^n SI_i$ .

The Indian water standards for drinking water, assigned weights ( $W_i$ ), calculated relative weights ( $RW_i$ ), and ideal value are presented in Table 10. The WQI for potable water for both Akelgarh and Rangpur is shown in Table 11.

The seasonal and annual WQI for Akelgarh fall (Fig. 5) under the category of “Good,” i.e., water is safe and can be consumed for drinking and cooking activities without any treatment. The WQI for Rangpur comes under the category of “Poor,” i.e., water is unsafe and cannot be used for drinking, cooking, and similar other activities without primary and secondary treatment depending upon the concentration of pollutants in river water. More than one dozen wastewater streams are directly linked with the river without any treatment before it reached Rangpur. Apart from this, solid and liquid waste generated from houses and industries situated nearby the bank of Chambal River, leachate from unauthorized solid waste dumping sites, soil erosion, reduction in the river’s self-purification capacity, and agricultural runoff are other reasons behind the poor category of river water at Rangpur sampling location.

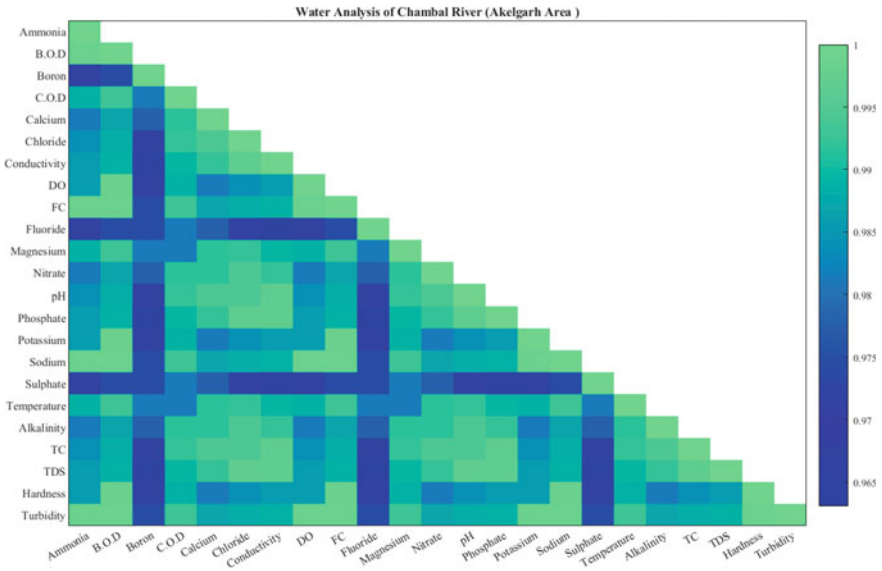


Fig. 3 Correlation matrix among all parameters at S-1

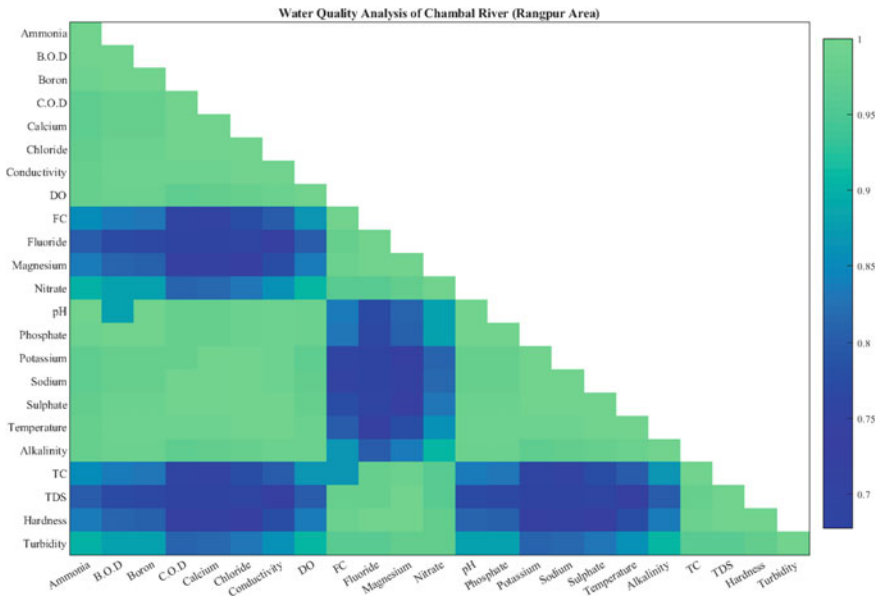


Fig. 4 Correlation matrix among all parameters at S-2

**Table 10** Indian standards, ideal value, weight, and relative weight for all parameters

Parameter	Indian standards	Ideal value	Weight	Relative weights
Ammonia (mg/l)	0.20	0.00	2.00	0.03
BOD (mg/l)	2.00	0.00	4.00	0.06
Boron (mg/l)	0.50	0.00	2.00	0.03
COD (mg/l)	2.50	0.00	4.00	0.06
Calcium (mg/l)	75.00	0.00	2.00	0.03
Chloride (mg/l)	250.00	0.00	3.00	0.04
Conductivity ( $\mu$ mho/cm)	400.00	0.00	3.00	0.04
Dissolved oxygen (mg/l)	6.00	14.00	4.00	0.06
Fecal coliform (MPN/100 ml)	50.00	0.00	4.00	0.06
Fluoride (mg/l)	1.00	0.00	4.00	0.06
Magnesium as Mg (mg/l)	30.00	0.00	3.00	0.04
Nitrate (mg/l)	45.00	0.00	4.00	0.06
pH	8.50	7.00	4.00	0.06
Phosphate (mg/l)	0.10	0.00	2.00	0.03
Potassium (mg/l)	8.00	0.00	1.00	0.01
Sodium (mg/l)	20.00	0.00	2.00	0.03
Sulfate (mg/l)	200.00	0.00	2.00	0.03
Temperature ( $^{\circ}$ C)	25.00	0.00	2.00	0.03
Bi-carbonate alkalinity (mg/l)	200.00	0.00	2.00	0.03
Total coliform (MPN/100 ml)	50.00	0.00	4.00	0.06
Total dissolved solids (mg/l)	500.00	0.00	4.00	0.06
Total hardness (mg/l)	200.00	0.00	4.00	0.06
Turbidity (JTU/NTU)	1.00	0.00	2.00	0.03

**Table 11** The water quality index for Akelgarh and Rangpur

Akelgarh (S-1)			Rangpur (S-2)		
Study time	WQI	Water quality	Study time	WQI	Water quality
Summer	98.66	Good	Summer	182.66	Poor
Rainy	100.08	Good	Rainy	147.58	Poor
Winter	77.54	Good	Winter	169.70	Poor
Annual	90.10	Good	Annual	175.65	Poor

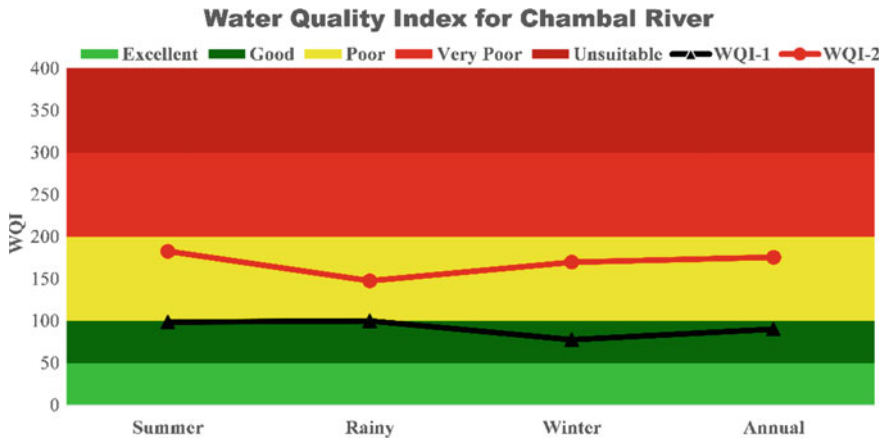


Fig. 5 Seasonal and annual variations in WQI for Akelgarh and Rangpur sampling points

Table 12 Various irrigation water quality indices [10]

IRRIGATION WATER QUALITY INDICES	
Index	Equation
Sodium Absorption Ratio (SAR)	$SAR = \frac{Na^+}{\sqrt{\frac{Ca^{2+} + Mg^{2+}}{2}}}$
Kelly Ratio (KR)	$KR = \frac{Na^+}{Ca^{2+} + Mg^{2+}}$
Soluble Sodium Percentage (SSP)	$SSP = \frac{Na^+}{Ca^{2+} + Mg^{2+} + Na^+} * 100$
Magnesium Hazard (MH)	$MH = \frac{Mg^{2+}}{Ca^{2+} + Mg^{2+}} * 100$
Sodium Percentage (Na%)	$Na\% = \frac{Na^+ + K^+}{Ca^{2+} + Mg^{2+} + Na^+ + K^+} * 100$
Permeability Index (PI)	$PI = \frac{Na^+ + K^+ + \sqrt{HCO_3^-}}{Ca^{2+} + Mg^{2+} + Na^+ + K^+} * 100$

Table 13 Standard limits for irrigation water parameters

Index	Range	Quality	Index	Range	Quality
SSP	<50	Good	KR	<1	Suitable
	>50	Unsuitable		>1	Unsuitable
MH	<50	Suitable	PI	<80	Good
	>50	Unsuitable		80–100	Moderate
Na%	< 20	Excellent		100–120	Poor
	20–40	Good	SAR	0–10	Excellent
	40–60	Permissible		10–18	Good
	60–80	Doubtful		18–26	Doubtful
>80	Unsuitable	>26		Unsuitable	

**Table 14** Various irrigation water quality indices

Sampling points	Study period	SAR	SSP	KR	Na %	MH	PI	Irrigation quality
S-1	Summer	09.79 (E)	54.21 (U)	1.18 (U)	55.58 (P)	22.83 (S)	68.69 (G)	Good and suitable
	Rainy	08.85 (E)	56.20 (U)	1.28 (U)	57.30 (P)	22.58 (S)	68.95 (G)	Good and suitable
	Winter	10.35 (G)	56.87 (U)	1.32 (U)	57.45 (P)	22.14 (S)	69.31 (G)	Good and suitable
	Annual	09.77 (E)	55.86 (U)	1.27 (U)	56.86 (P)	22.14 (S)	69.31 (G)	Good and suitable
S-2	Summer	12.82 (G)	55.09 (U)	1.23 (U)	56.54 (P)	32.62 (S)	66.54 (G)	Good and suitable
	Rainy	9.73 (G)	54.67 (U)	1.21 (U)	56.52 (P)	26.24 (S)	67.54 (G)	Good and suitable
	Winter	10.74 (E)	54.33 (U)	1.19 (U)	55.40 (P)	32.31 (S)	66.45 (G)	Good and suitable
	Annual	11.17 (G)	54.74 (U)	1.22 (U)	56.18 (P)	30.90 (S)	66.92 (G)	Good and suitable

E: Excellent, G: Good, S: Suitable, U: unsuitable, P: Permissible

### 4.3 Irrigation Water Quality Index

There are various parameters through which IWQI can be determined. Six parameters, namely, SSR, KR, SSA, NA%, MH, and PI, are selected from the literature, and their governing equations are mentioned in Table 12. Standard limits of irrigation parameters are given in Table 13. IWQI for Akelgarh and Rangpur is shown in Table 14.

The irrigation water quality index denotes its fitness for agricultural purposes and is determined by dissolved substances' concentration. The analysis of IWQI parameters shown in Table 14 suggests that Chambal River water flowing through Akelgarh to Rangpur is good and suitable for irrigation use, i.e., nutrients permissible limits to enhance crop yield.

## 5 Conclusion

The unavailability of clean and safe water in major cities is the most critical environmental concern worldwide. Polluted water used for drinking, cooking, and agricultural activities is a significant threat for human beings. After assessing water quality at two sampling points in Kota city, the study findings show that river quality at Akelgarh is clean and safe during the study period and making it fit for human consumption.



The seasonal and annual potable water quality at Rangpur was unsafe for human consumption. It is highly suggested not to use river water for human consumptions in the surrounding area without primary or secondary treatment depending upon the contaminants' concentration levels. Several wastewater streams, solid, and liquid waste generated from houses and industries situated nearby the bank of Chambal River, leachate from unauthorized solid waste dumping sites, soil erosion, reduction in the river's self-purification capacity, and agricultural runoff are the main reasons behind the poor quality of river water at Rangpur. Public awareness should be created, and wastewater streams should be treated before discharge into the river water to decrease the river water contamination load.

The overall IWQI accessed through SAR, SSP, KR, Na %, MH, and PI was good and suitable for irrigation, i.e., nutrients required for plant growth are in the range of acceptable limits. The present study may be used as baseline information both in concentration and trends by the regulating authorities. Heavy metals and radioactive materials can be included in monitoring parameters for future studies on the Chambal River and other rivers.

**Acknowledgements** The authors acknowledge the funding opportunities provided by the Technical Education Quality Improvement Programme (TEQIP-3) under the Ministry of Education, Government of India, required to carry out this study at the University Departments, Rajasthan Technical University, Kota (Rajasthan).

## References

1. Nations U (2018) Transforming our world: the 2030 agenda for sustainable development. A New Era Glob Heal. <https://doi.org/10.1891/9780826190123.ap02>
2. Marghade D, Malpe DB, Duraisamy K, Patil PD, Li P (2020) Hydrogeochemical evaluation, suitability, and health risk assessment of groundwater in the watershed of Godavari basin, Maharashtra, Central India. *Environ Sci Pollut Res*. <https://doi.org/10.1007/s11356-020-10032-7>
3. Adimalla N, Dhakate R, Kasarla A, Taloor AK (2020) Appraisal of groundwater quality for drinking and irrigation purposes in Central Telangana, India. *Groundw Sustain Dev* 10:100334. <https://doi.org/10.1016/j.gsd.2020.100334>
4. Balamurugan P, Kumar PS, Shankar K (2020) Dataset on the suitability of groundwater for drinking and irrigation purposes in the Sarabanga River region, Tamil Nadu, India. *Data Br* 29:105255. <https://doi.org/10.1016/j.dib.2020.105255>
5. Ahmed S, Khurshid S, Madan R, Abu Amarah BA, Naushad M (2020) Water quality assessment of shallow aquifer based on Canadian Council of Ministers of the environment index and its impact on irrigation of Mathura District, Uttar Pradesh. *J King Saud Univ Sci* 32 (1):1218–1225. <https://doi.org/10.1016/j.jksus.2019.11.019>
6. Kuldeep, Sisodiya S, Mathur AK (2020) Comparative assessment of noise models for Kota city. *Mater Today Proc*. <https://doi.org/10.1016/j.matpr.2020.09.513>
7. Kota District Census Handbook, Rajasthan, SERIES-09, PART XII-B Directorate of Census Operations, Census of India - 2011. [https://censusindia.gov.in/2011census/dchb/0829\\_PART\\_B\\_DCHB\\_KOTA.pdf](https://censusindia.gov.in/2011census/dchb/0829_PART_B_DCHB_KOTA.pdf)
8. Rajasthan Census (2011) Census Board of Rajasthan, Census of India -2011: Provisional Population. [https://censusindia.gov.in/2011-prov-results/prov\\_data\\_products\\_\\_rajasthan.html](https://censusindia.gov.in/2011-prov-results/prov_data_products__rajasthan.html)

9. Sisodiya S, Mehar RK, Mathur AK (2020) Statistical analysis for Urban lakes of Hadoti Region, Rajasthan 13(1):35–42
10. Sisodiya S, Mehar RK, Mathur AK (2020) Datasets for assessment of water quality indices for irrigation and drinking for Hadoti Lakes, Rajasthan 13(2):121–130

# Virtual Plan of the Domestic Enlistment Warming Framework to Reproduce Electromagnetic Boundaries



V. Geetha, M. Pushpavalli, P. Abirami, P. Sivagami,  
and R. Harikrishnan

## 1 Introduction

In the heating process, the electromagnetic field and the thermal field are strongly coupled. Induction heating process of the working material leads to rapid rise up in temperature due to the changes in the magnetic parameters like magnetic flux density (B), magnetic field intensity (H), permeability ( $\mu$ ), and electrical conductivity which leads to the changes in the electrical properties, which is harmful for the heating system and also affects the efficiency of the heating system. The measurement of these varied electrical and magnetic parameters with respect to temperature changes needs a computing resource. There are only few resources available for the computation of the electromagnetic parameters of the IH system. They are JMAG, COMSOL, CENOS, MULTIPHYSICS, EMS, etc., and survey on the simulation platform availability for the transient analysis of the heating system was made and the review states the usage of the EMS to compute the magnetic and thermal properties of the IH system developed for the domestic application. The state of the art of the review proves that the MULTIPHYSICS simulation of the induction heating system have the limitations over the finite element modeling. The requirement of the simulation software for the measurement of the electromagnetic parameters with high frequency is mandatory to have several iterations in the study. Researcher has integrated a virtual design to analyze the performance of the domestic induction heating system. CAD model for the designed system for thermal analysis is studied and compared with the simulated result, and also, real-time test and the results are depicted in [1]. The designers have identified the eco-design action of the developed hob. The most of the influenced parameters are approached

---

V. Geetha (✉) · M. Pushpavalli · P. Abirami · P. Sivagami  
EEE, Sathyabama Institute of Science & Technology, Chennai, India

R. Harikrishnan  
Symbiosis Institute of Technology, Symbiosis International Deemed University,  
Mulshi, India

in the article. The most food industry aims at satisfying the customer expectations in the product they buy. It aims on the taste, nutrition, and safety. The conventional method of heating the food directly gets reacted and reduces the taste, safety, and nutrition, so the direct induction heating method is innovated for a sample of a grape juice which is heated with a minimum temperature of 20 °C and a maximum of 100 °C for different frequency of the applied voltage. Here the study depicts that the induced current density in the medium is not detected and has to be demonstrated in the future research. The improvement in the intensity of the current can be attributed with the study of the transformer theory in [2, 3] have enhanced the induction heating technology to study the magnetic composites for the medical application. To test and measure the magnetic properties of the ferromagnetic material, a thermal transfer-based COMSOL simulation along with the experimental validation is performed resulting in the encouragement of usage of induction heating application in the field of medicine. The researcher has conducted the research to treat the varicose veins which is found to be a challenging task [4] and also demonstrated the all in one induction heating system for accommodating the all shapes of the vessel. The comparison of the flat bottomed vessel and the curved bottom vessel is been designed, simulated, and experimentally proves to have a good agreement. A 1500 W prototype model was built to evaluate the magnetic and thermal fields of the proposed topology. The FEM analysis of the simulated system was carried out to elaborate the heating performance of the designed system using JMAG software package [5] and has implemented an induction heating system with full bridge series resonant converter for different utensils made of materials like ferromagnetic conductive, non-ferromagnetic conductive, and non-ferromagnetic non-conductive with 500 W prototype. The system produced an average temperature of 83.8 °C, and efficiency of 96.9% at the maximum for the ferromagnetic material and various comparisons for magnetic properties regulating the output power flexibly and efficiently. The author has also focused on the magnetic coupling properties and temperature distribution of the proposed induction heating system [6]. A suitable optimization technique for the designed geometry was adopted for the uniform distribution of the heat. The author has approached with the numerical method to reach the desired temperature for the specimen to be heated [7] and has practically designed an induction heating cooker to determine the evolution of the temperature distributed over the surface, and a FEA was carried out considering the nonlinearity property of the pan used. Required governing equation was identified for the analysis which was made for a 220 V. Modeling of a single loop induction heating system to have optimal control of amplitude, frequency, and current, the key point of the study made was to have a desired temperature profile for the work piece made of non-ferromagnetic material. The optimization of the modeled system is carried out with genetic algorithm and compared with educated guess and optimum solution. The experimental validation of the proposed topology with the specific designed geometry proved that genetic algorithm holds good for the designed system. The genetic algorithm formulated in the proposed system reduced the heating time by 19% and energy by 11% in [8, 9] has modeled and optimized the induction cooking system for improving the temperature distribution.

The dimensions and the parameters are replaced by the iterative step carried out to minimize the error and calculated the temperature at each node of the designed and simulated study. Here the numerical mathematical representation was done to understand the design of the developed system. Researcher has presented a mathematical, numerical model for coupling the various physical phenomena like electromagnetic and thermomechanical computations. The research proved that the strategy developed has enabled the efficient parallel computation techniques and best suited for the global optimization procedures. The excellent output comparison was made between the numerical and experimental results in [10].

## **2 Geometric Model of the Induction Heating System**

### ***2.1 Coil Specification***

The cross-sectional view of the designed study depicts the dimensions of the coil geometry. The dimension depends on the length of the coil, thickness of the coil, and the material the coils made of. The coil is made of the material of copper. The air gap between the coils is concentrated during the coil design.

The coil with an outer and inner diameter of about 70 mm and 15 mm was designed using the solid works, and its cross sectional and isometric view are depicted in the following Figs. 1 and 2. The coil arrangement was made inside an air box to prevent the wastage of the magnetic flux in the space.

### ***2.2 Mesh Model of the Developed System***

Here the mesh model of the system with a pot arrangement is made, and the total geometry is kept in the air box arrangement, and the rms current of 5 A with a switching or the operating frequency of 29 kHz is applied at the terminals of the coil to measure the temperature in the coil and also along with the pot arrangement as in Fig. 3. The arrangement shown is the 3D view of the meshed system which is kept in the air chamber for the analysis. The system is kept in the air space such that the magnetic flux or the temperature developed on the application of the current in to the induction coil will not have scattering. The losses can be reduced such a way, and also, the system development in the EMS can be carried out only with the air spaces and with the mesh model. The geometry is based on the quantity of the medium to be warmed or heated here the water as the medium requires 100 °C to be developed in the work piece base such that the boiling point in water is achieved without any losses in the induction cooking system.

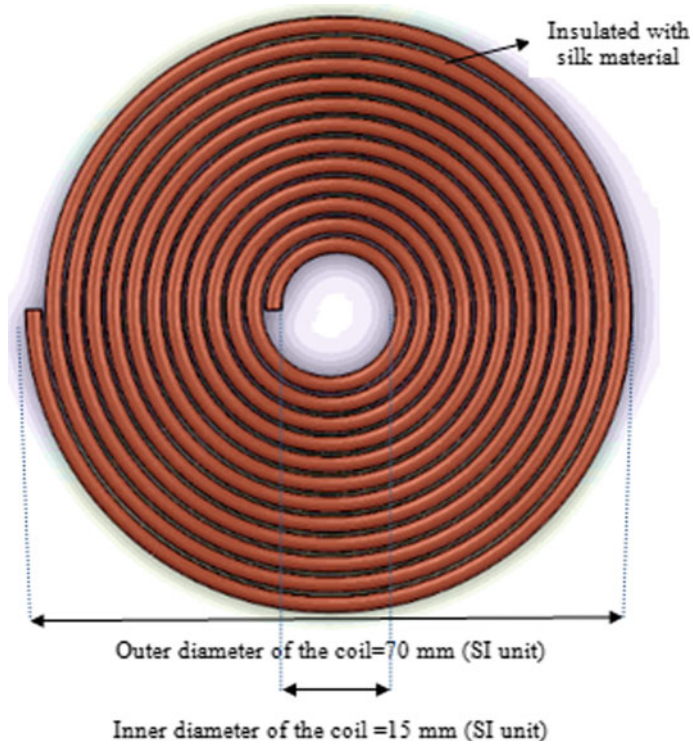


Fig. 1 Isometric view of the IH coil

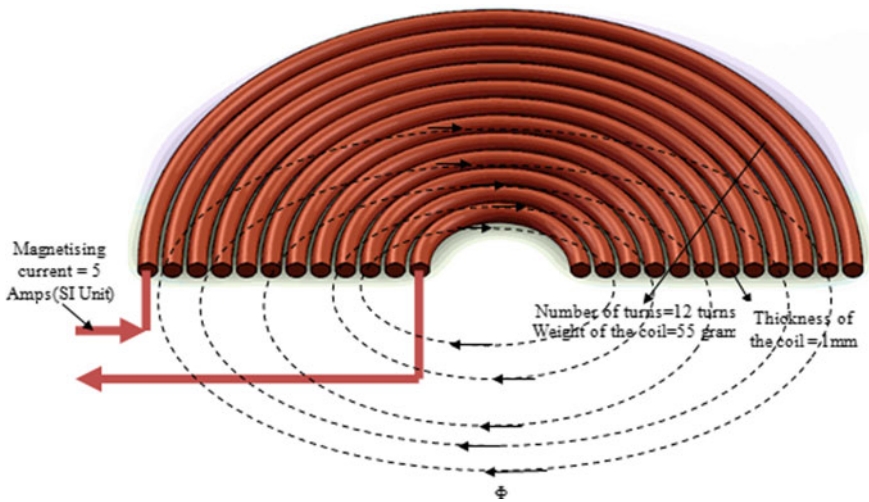
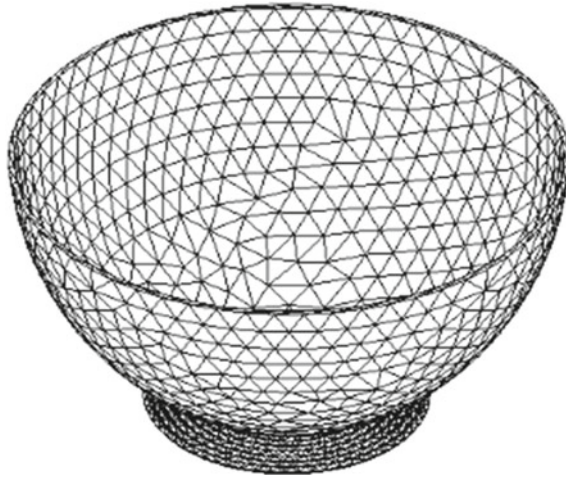


Fig. 2 Cross-sectional view of the IH coil



**Fig. 3** Mesh model of the IH geometry design

### 2.3 *Temperature Variation of the Developed Induction Coil*

The coil with 12 turns was developed to produce the required heat for the heating up of the medium water. The temperatures of the water is 100 °C, the transfer of heat from the coil to the work piece then to the medium are calculated and a temperature of 123.89 °C is produced in the coil. The coil carries a minimum temperature of 115.95 °C and a maximum of approximately 123.89 °C. Figure 4 represents the variation in the temperature in the coil.

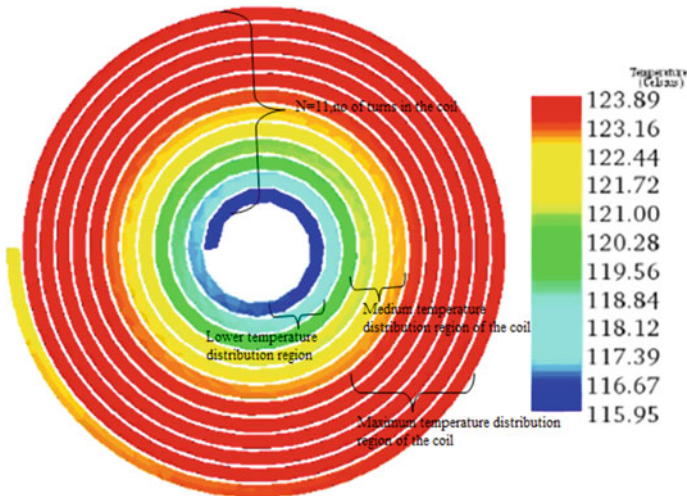


**Fig. 4** Temperature profile of the induction coil



## 2.4 Magnetic Flux Density of the Induction Cooking Coil

The density of the flux around the coil represents the amount of heat developed in the base of the cooking vessel. The developed flux in the coil is represented in the vector form. The coil is placed inside the air space that can be witnessed in Fig. 5. Here the current applied as the input to the induction coil is about 5 A.

We can observe the variation in the magnetic flux density in the vessel as a cross-sectional view and also the front view which clearly explains the variation in the distribution of flux over the vessel. In addition to all the magnetic parameters the thickness of the pan base is also a key factor for the amount of heat to be distributed uniformly. Figures 6 and 7 represent the vector representation of the movement of the magnetic flux density of the 3D model developed for the study. The thickness of the pan plays a major role in the heat distribution over the surface. The various thickness of the pan the temperature reaching the work piece is analyzed.

## 3 Heat Distribution of the Induction Heating System

The system designs using the solid works platform virtually implemented with various thickness of the base of the cooking system, and the parameters like the temperature gradient, magnetic flux density, and temperature are recorded after the number of iteration study carried out in the EMS platform. Figure 8 represents the variation in the temperature with the variation in the base thickness. The variation in

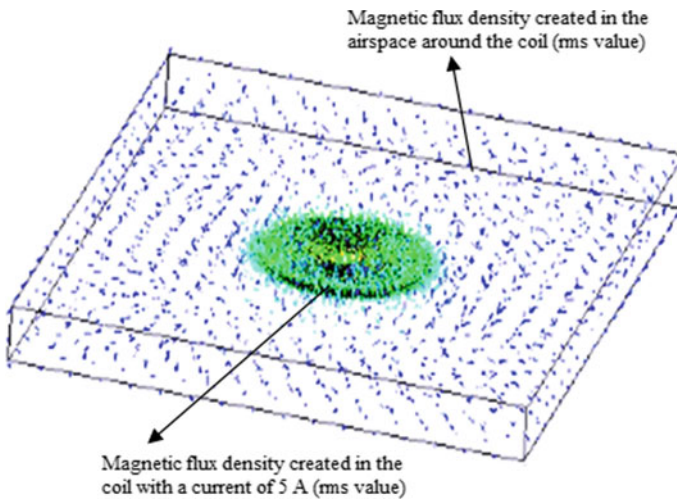


**Fig. 5** Vector representation of the magnetic flux density of the induction coil



**Fig. 6** Cross-sectional view of the geometry model of the induction cooking system

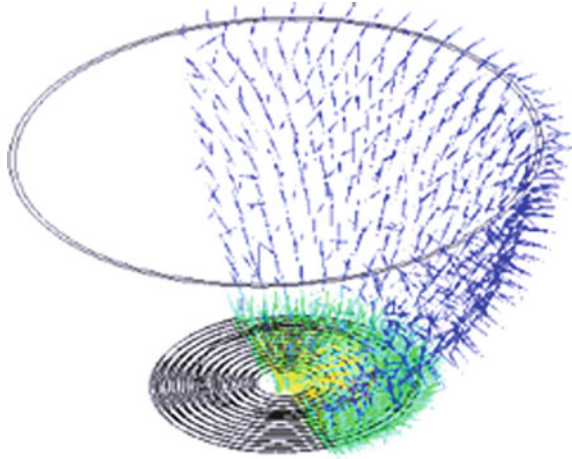
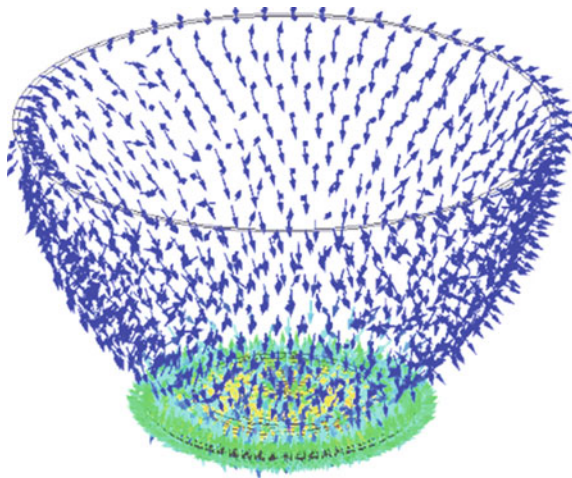


**Fig. 7** 3D model of the movement of the magnetic flux density ( $\text{wb/m}^2$ ) of the induction cooking system



the magnetic flux density with respect to thickness can be viewed in Figs. 9 and 10 which represents the temperature gradient that was measured for various thickness of the vessel base.

3D plot of the temperature distribution with a pan thickness of 3 mm is displayed after the study carried out with the virtual model of the induction cooking system, and the same is shown in Fig. 11. The various view of the cooking system, as shown in Fig. 11a–c, is viewed to demonstrate the distribution before implementing the actual induction cooking system. The FEA is carried out to the geometric model developed. The same study was carried out for the different thickness from 0.5 mm to 3 mm, as an illustration distribution of heat for the 3 mm thickness base is demonstrated.

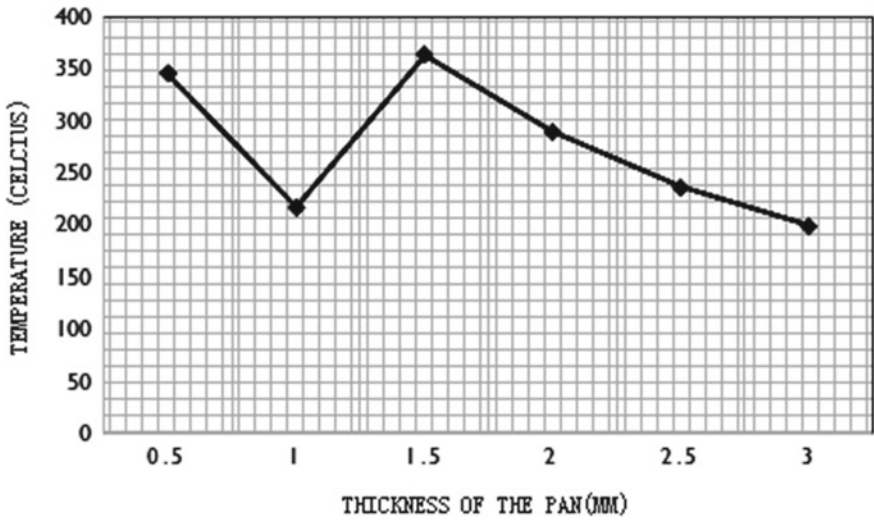


Fig. 8 Temperature versus base thickness of the induction cooking system

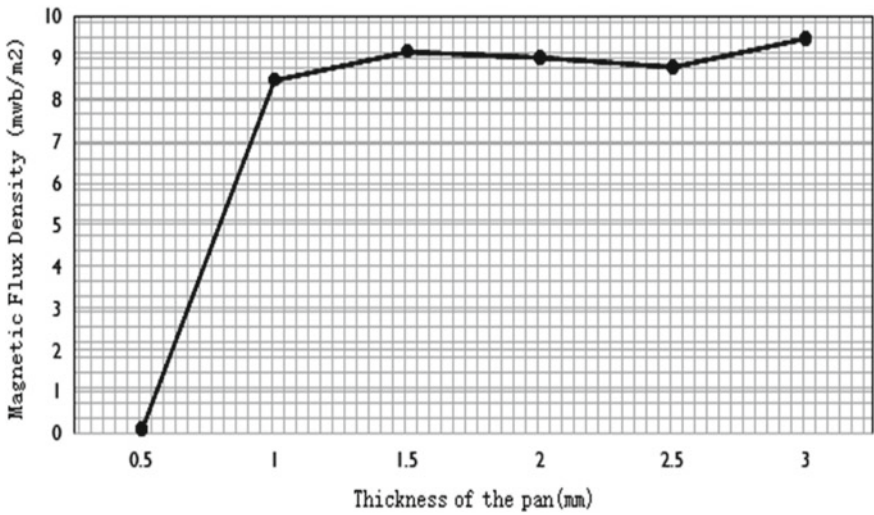


Fig. 9 Magnetic flux density versus base thickness of the induction cooking system

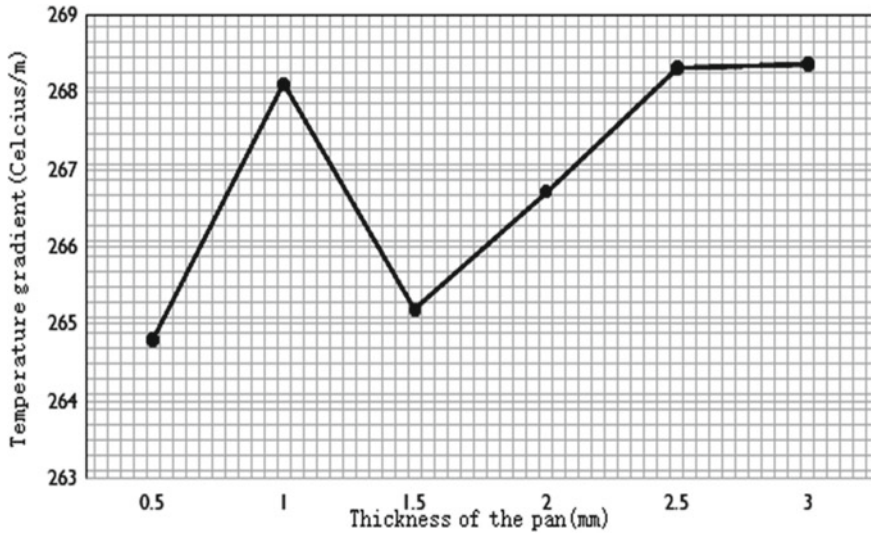


Fig. 10 Temperature gradient versus base thickness of the induction cooking system

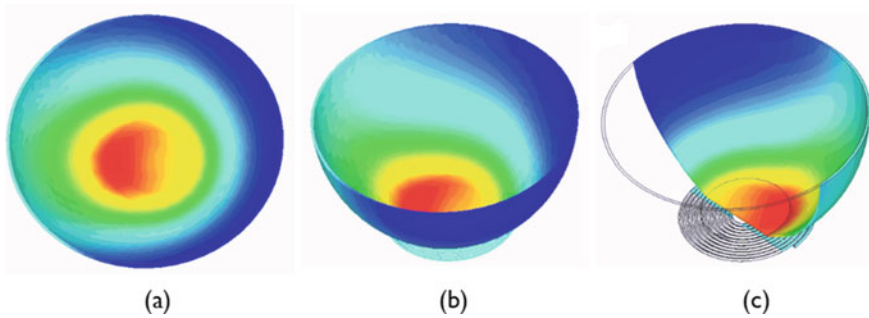


Fig. 11 **a** Top view of the heated pan with distribution of heat uniformly in the base, **b** isometric view of the heated pan with uniform distribution of heat, **c** cross-sectional view of the pan representing the coil with the pan

### 4 Conclusion

An induction cooking system with the 5 A current and a switching frequency of 29 kHz was virtually implemented with the induction coil with 12 turns wound coil. The cooking vessel has the mentioned geometry for the input provided for the study. The thermal and magnetic parameters are analyzed for the system with various base thickness, and the results are depicted in the research. The system virtually implemented to provide and verify the effectiveness of the cooking system to be implemented and produced as a product. In future, any induction cooking

system can be designed and verified for any specific quantity before developing the actual product. It can also be used for the heating system design for the sterilization process in the medical field.

## References

1. Landi D, Rossi M, Favi C, Brunzini A, Germani M (2019) A virtual design approach to simulate the hob energy performance. <https://doi.org/10.14733/cadaps.2020.1101-1115>
2. Jin Y, Yang N, Xu D, He C, Xu Y, Xu X, Jin Z (2020) Innovative induction heating of grapefruit juice via induced electric field and its application in *Escherichia coli* O157: H7 inactivation. *RSC Adv* 10(46):27280–27287
3. Xiang Z, Jakkpat KI, Ducharne B, Capsal JF, Mogniotte JF, Lermusiaux P, Cottinet PJ, Schiava ND, Le MQ (2020) Enhancing the low-frequency induction heating effect of magnetic composites for medical applications. *Polymers* 12(2):386
4. Han W, Chau KT, Wong HC, Jiang C, Lam WH (2019) All-in-one induction heating using dual magnetic couplings. *Energies* 12(9):1772
5. Han W, Chau KT, Lam WH (2019) All-utensil domestic induction heating system. *Energy Convers Manage* 195:1035–1043
6. Jakubovicova L, Andrej G, Peter K, Milan S (2016) Optimization of the induction heating process in order to achieve uniform surface temperature. *Procedia Engineering* 136:125–131
7. Al-Shaikhli AKM, Meka AT (2014) Design and implementation of practical induction heating cooker. *Int J Soft Comput Eng (IJSCE)* 4(4):73–76
8. Kranjc M, Županič A, Jarm T, Miklavcic D (2009) Optimization of induction heating using numerical modeling and genetic algorithm. In: 2009 35th annual conference of IEEE industrial electronics, pp 2104–2108. IEEE
9. Jiang YP, Wang D, Zhang QH, Chen JQ (2015) Electromagnetic-thermal coupling simulation by ANSYS multiphysics of induction heater. In: *Appl Mech Mater* 701:820–825
10. Bay F, Labbe V, Favennec Y, Chenot JL (2003) A numerical model for induction heating processes coupling electromagnetism and thermomechanics. *Int J Numer Meth Eng* 58(6):839–867

# Assessment of Urban Air Quality for Jodhpur City by the Air Quality Index (AQI) and Exceedance Factor (EF)



Kuldeep, Sohil Sisodiya, Anil K. Mathur, and Puneet Verma

## 1 Introduction

Air pollution is one of the major global threats to human health, with 4.2 million deaths in 2016 due to outdoor air pollution [1]. As per World Air Quality Report 2019, 39 cities of India were in the world's top 100 most polluted cities. Jodhpur's rank is 20th in the top 39 most polluted cities of India [2]. In Rajasthan (India), more than 90 thousand deaths in 2017 were related to air pollution. The state of Rajasthan has the highest death rate per one lakh population, which is 112.5 due to air pollution TOI, 2018.

Although seven nitrogen oxides are found in the atmosphere,  $\text{NO}$ ,  $\text{NO}_2$ ,  $\text{NO}_3$ ,  $\text{N}_2\text{O}$ ,  $\text{N}_2\text{O}_3$ ,  $\text{N}_2\text{O}_4$ , and  $\text{N}_2\text{O}_5$ , only two of these are harmful air pollutants: nitric oxide ( $\text{NO}$ ) and nitrogen dioxide ( $\text{NO}_2$ ). Nitric oxide ( $\text{NO}$ ) is a colorless gas whose concentration does not have any adverse health effects as it is found in the atmosphere. However,  $\text{NO}$  is oxidized to  $\text{NO}_2$ , which can cause bronchitis, pneumonia, and fewer respiratory infections in the lungs.  $\text{NO}_2$  also reacts with volatile compounds in sunlight to form photochemical oxidants that adversely affect health.

$\text{NO}_2$  has other environmental consequences besides being directly related to human health. It reacts with hydroxyl radicals ( $\text{OH}$ ) present in the atmosphere to form nitric acid ( $\text{HNO}_3$ ), which rusts on the metal surface and contributes to the acid precipitation problem. It also damages terrestrial plants and is an essential

---

Kuldeep · S. Sisodiya (✉) · A. K. Mathur  
Department of Civil Engineering, UD, RTU, Kota, Rajasthan 324010, India  
e-mail: [ssisodiya.npiu.ce@rtu.ac.in](mailto:ssisodiya.npiu.ce@rtu.ac.in)

P. Verma  
School of Earth and Atmospheric Sciences, Queensland University of Technology,  
Brisbane, Australia

P. Verma  
Mott MacDonald Pty. Ltd. Adelaide, Adelaide, Australia

cause of eutrophication. The reddish-brown color of smoke is due to nitrogen dioxide (e.g., Los Angeles Smoke) [3].

Sulfur dioxide ( $\text{SO}_2$ ) is a colorless, nonflammable, and non-explosive gas that causes suffocation at high concentrations. Sulfur dioxide is converted to sulfur trioxide; it can produce  $\text{H}_2\text{SO}_4$  by photochemical and catalytic reactions with other components in the atmosphere.

Sulfuric acid, sulfur dioxide, and sulfur salts irritate the respiratory tract's mucous membranes and promote chronic respiratory diseases, particularly bronchitis and pulmonary emphysema. Sulfur dioxide can damage trees, especially when trees are exposed to acid fog or clouds because they have high pH levels. Acidity damages plants by affecting their ability to extract nutrients from the soil. Under acidic conditions, nutrients are picked up from the soil more rapidly, and lower pH levels impede nutrient uptake. Sulfurous pollutants can discolor plants, corrode metals, and coach organic fibers to weaken.

Airborne sulfate significantly reduces visibility and discolors the atmosphere. Prolonged exposure to sulfate causes serious damage in the manufacture of marble, limestone, and mortar. The carbonates in these materials are replaced by the sulfates resulting product calcium sulfate, which arises from this reaction, is soluble in water and easily washes away, leaving a pitted, eroded surface. Many of the world's historical buildings and sculptures are rapidly deteriorating due to their high exposure [4].

The impact of  $\text{PM}_{10}$  on health occurs at the level of experience of most urban and rural populations in both developed and developing countries. There is a risk of heart and respiratory diseases due to continuous exposure to particles and can also cause lung cancer. Particulate matter causes leaf damage when it accumulates on the leaf surface in the presence of moisture.

Dust coating on leaves reduces photosynthesis, and increased plugging of stomata reduces plant growth; animals, which eat fluoride, arsenic-containing lead-coated plants, and lead, may suffer some ill effects. Particulate matter can damage materials by settling clothing and textile, corroding metals, eroding building surfaces, destroying discoloration, and destroying painted surfaces [3–5].

## 2 Study Area

Jodhpur, one of the large districts of Rajasthan, is located in the western region of the state, with a geographical area of 22,850  $\text{km}^2$ . According to the 2011 census, it has a population of 36.85 lakh. The district stretches between  $26^{\circ}00'$  and  $27^{\circ}37'$  at north latitude and between  $72^{\circ}55'$  and  $73^{\circ}52'$  at east longitude. The district comes under the arid zone and is situated at an altitude of 250–300 m above sea level. The average rainfall is reported to be 360 mm (36 cm) [6, 7].

The number of registered vehicles in Jodhpur is 1190627 as per the Transport Department, Government of Rajasthan. The total number of industrial units is 23,319 distributed in 22 industrial areas. For administration and development, the



**Table 1** Air quality monitoring stations along with GPS coordinates and monitoring agency

S. no.	Station name	Latitude	Longitude	Monitoring agency
1	Soorsagar Police Station	26.31	73.01	RSPCB
2	Sojati Gate	26.29	73.02	RSPCB
3	Shastri Nagar Police Station	26.27	72.99	RSPCB
4	RIICO Office, Basni	26.23	73.01	RSPCB
5	Maha Mandir	26.31	73.04	RSPCB
6	District Industries Centre Office	26.26	73.01	RSPCB
7	Kudi Mahila Police Station	26.21	73.02	RSPCB
8	Housing Board	26.26	72.97	RSPCB
9	Sangariya Sub-police Station	26.20	73.00	RSPCB
10	Collectorate Office	26.29	73.04	CPCB

district is divided into seven tehsils: Jodhpur, Osian, Phalodi, Bilara, Bhopalgarh, Luni, and Shergarh. Jodhpur city (tehsil) is selected for air quality study. There are ten air quality monitoring stations situated in the city’s crucial locations installed by RSPCB and CPCB, mentioned in Table 1 with GPS coordinates. The study area map is developed with the help of ArcGIS software and shown in Fig. 1.

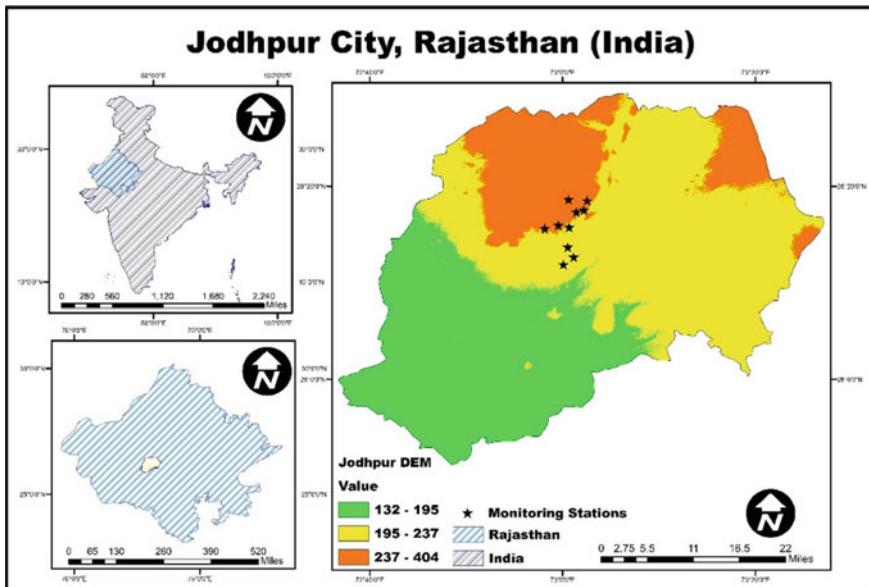


**Fig. 1** Study area demonstration along with digital elevation model

### 3 Observation and Calculation

The period of observation is one year, from January 1, 2019, to December 31, 2019. The study period is equally divided into three seasons to obtain seasonal variations in air pollutant concentrations. The monthly concentration levels of NO<sub>2</sub>, SO<sub>2</sub>, and PM<sub>10</sub> are presented in Tables 2, 3, and 4, respectively. Minimum, maximum, and average concentrations of these pollutants at each monitoring station are also computed annually. AQI is thus calculated from the concentration levels of these three criteria pollutants using CPCB step-by-step procedure and shown in Table 5.

**Table 2** Average, maximum, and minimum concentration of NO<sub>2</sub> at each monitoring station

Average, maximum, and minimum concentration of NO <sub>2</sub>											
Season	Conc.	MS-1	MS-2	MS-3	MS-4	MS-5	MS-6	MS-7	MS-8	MS-9	MS-10
Winter season	Avg	32.8	32.8	32.6	33.7	32.7	32.9	33.1	35.5	33.3	28.8
	Max	41.4	40.0	39.5	40.1	38.9	38.6	39.2	44.6	40.8	36.9
	Min	23.9	23.8	24.6	24.2	24.8	24.5	24.9	30.0	23.3	19.3
Summer season	Avg	21.6	21.1	21.2	21.4	21.3	22.3	21.2	21.5	21.0	34.7
	Max	24.2	24.0	24.0	24.8	23.3	25.3	24.0	24.1	23.2	40.5
	Min	19.8	19.7	19.8	19.9	20.2	20.9	19.8	20.1	19.9	29.5
Rainy season	Avg	17.5	16.9	18.1	17.4	18.1	19.2	18.3	18.2	17.9	27.6
	Max	19.2	19.4	19.5	19.9	19.5	20.2	19.4	19.8	19.6	30.1
	Min	14.7	11.8	16.0	12.1	16.3	17.8	17.0	17.0	16.0	24.3
Annual	Avg	24.0	23.6	24.0	24.2	24.0	24.8	24.2	25.1	24.1	30.4
	Max	41.4	40.0	39.5	40.1	38.9	38.6	39.2	44.6	40.8	40.5
	Min	14.7	11.8	16.0	12.1	16.3	17.8	17.0	17.0	16.0	19.3

**Table 3** Average, maximum, and minimum concentration of SO<sub>2</sub> at each monitoring station

Average, maximum, and minimum concentration of SO <sub>2</sub>											
Season	Conc.	MS-1	MS-2	MS-3	MS-4	MS-5	MS-6	MS-7	MS-8	MS-9	MS-10
Winter season	Avg	8.6	8.2	8.1	8.3	8.2	8.2	8.7	8.5	8.5	9.6
	Max	10.9	9.7	9.6	9.4	10.2	9.6	11.3	9.8	10.6	11.6
	Min	6.6	6.6	6.2	6.8	6.0	6.3	6.3	6.8	6.3	7.4
Summer season	Avg	5.7	5.6	5.5	5.6	5.6	5.8	5.6	5.7	5.6	9.3
	Max	6.2	6.0	5.9	6.0	5.9	5.9	5.8	6.0	5.9	12.5
	Min	5.4	5.4	5.3	5.3	5.4	5.6	5.4	5.5	5.4	7.0
Rainy season	Avg	5.6	5.1	5.5	5.1	5.8	6.0	5.8	5.6	5.6	7.6
	Max	6.9	5.7	6.4	5.5	7.6	7.9	7.8	7.1	6.9	10.0
	Min	5.0	4.6	5.0	4.8	5.1	5.1	5.1	4.9	5.0	6.5
Annual	Avg	6.6	6.3	6.3	6.3	6.5	6.7	6.7	6.6	6.6	8.9
	Max	10.9	9.7	9.6	9.4	10.2	9.6	11.3	9.8	10.6	12.5
	Min	5.0	4.6	5.0	4.8	5.1	5.1	5.1	4.9	5.0	6.5



**Table 4** Average, maximum, and minimum concentration of PM<sub>10</sub> at each monitoring station

Average, maximum, and minimum concentration of PM <sub>10</sub>											
Season	Conc.	MS-1	MS-2	MS-3	MS-4	MS-5	MS-6	MS-7	MS-8	MS-9	MS-10
Winter season	Avg	224	245	238	247	186	308	259	246	244	165
	Max	293	291	348	301	258	396	391	301	300	197
	Min	182	191	175	195	136	226	179	193	187	148
Summer season	Avg	224	338	259	250	254	350	341	280	310	199
	Max	272	389	318	300	366	412	460	345	434	241
	Min	154	304	214	202	183	272	276	256	244	151
Rainy season	Avg	116	154	126	125	108	188	178	146	138	147
	Max	175	239	178	188	139	259	257	209	183	192
	Min	76	115	71	98	75	126	130	100	95	106
Annual	Avg	188	246	208	207	182	282	259	224	231	170
	Max	293	389	348	301	366	412	460	345	434	241
	Min	76	115	71	98	75	126	130	100	95	106

**Table 5** Air quality index with categories

AQI value	Color	AQI category
0 to 50	Light green	Good
51 to 100	Green	Satisfactory
101 to 200	Yellow	Moderate
201 to 300	Orange	Poor
301 to 400	Red	Very poor
401 to 500	Maroon	Severe

## 4 Observation and Calculation

The arithmetic average concentration of NO<sub>2</sub> for winter, summer, and rainy seasons from all monitoring stations' observation data was 32.82 µg/m<sup>3</sup>, 22.71 µg/m<sup>3</sup>, and 18.93 µg/m<sup>3</sup>, respectively, as shown in Fig. 2. The topmost and lowermost values of NO<sub>2</sub> concentration were 44.58 µg/m<sup>3</sup> and 19.29 µg/m<sup>3</sup>, 40.55 µg/m<sup>3</sup> and 19.66 µg/m<sup>3</sup>, and 30.07 µg/m<sup>3</sup> and 11.79 µg/m<sup>3</sup>, for winter, summer, and rainy seasons, respectively. The range of NO<sub>2</sub> was 19.29–44.58 µg/m<sup>3</sup> in the winter season, 19.66–40.55 µg/m<sup>3</sup> in the summer season, and 11.79–30.07 µg/m<sup>3</sup> in the rainy season.

The annual range and average concentration of NO<sub>2</sub> were 11.79–44.58 µg/m<sup>3</sup> and 24.82 µg/m<sup>3</sup>. The maximum concentration of NO<sub>2</sub> was 44.58 µg/m<sup>3</sup> observed in January at Sojati Gate, Jodhpur, among all stations. The minimum concentration of NO<sub>2</sub> was 11.79 observed in October at Housing Board, Jodhpur, among all stations. The seasonal and annual concentration of NO<sub>2</sub> is within the acceptable limits prescribed by CPCB. The standard limit of NO<sub>2</sub> for 24 h is 80 µg/m<sup>3</sup> and for annual is 40 µg/m<sup>3</sup>.

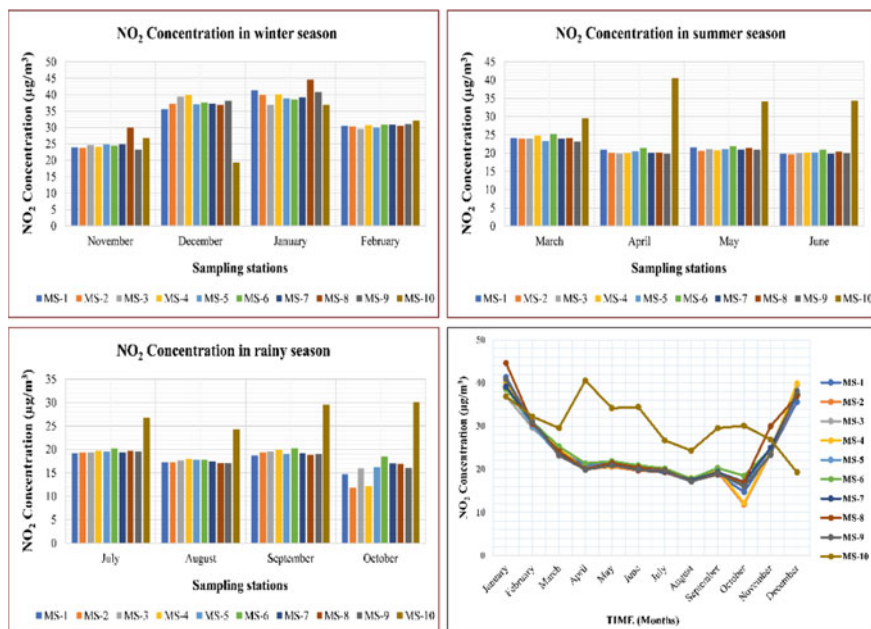


Fig. 2 Seasonal and annual variation in  $\text{NO}_2$  concentration

The arithmetic average concentration of  $\text{SO}_2$  for winter, summer, and rainy seasons from all monitoring stations' observation data was  $8.50 \mu\text{g}/\text{m}^3$ ,  $6.00 \mu\text{g}/\text{m}^3$ , and  $5.78 \mu\text{g}/\text{m}^3$ , respectively, as shown in Fig. 3. The topmost and lowermost values of  $\text{SO}_2$  concentration were  $11.59 \mu\text{g}/\text{m}^3$  and  $6.03 \mu\text{g}/\text{m}^3$ ,  $12.48 \mu\text{g}/\text{m}^3$  and  $5.32 \mu\text{g}/\text{m}^3$ , and  $9.99 \mu\text{g}/\text{m}^3$  and  $4.58 \mu\text{g}/\text{m}^3$ , for winter, summer, and rainy seasons, respectively. The range of  $\text{SO}_2$  was  $6.03\text{--}11.59 \mu\text{g}/\text{m}^3$  in the winter season,  $5.32\text{--}12.48 \mu\text{g}/\text{m}^3$  in the summer season, and  $4.58\text{--}9.99 \mu\text{g}/\text{m}^3$  in the rainy season.

The annual range and average concentration of  $\text{SO}_2$  were  $4.58\text{--}12.48 \mu\text{g}/\text{m}^3$  and  $6.76 \mu\text{g}/\text{m}^3$ , respectively. The maximum concentration of  $\text{SO}_2$  was  $12.48 \mu\text{g}/\text{m}^3$  observed in March at the DIC Office, Jodhpur, among all stations. The minimum concentration of  $\text{SO}_2$  was  $4.58 \mu\text{g}/\text{m}^3$  observed in October at Housing Board, Jodhpur, among all stations. The seasonal and annual concentration of  $\text{SO}_2$  is within the acceptable limits prescribed by CPCB. The standard limit of  $\text{SO}_2$  for 24 h is  $80 \mu\text{g}/\text{m}^3$  and for annual is  $50 \mu\text{g}/\text{m}^3$ .

The arithmetic average concentration of  $\text{PM}_{10}$  for winter, summer, and rainy seasons from all monitoring stations' observation data was  $236.08 \mu\text{g}/\text{m}^3$ ,  $280.56 \mu\text{g}/\text{m}^3$ , and  $142.36 \mu\text{g}/\text{m}^3$ , respectively, as shown in Fig. 4. The topmost and lowermost values of  $\text{PM}_{10}$  concentration were  $396.00 \mu\text{g}/\text{m}^3$  and  $136.00 \mu\text{g}/\text{m}^3$ ,  $460.00 \mu\text{g}/\text{m}^3$  and  $150.63 \mu\text{g}/\text{m}^3$ , and  $259.00 \mu\text{g}/\text{m}^3$  and  $71.00 \mu\text{g}/\text{m}^3$ , for winter, summer, and rainy seasons, respectively. The range of  $\text{PM}_{10}$  was  $136.00\text{--}$

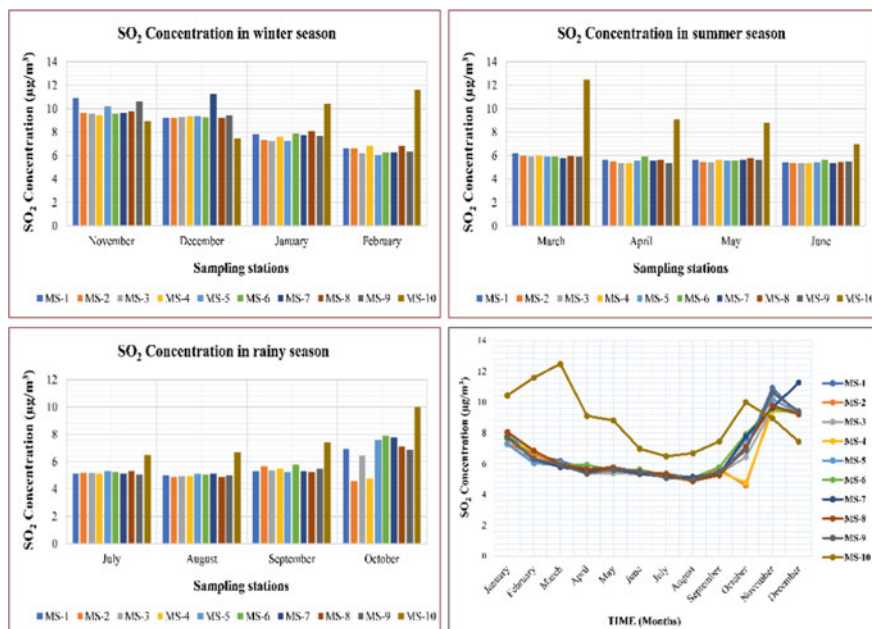


Fig. 3 Seasonal and annual variation in SO<sub>2</sub> concentration

396.00 µg/m<sup>3</sup> in the winter season, 150.63–460.00 µg/m<sup>3</sup> in the summer season, and 71.00–259.00 µg/m<sup>3</sup> in the rainy season.

The annual range and average concentration of PM<sub>10</sub> were 71.00–460.00 µg/m<sup>3</sup> and 219.67 µg/m<sup>3</sup>, respectively. The maximum concentration of PM<sub>10</sub> was 460.00 µg/m<sup>3</sup> observed in April at Shastri Nagar Thana, Jodhpur, among all stations. The minimum concentration of PM<sub>10</sub> was 71.00 µg/m<sup>3</sup> observed in September at Kudi Mahila Thana, Jodhpur, among all stations. The seasonal and annual concentration of PM<sub>10</sub> is violating the NAAQS prescribed by CPCB. The standard limit of PM<sub>10</sub> for 24 h is 100 µg/m<sup>3</sup> and for annual is 60 µg/m<sup>3</sup>.

### 5 Air Quality Index

The air quality index (AQI) is used to express the magnitude of air pollution of an area. AQI is defined as a composite scheme that transforms the weighted values of individual air pollutants (NO<sub>2</sub> SO<sub>2</sub>, CO, PM<sub>10</sub> visibility, etc.) into a single number or group of numbers. AQI is calculated from step-by-step procedure taken from the literature [8, 9]. Table 6 represents the monthly average values for AQI at each monitoring station.



Fig. 4 Seasonal and annual variation in PM10 concentration

Table 6 Average values for AQI at each monitoring station monthly

Month	MS-1	MS-2	MS-3	MS-4	MS-5	MS-6	MS-7	MS-8	MS-9	MS-10
January	243.0	241.0	298.0	251.0	149.3	272.0	212.0	251.0	225.0	165.0
February	174.6	240.0	166.0	230.0	208.0	346.0	341.0	229.0	250.0	132.0
March	187.3	254.0	176.0	168.0	166.6	287.0	242.0	206.0	196.0	133.0
April	193.3	339.0	268.0	250.0	316.0	328.0	430.0	213.0	259.0	175.0
May	222.0	296.0	213.0	205.0	217.0	362.0	285.0	295.0	404.0	193.0
June	136.0	264.0	194.6	195.3	155.3	222	226.0	207.0	204.0	160.0
July	150.0	192.6	152.0	158.6	126.0	209.0	207.0	172.6	155.3	161.0
August	90.0	110.0	79.0	104.0	90.0	123.3	142.0	100.0	118.6	103.0
September	76.0	122.0	71.0	98.0	75.0	117.3	120.0	100.0	95.0	115.0
October	114.0	119.3	150.6	104.0	118.0	187.3	140.6	148.6	129.3	145.0
November	154.6	160.6	150.0	163.3	124.0	238.0	152.6	162.0	158.0	132.0
December	173.3	172.6	187.3	173.3	149.3	184.0	169.3	172.6	176.0	142.0
<b>Avg</b>	<b>159.5</b>	<b>209.2</b>	<b>175.4</b>	<b>175.0</b>	<b>157.8</b>	<b>239.6</b>	<b>222.3</b>	<b>188.0</b>	<b>197.5</b>	<b>146.3</b>
<b>Max</b>	<b>243.0</b>	<b>339.0</b>	<b>298.0</b>	<b>251.0</b>	<b>316.0</b>	<b>362.0</b>	<b>430.0</b>	<b>295.0</b>	<b>404.0</b>	<b>193.0</b>
<b>Min</b>	<b>76.0</b>	<b>110.0</b>	<b>71.0</b>	<b>98.0</b>	<b>75.0</b>	<b>117.3</b>	<b>120.0</b>	<b>100.0</b>	<b>95.0</b>	<b>103.0</b>

The highest value of AQI was found at 430.00 in April at Shastri Nagar Thana (Fig. 5), Jodhpur, which shows the ambient air quality at that station is severe due to heavily populated commercial area, high vehicular movement, and massive population density. The lowest value of AQI was calculated 71.00 in September at

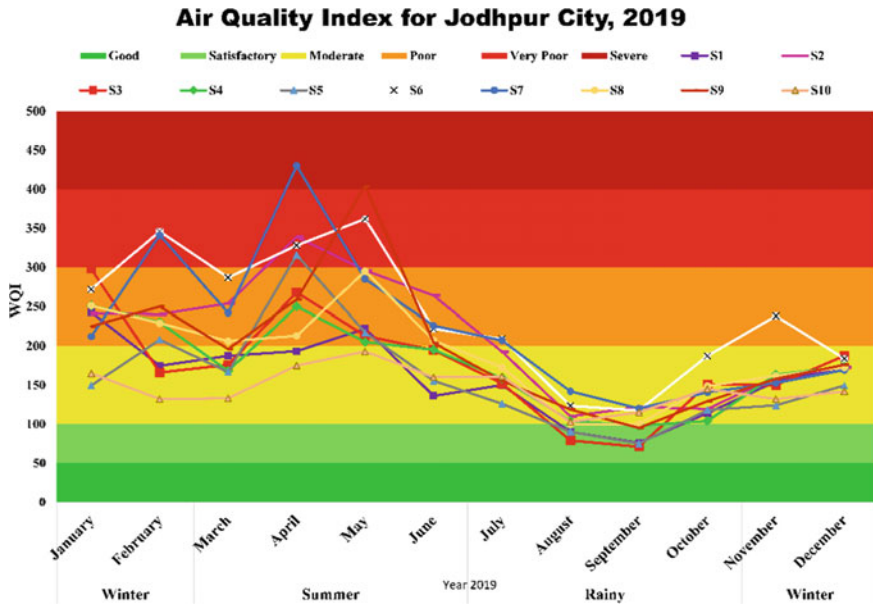


Fig. 5 Air quality index for Jodhpur city, 2019

Kudi Mahila Thana, Jodhpur, which shows that the ambient air quality at that station is satisfactory due to rainfall this month.

### 6 Exceedance Factor

The exceedance factor is the annual average concentration of critical pollutants and their corresponding national air quality standard. Exceedance factor is used to identify pollution (critical, high, moderate, and low). The following is the equation to find the exceedance factor [10]:

$$\text{Exceedance Factor} = \frac{\text{The annual average concentration of critical pollutant}}{\text{The annual standard for a particular pollutant}}$$

According to their critical pollution level, exceedance factor is divided into various categories as mentioned in Tables 7 and 8.

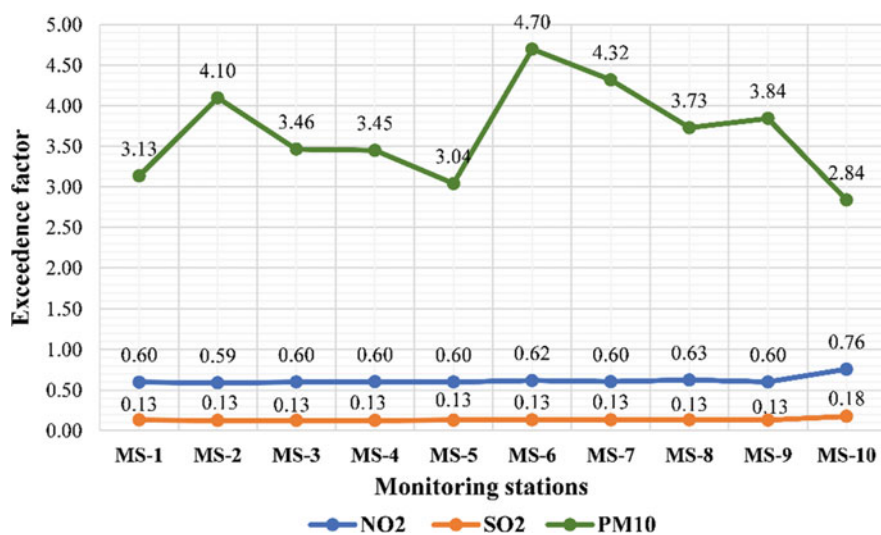
The PM<sub>10</sub> pollution level was critical at all monitoring stations in Jodhpur city because the exceedance factor for PM<sub>10</sub> is more than 1.5. The highest value of PM<sub>10</sub> exceedance factor was 4.70 at the RIICO Office as shown in Fig. 6, Basni Industrial Area, Jodhpur, indicating the critical pollution level of PM<sub>10</sub> at that location. The pollution level of NO<sub>2</sub> at all monitoring stations was moderate as the

**Table 7** Exceedance factor with their respective range

Level of pollution	Exceedance factor
Low pollution (L)	<0.5
Moderate pollution (M)	0.5–0.9
High pollution (H)	1.0–1.4
Critical pollution (C)	>1.5

**Table 8** Exceedance factors for various pollutants in the study area

Exceedance factor										
Pollutant	MS-1	MS-2	MS-3	MS-4	MS-5	MS-6	MS-7	MS-8	MS-9	MS-10
NO <sub>2</sub>	0.60	0.59	0.60	0.60	0.60	0.62	0.60	0.63	0.60	0.76
SO <sub>2</sub>	0.13	0.13	0.13	0.13	0.13	0.13	0.13	0.13	0.13	0.18
PM <sub>10</sub>	3.13	4.10	3.46	3.45	3.04	4.70	4.32	3.73	3.84	2.84

**Fig. 6** Exceedance factor in the study area

exceedance factor is between 0.59 and 0.76. The value of the exceedance factor for SO<sub>2</sub> was below 0.5, implying that the SO<sub>2</sub> pollution level was low at all monitoring locations.

## 7 Conclusions

The results from the assessment of air quality reveal that the seasonal and annual concentration of  $\text{NO}_2$  and  $\text{SO}_2$  is well below the safe limits indicating insignificant contribution in the bad air quality of Jodhpur. The absence of significant  $\text{SO}_2$  and  $\text{NO}_2$  production sources such as burning fossil fuels, the least emission through industrial and commercial activities, and government initiatives to reduce their ambient concentration like banning old vehicles promotes BS-VI motor vehicles' sulfur content in fuel, etc. The concentration of  $\text{PM}_{10}$  is exceeding the prescribed standards, both seasonally and annually. The main reasons behind the high concentration of  $\text{PM}_{10}$  are natural sandstorm, mining industries of Jasper, limestone, sandstone, masonry stone, rhyolite, granite, Bajri, marble, brick earth, cement and chemical industries, high vehicle density, etc. Hence, AQI for Jodhpur city is greatly influenced by  $\text{PM}_{10}$  concentration, making it responsible for worsening air quality of the city during all monitoring periods.

The range of AQI is between 71 and 430 from all monitoring stations' observation during the study period; i.e., the city's air quality varies from satisfactory to severe. EF for  $\text{PM}_{10}$  was greater than 2.5 at all monitoring stations verifying it as a more significant contributor for critical pollution with the negligible contribution of  $\text{SO}_2$  and  $\text{NO}_2$ . It is suggested that adequate managerial practice should be used to reduce the generation and dispersion of  $\text{PM}_{10}$ . Dense vegetation can be a very effective tool in the reduction of  $\text{PM}_{10}$  concentration in the city. The movement of old vehicles should be prohibited in the city, along with the promotion of electric vehicles.

This study can be performed for other cities in India and the rest of the world. Additionally, other pollutants such as  $\text{PM}_{2.5}$ ,  $\text{O}_3$ ,  $\text{CO}$ ,  $\text{NH}_3$ , and  $\text{Pb}$  can also be selected for air quality monitoring.

**Acknowledgements** The authors acknowledge the funding opportunities provided by the Technical Education Quality Improvement Programme (TEQIP-3) under the Ministry of Education, Government of India, required to carry out this study at the University Departments, Rajasthan Technical University Kota (Rajasthan).

## References

1. Neira DM and E and S. D. of H. Director of Public Health (2016) Ambient air pollution: a global assessment of exposure and burden of disease. [Online]. Available: <https://www.who.int/phe/publications/air-pollution-global-assessment/en/>
2. IQAir (2019) World air quality report. 2019 World Air Qual Rep 1–35. [Online]. Available: <https://www.iqair.com/world-most-polluted-cities/world-air-quality-report-2019-en.pdf>
3. Manisalidis I, Stavropoulou E, Stavropoulos A, Bezirtzoglou E (2020) Environmental and health impacts of air pollution: a review. *Front Public Heal* 8(February):1–13. <https://doi.org/10.3389/fpubh.2020.00014>

4. Morici G, Cibella F, Cogo A, Palange P, Bonsignore MR (2020) Respiratory effects of exposure to traffic-related air pollutants during exercise. *Front Public Heal* 8(December):1–8. <https://doi.org/10.3389/fpubh.2020.575137>
5. Chatterjee P (2019) Indian air pollution: loaded dice. *Lancet Planet Heal* 3(12):e500–e501. [https://doi.org/10.1016/S2542-5196\(19\)30247-5](https://doi.org/10.1016/S2542-5196(19)30247-5)
6. Jodhpur District Census Handbook, Rajasthan, SERIES-09, PART XII-B, Directorate of Census Operations, Census of India - 2011. [https://www.censusindia.gov.in/2011census/dchb/0815\\_PART\\_B\\_DCHB\\_JODHPUR.pdf](https://www.censusindia.gov.in/2011census/dchb/0815_PART_B_DCHB_JODHPUR.pdf)
7. Brief Industrial Profile of Jodhpur District 2011–12, Micro, Small and Medium Enterprises–Development Institute, Ministry of Govt. of India, pp 1–38 (2012). <https://www.msmedijaipur.gov.in/frontupload/JODHPUR.pdf>
8. Choudhary M, Gupta H (2016) Assessment of vehicular air pollution in Kota City, Rajasthan. *Assessment* 3(7). <https://doi.org/10.17148/IARJSET.2016.3756>
9. Rai NK, Sharma T, Vyas A, Singh SK (2017) Case study air quality index determination of residential areas of Jodhpur city: a case study 6(10):7046–7048
10. Banerjee T, Srivastava RK (2011) Assessment of the ambient air quality at the Integrated Industrial Estate-Pantnagar through the air quality index (AQI) and exceedance factor (EF). *ASIA-PACIFIC J Chem Eng* 6:64–70. <https://doi.org/10.1002/apj.450>